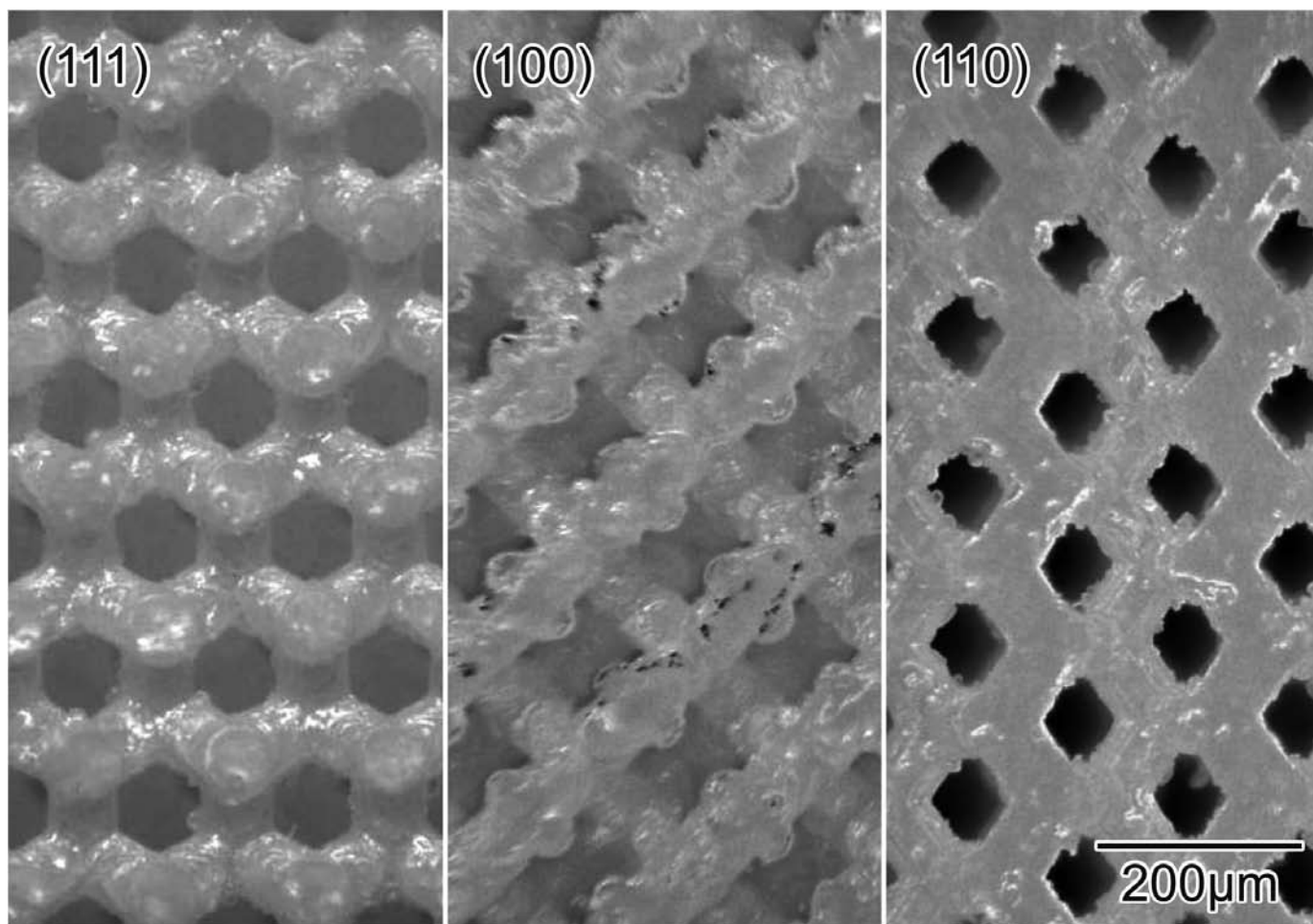


KONA Powder and Particle Journal

粉

No. 27 (2009)

Published by Hosokawa Powder Technology Foundation



KONA Powder and Particle Journal

<http://www.kona.or.jp>

KONA is a refereed scientific journal that publishes articles on powder and particle sciences and technology. KONA has been published annually since 1983 in Japan. KONA is distributed to researchers, members of the scientific community, universities and research libraries throughout the world.

About the Cover of Journal“ KONA”

The Chinese character “粉” is pronounced “KONA” in Japanese, and means “Powder” .

The hand written “粉” is after the late Mr. Eiichi Hosokawa, founder of the Hosokawa Micron Corporation.



Headquarters of Hosokawa Micron Corporation

Editorial Board

Y. Tsuji

Editor-in-Chief

(Professor Emeritus of Osaka Univ., JAPAN)

Asia / Oceania Editorial Board

H. Emi (Professor Emeritus of Kanazawa Univ., JAPAN)

Y. Fukumori (Kobe Gakuin Univ., JAPAN)

J. Hidaka (Doshisha Univ., JAPAN)

K. Higashitani (Kyoto Univ., JAPAN)

Y. Kang (Chungnam National Univ., KOREA)

Y. Kousaka (Professor Emeritus of Osaka Prefecture Univ., JAPAN)

J. Li (Chinese Academy of Science)

H. Masuda (Professor Emeritus of Kyoto Univ., JAPAN)

M. Naito (Osaka Univ., JAPAN)

K. Nogi (Osaka Univ., JAPAN)

Pradip (Tata Research Development and Design Centre)

M. Rhodes (Monash Univ., AUSTRALIA)

M. Takahashi (Nagoya Institute of Technology, JAPAN)

W. Tanthapanichakoon (National Science and Technology Development Agency, THAILAND)

T. Yokoyama (Hosokawa Powder Technology Research Institute, JAPAN)

Secretariat

T. Kawamura (Hosokawa Powder Technology Foundation, JAPAN)

Europe / Africa Editorial Board

M. Ghadiri (Chairman (Univ. of Leeds, UNITED KINGDOM)

B. Biscans (Univ. de Toulouse, FRANCE)

N.Z. Lyakhov (Institute of Solid State Chemistry, RUSSIA)

J. Marijnissen (Univ. of Delft, NETHERLANDS)

W. Peukert (Univ. Erlangen, GERMANY)

S.E. Pratsinis (ETH Zürich, SWITZERLAND)

Secretariat

P. Krubek (Hosokawa Micron GmbH, GERMANY)

J. Stein (Hosokawa Alpine AG)

American Editorial Board

B.M. Moudgil (Chairman (Univ. of Florida., U.S.A.)

D.W. Fuerstenau (Vice Chairman (Univ. of California, U.S.A.)

F. Concha (Univ. of Concepción, CHILE)

R. Flagan (California Institute of Technology, U.S.A.)

A.I. Hickey (Univ. of North Carolina, U.S.A.)

R. Hogg (Pennsylvania State Univ., U.S.A.)

Marple (Univ. of Minnesota, USA)

S.B. Savage (McGill Univ., CANADA)

Secretariat

C.C. Huang (Hosokawa Micron Powder Systems, U.S.A.)

■ Publication Office

Hosokawa Powder Technology Foundation

Shodai- Tajika 1-9, Hirakata, Osaka, 573-1132 Japan

e-mail : info@kona.or.jp

CONTENTS

The Letter from the Editor.....	1
Comment of the Cover Photograph	2
<Review Papers>	
Mixing and Segregation in Powders: Evaluation, Mechanisms and Processes	<i>R. Hogg</i> 3
Settling Velocities of Particulate Systems	<i>F. Concha</i>18
Mechanochemical Activation for Resolving the Problems of Catalysis	<i>R. A. Buyanov, V. V. Molchanov and V. V. Boldyrev</i>38
SHS Powders for Thermal Spray Coating Challenges and Opportunities in Direct Write Technology Using Nano-metal Particles	<i>T. Talako, A. Ilyuschenko and A. Letsko</i>55 <i>K. N. Han and N. S. Kim</i>73
Aerosol Route in Processing of Nanostructured Functional Materials	<i>O. Milosevic, L. Mancic, M.E. Rabanal, L. S. Gomez and K. Marinkovic</i>84
Structural Joining of Ceramics Nanoparticles: Development of Photonic Crystals for Terahertz Wave Control by Using Micro Stereolithography	<i>S. Kirihaara</i>107
Surface Modification for Improving the Stability of Nanoparticles in Liquid Media	<i>M. Iijima and H. Kamiya</i>119
Smart Powder Processing for Advanced Materials	<i>M. Naito, H. Abe, A. Kondo, T. Yokoyama and C. C. Huang</i>130
Numerical Simulations of Pulverized Coal Combustion	<i>R. Kurose, H. Watanabe and H. Makino</i>144
<Original Research Papers >	
The Improvement and Upscaling of a Laser CVP Reactor	<i>J. v. Erven, D. Munao, Z. Fu, T. Trzeciak. R. Janssen, E. Kelder and J. C. M. Marijnissen</i>157
Hydrotextural Description of an Unsaturated Humid Granular Media: Application for Kneading, Packing and Drying Operations	<i>E. Rondet, M. Rundgsiyopas, T. Ruiz, M. Delalonde and J.P. Desfours</i>174
Novel Material Properties Based on Flame-Synthesized Nanomaterials	<i>H. Wiggers</i>186
Drag on Gasborne Nanoparticles in the High Knudsen Number Regime	<i>T. Wu and A. P. Weber</i>195



Good Laboratory Practice in Particle Measurement Calibration: Cascade Impactor	<i>V. A. Marple and B. A. Olson</i>206
Improving Aerosol Dispersion through Processing and Dissemination Techniques	<i>S. Tedeschi, N. Stevens, K. Powers, A. Ranade, B. Moudgil, H. El-Shall</i>217
Modeling of Powder Deposition into Shallow Dies for Three Filling Methods	<i>S. S. Roudsari and V. M. Puri</i>228
Effect of Additives on the Dispersion Properties of Aqueous Based C/LiFePO ₄ Paste and its Impact on Lithium Ion Battery High Power Properties	<i>J. -H. Lee, H.-H. Kim, S. B. Wee, and U. Paik</i>239
< Information Articles >	
The 43rd Symposium on Powder Technology246
The 17th KONA Award247

The Letter from the Editor



Mojtaba Ghadiri
Europe/Africa Editorial Board Chairman

This year the Editor-in-Chief of KONA, Prof. Tsuji, suggested that the regional editorial boards contribute to writing the preface on a rota basis. As the Chairman of the Editorial Board for Europe and Africa, I have the privilege and honour to write the first letter in the new form.

KONA is now fully archival! It was registered last year with Thompson-Reuter, an achievement that has delighted the members of the three Editorial Boards and of course the contributors. KONA is a unique journal, as the contributions are solicited from leading researchers worldwide, providing a well-balanced coverage of the new developments in science and technology of powders and particle systems. It is published and distributed widely by Hosokawa Powder Technology Foundation. This provides an invaluable conduit for rapid knowledge transfer from the contributors to academic and industrial communities worldwide; and now with the newly acquired 'impact factor', it is hoped that its profile is further enhanced.

It has been a tough year for industry due to world recession, and it is a great relief that KONA has been protected from the upheavals by the Hosokawa Pow-

der Technology Foundation. The foundation operates completely independently from the Hosokawa Corporation, and has a charitable status which has been approved by the Japan government.

I would like to use this opportunity to convey a message from the Editor-in-Chief on a number of important changes in the content of the journal. From this issue onwards (No.27, 2009), the content of other Japanese journals in this field will no longer be listed, as it was found that the time to do it was so short that it was almost impossible to meet the printing deadline, and postponing it to the following year was too late. Another important change relates to the publication of selected papers translated from Japanese. Nowadays, Japanese researchers widely publish their work in archival journals in the English language, circumventing the market interest in translation. Furthermore, translation may not always accurately express the original intended views of the authors. It has therefore been decided not to publish translated papers from this issue onward.

Finally, the Editorial Boards welcome proposals for topics, papers and any comments the readers may have, as we wish to make the journal a 'must have' on desks of researchers in powders and particles as well on the shelves of libraries.

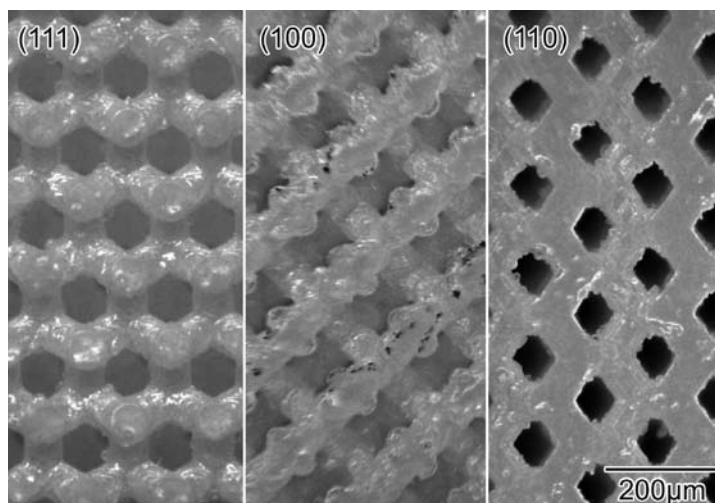
Mojtaba Ghadiri
Chairman of the Editorial Board for Europe and Africa
Leeds
21st October 2009

Comment of the Cover Photograph

Diamond Photonic Crystals with Alumina Micro Lattices

Soshu Kirihara

*Joining and Welding Research Institute
Osaka University*



Photonic crystals with periodic arrangements in dielectric constant can totally reflect electromagnetic waves by Bragg diffraction. Alumina micro lattices with diamond structure were fabricated in order to control terahertz wave expansions effectively by using micro stereolithography of a computer aided design and manufacturing (CAD/CAM) process. The photonic crystals composed of acrylic lattice with alumina nanoparticles dispersion were fabricated. In the micro stereolithography process, photo sensitive resin pastes with alumina nanoparticles dispersion were spread on a glass substrate with 10 μm in layer thickness by using a mechanical knife edge, and two dimensional images of ultra violet ray were exposed by using digital micro-mirror device (DMD) with 2 μm in part accuracy. Through the layer by layer stacking process, micrometer order three dimensional structures were formed. Dense alumina structures were obtained by successive dewaxing and sintering in an air atmosphere. The electromagnetic wave properties of these samples were measured by using a terahertz time domain spectroscopy (TDS) device. The micrometer order periodic structures exhibited perfect band gaps in the terahertz wave frequency range. In near future, the terahertz waves with micrometer order wavelength will be expected to apply for various types of novel sensors, which can detect gun powders, drugs, bacteria in foods, micro cracks in electric devices, cancer cells in human skin and other physical, chemical and living events. The fabricated alumina photonic crystals will be applied for the terahertz wave devices.

Mixing and Segregation in Powders: Evaluation, Mechanisms and Processes[†]

R. Hogg

Department of Energy and Mineral Engineering,
The Pennsylvania State University¹

Abstract

Mixing in powders generally results from relative motion of groups of particles – convective mixing – or of individuals – diffusive mixing. Segregation or demixing occurs when the motion of individual particles is biased according to their particular characteristics – size, shape, composition etc. In the absence of such bias, individual motion invariably leads to homogenization of the mixture. Relationships between mixing/segregation processes and the external and interparticle forces responsible for causing or opposing relative motion are reviewed. Specific examples of mixing and segregation in flow over surfaces, in rotating cylinders and other applications are described.

Keywords: Homogeneity, macromixing, micromixing, diffusive mixing, convective mixing, demixing, role of agitation and shear, percolation, mixing and segregation in flow systems

Introduction

Mixing of particulate solids is an important process in its own right, as in blending of the components of a mixed powder; it can also play a critical role in the performance of other particle processing operations such as grinding, granulation, classification and chemical treatment. In single-phase systems such as gases or miscible liquids, mixing proceeds spontaneously and irreversibly so that actions such as stirring are needed only to speed up the process. In contrast, solids mixing processes are neither spontaneous nor irreversible – some kind of mechanical agitation is required for mixing to occur and a tendency for different kinds of particles to segregate is commonly observed.

Segregation is typically described as a problem. While this is clearly appropriate for simple blending operations, there are cases where it is actually desirable by providing some degree of classification. Segregation due to agitation or flow of a powder is rarely an effective means of classification on its own but it can be a useful adjunct to other classification processes. For example, continuous screening op-

erations commonly involve movement of a layer of vibrated particles over the screen surface. Segregation of coarse (oversize) particles towards the top of the layer can improve screening efficiency by reducing blockage of the screen apertures. Agglomeration processes take advantage of segregation of large agglomerates to promote preferential discharge of the product from balling drums or pans.

It is important to distinguish between the results of active segregation processes and those due simply to inadequate mixing. If some of the components of a mixture are added in agglomerated form, complete mixing requires break-up and redistribution of this material. Low-shear devices such as tumblers may be incapable of performing this action. Indeed, they may actually enhance segregation by encouraging agglomerate formation and growth.

Another distinction can be made in the context of mixing as an element of some other process such as a continuous grinding operation. In liquid-phase reactors, “perfect” mixing refers to uniform distribution of the components throughout the vessel – intimate mixing at the molecular level usually follows automatically. The latter is often not true for particle systems. Spatial uniformity may be achieved while the components remain in the form of clumps. However, uniformity of this kind may be quite sufficient to regard the reactor as fully mixed for estimating process parameters such as residence time distributions.

[†] Accepted: July 22nd, 2009

¹ 213 Hosler Building, University Park, PA 16802
TEL: (814) 865-3802, FAX: (814) 865-3248
E-mail: rxh19@psu.edu

This paper is intended as an overview of the subject rather than a comprehensive review of published work in the area.

Assessment of Mixture Homogeneity

A generally accepted procedure for evaluating the relative homogeneity of a particulate mixture is to take a number of samples, at random, and determine the variance of their composition: the more homogeneous the mixture, the lower the expected variance. Because of the discrete nature of the particles, the expected variance of a random mixture is ultimately limited by the chance of different kinds of particles, especially those of minor components, being included in a sample. Based on simple statistics, it has been shown¹⁾ that the expected variance, σ^2 of the relative composition of samples containing N particles each taken from a completely random binary mixture is given by:

$$\sigma^2 = \frac{p(1-p)}{N} \quad (1)$$

where p is the overall number fraction of one of the components. The simple treatment has been extended to the more practical case of the expected variance in the mass fraction of a given component in samples of equal mass taken from a multi-component mixture^{2,6)}. The equivalent to Equation 1 then becomes

$$(\sigma_m^2)_i = \frac{f_i(1-f_i)w_i + f_i^2(\bar{w} - w_i)}{M} \quad (2)$$

where $(\sigma_m^2)_i$ is the expected variance of the mass concentration of component i in samples taken from a random mixture of all of the components; f_i is the overall mass fraction of component i in the mixture; w_i is the mass of a single particle of that component and \bar{w} is the overall mean particle mass, defined by:

$$\bar{w} = \sum_j f_j w_j \quad (3)$$

An observed sample variance that is greater than the expected value as determined using Equations 1 or 2 implies that the mixture is heterogeneous (non-random). It is possible, however, for such a result to be obtained, by chance, for a random mixture. Comparison of the ratio of the observed to expected variance using, for example, the simple F-test⁷⁾ gives an indication of whether or not the difference is significant statistically.

Dankwerts⁸⁾ used the terms *micromixing* and *macromixing* to distinguish between short-range

homogeneity, i.e., at the individual particle level, and long-range variations within a batch of material. The expected, randomly mixed variance described above refers to micromixing. Since the observed variance also includes the effects of errors in sample assay, it is necessary increase the expected variance by using small samples to ensure that incomplete micromixing is not masked by such errors. At the same time, however, the increase in the expected variance can mask the effects of small, but significant long-range variations. For example, in a study of axial mixing in a rotating cylinder⁹⁾ it was found, using samples of about 500 particles, that the observed sample variance became equal to the expected value after about 70,000 revolutions of the drum. At that stage, however, there remained a small but detectable and significant variation in composition along the length of the cylinder. To detect both long-range and short-range variations, it is necessary to sample at more than one level – small samples to identify local clustering of components and larger samples to test for the long-range variations. Typically, the latter can be minimized by further mixing while the former may require alternative procedures such as increased shear. Procedures for characterizing particulate mixtures have been described in greater detail in a recent publication by the author¹⁰⁾.

Mixing Mechanisms

Lacey¹¹⁾ proposed the following basic mechanisms for solids mixing: convective mixing which involves the collective transfer of groups of particles from one location to another; diffusive mixing defined as the distribution of particles over a freshly developed surface and shear mixing due to slipping planes set up within the mixture. Further consideration, however, suggests that, for free-flowing powders, the fundamental mechanisms are simply *convection* essentially as defined by Lacey and *diffusion* defined more broadly as the random motion of individual particles. Shear mixing can be regarded as a combination of convection and diffusion resulting from the redistribution of material across slipping planes. Shear is an important feature of the mixing process by providing the driving force for convection and diffusion. A third mechanism – transfer between agglomerates – is important for cohesive particles and is discussed below.

Typically, diffusion is a rather slow process while convection proceeds rapidly. Practical mixing systems employ combinations of these two primary mechanisms. Convection generally provides rapid

macromixing and substantially reduces the distances over which diffusion must occur to ensure complete micromixing. Agitation and shear are necessary for both mechanisms to occur. Convection is controlled primarily by the geometry of the system including the presence of elements such as paddles and baffles, that induce collective motion of the particles. This process can lead to a kind of diffusive macromixing, akin to turbulent diffusion in fluids. Diffusive micromixing is determined by the mobility of individual particles in response to agitation and shear. In free-flowing powders, mobility is generally high, promoting relatively rapid micromixing. In the case of cohesive powders, on the other hand, individual mobility is low and sometimes virtually absent. Mixing of these materials must rely heavily on shear to break up the material into smaller and smaller agglomerates. Since cohesive powders normally contain very fine particles and agglomerate breakage is a reversible process, liberation of individual particles is fleeting at best. Micromixing by simple diffusion is essentially eliminated and must occur by random transfer of particles between breaking and re-forming agglomerates.

Segregation Mechanisms

Micromixing by diffusion in a free-flowing powder requires that the motion of individual particles in response to agitation etc. be truly random and independent of the type of particle concerned. In other words, all particles in the system should have the same mobility. When there are differences in mobility among the components of a mixture, segregation becomes a possibility. Particle motion results from the effects of mechanical actions such as tumbling or stirring, and external forces, primarily gravity. Particle mobility is determined by the response to these forces and the resistance to motion due to other particles, their environment and the mixing device itself. In many ways, segregation in powders is analogous to differential settling of particles in a fluid.

Convective mixing does not normally depend on individual particle mobility; the mixing effect tends to be more or less random and is unlikely to contribute directly to segregation. At the same time, however, the actions that lead to convective mixing generally promote individual motion which can cause segregation. Because of restricted mobility, segregation is usually less prevalent in cohesive powders than in free-flowing material. Whereas convection and diffusion are complementary in mixing processes, they

generally work in opposition in segregation.

Segregation is caused by differences in the basic particle characteristics which can be defined in terms of size, shape, composition and structure¹⁰. As far as segregation is concerned, structure – the distribution of phases within a single particle – is unlikely to cause differences in mobility and can probably be discounted. Particle size and shape affect mobility largely through their effect on the resistance to motion whereas density (determined by particle composition) is more likely to influence the actual motion resulting from applied forces.

Size Segregation

Variations in individual particle mobility with size typically lead to segregation in a bed of particles subjected to vibration or flow. However, the form of the resulting segregation can vary widely depending on the actual conditions. This has led to a number of proposed mechanisms which are actually different manifestations of the same basic phenomenon: the ability of small particles to penetrate the bed more readily than coarser material.

Imposed vibration or particle-particle collisions in a flow stream cause some dilation of the bed and increased particle mobility. Gravitational forces lead to a net downward motion of the smaller particles which can readily pass through the voids in the expanded bed. This simple mechanism is especially important when the fine material is a minor component of the mixture and is commonly referred to as percolation or sieving^{12,13,14}. Segregation can also occur, by the same basic mechanism, regardless of the overall composition of the mixture. If the coarse particles are a minority – each surrounded by the finer components – their ability to move upwards is constrained only by the weight of the overlying material while downward motion requires either compaction of the material below or the unlikely possibility of encountering a sufficiently large void. At the same time, the void created by upward motion of the particle is easily filled by percolation of adjacent fines, which prevents a return to its original position¹⁵. The net result is a ratcheting upwards of the coarser particles. This effect has been described as displacement segregation^{12,13} or the “Brazil nut effect”¹⁶.

Size segregation is also widely observed when particles are poured onto a heap or in the filling of a container. Again the basic mechanism involved is the difference in the ability of small and large particles to penetrate a bed of material, although the result ap-

pears to be quite different. In contrast to a vibrated or agitated bed, a heap is essentially static with flow occurring only in the surface layers. Particles flow over the surface until they become trapped in a surface void. Since the finer material is more likely to encounter a sufficiently large void, the result is that coarse particles travel further down the slope and accumulate around the lower edges of the heap leaving excess fines in the core. This effect has often been called rolling segregation¹⁷.

The term trajectory segregation¹⁸ has been used to describe separation of coarse and fine particles projected from the end of a chute or fast-moving belt. Retardation of the lateral motion by aerodynamic drag is greater for small than for large particles. Projection of the particles individually would certainly lead to segregation. In practice, however, material is normally projected as a fairly dense, continuous stream carrying the adjacent air along with it. As a result, aerodynamic drag acts on the stream as a whole rather than on individual particles, thereby minimizing the segregation effect. Observation of segregation in such systems can probably be attributed to existing segregation, prior to projection. This effect was demonstrated by Augenstein^{19,20} and is illustrated in **Fig. 1**. Mixtures of coarse and fine particles projected from chute surfaces were collected in a sampling grid to determine the distributions of horizontal displacement. For smooth chute surfaces, the range of displacements was found to be narrow, indicating a narrow range of velocities, and the composition was essentially uniform (**Fig. 1a**). When the surface was rough, on the other hand, a much broader range of displacements was observed and a progressive increase in the concentration of coarse particles with displacement was found (**Fig. 1b**).

The extent of size segregation is generally limited by packing considerations. In the case of a binary mixture, segregation can be expected to lead to the development of two regions: one consisting essentially of the major component alone and the other containing both components under roughly optimum packing conditions.

Shape Segregation

Particle shape also affects mobility and differences are, therefore, a potential cause of segregation. It is generally agreed, however, that segregation by shape becomes significant only when the differences are substantial – smooth spheres from irregular particles, flakes or needles from roughly isometric particles,

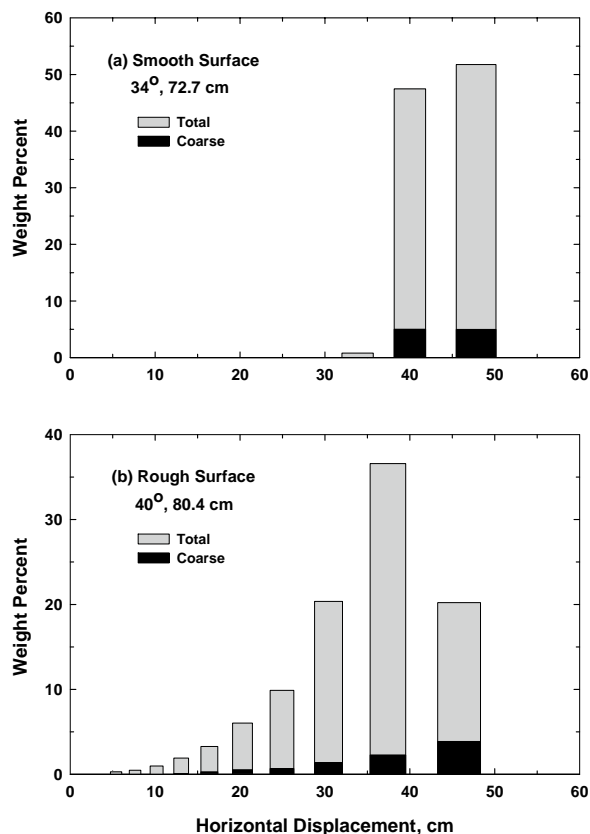


Fig. 1 Distribution of trajectories for mixtures of coarse (30×40 US mesh) and fine (70×100 US mesh) particles projected from inclined chute surfaces. Data of Augenstein¹⁹.

for example^{21,22}). In part, this may be an impression gained due to the difficulties involved in quantifying small differences in shape. Tang and Puri¹³ have noted that combinations of size and shape differences may lead to enhanced segregation.

Density Segregation

Differences in particle density are known to cause segregation, which might be anticipated from potential energy considerations. However, it is generally agreed that the effects are usually substantially less than those due to size differences²³. This may be partly due to the smaller range of densities found in particle systems – a 5:1 range in density is considered to be large while 1000:1 is a quite common size range. The analogy to sedimentation is again appropriate here. The (gravitational) force acting on a particle is affected by both size and density while the fluid drag (resistance to motion) is independent of density. It is likely that the same is largely true for segregation in powders. As noted above, a primary cause of segregation is the relative ability to penetrate a bed of particles; increased density provides

little advantage in this respect, especially in fairly compact systems such as vibrated or agitated beds or flow streams. A “push-away” mechanism²⁴ has been proposed in which a heavy particle is able to force its way between lighter components. Such an effect is unlikely to be significant in relatively compact beds since the weight of a single particle is generally much smaller than the force needed to shear the bed. For highly dilated beds subject to vigorous agitation or vibration, and especially for fully fluidized beds, a mechanism of this kind may indeed be viable, leading to an accumulation of the denser component(s) in the lower regions of the bed²⁵. These conditions could also have a significant effect on size segregation. By reducing the resistance to downward motion, a more open bed could actually reverse the segregation effect by allowing settling of the large particles. This could, in fact, account for some seemingly contradictory observations noted in the literature.

Segregation Due to Particle Interactions

In some circumstances interaction forces, either attractive or repulsive, can promote segregation. Selective agglomeration of certain components is an obvious example and could occur if particles of one component specifically attract particles of the same kind or repel other kinds. Typically, agglomeration is most prevalent among the fine, cohesive components of a mixture. Selective agglomeration is quite common in liquid suspensions but the close confinement of particles in dry or semi-dry powders is not generally conducive to selectivity. Most cases of segregation by clumping of fine components probably reflect incomplete micromixing due to low particle mobility, rather than a spontaneous segregation process.

Segregation due to interaction forces is possible when the forces are strong enough, or of sufficiently long range to affect relatively large, mobile particles. Magnetic particles are an obvious example. Other kinds of forces can produce similar effects as was observed by this author. For a mixing study using particles differing only in color, a narrow sieve fraction (40 × 50 US mesh) of crushed dolomite was dyed using a commercial food color. Attempts to prepare uniform mixtures of these particles with the same size fraction of the same dolomite, but not dyed, for use as calibration standards proved to be remarkably unsuccessful. Even when a reasonably homogeneous mixture was obtained by careful stirring of small quantities, any slight disturbance, by tapping or shaking the container, led to an immediate visible segrega-

tion. Apparently interaction forces, introduced by the surface coating, were sufficient to cause segregation of these relatively coarse (~0.35 mm) particles. In this particular study, the problem was circumvented by switching to a different color.

Role of Cohesion

By restricting the mobility of individual particles, cohesion generally serves to reduce the tendency for segregation to occur. However, cohesion in dry powders is normally associated with fine (e.g., < 20 μm) particles. Other than perhaps acquiring a coating of fines, coarser particles in a mixture can retain their mobility and be subject to segregation. Furthermore, the additional restriction of fine particle mobility may actually compound the problem. Agitation of a cohesive powder commonly leads to the formation of agglomerates which readily become segregated from the bulk (fine) powder. This effect is widely exploited in granulation processes.

Cohesion due to the presence of liquid phases generally extends over a broader range of particle sizes than that due to fine components and, in some situations, may provide a means of minimizing segregation problems.

Mixing and Segregation Processes

Mixing of free-flowing powders can generally be regarded as proceeding through some combination of the diffusion and convection mechanisms, convection being primarily responsible for macromixing while intimate micromixing relies on diffusion. The relative contributions of these two depend mostly on the geometry and operating conditions of the mixing device but may also be influenced by powder characteristics.

Mixing in Rotating Cylinders

The simple horizontal drum mixer has been studied extensively. For non-segregating powders (equal size, shape and density), it has been established that axial mixing proceeds through essentially pure diffusion^{9,11} while transverse mixing is dominated by convection with superimposed diffusion²⁶⁻²⁹. A bed of powder in a horizontal, rotating cylinder exists as two, fairly distinct regions: a “static” region in which particles follow the rotation with no relative motion and a “shear zone” where particles flow down the free surface of the bed. Conditions in the shear zone

depend on the Froude number: $Fr = R\omega^2/g$ where R is the cylinder radius, ω is the angular velocity and g is the acceleration due to gravity. At low rotational speeds (Froude numbers less than about 0.01), velocities in the shear zone are much higher than those in the static region so that the shear zone is thin and the free surface remains essentially planar. As the speed is increased, velocities in the static region increase relative to those in the shear zone, which are mostly determined by gravity; the zone increases in thickness and assumes a characteristic S-shape. With further increase in speed, cataracting occurs where particles are projected from the bed and follow a free-flight trajectory before re-entering the bed. At the critical speed, the centrifugal force acting on the layer of particles adjacent to the shell just balances that due to gravity ($R\omega^2 = g$) and centrifuging occurs. The critical speed ω_c is defined by:

$$\omega_c = \sqrt{\frac{g}{R}} \quad (4)$$

And corresponds to $Fr = 1$. Under steady flow conditions, continuity requires that a particle entering the shear zone at some axial location will, *on the average*, re-enter on the same transverse plane. Inter-particle collisions during flow down the surface cause the random lateral displacements that lead to axial diffusion^{30,31}. Convection in the transverse plane results primarily from differences in the time taken for particles at different radial locations to complete one pass through the static region. Random displacement of particles during flow through the shear zone provides the diffusive component.

Axial Mixing

Because of the absence of any contribution from convection, axial mixing in a simple drum proceeds very slowly. Experimental values of the diffusion coefficient for particles of about 0.2 mm in size rotated at relatively low speeds in cylinders with diameters in the 5-10 cm range are typically found to be about $1 \text{ mm}^2/\text{revolution}$ ^{9,32,33}.

It has been shown⁹ that, for a simple cylinder loaded end-to-end with equal quantities of two, essentially identical components, the expected sample variance due to incomplete macromixing can be estimated from:

$$\sigma^2 = \frac{2}{\pi^2} \exp\left(-\frac{2\pi^2 DN}{L^2}\right) \quad (5)$$

where D is the diffusion coefficient, N is the number

of revolutions of the cylinder and L is its length. Using the above value of D , Equation 4 predicts that more than 20,000 revolutions would be required to reduce the variance from an initial value of 0.25 to 0.0025 for a cylinder 10 cm long. This required time would increase with the square of mixer length.

Experimental studies by Rao et al.³³ indicated that the diffusion coefficient generally decreases with increased filling of the cylinder and increased particle size and increases with increased rotational speed. Higher diffusion coefficients at low filling levels were attributed to an increase in the number of passes through the shear zone per revolution, partially offset by the corresponding reduction in the path length in the zone. The particle size effect was thought to result from higher velocities in the shear zone due to higher dynamic angle of repose observed for finer particles. The increase with speed, even on a per revolution basis was also attributed to increases in the dynamic angle of repose. The approximate analysis presented by Rao et al. suggests that the diffusion coefficient (per revolution) should increase with the square of the cylinder diameter d for the same rotational speed. This would also be consistent with models used to describe axial transport through horizontal cylinders³⁴⁻³⁶. For conditions of dynamic similarity (constant Froude number) the diffusion coefficient (per time) should vary with $d^{3/2}$. Unfortunately, systematic investigations of the relationship between axial diffusion and cylinder diameter appear not to have been carried out.

The addition of mixing aids in the form of relatively large balls (usually plastic or rubber) has been shown to increase axial mixing rates significantly^{35,37}. Sawahata³⁷ and Chaudhuri and Fuerstenau³⁸ found that the axial diffusion coefficient was increased by a factor of about 3 for mixing aid additions comprising about 10% of the mixer volume but became constant after further addition. Shoji et al.³⁹ attributed the leveling off to segregation of the balls towards the central region of the cylinder and correspondingly high diffusion rates in that region. As the ball filling was increased further, their concentration in the central region became more or less constant while their distribution along the cylinder became more uniform. When the concentration of balls had become essentially uniform along the length of the cylinder, further ball additions again led to enhanced diffusion of the particles up to the condition where the volume of particles was just sufficient to fill the voids in the bed of balls. Abouzeid and Fuerstenau⁴⁰ demonstrated that the presence of mixing aids led to substantial

reduction of size segregation of particles in a rotating drum.

Transverse Mixing

The convection process that dominates mixing in the transverse plane of a rotating cylinder results from the different rates at which particles at different radial locations circulate the particle bed^{26,27}. As shown in **Fig. 2**, a particle at a radial distance r from the center of the cylinder travels through an angle 2θ in each pass through the static region. For a cylinder rotating at an angular velocity ω , the time to pass through the static region is equal to $2\theta/\omega$. If the filling of the cylinder with powder is less than 50%, the angle and the circulation time decrease with decreasing radial distance from the center. Thus, particles close to the center circulate several times in the time taken for a particle adjacent to the shell to circulate once.

The result of the difference in circulation time is that particles in the bed undergo a progressive angular displacement leading to the transformation of an initial side-by-side arrangement of two components into a series of spiral bands as illustrated in **Fig. 3**. The pattern shown in the figure was determined using the assumption that particles entering the shear zone on the upper part of the free surface reappear instantaneously at the same radial position on the lower part, i.e., the time spent in the shear zone is negligible²⁷. Modifying the calculations by allowing a finite time for passage through the shear zone leads to a retardation of the development of the pattern but to only minor changes in its form.

As the filling of the cylinder approaches 50%, the difference in circulation times is reduced until, ideally, at exactly 50%, the free surface passes through the center of rotation, the time for passage through the static region becomes the same for all radial locations and no convective mixing occurs. The time taken for particles to pass through the shear zone may actually assist the mixing process for this case. Due to the greater distances involved, particles entering the zone close to the cylinder wall require a longer time than those near the center. This effect again leads to an angular displacement of particles at different radial positions, resulting in a spiral pattern similar to those shown in **Fig. 3** but taking substantially longer to develop.

The patterns shown in the **Fig. 3** are the result of convection alone. In practice, random interchange between particles in different layers as they pass

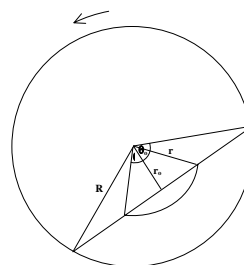


Fig. 2 Geometric arrangement used in the analysis of convective mixing in the transverse plane of a rotating cylinder.

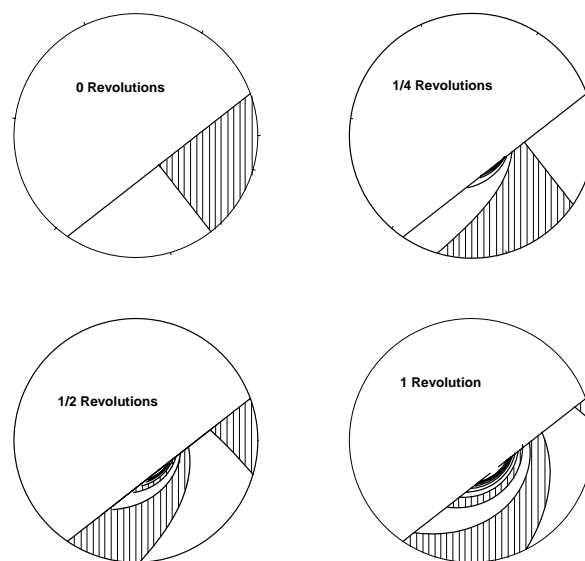


Fig. 3 Schematic representation of transverse mixing in a horizontal rotating cylinder at 30% filling.

through the shear zone (diffusion) causes a blurring of the boundaries and a rapid approach to complete mixing. Hogg and Fuerstenau²⁷ presented a simplified model for the overall process, treating the diffusion component as equivalent to simple diffusion between the alternate bands produced by convection. More recently, the analysis has been extended to include a description of the actual mixing process in the shear zone^{28,29}. Prigozhin and Kalman²⁹ presented a model which included an implicit assumption of perfect mixing in the shear zone which is essentially equivalent to the treatment by Inoue et al.²⁶ who assumed that particles entering the shear zone are redistributed at random as they reenter the rotating bed. Kharkhar et al.,²⁸ developed a simplified model for flow in the shear zone and described mixing in the zone as a process of diffusion between layers. Their results suggest that particles are not completely mixed in the shear zone and that description as a diffusion process is appropriate. Each of the models agrees qualitatively with experimental observation but, because of the many approximations involved

and the problem of obtaining precise measurements, quantitative comparisons are difficult to obtain.

Segregation in Rotating Cylinders

Both axial and transverse segregation are commonly observed in rotating cylinder systems⁴¹⁾. Transverse segregation usually proceeds rapidly and appears to be a necessary precursor to axial segregation⁴²⁾.

Transverse Segregation

Segregation of particles in the transverse plane of a horizontal rotating cylinder occurs during flow through the shear zone. Segregation by size, density and shape has been observed. Size segregation results from differences in resistance to flow. Large particles flow readily over the surface but encounter considerable resistance to penetration into the bed of flowing material. For smaller particles, on the other hand, trapping effects restrict their ability to flow over the surface but they are able to penetrate into and through voids in the bed. The combination of these two mechanisms leads to accumulation of the coarser components around the periphery of the rotating material and concentration of fines in a central core. Segregation by shape may also occur due to differences in resistance to flow. Again, it might be expected that particles that exhibit the greater resistance would accumulate in the central core, but experimental data in this area are very limited indeed. In the case of density segregation, the greater force of gravity acting on the denser particles causes a bias in the relative motion leading to accumulation of these particles in the central core⁴³⁾. The density effect may be enhanced at high rotational speeds where the shear zone becomes partially fluidized.

Transverse segregation occurs rapidly, approaching a steady state in a few revolutions of the cylinder⁴⁴⁻⁴⁶⁾. In practice, however, variations in the distribution of particles across the transverse plane may continue for substantially longer times due to the effects of simultaneous, but much slower, axial segregation. The limiting segregation pattern seems to be relatively independent of rotational speed and volumetric filling of the cylinder, except when a “dead zone” exists for fillings greater than 50%. Some attenuation of the segregation may be expected at higher rotational speeds due to enhanced diffusive mixing. The size distribution of the powder is obviously an important factor. Most research in the area has been carried out on

simple binary mixtures and has shown that even size differences as small as 20% can cause segregation. For such small differences, the concept of percolation seems inappropriate. Nevertheless, the differences in resistance to motion noted above still apply and lead to segregation. As might be expected, larger size differences promote faster segregation⁴⁵⁾.

Axial Segregation

Separation of dissimilar components in the form of alternate bands along the axis of the cylinder is commonly observed^{41,47)}. It appears that the process is a consequence of axial transport of particles caused by small variations in the inclination of the rotating bed due to friction at the end-walls and differences in internal friction of the mixture^{41,48-50)}. Axial transport due to the end-effect is illustrated in **Fig. 4** which shows schematically the expected trajectories of particles from different locations in the bed as they pass through the shear zone. The curved paths are the result of motion in the direction of steepest slope and are estimated using modification of the models developed for continuous flow through rotating cylinders^{34,35,51)}. As expected, particles originating from close to the outer shell of the cylinder are subject to greater axial displacement than those closer to the center of the bed. Since each of the trajectories shown returns to its original axial location, these estimates, based on independence of the individual paths, would predict no net axial displacement. However, the figure also shows that, especially for

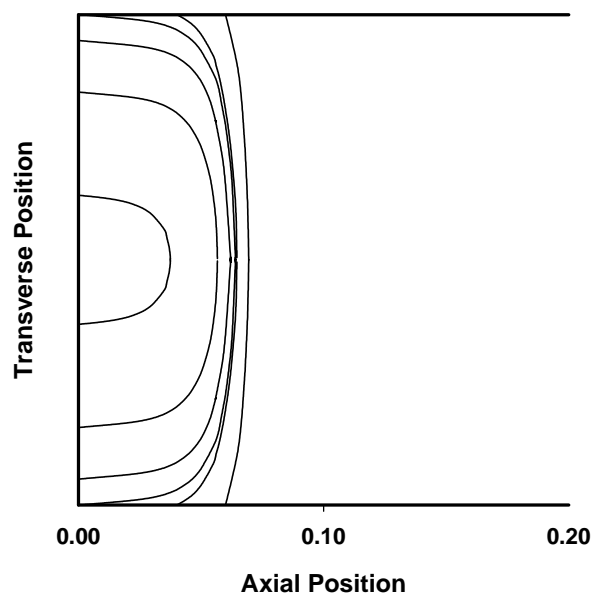


Fig. 4 Schematic illustration of particle trajectories in the surface layers adjacent to the end-walls of a rotating cylinder.

the outer layers, the paths of particles starting from different distances from the end-wall converge during passage through the shear zone. Obviously, therefore, the individual particle paths cannot really be independent, but there must nevertheless be a tendency for accumulation of those particles in that axial location. In order to maintain uniform loading of particles along the cylinder, migration of material away from that region must occur from all layers in the shear zone. Since there is less replenishment into the inner layers, the result is a reduction in the relative amount of that material. If transverse segregation has led to concentration of the finer (or heavier) particles in the central core and of the coarser (or lighter) material in the outer layers, the net effect of the axial transport described above is to form a band enriched in the outwardly segregating material close to but slightly removed from the end-wall, with corresponding regions of depletion on both sides.

Axial variations in the composition of the mixture due to the end-effects or even random fluctuations may lead to corresponding changes in inclination of the rotating charge and consequent axial migration by similar mechanisms to those described above and the formation of alternating bands along the length of the cylinder.

It is clear that the mechanisms of axial segregation are complex and the convective processes described here can only represent part of the picture. Individual particle mobility can be expected to vary with size and shape and perhaps with density. It follows that diffusivity should be similarly variable and could either promote or oppose segregation. In the case of segregation due to variations in inclination of the bed, Savage⁵²⁾ has shown that both migratory convection and random diffusion fluxes could be roughly proportional to the concentration gradient. Mathematically, the process could then be represented by a simple diffusion equation with an effective diffusion coefficient given by the difference between contributions from convection and true diffusion. Under some circumstances, this could result in a negative effective diffusion coefficient meaning that the process would lead to enhanced rather than reduced concentration gradients, i.e., to segregation. Simulation of the process using a cellular automaton showed that combinations of random (diffusion) and biased (convection) interchange of particles in an initially uniform mixture can indeed result in band formation and exhibit the kinds of instabilities observed in real systems.

It has been suggested that band formation away

from the ends of the cylinder may result from statistical fluctuations in bed depth or inclination^{48,49,53,54)}. However, it seems unlikely that such perturbations would be of sufficient magnitude and persistence to cause significant axial segregation. Propagation of disturbances from the end-walls appears to offer a more a more realistic explanation.

Mixing in Simple Flow

Both mixing and segregation in powders are generally promoted by flow of the material. Flow in powders can be considered to fall into one or other of two basic types: rapid flow as in the shear zone of a rotating cylinder or in the formation of a heap and slow flow as in internal motion during slow discharge of a hopper. Slow flow appears to be characterized by shearing at specific slip planes between otherwise static layers of powder. In rapid flow, on the other hand, the process involves the existence of a continuous velocity gradient, akin to that in flow of a viscous fluid.

Flow over an inclined surface such as a chute is a simple example of rapid flow. If the surface is smooth, motion occurs by sliding and there is little or no shearing within the powder. Since there is little relative motion of individual particles under such conditions, mixing effects are minimal. However, if the surface is roughened, to an extent equal to or greater than the surface of the powder bed itself, shear occurs within the powder and liquid-like flow occurs, provided of course the inclination of the surface exceeds the angle of friction between powder and surface. Particle-particle collisions due to shear provide a driving force for diffusional mixing.

If diffusion is promoted by shear, it is reasonable to expect that the rates should increase with increasing shear rate^{55,56)}. A simple linear relationship has been proposed⁵⁶⁾ of the form:

$$D = D_0 \left(1 + \alpha \frac{\partial v}{\partial y} \right) \quad (6)$$

where D is the diffusion coefficient, $\partial v / \partial y$ is the velocity gradient perpendicular to the flow direction, D_0 and α are constants. Experiments were carried out to evaluate the mixing of sand with garnet powder as a tracer fed as initially separate layers, one on top of the other onto the surface of an inclined chute whose surface was roughened using an attached layer of the same sand. Concentration profiles were determined for several distances of flow down the chute by a splitting procedure followed by magnetic

separation of the components⁵⁶). Velocity profiles were estimated using the trajectory procedure described by Augenstein and Hogg⁵⁷. An example of the distribution of tracer through the depth of the bed is shown in **Fig. 5** for increasing distance along the inclined surface. The solid lines are model predictions based on Equation 6 with fixed values of the parameters D_0 and α of $1.15 \times 10^{-2} \text{ cm}^2/\text{sec}$ and $7.03 \times 10^{-3} \text{ sec}$, respectively. The agreement between model and experiment is very good.

The results shown in **Fig. 5** are for the case where the tracer was added above the layer of sand. Because of the dependence of the diffusion coefficient on the velocity gradient, more extensive mixing should be expected if the tracer was added below the sand, due to the higher gradient closer to the chute surface. A comparison of the results for tracer addition above and below the sand layer is shown in **Fig. 6**. It is clear that placing the tracer in the high-shear region adjacent to the chute surface does indeed lead to enhanced mixing. Furthermore, the fact that the results could be fitted using the same values of the parameters D_0 and α provides strong support for the applicability of Equation 6 to this system. It appears that agitation of the powder due to flow is sufficient to promote diffusive mixing and is further enhanced by velocity gradients within the flow stream.

Segregation in Simple Flow

The conditions that promote mixing during simple flow of non-cohesive powders also favor segregation of particles with different characteristics. Some results of experiments carried out on initially homogeneous mixtures consisting of 10% coarse (20×30 US mesh) and 90% fine (50×70 US mesh) sand are shown in **Fig. 7**. It appears that segregation occurs rapidly during the initial stages of the flow, leading to significant depletion of the coarse particles close to the chute surface and corresponding enhancement near the upper, free surface of the stream. Further downstream, the process continues more slowly. Hwang^{20,58} proposed that the data were consistent with a simple extension to the diffusive mixing model described above with segregation assumed to occur through a constant upward convective velocity of the coarse particles. The solid lines shown in **Fig. 7** were obtained using this model. The slowing down of the segregation process following the initially high rate is attributed to the effects of diffusive mixing which assume greater importance as the concentration gradient develops.

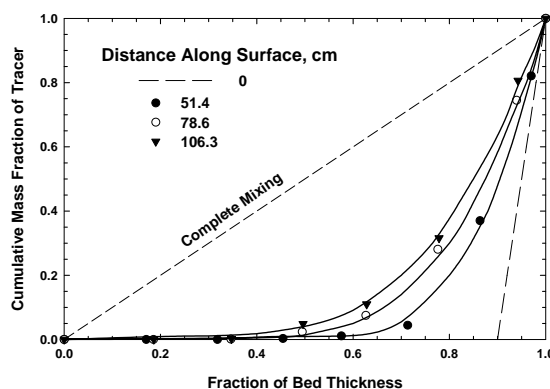


Fig. 5 Mixing of tracer particles during flow over an inclined surface. Tracer fed as a thin layer at the bottom of the stream. Points are experimental; lines are calculated based on Equation 6. Data of Hwang⁵⁸.

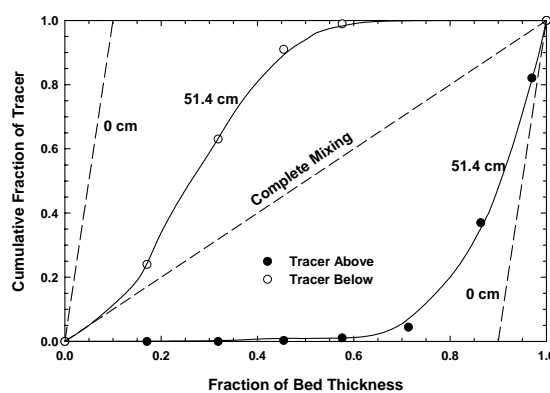


Fig. 6 Comparison of mixing behavior for tracer fed above and below the main flow stream. Calculated lines are based on the same values of the diffusion parameters. Data of Hwang⁵⁸.

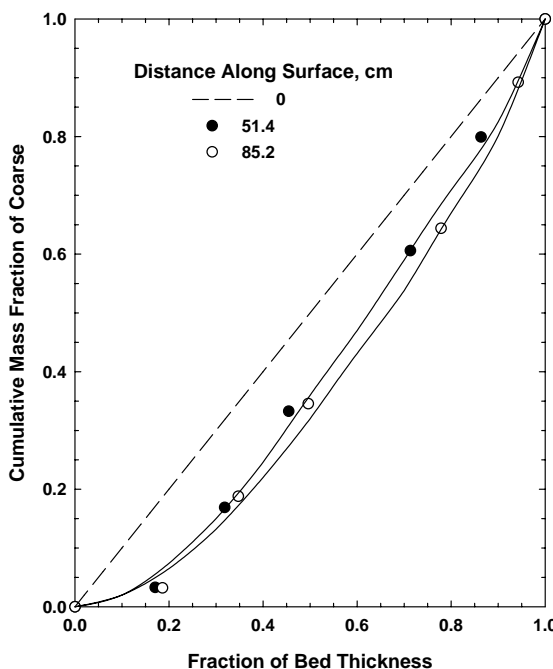


Fig. 7 Segregation of coarse (20×30 US mesh) and fine (50×70 US mesh) sand particles during flow of an initially homogeneous mixture over a rough surface. Data of Hwang⁵⁸.

Savage and Lun⁵⁹⁾ conducted similar experiments using mixtures of polystyrene beads but with the finer particles as the minor component. These authors proposed two segregation mechanisms: a “random fluctuating sieve” mechanism and a “squeeze expulsion” mechanism. The former corresponds to size-dependent percolation while the latter refers to the ejection of particles, by mechanical forces, from one layer to another and was assumed to be size-independent with no preferential direction. This combination represents a more realistic treatment of the segregation mechanisms than the simple convection process described above, in particular by providing the means to maintain mass conservation across the bed. Analysis of the two processes provides some predictive capability for the effects of variables such as particle size ratio on segregation rates. Diffusive mixing was not included in the model, leading to the rather unlikely conclusion that the process ultimately results in complete separation of the coarse and fine components.

Dolgunin et al.^{60,61)} conducted experiments similar to those described by Hwang et al.,^{20,58)}. They concluded that the bulk density was highest in the central region of the flowing stream as were the concentrations of the larger or denser particles in the mixture. It should be noted that these experiments were restricted to relatively thin layers – typically around 4 particle diameters – which might account for the form of the bulk density profiles. The authors correlated the observed segregation patterns to the bulk density profile which may also explain the differences in their observations from those typically seen in other studies: migration of coarse particles towards the upper region of the flowing bed.

Theoretical analyses have been used^{62,66)} to predict the effects of particle and system variables – size, density, elasticity, chute inclination, etc., – on segregation in flow over inclined surfaces. Different procedures appear to give equivalent results and to be in qualitative agreement with experimental data.

Segregation in Heap Formation

Flow over the surface of a heap has much in common with flow down a chute. However, the process is more complex due to the finite extent of the surface in the flow direction and the continuous development of the surface itself. Because the surface is inclined at essentially the angle of repose of the powder, flow can readily become unstable and subject to temporary build-up of particles followed by avalanching.

It is generally agreed²²⁾ that large particles encounter less resistance to flow over the surface than does finer material which is more easily trapped in surface voids. As a result the coarser components in a mixture can move further down the surface and tend to accumulate around the bottom of the heap. At the same time, build-up of the finer fractions in the upper regions of the surface can lead to periodic avalanching producing patches or streaks of fines within the accumulated coarse material. In the case of particles of similar size but different density, the heavier particles tend to be concentrated in the center of the heap with the lighter components towards the periphery^{22,24)}. The segregation patterns formed in binary mixtures have been shown to depend primarily on the relative sizes and densities of the components, their concentration and the velocity of impingement on the surface of the heap^{12,22)}.

Studies of the formation of two-dimensional heaps from binary mixtures with relatively small differences in size have shown the development of a regular pattern of striations over the entire heap, except at the central core formed during the initial stages of the process⁶⁵⁻⁶⁷⁾. However, there is reason to suspect that the highly regular pattern may be an artifact of the materials used and the nature of the test procedure.

In practice, pouring generally leads to the formation of three-dimensional, roughly conical heaps. This adds further complication to the formation process and any resulting segregation¹²⁾. Avalanching, due to local variations in slope, is unlikely to occur simultaneously around the heap leading to asymmetric radial distributions of the different particles. Flow over the surface is divergent, causing downstream thinning of the stream and possibly increased opportunity for trapping of particles.

Segregation in Bins and Hoppers

Segregation can be a serious problem in the storage of granular materials in bins or silos. While some segregation may occur across failure planes during flow through a bin⁶⁸⁾, such effects are probably small relative to surface segregation during filling and/or discharge. The problem of segregation is most pronounced in *funnel-flow* bins in which flow takes place through a channel formed within the mass of powder. *Mass-flow* bins, where material flows essentially *en masse* by sliding at the walls, provide little opportunity for segregation⁶⁹⁾.

Segregation can occur for both types if the material

is fed into the bin so as to form a heap leading, for example, to accumulation of coarse particles close to the walls, with a central core of finer particles. Segregation can also result from air entrainment of very fine particles during feeding¹²⁾. This effect can cause deposition of fines close to the walls leaving excess coarse material in the central region. In a mass-flow bin, the segregation pattern remains more or less intact during passage through the bin but becomes recombined in the converging hopper section at the discharge. The situation is more complicated for funnel-flow bins. Since flow is confined to an internal channel, the initial discharge comes from the fines-rich central core. As flow continues, a funnel-shape depression develops in the upper region of the bin contents. Coarse particles from the region close to the walls then begin to flow preferentially towards the center of the bin, reversing the segregation process. As a result, the discharge can switch from excess fines to excess coarse material. In many applications, bins are used to provide surge capacity with alternate or simultaneous feeding or discharge. The segregation patterns will then change according to whether feeding or discharge dominates and cycling of the discharge composition can occur.

Johanson⁷⁰⁾ and Carson et al.,⁷¹⁾ have described procedures for minimizing segregation in storage bins. A principal recommendation is to ensure that mass-flow conditions prevail. This should certainly be a priority in the design of new installations. However, despite more than 40 years of awareness of the advantages of such designs, the widespread use of funnel-flow bins remains. Conversion to or replacement by mass-flow systems is often considered to be economically impractical, especially for large-scale systems. Partial conversion can be achieved through the use of properly designed and placed inserts⁷⁰⁾. It should be noted that complete drainage should be avoided, even for mass-flow bins; a minimum filling level, somewhat above the converging hopper, should be maintained to ensure uniform flow of the material.

Segregation during bin filling, due to heap formation, can be reduced by distributing the feed over the bin cross section. Air entrainment effects can be largely eliminated by minimizing free-fall height during filling. A useful summary of procedures for suppressing segregation in storage systems has been presented by Tang and Puri¹³⁾.

Concluding Remarks

Mixing of solid particles generally proceeds

through combinations of two basic mechanisms: Convection and diffusion. Other proposed mechanisms such as “shear mixing” represent special cases or specific combinations of the two. Convection provides for rapid macromixing but is considerably less effective in promoting micromixing. Diffusion, on the other hand, is the primary mechanism for producing intimate micromixing. However, because the process occurs at the individual particle scale, mixing by diffusion alone proceeds very slowly. Convective mixing is controlled largely by the geometry and mechanical action of a mixing system while diffusion is more dependent on particle mobility and is severely hindered by cohesion of particles.

Segregation, i.e., de-mixing, is possible whenever different kinds of particles vary in mobility or response to external forces. Segregation by size can usually be attributed to differences in individual particle mobility – fines have higher mobility within a bed of particles while coarser material is more mobile on free surfaces. Shape effects can be expected to follow a similar pattern, with isometric particles having greater mobility than plates or needles, for example. Density differences can promote segregation due to the different gravitational force experienced by heavy or light particles. The actual form of segregation – top to bottom or side to side, for example – depends on the specific conditions of mechanical agitation of the system. Variations in both size and density can lead either to enhancement or reduction in segregation tendency depending on specific conditions.

Because segregation is normally a result of differences in individual particle mobility, its occurrence is most common in free-flowing powders. However, segregation of coarse particles is possible even in the presence of cohesive fine material. Aggregation of fines due to cohesion can also lead to segregation.

Procedures for minimizing segregation tend to be highly system-specific; there is no universal solution. Avoidance of mechanical agitation is generally appropriate – the use of completely, rather than partially, filled containers, for example. Introducing cohesion by liquid addition, where practical, can be effective but will, of course, exacerbate problems in mixing and storage.

Nomenclature

D	diffusion coefficient	$[L^2/T]$
D_0	diffusion parameter (Equation 6)	$[L^2/T]$
f_i	mass fraction of component i in a mixture	$[-]$
g	acceleration due to gravity	$[L/T^2]$

L	length of a mixing drum	[L]
M	sample weight	[M]
N_p	number of particles in a sample	[-]
r	radial coordinate	[L]
r_o	distance between powder bed and the center of a horizontal cylinder	[L]
R	radius of a cylinder	[L]
v	velocity	[L/T]
w_i	mean mass of a particle of component i	[M]
\bar{w}	overall mean particle mass in a mixture	[M]
y	vertical location in a flow stream	[L]
α	diffusion parameter (Equation 6)	[T]
θ	angular coordinate	[-]
θ_o	angle defining the filling of a cylinder	[-]
σ^2	expected variance (by number) of mixture composition	[-]
σ_m^2	expected variance (by mass) of mixture composition	[-]
ω_c	critical angular velocity of a rotating cylinder	[T ⁻¹]

References

- 1) Lacey, P.M.C. (1945): The Mixing of Solid Particles, *The Chemical Age*, 53. Aug. 11/18, pp. 119-124.
- 2) Buslik, D. (1950): Mixing and Sampling with Special Reference to Multi-Sized Granular Material, *ASTM Bull.*, 165. pp. 66-73.
- 3) Stange, K. (1954): Degree of Mixing in a Random Mixture as a Basis for Evaluating Mixing Experiments, *Chemie-Ing. Tech.*, 26. pp. 331-337.
- 4) Stange, K. (1963): Mixing Quality in a Random Mixture of Three or More Components, *Chemie-Ing. Tech.*, 35. pp. 580-582.
- 5) Poole, K.R., Taylor, R.F. and Wall, G.P. (1964): Mixing Powders to Fine-Scale Homogeneity: Studies of Batch Mixing, *Trans. Inst. Chem. Eng.*, pp. T305-T315.
- 6) Harnby, N. (1967): The Estimation of the Variance of Samples Withdrawn from a Random Mixture of Multi-Sized Particles, *Chem. Eng.*, 214. pp. CE270-CE271.
- 7) Walpole, R.E. and Myers, R.H. (1985): "Probability and Statistics for Engineers and Scientists, 3rd Ed." , Macmillan, New York.
- 8) Danckwerts, P.V. (1952): The Definition and Measurement of some Characteristics of Mixtures, *Appl. Sci. Res.*, 3 (A). pp. 279-296.
- 9) Hogg, R., Cahn, D.S., Healy, T.W. and Fuerstenau, D.W. (1966): Diffusional Mixing in an Ideal System, *Chem. Eng. Sci.*, 21. pp. 1025-1037.
- 10) Hogg, R. (2003): "Characterization of Relative Homogeneity in Particulate Solids," *Int. J. Miner. Process*, 72. pp. 477-487.
- 11) Lacey, P.M.C. (1954): Developments in the Theory of Particle Mixing, *J. App. Chem.*, 4. pp. 257-268.
- 12) Mosby, J., de Silva, S.R. and Enstad, G.G. (1996): Segregation of Particulate Materials – Mechanisms and Testers, *KONA Powder and Particle Journal*, No.14. pp. 31-42.
- 13) Tang, P. and Puri, V.M. (2004): Methods for Minimizing Segregation: a Review, *Part. Sci. Technol.*, 22. pp. 321-337.
- 14) Bridgewater, J. (1972): The Mixing of Cohesionless Powders, *Powder Technol.*, 5. pp. 257-260.
- 15) Williams, J.C. (1963): The Segregation of Powders and Granular Materials, *Fuel Soc. J.*, 14. pp. 29-34.
- 16) Rosato, A.D., Prinz, F., Standburg, K.J. and Svendsen, R. (1987): *Phys. Rev. Lett.* 58. pp. 1038-1040.
- 17) Matthée, H. (1968): Segregation Phenomena Relating to Bunkering of Bulk Materials: Theoretical Considerations and Experimental Investigations," *Powder Technol.*, 1. pp. 265-271.
- 18) Williams, J.C. (1976): The Segregation of particulate Materials. A Review, *Powder Technol.*, 15. pp. 245-251.
- 19) Augenstein, D.A. (1974): A Study of the Flow of Dry Particulate Solids, PhD Thesis, The Pennsylvania State University,.
- 20) Hogg, R., Augenstein, D.A. and Hwang, C.L. (1975): Segregation In Flowing Powders, Paper No. 98b, presented at the 68th Annual Meeting of AIChE, Los Angeles, CA.
- 21) Lawrence, L.R. and Beddow, J.K. (1969): Powder Segregation during Die Filling, *Powder Technol.*, 2. pp. 253-259.
- 22) Drahun, J.A. and Bridgewater, J. (1983): The Mechanism of Free Surface Segregation, *Powder Technol.*, 36. pp. 39-53.
- 23) Vallance, J.W. and Savage, S.B. (2000): Particle Segregation in Granular Flows down Chutes, in *IUTAM Symposium on Segregation in Granular Flows*, A.D. Rosato and D.L. Blackmore, eds., Kluwer Academic Publishers, Boston, pp. 31-51.
- 24) Tanaka, T. (1971): Segregation Models of Solid Mixtures Composed of Different Densities and Particle Sizes, *Ind. Eng. Chem., Proc. Des. and Dev.*, 10. pp. 332-340.
- 25) Geldart, D., Pope, D.J., Baeyens, J. and van de Wijer, P. (1981): Segregation in Beds of Large Particles at High Velocities, *Powder Technol.*, 30. pp.195-205.
- 26) Inoue, I., Yamaguchi, K. and Sato, K. (1970): Motion of Particle and Mixing Process in a Horizontal Drum Mixer, *Kagaku Kogaku*, 34. pp. 1323-1330.
- 27) Hogg, R. and Fuerstenau, D.W. (1972): Transverse Mixing in Rotating Cylinders, *Powder Technol.*, 6. pp. 139-148.
- 28) Khakhar, D.V., McCarthy, J.J. and Ottino, J.M. (1997): Transverse Flow and Mixing of Granular Materials in a Rotating cylinder, *Phys. Fluids*, 9. pp.31-43.
- 29) Prigozhin, L. and Kalman, H. (1998): Radial Mixing and Segregation of a Binary Mixture in a Rotating Drum: Model and Experiment, *Phys. Rev.*, 57. pp. 2073-2080.
- 30) Kaye, B.H., and Sparrow, D.B. (1964): Role of Surface Diffusion as a Mixing Mechanism in a Barrel-Mixer,

- Indust. Chemist, 5, pp. 246-250.
- 31) Cahn, D.S., Fuerstenau, D.W., Healy, T.W., Hogg, R. and Rose, H.E. (1966): Diffusional Mechanisms of Solid-Solid Mixing, *Nature*, 209, pp. 194-496.
 - 32) Abouzeid, A-Z.M., and Fuerstenau, D.W. (1972): Effects of Humidity on Mixing of Particulate Solids, *Ind. Eng. Chem., Proc. Des. and Dev.*, 11, pp. 296-301.
 - 33) Rao, S.J., Bhatia, S.K. and Khakhar, D.V. (1991): Axial Transport of Granular Solids in Rotating Cylinders. Part 2. Experiments in a Non-Flow System, *Powder Technol.*, 67, pp. 153-162.
 - 34) Vahl, L. and Kingma, W. G. (1951): Transport of Solids through Horizontal Rotary Cylinders, *Chem. Eng. Sci.*, 1, pp 253-258.
 - 35) Hogg, R., Shoji, K. and Austin, L.G. (1974): Axial Transport of Dry Powders in Horizontal Rotating Cylinders," *Powder Technol.*, 9, pp. 99-106.
 - 36) Karra, V.K. and Fuerstenau, D.W. (1978): Scale-up of the Axial Profile of Material Hold-up in Horizontal Rotating Cylinders, *Powder Technol.*, 19, pp. 265-269.
 - 37) Sawahata, Y. (1966): On the Mixing of Solids with Mixing Aids, *Kagaku Kogaku*, 30, pp. 178-179.
 - 38) Chaudhuri, P.K. and Fuerstenau, D.W. (1971): The Effect of Mixing Aids on the Kinetics of Mixing in a Rotating Drum, *Powder Technol.*, 4, pp. 146-150.
 - 39) Shoji, K., Hogg, R. and Austin, L.G. (1973): Axial Mixing of Particles in Batch Ball Mills, *Powder Technol.*, 7, pp. 331-336.
 - 40) Abouzeid, A-Z.M. and Fuerstenau, D.W. (1979): Effect of Mixing Aids on the Transport Behavior of Particulate Solids, *Powder Technol.*, 23, pp. 261-277.
 - 41) Donald, M.B. and Roseman, B. (1962): Mechanisms in a Horizontal Drum Mixer, *Br. Chem. Eng.*, 7, pp.749-752.
 - 42) Ottino, J.M. and Khakhar, D.V. (2000): Mixing and Segregation of Granular Materials, *Ann. Rev. Fluid. Mech.*, 32, pp. 55-91.
 - 43) Ristow, G.H. (1994): Particle Mass Segregation in a Two-Dimensional Rotating Drum, *Europhys. Lett.*, 28, pp. 97-101.
 - 44) Rogers, A.R. and Clements, J.A. (1972): The Examination of Segregation of Granular Materials in a Tumbling Mixer, *Powder Technol.*, 5, pp. 167-178.
 - 45) Nityanand, N., Manley, B. and Henein, H. (1986): An Analysis of Radial Segregation for Different Sized Spherical Solids in Rotary Cylinders, *Metall. Trans. B*, 17B, pp. 247-257.
 - 46) Cantelaube, F., Bideau, D. and Roux, S. (1997): Kinetics of Segregation of Granular Media in a Two-Dimensional Rotating Drum, *Powder Technol.*, 93, pp. 1-11.
 - 47) Oyama, Y. (1940): Mixing of Binary System of Two Sizes by Ball-Mill Motion, *Sci. Papers Inst. Phys. Chem. Research (Tokyo)* 37, pp. 17-29.
 - 48) Bridgwater, J., Sharpe, N.W. and Stocker, D.C. (1969): Particle Mixing by Percolation, *Trans. Inst. Chem. Eng.*, 47, pp. T114-119.
 - 49) Das Gupta, S. Bhatia, S.K. and Khakhar, D.V. (1991): Axial Segregation of Particles in a Horizontal Rotating Cylinder, *Chem. Eng. Sci.*, 46, pp. 1513-1517.
 - 50) Hill, K.M., Caprihan, A. and Kakalios, J. (1997): Axial Segregation of Granular Media Rotated in a Drum Mixer: Pattern Evolution, *Phys. Rev. E*, 56, pp. 4386-4393.
 - 51) Saeman, W.C. (1951): Passage of Solids through Rotary Kilns," *Chem. Eng. Progr.*, 47, pp. 508-514.
 - 52) Savage, S.B. (1993): Disorder, Diffusion and Structure Formation in Granular Flow, in "Disorder and Granular Media", D. Bideau and A. Hansen, eds., Elsevier, Amsterdam, pp. 255-285.
 - 53) Bridgwater, J. (1976): Fundamental Powder Mixing Mechanisms, *Powder Technol.*, 15, pp. 215-236.
 - 54) Zik, O., Levine, D., Lipson, S.G. Shtrickman, S. and Stavans, J. (1994). Rotationally Induced Segregation of Granular Materials, *Phys. Rev Lett.*, 73, pp. 644-647.
 - 55) Hogg, R. and Hwang, C.L. (1977): Mixing in Simple Flow Systems, *J. Powder and Bulk Solids Technol.*, 1, pp.72-75.
 - 56) Hwang, C.L. and Hogg, R. (1980): Diffusive Mixing in Flowing Powders, *Powder Technol.*, 26, pp. 93-101.
 - 57) Augenstein, D.A. and Hogg, R. (1978): An Experimental Study of the Flow of Dry Powders over Inclined Surfaces, *Powder Technol.*, 19, pp. 205-215.
 - 58) Hwang, C.L. (1978): Mixing and Segregation in Flowing Powders, PhD Thesis, The Pennsylvania State University.
 - 59) Savage, S.B. and Lun, C.K.K. (1988): Particle Size Segregation in Inclined Chute Flow of Dry Cohesionless Granular Solids, *J. Fluid Mech.*, 189, pp. 311-335.
 - 60) Dolgunin, V.N. and Ukolov, A.A. (1995): Segregation Modeling of Particle Rapid Flow, *Powder Technol.*, 83, pp. 95-103.
 - 61) Dolgunin, V.N., Kudy, A.N. and Ukolov, A.A. (1998) : Development of the Model of Segregation of Particles undergoing Granular Flow down an Inclined Plane, *Powder Technol.*, 96, pp. 211-218.
 - 62) Hsiau, S.S. and Hunt, M.L. (1996): Granular Thermal Diffusion in Flows of Binary-Sized Mixtures, *Acta Mech.*, 114, pp. 121-137.
 - 63) Hirschfeld, D. and Rapaport, D.C. (1997): Molecular Dynamics Studies of Grain Segregation in a Sheared Flow, *Phys. Rev. E*, 56, pp. 2012-2018.
 - 64) Khakhar, D.V., McCarthy, J.J. and Ottino, J.M. (1999): Mixing and Segregation of Granular Materials in Chute Flow, *CHAOS*, 9, pp. 594-610.
 - 65) Makse, H.N., Ciseau, P. and Stanley, H.E. (1997): Possible Stratification Mechanism in Granular Mixtures, *Phys. Rev. Lett.*, 78, pp. 3298-3301.
 - 66) Koeppel, J.P., Enz, M. and Kakalios, J. (1998): Phase Diagram for Avalanche Stratification of Granular Media, *Phys. Rev. E*, 58, pp. R4104-R4107.
 - 67) Boutreux, T. (1998): Surface Flows of Granular Mixtures: II. Segregation with Grains of Different Size, *Eur. Phys. J. B*, 6, pp. 419-424.
 - 68) Stephens, D.J. and Bridgwater, J. (1978): The mixing and Segregation of Cohesionless Particulate Materials Part II. Microscopic Mechanisms for Particles Differ-

- ing in Size, Powder Technol., 21, pp.29-44.
- 69) Jenike, A.W. (1964): Storage and Flow of Solids,” Bull. No. 123, Utah Eng. Expt. Stn.
- 70) Johanson, J.R. (1988): Solids Segregation: Causes and Solutions, Powder and Bulk Engineering, 2, No. 8, pp. 13-19.
- 71) Carson, J.W., Royal, T.A. and Goodwin, D.A. (1986): Understanding and Eliminating Particle Segregation Problems, Bulk Solids Handling, 6, pp. 139-144.

Author’s short biography



Richard Hogg

Richard Hogg is Professor Emeritus of Mineral Processing and GeoEnvironmental Engineering at the Pennsylvania State University. He received a B.Sc. from the University of Leeds and the M.S. and PhD degrees from the University of California at Berkeley. Dr Hogg’s research interests include fine particle processing, particle characterization, and colloid and surface chemistry.

Settling Velocities of Particulate Systems[†]

F. Concha

Department of Metallurgical Engineering
University of Concepción.¹

Abstract

This paper presents a review of the process of sedimentation of individual particles and suspensions of particles. Using the solutions of the Navier-Stokes equation with boundary layer approximation, explicit functions for the drag coefficient and settling velocities of spheres, isometric particles and arbitrary particles are developed.

Keywords: sedimentation, particulate systems, fluid dynamics

1. Introduction

Sedimentation is the settling of a particle, or suspension of particles, in a fluid due to the effect of an external force such as gravity, centrifugal force or any other body force. For many years, workers in the field of Particle Technology have been looking for a simple equation relating the settling velocity of particles to their size, shape and concentration. Such a simple objective has required a formidable effort and it has been solved only in part through the work of Newton (1687) and Stokes (1844) of flow around a particle, and the more recent research of Lapple (1940), Heywood (1962), Brenner (1964), Batchelor (1967), Zenz (1966), Barnea and Mitzrahi (1973) and many others, to those Turton and Levenspiel (1986) and Haider and Levenspiel (1989). Concha and collaborators established in 1979 a heuristic theory of sedimentation, that is, a theory based on the fundamental principles of mechanics, but with more or less degree of intuition and empirism. These works, (Concha and Almendra 1979a, 1979b, Concha and Barrientos 1982, 1986, Concha and Christiansen 1986), first solve the settling of one particle in a fluid, then, they introduce corrections for the interaction between particles, through which the settling velocity of a suspension is drastically reduced. Finally, the settling of isometric and non-spherical particles was treated. This approach, that uses principles of particle mechanics, receives the name of *discrete approach* to sedimentation, or *discrete sedimentation*.

Discrete sedimentation has been successful to establish constitutive equations in processes using sedimentation. It establishes the sedimentation properties of a certain particulate material in a given fluid. Nevertheless, to analyze a sedimentation process and to obtain behavioral pattern permitting the prediction of capacities and equipment design procedures, another approach is required, the so-called *continuum approach*.

The physics underlying sedimentation, that is, the settling of a particle in a fluid is known since a long time. Stokes presented the equation describing the sedimentation of a sphere in 1851 and that can be considered as the starting point of all discussions of the sedimentation process. Stokes shows that the settling velocity of a sphere in a fluid is directly proportional to the square of the particle radius, to the gravitational force and to the density difference between solid and fluid and inversely proportional to the fluid viscosity. This equation is based on a force balance around the sphere. Nevertheless, the proposed equation is valid only for slow motions, so that in other cases expressions that are more elaborate should be used. The problem is related to the hydrodynamic force between the particle and the fluid.

Consider the incompressible flow of a fluid around a solid sphere. The equations describing the phenomena are the continuity equation and Navier Stokes equation:

$$\begin{aligned} \nabla \cdot \mathbf{v} &= 0 \\ \rho \left(\frac{\partial \mathbf{v}}{\partial t} + \underset{\text{Convective force}}{\nabla \mathbf{v} \cdot \mathbf{v}} \right) &= -\nabla p + \underset{\text{Diffusive force}}{\mu \nabla^2 \mathbf{v}} + \rho \mathbf{g} \end{aligned} \quad (0.1)$$

[†] Accepted: July 22nd, 2009

¹ Edmundo Larenas 285, Concepción Chile,
E-mail: fconcha@udec.cl

where \mathbf{v} and p are the fluid velocity and pressure field, ρ and μ are the fluid density and viscosity and \mathbf{g} is the gravity force vector.

Unfortunately, Navier Stokes equation is non-linear and it is impossible to be solved explicitly in a general form. Therefore, methods have been used to solve it in special cases. It is known that the Reynolds number, $Re = \rho_f d u / \mu$ where ρ_f , d and u are the fluid density, the particle diameter and velocity respectively, is an important parameter that characterizes the flow. It is a dimensionless number representing the ratio of convective to diffusive forces in Navier Stokes equation. In dimensionless form, Navier-Stokes equation becomes:

$$\frac{1}{St} \frac{\partial \mathbf{v}^*}{\partial t^*} + \nabla^* \mathbf{v}^* \cdot \mathbf{v}^* = -\frac{1}{Ru} \nabla^* p^* + \frac{1}{Re} \nabla^{*2} \mathbf{v}^* - \frac{1}{Fr} \mathbf{e}_k \quad (0.2)$$

where the starred terms represent dimensionless variables defined by: $\mathbf{v}^* = \mathbf{v}/u_0$; $p^* = p/p_0$; $t^* = t/t_0$; $\nabla^* = L\nabla$ and u_0 , p_0 , t_0 and L are characteristic velocity, pressure, time and length in the problem, and St , Ru , Re and Fr are the Strouhal, Ruark, Reynolds and Froude numbers and \mathbf{e}_k is the vertical unit vector:

$$\text{Strouhal } St = \frac{t_0 u_0}{L}, \text{ Ruark } Ru = \frac{\rho u_0^2}{p_0},$$

$$\text{Reynolds } Re = \frac{\rho u_0 L}{\mu}, \text{ Froude } Fr = \frac{u_0^2}{Lg} \quad (0.3)$$

When the Reynolds number is small ($Re \rightarrow 0$), for example $Re < 10^3$, convective forces may be neglected in the Navier Stokes equation, obtaining the so called *Stokes Flow*. In dimensional form *Stokes Flow* is represented by:

$$\nabla \cdot \mathbf{v} = 0$$

$$\rho \frac{\partial \mathbf{v}}{\partial t} = -\nabla p + \mu \nabla^2 \mathbf{v} + \rho \mathbf{g} \quad (0.4)$$

2 Hydrodynamic Force on a Sphere in Stokes Flow

Do to the linearity of the differential equation in Stokes Flow, the velocity, the pressure and the *hydrodynamic force* in a steady flow are linear functions of the relative solid-fluid relative velocity. For the hydrodynamic force, the linear function, depend on the size and shape of the particle ($6\pi R$ for the sphere) and on the fluid viscosity (μ). Solving the boundary value problem and neglecting Basset term of added mass, yields (Happel and Brenner 1964):

$$F_D = -6\pi\mu R u \quad (2.1)$$

It is common to write the hydrodynamic force in its

dimensionless form known as *drag coefficient* C_D :

$$C_D = \frac{F_D}{(1/2\rho_f u^2)(\pi R^2)} \quad (2.2)$$

where ρ_f is the fluid density. Substituting (2.1) into (2.2), the drag coefficient of the sphere in Stokes flow is obtained:

$$C_D = \frac{24}{Re} \quad (2.3)$$

Macroscopic balance on a sphere in Stokes flow

Consider a small solid sphere submerged in a viscous fluid and suspended with a string. If the sphere, with density greater than that of the fluid, is in equilibrium, the balance of forces around it is zero. The forces acting on the particles are: gravity F_g , that pulls the sphere down, (2) buoyancy F_b , that is, the pressure forces of the fluid on the particle that pushes the sphere upwards and (3) the string resistance F_{string} , that supports the particle from falling. The force balance gives:

$$0 = F_{string} + \underbrace{F_g}_{-\rho_p V_p g} + \underbrace{F_b}_{+\rho_f V_p g} \quad (2.4)$$

$$0 = F_{string} - \rho_p V_p g + \rho_f V_p g \quad (2.5)$$

$$F_{string} = \underbrace{(\rho_p - \rho_f)}_{\Delta\rho} V_p g \equiv \Delta\rho V_p g \quad (2.6)$$

If the string is cut, forces become unbalanced and, according to Newton's law, the particle will accelerate. The initial acceleration can be obtained from the new force balance, where the string resistance is absent. The initial acceleration is:

$$\rho_p V_p a(t=0) = \Delta\rho V_p g$$

$$a(t=0) = \frac{\Delta\rho}{\rho_p} g \quad (2.7)$$

Once the particle is in motion, a new force, the drag, appears representing the resistance opposed by the fluid to the particle motion. This force F_D is proportional to the relative solid-fluid velocity and to the relative particle acceleration. Since the fluid is at rest it corresponds to the sphere velocity and acceleration. Once the motion starts, the drag force is added and the balance of forces becomes:

$$\rho_p V_p a(t) = \underbrace{\Delta\rho V_p g}_{\text{Net weight}} - \underbrace{6\pi\mu R u(t) - (1/2)\rho_p V_p a(t)}_{\text{Drag force}} \quad (2.8)$$

$$\frac{3}{2}\rho_p V_p a(t) = \Delta\rho g V_p - 6\pi\mu R u(t) \quad (2.9)$$

The term $(1/2)\rho_p V_p$ that was added to the mass $\rho_p V_p$ in the first term of equation (2.8) is called *added mass* induced by the acceleration.

Due to the increase in the velocity $u(t)$ with time, the

last term of (2.9) increases while the first term diminishes, and at a certain time becomes zero. The velocity becomes a constant called *terminal velocity* $u = u_\infty$ which is a characteristic of the solid-fluid system. From (2.9) with $a(t) = 0$,

$$u_\infty = \frac{2}{9} \frac{\Delta \rho R^2 g}{\mu} = \frac{1}{18} \frac{\Delta \rho d^2 g}{\mu} \quad (2.10)$$

This expression receives the name of *Stokes Equation* and is valid for small Reynolds numbers.

Sedimentation dynamics

Equation (2.9) is the differential equation for the settling velocity of a sphere in a gravity field. It can be written in the form:

$$\dot{u}(t) + \frac{2}{3} \frac{18\mu}{\rho_p d^2} u(t) - \frac{2\Delta\rho}{3\rho_p} g = 0 \quad (2.11)$$

Its solution is:

$$u(t) = \frac{1}{18} \frac{\Delta\rho d^2 g}{\mu} \left(1 - \exp\left(-\frac{2}{3} \frac{\mu}{18\rho_p d^2} t\right) \right) \quad (2.12)$$

The term inside the exponential term multiplying the time t is called *Stokes number* and the term outside the parenthesis is the *terminal velocity*, as we already mentioned in (2.10).

3. Hydrodynamic Force on a Sphere in Euler's Flow

When the Reynolds number tends to infinity ($Re \rightarrow \infty$), viscous forces disappear and the Navier Stokes equation becomes *Euler's Equation for Inviscid Flow*.

$$\nabla \cdot \mathbf{v} = 0$$

$$\rho \frac{\partial \mathbf{v}}{\partial t} \nabla \mathbf{v} \cdot \mathbf{v} = -\nabla p + \rho \mathbf{g} \quad (3.1)$$

In this case, the tangential component of the velocity at the particle surface is also a linear function of the relative solid-fluid velocity, but the radial component is equal to zero:

$$u_\theta(\theta) = \left(\frac{3}{2} \text{sen}\theta\right) u \text{ and } u_r = 0 \quad (3.2)$$

Now, the pressure is given by a non-linear function called *Bernoulli equation* (Batchelor 1967):

$$p(\theta) + 1/2 \rho_f u_\theta^2 = p + 1/2 \rho_f u^2 = \text{constante} \\ p(\theta) - p = \frac{1}{2} \rho_f u^2 \left(1 - \left(\frac{u_\theta}{u}\right)^2 \right) \quad (3.3)$$

Substituting (3.2) into (3.3), the dimensionless pressure, called *pressure coefficient* and defined by $C_p = (p(\theta) - p)/(1/2)\rho_f u^2$, may be expressed in Euler's flow by:

$$C_p = 1 - \frac{9}{2} \text{sen}^2 \theta \quad (3.4)$$

For an inviscid stationary flow, the hydrodynamic

force is zero. This result is due to the fact that the friction drag is zero in the absence of viscosity and that the form drag depends on the pressure distribution over the surface of the sphere and this distribution is symmetric leading to a zero net force.

4. Hydrodynamic Force on a Sphere in Prandtl's Flow

For intermediate values of the Reynolds Number, inertial and viscous forces in the fluid are of the same order of magnitude. In this case, the flow may be divided into two parts, an external inviscid flow far from the particle and an internal flow near the particle, where the viscosity plays an important role. This picture forms the basis of the *Boundary-Layer Theory* (Meksyn 1961, Rosenhead 1963, Golstein 1965, Schlichting 1968).

In the external inviscid flow, Euler's equations are applicable and the velocity and pressure distribution may be obtained from equations (3.2) and (3.3). The region of viscous flow near the particle is known as the boundary layer and it is there where a steep velocity gradient permits the non-slip condition at the solid surface to be satisfied.

The energy dissipation produced by the viscous flow within the boundary layer retards the flow and, at a certain point, aided by the adverse pressure gradient, the flow reverses its direction. These phenomena force the fluid particles outwards and away from the solid particle producing the phenomena called *boundary layer separation*, which occurs at an *angle of separation* given by (Lee and Barrow, 1968):

$$\theta_s = 214 Re^{-0.1} \quad \text{para } 24 < Re < 10.000 \quad (4.1)$$

For $Re=24$ the value of the angle of separation is $\theta_s=155.7$ and for $Re=10.000$ it is $\theta_s=85.2$. For Reynolds numbers exceeding 10.000, the angle of separation diminishes slowly from $\theta_s=85.2^\circ$ to 84° and then maintains this value up to $Re \approx 150.000$ (Tomotika 1937, Fage 1937, Amai 1938, Cabtree et al 1963).

Due to the separation of the boundary layer, the region of closed streamlines behind the sphere contains a standing ring-vortex, which first appears at Reynolds number of $Re \approx 24$. Taneda (1956) determined that beyond $Re \approx 130$ the ring-vortex began to oscillate and that at higher Reynolds numbers the fluid in the region of closed streamlines broke away and was carried downstream forming a wake.

The thickness " δ " of the boundary layer, defined as the distance from the solid surface to the region where the tangential velocity u_θ reaches 99% of the

value of the external inviscid flow, is proportional to $Re^{-1/2}$ and, at the point of separation, may be written in the form:

$$\frac{\delta}{R} = \frac{\delta_0}{Re^{1/2}} \quad (4.2)$$

McDonald (1954) gives a value of $\delta_0 = 9.06$.

The separation of the boundary layer prevents the recovery of the pressure at the rear of the sphere, resulting in an asymmetrical pressure distribution with a higher pressure at the front of the sphere. **Fig. 4.1** shows the pressure coefficient of a sphere in terms of the distance from the front stagnation point over the surface of the sphere in an inviscid flow and in boundary layer flow. The figure shows that the pressure has an approximate constant value behind the separation point at Reynolds numbers around $Re \approx 150,000$. This dimensionless pressure is called *base pressure* and has a value of $p_b^* \approx -0.4$ (Fage 1937, Lighthill 1963, p.108, Goldstein 1965, pp. 15 y 497, Schlichting 1968, p. 21).

The asymmetry of the pressure distribution explains the origin of the form-drag, the magnitude of which is closely related with the position of the point of separation. The farther the separation points from the front stagnation point, the smaller the form-drag. For a sphere at high Reynolds number, from $Re = 10,000$ up to $Re = 150,000$, the position of the separation point does not change very much, except with the change of flow from laminar to turbulent. Therefore, the *form-drag* will remain approximately constant. At the same time, the *friction-drag*, also called *skin friction*, falls proportional to $Re^{-1/2}$. From these observations, we can conclude that, for Reynolds numbers of about $Re=1,000$, the viscous interaction force has diminished sufficiently for its contribution

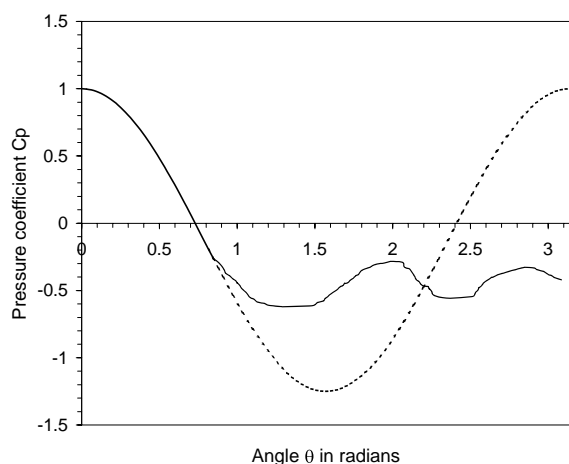


Fig. 4.1 Pressure coefficient as a function of the distance from the front stagnation point over the surface of a sphere in an inviscid and a boundary layer flow.

to the total interaction force to be negligible. Therefore, between $Re \approx 10,000$ to $Re \approx 150,000$ the drag coefficient is approximately constant at $C_D \approx 0.44$.

For Reynolds numbers greater than $Re \approx 150,000$, the flow changes in character and the boundary layer becomes turbulent. The increase in kinetic energy of the external region permits the flow in the boundary layer to reach further to the back of the sphere, shifting the separation point to values close to $\theta_s \approx 110^\circ$ and permitting also the base pressure to rise. The effect of these changes on the drag coefficient is a sudden drop and after that, a sharp increase with the Reynolds number. **Fig. 5.2** shows a plot of standard experimental values of the drag coefficient versus the Reynolds number (Lapple and Shepherd 1940, Perry 1963, p. 5.61) where this effect is shown. It shows the variation of the drag coefficient of a sphere for different values of the Reynolds number, and confirms that for $Re \rightarrow 0$, $C_D \propto Re^{-1/2}$ and that for $Re \gg 1$, $C_D \rightarrow 0.43$.

5. Drag Coefficient for a Sphere in the Range $0 < Re < 150,000$

To obtain a general equation relating the drag coefficient to the Reynolds number, we will use the concept of boundary layer and the knowledge that, for a given position at the surface of the sphere, the pressure inside the boundary layer is equal to the pressure in the inviscid region just outside the boundary layer before the separation point, and that it is a constant beyond it. We should also remember that the point of separation and the base pressure are constant for Reynolds numbers greater than $Re \approx 10,000$.

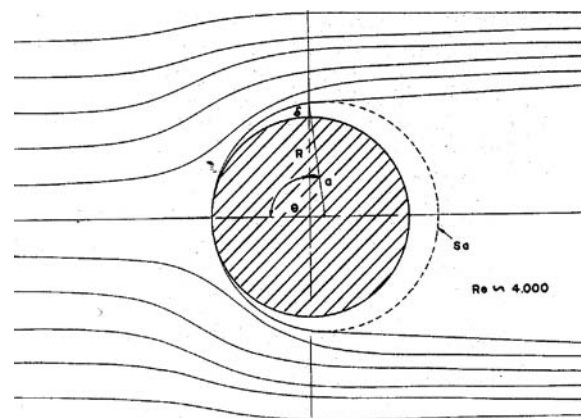


Fig. 5.1 Physical model for the flow in boundary layer around a sphere (Concha and Almendra 1979).

Consider a solid sphere of radius R with an attached boundary layer of thickness δ submerged in a flow at high Reynolds number (Abraham 1970). Assume that the system of sphere and boundary layer has a spherical shape with a radius equal to a , which can be approximated by $a = R + \delta$, as shown in **Fig. 3.1** (Abraham 1970, Concha and Almendra 1979).

Outside the spherical shell of radius a , and up to the point of separation $\theta = \theta_s$, the flow is inviscid and therefore the fluid velocity and the pressure distributions are given by:

$$u_\theta(\theta) = \frac{3}{2}u\sin\theta, \quad \text{for } 0 \leq \theta \leq \theta_s \quad (5.1)$$

$$p(\theta) = \frac{1}{2}\rho_f u^2 \left(1 - \left(\frac{u_\theta}{u}\right)^2\right), \quad \text{for } 0 \leq \theta \leq \theta_s \quad (5.2)$$

Beyond the separation point, a region exists where the pressure is constant and equal to the base pressure p_b :

$$p(\theta) = p_b, \quad \text{for } \theta_s \leq \theta \leq \pi \quad (5.3)$$

Since the effect of viscosity is confined to the interior of the sphere of radius a , the total drag exerted by the fluid on a , consists of a form drag only, Then:

$$F_D = \oint_{S_a} p(\theta) \cos\theta dS \quad (5.4)$$

The element of surface of the sphere of radius a is:

$$dS = a^2 \sin\theta d\theta d\phi \quad (5.5)$$

where ϕ is the azimuthally coordinate. Replacing into (5.4) results:

$$F_D = \int_0^{2\pi} \left(\int_0^\pi p(\theta) \sin\theta \cos\theta d\theta \right) d\phi$$

$$= 2\pi a^2 \int_0^\pi p(\theta) \sin\theta \cos\theta d\theta$$

Since the values of $p(\theta)$ is different before and after the separation point, separate the integrals into two parts, from 0 to θ_s and from θ_s to π .

$$F_D = 2\pi a^2 \left(\int_0^{\theta_s} p(\theta) \sin\theta \cos\theta d\theta + \int_{\theta_s}^\pi p(\theta) \sin\theta \cos\theta d\theta \right)$$

Substituting the values of $p(\theta)$ from (5.2) and from (5.3) and integrating we obtain:

$$F_D = \pi a^2 \rho_f u^2 \left(\frac{1}{2} \sin^2\theta_s - \frac{9}{16} \sin^4\theta_s - \frac{1}{2} p_b^* \sin^2\theta_s \right) \quad (5.6)$$

Substituting $a = R + \delta$ and defining the function $f(\theta_s, p_b^*)$ in the form:

$$f(\theta_s, p_b^*) = \frac{1}{2} \sin^2\theta_s - \frac{9}{16} \sin^4\theta_s - \frac{1}{2} p_b^* \sin^2\theta_s \quad (5.7)$$

we can write (5.6) in the form:

$$F_D = \rho_f u^2 \pi R^2 \left(1 + \frac{\delta}{R}\right)^2 f(\theta_s, p_b^*) \quad (5.8)$$

In terms of the drag coefficient we have:

$$C_D = 2f(\theta_s, p_b^*) \left(1 + \frac{\delta}{R}\right)^2 \quad (5.9)$$

and, defining the new parameter C_0 in the form:

$$C_0 = 2f(\theta_s, p_b^*) \quad (5.10)$$

and using equation (4.2) we obtain:

$$C_D = C_0(\theta_s, p_b^*) \left(1 + \frac{\delta_0}{Re^{1/2}}\right)^2 \quad (5.11)$$

Calculating the value of $f(\theta_s, p_b^*)$ for $\theta_s = 84^\circ$ and $p_b^* \approx -0.4$, we obtain $f(84, -0.4) = 0.142$ and from (5.10), $C_0 = 0.284 \approx 0.28$. Using the value of $\delta_0 = 9.06$, we finally obtain:

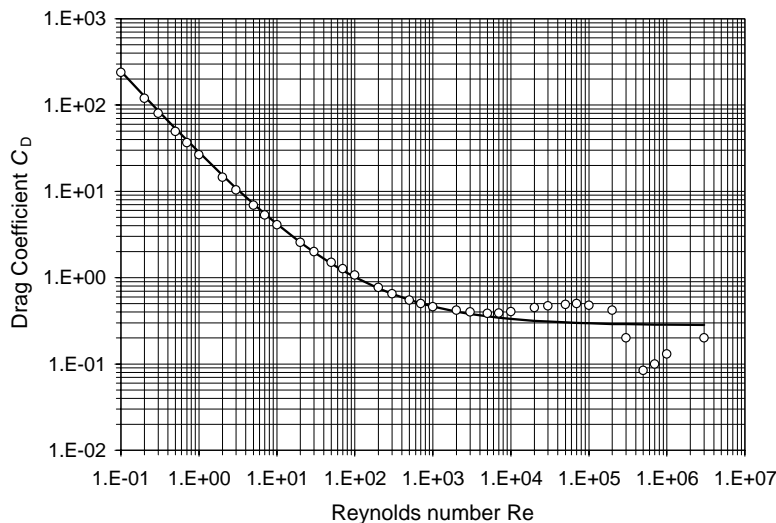


Fig. 5.2 Drag coefficient versus Reynolds number for a sphere. The continuous line is a simulation with equation (5.12). Circles are standard data from Lapple y Shepherd (1940 See table 4.1). See also Perry (1963) p. 5.61).

$$C_D = 0.28 \left(1 + \frac{9.06}{Re^{1/2}} \right)^2 \quad (5.12)$$

Expression (5.12) represents the drag coefficient for a sphere in boundary layer flow (Concha and Almendra 1979). A comparison with experimental data from Lapple and Shepherd (1940) is shown in **Fig. 5.2**.

Several alternative empirical equations have been proposed for the drag coefficient of spherical particles. See older articles reviewed by Concha and Almendra (1979), Zigrang and Sylvester (1981), Turton and Levenspiel (1986), Turton and Clark (1987) and Haider and Levenspiel (1989), and the more recent work of Ganguly (1990), Thomson and Clark (1991), Ganser (1993), Flemmer et al (1993), Darby (1996), Nguyen et al (1997), Chabra et al (1999) and Tsakalakis and Stamboltzis (2001).

It is worthwhile to mention the work of Brauer and Zucker (1976):

$$C_D = 0.49 + \frac{24}{Re} + \frac{3.73}{Re^{1/2}} - \frac{4.83 \times 10^{-3} Re^{1/2}}{1 + 3.0 \times 10^{-6} Re^{3/2}} \quad (5.13)$$

and that of Haider and Levenspiel (1989):

$$C_D = \frac{24}{Re} (1 + 0.1806 Re^{0.6459}) + \frac{0.4251}{1 + 6880.95/Re} \quad (5.14)$$

who presented alternative empirical equations for the drag coefficient of spherical particles in the range of Reynolds numbers less than 260,000. Both empirical equations, (5.13) and (5.14), give better approximations than Concha and Almendra's equation (5.12) for Reynolds numbers in the range of $5 \times 10^3 <$

$Re < 5 \times 10^5$. The merit of this last equation is its fundamental foundation.

6. Sedimentation Velocity of a Sphere

We have seen that when a particle settles at terminal velocity u_∞ , a balance is established between drag force, gravity and buoyancy:

$$F_{drag} + F_{gravity} + F_{buoyancy} = 0$$

$$F_{drag} = - (F_{gravity} + F_{buoyancy}), \equiv \text{net weight of the particle}$$

$$F_D = - (\rho_p V_p (-\mathbf{g}) + \rho_f V_p \mathbf{g}) \equiv \Delta \rho V_p \mathbf{g} \quad (6.1)$$

In (6.1) $\Delta \rho = \rho_s - \rho_f$ is the solid-fluid density difference. This equation shows that the drag force for a particle in sedimentation is known beforehand, once its volume and the density difference to the fluid are known. For a spherical particle, $V_p = 4/3 \pi R^3$, so that:

$$F_D = \frac{4}{3} \pi R^3 \Delta \rho \mathbf{g} \quad (6.2)$$

and the drag coefficient:

$$C_D = \frac{F_D}{1/2 \rho_f u_\infty^2 \pi R^2} \equiv \frac{4 \Delta \rho d \mathbf{g}}{3 \rho_f u_\infty^2} \quad (6.3)$$

where the sphere diameter is $d = 2R$ and u_∞ is the terminal settling velocity of a sphere in an infinite fluid.

Since the Reynolds number for the motion of one particle in an infinite fluid is defined by:

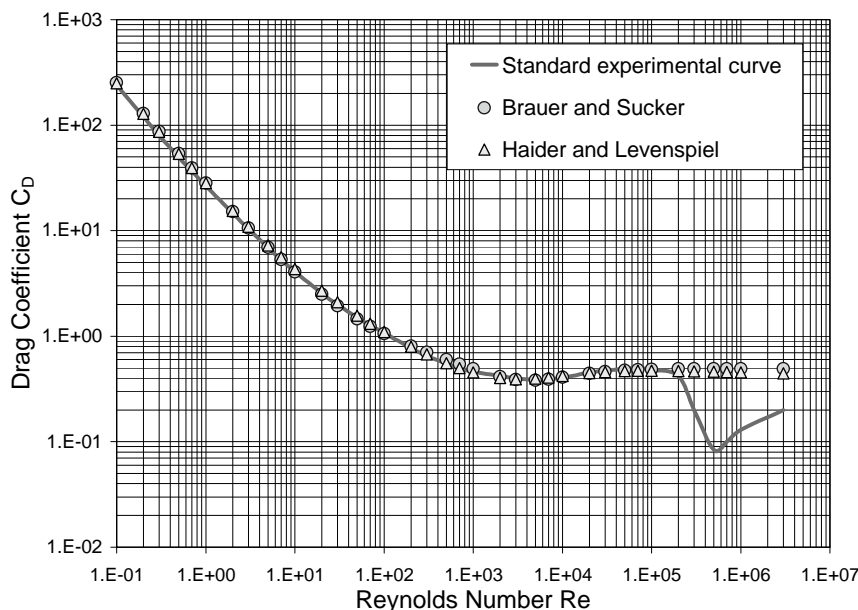


Fig. 5.3 Comparison of the Drag Coefficient for a sphere, simulated by Brauer and Zucker (1976) and by Haider and Levenspiel (1989), and standard experimental points from Lapple and Shepherd (1940).

$$Re_{\infty} = \frac{du_{\infty}\rho_f}{\mu_f}, \quad (6.4)$$

combining it with the drag coefficient yields two dimensionless numbers (Heywood 1962):

$$C_D Re_{\infty}^2 = \left(\frac{4 \Delta \rho \rho_f \mathbf{g}}{3 \mu_f^2} \right) d^3 \frac{Re_{\infty}}{C_D} = \left(\frac{3 \rho_f^2}{4 \Delta \rho \mu_f \mathbf{g}} \right) u_{\infty}^3 \quad (6.5)$$

Concha and Almendra (1979a) defined the characteristic parameters P and Q of the solid-liquid system:

$$P = \left(\frac{3 \mu_f^2}{4 \Delta \rho \rho_f \mathbf{g}} \right)^{1/3} \quad Q = \left(\frac{4 \Delta \rho \mu_f \mathbf{g}}{3 \rho_f^2} \right)^{1/3} \quad (6.6)$$

so, that equations (6.5) may be written in the form:

$$C_D Re_{\infty}^2 = \left(\frac{d}{P} \right)^3 = d^{*3} \quad \frac{Re_{\infty}}{C_D} = \left(\frac{u_{\infty}}{Q} \right)^3 \equiv u_{\infty}^{*3} \quad (6.7)$$

Expression (6.7) defines a dimensionless size d^* and a dimensionless velocity u^* , which are characteristics of a solid-liquid system:

$$d^* = \left(\frac{d}{P} \right) \quad u_{\infty}^* = \left(\frac{u_{\infty}}{Q} \right) \quad (6.8)$$

Since there is a direct relationship between the Drag Coefficient and the Reynolds Number, see for example equations (4.2) to (6.4), there must be a similar relationship between the dimensionless groups $C_D Re^2$ and Re/C_D . **Table 7.1** gives that relationship.

Multiplying the two terms in equation (6.7), we can observe that the Reynolds number may be written in terms of the dimensionless size and velocity:

$$Re_{\infty} = d^* u_{\infty}^* \quad (6.9)$$

Replacing (5.11) and (6.9) into (6.7) we obtain:

$$d^{*3} = C_0 \left(1 + \frac{\delta_0}{(u_{\infty}^* d^*)^{1/2}} \right)^2 (u_{\infty}^* d^*)^2$$

$$u_{\infty}^* d^* + \delta_0 (u_{\infty}^* d^*)^{1/2} - \frac{d^{*3/2}}{C_0^{1/2}} = 0$$

Solving these algebraic equation, explicit expressions are obtained for the dimensionless settling velocity u_{∞}^* of a sphere of dimensionless size d^* and for the dimensionless size d^* of a sphere settling at dimensionless velocity u_{∞}^* (Concha y Almendra 1979a):

$$u_{\infty}^* = \frac{1}{4} \frac{\delta_0^2}{d^*} \left(\left(1 + \frac{4}{C_0^{1/2} \delta_0^2} d^{*3/2} \right)^{1/2} - 1 \right)^2 \quad (6.10)$$

$$d^* = \frac{1}{4} C_0 u_{\infty}^{*2} \left(1 + \left(1 + \frac{4 \delta_0}{C_0^{1/2}} u_{\infty}^{*-3/2} \right)^{1/2} \right)^2 \quad (6.11)$$

Equations (6.10) and (6.11) are known as *Concha and Almendra's equations* for a sphere. These two equations are general for spheres settling in a fluid at any Reynolds number. Introducing the values of $C_0 = 0.28$ and $\delta_0 = 9.06$, the following final equations are obtained:

$$u^* = \frac{20.52}{d^*} \left((1 + 0.0921 d^{*3/2})^{1/2} - 1 \right)^2 \quad (6.12)$$

$$d^* = 0.07 u^{*2} \left(1 + (1 + 68.49 u^{*-3/2})^{1/2} \right)^2 \quad (6.13)$$

Using equation (6.12) the values of column

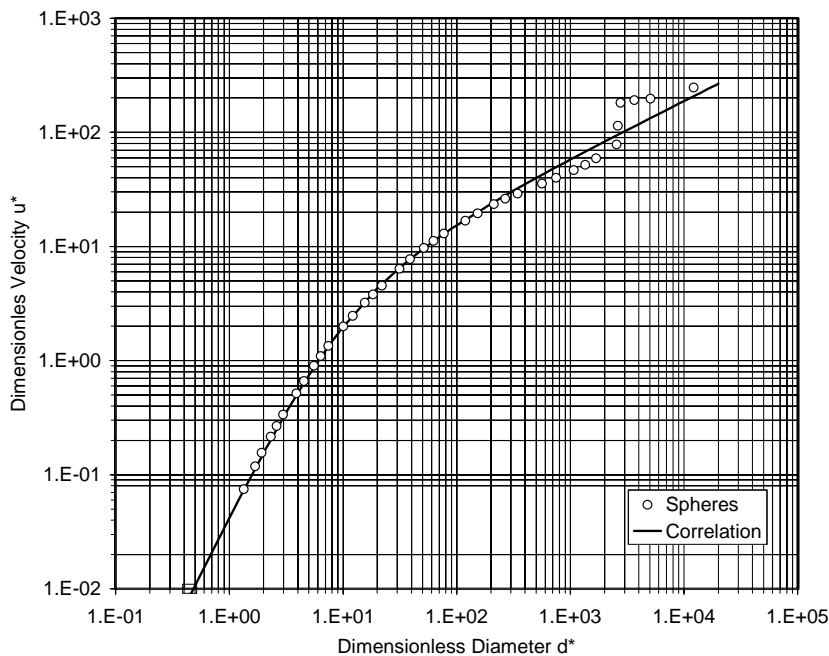


Fig. 6.1 Dimensionless velocity versus dimensionless diameter for the sedimentation of spheres according to equation (6.12) of Concha and Almendra. Circles are standard data from Lapple y Shepherd (1940) in table 3.1.

d^* sim and u^* sim are obtained. The plot of these data is shown in Fig. 6.1.

7. Sedimentation of a Suspension of Spheres

In a suspension, the spheres surrounding a given sphere, as it settles, hinder its motion. This hindrance is due to several effects. In the first place, when the particle changes its position, it can find the new site occupied by another particle, and will collide with it changing its trajectory. The more concentrate the suspension is the greater the chance of collision. The result is that hindrance is a function of concentration. On the other hand, the settling of each particle of the suspension produces a back flow of the fluid. This back flow will increase the drag on a given particle, retarding its sedimentation. Again, an increase in concentration will increase the hindrance. It is clear that in both cases, the hindrance depends on the fraction of volume occupied by the particles and not on their weight and therefore the appropriate parameter to measure hindrance is the volumetric concentration rather than the percent by weight.

Several theoretical works have been devoted to

study the interaction of particles in a suspension during sedimentation. These types of studies were discussed in Tory (1996).

In a recent approach, Quispe et al. (2000) used the tools of lattice-gas and cellular automata to study the sedimentation of particles and the fluid flow through an ensemble of settling particles. They were able to obtain some important macroscopic properties of the suspensions. Unfortunately, none of these works has yielded a sufficiently general and simple relationship between the variables of the suspension and its settling velocity to be used for practical purposes.

Concha and Almendra (1979b) assumed that the same equation used for individual spherical particles is valid for a suspension of particles. Then, the sedimentation of a suspension can be described by equation (6.12) replacing the parameters P and Q by $P(\varphi)$ and $Q(\varphi)$, parameters depending on the volume fraction of solids. Write equation (6.12) it in the form:

$$U^* = \frac{20.52}{D^*} \left(\left(1 + 0.0921 D^{*3/2} \right)^{1/2} - 1 \right)^2 \quad (7.1)$$

where

Table 7.1 Drag coefficient versus Reynolds Number and dimensionless velocity versus dimensionless diameter

LAPPLE AND SHEPHERD (1940)						CONCHA AND ALMENDRA		
		z	Re/C_D	$d^*=(C_D Re^2)^{1/3}$	$u^*=(Re/C_D)^{1/3}$	C_D sim	d^* sim	u^* sim
1.00E-01	2.40E+02	2.4	4.17E-04	1.34E+00	7.47E-02	246.158212	1.00E-01	4.35E-04
2.00E-01	1.20E+02	4.8	1.67E-03	1.69E+00	1.19E-01	126.541954	2.00E-01	1.73E-03
3.00E-01	8.00E+01	7.2	3.75E-03	1.93E+00	1.55E-01	86.1544439	3.00E-01	3.89E-03
5.00E-01	4.95E+01	12.4	1.01E-02	2.31E+00	2.16E-01	53.4219699	4.00E-01	6.88E-03
7.00E-01	3.65E+01	17.9	1.92E-02	2.62E+00	2.68E-01	39.1775519	5.00E-01	1.07E-02
1.00E+00	2.65E+01	26.5	3.77E-02	2.98E+00	3.35E-01	28.337008	6.00E-01	1.53E-02
2.00E+00	1.46E+01	58.4	1.37E-01	3.88E+00	5.15E-01	15.359281	7.00E-01	2.08E-02
3.00E+00	1.04E+01	93.6	2.88E-01	4.54E+00	6.61E-01	10.8703803	8.00E-01	2.70E-02
5.00E+00	6.90E+00	172.5	7.25E-01	5.57E+00	8.98E-01	7.1456645	9.00E-01	3.39E-02
7.00E+00	5.30E+00	259.7	1.3E+00	6.38E+00	1.10E+00	5.48098455	1.00E+00	4.16E-02
1.00E+01	4.10E+00	410.0	2.4E+00	7.43E+00	1.35E+00	4.18275399	1.10E+00	5.00E-02
2.00E+01	2.55E+00	1.02E+03	7.8E+00	1.01E+01	1.99E+00	2.56366185	1.20E+00	5.91E-02
3.00E+01	2.00E+00	1.80E+03	1.5E+01	1.22E+01	2.47E+00	1.97242199	1.30E+00	6.89E-02
5.00E+01	1.50E+00	3.75E+03	3.3E+01	1.55E+01	3.22E+00	1.45718355	1.40E+00	7.93E-02
7.00E+01	1.27E+00	6.22E+03	5.5E+01	1.84E+01	3.81E+00	1.21474559	1.50E+00	9.04E-02
1.00E+02	1.07E+00	1.07E+04	9.3E+01	2.20E+01	4.54E+00	1.01719408	1.60E+00	1.02E-01
2.00E+02	7.70E-01	3.08E+04	2.6E+02	3.13E+01	6.38E+00	0.75367474	1.70E+00	1.14E-01
3.00E+02	6.50E-01	5.85E+04	4.6E+02	3.88E+01	7.73E+00	0.64953579	1.80E+00	1.27E-01
5.00E+02	5.50E-01	1.38E+05	9.1E+02	5.16E+01	9.69E+00	0.55286511	1.90E+00	1.41E-01
7.00E+02	5.00E-01	2.45E+05	1.40E+03	6.26E+01	1.12E+01	0.5045975	2.00E+00	1.55E-01
1.00E+03	4.60E-01	4.60E+05	2.17E+03	7.72E+01	1.30E+01	0.46342473	2.10E+00	1.69E-01
2.00E+03	4.20E-01	1.68E+06	4.76E+03	1.19E+02	1.68E+01	0.40494085	2.20E+00	1.84E-01
3.00E+03	4.00E-01	3.60E+06	7.50E+03	1.53E+02	1.96E+01	0.38029197	2.30E+00	1.99E-01
5.00E+03	3.85E-01	9.63E+06	1.30E+04	2.13E+02	2.35E+01	0.35634822	2.40E+00	2.15E-01
7.00E+03	3.90E-01	1.91E+07	1.79E+04	2.67E+02	2.62E+01	0.34392446	2.50E+00	2.31E-01
1.00E+04	4.05E-01	4.05E+07	2.47E+04	3.43E+02	2.91E+01	0.33303434	2.60E+00	2.48E-01
2.00E+04	4.50E-01	1.80E+08	4.44E+04	5.65E+02	3.54E+01	0.31702494	2.70E+00	2.65E-01
3.00E+04	4.70E-01	4.23E+08	6.38E+04	7.51E+02	4.00E+01	0.31005856	2.80E+00	2.83E-01
5.00E+04	4.90E-01	1.23E+09	1.02E+05	1.07E+03	4.67E+01	0.3031495	2.90E+00	3.01E-01
7.00E+04	5.00E-01	2.45E+09	1.40E+05	1.35E+03	5.19E+01	0.29950474	3.00E+00	3.19E-01
1.00E+05	4.80E-01	4.80E+09	2.08E+05	1.69E+03	5.93E+01	0.29627397	3.10E+00	3.38E-01
2.00E+05	4.20E-01	1.68E+10	4.76E+05	2.56E+03	7.81E+01	0.29145983	3.20E+00	3.57E-01
3.00E+05	2.00E-01	1.80E+10	1.50E+06	2.62E+03	1.14E+02	0.2893397	3.30E+00	3.76E-01
5.00E+05	8.40E-02	2.10E+10	5.95E+06	2.76E+03	1.81E+02	0.28722112	3.40E+00	3.95E-01
7.00E+05	1.00E-01	4.90E+10	7.00E+06	3.66E+03	1.91E+02	0.28609695	3.50E+00	4.15E-01
1.00E+06	1.30E-01	1.30E+11	7.69E+06	5.07E+03	1.97E+02	0.28509658	3.60E+00	4.35E-01
3.00E+06	2.00E-01	1.80E+12	1.50E+07	1.22E+04	2.47E+02	0.28293691	3.70E+00	4.56E-01

$$D^* = \frac{d}{P(\varphi)} \quad \text{and} \quad U^* = \frac{u}{Q(\varphi)} \quad (7.2)$$

It is convenient to express the properties of a suspension, such as the viscosity and density, as the product of the property of the fluid with a function of concentration. Assume that $P(\varphi)$ and $Q(\varphi)$ can be related with P and Q in that form, then:

$$P(\varphi) = Pf_p(\varphi) \quad \text{and} \quad Q(\varphi) = Qf_q(\varphi) \quad (7.3)$$

Replacing (7.3) into (7.2), and using the definitions (6.7) of d^* and u^* , results in:

$$D^* = \frac{d^*}{f_p(\varphi)} \quad \text{and} \quad U^* = \frac{u^*}{f_q(\varphi)} \quad (7.4)$$

With these definitions equation (7.1) may be written in the form:

$$u^* = \frac{20.52}{d^*} f_p(\varphi) f_q(\varphi) \left(\left(1 + 0.0921 f_p^{-3/2} d^{*3/2} \right)^{1/2} - 1 \right)^2 \quad (7.5)$$

This expression, known as *Concha and Almendra's equation for a suspension of spheres*, permits the calculation of the settling velocity of a sphere of any size and density when it forms part of a suspension with volume fraction φ . To perform the calculations it is necessary to determine the parameters $f_p(\varphi)$ and $f_q(\varphi)$.

Asymptotic expressions for the sedimentation velocity

For small values of the Reynolds number, $Re \rightarrow 0$, the following expressions may be derived from (6.12) and (7.5), which reduce the settling equation to the expression indicated:

$$\begin{aligned} 0.0921 d^{*3/2} f_p^{-3/2} &<< 1 \Rightarrow \\ u^* &= 20.52 \left(\frac{0.0921}{2} \right)^2 d^{*2} f_p^{-2}(\varphi) f_q(\varphi) \\ 0.0921 d^{*3/2} &<< 1 \Rightarrow \\ u_\infty^* &= 20.52 \left(\frac{0.0921}{2} \right)^2 d^{*2} \end{aligned} \quad (7.6)$$

In these expressions, the symbols u_∞^* and u^* indicate the settling velocity of a particle in an infinite medium and the velocity of the same particle in a suspension respectively. The quotient between these two terms is:

$$\text{For } Re_\infty \rightarrow 0 \quad \frac{u^*}{u_\infty^*} = f_p^{-2}(\varphi) f_q(\varphi) \quad (7.7)$$

With a similar deduction we can write for high Reynolds numbers, equations (6.12) and (7.5) in the form:

$$\begin{aligned} 0.0921 d^{*3/2} f_p^{-3/2} &>> 1 \Rightarrow \\ u^* &= 20.52 x 0.0921 x d^{*1/2} f_p^{-1/2}(\varphi) f_q(\varphi) \\ 0.0921 d^{*3/2} &>> 1 \Rightarrow \quad u_\infty^* &= 20.52 x 0.0921 x d^{*1/2} \end{aligned}$$

The quotient between these two equations is:

$$\text{Para } Re_\infty \rightarrow \infty \quad \frac{u^*}{u_\infty^*} = f_p^{-1/2}(\varphi) f_q(\varphi) \quad (7.8)$$

To find functional forms for the functions $f_p(\varphi)$ and $f_q(\varphi)$, experimental values for the settling velocities u_∞ and u are needed.

Functional form for $f_p(\varphi)$ and $f_q(\varphi)$

Several authors have presented expressions for the velocity ratio u/u_∞ . See Concha and Almendra (1979b). Richardson and Zaki (1954), made the most comprehensive and most cited work on the relative particle-fluid flow under gravity. We will use their data in this paper.

Richardson and Zaki (1954) performed careful sedimentation and liquid fluidization test with mono-sized spherical particles in a wide range of particles sizes and fluid densities and viscosities. They expressed their result in the form:

$$\begin{aligned} u/u_\infty &= (1 - \varphi)^n \quad \text{for } Re \rightarrow 0 \quad \text{and} \quad u/u_\infty = (1 - \varphi)^m \\ &\text{for } Re \rightarrow \infty \end{aligned} \quad (7.9)$$

From (7.7), (7.8) and (7.9), we can write

$$\begin{aligned} f_p^{-2}(\varphi) f_q(\varphi) &= (1 - \varphi)^n \\ f_p^{-1/2}(\varphi) f_q(\varphi) &= (1 - \varphi)^m \end{aligned} \quad (7.10)$$

and, by solving this algebraic set we obtain:

$$f_p = (1 - \varphi)^{(2/3)(m-n)} \quad \text{and} \quad f_q = (1 - \varphi)^{(1/3)(4m-n)} \quad (7.11)$$

In **Table 7.1** the characteristics of these particles and fluid are given and values for u/u_∞ obtained from their experimental results are shown.

Using equation (7.6) and (7.7) and the calculated values in **Table 7.1**, the best values for m and n were:

$$n = 3.90 \quad \text{and} \quad m = 0.85 \quad (7.12)$$

Then,

$$f_p(\varphi) = (1 - \varphi)^{-2.033}, \quad f_q(\varphi) = (1 - \varphi)^{-0.167} \quad (7.13)$$

Fig. 6.1 shows a plot of the dimensionless settling velocity versus Reynolds number for spheres, according to the experimental data of Richardson and Zaki (1954) and the simulation of Concha and Almendra (1979) with equations (7.5) and (7.13). Data of u/u_∞ calculated from Richardson and Zaki (1954) are in **Table 7.2** and **Fig. 7.1**.

If all data of **Table 7.1** are plot in the form U^* versus D^* with the definitions (7.4), **Fig. 7.2** is obtained.

On the other hand, **Fig. 7.3** shows the settling ve-

Table 7.1 Experimental data of Richardson and Zaki (1954)

Experimental data from Richardson and Zaki (1954)								
N°	d (cm)	ρ_s (g/cm ³)	$\mu_f \times 10^2$ (g/cms)	ρ_f (g/cm ³)	v_{st} (cm/s)	Re_{∞}	n+1	n
P	0.0181	1.058	20.800	1.034	0.00206	0.000185	4.90	3.90
Q	0.0181	1.058	20.800	1.034	0.00206	0.000185	4.79	3.79
K	0.0096	2.923	62.000	1.208	0.01390	0.000216	4.75	3.75
L	0.0096	2.923	62.000	1.208	0.01390	0.000216	4.65	3.65
F	0.0358	1.058	20.800	1.034	0.00807	0.001430	4.92	3.92
G	0.0358	1.058	20.800	1.034	0.00807	0.001430	4.89	3.89
H	0.0096	2.923	20.800	1.034	0.04550	0.002180	4.76	3.76
I	0.0096	2.923	20.800	1.034	0.04550	0.002180	4.72	3.72
J	0.0096	2.923	20.800	1.034	0.04550	0.002180	4.69	3.69
R	0.0230	2.623	62.000	1.208	0.06590	0.002950	4.85	3.85
S	0.0230	2.623	62.000	1.208	0.06590	0.002950	4.80	3.80
T	0.0128	2.960	1.890	2.890	0.03307	0.064700	4.84	3.84
M	0.0128	2.960	1.890	2.890	0.03307	0.064700	4.72	3.72
C	0.0181	1.058	1.530	1.001	0.06640	0.078900	4.76	3.76
A	0.0181	1.058	1.530	1.001	0.06640	0.078900	4.90	3.90
B	0.0181	1.058	1.530	1.001	0.06640	0.078900	4.79	3.79
X	0.1029	2.976	112.900	1.221	0.89100	0.099500	5.30	4.30
Y	0.1029	2.976	112.900	1.221	0.89100	0.099500	5.20	4.20
D	0.0253	1.058	2.910	0.935	0.14750	0.120000	4.94	3.94
E	0.0253	1.058	2.910	0.935	0.14750	0.120000	4.90	3.90
N	0.0096	2.923	1.612	2.170	0.23400	0.030200	4.74	3.74
O	0.0096	2.923	1.612	2.170	0.23400	0.030200	4.65	3.65
2	0.0253	2.78	6.075	1.135	0.82700	0.391000	4.65	3.65
5	0.0253	1.06	1.000	1.000	0.19400	0.490000	4.53	3.53
8	0.0230	2.623	1.890	2.890	0.34900	1.227000	4.450	3.450
9	0.0230	2.623	1.890	2.890	0.34900	1.227000	4.520	3.520
12	0.0230	2.623	1.890	2.890	0.34900	1.227000	4.140	3.140
10	0.0230	2.623	1.612	2.170	0.65250	2.021000	4.300	3.300
11	0.0230	2.623	1.612	2.170	0.65250	2.021000	4.350	3.350
13	0.0230	2.623	1.612	2.170	0.65250	2.021000	4.240	3.240
6	0.0510	2.745	6.075	1.135	2.89000	2.745000	4.22	3.22
14	0.1029	2.976	10.960	1.153	6.03000	6.530000	4.300	3.300
15	0.1029	2.976	10.960	1.153	6.03000	6.530000	4.070	3.070
16	0.1029	2.976	10.960	1.153	6.03000	6.530000	4.000	3.000
4	0.0253	2.78	1.000	1.000	3.55000	8.971000	3.59	2.59
3	0.1029	10.6	15.010	0.875	19.60000	11.750000	3.72	2.72
1	0.1029	2.976	1.890	2.890	1.16000	18.180000	3.800	2.800
	0.1029	2.976	1.890	2.890	1.16000	18.180000	3.640	2.640
	0.1029	2.976	1.890	2.890	1.16000	18.180000	3.860	2.860
	0.1029	2.976	1.839	2.745	2.48000	38.260000	3.340	2.340
	0.1029	2.976	1.839	2.745	2.48000	38.260000	3.560	2.560
	0.1029	2.976	1.839	2.745	2.48000	38.260000	3.500	2.500
	0.0510	2.745	1.000	1.000	8.10000	41.720000	3.11	2.11
	0.1029	2.745	1.000	1.0	7.35000	14.450000	3.78	2.78
	0.1029	2.745	1.000	1.000	7.35000	14.450000	3.78	2.78
	0.4200	2.89	15.010	0.875	31.90000	78.250000	3.34	2.34
	0.1029	10.6	3.810	0.818	36.15000	79.800000	3.08	2.08
	0.2466	11.25	15.010	0.875	58.10000	80.350000	3.39	2.39
	0.3175	7.73	15.010	0.875	54.70000	101.200000	3.17	2.17
	0.4200	2.89	6.075	1.135	34.05000	267.000000	2.58	1.58
	0.1029	10.6	1.000	1.000	47.50000	488.700000	2.43	1.43
	0.4200	2.89	1.000	1.000	48.60000	2041.000000	2.33	1.33
	0.3175	7.73	1.000	1.000	79.70000	2530.000000	2.36	1.36
	0.6350	7.74	1.000	1.000	112.70000	7150.000000	2.38	1.38

locity u^* versus d^* for suspensions of spheres in water at 20°C for different values of the concentration φ . This figure can be used to visualize the state of flow of particulate system.

The relationship between the volume average velocity q , also known as *spatial velocity or percolation velocity*, to de solid velocity v_s and the relative solid fluid velocity v_r is given by:

$$q = v_s - (1 - \varphi) v_r \tag{7.14}$$

Fig. 7.3 divides the $u^* \times d^*$ plane into three regions: a *porous bed*, between the d^* axis and the line of constant concentration $\varphi = 0.585$ (Wen and Yu 1966 and Barnea and Mednick 1975 demonstrated that this concentration corresponds to the minimum fluidization velocity), a second region of fluidized bed between $0.585 \leq \varphi \leq 0$ and a third region of *hydraulic or pneumatic transport*, for values of velocities above

Table 7.2 Values of u/u_∞ from the experimental results of Richardson and Zaki (1954)

Re _∞	u/u _∞									
	0.000	0.010	0.050	0.100	0.150	0.200	0.300	0.400	0.500	0.585
0.00019	0.0021	0.96156	0.81869	0.66305	0.53056	0.41884	0.24882	0.13639	0.06699	0.03239
0.00019	0.0021	0.96263	0.82333	0.67078	0.54013	0.42925	0.25877	0.14428	0.07229	0.03568
0.00026	0.0139	0.96301	0.82502	0.67361	0.54365	0.43310	0.26249	0.14725	0.07433	0.03696
0.00026	0.0139	0.96398	0.82926	0.68075	0.55256	0.44287	0.27202	0.15497	0.07966	0.04035
0.00144	0.0081	0.96137	0.81786	0.66165	0.52884	0.41698	0.24705	0.13501	0.06606	0.03182
0.00144	0.0081	0.96166	0.81911	0.66375	0.53142	0.41978	0.24971	0.13709	0.06745	0.03267
0.00217	0.0455	0.96292	0.82460	0.67290	0.54277	0.43213	0.26156	0.14650	0.07381	0.03663
0.00217	0.0455	0.96330	0.82629	0.67574	0.54631	0.43601	0.26532	0.14953	0.07589	0.03794
0.00217	0.0455	0.96359	0.82756	0.67788	0.54898	0.43894	0.26817	0.15184	0.07748	0.03896
0.00295	0.0659	0.96205	0.82080	0.66655	0.53489	0.42354	0.25330	0.13992	0.06935	0.03384
0.00295	0.0659	0.96253	0.82290	0.67007	0.53925	0.42829	0.25785	0.14354	0.07179	0.03537
0.06473	0.0331	0.96214	0.82122	0.66725	0.53576	0.42449	0.25420	0.14064	0.06983	0.03414
0.06473	0.0331	0.96330	0.82629	0.67574	0.54631	0.43601	0.26532	0.14953	0.07589	0.03794
0.07579	0.0640	0.96292	0.82460	0.67290	0.54277	0.43213	0.26156	0.14650	0.07381	0.03663
0.07863	0.0664	0.96156	0.81869	0.66305	0.53056	0.41884	0.24882	0.13639	0.06699	0.03239
0.07863	0.0664	0.96263	0.82333	0.67078	0.54013	0.42925	0.25877	0.14428	0.07229	0.03568
0.09916	0.8910	0.95770	0.82027	0.63569	0.49717	0.38308	0.21574	0.11119	0.05077	0.02278
0.09916	0.8910	0.95867	0.80619	0.64242	0.50531	0.39172	0.22357	0.11701	0.05441	0.02488
0.11990	0.1475	0.96118	0.81702	0.66026	0.52712	0.41512	0.24529	0.13363	0.06515	0.03127
0.11990	0.1475	0.96156	0.81869	0.66305	0.53056	0.41884	0.24882	0.13639	0.06699	0.03239
0.30240	0.2340	0.96311	0.82544	0.67432	0.54454	0.43407	0.26343	0.14801	0.07484	0.03728
0.30240	0.2340	0.96398	0.82926	0.68075	0.55256	0.44287	0.27202	0.15497	0.07966	0.04035
0.39091	0.8270	0.96398	0.82926	0.68075	0.55256	0.44287	0.27202	0.15497	0.07966	0.04035
0.49082	0.1940	0.96514	0.83438	0.68941	0.56344	0.45489	0.28392	0.16477	0.08657	0.04484
1.22741	0.3490	0.96592	0.83781	0.69524	0.57081	0.46308	0.29214	0.17164	0.09151	0.04811
1.22741	0.3490	0.96524	0.83481	0.69013	0.56436	0.45591	0.28493	0.16561	0.08717	0.04524
1.22741	0.3490	0.96893	0.85124	0.71833	0.60031	0.49625	0.32629	0.20109	0.11344	0.06319
2.02024	0.6525	0.96738	0.84428	0.70632	0.58490	0.47885	0.30819	0.18531	0.10153	0.05490
2.02024	0.6525	0.96689	0.84212	0.70261	0.58017	0.47353	0.30275	0.18064	0.09807	0.05254
2.02024	0.6525	0.96796	0.84689	0.71080	0.59063	0.48530	0.31486	0.19108	0.10584	0.05787
2.75371	2.8900	0.96816	0.84775	0.71230	0.59256	0.48747	0.31711	0.19304	0.10732	0.05890
6.52757	6.0300	0.96738	0.84428	0.70632	0.58490	0.47885	0.30819	0.18531	0.10153	0.05490
6.52757	6.0300	0.96962	0.85430	0.72364	0.60718	0.50406	0.33454	0.20841	0.11908	0.06721
6.52757	6.0300	0.97030	0.85738	0.72900	0.61413	0.51200	0.34300	0.21600	0.12500	0.07147
8.98150	3.5500	0.97431	0.87560	0.76118	0.65644	0.56105	0.39701	0.26632	0.16609	0.10250
11.7571	1.9600	0.97303	0.86978	0.75083	0.64272	0.54501	0.37902	0.24921	0.15177	0.09143
18.2520	1.1600	0.97225	0.86622	0.74452	0.63441	0.53537	0.36836	0.23923	0.14359	0.08522
18.2520	1.1600	0.97382	0.87335	0.75718	0.65113	0.55483	0.38999	0.25961	0.16043	0.09810
18.2520	1.1600	0.97167	0.86355	0.73983	0.62826	0.52825	0.36056	0.23201	0.13774	0.08084
38.0915	2.4800	0.97676	0.88690	0.78150	0.68366	0.59324	0.43404	0.30260	0.19751	0.12771
38.0915	2.4800	0.97460	0.87695	0.76359	0.65965	0.56482	0.40128	0.27044	0.16958	0.10525
38.0915	2.4800	0.97519	0.87965	0.76843	0.66611	0.57243	0.40996	0.27885	0.17678	0.11095
41.3100	8.1000	0.97902	0.89742	0.80067	0.70970	0.62448	0.47115	0.34033	0.23165	0.15634
75.6315	7.3500	0.97245	0.86710	0.74610	0.63648	0.53776	0.37100	0.24169	0.14559	0.08673
75.6315	7.3500	0.97245	0.86710	0.74610	0.63648	0.53776	0.37100	0.24169	0.14559	0.08673
78.1029	31.900	0.97676	0.88690	0.78150	0.68366	0.59324	0.43404	0.30260	0.19751	0.12771
79.8642	36.150	0.97931	0.89880	0.80320	0.71317	0.62868	0.47622	0.34558	0.23651	0.16052
83.5212	58.100	0.97627	0.88463	0.77739	0.67813	0.58666	0.42637	0.29497	0.19078	0.12222
101.241	54.700	0.97843	0.89466	0.79562	0.70281	0.61618	0.46117	0.33006	0.22221	0.14831
267.187	34.050	0.98425	0.92215	0.84665	0.77354	0.70288	0.56919	0.44615	0.33448	0.24918
488.775	47.500	0.98573	0.92928	0.86014	0.79263	0.72681	0.60047	0.48168	0.37113	0.28432
2041.20	48.600	0.98672	0.93405	0.86925	0.80561	0.74321	0.62227	0.50692	0.39777	0.31046
2530.48	79.700	0.98642	0.93262	0.86650	0.80170	0.73825	0.61565	0.49921	0.38958	0.30237
7156.45	112.70	0.98623	0.93166	0.86468	0.79909	0.73496	0.61127	0.49414	0.38422	0.29710

concentration $\varphi = 0$.

Drag Coefficient for a suspension of spheres

From equations (6.10) and (7.5) we deduce that:

$$\tilde{\delta}_0^2 = \delta_0^2 f_p(\varphi) f_q(\varphi) \quad (7.15)$$

$$\tilde{C}_0^{1/2} \tilde{\delta}_0^2 = C_0^{1/2} \delta_0^2 f_p^{3/2}(\varphi) \quad (7.16)$$

therefore, the parameters of the Drag Coefficient are:

$$\tilde{C}_0 = C_0 f_p(\varphi) f_q^{-2}(\varphi) \quad (7.17)$$

$$\tilde{\delta}_0 = \delta_0 f_p^{1/2}(\varphi) f_q^{1/2}(\varphi) \quad (7.18)$$

and the Drag Coefficient of the sphere can be written

in the form:

$$C_D = C_0 f_p(\varphi) f_q^{-2}(\varphi) \left(1 + \frac{\delta_0 f_p^{1/2}(\varphi) f_q^{1/2}(\varphi)}{Re^{1/2}} \right)^2 \quad (7.19)$$

and substituting the values of the parameters:

$$C_D = 0.28 f_p(\varphi) f_q^{-2}(\varphi) \left(1 + \frac{\delta_0 f_p^{1/2}(\varphi) f_q^{1/2}(\varphi)}{Re^{1/2}} \right)^2$$

8. Sedimentation of Isometric Particles

The behavior of non-spherical particles is different than that of spherical particles during sedimentation.

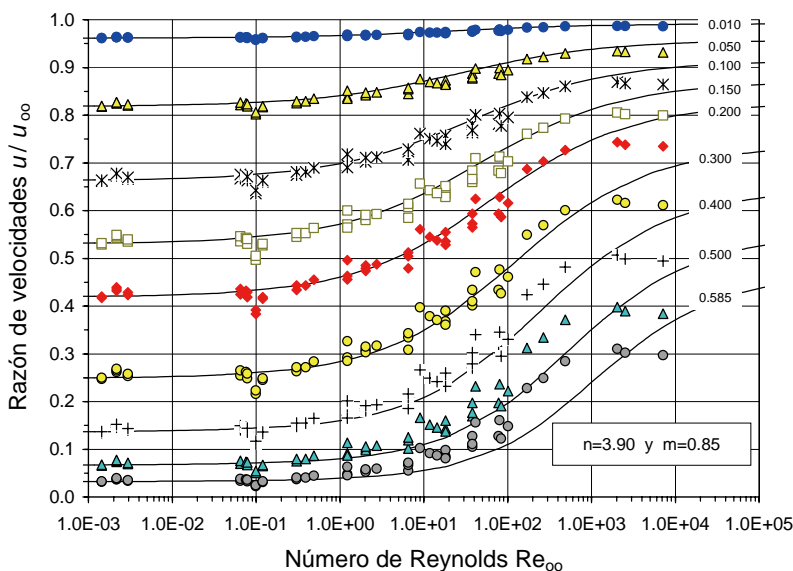


Fig. 7.1 Dimensionless settling velocities versus Reynolds number, together with data obtained from Richardson and Zaki (1954) experimental results.

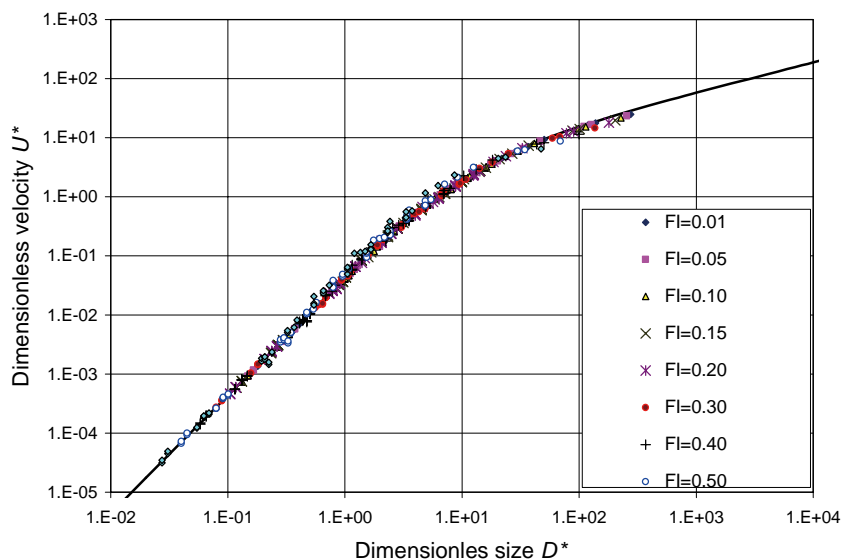


Fig. 7.2 Dimensionless velocity U^* for suspensions of spheres of any size and density versus the dimensionless diameter D^* , with experimental data of Richardson and Zaki (1954).

While spherical particles fall in a vertical trajectory, non-spherical particles rotate, vibrate and follow spiral trajectories. Several authors have studied the sedimentation of *isometric particles*, which have a high degree of symmetry with three equal mutually perpendicular symmetry axes, such as the tetrahedron, octahedron and dodecahedron. Wadell (1932, 1934), Pettyjohn and Christiansen (1948) and Christiansen and Barker (1965) show that isometric particles follow vertical trajectories at low Reynolds numbers, but rotate and vibrate and show helicoidally trajectories for Reynolds numbers between 300 and 150.000.

Pettyjohn and Christiansen (1948) demonstrate

that velocities in Stokes flow for isometric particles may be described with the following expression:

$$\frac{u_p}{u_e} = 0.843 \log \left(\frac{\psi}{0.065} \right) \quad \text{with} \quad u_e = \frac{\Delta \rho d_e^2 g}{18 \mu_f} \quad (8.1)$$

where d_e is the volume equivalent diameter, that is, the diameter of a sphere with the same volume as the particle, and u_e is its settling velocity

In the range of $2.000 \leq Re \leq 17.000$, the same authors derived the following equation for the settling velocity:

$$u_e = \frac{4}{3} \frac{\Delta \rho d_e g}{\rho_f C_D}, \quad (8.2)$$

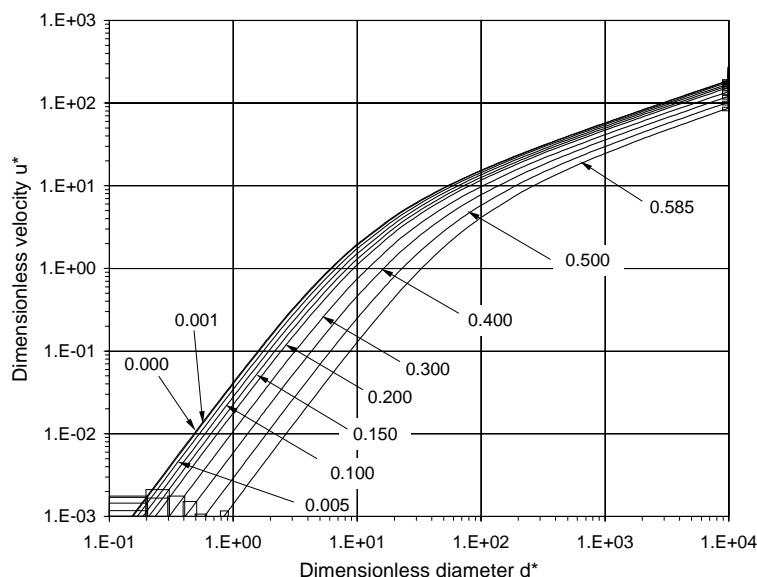


Fig. 7.3 Simulation of the dimensionless velocity u^* versus the dimensionless size d^* for spherical particles settling in a suspension in water at 20°C with the volume fraction of solids a parameter.

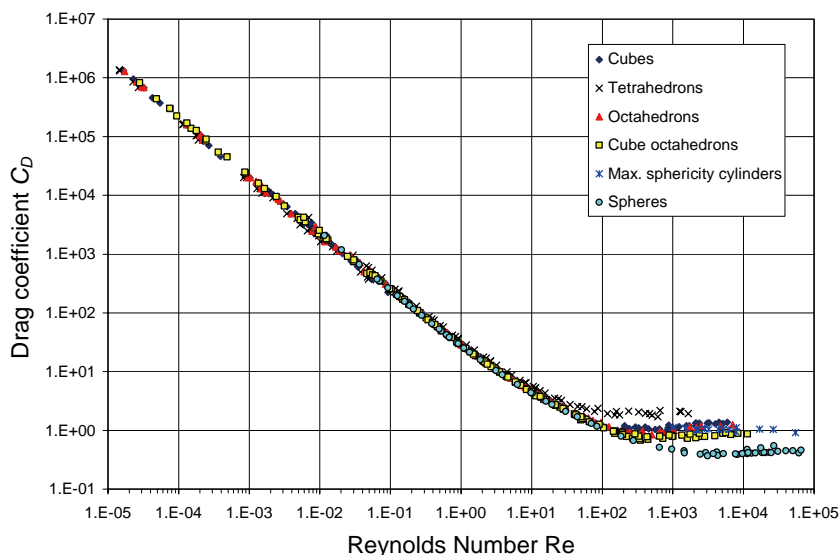


Fig. 8.1 Plot of the drag coefficient versus de Reynolds number for the settling of isometric particles according to Pettyjohn and Christiansen (1948), and Barker (1951).

with the drag coefficient C_D given by: $C_D = (5.31 - 4.88\psi)/(1.433 \times 0.43)$. The value of 1.433 in the denominator of this equation is a factor that takes the theoretical value of $C_D = 0.3$ to the average experimental value $C_D = 0.43$.

As we have already said, for $Re > 300$, the particles begin to rotate and oscillate, which depends on the particle density. To take into account these behaviors, Barker (1951) introduced the particle to fluid density ratio as a new variable in the form:

$$C_D(\psi, \lambda) = \lambda^{1/18} \frac{(5.31 - 4.88\psi)}{0.62}, \quad (8.3)$$

where λ is the quotient between the solid and fluid densities $\lambda = \rho_p/\rho_f$. Data from Pettyjohn and Christiansen (1948) and from Barker (1951) are plotted in **Fig. 8.1**. **Fig. 8.2** gives details of the higher Reynolds end.

Drag coefficient and sedimentation velocity

All the results obtained for spherical particles (Concha y Almendra 1979a, 1979b), may be used to develop functions for the drag coefficient and sedimentation velocity of isometric particles.

Assume that equation (5.11) and (6.10) are valid

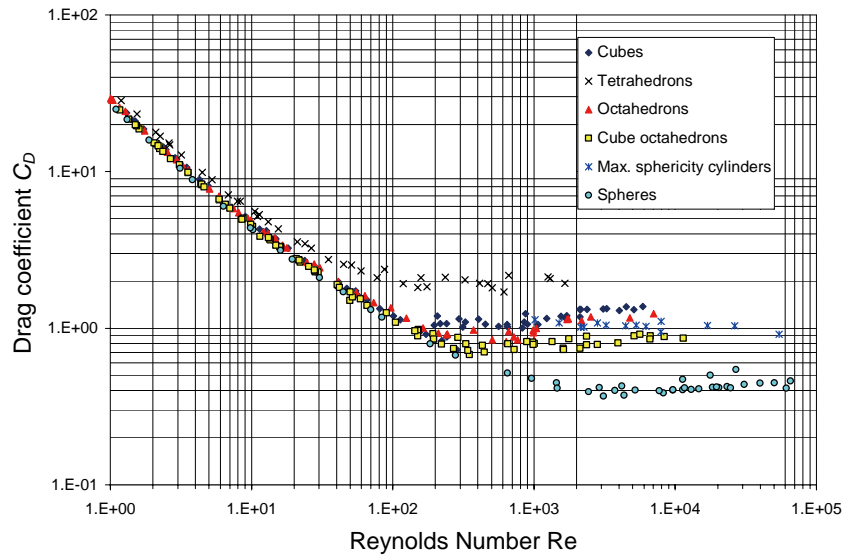


Fig. 8.2 Details for Fig 4.17 at the high Reynolds number end. (Pettyjohn and Christiansen 1948, and Barker 1951).

for isometric particles, with values of C_0 and δ_0 as functions of the sphericity ψ and of the density quotient λ (Concha y Barrientos 1986):

$$C_D(\psi, \lambda) = \tilde{C}_0(\psi, \lambda) \left(1 + \frac{\delta_0(\psi, \lambda)}{Re^{1/2}}\right)^2 \quad (8.4)$$

$$u_p^* = \frac{1}{4} \frac{\tilde{\delta}_0^2(\psi, \lambda)}{d^*} \left\{ \left(1 + \frac{4}{\tilde{C}_0^{1/2}(\psi, \lambda) \tilde{\delta}_0^2(\psi, \lambda)} d^{*3/2}\right)^{1/2} - 1 \right\}^2 \quad (8.5)$$

where the Reynolds number is defined using the volume equivalent diameter.

To determine the equation's parameters assume that:

$$\tilde{C}_0(\psi, \lambda) = C_0 f_A(\psi) f_C(\lambda) \quad (8.6)$$

$$\tilde{\delta}_0(\psi, \lambda) = \delta_0 f_B(\psi) f_D(\lambda) \quad (8.7)$$

where C_0 and δ_0 are the same parameters of a sphere.

Assume that we can approximate the velocity of isometric particles at low Reynolds number, $Re \rightarrow 0$, in the same way as for spherical particles. Then:

$$u_e^* = \frac{d_e^{*2}}{C_0 \delta_0^2} \quad \text{and} \quad u_p^* = \frac{d_e^{*2}}{\tilde{C}_0(\psi, \lambda) \tilde{\delta}_0^2(\psi, \lambda)} \quad (8.8)$$

Taking the quotient of these terms and substituting (8.6) and (8.7), results in:

$$Re \rightarrow 0, \quad \frac{u_e^*}{u_p^*} \equiv \frac{u_e}{u_p} = f_A(\psi) f_B^2(\psi) f_C(\lambda) f_D^2(\lambda) \quad (8.9)$$

On the other hand, for $Re \rightarrow \infty$:

$$\frac{C_D(\psi, \lambda)}{C_D} = \frac{\tilde{C}_0(\psi, \lambda)}{C_0} \quad \text{and} \quad \frac{C_D(\psi, \lambda)}{C_D} = f_A(\psi) f_C(\lambda) \quad (8.10)$$

To determine the functions f_A , f_B , f_C and f_D we will use the correlations presented by Pettyjohn and Christiansen (8.13) and (8.15), and by Barker (1951). From (8.9) and (8.10) we can write:

$$f_A(\psi) f_B^2(\psi) f_C(\lambda) f_D^2(\lambda) = \left\{ 0.843 \log \frac{\psi}{0.065} \right\}^{-1} \quad (8.11)$$

$$f_A(\psi) f_C(\lambda) = \lambda^{1/18} \frac{5.31 - 4.88\psi}{0.62} \quad (8.12)$$

From (8.10) and (8.12) we deduce that:

$$f_A(\psi) = \frac{5.31 - 4.88\psi}{0.62} \quad f_C(\lambda) = \lambda^{1/18} \quad (8.13)$$

Since in Stokes regime the density does not influences the flow, equation (8.11) implies that:

$$f_C(\lambda) f_D^2(\lambda) = 1 \quad \Rightarrow \quad f_D(\lambda) = \lambda^{-1/36} \quad (8.14)$$

therefore

$$f_B(\psi) = \left\{ \frac{5.31 - 4.88\psi}{0.62} \times 0.843 \log \frac{\psi}{0.065} \right\}^{-1/2} \quad (8.15)$$

The following figures show the drag coefficients of isometric particles and the dimensionless settling velocities versus the dimensionless particle size.

The experimental data used in the previous correlations are 655 points including spheres, cubes-octahedrons, maximum sphericity cylinders, octahedrons and tetrahedrons in the following ranges:

0.1cm	<de<	5cm
1.7g/cm ³	<p _s <	11.2 g/cm ³
0.67	<ψ<	1
0.87g/cm ³	<p<	1.43g/cm ³
9 × 10 ³ g/cm-s	<μ<	900g/cm-s
5 × 10 ³	<Re<	2 × 10 ⁴

with the following values for the particles sphericity

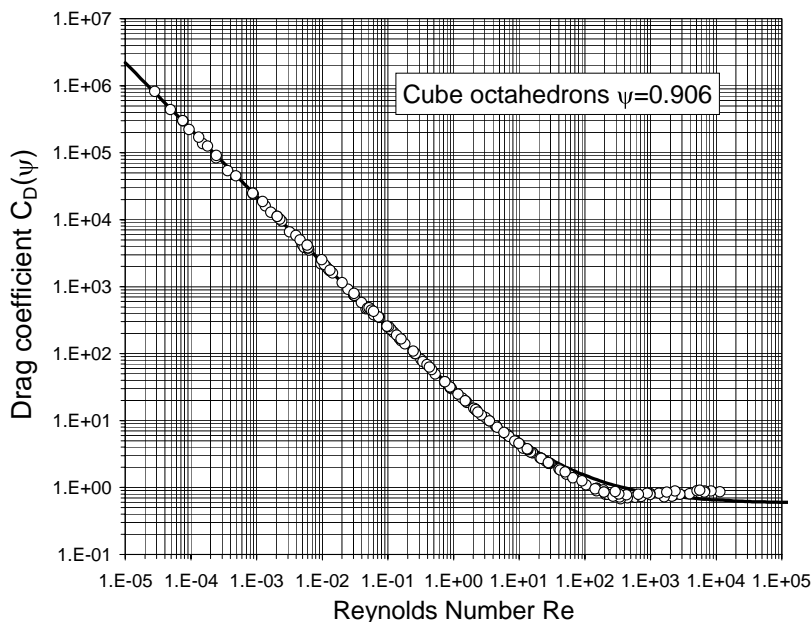


Fig. 8.3a Simulation with Concha and Barrientos' equation (8.4) and experimental values for isometric particles from Pettyjohn and Christiansen (1948) and Barker (1951) for cube octahedrons.

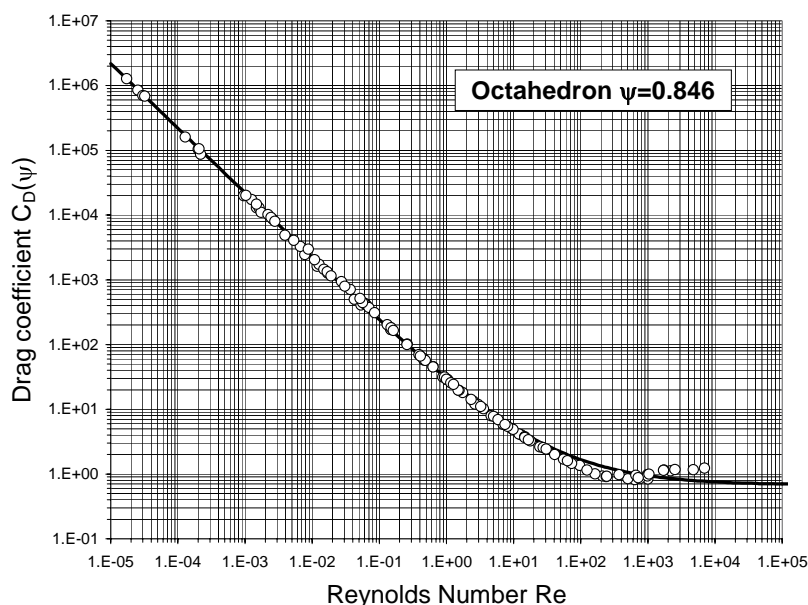


Fig. 8.3b Simulation with Concha and Barrientos' equation (8.4) and experimental values for isometric particles from Pettyjohn and Christiansen (1948) and Barker (1951) for octahedrons.

(Happel and Brenner 1965; Barker 1951) and the parameters of Concha and Barrientos (1986)

Alternative equations for isometric particles were proposed by Ganser (1993):

$$C_D = \frac{1}{K_1} \frac{24}{Re} \left\{ 1 + 0.1118 (K_1 K_2 Re)^{0.6567} \right\} + \frac{0.4305 K_1 K_2^2 Re}{3305 + K_1 K_2 Re} \quad (8.16)$$

	ψ	$f_A(\psi)$	$f_B(\psi)$
Sphere	1.000	1.0000	1.0000
Cube octahed	0.906	1.4334	0.8826
Octahedron	0.846	1.9057	1.2904
Cube	0.806	2.2205	1.5468
Tetrahedron	0.670	3.2910	2.3108
Max sph cylin	0.875	1.6774	1.0966

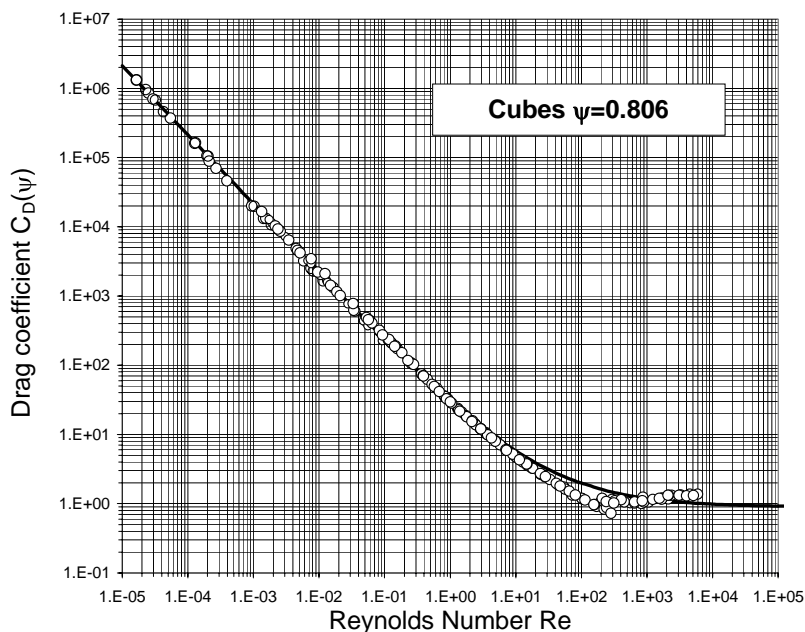


Fig. 8.3c Simulation with Concha and Barrientos' equation (8.4) and experimental values for isometric particles from Pettyjohn and Christiansen (1948) and Barker (1951) for cubes.

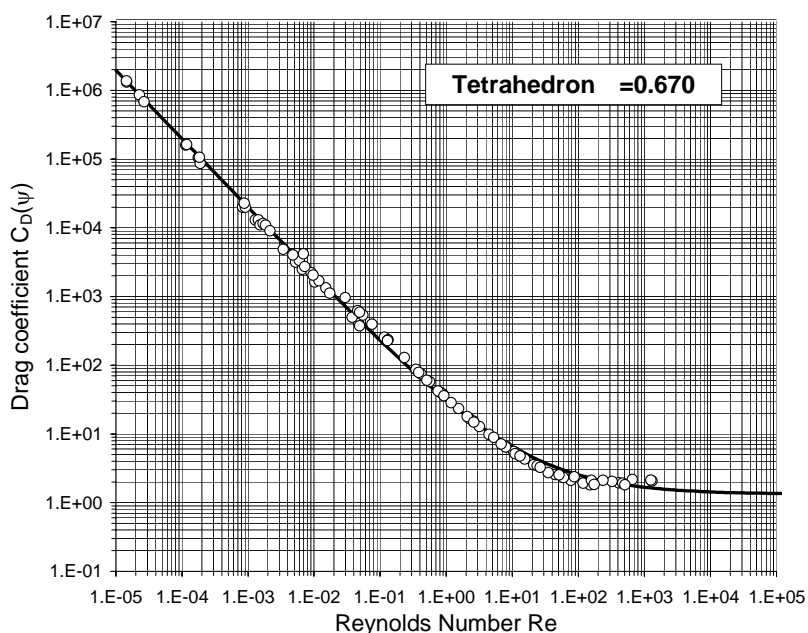


Fig. 8.3d Simulation with Concha and Barrientos' equation (8.4) and experimental values for isometric particles from Pettyjohn and Christiansen (1948) and Barker (1951) for tetrahedrons.

where

$$K_1 = \left(\frac{1}{3} + \frac{2}{3} \psi^{-1/2} \right)^{-1},$$

$$K_2 = 10^{1.8148(-\log \psi)^{0.5743}} \quad (8.17)$$

9. Sedimentation of Particles of Arbitrary Shape

Concha and Christiansen (1986) extended the validity of equations (6.4) and (6.5) to suspensions of

particles of arbitrary shape.

$$C_D(\psi, \lambda, \varphi) = \tilde{C}_0(\psi, \lambda, \varphi) \left(1 + \frac{\delta_0(\psi, \lambda, \varphi)}{Re^{1/2}} \right)^2 \quad (9.1)$$

$$u_p^*(\psi, \lambda, \varphi) = \frac{1}{4} \frac{\delta_0^2(\psi, \lambda, \varphi)}{d_*} \left\{ \left(1 + \frac{4}{\tilde{C}_0^{1/2}(\psi, \lambda, \varphi) \delta_0^2(\psi, \lambda, \varphi)} d_*^{3/2} \right)^{1/2} - 1 \right\}^2 \quad (9.2)$$

where ψ , λ and φ are the *hydrodynamic sphericity* of the particles, the density ratio of solid and fluid and

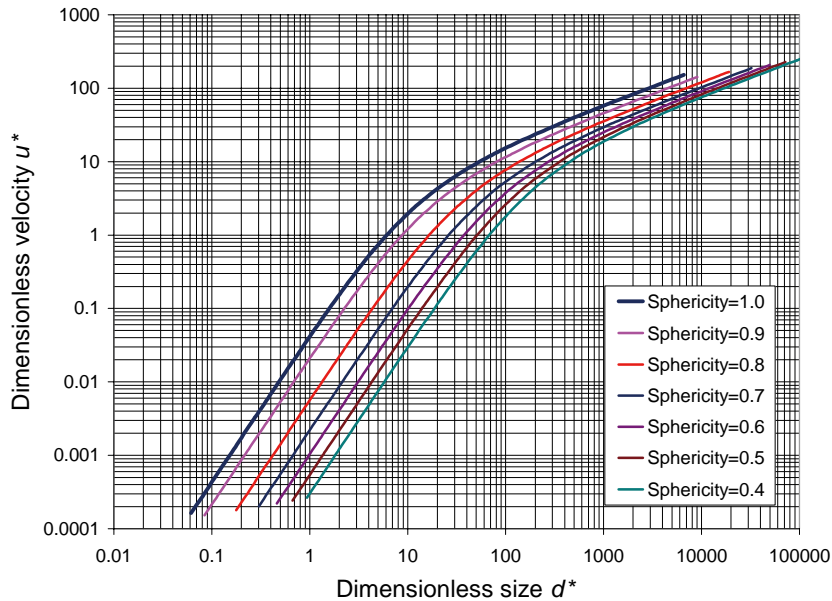


Fig. 8.4 Dimensionless size versus dimensionless velocity for isometric particles according to Concha and Barrientos equation (8.5).

the volume fraction of solid in the suspension.

Similarly as in the case of isometric particles, they assumed that the functions \tilde{C}_0 and $\tilde{\delta}_0$ may be written in the form:

$$\tilde{C}_0(\psi, \lambda, \varphi) = C_0 f_A(\psi) f_C(\lambda) f_p(\varphi) f_q^{-2}(\varphi) \quad (9.3)$$

$$\tilde{\delta}_0(\psi, \lambda, \varphi) = \delta_0 f_B(\psi) f_D(\lambda) f_F(\varphi) f_p^{1/2}(\varphi) f_q^{1/2}(\varphi) \quad (9.4)$$

with $f_A(\psi) = \frac{5.31-4.88\psi}{0.62}$ (9.5)

$$f_B(\psi) = \left\{ \frac{5.31-4.48\psi}{0.62} \times 0.843 \log \frac{\psi}{0.065} \right\}^{-1/2} \quad (9.6)$$

$$f_C(\lambda) = \lambda^{1/18} \quad f_D(\lambda) = \lambda^{-1/36} \quad (9.7)$$

$$f_p(\varphi) = (1 - \varphi)^{-2.033}, \quad f_q(\varphi) = (1 - \varphi)^{-0.167} \quad (9.8)$$

Hydrodynamic sphericity

Concha y Christiansen (1986) found it necessary to define a *hydrodynamic shape factor* to be used with the above equations, since the usual methods to measure sphericity did not gave good results. They defined the *effective hydrodynamic sphericity* of a particle as the *sphericity of an isometric particle having the same drag (volume) and the same settling velocity as the particle*.

The hydrodynamic sphericity may be obtained by performing sedimentation, or fluidization experiments, calculating the drag coefficient for the particle using the volume equivalent diameter and obtaining the sphericity (defined for isometric particles) that fit the experimental value.

Modified drag coefficient and sedimentation velocity

A unified correlation can also be obtained for the drag coefficient and the sedimentation velocity of irregular particles forming a suspension. Defining C_{DM} , Re_M , d_{eM}^* and u_{pM}^* in the following form:

$$C_{DM} = \frac{C_D(\psi, \lambda)}{f_A(\psi) f_C(\lambda) f_p(\varphi)} \quad Re_M = \frac{Re}{f_B^2(\psi) f_D^2(\lambda) f_p^2(\varphi)}$$

$$d_{eM}^* = \frac{d_e^*(\psi, \lambda)}{f_p(\varphi) \times (f_A(\psi)^{1/2} \times f_B^2(\psi) \times f_C(\lambda)^{1/2} \times f_D^2(\lambda))^{2/3}} \quad (9.9)$$

$$u_{pM}^* = \frac{u_p^*(\psi, \lambda)}{f_B(\psi) f_D(\lambda) f_q(\varphi)} \quad (9.10)$$

$$u_{pM}^* = \frac{u_p^*(\psi, \lambda)}{f_B(\psi) f_D(\lambda) f_q(\varphi)} \quad (9.11)$$

Fig. 9.1 and **9.2** show the unified correlations for the data from Concha and Christiansen (1986).

Ganser (1993) proposed an empirical equation for the drag coefficient of non-spherical non-isometric particles, including irregular particles, similar to that given earlier for spherical particles (8.16), but with different values for the parameters K_1 .

$$C_D = \frac{1}{K_1} \frac{24}{Re} \left\{ 1 + 0.1118 (K_1 K_2 Re)^{0.6567} \right\} + \frac{0.4305 K_1 K_2 Re}{3305 + K_1 K_2 Re} \quad (9.12)$$

where

$$K_1 = \left(\frac{1}{3} \frac{d_p}{d_e} + \frac{2}{3} \psi^{-1/2} \right)^{-1}, \quad K_2 = 10^{1.8148(-\log \psi)^{0.5743}} \quad (9.13)$$

In equation (9.13) for K_1, d_e and d_p are the *volume equivalent* and the *projected area equivalent* diameters of the irregular particle respectively.

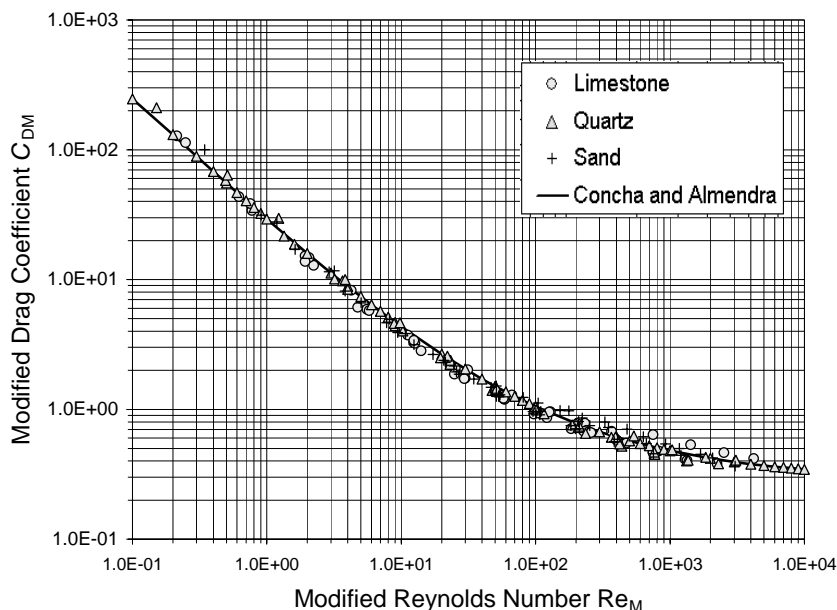


Fig. 9.1 Unified drag coefficient versus Reynolds number for quartz, limestone and sand particles (The same data of Fig. 4.20 (Concha y Christiansen 1986).

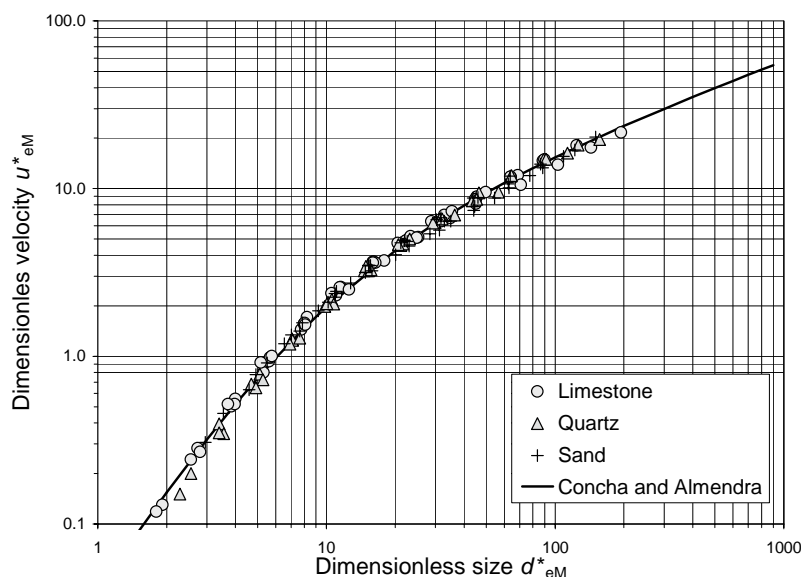


Fig. 9.2 Unified sedimentation velocity versus size for limestone, quartz and sand particles (The same data of Fig. 4.20 (Concha y Christiansen 1986).

Finally, it is interesting to mention the work of Yin et al (2003) who analyzed the settling of cylindrical particles analytically, and obtained, by linear and angular momentum balances, the forces and torques applied to the particle during its fall. Using Ganser's equation for the drag coefficient, they solved the differential equations of motion numerically obtaining results close to those measured experimentally by them.

Acknowledgments

This paper was financed by INNOVA Project CM0117 and AMIRA Project p996.

References

Abraham, F.F. (1979): Functional dependence of the drag coefficient of a sphere on Reynolds Number. Phys. Fluid, 13, pp.2194-2195.

- Barker H. (1951): The effect of shape and density on the free settling rates of particles at high Reynolds Numbers, Ph.D. Thesis, University of Utah, Table 7, pp.124-132; Table 9, pp.148-153.
- Barnea, E. and Mitzrahi, J. (1973): A generalized approach to the fluid dynamics of particulate systems, 1. General correlation for fluidization and sedimentation in solid multiparticle systems, Chem. Eng. J., 5, pp.171-189.
- Barnea, E. And Mednick, R.L. (1975): Correlation for minimum fluidization velocity, Trans. Inst. Chem. Eng., 53, pp.278-281.
- Batchelor, G.K. (1967): "An Introduction for Fluid Dynamics", Cambridge University Press, Cambridge, 262p.
- Brauer, H. and Sucker, D. (1976): Umströmung von Platten, Zylindern un Kugeln, Chem. Ing. Tech., 48, 665-671.
- Chabra, R. P., Agarwal, L. And Sinha, N.K. (1999): Drag on non-spherical particles: An evaluation of available methods., Powder Tech., 101, pp.288-295.
- Concha F., and Almendra, E.R. (1979a): Settling Velocities of Particulate Systems, 1. Settling velocities of individual spherical particles. Int. J. Mineral Process., 5, pp.349-367.
- Concha F., and Almendra, E.R. (1979b): Settling Velocities of Particulate Systems, 2. Settling velocities of suspensions of spherical particles. Int. J. Mineral Process., 6, pp.31-41.
- Concha F., and Barrientos, A. (1986): Settling Velocities of Particulate Systems, 4. Settling of no spherical isometric particles. Int. J. Mineral Process., 18, pp.297-308.
- Concha F., and Christiansen, A. (1986): Settling Velocities of Particulate Systems, 5. Settling velocities of suspensions of particles of arbitrary shape. Int. J. Mineral Process., 18, pp.309-322.
- Christiansen, E.B. and Barker, D.H. (1965): The effect of shape and density on the free settling rate of particles at high Reynolds Numbers, AIChE J., 11(1), pp.145-151.
- Darby, R. (1996): Determining settling rates of particles, Chem. Eng., December, pp.109-112.
- Fage, A. (1937): Experiments on a sphere at critical Reynolds Number, Rep. Mem. Aero. Res. Counc. London, N° 1766, pp. 108, 423.
- Flemmer, R. L., Pickett, J. and Clark, N.N. (1993): An experimental study on the effect of particle shape on fluidization behavior, Powder Tech. 77, pp.123-133.
- Ganguly, U.P. (1990): On the prediction of terminal settling velocity in solids-liquid systems, Int. JI. Mineral Process., 29, pp.235-247.
- Ganser, G.H. (1993): A rational approach to drag prediction of spherical and non-spherical particles, 1993. Powder Tech., 77, pp/143-152.
- Goldstein, S., Editor (1965): "Modern Development in Fluid Dynamics, Vol. I and II", Dover, New York, N.Y., 702 pp.
- Gurtin, M.E. (1981): "An Introduction to Continuum Mechanics", Academic Press, New York, p.121.
- Haider, A. and Levenspiel, O. (1998): Drag coefficient and terminal velocity of spherical and non-spherical particles, Powder Techn., 58, pp.63-70.
- Happel, J. and Brenner, H. (1965): "Low Reynolds Hydrodynamics", Prentice-Hall, Inc, Englewood Cliffs N.J., USA, p.220.
- Heywood, H. (1962): Uniform and non-uniform motion of particles in fluids. In Proceeding of the Symposium on the Interaction between Fluid and Particles, Inst. of Chem. Eng., London, pp.1-8.
- Isaacs, J. and Thodos, G. (1967): The free-settling of solid cylindrical particles in the turbulent regime., The Canadian J. of Chem. Eng., 45, pp.150-155.
- Lapple, C.E. and Shepherd, C.B. (1940): Calculation of particle trajectories, Ind. Eng. Chem., 32, p.605.
- Lee, K and Barrow, H. (1968): Transport process in flow around a sphere with particular reference to the transfer of mass, Int. JI. Heat and mass Transfer, 11, p.1020.
- Massarani, G. e Costapinto, C. (1980): Forca resistiva sólido.fluido em sistemas particulados de porosidad elevada, Revista Brasileira de tecnologia, 11, (1) pp.45-50.
- Massarani, G. (1984): Problemas em Sistemas Particulados, Blücher Ltda., Rio de Janeiro, Brazil, pp.102-109.
- Newton, I. (1687): "Filosofiae naturalis principia mathematica", London.
- Nguyen, A.V., Stechemesser, H., Zobel, G. and Schulze, H. J. (1997): An improved formula for terminal velocity of rigid spheres, Int. JI. Mineral Process., 50, pp.53-61.
- Richardson, J. F. and Zaki, W.N. (1954): Sedimentation and fluidization: Part I. Trans. Inst. Chem. Eng., 32, pp.35-53.
- Pettyjohn, E. S. and Christiansen, E. B. (1948): Effect of particle shape on free-settling of isometric particles, Chem. Eng. Progress, 44 (2), pp.157-172.
- Rosenhead, L. Editor (1963): "Laminar Boundary Layers", Oxford University Press, , pp.87, 423, 687.
- Schlichting, H. (1968): "Boundary Layer Theory", McGraw-Hill, New York, N.Y., p. 747.
- Stokes, G.G. (1844): On the theories of internal friction of fluids in motion and of the equilibrium and motion of elastic solids, Trans. Cambr. Phil. Soc., 8 (9), pp.287-319.
- Taneda, S. (1956): Rep. Res. Inst. Appl. Mech., Kyushu University, 4, p.99.
- Thomson, T. and Clark, N.N. (1991): A holistic approach to particle drag prediction, Powder tech., 67, pp.57-66.
- Tomotika, A. R. A. (1936): Reports and Memoranda N° 1678,. See also Goldstein 1965, p.498.
- Tory, E. M. (1996): Sedimentation of small particles in a viscous fluid, Computational Mechanics Publications Inc., Ashurst Lodge, Ashurst Southampton, UK.
- Tsakalis, K. G. and Stamboltzis, G.A. (2001): Prediction of the settling velocity of irregularly shaped particles, Minerals Engineering, 14 (3), pp.349-357.
- Tourton, R. and Clark, N.N. (1987): An explicit relationship to predict spherical terminal velocity, Powder Techn., 53, pp.127-129.
- Tourton, R. and Levenspiel, O. (1986): A short Note on the drag correlation for spheres, 47, pp.83-86.
- Zigrang, D.J. and Sylvester, N.D. (1981): An explicit equation for particle settling velocities in solid-liquid systems, AIChE J., 27, pp.1043-1044.

Author's short biography



Fernando Concha Arcil

Fernando Concha Arcil obtained a Bachelor degree in Chemical Engineering at the University of Concepción in Chile in 1962 and a Ph.D. in Metallurgical Engineering from the University of Minnesota in 1968. He is professor at the Department of Metallurgical Engineering, University of Concepción. His main research topic is the application of transport phenomena to the field of Mineral Processing. He has published four books: *Modern Rational Mechanics*, *Design and Simulation of Grinding-Classification Circuits and Filtration and Separation*, all in Spanish, and *Sedimentation and Thickening: Phenomenological Foundation and Mathematical Theory* in English. He also has published more than 100 technical papers in international journals. For his work in sedimentation with applications to hydrocyclones and thickeners he received the Antoine Gaudin Award 1998, presented by the American Society for Mining Metallurgy and Exploration, SME.

Mechanochemical Activation for Resolving the Problems of Catalysis[†]

R.A. Buyanov, V.V. Molchanov and V.V. Boldyrev

Institute of Catalysis RAS, Institute of Solid State Chemistry and Mechanochemistry, Novosibirsk State University¹

Abstract

The role of structure-energy properties of the mechanically induced defects of the crystal structure of heterogeneous catalysts is considered here. The main concepts of the effect of mechanochemical activation on the activity and selectivity of catalysts are theoretically stated. The most promising research trends are presented.

Keywords: mechanochemistry, catalysis, catalysis preparation change of activity and selectivity

1. Introduction and Definition of the Problem

The development of mechanochemical activation (MCA) of solids and the appearance of high-energy tense mills have shown the considerable promise of this method. In the last years, the possibilities of MCA have drawn the attention of specialists in catalysis.

During MCA, a solid (a catalyst in our case) accumulates excess potential energy as elastic and plastic deformations and a great variety of defects, which is accompanied by an increase in its reactivity. The reactivity of a system is universal in that a simultaneous decrease in its thermodynamic potential tend to a simultaneous decrease. This tendency can involve different relaxation channels, which allow synthesis of catalysts with new properties, reduction of the number of stages in its production, and also acceleration of the catalytic reactions.

In the present work we make an attempt to consider peculiarities of the synthesis process and the preparation of catalysts using MCA, the nature of its effect on catalytic activity and selectivity and thus to define the problem in detail.

2. Plausible MCA Applications in Catalysis

The Principle Sections of Catalysis are as Follows:

2.1. Development of the scientific basis of catalyst preparation.

The content of this division/section is determined by its main problem, i.e. development of the methods of preparation of catalysts with the desired properties. These are: specific surface area, porous structure, phase composition, crystallization degree, morphological properties of crystals, defectiveness, dispersion, thermal stability, structural and mechanical properties, component distributions on the supports, etc.

To solve the problem, one should investigate the physicochemical regularities which determine the features of synthesis and the action of materials during all stages of the method chosen for the preparation of separate families of similar materials, catalysts in our case¹⁾.

2.2. Development of the scientific basis for prediction of catalytic action

This section includes the most complicated and important problems, such as:

- Chemical nature, structure and mechanism of action of active sites during operation on the catalyst surface;
- Nature and relationships between the main and side reactions of catalytically active sites, the means and methods of influencing the above in order to increase selectivity towards the desired product;

[†] Accepted: September 25th, 2009

¹ Inst. Solid State Chemistry, Kutateladze, 18, 630128 Novosibirsk, Russia

* Corresponding author

E-mail: boldyrev@solid.nsk.su

TEL : 7-383-332 1550 FAX : 7-383-332 2847, 7-383-332 1550

- Nature of the effect and input of physical characteristics of the catalyst surface. The role of defects and energy-non-equilibrium states in the chemical nature and efficiency of active sites;
- Stability, resistance, lifetime of the active sites and reasons for their deactivation.

Let us consider specific features and potentialities of MCA in catalysis.

3. Preparation of Catalysts using MCA.

3.1. Brief review of the theoretical and practical backgrounds of the MCA application for catalyst preparations.

Traditional preparations of heterogeneous catalysts include, as a rule, several stages and exhibit a number of serious disadvantages. Thus, reactivity is usually increased by performing processes in solutions or high-temperature treatments. As a result, the known methods do not meet the present-day ecological and energetic requirements.

The development of high-efficiency mechanical activators made it possible to use MCA as an independent and in some cases as the main stage for increasing the reactivity of the solids involved in the catalyst preparation.

A considerable body of articles, reviews and monographs^{2,9)} is devoted to the theory and practical applications of MCA in the preparation of multicomponent solid systems. In this application field, the emphasis is placed on the processes occurring in the bulk mass. Phenomena occurring on the solid surface are of secondary importance and only assume critical importance if one considers the nature of catalytic actions.

Catalysts are specific products. For this reason, their synthesis by the interaction of solids should take into account the requirements imposed on the characteristics of such a product. Nevertheless, the main and already stated theoretical basis remains. The concepts described in the above works are as follows.

The MCA-based preparation technologies of two- and multi-component solid systems involve chemical and other interactions between solid ingredients. The rate of interactions is limited by such parameters as contact area, mass transfer processes and activation barriers.

Dispergation of solid phases increases a ratio between particle surfaces and their volumes and thus

increases the total contact area between the solid phases.

It was established²⁾ that MCA reactions in the solid mixtures follow two regimes. At a low intensity of MCA, solids undergo crushing. In this case, the reaction rate depends on the number and area of contacts between the reacting particles. At a high intensity of MCA, we observed the regime of plastic deformation, at least of one reacting component. This results in a contact throughout the whole surface of a hard-to-grind material. Note that in the initial period, the chemical interaction of components is a limiting process stage. As the formed product layer begins to isolate the reacting products from each other, the diffusion mass transfer regime begins to define the reaction rate.

Under conditions of plastic deformation, the solid phase takes on the properties of «a quasi-liquid». This state is associated with the formation of dislocations, linear and point defects, anion and cation vacancies and the appearance of external and internal interfaces, i.e. total disorder of crystals. Available data³⁾ suggest that for the vacancy mechanism of material transfer, the diffusion coefficient is proportional to the vacancies concentration. As the intensity of MCA is sufficiently high, the saturation with defects reaches the point where a solid transforms into «a cold melting» state.

The tension gradient noticeably affects mass transfer in such dissipative systems. The non-equilibrium system is responsible for the formation of a broad structure, energy, chemical and physical variety depending on the MCA intensity. This extends the area of objects and potentialities which may be of interest for catalysis and catalysts.

Allied mixtures (ionic salts, metals) subjected to MCA may be mixed at the atomic level via a dislocation-diffusion mechanism. Thus, mass transfer of substance occurs due to plastic yielding and diffusions resulting from moving of linear and point defects.

It was shown³⁾ that under conditions of elastic crystal deformation, the excess energy of MCA is distributed throughout the volume of dislocations and defects. Such energy distribution is thermodynamically more efficient than the uniform distribution through all interatomic bonds. This peculiarity of the substance crystalline state defines the nature of MCA conversions.

Synthesis of multicomponent systems under MCA conditions should be considered with regard to the thermodynamics of the processes. During MCA, the reacting solid phases increase the free energy store

(isobaric potential) $\Delta G = \Delta U - T \Delta S$, which is associated with equilibrium constant K by equation $\Delta G = -RT \ln K$. Such a relationship permits a seemingly paradox conclusion that it is possible to create super-equilibrium systems. However, this paradox can be explained from the standpoint of thermodynamics. Under MCA conditions, the energy of the reacting phases significantly differs from the reference data corresponding to the standard conditions. For this reason, non-equilibrium systems can appear under such conditions. As the energy stops dissipating, such energy-intensive systems undergo an extinction relaxation process towards standard characteristics. This is an activation process. Owing to internal friction and retardation of atoms, relaxation decays and complete equilibrium is not attained. A metastable non-equilibrium system appears^{7,9)}.

It is pertinent to note that some individual crystal materials, which were treated by MCA but did not experience chemical conversion, change their structure and properties to an extent that they could be taken as new substances having the composition of the initial substance.

This brief description of the present-day concepts of the mechanism, regularities and peculiar features of MCA is aimed at promoting an interest in this promising method and its application in the development of a scientific basis of the preparation technologies of catalysts¹⁾.

Let us mention some areas where significant results have been already obtained:

1. Changes of the technology stages employing solutions by the mechanically activated homogenization of systems or mechanical alloying, which permits one to obtain new structures and prevent ecologically harmful waste. The performance of direct synthesis of catalysts under MCA conditions (mechanochemical synthesis).
2. Syntheses of new solid materials (catalysts) due to an increase in the reactivity of the reacting solid phases under MCA conditions.
3. Preparations of non-equilibrium solid systems that cannot be prepared by traditional methods, including solid solutions whose concentrations are significantly higher than the equilibrium one.
4. A decrease in temperature and provision of an easy interaction of phases during further treatments as calcination, hydration, sorption, reduction, etc.
5. A decrease in the temperature of the synthesis of binary and more complex systems owing to MCA, resulting in improved structural and other characteristics.

6. Modifications of operation properties (formability, strength, texture, etc.).
7. Preparations of highly dispersed and nano-sized systems.
8. Simplifications of technologies by reducing the number of stages and aggregate costs.

3.2. Some results of MCA applications for catalyst preparations

We want to present several examples and researches to illustrate the potentialities of MCA in the preparation of catalysts.

Thus, by exposing the powder mixtures of metallic magnesium and iron group metals to MCA, it is possible to obtain a number of mechanical alloys that after subsequent hydrogenation in a hydrogen medium at 10-17 atm, permit the synthesis of new intermetallic hydrides Mg_2MH_x (where $M=Co, Fe$ and $x=5 \div 6$). These hydrides are unique catalysts of the hydrogenation of acetylene and diene hydrocarbons to mono olefins, the process selectivity being about 100%¹⁰⁾. The mechanism of hydrogenation has been established. Hydrogenation follows the stage mechanism in the low-temperature region and the heterogeneous-homogeneous radical mechanism at relatively high temperatures¹¹⁾.

The mechanochemical activation of the metal powders at a hydrogen pressure of 100 atm permitted the synthesis of two formerly unknown intermetallic hydrides as Mg_2NiH_6 and $MgCuH_2$ exhibiting hydrogenating abilities¹²⁾.

It was established that MCA strongly affects the properties of supports as well as nickel chlorides and nickel metals supported on them.

For Al_2O_3 , TiO_2 , ZnO , and $ZnAl_2O_4$, the following phenomena were observed: (1) an increase in the sorption ability of the supports regarding the metal; (2) a decrease in the temperature of reduction of nickel chloride with hydrogen by 200-300°, and (3) an increase in the activity of the supported metals in a number of catalytic reactions. MCA of $\gamma-Al_2O_3$ makes it possible to increase coke resistance, dispersion of the supported metals and catalytic activity of the supported catalysts^{13, 14)}.

We suggest a new synthesis method of heteropoly acids from molybdenum, tungsten and vanadium oxides. The method is very efficient for the synthesis of phosphorous-vanadium-molybdenum and phosphomolybdic acids. In contrast to the traditional syntheses including 6-8 stages, our method involves only 2-3 stages: MCA of oxides or their mixtures and the interaction with an aqueous phosphoric acid. We

synthesized a number of heteropoly acids described by the following formulae:



and $H_6P_2M_{18}O_{62}$, where $M=Mo$ or W , and $m = 0 \div 4$. These HPA are efficient catalysts in a series of commercial processes¹⁵⁾.

We have developed an absolutely new catalytic system based on the metal particles that are definitely incorporated into carbon filaments via the catalytic decomposition of hydrocarbons on such particles. The as-prepared catalysts make it possible to perform a number of catalytic processes.

Dispersed particles of the iron group metals and their alloys with some other metals were prepared by mechanical grinding of the corresponding metal oxides in high-power activators with subsequent reduction. To prevent sintering of the metal particles, the substances with a layer-type structure, i.e. magnesium or aluminum hydroxides, were introduced into the activated mixture¹⁶⁾.

MCA enabled the synthesis of new alumina forms such as π - Al_2O_3 . This crystal modification results from dehydration of the mechanically activated gibbsite. The modification is characterized by a layer structure similar to that of gibbsite and the presence of four, five and six coordinated ions. Two neighboring ions Al(III), that are five-coordinated towards oxygen, are paired Lewis centers exhibiting catalytic activity^{17, 18)}.

It was established that the preliminary activation of gibbsite, boehmite and bayerite reduces the temperature of their phase transfer into corundum by 200-300°¹⁸⁾.

For the analysis of some components polluting an environment, the conducting composites possessing catalytic properties are required. One of such systems is the composite nano-sized platinum and conducting carbon. Works on the synthesis of such systems by a mechanochemical activation method have been started.

The sample of conducting carbon black of mark E-245 was impregnated with a water solution of H_2PtCl_6 , dried at 1200 C and then exposed to mechanochemical activation in a planetary mill AGO-2 at a rotational speed of the barrels of 10 s⁻¹. The analysis of products was carried out by XRD. Mechanical activation of a mix of carbon black and H_2PtCl_6 results in a reduction of the last up to metal platinum. The particle size of platinum determined by XRD is 5 nm. Catalytic activity was determined in a modeling reaction of hydrogenation of butadiene in a flowing installation at speeds of hydrogen - 7 l/hour and bu-

tadiene - 1.4 l/hour. The temperatures of reaction were 80-1800 C. A shot of the catalyst - 0.5 g. Before definition of catalytic activity, samples of catalysts were reduced in a current of hydrogen at temperatures between 250 and 3500C. The obtained sample displays catalytic activity in reaction of hydrogenation of butadiene. After the reduction of a sample at 350 °C, conversion of butadiene makes 78%, selectivity on butenes of 68%, on butane - 32%.

4. Development of Concepts of the MCA Effect on the Activity and Selectivity of Catalysts

4.1. The problem description

In section 2.2, we presented the main problems whose solution will make it possible to develop a theory for predicting the catalytic actions. However, the task is complicated by the fact that a traditional problem definition also involves phenomena of the MCA system.

In this context, we suggest two possible applications of MCA for increasing catalytic action¹⁹⁾:

1. Effect on the catalytic properties of the preliminary MCA treatment of a catalyst. In this case, the action of MCA manifests itself in as much as a partially relaxed catalyst system preserves some part of its defectiveness and the excess free energy associated with it.
2. Effect on the catalytic properties of MCA during the catalytic process. In this case, manifestation of the MCA action depends on the power density of MCA, i.e. on the level of energy dissipation and properties of the catalyst dissipation state. Catalysis occurs on the surface of heterogeneous catalysts. The properties of the atoms on the solid surface differ from those in the solid bulk. Their reactivity is affected by steric and power properties of the defects on the surface. For this reason we are primarily interested in the phenomena and processes occurring on the surface under MCA action^{5, 8)}.

In some reports, defects in the crystal structure are given with a catalytic action, whereas the chemical nature of the catalytic action is not mentioned at all. Meanwhile, catalytic action is based on the formation of a chemical mediator (active complex) on the surface. In other words, catalysis is a chemical phenomenon. The question now arises: What are the relations and the input of chemical and structure-energy components into the nature and properties of catalytically active centers? This question can be subdivided into a number of specific questions as:

1. What is the nature of the MCA effect on the activ-

- ity of the catalysis centers?
2. Are there individual active centers of the target and side reactions?
 3. Can MCA destroy active centers or initiate generation of alternative active centers?
 4. If 100% conversion of the initial product is composed of selectivity of the desired and by-products, can we use MCA to control selectivity of the desired product, etc.?

At present, definition of the above questions is still underway and there are no unambiguous answers to the above questions. We have just indicated the problems as guidelines to assist in the performance of future researches.

4.2. Brief review of the information concerning the MCA effect on the activity and selectivity of catalysts

The nature of chemical bonds in the crystal lattice defines physicochemical properties of solids, including reactivity. This nature varies over a wide range: ionic, covalent, metallic, molecular, hydrogen. MCA affects chemical bonds in different ways. These are responsible for anisotropy of the properties of crystals and distinctions between different crystal faces in surface energy and reactivity.

Catalytic action in heterogeneous catalysis begins with adsorption or chemisorption of the reacting molecules. The processes rely on the chemical nature of bonds. The solid surface of catalysts is energetically and chemically inhomogeneous. As a consequence of chemical inhomogeneity in the composition and bonds saturation, the interaction with the molecule surface results in complexes with different binding energies. The catalytic action itself significantly depends on the energy properties of the adsorbed complexes, i.e. on the properties of the surface where the reacting molecules are adsorbed.

During MCA, the range of inhomogeneity of the catalyst surface properties sharply increases, which extends the variety of active centers.

In our case, the question of the nature and mechanisms of MCA's effect on the efficiency of active centers is reduced to the explanation of a relationship between structure-energy properties of an active center and its reactivity. Furthermore, one should assume that different defects (i.e. carriers of excess energy in the solid) have a different effect on the chemical, catalytic and other properties of catalysts.

Relaxation in a heterogeneous catalyst structure can proceed through several channels of different natures. However, the main reason of increasing

catalytic activity is that a feature of the defects in the crystal structure. The system tends to minimize its free energy by localizing it on the defects³⁾. Such distribution of free energy is thermodynamically more efficient than the uniform distribution of elastic stresses throughout the crystal lattice bonds. As follows from ref. ⁸⁾, the chemical activity of the catalytic centers is increased by extended defects such as interblock boundaries formed by dislocation array and shift defects resulting from shifts and turns of the layers. Such areas are characterized by maximal concentrations of the surface atoms with unsaturated bonds and increased reactivity. An increase in free energy of the above areas reduces a potential barrier of activation of the catalytic reactions.

One would expect the highest effect of MCA on the catalytic activity from a combination of a catalytic action and MCA. In this case, a catalytic system can be approximately treated as a dissipative one²⁰⁾. The system state will depend on the intensity of energy dissipation. On each dissipation level, the corresponding dynamic order and a non-equilibrium stationary structure will appear. Thus, as the process of catalysis and MCA action are used at the same time, one may speak about a statistically defined set of the system dynamic states with its own potentials. These states appear only in the area of impact action, but not in the whole bulk of particles. For this reason, the observed increase in catalytic activity should be attributed to the input of this area alone.

Pulse action of MCA on the catalyst is responsible for two counter processes, occurring in the system at each instant of time, i.e. deformation accompanied by increasing free energy and relaxation. For each constant regime of MCA, the processes come to equilibrium. Owing to self-organization, the structure of the system assumes both spatial order and specific properties, including catalytic ones.

A dynamic equilibrium between all defects depends on the intensity of dissipation (MCA)⁹⁾. After MCA, the process of relaxation occurs accompanied by condensation of the dispersed defects in linear and planar formations. Note that a possibility to obtain states with different defect saturations depends on the MCA intensity and the type of chemical bonds in a solid. As the MCA action decreases, the main part is played by the rate of "hardening" in the relaxation process. One can suggest that after MCA, the rate of relaxation is described by equations as one of radioactive elements half-life.

Relaxation energy can be rather high due to the conversion of elastic energy into vibration energy.

For this reason, an excited bond can initiate a chemical reaction. Annihilation of the structural defects is accompanied by release of the energy sufficient for the electron excitation and bonds destruction, which also increases activity of the catalytic centers^{3,4}. In any case, the as-activated catalytic complex acquires some excess energy providing a penetration of the potential barrier of a catalytic reaction. This is a manner in which a specific channel of energy relaxation (here it is a catalytic reaction) acts. Qualitative analysis of the varying thermodynamic and kinetic parameters of the catalytic processes under MCA conditions¹⁹ has shown that catalyst activity should increase if the nature of active centers does not change. In this case, selectivity can vary with the relation between the rates of main and side reactions. Some information on the nature of selectivity can be received by studying correlations between the rates of separate reactions and the presence of the corresponding structural defects.

As MCA is combined with a catalytic process, a special channel for the process performance appears. Under these conditions, fresh surfaces with broken and distorted bonds, where active centers have a radical character, are continuously generated. The appearance of excited atoms on the above surface determines their reactivity. The lifetime of these atoms is comparable with the rate of chain breaking. In this case, the reaction with gas proceeds without activation². Radical reactions are defined by the rate of formation and spending of active centers that is proportional to the rate of reproduction of fresh surfaces. The centers are destroyed via: spontaneous annihilation and interaction with gases during the catalytic act².

4.3. MCA as a means of affecting both the activity and selectivity of catalysts

In ref.⁸ we presented a detailed analysis of the publications that consider the effect of MCA on the activity and selectivity of catalysts. The present article considers a number of new examples.

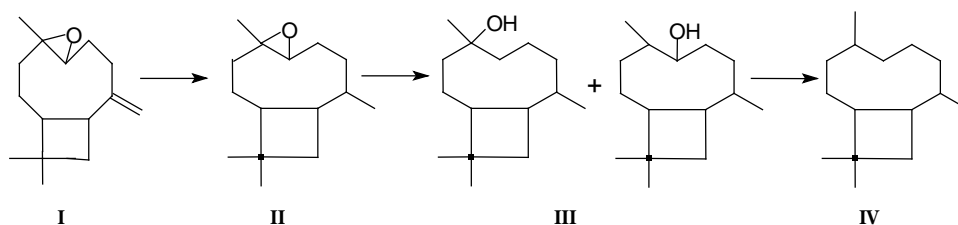
Thus, the performance of catalytic reactions under

MCA conditions permits an increase in activity and selectivity and an essential extension of the range of plausible processes. Of particular interest are new potentialities of the MCA performance under reaction medium pressure: synthesis of new compounds, selective performance of catalytic reactions in the solid phase, new efficient ways of reactions performance. Thus, the hydrogenation in the solid phase of a number of organic compounds promotes a selective reduction of functional groups and unsaturated bonds. The most illustrative example is the hydrogenation of caryophyllene- α -oxide (**Scheme 1**). The activation of caryophyllene- α -oxide (I) for 10 min at the barrels' rotational frequency of 10 s⁻¹ in the presence of the hydride Mg₂NiH₄ at hydrogen pressure 5 atm leads to hydrogenation of the double bond and the quantitative transformation into dihydrocaryophyllene- α -oxide (II). An increase of MCA time to 90 min under the same conditions leads to the reduction of the epoxy group to form a hydroxyl group at a selectivity of 90%. Fourteen isomers of alcohols (III) are formed. Finally, at a barrel speed of 17 s⁻¹, the complete removal of hydroxyl groups occurs within 20 min resulting in the formation of dihydrocaryophyllene (IV). According to the data of X-ray phase analysis, no changes in the composition of hydride occur. Hence we may suppose that catalytic hydrogenation of caryophyllene- α -oxide takes place.

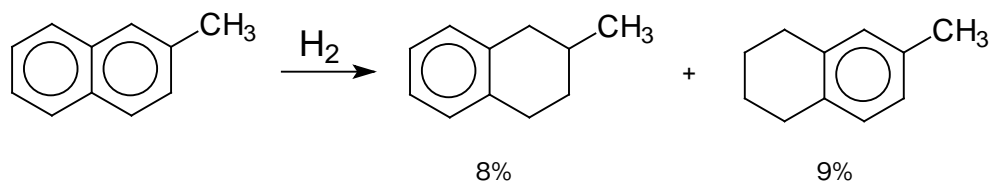
The MCA of 2-methylnaphtalene for 30 min at a hydrogen pressure of 20 atm (barrels' rotational frequency 17 s⁻¹) in the presence of hydride Mg₂NiH₄ results in hydrogenation of one of the benzene rings with the formation of a mixture of tetralines (**Schematic 2**).

Quantitative transformation of benzamide into benzamine observed on the hydride Mg₂NiH₄ after MCA for 30 min at barrels' rotational frequency of 17 s⁻¹ and hydrogen pressure of 15 atm (**Schematic 3**).

The high efficiency this method demonstrate for the hydrogenation of. The MCA of a number of nitroaromatic compounds for 30 min at hydrogen pressure of 50-100 atm (barrels' rotational frequency 17 s⁻¹) in the presence of hydride Mg₂NiH₄ results in



Schematic 1.



Schematic 2.



Schematic 3.

hydrogenation of nitro groups with the formation of corresponding amines (**Schematic 4**).

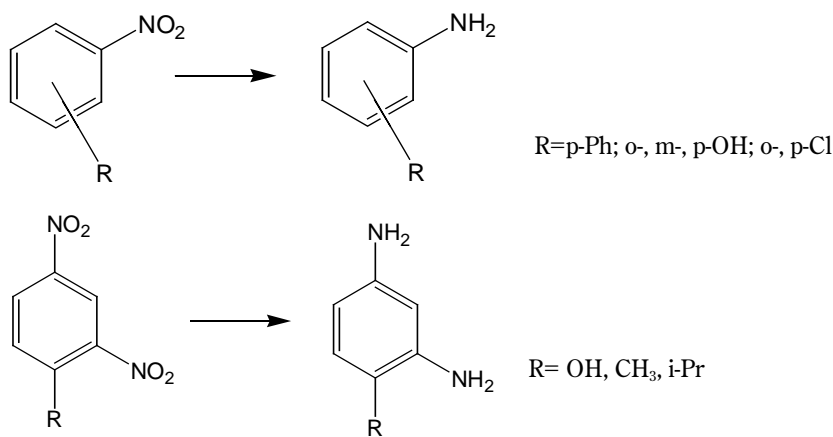
This method also demonstrates a high efficiency for the reaction of catalytic oxidation. The MCA of organic solids at pure oxygen pressure 30-80 atm in the presence of transition metal oxides results in full oxidation. This phenomenon may be used for the sterilization of toxic substances including poisonous gases. The hexamethylphosphoramide was used as a model poisonous gas (**Schematic 5**). The oxides of iron and manganese were used as catalysts.

The reactions of partial oxidation take place if the high pressure in the barrels is created by the mix-

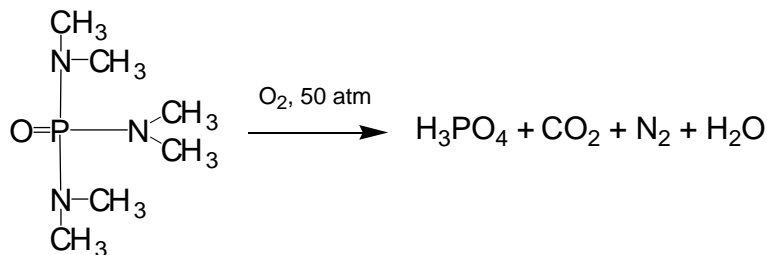
ture of oxygen and inert gases (argon, nitrogen). The following reactions of partial oxidation were realized (**Schematic 6**):

Ursolic acid was oxidized at elevated oxygen pressure²¹. The structure of ursolic acid (**Schematic 7**) allows the synthesis of biologically active substances.

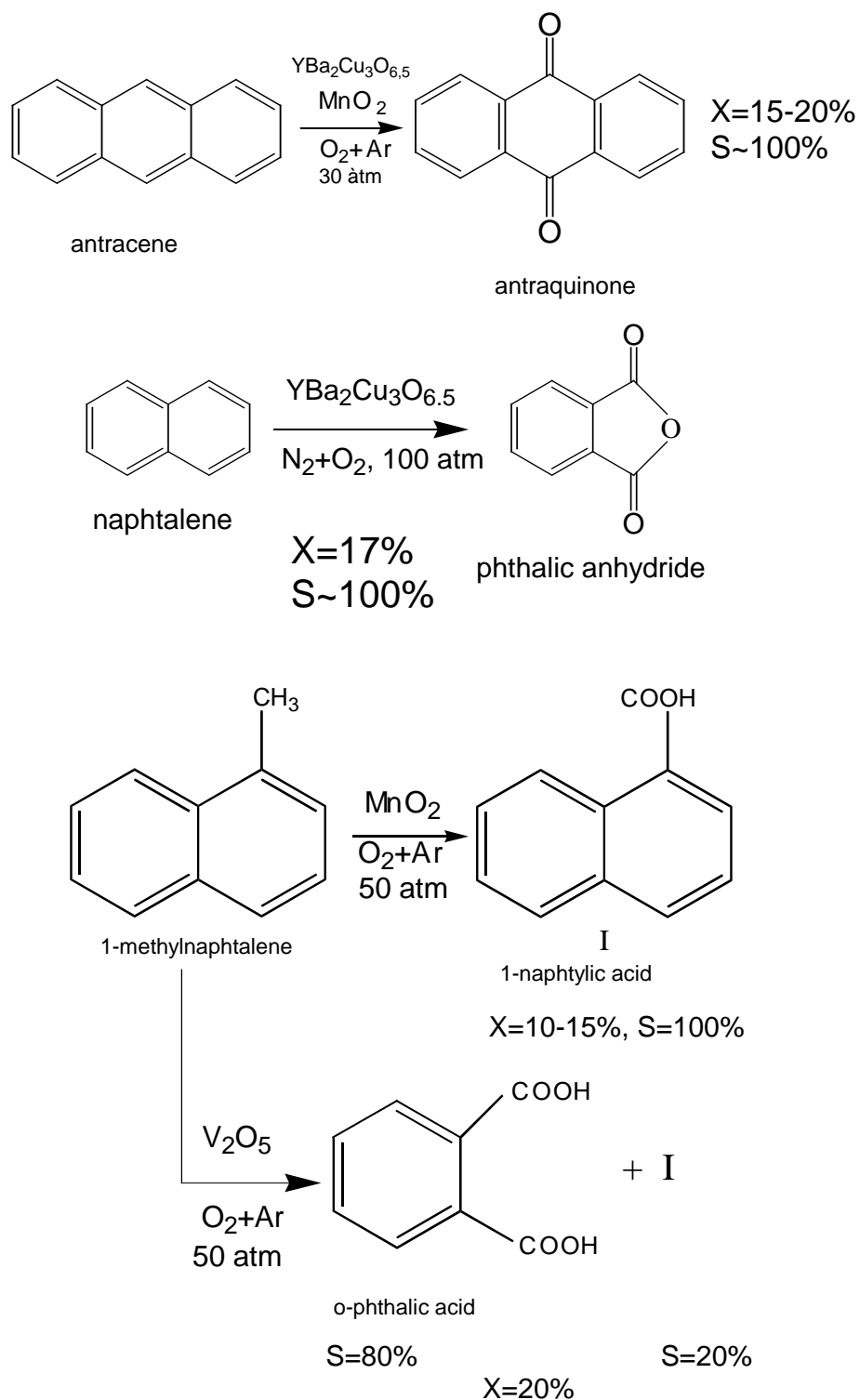
Practically all the known derivatives of ursolic acid exhibit physiological activity. Possible syntheses are hindered because of the low reactivity of ursolic acid. The development of methods to integrate ursolic acid into chemical processes will open the way for new large-scale sources of raw materials for the chemical industry, because this acid is present in a series of



Schematic 4.



Schematic 5.

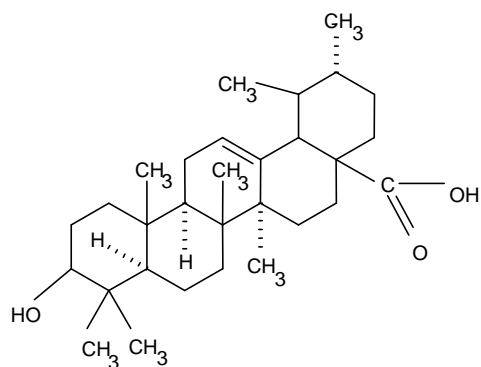


Schematic 6.

plants in large amounts. Investigation of the catalytic oxidation of ursolic acid was carried out under MCA, increased oxygen pressure and the use of traditional metal oxides as catalysts (MnO_2 , Fe_2O_3 , WO_3). Four compounds are the major oxidation products after the reaction under MCA, increased oxygen pressure

and MnO_2 as the catalyst. Fragments of the structural formula of ursolic acid that undergo transformation during oxidation are shown in **Schematic 7**.

Ursolic acid amide was obtained at elevated ammonium pressure. Cooper salts were used as catalysts. Without solvents, the amide yield was no higher



Ursolic acid

Schematic 7.

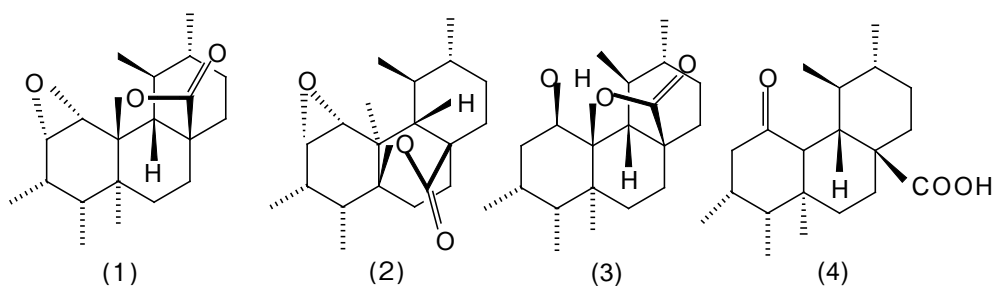
than 8-10%. Amination in the presence of methanol or acetic acid as the solvent made it possible to obtain amide of ursolic acid at a yield of 65% (Schematic 9).

Under the same conditions but without the catalysts, ammonia salt of ursolic acid was obtained.

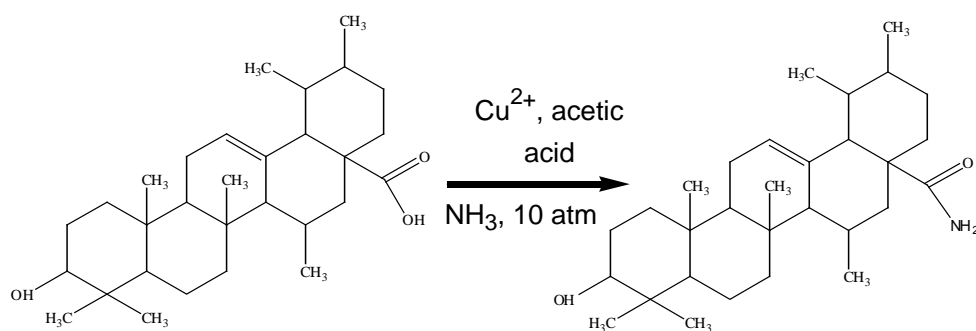
The phthalimide was obtained (Schematic 10) by amination of phthalic anhydride at ammonia pressure 10 atm.

The reactions of hydro-dechlorination of toxic chlorine aromatic compounds, including complete destruction of 1,2,3,4-tetrachlorodibenzo-p-dioxin (Schematic 11), were performed²¹.

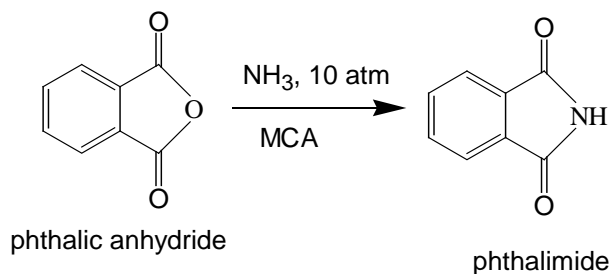
Of particular interest is the catalytic action of ammonia observed in the synthesis of intermetallic compound hydrides performed during mechanochemical activation of the reacting metals at the gas-phase pressure ($H_2 + 5\% NH_3$). Adding ammonia into the hydrogen medium made it possible to change the mechanism and the rate of formation of nickel-magnesium intermetallide hydrides. Ammonia was adsorbed on the solid activated particles (reaction



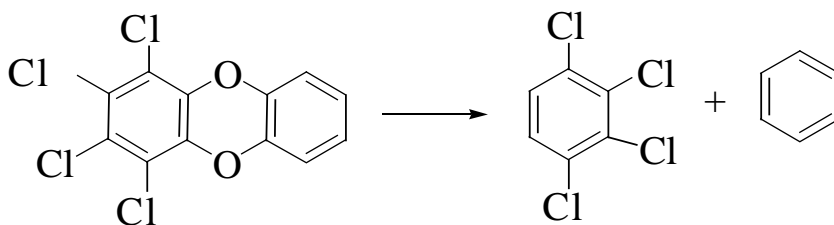
Schematic 8.



Schematic 9.



Schematic 10.



Schematic 11.

participants), was activated by them and provided the stage mechanism for the transfer of hydrogen atoms²³⁾.

It was established²⁴⁾ that the specific rate of oxidation of CO on TiO₂ linearly depends on the concentration of crystal shear planes which was measured by ESR of Ti₂⁷⁺ dimers (Fig. 1). This dependence can be considered as unambiguous proof of the role of extensive defects.

MCA tripled the specific catalytic activity of zinc oxide in the reaction of CO oxidation. This was accompanied by an essential decrease of activation energy, which indicated the generation of alternative active centers. This observation was associated with the formation of low-angle interblock boundaries and the appearance of exits of dislocations and packing defects onto the surface. The linear dependence of the specific rate of oxidation of CO and the quantity of microstrange was established (Fig. 2). The ions of Zn²⁺ involved in the defects are the centers of chemisorption of oxygen, which is a catalytically active cen-

ter providing the stage mechanism of CO oxidation. It was also established that point defects do not affect the activity of ZnO in this reaction²⁵⁾.

Experimental evidence was obtained that the stacking fault generated during MCA of zinc ferrite is responsible for increasing the specific rate of CO oxidation. The linear relationship of the specific rate of CO oxidation is observed from the concentration of defects determined by Moessbauer spectroscopy (Fig. 3) and X-ray diffraction (Fig. 4) methods.

Of special interest are our recent results (unpublished) concerning the changes in catalyst selectivity towards desired and by-products caused by MCA action. The results prove the possibility of generating one active center and the annihilation of other centers. It was established that MCA affects the selectivity of vanadium oxide in the oxidation of formaldehyde into formic acid and by-products. In addition, the selectivity of zinc oxide changes in the conversion of isopropyl alcohol, which follows two routes such as

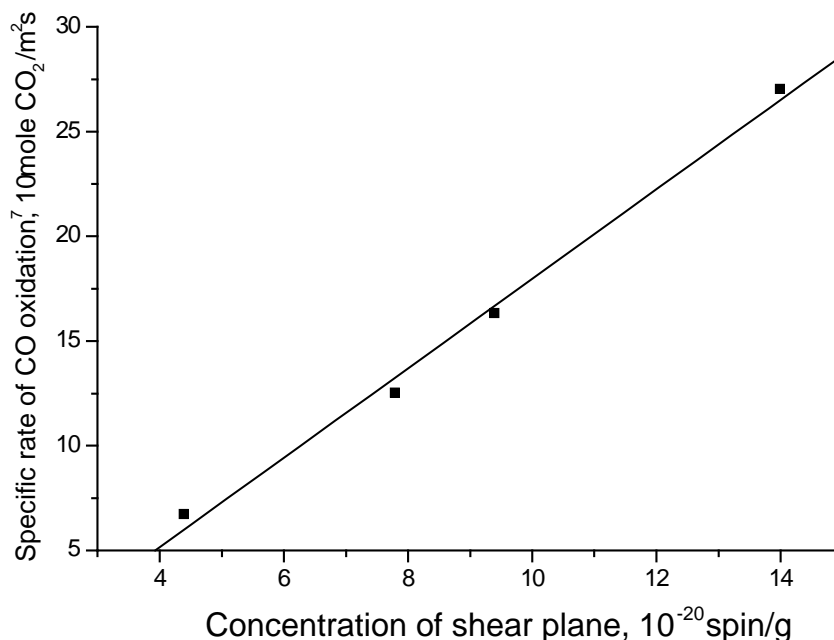


Fig.1 Dependence of the specific rate of CO oxidation vs. concentration of shear plane.

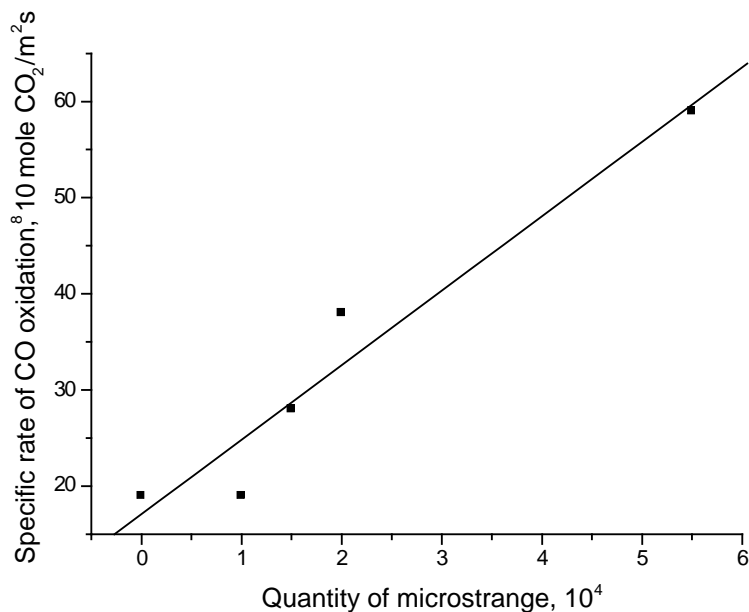


Fig.2 Dependence of the specific rate CO oxidation on the quantity of microstrange.

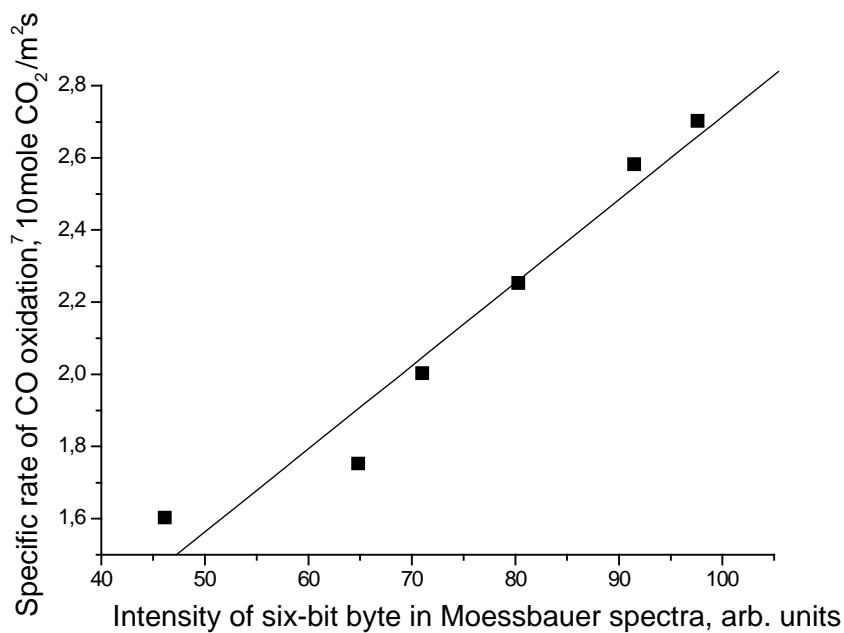


Fig.3 Dependence of the specific rate CO oxidation vs. the concentration of stacking fault measured by Moessbauer spectroscopy.

dehydrogenation yielding acetone, and dehydration resulting in propylene.

In both cases, the selectivity was changed by the formation of aprotonic acid centers under MCA action and a decrease in the number of protonic acid centers.

The comparison of the effect of MCA on properties of solids indicates that the same mechanically induced defects of the crystal structure exhibit a higher activity in the three chemical processes differing by their nature and mechanisms: simple chemical transformations, sorption and catalysis (**Table 1**).

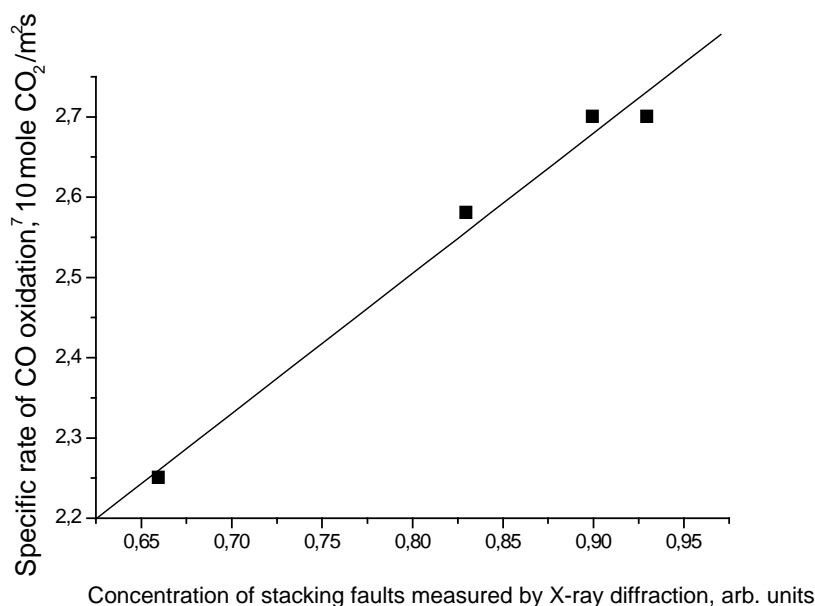


Fig.4 Dependence of the specific rate CO oxidation vs. the concentration of stacking fault measured by X-ray diffraction.

Table 1 Influence of defects in the catalyst structure on chemical processes

Catalyst	Chemical transformation	Sorption	Catalytic reaction
ZnO	Oxidation-reduction	O ₂ , H ₂ Se, Ni ²⁺	Oxidation of CO
TiO ₂	Oxidation, dissolution in acids	Ni ²⁺	The same
ZnAl ₂ O ₄ , ZnFe ₂ O ₄	Leaching	Ni ²⁺ , H ₂ S	The same
Fe ₂ O ₃	Dissolution in acids	H ₂ S	The same
V ₂ O ₅	Dissolution in hydrogen peroxide	NH ₃	Oxidation formaldehyde to formic acid

In the literature there are not so many works on the application of MCA in catalysis. We summarized these works in tables. In **Table 2**, works on the preparation of catalysts using MCA are given. In **Table 3**, works on the influence of MCA on catalytic properties are given.

5. Conclusions

Our review considers the role of structure-energy properties of the mechanically induced defects in the crystal structure of the heterogeneous catalysts. The main theoretical concepts of the effect of MCA on the activity and selectivity of catalysts are stated. We considered the most promising trends in the research activities in this field. The use of literary and our own data on high-performance MCA in three areas makes it is possible to judge:

- Preparation of catalysts with decreasing power

consumption, less time for synthesis and the absence of a harmful drain

- Increase of the activity and change of the selectivity of catalysts after MCA
- Performance of catalytic reactions using MCA with the quantitative yields and high selectivity

The increasing interest in MCA applications in catalysis reflects the tendencies in this field. There is good reason to believe that the basic researches of the nature and mechanisms of MCA actions performed in all divisions of the science of catalysis and catalysts will promote general progress in the practical realization of the method.

References

- 1) Buyanov R.A. (1991): *Sibirskii Khimicheskii Zhurnal*, No 1, pp.5-19.
- 2) Avvakumov Ye.G. (1986) "Mechanical methods of acti-

Table 2 Results of the MCA application for the preparation of catalysts

Initial product	Final product or derived result	Apparatus for MCA	Additional effects	Reference
α -TiCl ₃ , γ -TiCl ₃	δ -TiCl ₃	BM	Increased activity in the reaction of propylene polymerization	26, 27
TiCl ₃ +AlCl ₃ +R ₃ Al	δ -TiCl ₃	BM	–	28
TiCl ₃ +AlCl ₃	Solid solution with δ -TiCl ₃ structure	BM	Increased activity in the reaction of ethylene polymerization	29-31
TiCl ₄ +MgCl ₂	Fixation of TiCl ₄ on the MgCl ₂ surface	BM	ditto	32-34
α -Fe ₂ O ₃ or α -Al ₂ O ₃ +H ₂ CrO ₄ , Fe ₂ O ₃ +H ₂ CrO ₄	Catalysts of vapor conversion of CO	–	Increased activity, enhanced strength	35, 36
ZnO+H ₂ CrO ₄	Catalyst of methanol synthesis	–	Increased activity	37, 42
MgO+Cu ²⁺ in ACS	Catalysts of vapor conversion of CO	BM	Increased activity	38
H ₂ CrO ₄ +Al(OH) ₃ +ZnO+CuCO ₃ × Cu(OH) ₂	Catalyst of vapor conversion of CO	–	Increased activity	39
CuAl ₂ O ₄ +ethanol or acetone solution	Improved quality of binding agent	–	Enhanced strength	40
ZnO+Al ₂ O ₃ in ACS	Sulfur adsorbent	–	Enhanced strength, increased sulfur capacity	41
ZnO	The same	VM, PM	The same	43, 44
Cu(OH) ₂ CuCO ₃ + ZnO	Solid solution Zn-Cu-O	PM		45
Cu(OH) ₂ CuCO ₃ + Ni(OH) ₂ NiCO ₃	Solid solution Ni-Cu-O	PM		46
Al(OH) ₃ +CuO, MgO, ZnO, CaO, Cu(OH) ₂ CuCO ₃	Amorphization of aluminum hydroxide	PM	Substitution of the wet method of aluminum hydroxide preparation	47
CoO+CuO	Catalyst of after-burning	PM		48, 49
CuO, Co ₃ O ₄	Improved capacity for founding by extrusion	PM	Increased activity in CO oxidation, resistance to poisoning with SO ₂	50
La ₂ O ₃ +Co ₃ O ₄ , La ₂ (CO ₃) ₂ +CoCO ₃ × Co(OH) ₃	LaCoO ₃ (catalyst of after-burning of gas emissions)	PM	Increased CuO activity in butane oxidation	51
La ₂ O ₃ +Mn ₂ O ₃ (or MnO ₂ or Mn ₃ O ₄)	LaMnO ₃ (catalyst of after-burning of gas emissions)	PM	–	52
Al-Ni (alloy)	Raney Ni	VM		53
Ni+Al	Alloys, precursors of Ra/Ni	PM	Increased activity in cyclohexene hydrogenation, Pr ³ OH dehydrogenation	54-57
Ni+Al+M (M = V, Cr, Mn, Fe, Co, Mo, W)	Modified Raney nickel	PM	Increased activity in reactions of hydrogenation	58
Ra/Ni (used)+Al	Ra/Ni	–	ditto	59
M ₂ CO ₃ +Fe ₂ O ₃ (M = K, Rb, Cs)	Catalyst of ethylbenzene dehydrogenation	DS	ditto	60,61
Aluminum hydroxides+SiO ₂	Aluminosilicates, zeolites	PM	Increased activity, enhanced strength	62,63
Ca-Cr-Ni-phosphate catalyst IM-22O ₄	Regulation of the processes of crystallization and baking	PM	–	64
			Enhanced strength	

Note. Abbreviations: ACS, ammonium carbonate solution; CMC, carboxymethylcellulose; PVA, poly(vinyl alcohol); PEG, poly(ethylene glycol); Ra/Ni, Raney nickel; BM, ball mill; USD, ultrasonic disintegrator; VM, vibratory mill; PM, planetary mill; DS, disintegrator.

Table 3 Influence of MCA on catalytic properties of various compounds

Catalyst	Reaction	Active centre	Reference
Cu	Dehydrogenation of ethanol	Dislocations	65
Ni	Hydrogenation of cinnamic acid, dehydrogenation of ethanol, decomposition of H ₂ O ₂ , <i>ortho-para</i> conversion of hydrogen	Vacancies, dislocations	66, 67
Ag	Decomposition of formic acid, decomposition of H ₂ O ₂ , oxidation of ethanol	Dislocations	68
Au	Decomposition of H ₂ O ₂	ditto	69
Pt	Decomposition of formic acid, hydrogenation of cinnamic acid	Point defects, dislocations	70
Co	Decomposition of H ₂ O ₂ , hydrogenation of benzene	Defects and distortions of the structure	71, 72
Ni	Hydrogenation of benzene	Distortions of the lattice	73, 74
Ni	Hydrogenation of phenol and mixtures of higher unsaturated alcohols	ditto	75
Ni	Hydrogenation of fats, <i>ortho-para</i> conversion of hydrogen	Dislocations	76, 77
V ₂ O ₅	Oxidation of SO ₂ to SO ₃	Distortions of the lattice	78
Fe ₂ O ₃ , Fe ₃ O ₄	The same	ditto	79
Fe ₂ O ₃ , Fe ₃ O ₄	Oxidation of CO	–	80
Fe ₂ O ₃ , Fe ₃ O ₄	Vapor conversion of CO	Distortions of the lattice	81
CuO	Decomposition of N ₂ O, <i>ortho-para</i> conversion of hydrogen	Defects of the lattice	82, 83
CaO	Decomposition of N ₂ O	ditto	84
NiO	Decomposition of H ₂ O ₂	Distortions of the lattice	85
KHSO ₄	Polymerization of acetaldehyde	New acidic centers	86
H ₂ WO ₄	Hydration of propylene	New proton centers	87
Cr ₂ O ₃ + CuO or ZnO	Dehydrogenation of PriOH	Distortions of the lattice	88, 89
TiO ₂ , ZnO, BaTiO ₃ , NiO	Oxidation of CO	Anionic vacancies	90
TiO ₂ + WO ₃ , TiO ₂ + Fe ₂ O ₃ , TiO ₂	ditto	Distortions of the lattice	91
CaF ₂	Dehydrogenation and dehydration of PriOH	–	92
V ₂ O ₅ + SiO ₂	Oxidation of methane to formaldehyde	–	93
CuO	Oxidation of butane	Surface Cu ⁺ ions	94
Co ₃ O ₄	ditto	Excess oxygen	95
Fe ₂ O ₃	Oxidation of CO	Defects with a local symmetry of spinel	95, 96
MnO ₂ , MnO, Mn ₃ O ₄ , Mn ₂ O ₃	ditto	Extended defects, steps	95

- vation of chemical processes”. Novosibirsk, Nauka.
- Butyagin P.Yu. (1984): Russian Chemical Reviews, vol. 53, pp. 1025-1038.
 - Butyagin P.Yu. (1994): Russian Chemical Reviews, vol. 63, pp.965-976.
 - Boldyrev V.V. (1997) “Reactivity of Solid materials”. Novosibirsk, SB RAS.
 - Boldyrev V.V. (1991) In: “Mechanochemical synthesis in inorganic chemistry”. Novosibirsk, Nauka SB of USSR Acad. Sci. (Ed. Avvakumov Ye.G.), pp. 5-32.
 - Boldyrev V. V. (2006): Russian Chemical Reviews, vol. 75, pp. 177-189.
 - Molchanov V. V., Buyanov R. A. (2000): Russian Chemical Reviews, vol. 69, pp. 435-450.
 - Buyanov R. A., Molchanov V. V. (2001): Chemistry for Sustainable Development, vol. 9, pp.369-377.
 - Goidin V. V., Molchanov V. V., Buyanov R. A. et al. (1997): Chemistry for Sustainable Development, vol. 5, pp.585-589.
 - Molchanov V.V., Goidin V.V., Buyanov R. A., (2006): Kinet. Catal., vol. 47, pp.744-746.
 - Goidin V. V., Molchanov V.V., Buyanov R. A., (2004): Inorganic materials, vol. 40, pp. 1165-1168.
 - Buyanov R.A., Molchanov V.V., (1996): Khimicheskaya Promyshlennost., No 3, pp. 152-157.
 - Molchanov V. V., Buyanov R. A., (2001): Kinet. Catal., vol. 42, pp. 366-374.
 - Molchanov V. V., Maksimov G. M., Maksimovskaya R.I. et al. (2003): Inorganic materials, vol. 30, pp.687-693.
 - Molchanov V. V., Chesnokov V.V., Buyanov R. A. et al. (2005): Kinet. Catal., vol. 46, pp.660-668.
 - Paramzin S.M., Zolotovskii B.P., Krivoruchko O.P., Buyanov R.A. (1987): In Proc. IV Intern. Heterog. Catalysis, Bulgaria, Sofia. Part.2, p.369.
 - Paramzin, S.M., Zolotovskii B.P., Krivoruchko O.P., Buyanov R.A. (1989): Izvestiya Sibirskogo Otdeleniya Akad. Nauk SSSR, ser. Khim. Nauk, No 1, pp.33-39.

- 19) Buyanov R.A., Molchanov V.V. (2003): Chemistry for Sustainable Development, vol. 11, pp.467-470.
- 20) Glansdorff P., Prigogine I. (1971) Thermodynamic theory of structure, stability, and fluctuations, N.Y., Wiley-Interscience.
- 21) Molchanov V. V., Goidin V.V., Buyanov R.A. et al. (2002): Chemistry for sustainable development, vol. 10, pp.133-140.
- 22) Molchanov V.V., Plyasova L.M., Goidin V.V., Buyanov R.A. (1995): Inorganic materials, vol. 31, pp.1125-1229.
- 23) Goidin V.V., Molchanov V.V., Buyanov R. A. (2005): Doklady Chemistry, vol. 402, pp.101-104.
- 24) Avvakumov Ye.G., Molchanov V.V., Buyanov R.A., Boldyrev V.V. (1989): Dokl. Akad. Nauk, vol. 306, pp.367-370.
- 25) Molchanov V.V., Buyanov R.A., Tsybulya S.V. et al. (2004): Kinet. Catal., vol. 45, pp.684-693.
- 26) Natta G., Pasquon I. (1959): In: Adv. Catal., N.-Y., Academic Press Inc., vol. 11, pp.2-66.
- 27) Natta G., Corradini P., Allegra G. (1961): J. Polym. Sci. vol. 51 pp.399-410.
- 28) Seelbach C. W., Tornqvist E. (1962) US Patent 3034992.
- 29) Tornqvist E. G. M., Richardson J. T., Wilchinsky Z. W. Looney R. W. (1967): J. Catal., vol. 8, pp.189-196.
- 30) Carradine W. R., Rase H. F. (1971): J. Appl. Polym. Sci., vol. 15, pp.889-912.
- 31) Wilchinsky Z. W., Looney R.W., Tornqvist E.G.M. (1973): J. Catal., vol. 28, pp.351-367.
- 32) Kashiwa N. (1980): Polymer J., vol. 12, pp.603-608.
- 33) Zakharov V. A., Perkovets D.V., Bukatov G. D. et al. (1988): Kinet. Catal., vol. 29, pp.903-908.
- 34) Zakharov V. A., Perkovets D.V., Bukatov G. D. et al. (1988): Kinet. Catal., vol. 29, pp.1202-1205.
- 35) Shirokov Yu.G., Iliin A.P., Kirillov I.P. (1979): Izvestiya Sibirskogo Otdeleniya Akad. Nauk SSSR, ser. Khim. Nauk, No 3, pp.45-50.
- 36) Shirokov Yu. G., Iliin A. P., Nizov G. A., Sitnikova N.N. (1986): RU Patent 1235523.
- 37) Shirokov Yu.G. (1997): J. Appl. Chem. (Russian), vol. 70, pp.961-977.
- 38) Smirnov N. N., Iliin A. P., Novikov E. N., Shirokov Yu.G. (1989): Izvestiya VUZov. Chem. and chem.. techol., vol. 32, pp.83-86.
- 39) Shirokov Yu.G. (1984): The Questions of Kinetic and Catalysis, Ivanovo, pp.3-9.
- 40) Iliin A. P., Shirokov Yu. G., Saushkina L.A. (1986): RU Patent 1253661.
- 41) Iliin A. P., Kirillov I. P., Shirokov Yu.G. (1979): Izvestiya VUZov. Chem. and chem.. techol., vol. 22, pp.246-248.
- 42) Mukhina M. I., Afanasiev D.V., Shirokov Yu.G. (1987): The questions of kinetic and catalysis, Ivanovo, pp.22-24. Prokofiev V.Yu., Iliin A.P., Shirokov Yu.G. (1993): Izvestiya VUZov. Chem. and chem.. techol., vol. 36, pp.68-72.
- 43) Ikonnikov V.G., Titelman L.I., Rastegaev O.V., Shirokov Yu.G. (1986): The Questions of Kinetic and Catalysis, Ivanovo, pp.93-99.
- 44) Shirokov Yu.G., Iliin A.P., Kirillov I.P. et al. (1979): J. Appl. Chem. (Russian), vol. 52, pp.1228-1233.
- 45) Shirokov Yu.G. (1987): J. Appl. Chem. (Russian), vol. 70, pp.961-977.
- 46) Iliin A.P., Smirnov N. N., Shirokov Yu.G., Efremov V.N. (1994): Izvestiya VUZov. Chem. and chem.. techol., vol. 37, pp.79-82.
- 47) Smirnov N.N., Iliin A. P., Shirokov Yu.G. (1993): Izvestiya VUZov. Chem. and chem.. techol., vol. 36, pp.48-52.
- 48) Angelov S.A., Bonchev R. P. (1986): Appl.Cat., vol. 24, pp.219-225.
- 49) Angelov S. A., Bonchev R. P. (1987): Doklady BAN, vol. 40, pp.63-66.
- 50) Isupova L. A., Aleksandrov V.Yu., Popovskii V.V., Moroz E.M. (1988): J. Appl. Chem. (Russian), vol. 61, pp.1976-1980.
- 51) Pauli I.A., Avvakumov E.G., Isupova L.A. et al. (1992): Sibirskii Khimicheskii Zhurnal, No 3, pp.133-137.
- 52) Isupova L.A., Sadykov V.A., Solovyova L.P. et al. (1994): In: 6th Intern. Symp. "Scientific bases for the preparation of heterogeneous catalysts" (Louvian-La-Neuve, 1994); Preprints vol. 2, pp.231-239.
- 53) Kiperman S. L., Balandin A.A., Davydova I.R. (1957): Izv. Akad. Nauk SSSR Otd. Khim. Nauk, No 12, pp.1482-1484.
- 54) Boldyrev V.V., Golubkova G.V., Grigorieva T.F. et al. (1987): Dokl. Akad. Nauk, vol. 297, pp.1181-1184.
- 55) Ivanov E.Yu., Grigorieva T.F., Golubkova G.V. et al. (1988): Izvestiya Sibirskogo Otdeleniya Akad. Nauk SSSR, ser. Khim. Nauk, No 6, pp.80-83.
- 56) Fasman A.B., Mikhailenko S.D., Kalinina O.T. et al. (1988): Izvestiya Sibirskogo Otdeleniya Akad. Nauk SSSR, ser. Khim. Nauk, No 6, pp.83-85.
- 57) Nischenkova L. G., Gostikin V.P., Litvinova S.V. (1991): Highly refined materials on the based on platinum metals and their compounds in catalysis and current technology, Ivanovo, pp.81-85.
- 58) Nischenkova L. G., Ivanov E.Yu., Golubkova G.V. (1991): Highly refined materials on the based on platinum metals and their compounds in catalysis and current technology, Ivanovo, pp.76-79.
- 59) Nischenkova L.G., Golubkova G.V. (1991): Highly refined materials on the based on platinum metals and their compounds in catalysis and current technology, Ivanovo, pp.79-81.
- 60) Volkov M. I., Stepanov E. G., Strunnikova L. V., Kotelnikov G. R. (1986): The Questions of Kinetic and Catalysis, Ivanovo, pp.100-104.
- 61) Volkov M. I., Stepanov E.G., Suzdilovskaya T. N., Kotelnikov G. R. (1988): The Questions of Kinetic and Catalysis, Ivanovo, pp.36-39.
- 62) Klevtsov D. P., Krivoruchko O.P., Mastikhin V. M. et al. (1988): React. Kinet. Catal. Lett., vol. 36, pp.319-324.
- 63) Avvakumov E. G., (1994): Chemistry for sustainable development, vol. 11, pp.541-558.
- 64) Molchanov V. V., Goidin V.V. (1993): Khim. Promst, No 12, pp.613-615.

- 65) Uhara I., Yanagimoto S., Tani K. et al. (1962): J. Phys. Chem., vol. 66, pp.2691-2694.
- 66) Uhara I., Hikino T., Numata Y. et al. (1962): J. Phys. Chem., vol. 66, pp.1374-1375.
- 67) Uhara I., Kishimoto S., Hikino T. et al. (1963): J. Phys. Chem., vol. 67, pp.996-1001.
- 68) Uhara I., Kishimoto S., Yoshida Y., Hikino T. (1965): J. Phys. Chem., vol. 69, pp.880-882.
- 69) Kishimoto S., Nishioka M. (1972): J. Phys. Chem., vol. 76, pp.1907-1908.
- 70) Kishimoto S. (1963): J. Phys. Chem., vol. 67, pp.1161-1162.
- 71) Tetzner G., Schrader R. (1974): Z. Anorg. Allg. Chem., vol. 407, pp.227-236.
- 72) Tetzner G., Schrader R. (1974): Z. Anorg. Allg. Chem., vol. 409, pp.77-88.
- 73) Schrader R., Grund H., Tetzner G. (1963): Z. Chem., vol. 3, pp.356-357.
- 74) Schrader R., Grund H., Tetzner G. (1967): Chem. Ingen. Techn., vol. 39, pp.806-812.
- 75) Schrader R., Staedter W. (1968): Acta Chim. Acad. Sci. Hung., vol. 55, pp.39-47.
- 76) Schrader R., Staedter W., Oettel H. (1971): Chem. Techn., vol. 23, pp.363-367.
- 77) Schrader R., Staedter W., Oettel H. (1972): Z. Phys. Chem., vol. 249, pp.87-100.
- 78) Paudert R. (1965): Chem. Techn., vol. 17, pp.449-453.
- 79) Paudert R. (1967): Monatsber. Dtsch. Akad. Wiss. Berlin, vol. 9, pp.719-724.
- 80) Schrader R., Jacob G. (1966): Chem. Techn., vol. 18, pp.414-416.
- 81) Schrader R., Vogelsberger W. (1969): Z. Anorg. Allg. Chem., vol. 368, pp.187-195.
- 82) Schrader R., Deren J., Fritsche B., Ziolkowski J. (1970): Z. Anorg. Allg. Chem., vol. 379, pp.17-24.
- 83) Schrader R., Deren J., Fritsche B., Ziolkowski J. (1970): Z. Anorg. Allg. Chem., vol. 379, pp.25-34.
- 84) Schrader R., Thiem E. (1968): Z. Phys. Chem., vol. 238, pp.41-50.
- 85) Sadahiro Y., Shimidzu K. (1968): J. Chem. Soc. Japan, vol. 71, pp.1374-1378.
- 86) Ogino Y., Kawakami T., Tsurumi K. (1966): Bull. Chem. Soc. Japan, vol. 39, pp.639-642.
- 87) Ogino Y., Kawakami T., Matsuoka T. (1966): Bull. Chem. Soc. Japan, vol. 39, pp.859-863.
- 88) Ogino Y., Nakajima S. (1967): J. Catal., vol. 9, pp.251-262.
- 89) Ogino Y., Ono T. (1967): Bull. Chem. Soc. Japan, vol. 40, pp.2223-2228.
- 90) Batsanov S.S., Boreskov G.K., Gridasova G.V. et al. (1967): Kinet. Catal., vol. 8, pp.1348-1355.
- 91) Golden J., Williams F., Morosin B. et al. (1981): Shock Waves Condens (Menlo Park, Calif, 1981), pp.72-76.
- 92) Batsanov S. S., Bokarev V. P., Kostenchuk I.A. et al. (1982): React. Kinet. Catal. Lett., vol. 20, pp.43-45.
- 93) Krylov O. V., Firsova A. A., Bobyshev A.A. et al. (1992): Cat. Today, vol. 13, pp.381-390.
- 94) Isupova L. A., Aleksandrov V. Yu., Popovskii V.V. et al. (1986): React. Kinet. Catal. Lett., vol. 31, pp.195-202.
- 95) Sadykov V.A., Isupova L.A., Bulgakov N.N. (1998): Chemistry for Sustainable Development, vol. 6, pp. 215-222.
- 96) Sadykov V.A., Isupova L.A., Tsybulya S.V. et al. (1996): J. Solid State Chem., vol. 123, pp.191-202.

Author's short biography



Roman A. Buyanov

The corresponding member of the Russian Academy of Sciences, professor, RAS adviser.

For a long time he is a vice-director of the Boreskov Institute of Catalysis SB RAS. The expert in the field of inorganic and physical chemistry, catalysis, chemical technology.

The author more than 400 scientific publications and 110 patents.

Author's short biography



Victor V. Molchanov

Victor V. Molchanov is head of laboratory in Boreskov Institute of Catalysis. In 1981 he received his Ph. D. in catalysis. In 2002 Victor V. Molchanov received his Sci. D. degree in catalysis. His research interest are applying mechanochemistry in catalysis, scientific bases of catalysts preparation, carbon nanomaterials. Victor V. Molchanov is the author more than 100 scientific papers and 30 patents.



Boldyrev

Graduated in 1948 from Tomsk State University. Ph.D. in chemistry in 1951 at Tomsk State University, Doctor of Sciences in Chemistry in 1961, Professor of Chemistry since 1963. 1979 - a Corresponding Member of the Academy of Sciences USSR, since 1991 - a Full Member of Russian Academy of Sciences. President of the International Advisory Committee on the Reactivity of Solids (1992-1996) and of the International Mechanochemical Association (1989-1997). He was president of International Mechanochemical association of IUPAC (1987-1991), 1993 - State Prize of Russia for the Highest Achievements in Science.

1948-1956 - a lecturer at Tomsk State University. 1957-1963 - Head of the Department of Radiation Chemistry at Tomsk Technical University and the Head of the Project at the Institute of Nuclear Physics in Tomsk. 1964-1974 - the Head of the Laboratory of Solid State Kinetics at the Institute of Chemical Kinetics and Combustion Siberian Department of the USSR Academy of Sciences in Novosibirsk. 1975-1998 - Director of the Institute of Solid State Chemistry Russian Academy of Sciences in Novosibirsk, since IV.1998 - Adviser of Russian Academy of Sciences. Since 1983 - Head of the Department of Solid State Chemistry of Novosibirsk State University. To date he is director of Centre of Molecular Design and Ecologically Safe Technologies at Novosibirsk State University. Author of more than 800 paper, 13 books and 92 patents.

SHS Powders for Thermal Spray Coating[†]

T. Talako*, A. Ilyuschenko and A. Letsko
Powder Metallurgy Institute¹

Abstract

The possibilities of preparing advanced powders for thermal spraying functional coatings by the method of self-propagating high-temperature synthesis are discussed in this review. Besides important economical and ecological benefits, the method allows the formation of powders with improved or unique structure and properties in size ranges and with an external morphology suitable for different thermal spray processes. A number of novel powders and recent achievements are presented.

Keywords: self-propagating high-temperature synthesis, powder, thermal spray coating

Introduction

Modern industrial technologies call for the development of novel materials with improved properties, lower costs and environmentally suitable processes. Surface engineering that attempts to create functional layers on the surface is obviously the most economical way to provide high performance to machinery and equipment. Among the wide range of available methods (including varieties of atomistic and particulate deposition, bulk coatings wetting processes and surface modification), thermal spray coatings offer the most versatile solutions. Thermal spray processes form a continuous coating by melting the consumable material (feedstock) to form droplets and impinging these droplets on the substrate. The mechanism of bonding to the substrate in thermal sprayings (TS) is the same as plating, both mechanical interlocking and atomic interaction, with the shear strength around 7 MPa¹⁾. The thickness of the coatings can range from 10 μm to a few millimeters²⁾. Other advantages of thermal spraying include a practically unlimited assortment of powders to be sprayed, high efficiency and relatively low substrate temperature (373-583 K), thus minimizing shape distortion, oxidation and phase transformations in the near-surface layer. Demanded characteristics for thermal spray feedstock powders can be very differ-

ent, depending on the spraying process, the operating conditions, the desired properties of the final coating, etc. Besides the intrinsic material properties, the technical requirements for the TS feedstock powders include good flowability and sprayability. They are greatly affected by the particle size, shape and morphology as well as particle size distribution. That is why thermal spray feedstock powder production processes must be reliable and flexible, while remaining as inexpensive as possible.

Self-propagating high-temperature synthesis (SHS) or combustion synthesis, discovered by A.G. Merzhanov and colleagues in 1967, is known as a very promising technique for processing materials (ceramics, intermetallics, cermets, etc.) with good physical and chemical properties at relatively low costs^{3,4)}. The main point of the process is that after localized initiation, the reaction propagates as a narrow zone – combustion wave – along a sample driven by the exothermic reaction between components of the charge mixture without the application of external heating (furnaces, etc.). Because of the extreme conditions in the SHS wave (high temperature of up to 3500°C, fast heating of up to 10⁶K/s, steep temperature gradient of up to 10⁵ K/cm, rapid cooling in the after-burn zone of up to 100 K/s, and fast accomplishment of reaction, 0.5 s to 1 min), chemical interaction mechanisms during the SHS are often non-equilibrium, resulting in the formation of materials with improved structure and properties, especially in multi-component composite systems^{3,6)}. Moreover, a product with increased purity can be obtained due to evaporation of volatile impurities at the high temperatures of the

[†] Accepted: September 25th, 2009

¹ 41, Platonov str., 220005 Minsk, Belarus

* Corresponding author:

TEL: +375 17 293 98-27, FAX: +375 17 210 05 74,
E-mail: talako@tut.by

process. Besides the important economical benefits connected with low energy requirements and short reaction times, the method is promising from an environmental point of view^{7,8)}. Two ecological aspects related to SHS are usually considered: ecological cleanness of the SHS technologies and possibilities of industrial waste inertation, minimization and reuse in SHS reactions. Generally, the SHS process is believed to be ecologically clean. However, for some large-scale production, gas emission of volatile impurities during synthesis can be an environmental threat. The major achievements in the exploitation of SHS for environmental protection include: the fixation and consolidation of high-level radioactive wastes; the treating and recycling of a highly toxic solid waste from electrolytic zinc plants; the recycling of silicon sludge from semiconductor industries, aluminum dross produced by aluminum foundries, nonferrous metal cutting and grinding waste, Fe₃O₄ dross and dead catalysts; the degradation of chlorinated aromatics^{7,8)}.

The first works available in the literature that take advantage of SHS materials for TS were devoted to plasma spraying (PS) of carbides, intermetallics and carbide-based composite powders⁹⁻¹⁸⁾. It was noted that at equal coating properties, SHS powders provide 20-25-fold energy savings and half the labor input as compared with conventional methods of powders preparation. Since then, a great number of researchers have been engaged in investigating thermal spray coatings from SHS powders¹⁹⁻⁸²⁾. Most of them dealt with wear-resistant coatings formed by different thermal spray methods from 'titanium carbide/metal binder' compositions. It was conditioned by the high exothermal effect of TiC formation (giving full scope for the choice of binder material acting as diluents in the synthesis process) and good coating properties (comparable with or even better than that of conventionally used WC/Co and Cr₃C₂/NiCr coatings). The chemical and morphological features of different SHS powders were described, and their technical characteristics of flowability and sprayability were outlined³⁰⁻³⁸⁾. Wear performance and hardness test results for various TS coatings were also reported^{21-23, 25, 26, 30-39, 42, 43)}. Further progress was connected with widening sprayed materials including improvement of TiC-based powders (forming double (Ti, Cr)C, (Ti, W)C and (Ti, Mo)C carbides, complex alloyed binders, introducing additional solid lubricant phases, etc.), as well as the development of other compositions⁴⁴⁻⁸¹⁾. At present, more than 90 different SHS powders have been investigated as feedstock materials

for TS coatings. Different kinds of plasma spraying methods (air plasma spraying (APS), supersonic air plasma spraying (SAPS), low-pressure plasma spraying (LPPS), underwater plasma spraying (UPS)), as well as detonation spraying (DS), flame spraying (FS) and high-velocity oxygen-fuel spraying (HVOF) are in common use for depositing protective coatings from SHS powders. The first attempt to systematize results on using self-propagating high-temperature synthesis for thermal spraying was made recently by A.L. Borisova and Yu.S. Borisov⁸²⁾. The compositions of the most widely reported thermal sprayed SHS powders as well as methods of their deposition and properties of the coatings have been listed. However, only general information about some of the SHS powders and their processing is presented in this review, while some promising powders and recent achievements were not mentioned. The aim of this work is to summarize relevant up-to-date literature and results of the author's research on producing advanced SHS powders for thermal spraying functional coatings.

1. Fundamentals of Powder SHS Technology

As stated above, the main condition for implementation of the SHS process is a high enough exothermicity of the charge mixture. According to experimental data, SHS normally takes place when the adiabatic temperature is higher than 1800 K⁸³⁾ or at a ratio of reaction heat to a specific thermal capacity of a product at room temperature $\Delta H_{298}/C_{298} > 2000$ K⁸⁴⁾.

The powder SHS technology is based on burning green powder mixtures in special reactors in the environment of an inert or reacting gas, and also in vacuum or in the open air⁸⁵⁾. The chemistry of the SHS process is versatile. Materials can be produced from elements and using compounds, mineral raw materials and industrial waste as reactants. Combustion products are usually porous sinters which are exposed to subsequent processing to produce powders of a different function. The general technological configuration of SHS powder production includes the following operations: (1) preparation of a green mixture: sieving, milling, drying of components (if necessary) and mixing; (2) filling of a reactor with a green mixture and gases; (3) synthesis after a short-term thermal initiation and (4) subsequent processing of the synthesized products. In the case of synthesis from elemental powders, the subsequent processing of the synthesized product includes only mechanical treatment: scraping, crushing, milling and classification.

Some additional operations can be necessary in the case of the more complicated routes. For example, magnesiothermy synthesized product after crushing is exposed to acid enrichment to remove magnesium oxide, and is then dried and mechanically processed.

The main parameters to control the synthesis process are composition and structure of the charge mixture (including type and amount of additives and fillers); reactant's dispersity; relative density and charge volume; initial temperature of the sample; composition and pressure of ambient gases; external influences (preliminary mechanical activation of charge mixtures, electric and magnetic fields, ultrasonic, centrifugal and gravitation forces, shock waves, etc.). Detailed information about the relationships between SHS process parameters and combustion product structure and properties can be found elsewhere^{3-6, 8, 83-85}. In this review, we summarize the main approaches to the synthesis of powders for thermal spraying. A number of novel powders and recent achievements are presented.

2. Thermal Sprayed Powders

All the powders that have proven themselves for thermal spraying can be divided into two main groups: refractory compounds and composite powders. The most representative powders and characteristic features of their processing are given below.

2.1. Refractory compounds

The most common route for manufacturing powders of **carbides, borides, silicides**, etc. is conventional synthesis from elemental powders ($\text{Ti}+\text{C}=\text{TiC}$; $\text{Ti}+2\text{B}=\text{TiB}_2$; $\text{Mo}+2\text{Si}=\text{MoSi}_2$) in a pressure-defined reactor. High-caloric mixtures (for example, $\text{Ti}+\text{C}$ and $\text{Ti}+2\text{B}$) are normally diluted with 15-20% wt.% of combustion product. To provide stoichiometric composition of titanium carbide, 1-1.5% carbon excess is usually required. Other details of manufacturing techniques for TiC , TaC , NbC , TiB_2 and MoSi_2 powders can be found in⁸⁵.

For low-caloric mixtures (for example, $\text{Cr}+\text{C}$), liquid-phase processes with aluminothermal reactions can be used. This process is called SHS with reducing stage. Two competitive reactions $\text{MeO}_x+\text{Al}\rightarrow\text{Me}+\text{Al}_2\text{O}_3$ and $\text{MeO}_x+\text{C}\rightarrow\text{Me}+\text{CO}$ proceed simultaneously in the first stage of the process. The SHS proper, i.e. synthesis of carbide from the metal and carbon, takes place in the second stage. A two-phased melt consisting of carbide and alumina is finally formed. Phase separation resulting from differences

in carbide and oxide density occurs under gravitational or centrifugal forces. A chromium carbide powder is hereby produced from a mixture containing 37 wt.% CrO_3 , 27 wt.% Cr_2O_3 , 27.5 wt.% Al and 8.5 wt.% graphite. The respective technology is described in⁸⁵.

Nitride powders (TiN , ZrN , etc.) are usually formed by the combustion of metal powders in gaseous nitrogen spontaneously entering into the reaction zone after being "filtered" through the pores. One of the critical parameters for this route is careful control of the reacting gas pressure. A 40-70% dilution with coarse-grained combustion product powder is also necessary to provide the filtration processes.

In open (continuous-flow) reactors with a directed flow of the reacting or doped gas through the loose powder, so-called "Filtration SHS Technology" is implemented^{85,86}. The main advantages of the process include the possibility of synthesizing titanium nitride at a low pressure of supplied nitrogen (less than 5 MPa) without charge mixture dilution. Moreover, it is possible to remove emitted gases, thus increasing the purity of the product, and allows cutting wastes and sludge to be used as reactants without precleaning.

So-called azide technology is based on using solid azide powder as the nitrating reactant instead of gaseous or liquid nitrogen⁸⁶. The chemical equation of TiN synthesis is written as follows: $4\text{Ti}+\text{NaN}_3+\text{NH}_4\text{Cl}=4\text{TiN}+\text{NaCl}+2\text{H}_2\uparrow$. As compared to systems with gaseous nitrogen, this route allows increasing the reactant concentration in the synthesis zone, eliminating filtration problems and producing more fine-grained powder (because of the lower combustion temperature) at high efficiency (no charge dilution is used). However, NaN_3 is toxic and more expensive than gaseous nitrogen.

Complex refractory compounds such as double carbides, carbonitrides, etc., can be produced using three- and more-component charge mixtures. For example, the production route for double titanium-chromium carbide $\text{Ti}_{0.7}\text{Cr}_{0.3}\text{C}$ is similar to TiC synthesis process except for the addition of chromium powder into the powder mixture and 2% carbon excess. SHS of titanium carbonitride $\text{TiC}_{0.5}\text{N}_{0.5}$ is formed by combustion of the powder mixture comprising titanium and carbon-blake with 30% diluent of carbonitride powder in nitrogen media.

SHS powders of carbides, nitrides and silicides are intended for wear-resistant and high-temperature TS-coatings. Among the developed thermal sprayed powders worthy of note are powders of molybdenum disilicide (for high-temperature oxidation-resistant

coatings), chromium and double titanium-chromium carbides (for wear-protective coatings).

Another class of refractory compounds showing growing interest for thermal spray applications is **intermetallics**. The general chemical equation of intermetallics combustion synthesis can be written as follows: $Me' + Me'' \rightarrow Me'_x Me''_y$.

Due to the fact that the exothermal effect of most intermetallic compound formation from elemental powders is not high enough¹¹⁾, preheating of the charge mixture before ignition is normally used. Preliminary mechanical activation (MA) of the reacting mixtures allows synthesis to be performed without heating at higher conversion completeness. Single-phase equilibrium and ultrafine (nanocrystalline) intermetallic compounds were reported to be formed through the mechanically activated self-propagating high-temperature synthesis (MASHS) route^{87,88)}.

Of the intermetallics, nickel, iron and titanium aluminide-based powders are currently in use for thermal spray protective coatings. Some examples of novel SHS powders developed in the Powder Metallurgy Institute are presented below.

NiAl powders modified with nanoadditives. Due to the high melting temperature, good high-temperature strength, low density, high thermal conductivity and excellent oxidation resistance^{89,90)}, NiAl protective coatings can be used effectively for high-temperature applications.

As was mentioned before, the powder for thermal spraying has to have good flowability and this property is greatly affected by the particle size distribution and particle morphology. The best flowability is achieved for particles of spherical shape. While particle size requirements vary for different TS methods, the particle size distribution is a critical parameter for thermal sprayed powders. Powder particles that are too coarse cannot be heated sufficiently during spraying to deposit on the substrate. Conversely, particles that are too fine can be overheated and suffer thermal degradation (decomposition) during spraying. That is why precise control of formation of the necessary particle size distribution is a very important task of the TS feedstock powder production process.

Interesting results have been obtained when adding nanoadditives (nanopowders of ultradispersed diamond (UDD) and SiO₂) to the charge mixture for the synthesis of NiAl powders⁹¹⁾. The as-synthesized powder particle size appeared to be strongly dependent on the nanoadditive aggregate size (the less the nanoadditive aggregate size, the finer the powders that can be formed). **Fig. 1** represents cross-sections

of conventional SHS **(a)** and modified with 5 vol.% UDD (200-nm sized aggregates consisting of particles of about 20-40 nm) NiAl SHS powder **(d)**. As can be seen from the figure, the modified powder has a more uniform particle size distribution with 4-8-fold smaller particles. Close to spherical shape is kept in the powder. This dispersive effect can be explained by the fact that nanoadditives, being the nucleus of heterogeneous crystallization, promote quicker and more uniform intermetallic phase formation in the early stage of SHS, meanwhile preventing intensive sintering and grain growth processes because of lower combustion temperature. Nanoadditives can also essentially improve internal oxidation behavior of the material: an intergranular oxidation resulting in material fracture has been observed in the conventional NiAl SHS-powder **(Fig. 1b)**. In contrast, fine oxide inclusions sufficiently uniformly distributed in the material are formed in the modified powder **(Fig. 1e)**. Finally, modification of powders with nanoadditives results in an increase of the powder's deposition efficiency. For example, the thickness of detonation spray coatings from the modified NiAl SHS powder is 1.5-2.5 times higher than that of the unmodified one at the same spraying conditions (compare **Fig. 1e** and **f**). It seems to be connected with a more even particle size distribution and a more fine-grained structure⁹²⁾.

Ni-Al-Cr powder. It is known that chromium is one of the most widely used alloying elements to improve properties of nickel aluminides⁹³⁾. It increases the oxidation resistance of NiAl, suppressing the formation of metastable aluminum oxides in a temperature range of 900-1000°C and promoting the formation of a dense fine-grained α -Al₂O₃ protective film, providing high corrosion resistance⁹⁰⁾, and also improves the mechanical properties of NiAl by solid solution hardening and hardening by thin inclusions of α -Cr⁸⁹⁾.

Recently, we have developed a novel SHS powder based on nickel monoaluminide alloyed with chromium and strengthened with dispersed inclusions of chromium-based solid solution **(Fig. 2a)**⁹⁴⁾. The powder is produced using preliminary mechanical activation of the reacting mixture of Ni-20 wt.% Cr alloy with aluminum before synthesis. In the developed powder, the NiAl phase contains 3-6 wt.% Cr and secondary inclusions on the basis of chromium up to 25 wt.% of nickel and up to 15 wt.% of aluminum. The increased content of chromium dissolved in NiAl is evidently connected with the fact that chromium substitutes not only for nickel but also for aluminum sites in a B2 lattice. The powder microhardness is 320-550

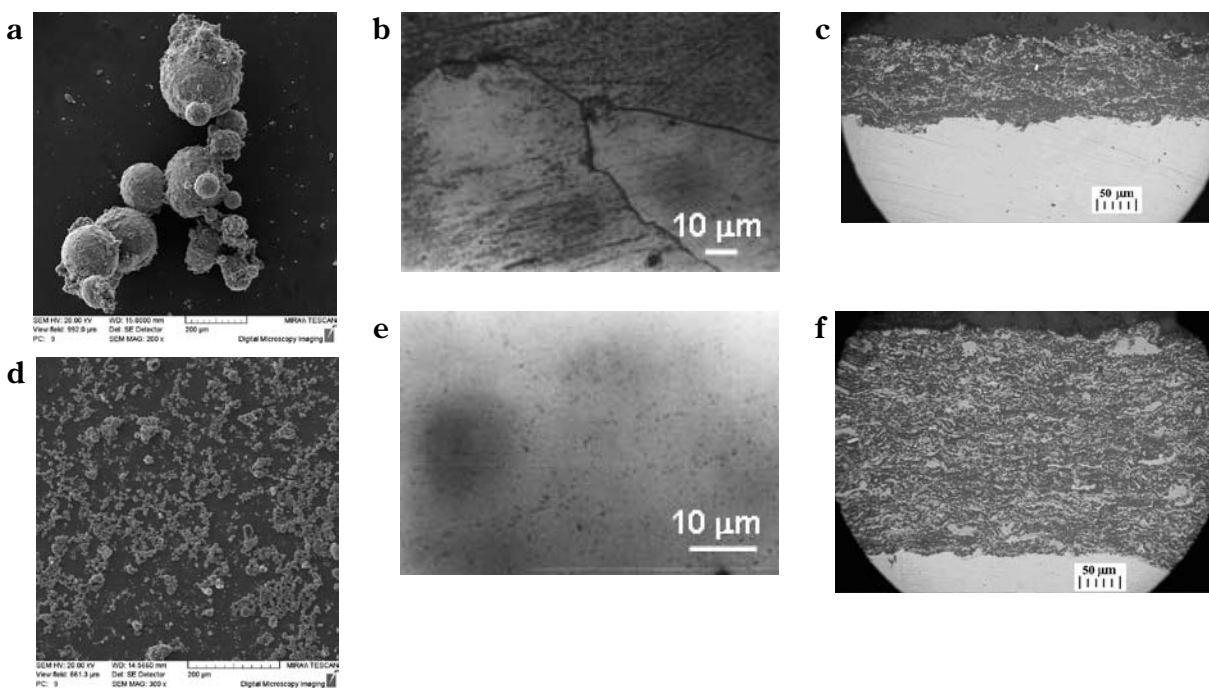


Fig.1 Morphology (a, d) and cross-sections of NiAl powders (b, e); cross-sections of detonation spray coating from them (c, f): a-c – conventional SHS powder; d-f – modified with 5 vol.% UDD SHS powder.

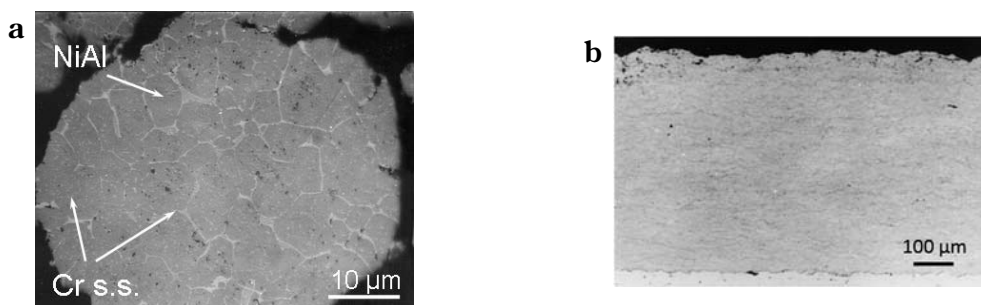


Fig.2. Cross-sections of NiAlCr powder (a) and HVOF coating from it (b).

Hv50. The high-velocity oxy-fuel flame (HVOF) spray coating from the developed NiAlCr powder (**Fig. 2b**) demonstrates good mechanical properties and excellent oxidation behavior up to 1300 K.

FeAl-Fe_xAl_y powder. Due to the high Young's modulus, high elevated temperature strength retention, excellent corrosion resistance in oxidizing, sulfiding or carburizing environments up to 1000°C, relatively low density as compared with stainless steels and nickel superalloys, and low price of raw materials⁹⁵, FeAl intermetallic alloys based on the ordered B2 structure are very attractive materials for medium-temperature applications. However, poor room temperature ductility, low creep resistance and sensibility to environmental embrittlement restrict their industrial applications as structural parts.

Recently, a new FeAl-Fe_xAl_y powder with improved

characteristics and low cost has been developed^{67, 96,97}. Creation of the powder was based on the idea of strengthening the material with inclusions of secondary precipitates of other iron aluminides formed during synthesis. The powder was prepared through the MASHS route⁹⁶. **Fig. 3a,b** shows the morphology and cross-section of the developed powder. The powder is characterized by the typical eutectoid structure with lamellar morphology of aluminum-enriched crystals. According to energy dispersive X-ray analysis (EDX) results^{67, 96,97}, the light-gray contrast of matrix phase corresponds to the composition of B2 FeAl with some aluminum excess. The composition of the lamellae crystals with dark-gray contrast is close to that of the FeAl₂ compound. However, the X-ray diffraction pattern (**Fig. 4**) clearly shows the evidence of a three-phased composition: Fe₂Al₅ typical reflexes

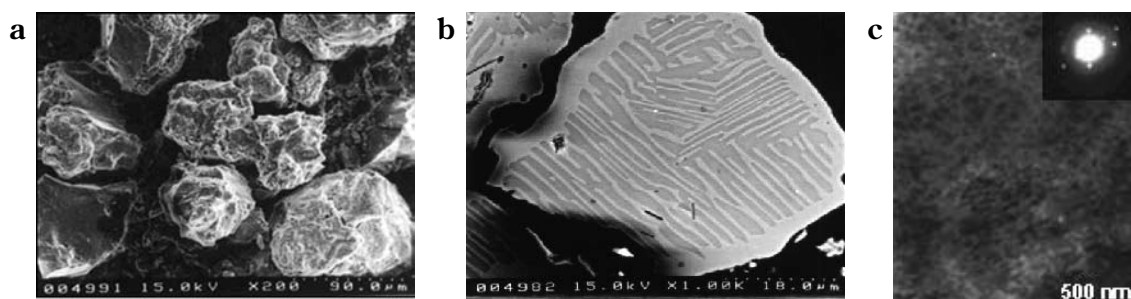


Fig.3 Morphology (a), cross-section (b) and TEM micrograph (c) of FeAl-Fe_xAl_y powder.

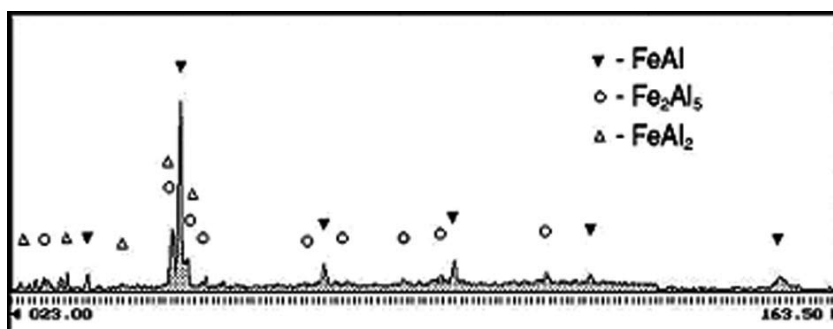


Fig.4 X-ray diffraction pattern of FeAl-Fe_xAl_y powder.

are also found in the spectrum. An Fe₂Al₅ phase is likely to be located on the particle surface and is presented as fine inclusions within the lamellae crystals' volume (see Transmission Electron Microscopy (TEM) micrograph, **Fig. 3c**)⁶⁷. The phase mixture formation evident in the TEM micrograph and identified as FeAl₂+Fe₂Al₅ is probably from the result of the non-equilibrium conditions of structure formation during synthesis, similar to that described in⁹⁸.

The microhardness of the powder is about 500-850 Hv₅₀. It is significantly higher than the typical microhardness of B2 alloys (250-450 Hv₅₀). It should be noted that no cracks were observed in the material even after microindentation tests in spite of the fact that the structure consists completely of intermetallic phases. It is likely that the increased mechanical properties of the powder are provided by the eutectoid structure of multiphased composition of iron aluminides similar to a Ti-Al system, for which superplasticity was observed in the two-phase area ($\gamma + \alpha_2$)⁹⁹. Nanoprecipitates of the Fe₂Al₅ phase can also contribute to the increased crack resistance.

High-quality coatings from the FeAl-Fe_xAl_y powder can be obtained using detonation and high-velocity oxy-fuel flame spraying techniques with a porosity of less than 1% and microhardness of 834 and 831 HV200, respectively⁶⁷. Material peculiarities (high aluminum content and fine-grained structure of multiphased intermetallic composition) provide the coat-

ings with good corrosion- and wear-resistance. The tribological performance of the coatings (abrasion, sliding and erosion behavior) is close to that of composites based on alloyed iron and nickel aluminides with oxide and carbide strengthening⁶⁷. The oxidation resistance of the FeAl-Fe_xAl_y coating is comparable with that of NiCrAl-Al₂O₃: dense and protective alumina film is formed during oxidation tests (**Fig. 5**)⁹⁷.

Ti-Al-Cr powder. Titanium aluminide alloys are known as a promising material for structural use in automotive and aerospace applications due to their low density, relatively high strength and low creep properties even at 1200 K¹⁰⁰. However, they are limited by the poor oxidation resistance at elevated temperatures (>1000K) and poor toughness at ambient temperature. The addition of suitable alloying elements can improve the above characteristics. **Fig. 6 a, b** shows the morphology and cross-section of the novel Ti - 46at.%Al - 8 at.% Cr powder produced using the MASHS route^{101,102}. The powder is characterized by the multiphase dispersed strengthened structure with coherent precipitates/matrix bonding. The main structural constituents of the powder are titanium aluminides alloyed with chromium¹⁰²: (γ -TiAl(Cr), α_2 -Ti₃Al(Cr) and Al_{0.67}Cr_{0.08}Ti_{0.25}) (**Fig. 7**). In spite of the high total intermetallic content of the synthesized powder (about 95%), no cracks are observed in the material, even during microhardness tests. The

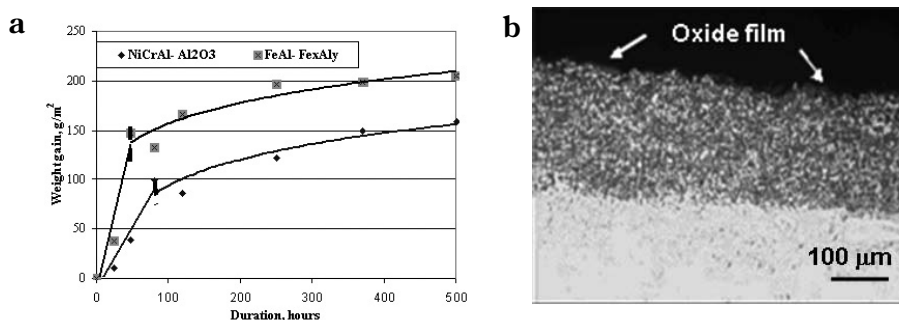


Fig. 5 Comparative oxidation behavior of HVOF coatings (a) and cross-section of HVOF coating from FeAl-Fe_xAl_y powder after 48 hour duration in air at 950°C (b) ⁹⁷.

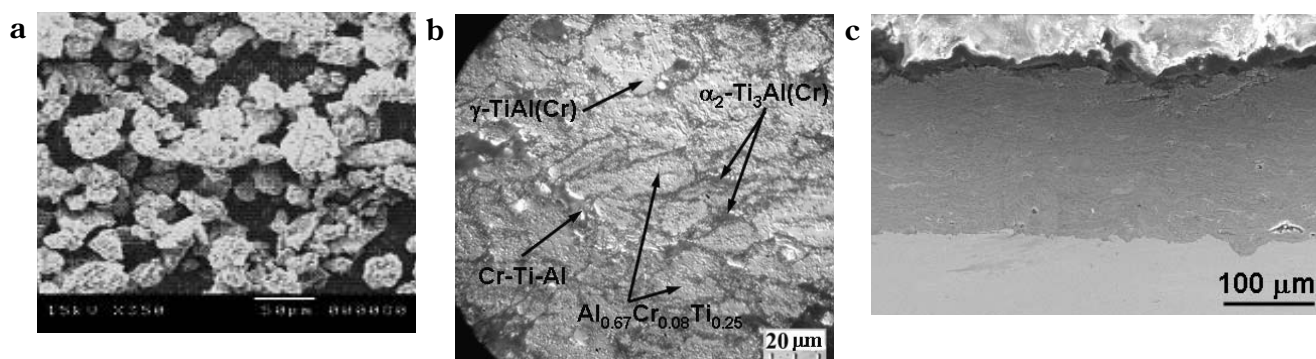


Fig. 6 Morphology (a) and cross-section (b) of TiAlCr powder; cross-section of detonation spray coating from the powder (c).

powder is characterized by the higher hardness as compared to known gamma-alloys (average microhardness value was 313 Hv_{0.25}) and improved oxidation resistance.

High-quality detonation spray coatings with high hardness (940-1100 HV) and low porosity (less than 1%) have been obtained from the developed powder (Fig. 6c)¹⁰². The coatings exhibit good oxidation behavior up to 1173 K. The main phases identified in the oxide scale are (Al_{0.948}Cr_{0.052})₂O₃ with corundum structure and TiO₂ (rutile) alloyed with some aluminum.

Over the last years, there has been much interest in producing thick ferrite films for electromagnetic applications. Ferrites are iron-containing non-conducting ceramic materials with special magnetic properties. Traditionally, ferrites have been manufactured by conventional ceramic powder processing routes which involve milling the component oxides (in the correct proportions) with an organic binder in a ball mill, compacting, drying, pre-firing to burn out the binder and then sintering to form the ferrite crystal structure. Self-propagating high-temperature synthesis provides the important economical benefit connected with substitution of the rather long and ex-

pensive furnace ferritization stage for the fast and energy-efficient combustion process. The characteristic of an SHS process is that it requires the presence, in the initial mixture, of a combustible and an oxidant to implement the combustion reaction. Iron is usually used as a combustible, which is incorporated into the composition of the ferrite. Oxygen is used as the oxidant, obtained from one of two sources: an internal source, for example due to the oxygen evolution during decomposition of NaClO₄¹⁰³ added to the reactive mixture, or an external source, for example oxygen in the air or bottled oxygen. Combined sources can be also used. Preliminary MA of a charge mixture in

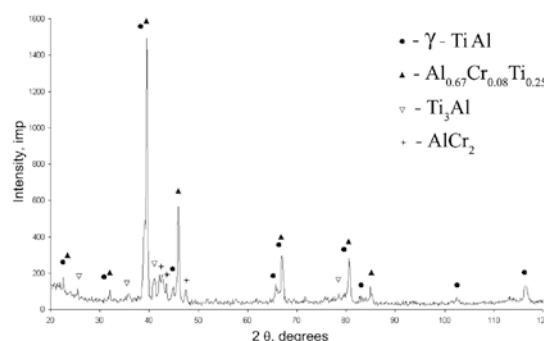


Fig. 7 X-ray diffraction pattern of TiAlCr powder.

high-energy mills has a strong influence on the combustion parameters as well as on the structure and phase-formation mechanisms during SHS, resulting in improved conversion completeness and the formation of a fine homogeneous structure with uniform elemental distribution within the ferrite powder particles¹⁰⁴.

Recently, novel **Ni,Zn-ferrite** SHS powders with additions of Co and Mn have been developed for thermal spraying¹⁰⁵. The ferrite powder is manufactured via the MASHS route from reactive mixtures consisting of the constituent oxides and NaClO₄ as an oxidant. The investigation results have shown that the as-synthesized powder can be produced in size ranges and with an external morphology suitable for both high-velocity oxy-fuel flame and atmospheric plasma spraying. The powder has a single-phase spinel crystal structure and powder particles comprise sintered sub-micron grains (**Fig. 8a**). The spinel crystal structure of the original feedstock powder can be wholly or largely retained in the sprayed deposit (**Fig. 8b**), providing the necessary electromagnetic properties. The composition can be adjusted to match special requirements.

2.2. Composite powders

Composite powders are the most widely used for thermal spraying group of SHS powders. Self-propagating high-temperature synthesis provides an

opportunity to produce composites via a single-stage process even in systems of materials with significantly different properties (for example, melting temperatures) as well as compositions that cannot be formed by the other methods.

Composite powders of the type “**refractory compound / metallic binder**” are produced by the synthesis of a refractory compound in the presence of metal binders, so-called “diluent”, using a high-temperature exothermal reaction of refractory compound formation. A wide range of compositions for wear-resistant coatings has been developed¹⁸².

The most popular powders becoming widespread for thermal spray applications are titanium- and chromium carbide-based powders as well as titanium diboride-containing composites. Iron, nickel, cobalt, aluminum, copper and their alloys can be used as binders. A typical structure of a titanium carbide-based powder is presented in **Fig. 9a**. The principal advantages of the synthesized powders were fine distribution of carbide grains in the material volume and high cohesive bond strength between components of the composite (due to melting of metal binder during synthesis). The structure peculiarities of SHS powders provided the good coating properties. In general, the deposition efficiency, density, hardness and wear-resistance of TS coatings from the composite SHS powders were higher than that from plated or agglomerated ones (**Table 1, 2**).

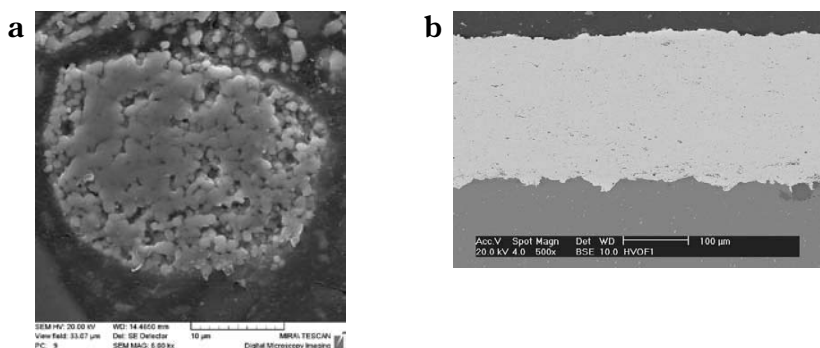


Fig.8 Cross-sections of (Ni,Zn,Co,Mn)Fe₂O₄ powder (a) and HVOF coating from it (b)¹⁰⁵.

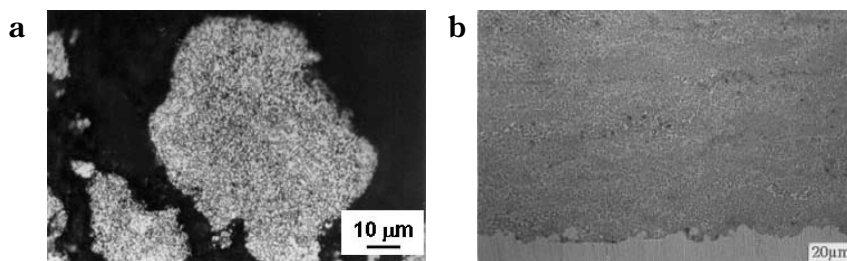


Fig.9 Cross-sections of NiCr / TiC powder (a) and LPPS coating from it (b)¹⁰⁵.

Table 1 Properties of HVOF coatings from Cr₃C₂ / NiCr powders

Property	81 UF-NS, METCO: mechanical blend 75% Cr ₃ C ₂ + 25% Ni20Cr, wt.%	SHS composite powder of the same composition
Deposition efficiency, %	32	50
NiCr content, wt.%	38	20
Oxygen content, wt.%	9-10	6-7
Phase composition	Cr ₇ C ₃ , Ni-solid solution	Cr ₇ C ₃ , Cr ₃ C ₂ , Ni-solid solution

Table 2 Erosion resistance of TS coatings under 0.05-0.20 mm SiO₂ erodent impact (16 g/mm², 60 m/s, 90°)

Material (Composition in wt.%)	Spraying features	Thickness loss, R _{max} , μm	Wear intensity, I, mg/(mm ² · g)
81 UF-NS, METCO: mechanical blend 75% Cr ₃ C ₂ + 25% Ni20Cr	HVOF	110	0.028
SHS composite powder 75% Cr ₃ C ₂ / 25% Ni20Cr	HVOF	100	0.015
	LPPS, Ar-H ₂	60	less than 0.005
	LPPS, Ar-He	100	0.024
SHS composite powder 55% TiC / 45% Ni20Cr	HVOF	80	0.013
	LPPS, heated substrate	70	less than 0.005
	LPPS, cooled substrate	100	0.038
SHS composite powder 50% TiC / 50% Fe30Cr	HVOF	140	0.038
	LPPS, heated substrate	70	0.009

Further improvement can be achieved with the formation of complex compounds. A typical example is powder based on double chromium and titanium carbides^{57, 106}. The idea of creating such a composition was based on the attempt to combine the excellent wear-resistance and extreme high hardness of titanium carbide with the high corrosion-resistance of chromium carbide. The powder was obtained by the simultaneous synthesis of chromium and titanium carbides in the presence of a nickel-chromium binder. To provide conversion completeness in systems with a high chromium carbide content, preheating as well as mechanical and chemical activation of the process were applied^{57, 106}.

SHS yielded a fine-grained product with a composite structure. X-ray analysis identified three phases: titanium carbide, chromium carbide and a solid solution based on gamma-nickel. Depending on the Ti-C/Cr-C ratio in the charge mixture and the synthesis conditions, chromium can be mostly dissolved in titanium carbide, forming titanium-chromium carbide solid solution (double titanium-chromium carbide) or can make up its proper carbides⁵⁷.

Table 3 represents the oxidation resistance of the SHS composite powder 75wt.% (Cr₃C₂-TiC)/25 wt.% (Ni20Cr) - depending on the carbide phase composition. To control the content of chromium dissolved in the double carbide solid solution, titanium carbide lattice parameter measurements are presented

(chromium is known to occupy titanium sites in TiC, decreasing its lattice parameter¹⁰⁷). In general, dissolving chromium in the titanium carbide lattice during synthesis ensures a higher oxidation resistance of the material. For the composition with 30 wt.% Cr₃C₂, in spite of significantly lower weight gain, the oxidation kinetics is still controlled by the formation of titanium oxides that do not exhibit a high protective ability. A protective chromia layer is formed at a titanium-to-chromium carbide ratio of 30:70 (see **Table 3**, line 6). The material oxidation behavior is practically the same as that of the composite with pure chromium carbide. Interestingly, when the synthesis conditions assist chromium to form its proper carbide, leading to a lower Cr content in titanium-chromium solid solution, the oxidation resistance of the composition drops again (compare line 5 and 6, **Table 3**).

Fig. 10a illustrates the structure of the developed powder. Gray fields consist of double carbide grains that are round in shape of up to 0.5-1 μm in size surrounded by the very thin layers of nickel solid solution (light in color). The chromium content is practically constant through the crystals. It was evaluated as about 3 wt.% based on the electron probe microanalysis results. The microhardness of these areas is 766-1449 H_{V50}. The material also contains Cr₃C₂ polyhedral crystals (light-gray) of 5-10 μm in size and a microhardness of 1449-1648 HV50. There are some

Table 3 Weight gain of the SHS powders 75(Cr₃C₂-TiC) / 25 Ni20Cr, wt.%, with particle size less than 50 μm during oxidation in air

N	Carbide phase composition, wt.%	TiC lattice parameter, nm	Weight gain, mg/g at temperature (°C)					
			300	400	450	500	550	600
1	100TiC	0.4345	33	36	38	63	73	362
2	10Cr ₃ C ₂ -90TiC	0.432	53	48	49	78	127	130
3	20Cr ₃ C ₂ -80TiC	0.4315	0	3	7	39	131	139
4	30Cr ₃ C ₂ -70TiC	0.4290	0	2	6	71	78	79
5	70Cr ₃ C ₂ -30TiC	0.4320	0	4	12	26	40	100
6	70Cr₃C₂-30TiC	0.4280	0	4	10	14	15	13
7	100Cr ₃ C ₂	-	0	0	3	5	10	9

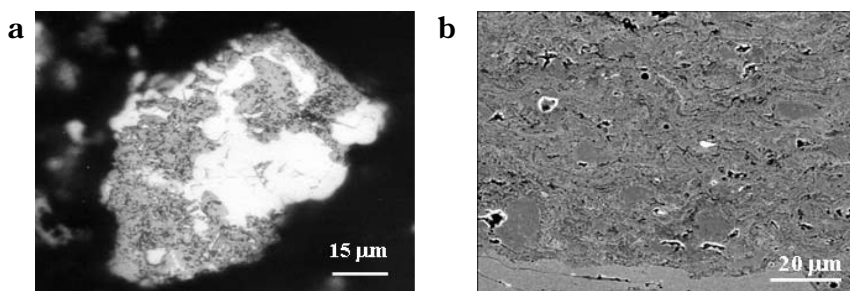


Fig.10 Cross-sections of (Cr₃C₂-TiC) / NiCr powder (a) and HVOF coating from it (b).

fine inclusions of nickel solid solution in chromium carbide areas, too.

HVOF coatings from the synthesized (Cr₃C₂-TiC) / NiCr powder (**Fig. 10 (b)**) demonstrate an extremely high thermal cycling lifetime (8-10 times higher than that of HVOF coatings from conventionally used WC-17%Co and 25NiCr-75Cr₃C₂ powders (Praxair Specialty)⁵⁷). Elevated temperature erosion in a wide range of test conditions did not reveal any signs of the material corrosion⁵⁷). The main mechanism of the surface degradation is mechanical wear caused by the impacting particles. The surface morphology of the erosion grooves is indicative of a ductile wear mechanism.

The industrial-scale production of the developed (Cr₃C₂-TiC) / NiCr powder has been approved in PMI with a deviation of the titanium carbide lattice parameter less than ±0.0001 nm. Since 1996, the powder has been employed in coal-fired boilers of energy plants and also in waste-incinerating systems as well as in the paper and chemical industries in the USA, Sweden, Germany and Poland.

Another approach to improvement of metal/ceramic composite powders is the development of binder materials. A big advance was achieved with complex binders^{35, 37, 42, 54, 73}) and the introduction of solid lubricant phases such as graphite, calcium fluoride and molybdenum disilicide^{44, 48, 60, 65, 75}) (by adding corresponding powders to the charge mixture). For exam-

ple, SHS powders with solid lubricants (TiC/NiCr / MoS₂, TiC/NiCr / CaF₂, TiC / FeCr / graphite, TiC / Fe-CrMo / graphite and Cr₂O₃ / TiO₂ / CaF₂) provide good coating performance under dry or limited lubricated friction conditions and at high temperatures⁶⁵).

One more class of composite powders showing promise for TS applications is lightweight high-performance **intermetallic-oxide composites** which enable a significant decrease in weight whilst providing top performance as compared to existing materials.

In general, SHS intermetallic/oxide powders can be produced using two main approaches: (1) synthesis of intermetallics from the corresponding metal powders in the presence of dispersed alumina particles and (2) formation of necessary compositions using aluminothermal reduction of metal oxides. Both routes have some limitations connected with too low (in the first case) and too high (in the second one) exothermal reaction effects. In both cases, preliminary mechanical activation provides for the efficient solution of the problems and results in the formation of homogeneous fine-grained materials.

Fig. 11a represents the microstructure of a NiAl / Al₂O₃ composite powder produced by the synthesis of nickel monoaluminide from elemental powders in the presence of dispersed alumina particles⁴⁵). The powder microhardness is 350-650 Hv₅₀. The amount of alumina is optimized in such a way that the mate-

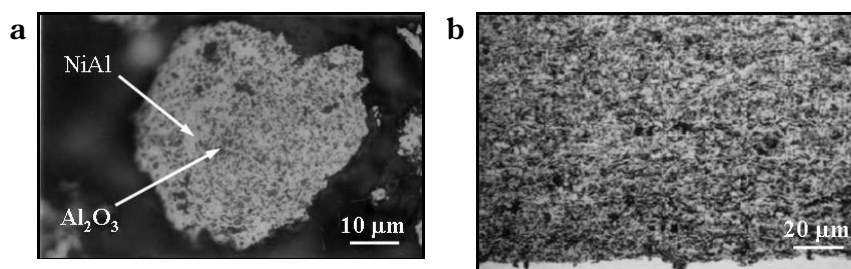


Fig. 11 Cross-sections of NiAl / Al₂O₃ powder (a) and high-velocity plasma spray coating from it (b).

rial's thermal expansion coefficient is close to that of a carbon steel substrate, providing high performance of the coatings under thermal shock conditions. Plasma coatings from the powder (**Fig. 11b**) also exhibit good wear-resistance⁴⁵.

Nanocomposite powders. The processing of nanostructured materials has attracted more attention in recent years due to the fact that the nanometer size scale brings substantial changes into physicochemical and mechanical properties, in comparison with bulk properties¹⁰⁸. To produce nanostructural feedstock from micron- and submicron-grained composite powders, the post-synthesis treatment of SHS powders in attrition mills and high-energy mills is used⁷⁷⁻⁷⁹. Nanocomposite coatings have been ob-

tained from these feedstocks.

Recently, together with our colleagues from the Institute of Solid State Chemistry and Mechanochemistry, Novosibirsk, Russia, we have developed a new approach to produce SHS nanocomposite powders using mechanocomposite precursors¹⁰⁹⁻¹¹¹. It can be illustrated by the example of producing intermetallic/oxide powders in systems with aluminothermal reactions. The point of the process is that the aluminothermal reduction of metal oxides, fully or partially completed during the mechanical activation step, forms nanocomposite precursors containing nanosized alumina inclusions. In the second step, SHS proceeded in the precursors thus formed. The as-synthesized powders completely inherit the pre-

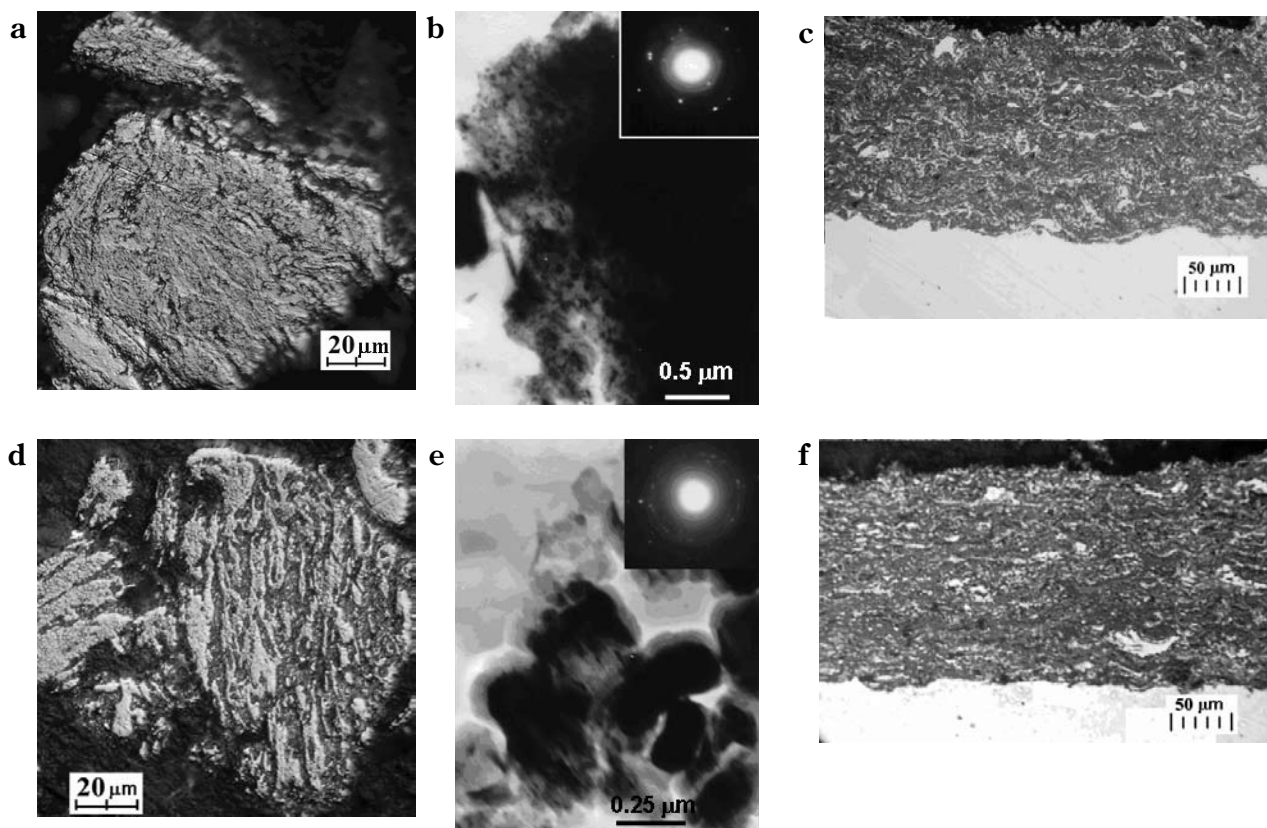


Fig. 12 Microstructure of nanocomposite SHS powders (a-b, d-e) and detonation spray coatings from them (c, f): a-c – FeAl / Al₂O₃ powder; d-f – FeAl(Cr) / Al₂O₃ powder.

cursor's structural morphology^{110,111}. It is probably connected with the high rate of chemical reactions in the nanocomposite precursors and implementation of non-equilibrium phase formation mechanisms at the lowered temperatures¹¹¹.

This approach was used to develop nanocomposite powders FeAl/Al₂O₃ and FeAl(Cr)/Al₂O₃ with so-called interpenetrating structure with improved interfacial strength¹¹² (**Fig. 12 a, b, d, e**). Detonation spray coatings from the powders (**Fig. 12c, f**) also have a nanocomposite structure with average crystallite size of the intermetallic phase 15-57 nm, porosity less than 1%, microhardness 750-850 Hv200 and high antifriction properties at conditions of lubricated friction of sliding and rolling (friction ratio of coatings FeAl/Al₂O₃ and FeAl(Cr)/Al₂O₃ at loading of 5 MPa, sliding velocity 4.2 m/s and use of samples of hardened steel 45 subjected to nitrocementation as a counterbody is 0.05 and 0.045, respectively)¹¹³.

Thus, the SHS method opens up a great deal of opportunities for creating advanced powders for thermal spraying. A summarized list of thermal sprayed powders, methods of their deposition and coating properties is given in **Table 4**. At present, SHS powders for thermal spraying are developed and produced by the Institute of Structural Macrokinetics (Russia), Powder Metallurgy Institute (Belarus), London & Scandinavian Metallurgy Co., Ltd. (Great Britain), Exotherm Co. (USA), Xform Inc. (USA) and Kyoritsu Ceramic Co. Ltd. (Japan).

Summary

From the results obtained it is evident that self-propagating high-temperature synthesis is a promising method for the preparation of advanced powders for thermal spraying functional coatings. Besides important economical and ecological benefits, the method allows the formation of powders with improved or

Table 4 SHS powders for thermal spraying

Powder composition	Spraying method	Coating function (properties)	Ref.
MoSi ₂	PS, HVOF	High-temperature oxidation-resistant coating	21, 24
Cr ₃ C ₂ ; (Ti, Cr)C; Cr ₃ C ₂ /Ti _k Cr _{1-x} Cy	PS	Wear protection	17, 51, 85
TiC-Cr ₃ C ₂ (clad with nickel)	PS	Long-term oxidation resistance at 500°C	14, 17
TiB ₂ (SHS) + MoSi ₂	APS	Composite-coated cathodes for aluminum electrolysis process	76
TiN, ZrN	PS	Coatings on carbon fibers	86
non-stoichiometric TiN _x	TS	Wear-resistant coating	85
NiAl; Ni ₃ Al; NiAlCr; NiAl modified with nano SiO ₂ and UDD	PS, DS	High-temperature applications, high oxidation resistance	29, 94, 91-92
TiAl; TiAl ₃	PS, DS	Lightweight, oxidation- and corrosion-resistant, Aircraft fuel coupling	8, 27, 81
TiAlCr	DS	Oxidation-resistant up to 900°C	102
FeAl-Fe _x Al _y	HVOF, DS, PS	Wear and corrosion protection Size restoration	64,67
(Ni, Zn, Co, Mn) Fe ₂ O ₄	HVOF, APS	Electromagnetic applications	105
TiC/Al, SiC/Al, SiC/Al-Si	UPS, APS, LPPS	Wear protection of Al alloys	25, 31
TiC/Ni	PS	Modifying additive for CoNiCrAlY intermediate layer for thermal-barrier coating	78
TiC _{0.5} N _{0.5} /Ni	TS	Wear-resistant coating	85
(Ti, Cr)C/Ni; Ti _k Cr _{1-x} Cy/Ni; (TiC-Cr ₃ C ₂)/Ni	PS	Wear protection, erosion- and corrosion-resistant coatings	8, 13, 85
Ti _k Cr _{1-x} Cy/Ni-P	PS	Wear protection	15
TiC/Fe; TiC/Co; TiC/Al; TiC/Fe ₃ C/Fe; TiC/FeCr TiC/NiCr; TiC/FeCu; TiC/FeCrNi; TiC/FeCrMoC; TiC/FeCrWMo, TiC/CrNiMo TiC/FeNiCrMo; TiC/NiCr; TiC/NiCrMoW; TiC/NiTiCrAl	HVOF, PS, UPS,LPPS,	Wear protection	23, 31, 34, 42, 46, 52-56, 58, 66, 73
(Ti, W)C/Ni, TiC/NiTi; TiC/NiCr; (Mo, Ti)C/ NiCr; (W, Ti)C/NiCr; (Ti, W)C/NiCr TiC/NiTiCrAl	PS, HVOF	Protection against corrosion and wear Corrosion resistance of coatings is higher than that of WC-Co, WC-Ni coatings	35, 53, 56, 63
TiC/NiCr	PS	High sliding wear resistance	32
TiC/NiAl	TS	Protection against oxidation and wear in sulfur-containing area	28
TiC/NiCr; TiC/FeCr; Cr ₃ C ₂ /NiCr	LPPS, HVOF	Protection against erosion at temperatures up to 400°C for TiC-based powders; up to 600°C for Cr ₃ C ₂ -based powder	30, 32

Cr ₃ C ₂ /NiCr	HVOF	High resistance in fuel combustion products, protection against erosion wear	20, 56
Cr ₃ C ₂ /NiMo	PS	Wear protection	51
Cr ₃ C ₂ /TiC/NiCr; Cr ₃ C ₂ /TiC/NiCrMo	FS, HVOF	Protection against erosion and corrosion at elevated temperatures	56, 57
Cr ₃ C ₂ /NiAl	PS	Wear-resistant coating	8
NbC/Fe, (Nb, Ti)C/Fe (W, Ti)C/Fe	TS	Wear-resistant coatings	8
TiB ₂ /Fe; TiB ₂ /FeCr; TiB ₂ /NiCr; TiB ₂ /NiCrB	HVOF	High abrasive and sliding wear resistance	56, 62, 70, 72
TiB ₂ /Al ₂ O ₃	PS	Abrasive-wear-resistant coating	80
TiB ₂ /Cu	PS	Nanostructured coatings on copper substrate	79
TiC/FeCr/C; TiC/FeCrMoC; TiC /NiCrFe/ MoS ₂ ; TiC/NiCrFe/CaF ₂ ; Cr ₂ O ₃ /TiO ₂ /CaF ₂ ;	DS, SAPS, PS	Antifriction coatings	44, 48, 60, 65, 75
MoSi ₂ /SiC	APS, LPPS, HVOF	High-temperature applications, oxidation-resistant	21, 24
MoSi ₂ /Si ₃ N ₄	PS	Wear- and oxidation-resistant coatings	40, 41
Al ₂ O ₃ /B ₄ C/SiC; Al ₂ O ₃ /TiN; B ₄ C/SiC; TiSi ₂ / Al ₂ O ₃ /Cu/BN; TiSi ₂ /Al ₂ O ₃ /Ni/Cr ₃ C ₂ ; Cr ₃ C ₂ / Al ₂ O ₃ /NiAl/TiSi ₂ /TiC	DS	Coatings are promising for propulsion engineering, energy, metallurgy and oil industry to protect parts from oxidation and erosion	74
NiAl/Al ₂ O ₃ ; FeAl/Al ₂ O ₃	FS, PS, SAPS	Wear protection	38, 45
Nanocomposite powders FeAl/Al ₂ O ₃ ; FeAl(Cr)/Al ₂ O ₃	DS	Antifriction coatings	113
Al ₂ O ₃ /Cr	PS	Wear in unshocked impacts and high temperatures, intermediate layer for thermal-barrier coatings	12, 16, 19
Al ₂ O ₃ /TiC	PS	Wear protection	49
Al ₂ O ₃ /Cr ₃ C ₂	APS	High wear resistance in liquid fuel	9
Al ₂ O ₃ /NiAl	PS	Intermediate layer for thermal-barrier coatings	19
FeCrAl-FeAl/Cr ₃ C ₂ -Al ₂ O ₃ ; NiCrAl-FeAl/TiC- Al ₂ O ₃	APS, DS	Wear-resistant, promising for automotive industry as brake facing material	69

unique structure and properties in size ranges and with an external morphology suitable for different thermal spray processes. Usage of different kinds of the SHS process activation plays an important role in structure and phase-formation mechanisms, providing good flexibility and reliability even for industrial-scale powder production.

References

- 1) Pawlowski, L. (1995): "The Science and Technology of Thermal Spray Coatings", New York, Wiley.
- 2) Fauchais, P. and Montavon, G. (2008): Thermal and cold spray: Recent developments, Key Engineering Materials, Vol. 384, pp.1-59.
- 3) Merzhanov, A. G. (1990): Self-propagating high-temperature synthesis: twenty years of research and findings, In: "Combustion and plasma synthesis of high-temperature materials", VCH Publishers Inc., New York, pp.1-53.
- 4) Varma, A., Rogachev, A.S., Mukas'yan, A.S., Hwang, S. (1998): Combustion synthesis of advanced materials: Principles and applications, Adv. Chem. Eng, Vol. 24, pp.79-226.
- 5) Levashov, E. A., Rogachev, A.S., Yuxhvid, V.I., Borovinskaya, I. P. (1999): Physico-Chemical, and Technological Fundamentals of Self-Propagating High-Temperature Synthesis, BINOM, Moscow (in Russian).
- 6) Merzhanov, A. G., Mukasyan, A.S. (2007): "Solid-Flame Combustion", Torus Press, Moscow (in Russian).
- 7) Cao, G., Orrù, R. (2002): Self-propagating reactions for environmental protection: State of the art and future directions, Chemical Engineering Journal, Vol. 87 (2), pp.239-249.
- 8) Concept for Further Development of SHS as a Branch of Modern R & D (2003), ed. Merzhanov, A. G., Territoriya, Chernogolovka [in Russian].
- 9) Borisov, Yu.S., Polyandin, B.A., Gorbatov, I.N. (1981): Production and properties of plasma-sprayed composite-powder coatings based on refractory compounds, Abstracts of Sci.-tech. Conf. on Composite Coatings, Zhitomir, pp.24-25 [in Russian].
- 10) Borisov, Yu., Borisova, A., Shvedova, L. (1986): Transition metal - Nonmetallic refractory compound composite powders for thermal spraying, Proc. of ITSC'86, Montreal, Canada, September 8-12, 1986, Pergamon Press, pp.323-330.
- 11) Itin, V. I., Naiborodenco, Yu.S. (1989): "High-Temperature Synthesis of Intermetallic Compounds", Tomsk State University Publishing House, Tomsk, (in Russian).
- 12) Vepruk, B. A., Kurylev, M.V., Korenkov, V. A., Mu-

- kazhanov, V. A. (1990): Composite SHS-powder of aluminum oxide with chrome for a plasma spraying, Abstracts Region. Conf. of Young Scientists and Experts of Research Organizations and Enterprises on Modern Materials in Mechanical Engineering, Perm, p. 14 [in Russian].
- 13) Gorbatov, I. N., Shkiro, V. M., Terent'ev, A.E., Shvedova, L.K., Martsenyuk, I. S., Karpenko, S.V. (1991): Study of properties of gas-thermal coatings from composite powders of titanium and chromium carbides and nickel, *Fizika i Khimiya Obrabotki Materialov*, No 4, pp.102-106.
 - 14) Gorbatov, I. N., Il'chenko, N. S., Terent'ev, A. S. (1991): Effect of cladding double titanium-chrome carbide on the properties of plasma-sprayed coatings, *Fizika i Khimiya Obrabotki Materialov*, No 3, pp.69-73.
 - 15) Gorbatov, I.N., Panasyuk, A. D., Shvedova, L.K. (1991): Thermal-sprayed composite-powder coatings based on titanium-chrome carbide, *Zashch. Pokryt. Metal.*, Vol. 25, pp.22-25.
 - 16) Veprik, B. A., Kurylev, M.V., Korenkov, V.A. (1991): Structure of Cr-Al₂O₃ SHS-composite coatings, Superhard and Composite Materials and Coatings and Their Application, Kiev, pp.57-59 [in Russian].
 - 17) Merzhanov, A. G. (1992): Self-propagating high-temperature synthesis and powder metallurgy: Unity of goals and competition of principles, *Advances in Powder Metallurgy*, No 9, pp.341-368.
 - 18) Borisov, Yu., Borisova, A. (1993): Application of self-propagating high-temperature synthesis in thermal spraying technology, Proc. of NTSC'93, Anaheim, USA, June 7-11, 1993, ASM Int., pp.139-144.
 - 19) Show, K. G., Mc. Coy, K. P., Trogolo, J.A. (1994): Fabrication of composite spray powders using reaction synthesis, Proc. 7th NTSC, Boston, USA, June 20-24, 1994, ASM Int. Boston, pp.509-514.
 - 20) Wang, B. Q., Luer, K. (1994): The relative erosion-corrosion resistance of commercial thermal sprayed coating in a simulated circulating fluidized bed combustor (CFBC) environment, Proc. 7th NTSC, Boston, USA, June 20-24, 1994, ASM Int. Boston, pp.115-120.
 - 21) Smith, R.W., Mohanty, M., Shtessel, E., Verstak, A. (1995): Self-propagating High-Temperature Synthesis (SHS) of Thermal Spray Powders, Proc. ITSC'95, Kobe, Japan, 22-26 May, 1995, High-temperature Society of Japan, 1995, pp.1121-1126.
 - 22) Lugscheider, E., Remek, E., Borisov, Yu. (1995): NiCr-Cr₃C₂ and NiCr-TiC high wear-resistant coatings for protective applications in steam turbines, Proc. ITSC'95, Kobe, Japan, 22-26 May, 1995, High-temperature Society of Japan, 1995, pp.235-240.
 - 23) Mohanty, M., Smith, R. W. (1995): Plasma spray processing of TiC-reinforced coatings for wear protection, Proc. 8th NTSC, Houston, USA, September 11-15, 1995, ASM Int. Houston, pp.561-566.
 - 24) Knight, R., Smith, R.W., Mohanty, M., Shtessel, E.A. (1995): Low pressure plasma sprayed SHS MoSi₂/SiC composite coatings, Proc. 8th NTSC, Houston, USA, September 11-15, 1995, ASM Int. Houston, pp.743-748.
 - 25) Vitiaz, P., Verstak, A., Lugscheider, E., Remer, P., Steinhäuser, Z., Borisov, Yu., Azarova, T., Beliaev, A., Talako T. (1995): Novel metal-carbide coatings from the synthesized powders for protection of aluminium and titanium alloys from wear, *Powder Metallurgy (Minsk)*, Issue 17, pp.100-109 (in Russian).
 - 26) Saidi, A., Wood, J.V., Kellie, J.L.F. (1995): Development of carbide coating materials for thermal spraying, Proc. 5th World Seminar on Heat Treatment and Surface Engineering, Iranian Soc. Sci. Eng. Technol. Isfahan, pp.451-456.
 - 27) Vol'pe, B. M., Yevstigneev, V.V., Milyukov, I.V. (1995): SHS of disperse Ti-Al materials and their protective coatings, *Fizika i Khimiya Obrabotki Materialov*, No 2, pp.73-79.
 - 28) Shaw, K. G., Reinshagen, J.H. (1996): Powder production of nickel and iron aluminides Proc. 4th Conf. on Nickel and Iron Aluminides, Cincinnati, USA, pp.1-11.
 - 29) Vol'pe, B. M., Evstigneev, V.V., Milyukova, I.V., Sajgutin, G. V., Glechikov, S.V., Konoplin, Yu.P. (1996): Self-propagating high-temperature synthesis of fine nickel aluminides and protective coatings on their basis, *Fizika i Khimiya Obrabotki Materialov*, No 1, pp.50-54.
 - 30) Verstak, A., Vitiaz, P., Lugscheider, E., Belyaev, A., Talako, T., Azarova, T., Koval, V. (1996): New coatings for elevated temperature erosion application (1996) Proc. TS' 96, Essen, Germany, March 6-8, 1996, DVS-Verl. Essen, pp.71-75.
 - 31) Vitiaz, P., Verstak, A., Lugscheider, E., Azarova, T., Talako, T. (1996): Titanium carbide in wear resistant coatings, Proc. of the 9-th National Thermal Spray Conference NTSC' 96 "Thermal Spray: Solutions of Engineering problems", Cincinnati, USA, October 7-10, 1996, ASM Int. Cincinnati, pp.169-176.
 - 32) Bartuli, C., Smith, R.W. (1996): Comparison between Ni-Cr-40vol%TiC wear-resistant plasma sprayed coatings produced from self-propagating high-temperature synthesis and plasma densified powders, *Journal of Thermal Spray Technology*, Vol. 5, No 3, pp.335-342.
 - 33) Bartuli, C., Smith, R. W., Shtessel, E. (1997): SHS powders for thermal spray applications, *Ceramics International*, Vol. 23, Issue 1, pp.61-68.
 - 34) Vitiaz, P., Azarova, T., Talako, T., Ilyuschenko, A. (1997): Composite Fe/TiC powders for wear resistance coatings using plasma spray process, Proc. 1st UTSC, Indianapolis, USA, September 15-18, 1997, ASM Int. Indianapolis, pp.131-139.
 - 35) De Paco, J. M., Nutting, J., Guilemany, J.M. (1997): Structure-properties relationships of TiC-Ni-Ti and (Ti, W)C-Ni powders manufactured by the SHS process and the resultant HVOF-sprayed coatings, Proc. 1st UTSC, Indianapolis, USA, September 15-18, 1997, ASM Int. Indianapolis, pp.935-942.
 - 36) Kunrath, A. O., Upadhaya, K., Reimanis, I.E., Moore, J. J. (1997): Synthesis and application of composite TiC-Cr₃C₂ targets, *Surface and Coatings Technology*, Vol. 94-95, pp.237-241.

- 37) Ilyuschenko, A., Azarova, T., Talako, T., Wielage, B., Steinhauser, S. (1998): Wear resistant thermal sprayed coatings from Fe/TiC powders, III konferencja Naukowo-Techniczna Materiały i technologie zwiększajace trwalose elemetow maszyn i urzadzzen w przemyśle energetycznym, Ustron, 1998, p.99-104.
- 38) Manoilo, E. D., Talako, T. L., Belyaev, A.V. (1998): Gas-flame spraying of coatings of synthesized composite materials with solid-phase inclusions, Powder Metallurgy (Minsk), Issue 21, pp.69-73 (in Russian).
- 39) Guilemany, J. M., De Paco, J. M., Miguel, J.R., Sanchez, J., Smith, P. (1998): Corrosion resistance of HVOF coatings based upon TiC+NiTi and (Ti,W)C+Ni, Proceedings of the International Thermal Spray Conference, 1, pp.57-61.
- 40) Bartlett, A. H., Castro, R.G. (1998): Elevated temperature mechanical properties of MoSi₂/Si₃N₄, MoSi₂/SiC composites produced by self-propagating high temperature synthesis, Journal of Materials Science, Vol. 33, No 6, pp.1653-1660.
- 41) Kung, H., Lu, Y.C., Bartlett, A.H., Castro, R.G., Petrovic, J. J. (1998): Structural characterization of combustion synthesized MoSi₂-Si₃N₄ composite powders and plasma sprayed MoSi₂-Si₃N₄ composites, J. Mater. Res., Vol. 13, No 6, pp.1522-1529.
- 42) Ilyuschenko, A., Azarova, T., Wielage, B. (1999): Microstructure-properties relationship, Proc. UTSC, Dusseldorf, Germany, March 17-19, 1999, DVS-Verl. Dusseldorf, pp.35-38.
- 43) L.-M. Berger, M. Nebelung, P. Vuoristo, M. Heinonen, T. Mäntylä, T. Reinhardt, M. Delaet. (1999): Development and application of TiC-Ni based plasma sprayed coatings, Proc. UTSC, Dusseldorf, Germany, March 17-19, 1999, DVS-Verl. Dusseldorf, pp.128-133.
- 44) Borisova, A., Borisov, Yu., Tunik, A. (1999): Thermal spraying of coatings containing solid lubricants, Proc. UTSC, Dusseldorf, Germany, March 17-19, 1999, DVS-Verl. Dusseldorf, pp.174-181.
- 45) Vityaz, P.; Beliaev, A.; Talako, T.; Koval, V. (1999): Plasma coatings from the synthesized composite powders, Proc. UTSC, Dusseldorf, Germany, March 17-19, 1999, DVS-Verl. Dusseldorf, pp.293-295.
- 46) Wielage, B., Steinhauser, S., Schnick, T. (1999): Thermal spraying of titanium carbide composite materials, Proc. UTSC, Dusseldorf, Germany, March 17-19, 1999, DVS-Verl. Dusseldorf, pp.301-305.
- 47) Guilemany, J.M., Sanchez, J., de Paco, J.M. (1999): Spray gun influence on the oxidation of TiC+Ni-Ti based powders during HVOF spraying, Proc. UTSC, Dusseldorf, Germany, March 17-19, 1999, DVS-Verl. Dusseldorf, pp.446-451.
- 48) Borisova, A.L., Adeeva, L.I., Tunik, A.Yu. (1999): Structure and properties of thermal-sprayed coatings based on titanium carbide and titanium and chrome oxides with solid lubricants Avtomat. Svarka, No 1, pp.22-27.
- 49) Lintula, P., Maunu, J., Vuoristo, P., Mantyla, T. (1999): Production of TiC-based cermet and TiC-Al₂O₃ thermal spray powders by SHS, 5th Int. Symp. Self-propagating High-temperature Synthesis (SHS-99), Moscow, pp.81-82.
- 50) Wang, B.-Q., Verstak, A. (1999): Elevated temperature erosion of HVOF Cr₃C₂/TiC-NiCrMo cermet coating, Wear, Vol. 233-235, pp.342-351.
- 51) Sharivker, S.Yu., Merzhanov, A.G. (2000): SHS-Powders and Their Processing, ISMAN, Chernogolovka (in Russian).
- 52) Vaisanen, M., Vuoristo, P., Mantyla, T., Maunu, V., Lintunen, P., Lintula, P. (2000): Microstructure and Properties of TiC-CrNiMo SHS Spray Powder and Thermally Sprayed Coating, Proceedings of the International Thermal Spray Conference, pp.429-434.
- 53) Blatchford, M.T., Horlock, A.J., McCartney, D.G., Shipway, P.H., Wood, J.V. (2000): Production and Characterization of HVOF Sprayed NiCr-TiC Coatings Using SHS Powder Feedstock, Proceedings of the International Thermal Spray Conference, pp.515-522.
- 54) Wielage, B., Steinhauser, S., Schnick, T., Ilyuschenko, A., Azarova, A. (2000): HVOF Sprayed Titanium Carbide Composite Coatings for Wear Protection, Proceedings of the International Thermal Spray Conference, pp.537-542.
- 55) Steinhauser, S., Wielage, B., Hofmann, U., Schnick, Th., Ilyuschenko, A., Azarova, T. (2000): Plasma-sprayed wear-resistant coatings with respect to ecological aspects, Surface and Coatings Technology, Vol. 131, No 1-3, pp.365-371.
- 56) Blatchford, M.T., Jones, M., Horlock, A.J., McCartney, D.G., Shipway, P.H., Wood, J.V. (2001): Improvements in HVOF sprayed cermet coatings produced from SHS powders, Proceedings of the International Thermal Spray Conference "Thermal Spray 2001: New Surfaces for a new Millennium", (Ed.) C.C. Berndt, K.A. Khor and E.F. Lugscheider, Published by ASM International, Materials Park, Ohio, USA, pp.221-230.
- 57) Ilyushchenko, A., Vitiaz, P., Beliaev, A., Talako, T. (2001): SHS powder materials for protective coatings in power industry, Proceedings of the International Thermal Spray Conference "Thermal Spray 2001: New Surfaces for a new Millennium", (Ed.) C.C. Berndt, K.A. Khor and E.F. Lugscheider, Published by ASM International, Materials Park, Ohio, USA, pp.1299-1302.
- 58) Jones, M., Horlock, A.J., Shipway, P.H., McCartney, D.G., Wood, J.V. (2001): Microstructure and abrasive wear behavior of FeCr-TiC coatings deposited by HVOF spraying of SHS powders, Wear, Vol. 249, No 3-4, pp.246-253.
- 59) Jones, M., Horlock, A.J., Shipway, P.H., McCartney, D.G., Wood, J.V. (2001): A comparison of the abrasive wear behaviour of HVOF sprayed titanium carbide and titanium boride-based cermet coatings, Wear, Vol. 251, pp.1009-1016.
- 60) Beliaev, A.V., Ilyuschenko, A.Ph., Vitiaz, P.A., Talako, T.L., Sobolevsky, S.B. (2001): Art of manufacturing of composite ceramic material, Patent RB No 4163 (in Russian).

- 61) Horlock, A.J., McCartney, D.G., Shipway, P.H., Wood, J.V. (2002): Thermally sprayed Ni(Cr)-TiB₂ coatings using powder produced by self-propagating high temperature synthesis: Microstructure and abrasive wear behaviour, *Materials Science and Engineering*, Vol. A 336, No 1-2, pp.88-98.
- 62) Degnan, C. C., Shipway, P. H. (2002): A comparison of the reciprocating sliding wear behaviour of steel based metal matrix composites processed from self-propagating high-temperature synthesised Fe-TiC and Fe-TiB₂ masteralloys, *Wear*, Vol. 252, No 9-10, pp.832-841.
- 63) Azarova, T., Vitiaz, P., Wielage, B. (2002): Coherences between structure and properties of TiC containing thermal spraying coatings, *Proc. ITSC, Essen, Germany, March 4-6, 2002, DVS-Verl. Essen*, pp.96-101.
- 64) Ilyushchenko, A., Talako, T.L., Beliaev, A.V., Letsko, A. I., Formanek, B. (2002): "Coatings of powders based on Iron aluminides, *Proc. ITSC, Essen, Germany, March 4-6, 2002, DVS-Verl. Essen*, pp.136-138.
- 65) Ilyushchenko, A., Shevtsov, A., Azarova, T., Okovityi, V., Smurov, V., Ignatiev, M., Kovalion, E. (2002): Investigation of composite powders with hard lubricant components for thermal spraying of coatings, *Proc. ITSC, Essen, Germany, March 4-6, 2002, DVS-Verl. Essen*, pp.1029-1032.
- 66) Azarova, T. A., Vitiaz, P. A., Vilage, B., Shteinhauzer, Z. (2002): Structure and properties of composite materials based on titanium carbide with copper additives, *Powder Metallurgy (Minsk)*, Issue 25, 85-89 (in Russian).
- 67) Vitiaz, P. A., Ilyushchenko, A.Ph., Talako, T.L., Beliaev, A. V., Letsko, A.I., Formanek, B, Yakovleva, M.S. (2003): High-velocity oxy-fuel flame and detonation spraying of powders of iron aluminides produced by the method of self-propagating high-temperature synthesis, *Powder Metallurgy (Minsk)*, Issue 26, pp.135-141 (in Russian).
- 68) Licheri, R., Orrù, R., Cao, G., Crippa, A., Scholz, R. (2003): Self-propagating combustion synthesis and plasma spraying deposition of TiC-Fe powders, *Ceramics International*, Vol. 29, No 5, pp.519-526.
- 69) Bach, Fr.-W., Babiak, Z., Rothardt, T., Formanek, B. (2003): Properties of Plasma and D-gun sprayed Metal-Matrix-Composite (MMC) Coatings based on Ceramic Hard Particle Reinforced Fe-, Ni-aluminide Matrix, *Proc Thermal Spray 2003: Advancing the Science & Applying the Technology*, Ed. C. Moreau and B. Marple, Published by ASM International, Materials Park, Ohio, USA, 2003, pp.249-253.
- 70) Lotfi, B., Shipway, P. H., McCartney, D.G., Edris, H. (2003) Abrasive wear behaviour of Ni(Cr)-TiB₂ coatings deposited by HVOF spraying of SHS-derived cermet powders, *Wear*, Vol. 254, No 3-4, pp.340-349.
- 71) Licheri, R., Orru, R., Cao, G., Crippa, A., Scholz, R. (2003): Self-propagating combustion synthesis and plasma spraying deposition of TiC-Fe powders, *Ceramics International*, Vol. 29, No 5, pp.519-526.
- 72) Lotfi, B., Sadeghian, Z. (2004): Microstructure and sliding wear behaviour of Ni(Cr)-TiB₂ coatings deposited by HVOF spraying of SHS powders, *Transactions of Materials and Heat Treatment*, Vol. 25, No 5, pp.1183-1186.
- 73) Licheri, R., Orru, R., Locci, A.M., Cao, G. (2004): Combustion synthesis of TiC-metal composites and related plasma spraying deposition, *International Journal of Materials and Product Technology*, Vol. 20, No 5-6, pp.464-478.
- 74) Borisova, A., Borisov, Yu., Adeeva, L. (2005): Heat-resistance of plasma spray coatings from composite powders produced by SHS-method, *Proc. 16th Int. Plansee Seminar, Austria, 30 May-3 June, 2005, RVF Vienna*, pp.434-447.
- 75) Ilyushchenko, A. F., Okovityi, V.A., Shevtsov, A.I. (2005): Formation of Wear-Resistant Plasma-Sprayed Coatings Based on Self-Lubricating Composite Materials, *Bestprint, Minsk (in Russian)*.
- 76) Lu, H., Jia, W., Ma, R., Yuan, W., Wang, Y. (2005): Titanium diboride and molybdenum silicide composite coating on cathode carbon blocks in aluminum electrolysis cells by atmospheric plasma spraying, *TMS Light Metals*, pp.785-788.
- 77) Dercz, G., Formanek, B., Prusik, K., Pajak, L. (2005): Microstructure of Ni(Cr)-TiC-Cr₃C₂-Cr₇C₃ composite powder, *Journal of Materials Processing Technology*, Vol. 162-163 (SPEC. ISS.), pp.15-19.
- 78) Solonenko, O.P., Cherepanov, A.N., Marusin, B.A., Poluboyarov D.F. (2007): Combined technologies for processing perspective powder materials, coating deposition and surface hardening with controlled micro- and nanostructure, *Tyazheloe mashinostroenie*, No 10, pp.10-13 (in Russian).
- 79) Lomovsky, O. I., Dudina, D.V., Ulianitsky, V.Yu., Zlobin, S.B., Kosarev, V.F., Klinkov, S.V., Korchagin, M.A., Kwon, Y.-S. (2007): Cold and detonation spraying of TiB₂-Cu nanocomposites, *Materials Science Forum*, 534-536, pp.1373-1376.
- 80) Cheng, H., Li, Z., Shi, Y., Li, Q., Li, S. (2008): Effects of nanoscale powder on coating deposited by axial plasma spraying TiB₂/Al₂O₃ composite powders, *Transactions of the China Welding Institution*, Vol. 29, No 1, pp.40-44.
- 81) Filimonov, V.Yu., Yakovlev, V. I., Korchagin, M. A., Loginova, M.V., Semenchina, A. S., Afanas'ev, A. V. (2008): Structure formation during gas-detonation spraying of coatings from composite powders TiAl₃ and Ni₃Al, *Combustion, Explosion and Shock Waves*, Vol. 44, No 5, pp.591-596.
- 82) Borisova, A.L., Borisov, Yu.S. (2008): Self-propagating high-temperature synthesis for the deposition of thermal-sprayed coatings, *Powder Metallurgy and Metal Ceramics*, Vol. 47, No 1-2, pp.80-94.
- 83) Munir, Z.; Anselmi-Tamburini, V. (1989): Self-Propagating Exothermic Reactions: The Synthesis of High-Temperature Materials by Combustion, *Mater. Sci. Rep.*, Vol. 3, pp.277-365.

- 84) Moore, J. J.; Feng, H. J. (1995): Combustion synthesis of advanced materials. Part I. Reaction parameters, *Progress in Mater. Sci.*, Vol. 39, No 4-5, p. 243-273.
- 85) Amosov, A. P., Borovinskaya, I.P., Merzhanov, A.G. (2007): "Powder Technology of Self-Propagating High-Temperature Synthesis of Materials", Ed. Antziferov, V.N, Mashinostroenie-1, Moscow (in Russian).
- 86) Amosov, A.P., Bichurov, G.V. (2007): Azide Technology of Self-Propagating High-Temperature Synthesis of Micro- and Nanopowders, Mashinostroenie-1, Moscow (in Russian).
- 87) Bernard, F., Gaffet, E. (2001): Mechanical alloying in SHS research, *Int. J. SHS*, No 2, pp.109–131.
- 88) Grigorieva, T., Korchagin, M., Lyakhov, N. (2002): Combination of SHS and mechanochemical synthesis for nanopowder technologies, *KONA Powder and Particle Journal*, No. 20, pp.144–158.
- 89) Walston, W.S., Field, R.D., Dobbs, J.R., Lahrman, D.F., Darolia, R. (1999): Microstructure and high temperature strength of NiAl alloys, *Intermetallics*, Vol. 7, pp.523-532.
- 90) Grabke, H.J. (1999): Oxidation of NiAl and FeAl, *Intermetallics*, Vol. 7, pp.1153-1158.
- 91) Talako, T. L., Letsko, A. I., Vitiaz, P. A., Beliaev, A. V., Zabavsky, V. M. (2008): Art of manufacturing modified powder by the method of self-propagating high-temperature synthesis, Patent RB No 10781 (in Russian).
- 92) Talako, T.L.; Yakovleva, M. S., Letsko A.I.; Vitiaz P.A.; Kovaleva, S.A., Mosunov, E. I. (2008): Structure and properties of detonation spray coatings from SHS powders modified with nanoadditives, *Proc I-st Int. Sci. Conf. "Nanostructural materials-2008: Belarus-Russia, Ukraine"*, Minsk, p. 289 (in Russian).
- 93) Cotton, J.D., Noebe, R. D. and Kaufman, M.J. (1993): Ternary alloying effects in polycrystalline β -NiAl, *Structural intermetallics*, ed. by R. Darolia, the Minerals, Metals & Materials Society, pp.513-522.
- 94) Beliaev, A. V., Talako, T. L., Letsko, A.I., Vitiaz, P.A., Ilyushchenko, A. Ph.(2008): Powder material based on nickel monoaluminide and art of its manufacturing, Patent RB No 10317 (in Russian).
- 95) Liu, C. T., Stringer, J., Mundy, J.N., Horton, L.L, Angelini, P. (1997): Ordered intermetallic alloys: an assessment, *Intermetallics*, Vol. 5, pp.579-596.
- 96) Talako, T.L., Beliaev, A.V., Ilyushchenko, A.Ph., Letsko, A.I. (2004): Powder material based on iron monoaluminide and art of its manufacturing, Patent RB No 6545 (in Russian).
- 97) Formanek, B., Szczucka-Lasota, B., Szymanski, K., Ilyushchenko, A.Ph., Talako, T.L., Beliaev, A.V., Letsko, A.I. (2004): Corrosion resistance of coatings sprayed from the powder based on intermetallic FeAl, *Powder Metallurgy (Minsk)*, Issue 27, pp.135-140 (in Russian).
- 98) Allen, C. M., O' Reilly, K. A. Q., Cantor, B., Evans, P.V. (1998): Intermetallic phase selection in 1XXX Al Alloys, *Progress in Materials Science*, Vol. 43, pp.89-170.
- 99) Nieh, T.G., Wadsworth, J. (1997): Microstructural characteristics and deformation properties in superplastic intermetallics, *Materials Science and Engineering*, Vol. A 239-240, pp.88-96.
- 100) Dimiduk, D. M. (1999): Gamma titanium aluminide alloys – an assessment within the competition of aerospace structural materials, *Materials Science and Engineering*, Vol. A263, pp.281-288.
- 101) Talako, T. L., Letsko, A. I., Beliaev, A. V., Ilyushchenko, A.Ph., Hasak, T.V. (2008): Art of manufacturing powder material based on titanium aluminides, Patent RB No 10752 (in Russian).
- 102) Talaka, T., Ilyushchenko, A., Letsko, A., Hasak, T.(2007): Structure and Properties of MASHS Titanium Aluminide-Based Powder Alloyed with Chromium, *Materials Science Forum*, Vol. 534-536, p. 1589-1592.
- 103) Cross, W. B., Affleck, L., Kuznetsov, M.V., Parkin, I.P., Pankhurst, Q.A. (1999): Self-propagating high-temperature of ferrites MFe₂O₄ (M=Mg, Ba, Co, Ni, Cu, Zn); reactions in an external magnetic field, *J. Mater. Chem.*, Vol. 9, pp.2545-2552.
- 104) Talako, T. L., Beliaev, A.V., Letsko, A.I., Okatova, G.P., Kuznetsov, M.V., Morozov, Yu.G. (2002): Peculiarities of mechanically-activated self-propagating high-temperature synthesis of barium hexaferrite, *Powder Metallurgy (Minsk)*, Issue 25, pp.140-145 (in Russian).
- 105) McCartney, D.G., Zhang, D., Yellup J. Y., Bruhl M., Bobzin K., Richardt K., Talako T., Ilyushchanka A. (2009): Novel NiZn-Ferrite Powders and Coatings for Electromagnetic Applications, *Proc of International Thermal Spray Conference ITSC'09 "Expanding Thermal Spray Performance to New Markets and Applications or Thermal Spray"*, Las Vegas, May 2009, Ed. Basil, R. Marple, Margaret M., Hyland, Yuk-Chiu Lau, Chang-Jiu Li, Rogerio S. Lima, Ghislain Montavon. ASM international, pp.818-823.
- 106) Beliaev, A.V., Verstak, A.A., Talako, T.L., Vitiaz, P.A., Ilyushchenko, A.Ph. (2003): Art of manufacturing of composite powder material based on chromium and titanium carbides, Patent RB No 5947 (in Russian).
- 107) Sloof, W.G., Delhez, R., de Keijser, Th.H., Schalkoord, D., Ramaekers, P.P.J., Bastin, G.F. (1988): Chemical constitution and microstructure of TiC_x coatings chemically vapour deposited on Fe-C substrates; effects of iron and chromium, *J. of Mater. Sci.*, Vol. 23, pp.1660-1672.
- 108) Gusev, A. I., Rempel, A. A. (2001): Nanocrystalline materials, *Physmatlit*, Moscow (in Russian).
- 109) Lyakhov, N.Z., Vityaz, P. A., Grigor'eva, T.F. Talako, T.L., Barinova, A.P., Letsko A.I. (2005): Mechanochemically Synthesized Precursors for the Preparation of Intermetallic Compound/Oxide Nanocomposites by SHS, *Doklady Chemistry*, Vol. 405, Part 2, pp.255- 257.
- 110) Talaka, T., Grigorieva, T., Vitiaz, P., Lyakhov, N., Letsko A., Barinova A. (2007): Structure Peculiarities of Nanocomposite Powder Fe₄OAl/Al₂O₃ Produced by MASHS, *Mater. Sci. Forum*, Vols. 534-536, pp.1421-1424.
- 111) Talako, T. L., Grigor'eva, T. F., Letsko, A.I., Barinova, A. P., Vitiaz, P.A., Lyakhov, N.Z. (2009) Mecanoacti-

vated SHS of FeAl-Based Nanocomposite Powders, International Journal of Self-Propagating High-Temperature Synthesis Int. J. of SHS, Vol. 18, No2, pp.125-132.

- 112) Subramanian, R., McKamey, C. G., Schneibel, J.H., Buck, L. R., Menchhofer, P. A. (1998): Iron-aluminide- Al_2O_3 composites by in situ displacement reactions: processing and mechanical properties, Mater. Sci.

Eng. A, Vol. 254, pp.119-128.

- 113) Talako, T. L., Yakovleva, M. S., Letsko, A.I., Mosunov, E. I., Shipitsa, N. A., Saroka, D. I., Vitiaz, P.A. (2008): Structure and properties of detonation spray coatings from nanocomposite SHS powders intermetallide / oxide, Powder Metallurgy (Minsk), Issue 31, pp.281-285 (in Russian).

Author's short biography



Tatiana Talako

Tatiana Talako is currently Leading Researcher of the Department of machine building materials of the State Scientific Institution "Powder Metallurgy Institute", Minsk, Belarus. She graduated from the Byelorussian Polytechnic Institute (1988), Minsk, and received her PhD in Technical Sciences (1997) at the Powder Metallurgy Institute. Dr. Talako's research interests include materials science of advanced multifunctional powders and thermal spray coatings from them, processing materials using high-energy mechanical treatment and self-propagating high-temperature synthesis. She has coauthored about 25 scientific refereed journal papers, 2 books/chapters, and 9 patents.



Alexander Ilyuschenko

Corresponding Member of the National Academy of Sciences of Belarus, Professor Alexander Ilyuschenko is Director of the State Scientific Institution "Powder Metallurgy Institute", Minsk, Belarus. He graduated from the Byelorussian Polytechnic Institute (1978), Minsk. He received his PhD in Technical Sciences in 1985 at the Powder Metallurgy Institute, his doctor of sciences in 1998. His research has touched many aspects of powder metallurgy and thermal spray coatings science and technology, from fundamental investigations on thermal spray coatings formation to the development of advanced composite powder materials using high-energy processes.

Prof. Ilyuschenko has received numerous honors and awards, including the State Premium of Belarus in 2001. He takes an active part in international activities and has been a member of ASM since 1997 (ID 262841). His research has been reported in more than 500 scientific papers, 17 books, 17 inventor's certificates and 38 patents.



Andrey Letsko

Andrey Letsko is Head of Laboratory of New Materials & Technologies of the Department of machine building materials of the State Scientific Institution "Powder Metallurgy Institute". He graduated from the Byelorussian State Polytechnic Academy (1999), Minsk, and received his PhD in Technical Sciences (2008) at the Powder Metallurgy Institute. Dr. Letsko's research interests include the development and processing of advanced multifunctional powders using methods of high-energy mechanical treatment and self-propagating high-temperature synthesis. He has coauthored about 20 scientific refereed journal papers, 1 book chapter and 4 patents.

Challenges and Opportunities in Direct Write Technology Using Nano-metal Particles[†]

Kenneth N. Han^{1,2*} and Nam Soo Kim²
South Dakota School of Mines & Technology¹
KEN Research Laboratory, Seo Kyeong University²

Abstract

Direct write technology assists the electronic industry in their effort to miniaturize electronic circuits and enhance speed of printing capability. The technology allows printing various patterns without employing a mask or a resist with an enhanced speed with the aid of computer.

This paper describes the current status of the synthesis of conductive inks, a key to success in this technology. There are numerous factors to overcome in manufacturing inks which meet all the necessary conditions of conductivity, viscosity, and stability. In order to achieve the required conductivity, nano-particles used in the ink have to be made from gold, silver or copper. Inherent problems involved in these metal powders include high melting point, coagulation, impurities, cost, and, in the case of copper, oxidation. The direction of research currently being carried out in meeting and overcoming various challenges in this technology is reviewed and discussed. Other salient applications of nano-sized metal powders are also briefly examined.

Keywords: nano metals, direct write, catalysis, reduction, inverse micelle

Introduction

The power of nano-technology was first mentioned at an international conference in 1959 by Dr. Richard Feynman, a Physics Nobel Laureate when he commented on nano-science in relation to atomic theory. It was suggested that one day all of the information known to the world will be stored in a space of the size of a grain. The significance of this statement was hardly comprehended at the time, but as time progresses many people feel that we are approaching closer to the reality of the nano-world.

The term “nano” is used in conjunction with objects of a size between 10Å and 1000Å, meaning 1 nm and 100 nm respectively. One nanometer is 10⁻⁹ meters which is too small for most people to grasp its meaning and potential applications. In order to get perspective on this measurement, let us imagine a comparison between an object of micro-size and an object of nano-size in terms of a comparison between

the wave-length of ultra-violet light and the wave-length of X-rays. When the size of an object is comparable to the wave-length of infrared and visible light, the size is referred to as micro-size, which we are more accustomed to and is often known as the colloidal size.

When the size of an object is in the nano-size range, the characteristics and behavior of the material is changed dramatically. This might be illustrated with silver, which has an atomic weight of 108, an atomic diameter (b) of 2.9 Å, and a density (ρ) of 10.5 g/cm³. A cube of silver 1 cm on a side would have a surface area of 6 cm², or a specific surface of 0.6 cm²/g. The specific surface of a cubic or spherical particle is simply given by $6/\rho d$ where d is the diameter of the particle. For a silver particle 1 μ m in diameter, the specific surface is 6×10^3 cm²/g, whereas that of a particle 10 nm (0.01 μ m) in diameter would increase sharply to 6×10^5 cm²/g. If a solid is made up of atoms of linear dimensions, b, then the molecular volume is approximately b³ and the fraction of atoms in the surface layer is approximately 6(b/d). Thus, for a 1-mm particle, about 0.2 % of the atoms will be in the surface, but in the case of a 10-nm particle about 20 % of the atoms lie in the surface. So for the 1-cm cube, only 2 or 3 atoms in ten million are surface

[†] Accepted: July 22nd, 2009

¹ Rapid City, SD., USA

² #16-1 Chungnung-dong, Song- buk-ku, Seoul, 136-704 Korea

* Corresponding author

E-mail: hknkorea@gmail.com

TEL: 503-644-7014

atoms, but when divided into 10^{12} particles of $1\text{-}\mu\text{m}$, one atom in 450 is a surface atom. At 10 nm, one silver atom in five is a surface atom, and surface effects dominate. So when dealing with nano-particles, we must be concerned with large numbers of particles, extremely small size, large specific surface area, and particles dominated by surface effects.

In 1856, Michael Faraday first prepared colloidal gold by reducing an aqueous solution of gold chloride with phosphorous to yield a ruby-colored liquid, proving that he had finely divided gold particles. He found that a small addition of salts to the solution changed the color to blue, and studied various phenomena associated. More modern work shows that gold nano-sized particles exhibit red. Gold nano-sized particles exhibit red, orange, and purple colors depending upon their size and shape, and the melting point of gold can be lowered from 1060°C , for bulk gold, to about $300\text{-}400^{\circ}\text{C}$ when the size becomes $5\text{-}10\text{ nm}$.¹⁾ In addition, chemical reactivity changes significantly when the size of particles enters in the nano-size range and many nano-sized particles are used in conjunction with catalytic reactions.

There has been a great deal of interest in the synthesis of conductive ink using nano-sized metal powders since such ink finds numerous applications in the electronic industry. Numerous attempts have been made to produce conductive ink using primarily gold and silver nano-sized particles but commercial production of such an ink has not yet occurred. If successful, the applications of the ink are numerous. Examples can be found in display backplanes, radio frequency identification (RFID) antennas and tags, printed sensors, smart packages, e-paper, advanced layered electronics and many more.

Micro-fabrication of electronic components at the submicron scale will also help industry in its effort to miniaturize electronic circuits. Many researchers believe that the direct write technology will undoubtedly revolutionize the electronic industry. The term direct write process represents a printing process in which electronic circuit patterns are written directly from a pen-like system without going through a series and the tedious process of fabricating the patterns with masking and etching. The direct write process is flexible, versatile and accurate to a high degree of precision since a computer is an essential part of the process. Manufacturing sub-micron sized electronic circuits using traditional lithographic techniques is a very time-consuming and expensive process.

Reduction of metal ions into their elemental state

in an aqueous solution is routinely carried out by hydrometallurgists. The skills and fundamental techniques used by this branch of metallurgy can easily be applied to manufacturing nano-metal powders in solution with a few significant variations. In this paper, the authors will attempt to introduce and discuss how such small metal powders can be synthesized and the challenges one faces during the process of synthesizing such nano-sized metal powders.

Synthesis of Nano-Metal Powders

Various methods are used to synthesize nano-metal powders. Four commonly used methods are given below:

- Laser/Plasma Method
- Electro-chemical Method
- Vacuum Decomposition Method
- Wet Method

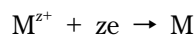
Laser/Plasma Method

This method uses a metal target bombarded with high energy with an intensity flux greater than 10^7 watts/cm^2 . As a result, the atoms on the surface of the target will generate plasma gas. The temperature of the system can rise up to $10,000\text{ deg-K}$ and about $10^4\text{-}10^5$ atoms on the 0.01 cm^2 target area are generated in 10^{-8} seconds.²⁾ Atoms produced in such a system are usually in nano-size but the cost of the process is usually very high.

Metal gas produced in such a system can then be cooled off and various sizes of nano-metal powders can be manufactured by adjusting the rate of cooling. In this process, Ar or N_2 gas is used as a carrier gas to prevent oxidation.

Electro-Chemical Method

This process method is the same technique used in the electrochemical deposition of metal ions in aqueous solution often used in hydrometallurgical processes. In this method, metal salts are dissolved in aqueous media which is then subjected to an electrical field. Positively charged metal ions will be attracted to the cathode and form elemental metal by receiving electrons from the electrode.

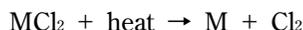


The metals collected on the surface of the cathode are separated from it and broken into various sizes. It

is very difficult to control the size of metal powders generated in this fashion, however. Principles involved in this process are described well in common references used in hydrometallurgy.^{3,4)}

Vacuum Decomposition Method

This method uses vacuum and heat to decompose metal salts. Size control is also a problem with this method.



Information on the temperature of decomposition of various metal salts is readily available in the literature.⁵⁾

Wet Method

This is the most common method in the synthesis of nano-metal powders. This method is a relatively easy method and also very effective. Metal salts are dissolved in liquid media, and then a reducing agent is introduced to the system to reduce metal ions to elemental metal. There are, in general, two types of carrying out this method. One is to reduce metal ions in solution by adding a reducing agent directly into the system. The other method is very similar to the above process but the reduction is carried out in the presence of organic chemicals. These will be discussed in more detail below.

a. Direct Reduction in Aqueous Phase

When metal ions are introduced in water, these metal ions are uniformly dispersed in the liquid phase. As a reducing agent is introduced to the solution containing metal ions, the metal ions are subjected to reduction resulting in an elemental state upon reduction if the reductant used is effective.^{6,17)} It is important to note that reductants suitable for some metals are not necessarily suitable for others. Significant difference in the emf (electro-motive force) value between the metal ion and the reducing agent must exist in order to achieve an effective reduction. Difference in the emf is a necessary, but not sufficient, condition for satisfactory reduction.

As metal particles are generated, they should be individual metal atoms first. However, the metal atoms in the aqueous phase are unstable by nature, and these metal atoms try to get together and grow. In addition, some metals serve as nuclei for others to grow on. The rate of growth of these metal powders

will depend upon various variables, including the concentration of metal ions, the type of reductant, temperature, and very frequently the pH of the system.

In general, the lower the concentration of metal ion and reducing agent the smaller the size of metal powders which results.⁶⁾ The size of the produced metal powders is relatively small when the rate of reduction is slow. Consequently, less powerful reductants are favorable for generating smaller sizes of metal powders.

When metal powders produced by reduction are highly charged, the growth of the particles is adversely affected. Unfortunately, most metals, except gold and some of other precious metals, are subject to dissolution at low pH: therefore this method of producing small-sized particles has its limit. On the other hand, if the pH of the solution is raised too much, most metals are subjected to hydration or oxidation to become hydroxides or oxides, which may not be desirable in many applications.⁶⁾

Another way of controlling the size is to add dispersants. Dispersants frequently used may include starch, silicates, and various polymers.^{6,18)} This approach is widely used in the synthesis of nano-metal powders but it should be noted that these dispersants are impurities added to the system, which could cause problems in later applications.

b. Choice of Reductants

Table 1 lists selected various metals with their standard emf value, melting point, and conductivity, which are compared with those of the hydrogen ion

Table 1 Emf, melting point, and conductivity value of various metals^{19,21)}

Metal/ion	EMF	Melting pt	Conductivity
	(volts SHE)	(deg-C)	$\times 10^6$ (ohm ⁻¹ cm ⁻¹)
Au/Au ⁺⁺⁺	1.5	1064.6	0.452
Pt/Pt ⁺⁺	1.19	1771.8	0.096
Ag/Ag ⁺	0.799	960.8	0.63
Cu/Cu ⁺⁺	0.337	1084.4	0.596
Sb/SbO ⁺	0.212	630.8	0.028
H ₂ /H ⁺	0	-259.2	0.108
Pb/Pb ⁺⁺	-0.126	327.4	0.048
Sn/Sn ⁺⁺	-0.136	231.8	0.091
Ni/Ni ⁺⁺	-0.25	1452.8	0.143
In/In ⁺⁺	-0.269	156.6	0.116
Co/Co ⁺⁺	-0.277	994.8	0.172
Cd/Cd ⁺⁺	-0.403	321	0.138
Fe/Fe ⁺⁺⁺	-0.44	1535.7	0.093
Ga/Ga ⁺⁺⁺	-0.529	29.7	0.067
Al/Al ⁺⁺⁺	-1.663	660.1	0.377

as a reference. When these metal ions are dispersed in water and an appropriate reducing agent is introduced, these metals will be reduced to elemental metals.

As noted from this table, noble metals such as gold, silver, platinum and copper are easily reduced by most common reductants but many other metals would require stronger reductants to be reduced. In addition to the reducing power, i.e. emf, the melting point of these metals is an important factor in certain applications. For example, in most electronic industry applications, good conductivity is essential to the function of the resulting product.

Most of the ink produced to date requires a post-heat treatment. The ink usually contains liquid, such as water, containing organic chemicals, which have to be removed to secure acceptable circuits with a desired value of conductivity. As a result, a post-heat treatment is needed to remove water and organic matters. Since most substrates are made of organic materials, the temperature applied in this heat process should not exceed the temperature beyond which the substrate can be damaged. In addition, it is necessary to ensure good mechanical adherence between the ink materials and the substrate. It is also important to maintain good fluidity of the ink with an acceptable level of viscosity.

Table 2 lists commonly used reductants with their emf values. As noted, most of these reductants will easily reduce gold, silver and copper, but in order to reduce most other metals, only a few of these reductants will be effective. It should be noted, however, that some of the reductants that produce gases as products are usually effective reductants: the partial pressure of these gases would be very low, as their solubility in water is low. As a result, the standard emf values can be misleading in representing their true power of reduction. In other words, the emf values of these reductants can be very small, as long as these gases are immediately removed from the system.

Table 2 Common reductants with their emf values^{19,20)}

Reductants	Emf values
$\text{H}_2\text{S} \rightarrow \text{S} + 2\text{H}^+ + 2\text{e}$	(0.142V)
$\text{H}_2\text{SO}_3 + \text{H}_2\text{O} \rightarrow \text{SO}_4^{2-} + 4\text{H}^+ + 2\text{e}$	(0.172V)
$\text{HCOOH} \rightarrow \text{CO}_2 + 2\text{H}^+ + 2\text{e}$	(-0.199V)
$\text{N}_2\text{H}_4 + 4\text{OH}^- \rightarrow \text{N}_2 + 4\text{H}_2\text{O} + 4\text{e}$	(-1.16V)
$\text{NaBH}_4 + 4\text{H}_2\text{O} \rightarrow \text{NaOH} + \text{H}_3\text{BO}_3 + 8\text{H}^+ + 8\text{e}$	(-0.350V)
$\text{NaBH}_4 + \text{O}_2 + 2\text{H}_2\text{O} \rightarrow \text{NaOH} + \text{H}_3\text{BO}_3 + 4\text{H}^+ + 4\text{e}$	(-1.928V)
$2\text{BH}_4^- \rightarrow \text{B}_2\text{H}_6 + 2\text{H}^+ + 4\text{e}$	(-0.368V)

As will be discussed later, the stronger the power of reductants in terms of the emf becomes, the faster the reduction reaction will generally take place. However, a fast reduction does not necessarily represent desirable conditions for the formation of the desired size of nano-particles. It is frequently found that the slower the reduction is the smaller the final size of the nano-particles becomes. Another consideration should be taken into account in selecting the reductant is the kind of products it produces. In general, inorganic products such as sulfur or other solids are undesirable, since they become undesirable impurities which will stay with the nano-particles.

The majority of the studies on the manufacturing of nano-metal particles have been conducted on gold and silver. Since gold and silver are very noble as noted in **Table 1**, the reduction of these metals in solution can be easily carried out using even mild reductants. In view of these metals being noble and also environmental concerns, organic based reductants have been widely used in this practice. These include trisodium citrate ($\text{C}_6\text{H}_5\text{O}_7\text{Na}_3$),^{14,22,23)} formaldehyde (CH_2O),^{8,12)} polyethylene glycol ($\text{C}_{2n+2}\text{H}_{4n+6}\text{O}_{n+2}$),²⁴⁾ glucose ($\text{C}_6\text{H}_{12}\text{O}_6$),²²⁾ ascorbic acid ($\text{C}_6\text{H}_8\text{O}_6$),²⁵⁾ tannic acid ($\text{C}_{34}\text{H}_{28}\text{O}_{21}$),²⁶⁾ polyvinylpyrrolidone (PVP: $\text{C}_6\text{H}_9\text{NO}$),^{14,22,27)} polyvinylalcohol (PVA: $(\text{C}_2\text{H}_4\text{O})_n$),^{22,27)} oleyl amine ($\text{C}_{18}\text{H}_{37}\text{N}$),¹¹⁾ and many more. In addition, the literature mentions a host of other organic reductants. These include alkyl acid phosphate ($\text{C}_5\text{H}_{11}\text{H}_2\text{PO}_4$ - amyl),^{28,29)} dendrimers,³⁰⁾ 3-thiopheneacetic acid ($\text{C}_6\text{H}_6\text{O}_2\text{S}$),³¹⁾ superhydrides,³²⁾ glucose ($\text{C}_6\text{H}_{12}\text{O}_6$),³³⁾ aspartic acid ($\text{C}_4\text{H}_7\text{NO}_4$ - $\text{HO}_2\text{CCH}(\text{NH}_2)\text{CH}_2\text{CO}_2\text{H}$),³⁴⁾ sodium formaldehyde sulfoxylate ($\text{CH}_3\text{NaO}_3\text{S}$),³⁵⁾ arginine ($\text{C}_6\text{H}_{14}\text{N}_4\text{O}_2$),³⁶⁾ 1,2-hexadecanediol ($\text{C}_{16}\text{H}_{34}\text{O}_2$),³⁷⁾ tetrakis (hydroxymethyl) phosphonium chloride ($(\text{HOCH}_2)_4\text{PCl}$),³⁸⁾ polyacrylamide ($-\text{CH}_2\text{CHCONH}_2$),³⁹⁾ quercetin ($\text{C}_{15}\text{H}_{10}\text{O}_7$),⁴⁰⁾ Geranium leaf,⁴¹⁾ aldehyde (RCOH),⁴²⁾ phosphorous,⁴³⁾ dimethylformamide ($\text{C}_3\text{H}_7\text{NO}$),⁴⁴⁾ trioctyl phosphine,⁴⁵⁾ destrin,⁴⁶⁾ dimethylamineborane,^{47,48)} and toluene⁴⁹⁾.

It should be noted however, that the most widely used reductants in manufacturing nano-metal powders is sodium borohydride, followed by hydrazine, and occasionally hydroxylamine hydrochloride, which are frequently used in hydrometallurgical applications. These reductants are very powerful and can be applied not only to gold, silver and copper, but also to other metals including iron, cobalt, and nickel. When these more powerful reductants are used, the reduction of ions is almost immediate, unlike with some organic reductants which are inherently weak reductants and often require high temperatures. The

emf values of the majority of organic reductants have not been determined, although they are assumed to be around -0.2 to -0.8 volts. Many of these organic reductants contain a carboxylate group that produces carbon dioxide and a hydrogen ion accompanied by electrons upon the oxidation reaction. The half cell reaction by the formic acid shown in **Table 2** is a good example.

c. Oxidation of Metal Powders

As noted earlier, most investigations into manufacturing nano-metal powders have reported on gold and silver. However, there is a natural incentive to produce nano-metal powders using copper. This is because copper exhibits the second highest conductivity among metals, and is very abundant. In terms of economical consideration, the price of copper is about 1/85 and 1/6,000 respectively of silver and gold based on the price in May of 2009.

As can be seen in **Table 3**, gold and silver are difficult to oxidize but copper is easily oxidized with a small amount of oxygen present. This indicates that most metals except gold and silver are easily oxidized in aqueous media. This is a problem in manufacturing nano-metal particles other than gold and silver. Prevention of oxidation of other metals including copper is almost impossible even in the inert gas atmosphere. The prevention of oxidation of these oxides can be accomplished with the help of CO or H₂ gas, as shown in **Table 4**. This means that oxidation of copper nano-particles can be eliminated if the synthesis of the copper nano-particles is conducted in the presence of CO or H₂. However, handling these gases is rather cumbersome, and practitioners prefer to avoid using such gases when possible.

Table 3 Gibbs standard free energy for copper, gold, and silver oxides and partial pressure of oxygen required to stop oxidation at 25°C. [Thermodynamic values were taken from references^{19,20}]

Metal Oxides	$\Delta G_{f, 25}^{\circ}, \text{cal/mol}$	P_{O_2}, atm
CuO	-30,400	2.60×10^{-45}
AuO ₂	48,000	1.58×10^{-35}
Ag ₂ O	2,600	6.51×10^{-3}

Table 4 The ratio of CO/CO₂ or H₂/H₂O for prevention of these oxides from oxidation. [Thermodynamic data for calculations were taken from references^{19,20}]

Metal Oxides	CO/CO ₂	H ₂ /H ₂ O
CuO	1.35×10^{-24}	2.43×10^{-19}
AuO ₂	2.22×10^{-66}	2.95×10^{-24}
Ag ₂ O	6.08×10^{-50}	1.09×10^{-44}

d. Concentration Effect

The concentration and size of these nano-metal powders play an important role in creating an acceptable conductive ink. When metal ions suspended in water are subjected to reduction by a reducing agent, metal ions will be reduced to a metallic state, first as an atom, and then will grow by combining with other reduced metal atoms. The growth of these metals in water is a very fast process exhibiting the growth by a few micron sizes in a couple of minutes, if not seconds.

It is obvious that the more diluted these ions are in the system, the easier it is to maintain particles in the state of dispersion, and hence prevent agglomeration. However, this creates a dilemma, since an effective ink should maintain a certain concentration of these ions in the first place. It should be noted that there is a threshold concentration of these ions in the solution in the production of the conductive ink. The main objective of the ink is to render the final product sufficiently conductive, and therefore, the concentration of metal powders in the ink should be high enough to have sufficient amounts of metal powder accumulating on the substrate to ensure good conductivity through the patterns.

In order to illustrate the importance of the metal concentration to the formation of the ink, let us assume that we desire to make a one micron size pattern consisting of 1 μm width × 1 μm depth, using 100 nm size silver particles dispersed in the ink. When the ink is deposited on the substrate and water is subsequently evaporated via the post heat-treatment, only metal powders will remain on the substrate. Let us also assume that the metal powders at the 1 μm depth are all deposited on the substrate to form a monolayer. At this stage, it is vital to have sufficient amounts of metal powder in the ink to have a continuous metal powders aligned in the drawn pattern, so that electrons can flow through these metal powders. In order to achieve this objective, a monolayer formation, at the minimum, of these particles on the substrate is required. **Table 5** shows the percent of the metal powders concentrated on the substrate for a given concentration of metal in the ink.

As noted in the table, when the concentration of solids is 0.1%, which is equivalent to 1000 ppm of metal powders in the solution, the solution will yield only 0.14% coverage, which is far from the monolayer required. Even at the concentration of 40%, which is equivalent to 620,000 ppm of solids, the solution will yield less than 100% monolayer coverage. It should be noted that even if the coverage is 100%, there is

Table 5 Comparison of nano-particles and the percent are occupied on the substrate

% Wt of Ag particles	% Monolayer coverage
0.1	0.1
0.5	0.7
1.0	1.4
2.0	3
4.1	6
11	16
41	58
62	89
75	107

no guarantee that the overall conductivity will be satisfactory, due to the unavoidable contact resistance between particles. It is noted that a 75% concentration of solids in the solution is by no means normally recognized as a fluid ink, but is rather a paste. This is one of the most difficult challenges to overcome in making a successful conductive ink.

Even if the resulting ink product in the substrate is multi-layered, there exists the problem of packing, which leads to voids resulting in poor conductivity.⁵⁰⁻⁵²⁾ Since the melting point of silver is 960°C, the contact resistance is very difficult to resolve, due to the fact that most substrates are made of organic compounds and will be damaged over 250°C, a recommended maximum temperature allowed to sustain the integrity of the organic substrate used in the electronic industry. One way to overcome this problem is to mix silver with a metal or alloy whose melting point is rather low. As seen in **Table 1**, the melting point of some metals, such as tin, indium, and gallium, is less than 250°C. Therefore, mixing silver with these metals yields better electrical contact after heat treatment at this temperature. Even if the melting point of a metal is more than this temperature, when this metal is mixed with other metals, the resulting eutectic temperature can be less than 250°C (see **Fig. 1**).⁵³⁾ As seen in this figure, when indium and tin are mixed at about 50%, the melting point drops to about 120°C. Such an attempt has been carried out in the authors' laboratory and the results are encouraging.

e. Stability of Nano-Metal Powders

Another problem using the direct reduction in aqueous media is the stability of metals in suspension. When these metals are formed by reduction, they are subject to coagulation and grow, resulting in non-uniform sized particles. When these particles grow, they settle easily and do not maintain nano-

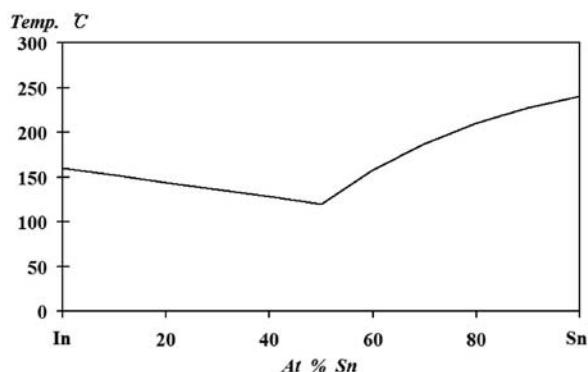


Fig. 1 Binary system of indium and tin showing the eutectic temperature of about 120°C.

size. The settled particles are consolidated and become very difficult to return to suspension and re-dispersion, even with strong agitation by a stirrer or agitation by sonic waves.

Some applications of these nano-sized metal powders require dry forms of these nano-particles. However, when these wet nano-sized particles are subject to dry conditions, the particles agglomerate easily. There are ways to overcome the aggregation of particles due to drying, which include freeze drying and spray drying. However, these processes are tedious and expensive.

Many researchers have found that nano-metal powders manufactured in an oil phase are easily re-dispersed after drying. However, metal ions are not usually soluble in these oils. Therefore, the two-phase system using oil and water is introduced to solve this problem. Metal ions are dissolved in the water phase and the reduction is carried out in the water phase and then the reduced metals are transferred into the oil phase and then dry them, which often produces satisfactory results. Organic chemicals trapped between nano-particles become soluble in a proper solvent and help to re-disperse nano-particles at a later stage when they are needed.

f. Reduction with Organic Phase

Many investigators have synthesized gold and silver nano-particles using the organic phase in the presence of the aqueous phase with various surfactants. The so called "inverse micelle method" is frequently used in the synthesis of nano-metal particles, and utilizes such a two-phase system.^{22,26)} As depicted in **Fig 2**, a group of metal ions dissolved in a water droplet are surrounded by organic surfactants which have a special affinity with the metal ions. These metal ions can be negative, as in the case of AuCl_4^- or positive as in the case of Ag^+ inside the droplets.

These water droplets can be a result of emulsification of water in oil phase. Metal ions can form a group in the aqueous phase with the aid of surfactants which have affinity with these ions. For negative ions, cationic surfactant such as alkyl amines, and for cationic ions, anionic surfactants such as carboxyl and sulfonate are used to surround the metal ions. These metal ions are then subjected to reduction with the aid of a reductant such as sodium borohydride, citric acid, or alkane tetrakis phosphonium chloride.¹⁰

The tail end of the surfactants is hydrophobic, and therefore they are attracted to the oil phase. These droplets can then be easily transferred to the oil phase as shown in **Fig. 3**. The oil phase is then separated from the water phase and subject to drying. After drying and evaporating, the residual organic phase will result in nano-sized metal powders which can be stored in an air-tight container for future use. The size of the reduced nano-metal powders is determined by the size of water droplets in oil as in the continuous phase.

The size of water droplets in the oil phase is determined by an effective emulsification of the oil/water mixture. The parameter known as “W,” which is the molar ratio of water to surfactant for the emulsification system is an important factor governing the size of these droplets.²² In general, the less water present in comparison to the surfactant, the smaller the water droplets are and hence the smaller the produced nano-metal powders becomes. Surfactants used in the emulsification can be cationic, like cetyltrimethylammonium bromide, anionic, like bis(2-ethylhexyl)sulfosuccinate, and nonionic, like Triton X-100. Nano-metals produced in the water droplets can grow by agglomeration within the confinement of the size of the water droplets but the maximum size is limited by the size of the droplets.

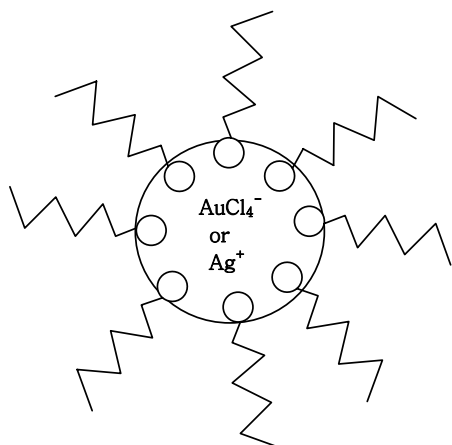


Fig. 2 Pictorial presentation of inverse micelle formation.

Such prepared nano-particles in the oil phase can be stored for the future use. Even if the nano-particles in the oil phase become somewhat flocculated, they can be easily re-dispersed at a later time by methods such as ultra-sonic wave if necessary. The organic phase can be easily evaporated to isolate the nano-particles, as mentioned earlier. The surfactants adhered to metal nano-particles help metal nano-particles re-disperse. These surfactants can be removed by dissolution with a proper solvent, by evaporation or even by burning.

The reduction of metals trapped in the water droplets can be done while they are in the aqueous phase or after transferring into the oil phase. If these metal powders are reduced while in the water phase, after reduction, they can be transferred to the oil phase. The rest of the process will be identical as described above for the direct reduction process. In order to reinforce the stability of the water droplets, thiol group organic chemicals are often added, since thio group organic chemicals have affinity of these metal ions. Such a method of preparing nano-metal powders using the two phase system was first demonstrated by Faraday⁵⁴ as early as 1857, and more recently by others.⁵⁵⁻⁶⁷

Nano gold and silver powders can be synthesized in the aqueous phase but in the presence of organic stabilizers such as poly-vinyl pyrrolidone (PVP) which also happens to be a reducing agent.^{8,18,43} The molecular weight of this organic chemical ranges between 10,000 and 60,000, and it serves as a dispersing agent to separate metal ions from each other. A solution containing metal ions is added to the solution containing this organic chemical and then the mixture is usually heated to about 60°C. Silver is then reduced to give a pink, purple, red or green color, depending upon the size and shape.

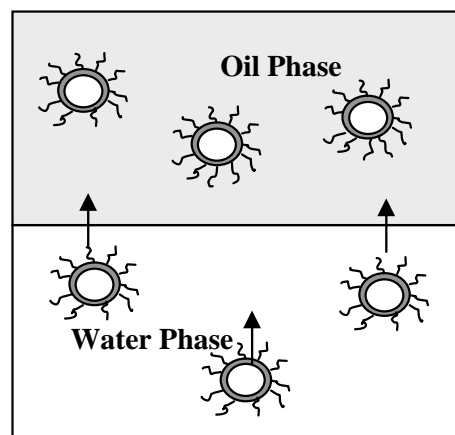


Fig. 3 Pictorial presentation of micelle transferring to oil phase.

Other Applications of Nano-Metal Particles

Applications of nano-metal powders are found in materials, devices, and process technology. Nano-particles are used in catalysts, nano-membrance, nano-carbon tubes, high strength materials, composite materials, and medical materials. Applications in nano-devices are found in short-wave electronic devices, molecular devices, bio-electronic devices, and optical devices. In addition, the nano-technology has applications in process technology including nano-patterning, nano-circuit, organic and inorganic nano-materials processing, nano-electrical system, nano-computers, nano-measuring processes, and nano-medical processes.

Let us take a close look at a number of practical examples. Nano-sized gold and silver offer various colors depending upon size and shape.⁶⁶⁾ This property is used in paint applications.⁶⁷⁾ There are evidences that nano-particles can be used in deodorant and sunscreens, but much more investigation on the side and after effects of such applications is required for safe applications in these areas.

One of the most remarkable and promising applications of nano-metal powders would be in catalysis. It has been found that oxidation of carbon monoxide is possible even at room temperature on gold nano-powders.^{68,69)} Cartoons showing the reactions between carbon monoxide and oxygen, and also cyanide and ferric ions, on gold nano-particles are shown in **Figs. 4 and 5**. In this case, since metal powders are nano-sized, huge surface area per given volume is available. In the case of cyanide with ferric ions, since gold has a special affinity with cyanide, gold nano-particles will catch cyanide, helping ferric ion to react with cyanide. Therefore, the chemical reaction will be facilitated simply because of the availability of a large surface area, and, at the same time, the affinity of gold with cyanide, enabling it to hold cyanide for the reaction with ferric ions.

Summary and Comments

It is apparent that the fundamentals of hydrometallurgy, known to many who have been working on applied interfacial phenomena such as, mineral processing researchers, or chemical engineers, are easily applied to the manufacture of nano-metal powders. Manufacture of nano-metal powders utilizes the principles and technologies which have been already employed in these or many other related areas for a century. For example, mineral process engineers

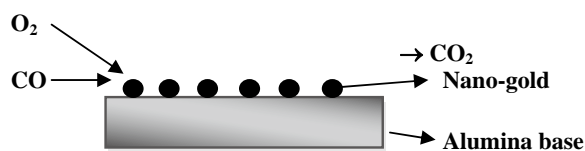
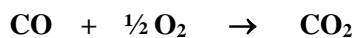


Fig. 4 Pictorial presentation of carbon monoxide reacting with oxygen with the help of gold nano-particles on alumina substrate.

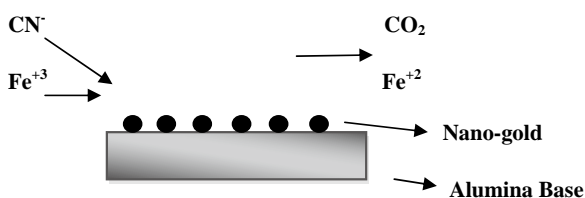
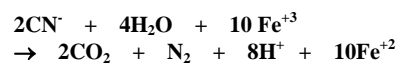


Fig. 5 Pictorial presentation of cyanide reacting with ferric ion with the help of gold nano-particles.

who are familiar with the metal reduction technology and interfacial phenomena used in froth flotation can immediately contribute their knowledge to the advancement of this exciting and emerging technology.

Nano-technology offers exciting opportunities, not only making nano-sized metal powders which can be used in the electronic industry, but also in medical, chemical, pharmaceutical, agricultural, civil, mechanical, electronics, materials, and environmental industries, and many other areas.

Acknowledgement

The authors acknowledge the financial supports from World Class University Program (R33-2008-000-10004-0), Korea.

References

- 1) Corti, C. W., Holliday, R. J. and Thompson, D. T. (2002): Developing New Industrial Applications for Gold, Gold Bulletin. Vol. 35. pp.111-117.
- 2) Daun, K. J., Stagg, B. J., Liu, F., Smallwood, G. J. S, and Snelling, D. R. (2007): Determining Aerosol Particle Size Distributions Using Time-Resolved Laser-Induced Incandescence, Appl. Phys. B, Vol. 87, No. 2, pp.363-372.
- 3) Han, K. N. (2002): "Fundamentals of Aqueous Metallurgy", SME, Denver, p. 212.
- 4) Mantell, C. L. (1960): "Electrochemical Engineering", McGraw-Hill, New York, 1960. p.680.

- 5) West, R. C. ed. (1985): "CRC Handbook of Chemistry and Physics", CRC Press. pp. 1-37.
- 6) Han, K. N., Kim, N. S. and Lee, H. J. (2005): Manufacturing of Nano-metal Powders in Aqueous Media, *Enbion Report*. p. 7.
- 7) Gomez, S. et al.,(2000): Gold Nanoparticles from Self-assembled Gold(I) Amine Precurseors, *Chem. Commun.*, pp.1945-1946.
- 8) Chou, K. S. and Ren, C. Y. (2000): Synthesis of Nano-sized Silver Particles by Chemical Reduction Method, *Mat. Chem. Phys.* Vol. 64. pp.241-246.
- 9) Solomon, S. D., Bahadory, M., Jeyarajasingam, A. V., Rutkowsky, S. A., and Boritz, C. (2007): Synthesis and Study of Silver Nanoparticles, *J. Chem Edu.* Vol. 84. pp.322-325.
- 10) Wu, S. H., and Chen, D. H. (2004): Synthesis of High-concentration Cu nanoparrticles in Aqueous CTAB Solutions, *J. Coll. Int. Sci.* Vol. 273. pp.165-169.
- 11) Aslam, M., Fu, L., Su, M., Vijayamohanan, K. and Dravid, V. P. (2004): Novel One-step Synthesis of Amine-stabilized Aqueous Colloidal Gold nanoparticles, *J. Mater. Chem.* Vol. 14. pp.1795-1797.
- 12) Khanna, P. K., Kale, T. S., SXhaikh, M., Koteswar, N. and Satyanarayana, C. V. V. (2008): Synthesis of Oleic Acid Capped Copper Nano-particles via Reduction of Copper Salt by SFS, *Mat. Chem. Phys.* Vol. 110. pp.21-25.
- 13) Yang, J. G., Okamoto, T., Ichino, R., Bessho, T., Satake, S., and Okido, M. (2006): A Simple Way for Preparing Antioxidation Nano-copper Powders, *Chem Lett.*, Vol. 35. pp.648-649.
- 14) Khanna, P. K., Singh, N., Kulkarni, D., Deshmukh, S., Charan, S., and Adhyapak, P. V. (2007): Water Based Simple Synthesis of Re-dispersed Silver Nano-particles, *Mat. Letters.* Vol. 61. pp.3366-3370.
- 15) Turkevich, J., Garton, G.. and Stevenson, P. C. (1954): The Color of Colloidal Gold, *J. Coll. Sci.* Vol. 9. pp.26-35.
- 16) Handley, D. A. (1989): Methods for Synthesis of Colloidal Gold, in *Colloid Gold: Principles, Methods and Applications*, (ed. M. A. Hayat), Academic Press, San Diego. 1989. Vol. 1. pp.13-32.
- 17) Duff, D. G., Baiker, A. and Edwards, P. P. (1993): A New Hydrosol of Gold Clusters. 1. Formation and Particle Size Variation, *Langmuir.* Vol. 9. pp.2301-2309.
- 18) Washio, I., Xiong, Y., Yin, Y. and Xia, Y. (2006): Reduction by the End Groups of Poly(vinyl pyrrolidone): A New and Versatile Route to the Kinetically Controlled Synthesis of Ag Trangular Nanoplates, *Adv. Mater.* Vol. 18. pp.1745-1749.
- 19) Pourbaix, M. (1974): *Atlas of Electrochemical Equilibria NACE*, Houston, USA. p.644.
- 20) West, R. C. ed. (1985): "CRC Handbook of Chemistry and Physics", CRC Press. p.I-37.
- 21) <http://www.standnes.no/chemix/periodictable/electrical-conductivity-elements.htm>
- 22) Zhang, W., Qiao, X. and Chen, J. (2007): Synthesis of Silver Nanoparticles- Effects of Concerned Parameters in Water/oil Microemulsion, *Mat. Sci and Eng. B.* Vol. 142. pp.1-15.
- 23) Silcikaite, A., Prosycevas, I., Puiso, J., Jurfaitis, A., and Guobiene, A. (2006): Analysis of Silver Nanoparticles by Chemical Reduction or Silver Solution, *Mat. Sci. Vol. 12. No. 4.* pp.287-291.
- 24) Luo, C., Zhang, Y., Zeng, X., Zeng, Y., and Wang, Y. (2005): The Role of Poly(ethylene glycol) in the Formation of Silver Nano-particles, *J. Coll. Int. Sci.* Vol. 288. pp.444-448.
- 25) Sau, T. K. et al.. (2001): Size Controlled Synthesis of Gold Nanoparticles Using Photochemically Prepared Seed Particles, *J. Nanoparticle Res.* Vol. 3. pp.257-261.
- 26) Zhao, S. Y., Chen, S. H., Li, D. G., Yang, X. G., and Ma, H. Y. (2004): A Convenient Phase Transfer Route for Nano-particles, *Physica E.* Vol. 23. pp.92-96.
- 27) Park, H. P. et al. (2003): Effect of Nonionic n-octyl β -D-glucopyranoside Surfactant on the Stability Improvement of Silver Polymer Electrolyte Membranes for Olefin/paraffin Separation., *J. Membrane Sci.* Vol. 217. pp.285-293.
- 28) Hwang, M. J., Lee, S. Y. and Han, C. S. (2006): A Study on Electric Conductivity of Phosphoric Acid Supported on Nano-pore Rice Husk Silica in $H_2/Pt/H_3PO_4$ /RHS/Pt/ O_2 fuel cells., *J. Nanosci. Nanotechnol.* Vol.6. pp.3491-3493.
- 29) Mei, Y.F. et al. (2004): Formation of Si-based Nanoisland Array on Porous Anodic Alumina, *Acta Materialia.* Vol.52. pp.5633-5637.
- 30) Swanson, S. D. et al. (2008): Targeted Gadolinium-loaded Dendrimer Nanoparticles for Tumor-specific Magnetic Resonance Contrast Enhancement, *Int.J. Mamomecicine.* Vol.3. pp.201-210.
- 31) Cuendias, A. d., Backov, R., Cloutet, E. and Cramail, H. (2005): Synthesis of Gold Nanoparticles Coated onto Polyurethane Microspheres, *J. Mater.Chem.* Vol.15. pp.4196-4199.
- 32) Sun, S. et al. (2003): Controlled Synthesis and Assembly of FePt Nanoparticles *J.Phys.Chem.* Vol.107. pp.5419-5425.
- 33) Meng, X., Ren, X. and Tang, F. (2003): A Glucose Biosensor Using Au Nanoparticle Modified Glucose Oxidase, *Tech. Institute of Phys.and Chem.* Vol.3. pp.404-407.
- 34) Guan, H., Zhou, P., Zhou, X. and He, Z. (2008): Sensitive and Selective Detection of Aspartic Acid and Glutamic Acid Based on Polythiophene-gold Nanoparticles Composite, *Talanta.* Vol.77. pp.319-324.
- 35) Khanna, P. K. et al. (2009): Synthesis of Hydrophilic Copper Nanoparticles: Effect of Reaction Temperature, *J. Nanoparticle Res.* Vol. 11. pp.793-799.
- 36) Gao, Y., Xu, Z., Chen, S., Gu, W., Chen, L. and Li, Y. (2008): Arginine-chitosan/DNA Self-assemble Nanoparticles for Gene Delivery: In Vitro Characteristics and Transfection Efficiency, *Int. J. Pharma.* Vol.359. pp.241-246.
- 37) Chen, M., Nikles, D. E., Yin, H., Wang, S., Harrell, J. W. and Majetich, S. A. (2003): Patterning Self-assem-

- bled FePt Nanoparticles, *J. Magnetism and Magnetic Mat.* Vol.266. pp.8-11.
- 38) Grunwaldt, J.D., Kiener, C., Wögerbauer, C. and Baiker, A. (1998): Preparation of Supported Gold Catalysts for Low-Temperature CO Oxidation via Size-Controlled Gold Colloids, *J. Catalysis.* Vol.181. pp.223-232.
 - 39) Tang, W., Xu, H., Park, E. J., Philbert, M. A. and Kopelman, R. (2008): Encapsulation of Methylene Blue in Polyacrylamide Nanoparticle Platforms Protects its Photodynamic Effectiveness, *Biochem. Biophys. Res. Commun.* Vol.369. pp.579-583.
 - 40) Zhang, Y., Yang, Y., Tang, K., Hu X., and Zou, G. (2008): Physicochemical Characterization and Antioxidant Activity of Quercetin-loaded Chitosan Nanoparticles, *J. Appl. Polymer Sci.* Vol.107. pp.891-897.
 - 41) Sharma, N. C., Sahi, S. V. Nath, S., Parsons, J. G., Gardea-Torresdey, J. L. and Pal T. (2007): Synthesis of Plant-mediated Gold Nanoparticles and Catalytic Role of Biomatrix-embedded Nanomaterials, *Environ. Sci. Technol.* Vol.41. pp.5137-5142.
 - 42) Singh, P., Katyal, A., Kalra, R. and Chandra, R. (2008): Copper Nanoparticles in Ionic Liquid: An Easy and Efficient Catalyst for the Coupling of Thiazolidine-2,4-dione, Aromatic Aldehyde and Ammonium Acetate, *Catalysis Commun.* Vol.9. pp.1618-1623.
 - 43) Wang, F., Arai, S., Park, K. C., Takeuchi, K., Kim, Y. J. and Endo, M. (2006): Synthesis of Carbon Nanotube-supported Nickel-phosphorus Nanoparticles by an Electroless Process, *Lett. Edit.* Vol.44. pp.1298-1352.
 - 44) Pastoriza-Santos, I. and Liz-Marzan, L. M. (2009): N,N-Dimethylformamide as a Reaction Medium for Metal Nanoparticle Synthesis, *Adv. Func. Mat.* Vol. 19. pp.679-688.
 - 45) Henkes, A. E. and Schaak, R. E. (2007): Trioctylphosphine: A General Phosphorus Source for the Low-Temperature Conversion of Metals into Metal Phosphides, *Chem.Mater.* Vol.19. pp.4234-4242.
 - 46) Goncalves, C. and Miguel, F. (2008): Characterization of the Self-assembly Process of Hydrophobically Modified Dextrin, *European Polymer Journal* Vol. 44. pp.3529-3534.
 - 47) Miyoshi, K., Fujikawa, S. and Kunitake, T. (2008): Fabrication of Nanoline Arrays of Noble Metals by Electroless Plating and Selective Etching Process, *Colloids and Surfaces A.* Vol.321. pp.238-243.
 - 48) Esumi, K., Sarashina, S. and Yoshimura, T. (2004): Synthesis of Gold Nanoparticles from an Organometallic Compound in Supercritical Carbon Dioxide, *Langmuir.* Vol.20. pp.5189-5191.
 - 49) Rao, C. R. K. and Trivedi, D. C. (2005): Synthesis and Characterization of Fatty Acids Passivated Silver Nanoparticles-their Interaction with PPy, *Synthetic Metals.* Vol.155. pp.324-327.
 - 50) Kim, N. S., Amert, A. K., Woessner, S. M., Decker, S., Kang, S. M., and Han, K. N. (2007): Effect of Metal Powder Packing on the Conductivity of Nanometal Ink., *J. Nanoscience and Nanotechnology*, Vol. 7. pp.3902-3905.
 - 51) Han, K. N. and Kim, N. S. (2008): Theory and Application of Conductive Inks Manufactured with the Help of Low Melting Metals, *The Korea Soc. Mach. Tool Eng.* Vol. 17. pp.126-131.
 - 52) Kwon, D. H., Jeong, T. E., Kim, N. S. and Han, K. N. (2007): Effect of Metal Powders on the Conductivity of Conductive Inks, *Proceedings of Korean Society of Machine Tool Engineers Spring Conference*, May, 18. pp.35-41.
 - 53) Villars, P., Prince, A., and Okamoto, H., "*Handbook of Ternary Alloy Phase Diagrams*" (ASM Publication: 10 vol set.)
 - 54) Faraday, M. (1857): Experimental Relations of Gold (and other metals) to Light, *Philos. Trans. R. Soc. London.* Vol. 147. pp.145-181.
 - 55) Pal, A., Shah, S. and Devi, S. (2007): Preparation of Silver, Gold and Silver-gold Bimetallic Nanoparticles in w/o Microemulsion Containing Triton X-100. *Colloids and Surfaces A.* Vol. 302. pp.483-487.
 - 56) Leopold, N. and Lendl, B. (2003): A New Method for Fast Preparation of Highly Surface-Enhanced Raman Scattering Active Silver Colloids at Room Temperature by Reduction of Silver Nitrate with Hydroxylamine Hydrochloride, *J. Phys. Chem. B* 107. pp.5723-5727.
 - 57) Caswell, K. K., Bender, C. M. and Murphy, C. J. (2003): Seedless, Surfactantless Wet Chemical Synthesis of Silver Nanowires, *Nano Letters* 3. pp.667-669.
 - 58) Sun, Y. G. and Xia, Y. N. (2002): Shape-controlled Synthesis of Gold and Silver Nano-particles, *Science* Vol. 298. pp.2176-2179.
 - 59) Pillar, Z. S. and Kamat, P. V. (2004): What Factors Control the Size and Shape of Silver Nanoparticles in the Citrate Ion Reduction Method?, *J. Phys Chem. B.* Vol. 108. pp.945-951.
 - 60) Brust, M. et al. (1994): Synthesis of Thiol-derivatised Gold Nanoparticles in a Two-phase Liquid-Liquid System, *J. Chem. Soc., Chem. Commun.*, pp.801-802.
 - 61) Porter, M. D. et al. (1987): Spontaneously Organized Molecular Assemblies. 4. Structural Characterization of n-alkyl Thiol Monolayers on Gold by Optical Ellipsometry, Infrared Spectroscopy, and Electrochemistry, *J. Am. Chem. Soc.* Vol. 109. pp.3559-3568.
 - 62) Adam, M. et al. (2004): Novel One-step Synthesis of Amine-stabilized Aqueous Colloidal Gold Nanoparticles, *J. Mater. Chem.* Vol. 14. pp.1795-1797.
 - 63) Song, X., Sun, S., Zhang, W. and Yin, A. (2004): A Method for the Synthesis of Spherical Copper Nanoparticles in the Organic Phase, *J. Coll. Inter. Sci.*, Vol. 273. pp.463-469.
 - 64) Sastry, M. (2003): Phase Transfer Protocols in Nanoparticle Synthesis, *Current Sci.* Vol. 85. pp.1735-1745.
 - 65) Sun, Y., Mayers, B., Herricks, T. and Xia, Y. (2003): Polyol Synthesis of Uniform Silver Nanowires: A Plausible Growth Mechanism and the Supporting Evidence, *Nano Lett.* Vol. 3. pp.955-960.
 - 66) Liz-Marzan, L. M. (2004): Nanometals Formation and Color, *Materials Today.* Vol 7. pp.26-31.

- 67) Liu, H. B. et al. (2001): Melting Behavior of Nanometer Sized Gold Isomers, *Surface Sci.* Vol. 491. pp.88-98.
- 68) Haruta, M. (1997): Size- and Support-dependency in the Catalysis of Gold, *Catalysis Today.* Vol. 36. pp.153-166.
- 69) Haruta, M. (2003): When Gold is Not Noble: Catalysis by Nanoparticles. *The Chemical Record.* Vol. 3. pp.75-87.

Author's short biography



Kenneth N. Han

Kenneth N. Han received his B.S. and M.S degrees from Seoul National University, Seoul, Korea again M.S. degree from University of Illinois, and PhD from University of California, Berkeley. He served as Lecturer and Senior Lecturer at Monash University in Melbourne, Australia; Professor, Department Head, Dean of Materials Science and Engineering, Dean of Graduate Studies, and Professor Emeritus at South Dakota School of Mines and Technology, Rapid City, SD. He is Founding Director and Chair Professor of KEN Research Center at Seokyeong University in Seoul, Korea. His research interests include Synthesis of Nano-metal Powders; Hydrometallurgy; Corrosion Inhibition; Precious Metals Recovery and Refining; Fine Particles Recovery; Electrometallurgy.



Nam-Soo Kim

Nam-Soo Kim received his B.S. and M.S degrees in Material Science and Engineering from Korea University, Seoul. He received his Ph.D. degree from South Dakota School of Mines and Technology, Rapid City, USA. He is currently Professor of the School of bio & Chemical Engineering and also Director of KEN Research Center at Seokyeong University in Seoul, Korea. His research interests include Direct Writing and Printing Technology in Nano- technology, Hydrometallurgy and Recycling.

Aerosol route in Processing of Nanostructured Functional Materials[†]

O.Milosevic^{*1}, L.Mancic¹, M.E. Rabanal², L.S.Gomez², K.Marinkovic¹
Institute of Technical Sciences of the Serbian Academy of Sciences and Arts¹
Universidad Carlos III de Madrid²

Abstract

The diversity and potentials of the aerosol route for making functional materials at the nano size level are reviewed. Among the methods currently used for nanophase processing, synthesis through dispersion phase (aerosol) enables generation of ultrafine, either single or complex powders with controlled stoichiometry, chemical and phase content provided by high surface reaction, high heating and cooling rates and short residence time. It represents a "bottom-up" chemical approach and provides control over a variety of important parameters for particle processing. This may favor to the formation of either amorphous, nanocrystalline or metastable phases implying a huge impact in the search for advanced functional materials having novel and unique structures and properties. Particularly, the opportunities of the hot wall aerosol synthesis, i.e. spray pyrolysis, for the generation of ultrafine spherical particles with uniformly distributed components, phases and nano-clustered inner structure and luminescence properties is demonstrated with various analyzing techniques like XRPD, FE-SEM, HR-TEM, STEM and nanotomography. Following the initial attempts, a more detailed aspect of the several phosphor particles generation based on $Gd_2O_3:Eu$, $Y_2O_3:Eu$, $(Y_{1-x}Gd_x)_2O_3:Eu$ and $Y_3Al_5O_{12}:Ce$ is reviewed highlighting the research activities in the Institute of Technical Sciences of SASA, Serbia.

Keywords: aerosol, nanoparticles, synthesis, phosphors, luminescence

1. Introduction

Tremendous technological and scientific trend in material science for miniaturization and microstructure refinement is basically followed with the increasing interest for nanophase characterization and understanding. The field of nanoscience and nanotechnology has an exciting progress in recent years, particularly regarding the control synthesis of ultrafine particles or nanoparticles that might have a great potential for use in solid-state functional materials and devices, like phosphors, sensors, catalysts, drug delivery carriers etc.¹⁾ The key points important for the future research and development of nanophased materials represent the ability for further improvement of material properties through nanostructuring and fundamental research of structure-properties

relationship, from one side, as well as development of assigned and controlled synthesis route with the ability to ensure nanophase synthesis in a controlled manner, from another. Synthesis of submicronic and nanosized powders and thin films represent an area of increasingly high interest and offers new opportunities in materials engineering whether one or multi component systems are considered.

The chemical synthesis routes, like liquid precipitation, sol-gel or hydrothermal methods, offer many advantages over conventional procedures for nanoscaled materials processing. Since the precursors are mixed at the molecular level in a solution, a high degree of structural homogeneity is achievable; doping is effective, surface area of powder produced is very high, leading to lower processing temperature. Moreover, the solution routes and low temperature processing minimize the potential for contamination, which is very important for the most applications in the electronic, optoelectronic, chemical industries etc. that are sensitive to some of the impurities.

Compared to other processing techniques, powder

[†] Accepted: August 27th, 2009

¹ K. Mihailova 35/IV, 11000 Belgrade, Serbia

² Avda. de la Universidad 30, Leganes, Madrid, Spain

* Corresponding author

E-mail: olivera.milosevic@itn.sanu.ac.rs

synthesis through aerosol routes enable the generation of fine, submicronic to nanoscale, either single or complex, powders from a variety of precursor solutions²⁻⁶. It represents basically chemical route having a “bottom-up” approach for powder processing. The diversity of aerosol routes, depending mainly on the nature of aerosol and the manner how the aerosol decomposition energy is transferred to the system are presented on **Fig.1**. Two cases are roughly evident in aerosol routes: gas-to-particle route, which relates to the particle formation from the gaseous precursors and droplet-to-particle route, that relates to the formation of discrete aerosol droplets and control of the aerosol decomposition into particles³. Depending on how the thermal energy is provided to the precursors, affecting the most important particle formation parameters: residence time and temperature distribution, the main aerosol decomposition methods could be presented as is on **Fig.1**. The advantages of aerosol synthesis are as follows: it represents a simple method for production of oxide, non-oxide, metal and composite powders of complex composition, either in amorphous, crystalline or nanocrystalline state. Solution chemistry approaches offer design of materials at the molecular level, spherical particle morphology with full or hollow spheres, with narrow particle size distribution and a very homogeneous composition can be achieved by properly adjustment of the process parameters. For the case of film processing, this method provides easy control of deposition rate and thickness, simple doping of films using any element in any proportion by addition of a suitable dopant into the starting solution, possible production of layered films and films with concentration gradient, vacuum not required in any step of the process and there are no limits concerning dimensions and shape of sub-

strate.

In the case of hot-wall processing^{2-5,7-10}, energy source for reaction and particle formation is usually provided through tubular flow reactor, flame synthesis use combustion enthalpy of vapor flame¹¹⁻¹³, self sustaining flame reactors use combustion enthalpy of dispersed oil phase in the form of emulsion¹⁴, self combustion aerosol synthesis use combustion enthalpy of entire solution being chemically modified^{15,16}. Tubular hot-wall flow reactor provide a well-controlled temperature profile over long residence times, while in the case of flame synthesis the decomposition temperatures are higher and the residence time is shorter. In aerosol assisted thin film preparation (Pyrosol process) there is precursor decomposition in the vicinity on the heated substrate¹⁷⁻¹⁹. Under certain circumstances, Pyrosol could be assimilated to a chemical vapor deposition process, but it removes restrictions of CVD such as high vapor pressure of precursors and their good thermal stability. In comparison to the pneumatic atomizers, the aerosol produced by ultrasonic atomization enables better controlling of droplet size and size distribution.

2. Hot-Wall Aerosol Synthesis (Spray pyrolysis)

Hot-wall aerosol synthesis is based on the formation of aerosols of precursor solutions and control over the aerosol decomposition in a high temperature tubular flow reactor through the successive processes of droplet evaporation, drying, solute precipitation and decomposition. Since the heterogeneous gas/liquid-solid reaction occurs in a dispersed system-aerosol at the level of few micrometers sized droplets, compositional segregation is prevented and high heating rates (20-300°C/s), as well as high surface

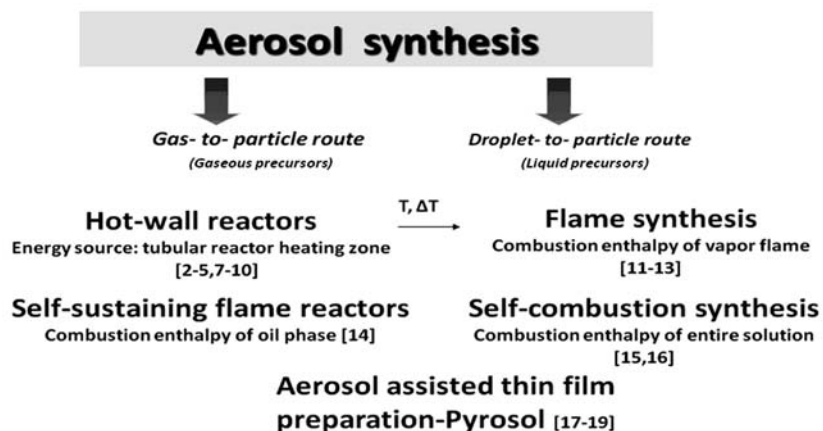


Fig. 1 The diversity of the aerosol routes, depending on the nature of aerosol (upper) and the manner of how the aerosol decomposition energy is provided to the system (down).

reaction could be achieved²⁾. During decomposition, the aerosol droplets undergo evaporation/drying, precipitation and thermolysis in a single-step process. Consequently, spherical, solid, agglomerate-free, either submicronic, nanostructured or nanoscaled particles are obtained through the mechanisms of primary nano- particles coalescence, collision and sintering. Schematic of the hot-wall aerosol synthesis routes is presented in **Fig. 2**. The process involves formation of discrete droplets of precursor solution in the form of aerosol and control over their thermally induced decomposition and phase transformation.

Synthesis I refers to the chemical synthesis and solution preparation that could be in the form of true solutions, colloids or emulsions. In addition, the modification of the chemistry of the solution, i.e. additives like glycine, urea, suchrose etc. alters the morphology of the particles derived as well as the particle size, size distribution and agglomeration state. The precursors and precursors chemistry are usually characterized for their physico-chemical properties like determination of the solution surface tension, viscosity, density, concentration, pH, as well as the decomposition behavior of the precursors since there is a strong relationship between the mentioned solution properties and the droplet/particle size^{21,22)}.

Aerosol is most frequently formed ultrasonically, using high-frequency (100KHz - 10MHz) ultrasonic beam¹⁷⁾ directed to the gas-liquid interface. Liquid atomization and aerosol formation occur for the certain values of the acoustic waves amplitude, where the average droplet size depends mostly on the solution

properties (viscosity, surface tension, concentration, density etc.) as well as the ultrasound frequency. It was already shown that this technique is suitable for the aerosol formation with the narrow size of droplet distribution, thus affecting narrow particle size distribution.

Depending on the atomization technique, either monodispersed or polydispersed particles could be obtained. The monodispersed nano particles are formed either through the evaporation-condensation mechanisms, using electro spray atomizer or differential mobility classifier^{23,24)}. Twin-fluid and ultrasonic atomization techniques usually led to the formation of polydispersed particles. The droplet size and size distribution depend on the type of atomization and the precursor properties, as presented in **Table 1**.

The particle size is then defined by the following equation for the case that one particle is derived from one droplet²²⁾:

$$D_p = D_d \left(\frac{c^* M_s}{\rho_p M_p} \right)^{1/3} \quad (1)$$

Where: D_p - particle diameter [μm], c^* - initial solution concentration [gcm^{-3}], M_s - molecular mass of resulting powder [gmol^{-1}], M_p - molecular mass of precursor [gmol^{-1}], ρ_p - powder density [gcm^{-3}]

The aerosol is carried out by the flowing gas stream into high-temperature tubular flow reactor. Differential mobility analyzer (DMA) or Scanning Mobility Particle Sizer (SMPS) can be used for on-line determination of the aerosol-born particle's size, size distribution and concentration²⁴⁾.

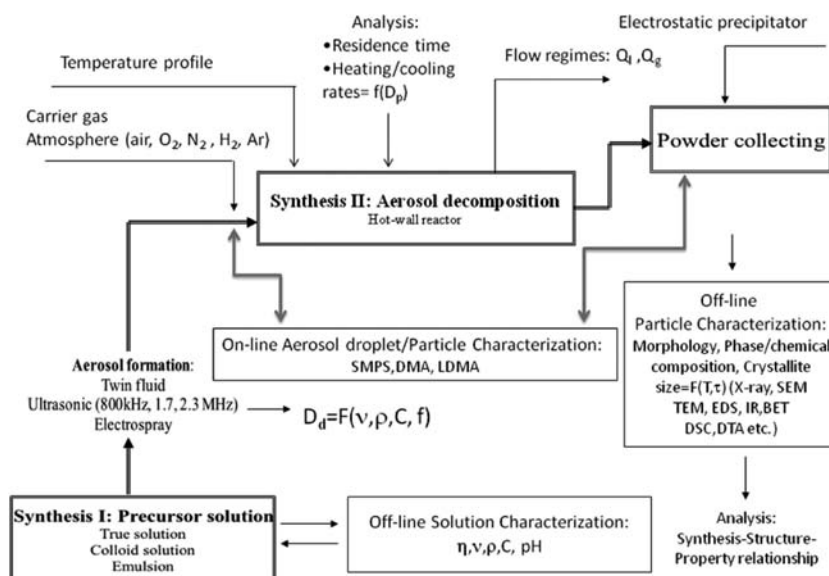


Fig. 2 Schematic of the hot-wall aerosol synthesis route methodology²⁰⁾.

Table 1 The manner of the aerosol formation and droplet/particle size distribution

Aerosol formation /Droplet size equations, μm	
Monodispersed droplets/particles	Evaporation-Condensation ²⁵⁾
	Electrospray aerosol route ²³⁾
	Differential mobility classifier ²⁴⁾
Polydispersed droplets/particles	Twin-fluid atomization Empirical relationship S.Nukiyama, Y.Tanasawa ²⁶⁾ **
	$D_d = \frac{585}{V} \left(\frac{\gamma}{\rho} \right)^{0.5} + 597 \left(\frac{\mu}{(\gamma\rho)^{0.5}} \right)^{0.45} \left(\frac{1000F_L}{F_G} \right)^{1.5}$
	Ultrasonic atomization Lang ²¹⁾ ***
	$D_d = 0.34 \left(\frac{8\pi\gamma}{\rho f} \right)^{1/3}$

** D_d - droplet diameter [μm]; V - relative carrier gas- to -liquid velocity at the nozzle exit [ms^{-1}]; γ - solution surface tension [10^3Nm^{-1}]; ρ - solution density [gcm^{-3}]; μ - solution viscosity [Pas]; F_G - gas flow rate [cm^3s^{-1}]; F_L - liquid flow rate [cm^3s^{-1}]

*** D_d - droplet diameter [μm]; γ - solution surface tension [dyncm^{-1}]; ρ -solution density [gcm^{-3}]; f - ultrasound frequency [10^3s^{-1}]

The flow rate of the carrier gas represents one of the most important process parameters enabling the supporting atmosphere as well as the aerosol flow rate and the droplets residence time to be controlled. During the main process, denoted as *Synthesis II*, aerosol droplets undergo evaporation, drying and solute precipitation in a single-step process caused by the mechanisms of heat and mass transfer inside the droplets and between the droplets and surrounding gas. Such mechanism enables high surface reaction, solution stoichiometric retention as well as segregation suppression to the droplet scale. As a result, spherical, solid, agglomerate-free, either nano scale or submicronic particles are obtained having composite inner nano structure²⁷⁻³⁴⁾.

After solvent evaporation/drying stage and consecutively solute precipitation and decomposition that occurs at the droplet level, the primary particles arise through the thermally induced processes of nuclei formation, collision and coalescence. Resulting particles then arise through the growth and aggregation of nano scaled “primary particles” arranged in spherical so called “secondary particles”. The secondary particle size and size distribution are mainly influenced by the properties of aerosol generator and precursor solutions. Primary particles, that represent either crystallites or block-mosaic assemblies, sizing mainly below 50nm, could coalesced entirely or densified with existing nanoporosity and exhibiting high surface area. The Summary of the particle morphology hierarchy is presented at **Fig. 3**. The size of primary particles depends on the time-temperature history and materials properties. For low tempera-

tures and short residence time particle coalescence proceeds slowly compared to collisions, producing weak agglomerates having a high specific surface area. On the contrary, at high temperatures and for small particles, particle coalescence is dominant process resulting in primary particle growth, hard agglomerates and small specific surface area³⁵⁾.

Nanophase particles can be generated in accordance to this method by properly controlling over the initial aerosol droplet size, the mechanisms of the droplet collision and coalescence as well as by suppressing the excessive grain growth and grain coarsening. As a result, it is possible to obtain either nanoparticles directly from nano-sized droplets or to obtain submicronic sized particles, that offer a composite nanograin particle structure^{27, 34, 36)}. **Fig. 4**. represents the methodology for directly producing of nanoscaled particles by spray pyrolysis. By following the proportionality of particle size with solution concentration and the droplet size (eq.1) and the basic concept of spray pyrolysis where one particle is derived from one droplet, directly producing of nano particles can be achieved from dilute solutions and small aerosol droplets²⁾. Decrease of the droplet size can be achieved either by using electrospray atomizer, that is able to directly produce nanoscaled monodispersed particles or by the modification of the atomizing technique, like filter expansion aerosol generator (FEAG), developed for the synthesis of nanoscaled phosphor particles by low-pressure spray pyrolysis^{23,36)}. On the other hand, self combustion spray pyrolysis, associated with the modification of precursor chemistry by using of exothermic reacting

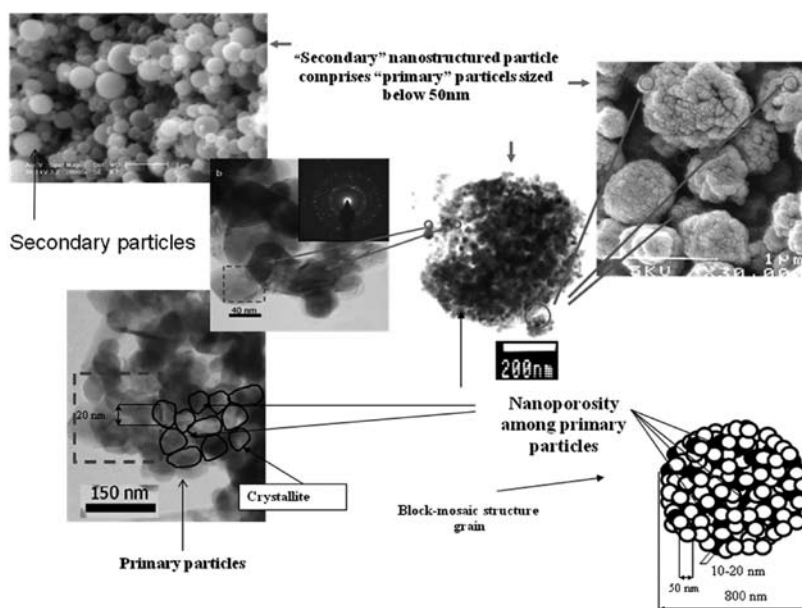


Fig. 3 Summary of the particle morphology hierarchy.

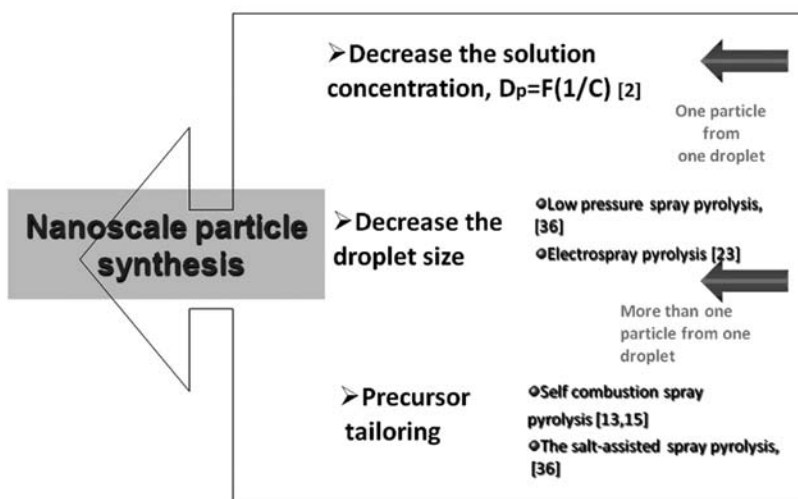


Fig.4 Nanoscale particle synthesis through aerosol route.

species, that cause droplets/particles to be decomposed with additional heat and exploding during the process, leads to the direct synthesis of nanoparticles^{13,15}.

The choice of precursors, their thermal and decomposition behavior play an important role in nanoscaled particles synthesis, as well^{36,37}. The mechanisms of nucleation and growth of primary particles, ranging from few to several tens of nanometers, which gather together during decomposition process into spherical agglomerates, or so called “secondary particles” the mean size below 1000nm, play a crucial role in formation of particle size and morphology^{15,38}.

Salt assisted spray pyrolysis (SAD) enable releasing the nano-scaled primary particles by modification of the solution chemistry and preventing formation of hardly aggregated primary particles into the secondary particles³⁶.

From the viewpoint of the application of the as-generated particles for advanced materials synthesis, particle morphology is of great interest. Aerosol synthesis enables synthesis of various particle morphology, either as hollow or dense spheres. It is presumed that certain particle morphology is formed during the evaporation/drying stage that encountered processes of evaporation and diffusion of both the solvent, and

solute, changing in droplet temperature and crust formation. They are governed by the basic laws of heat and mass transfer so several models describing the above mentioned phenomena are developed and can be applied in prediction of particle morphology³⁹⁻⁴¹). The problems regarding droplet collision and consequently droplet coalescence or agglomerated particles formation are often associated with ultrasonic spray pyrolysis, since reducing droplet size significantly increases the probability for collision²). Agglomerated particles are undesirable especially for afterwards sintering purposes, causing hard agglomerates formation and inducing local grain growth and inhomogeneity.

On the contrary of the reports on the mechanisms of particle formation from inorganic salts, solid particles are often generated from metal alkoxides or organic solutions if they undergo polymerization process^{29, 33, 42-43}). Another feature that strongly alters the particle morphology is transferring ions into gas phase in the case of volatile precursors⁴⁴). In this case the particles are formed both from gas as well as liquid (solid) phase, leading to the broad size of particle distribution and to the differences in particle morphology. From the viewpoint of difficulties for the stoichiometry retention in the case of multicomponent systems, this feature has to be controlled carefully.

Depending on the process parameters – tem-

perature and residence time, either amorphous or crystalline particles can be obtained. It was shown that proper adjusting of the mentioned parameters enables synthesis of either nanophase, polycrystalline or single-crystal particles by controlling over the mechanisms of grain growth and sintering^{2, 28}). Numerous materials, either in the form of thin films or nanostructured/nanoscaled particles as metal oxides, mixed metal oxides, nonoxides and metals have been obtained by this method and have reviewed in literature^{2,3,6,13,45,46,47}). The potentials of the aerosol routes for making solid-states structures at the nano size level are virtually unlimited, providing possibilities for new and unique applications in electronics, optoelectronics, catalysis, energy conversion systems, drug delivery etc. It has been reported synthesis of electrode material for solid oxide fuel cells^{48, 49}, phosphors^{47,50}, metal-ceramic and ceramic-ceramic nanocomposite particles synthesized in environmental conditions^{51, 52}) and under microgravity⁵³). The examples of experimental set-up for the spray pyrolysis developed at the several research centers and universities are presented at **Fig. 5**.

The program of controlled and sophisticated powders and films synthesis has been realized in the Institute of Technical Sciences of the Serbian Academy of Sciences and Arts (ITS SASA) since past two decades. In the framework of this research, the method of aerosol synthesis of nanophased powders

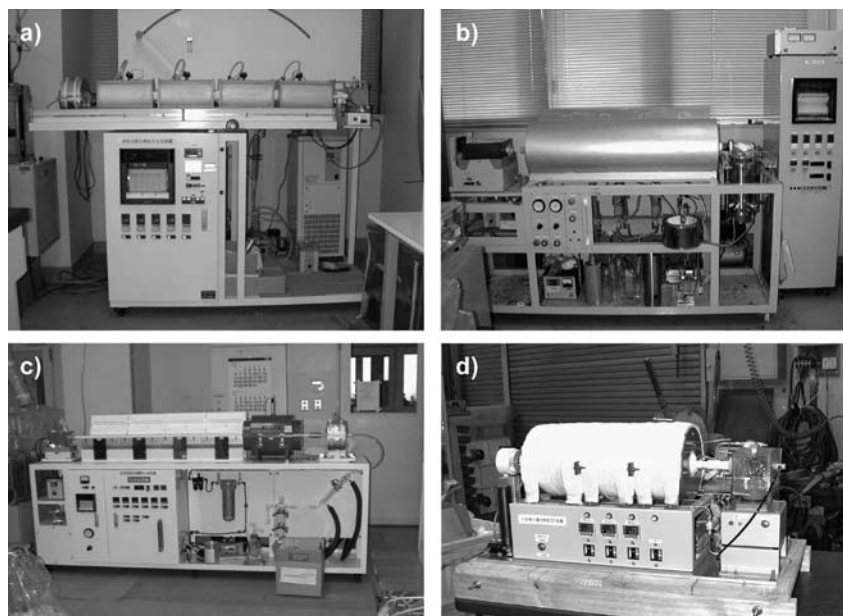


Fig. 5. Experimental set-up in Japan Fine Ceramic Centre, Nagoya (a,b,c), with 4 heating zones, $T_{\max}=1000^{\circ}\text{C}$ ^{48,50}); 4 separating heating zones, $T_{\max}=1000^{\circ}\text{C}$ for the synthesis of ceramic-metal nanocomposites; 5 heating zones, $T_{\max}=1200^{\circ}\text{C}$ for the synthesis of ceramic-ceramic nanocomposites^{51, 52}), respectively; Osaka University, JWRI (d) for the synthesis of ceramic nanoparticles under microgravity⁵³) (with courtesy of Dr. Ohara, Osaka University, JWRI, Japan).

and films is developed together with the experimental and pilot set-up [Fig. 6]: the experimental set-up is based both on electrospray (TDI) and ultrasonic (800kHz, 1.3, 1.7 and 2.5 MHz, RBI) atomizing systems, while a pilot plant is based on twin-fluid atomization technique, equipped with a Scanning Mobility Particle Sizer (TDI) for in-situ determination of aerosol properties. It offers the opportunity for the synthesis of both monodisperse and polydisperse nanoscaled particles in different oxide and nonoxide systems. Moreover, a Pyrosol technique for thin film synthesis through aerosols is developed, too. Based on these techniques, the synthesis of fine, spherical, submicronic powders either in crystal or amorphous state based on oxides, metals and non-oxides have been processed as follows: ZnO^{38,41,54,55}, ZnO-Pt(IV)⁵⁶, ZnO-Ru(III)⁵⁷, BaTiO₃⁴², ZnO-Cr₂O₃ spinel³⁴, Al₂O₃ based materials^{58,59}, Ni, NiO⁶⁰, SiC⁶¹, Q-TiO₂⁶², nanocomposites Ag:(Bi,Pb)-2223^{15,63,64}, phosphors, Gd₂O₃:Eu^{10,65,66,67}, Y₂O₃:Eu, (GdY)₂O₃:Eu^{20,68,69}, Y₃Al₅O₁₂:Ce^{10,70-74}, LiFePO₄⁷⁵. Those materials are applicable for electronics, optoelectronics, engineering ceramics, catalysts, biomaterials etc.

3. Opportunities of Hot Wall Aerosol Route (Spray Pyrolysis) for Phosphor Materials Processing

The opportunities for the synthesis of spherical, nonagglomerated particles with uniformly distributed components and phases are of special importance when phosphor materials having luminescence properties are considered. Phosphors represent inorganic crystal structures capable of emitting definite quantities of radiation within visible and/or ultraviolet spectrum as a result of excitation by an external energy source such as electron or a photon beam^{76,77,78}. Such properties of these materials are an outcome from the atomic state interactions that occur between luminescent centers and the host lattice material after the excitation. Rare earth ions (Eu^{2+,3+}, Ce³⁺, Tm³⁺, Tb³⁺, Nd³⁺) and transition metal ions (Cr³⁺, Mn²⁺) are commonly used as luminescent centers^{79,80}. Luminescent materials are normally utilized in cathode ray tubes for television screens and due to excellent characteristics of these materials their use has increased in the past years due to their application in modern emissive display industry such as flat screens, plasma and electroluminescence screens, etc. The most important properties that luminescent materials should pos-

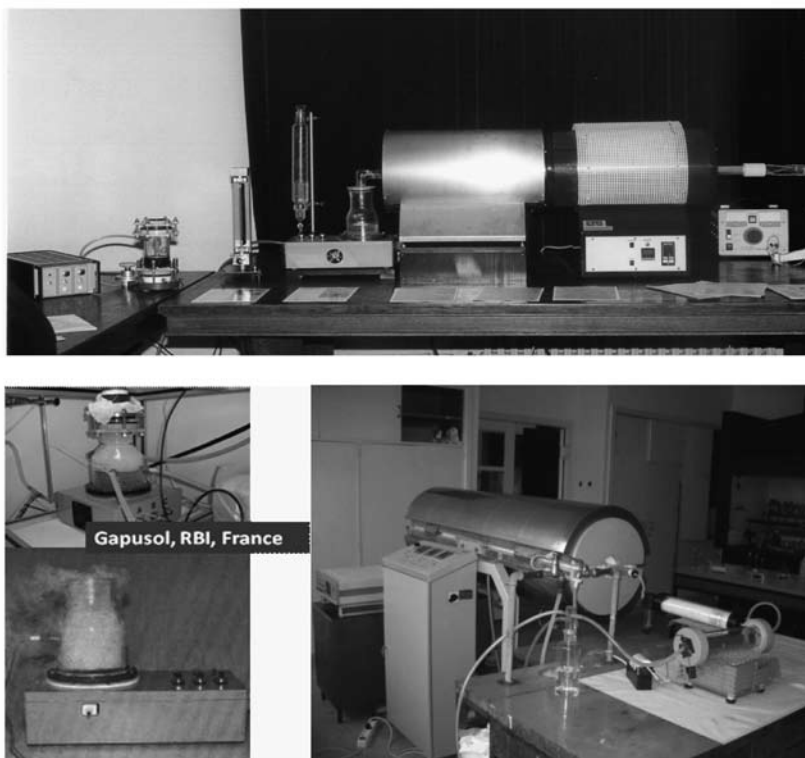


Fig. 6 Experimental set-up at ITS SASA having two (upper) and three (down) heating zones, equipped with an electrostatic precipitator for powder collecting and ultrasonic atomizers, 800 kHz, 2.1 MHz, RBI, Meylan, France (down).

sess are their brightness, spectral energy distribution and decay time⁸¹). Since luminescence properties are strongly affected by the phosphor crystallinity, phase purity, distribution of activator, surface area and particle morphology⁸²⁻⁸⁴), more efforts have been done in promoting the researches toward new methods for nanoparticles synthesis. Spray pyrolysis method has been recognized as a successful to obtain phosphor powders with high purity, homogeneous distributions of activator centers, narrow distribution of particle size and spherical morphology in nanometric scale⁴⁷).

3.1. Gd₂O₃:Eu³⁺

Gadolinia doped with europium has been used in several applications for display devices as effective red phosphor material having improved stability in high vacuum and the absence of corrosive gas emissions under electron bombardment⁸⁵). Since the luminescent behavior is greatly affected by the phosphor particle morphology and compositional homogeneity, the advantages of spray pyrolysis over conventional solid-state synthesis are huge, as already reported in literature^{47,82,85,86}).

As part of a programme to develop high grade phosphor particles, spherical in shape, agglomerated-free and with a narrow size distribution, efforts have been made to prepare material using a hot wall spray

pyrolysis approach^{10,50,65}). With regards to that, nanostructured, spherical Gd₂O₃:Eu³⁺ phosphor particles sizing bellow 800nm were synthesized from ultrasonically generated common nitrates solutions (**Fig.7**). As seen, the particle inner structure clearly resolved by the low and high magnification TEM implies the typical particle morphology obtained by spray pyrolysis composed of nano sized primary particles assembled in a spherical secondary particle. Visual inspection of the particle morphology is done by means of STEM nanotomography corresponding to the particle annealed at low temperature (900°C/12h), as shown in **Fig. 8**⁸⁶). The contrast obtained with HAADF-STEM implies bright and dark areas in a spherical shaped particle sized approx 500nm where dark contrast observed in the tilt series indicates the presence of voids and a rough particle surfaces. In the reconstructed images (**Fig. 8**, right), the better contrast than the original image allows confirming the porous and rough surfaces. It was supposed that the particle roughness is presumably a consequence of the primary particles crystallization, aggregation and growth in the secondary particles caused by the temperature increase.

In comparison to the particle morphology of conventionally obtained phosphor materials, here spherical particle morphology enables high packing

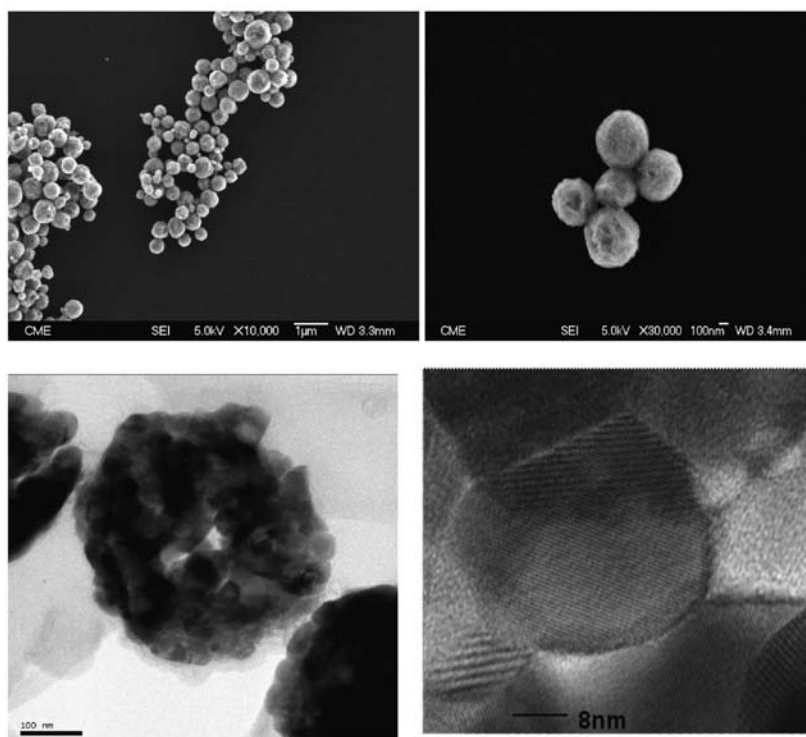


Fig. 7 Field emission scanning electron microscopy (FE-SEM) (upper), TEM, HR-TEM (400 KV JEOL JEM 4000 EX) of the as-prepared Gd₂O₃:Eu particles (down), respectively.

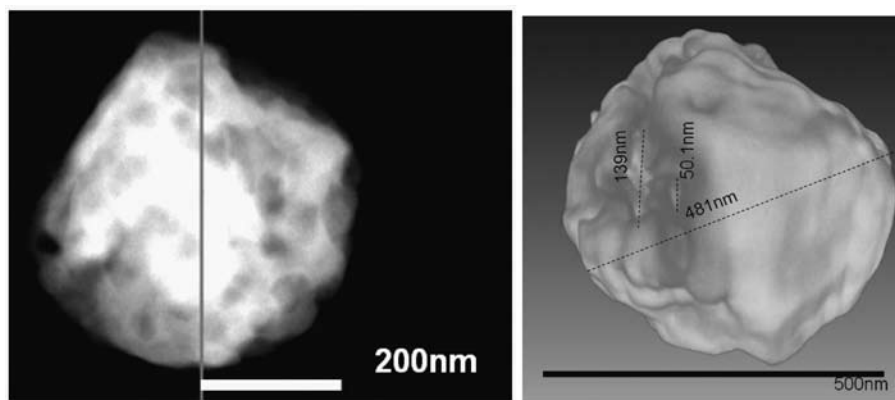


Fig. 8 STEM image of the tomographic tilt series. The vertical line indicates the rotation axis. A Tecnai TEM G² F20 X-TWIN with Fischione “single tilt” stage in HAADF mode operated at 200kV TEM was employed (left); reconstructed tomographic image: the inspect 3d v 2.5 X press Edition software and AMIRA software in cross correlation mode was employed (right).

densities, higher brightness and resolution⁸²). On the other side, hollow and porous particles have lower signal intensity in comparison with dense spherical particles⁸⁶. Besides, particle roughness and the agglomeration state are very important factors that affect the luminescence signal, implying the necessity to follow the morphology features and correlate them with the process parameters, like temperature, residence time, precursor decomposition behavior etc. In addition, the sensitization of the as-prepared particles is a critical stage in phosphor preparation and sensitivity improves with increasing the crystallinity and homogenization of the Eu dopants within the particles. Success in this processing have been obtained with additional thermal treatments of the as-prepared particles above 800 °C, where the thermally induced interparticle sintering did not occur and initially obtained morphological features were preserved⁶⁵).

Detailed phase and structural analysis proceeded in accordance to XRPD, TEM-HRTEM and EFTEM

analysing methods, proved uniform compositional distribution of the constitutive elements along the particles obtained *via* spray pyrolysis as seen from the corresponding gadolinium and europium EFTEM spectra (**Fig. 9**). EFTEM-EELS spectrum obtained for Gd₂O₃:Eu³⁺ particles additionally annealed at 900°C/12h (gray line) and 1000°C /12h (black line) in the ELNES region show the Gd M4 and Gd M5 signal for both samples (around 1185ev-1187ev) and the Eu M5 and Eu M4 signal around 1131ev-1186ev. The comparison between the spectrum indicates the incorporation of the Eu in the Gd matrix, while no changes in the energy and intensity M4/M5 ratio (0.83) indicates a (+3) oxidation state in the samples with different Eu content and thermal treatment (**Fig. 10**).

Host gadolinium oxide exhibits two polymorphic forms, low temperature (cubic) and high temperature (monoclinic), so several studies dealing with the investigation of Gd₂O₃ crystal phases development dur-

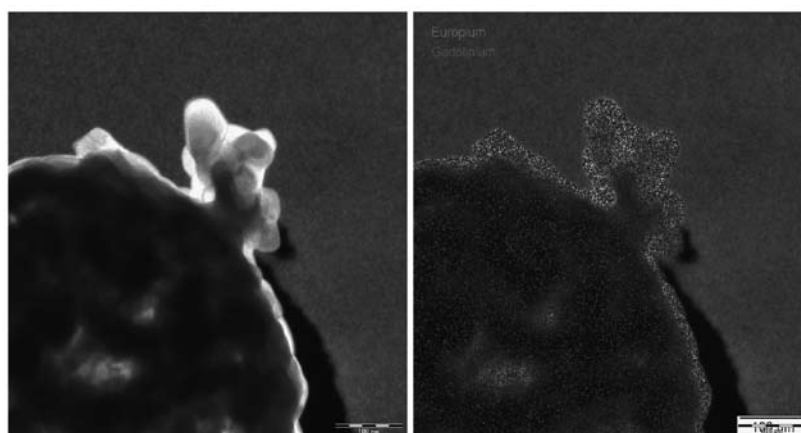


Fig. 9 The low magnification EFTEM images, Libra, 120kV, with a corrected 90° OMEGA energy filter.

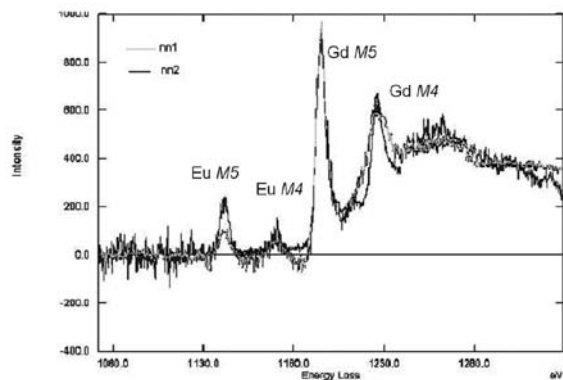


Fig. 10 EFTEM-EELS spectrum obtained for $Gd_2O_3:Eu$ particles treated at $900^\circ C/12h$ (gray line) and $1000^\circ C/12h$ (black line) in the ELNES region. A 120 KV LIBRA transmission electron microscope with omega filter in column and EELS spectrum (three windows method) was used.

ing aerosol synthesis and their relationship with luminescence properties were reported^{10,82,87,89}. XRPD revealed here the presence of two crystalline cubic phases in as-prepared powders: a bcc phase with $Ia3$ space group ($a \approx 10.829(3) \text{ \AA}$); and a fcc phase with $Fm-3m$ space group ($a \approx 5.6242(1) \text{ \AA}$) for the Eu^{3+} less doping concentration⁵⁰. After thermal treatment only the cubic $Ia3$ phase has been observed, with the cell parameters affected with Eu^{3+} doping concentration, followed with progressive increase in crystallite size. HR-TEM implied the primary nano particles of the as-prepared powders are associated with the defect structure (**Fig. 7**). After annealing above $900^\circ C$, it is evident the better order related to the orientation in the atomic frames and a decreasing of defects content. In confirmation of the stated above, a HRTEM image of the cubic phase with $Ia3$ symmetry taken along the $[100]$ zone axis is presented at **Fig. 11** indicating high crystallinity and clearly resolved the (002) and (020) atomic planes. In addition, HRTEM

analysis also proved the locally appearance of a monoclinic phase with $C2/m$ symmetry taken along the $[1-10]$ zone axis. The atomic distance (110) is resolved in the image (**Fig. 11**, right). The appearance of the higher density metastable monoclinic structure is probably a consequence of the extreme synthesis conditions during spray pyrolysis, i.e. high heating rates and short residence time and attributable to the Gibbs-Thomson effect, associated with increased surface tension with nanostructuring⁶⁵, (**Fig. 11**).

Luminescence studies carried out in $Gd_2O_3:Eu^{3+}$ phosphor system have demonstrated that annealing and crystalline phases control both the thermoluminescence and radioluminescence signals⁶⁵. Characteristic bands in the emission spectra are assigned to Eu^{3+} ion radiative ${}^5D_0 \rightarrow {}^7F_i$ ($i=0,1,2,3,4$) transitions. In all the samples maximum intensity peak is at 611 nm wavelength belonging to ${}^5D_0 \rightarrow {}^7F_2$ transition^{10,50}. All observed transitions are due to the Eu^{3+} in C_2 crystallographic site except one line, at 581 nm (attributed to ${}^5D_0 \rightarrow {}^7F_1$ transition) that belongs to Eu^{3+} in S_6 crystallographic site.

3.2. $Y_2O_3:Eu^{3+}$

Y_2O_3 doped with europium is a well known red phosphor material employed in modern high-resolution display devices such as plasma display panels (PDP) and field emission displays (FED)⁴⁷. The incorporation of gadolinium in the yttria matrix may significantly contribute to the luminescent properties and x-ray absorption coefficient thus increasing the field of application in optoelectronic devices such as ceramic scintillators for computed tomography.

The interest of the Y_2O_3 has been broadly known due to its particularly relevant physical and functional properties, including the crystallographic stability, a

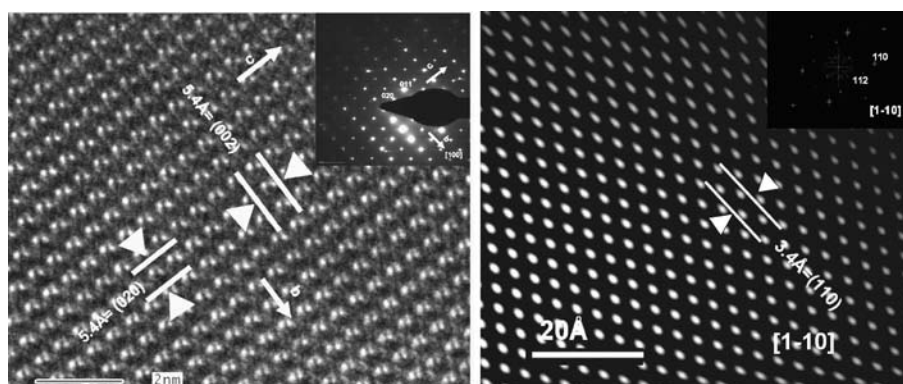


Fig. 11 HRTEM images of the cubic $Ia3$ phase with the corresponding indexed electron diffraction pattern (left) and monoclinic $c2/m$ phase with the fft indexed along the $[1-10]$ (right) taken by Titan 80-300TM TEM, 300KV and Tecnai F 20 TEM, 200 KV, respectively.

wide band energy gap (5.5e.v.) and the ability to be a host material for rare earth ions. Yttrium oxide is a good phosphor material with different luminescent spectra depending on the luminescent center by which it is activated (for example Eu, Tb, Dy, Tm or Nd); doped with Eu^{3+} is a well known red phosphor in flat panel displays^{90,92}. In particular, it has been shown that if in nanostructure form it possesses improved quantum efficiency while the mixed oxide with rare earth ions (RE), the $\text{RE}_x\text{Y}_{2-x}\text{O}_3$ type, represents a new group of superconducting materials⁹³. Yttria represents one of the best host materials for rare earth ions due to the fact that its ionic radii and crystal structure are very similar to the ionic radii and crystal structure of the rare earth ions⁸². There are several crystal structures of Y_2O_3 : cubic, type Mn_2O_3 , which represents a stable equilibrium structure under stationary conditions and monoclinic structure with space group $C2/m$ that can be formed under extreme synthesis conditions^{65,94}.

The nanostructured particles of Y_2O_3 doped with Eu^{3+} were processed through the spray pyrolysis method from nitrate precursors²⁰. Synthesis was carried out with an ultrasonic aerosol device operating at 1.3 MHz in air atmosphere connected with a triple-zone tubular flow reactor (200-700-900°C) (**Fig. 6**). Particles were submitted to post-thermal treatments at temperatures among 1000 and 1200°C for 12 hours in order to increase the crystallinity and uniform distribution of doped centers. The particles obtained were spherical, having narrow size distributions, high compositional homogeneity and were in unagglomerated state (**Fig. 12**). Exceptionally, sintering start point was noticed in the case of the samples thermally treated at 1200°C. That is, TEM analysis revealed neck formation between secondary spherical particles^{10, 69}.

The $Ia3$ phase has been identified by XRD and TEM-HRTEM/FFT in both as-prepared and thermally treated samples. No intermediate phase is

observed along the particles. Rietveld refinement revealed that crystallite size of the as-prepared powders was around 20nm while sufficient energy supply during the thermal treatment led to crystallite growth (40-130nm for annealing temperatures 1000-1200°C, respectively) and affected structural relaxation (lower values of microstrain in comparison to the values for ap samples) (**Table2**).

Functional characterization done through the determination of photoluminescent characteristics showed typical emission spectra of Eu^{3+} ion incorporated into yttrium oxide. Emission spectra were obtained at room temperature through excitation of Eu^{3+} ion into $^5\text{L}_6$ energy level under 393nm wavelength (**Fig. 13**). The emission lines of Eu^{3+} were ascribed to $^5\text{D}_0 \rightarrow ^7\text{F}_j$ ($j=1, 2, 3, 4$) spin forbidden $f-f$ transitions and the main emission peak corresponded to clear red emission at 611nm. Detailed analysis of the emission spectra showed that they consist out of sharp peaks, originating from Eu^{3+} ion incorporated into C_2 site, while only one weak line belonging to Eu^{3+} ion incorporated into S_6 site was observed. Maximum Stark splitting (ΔE) of the $^7\text{F}_1$ manifold, occurring under the influence of the crystal field, was in agreement with theoretical values $\text{Y}_2\text{O}_3:\text{Eu}^{3+}$ ($\Delta E(\text{Y}_2\text{O}_3) = 355\text{cm}^{-1}$)⁹⁵.

Based on the fluorescence decay curves of the $^5\text{D}_0$ emitting level it was concluded that applied synthesis method (spray pyrolysis) leads to the formation of nanostructured powders having longer lifetimes in comparison to $\text{Y}_2\text{O}_3:\text{Eu}^{3+}$ in its bulk form ($\tau(^5\text{D}_0 \rightarrow ^7\text{F}_2)_{\text{theor}} = 1.0\text{ms}$ (Y_2O_3)⁹⁶). Also, it was shown that samples with doping concentration of 10 at% Eu^{3+} had lower $^5\text{D}_0$ lifetimes (around 1.2 ms) in comparison to 5 at% (around 1.4 ms) leading to a conclusion that in the case of higher doping level concentration quenching occurs (**Table 2**).

Through the analysis of lifetime values for Eu^{3+} $^5\text{D}^1$ emitting level for Y_2O_3 with 5at% of Eu^{3+} the influence of thermal treatment was monitored (**Fig. 13**).

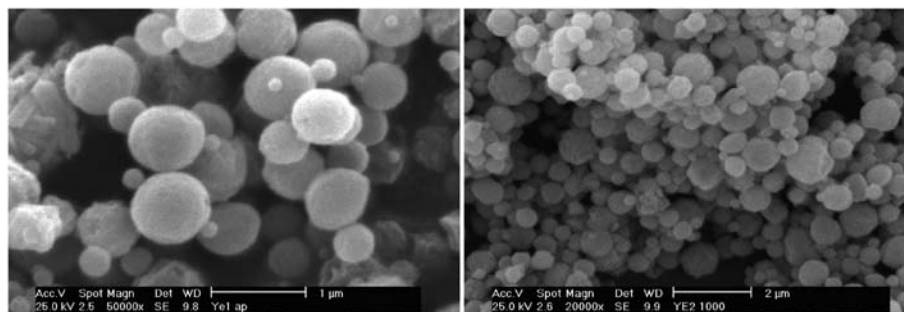


Fig. 12 $(\text{Y}_{0.95}\text{Eu}_{0.05})_2\text{O}_3$ (left) and $(\text{Y}_{0.90}\text{Eu}_{0.10})_2\text{O}_3$ (right) thermally treated at 900°C and 1000°C, respectively.

Table 2 Main structural parameters derived through Rietveld refinement and characteristics of the luminescent measurements for $Y_2O_3:Eu^{3+}$ system²⁰⁾

	$Y_2O_3:Eu^{3+}$							
	ye ₅ B A-doping concentration Eu ³⁺ (at%) B- annealing temperature(°C)				ap- as-prepared sample			
	ye ₅ ap	ye ₅ 1000	ye ₅ 1100	ye ₅ 1200	ye ₁₀ ap	ye ₁₀ 1000	ye ₁₀ 1100	ye ₁₀ 1200
cs (nm)	19.14	40.55	60.06	129.53	20.11	40.94	66.99	132.89
a (Å)	10.620	10.616	10.616	10.616	10.632	10.628	10.623	10.628
ms (%)	0.432	0.189	0.0607	0.0963	0.529	0.197	0.0794	0.0402
⁵ D ₀ → ⁷ F ₀ (C ₂) (nm)	580.3	580.4	580.4	580.4	580.4	580.4	580.4	580.4
⁵ D ₀ → ⁷ F ₁ (S ₆) (nm)	582.1	582.3	582.2	582.2	582.2	582.0	582.1	582.1
⁵ D ₀ → ⁷ F ₁ (C ₂) (nm)	587.1	587.2	587.1	587.2	587.1	587.2	587.2	587.2
	592.9	592.8	592.8	592.9	592.8	592.8	592.8	592.8
	599.2	599.1	599.2	599.4	599.2	599.2	599.2	599.2
Δ E (cm ⁻¹)	344.0	338.2	344.0	346.5	344	341	341	341
τ (⁵ D ₀ → ⁷ F ₂) (ms)	1.47	1.46	1.40	1.42	1.24	1.21	1.14	1.14
τ _{avr} (⁵ D ₁ → ⁷ F ₂) (μ s)	11.33	18.97	19.74	19.78	/	/	/	/

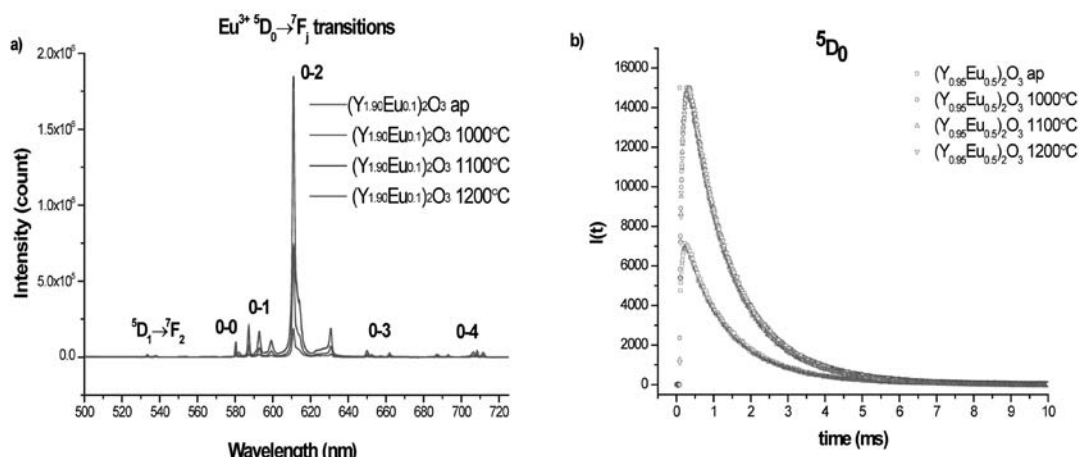


Fig. 13 Emission spectra of $(Y_{0.90}Eu_{0.10})_2O_3$ system (left) and lifetime values of $(Y_{0.95}Eu_{0.05})_2O_3$ system under $\lambda_{ex}=393nm$ ($\lambda_{em}=611nm$) (right)²⁰⁾.

Namely, as-prepared powders had a lower value of these parameter (around 11 μ s) while the value for thermally treated was slightly higher (around 20 μ s). Knowing that decrease of emission intensity from ⁵D₁ emitting level is due to increased probability of cross-relaxation mechanism which occurs when there is an increase of Eu³⁺ concentration in the yttria host lattice⁹⁷⁾ it was concluded that cross-relaxation effect was stronger in the case of as-prepared samples. Above stated observations indirectly depicted more homogeneous distribution of Eu³⁺ ions in case of the annealed samples.^{68,98,99)}

3.3. (Y,Gd)₂O₃:Eu³⁺

$(Y_{1-x}Gd_x)_2O_3:Eu^{3+}$ system, where the gadolinium content was varied ($x=0.25, 0.50, 0.75$), has been

synthesized throughout the same conditions as $Y_2O_3:Eu^{3+}$. TEM investigations revealed that these systems poses the same morphological features as yttrium oxide system i.e. particles possess spherical filled morphology. Additionally SAED patterns revealed polycrystalline nature of the particles, while the ring width implied high defect content in as-prepared samples **Fig. 14**. Through XRD and TEM/SAED analysis it was also shown that gadolinium content had influence on the structural phase characteristics. To be exact, as-prepared samples with composition $x=0.25, 0.50$ had solely $Ia\bar{3}$ phase, but the sample compositionally closest to pure Gd_2O_3 , with $x=0.75$, showed the same characteristics as gadolinium oxide synthesized under similar conditions. Apart from primary, cubic bcc $Ia\bar{3}$ phase a second cubic fcc

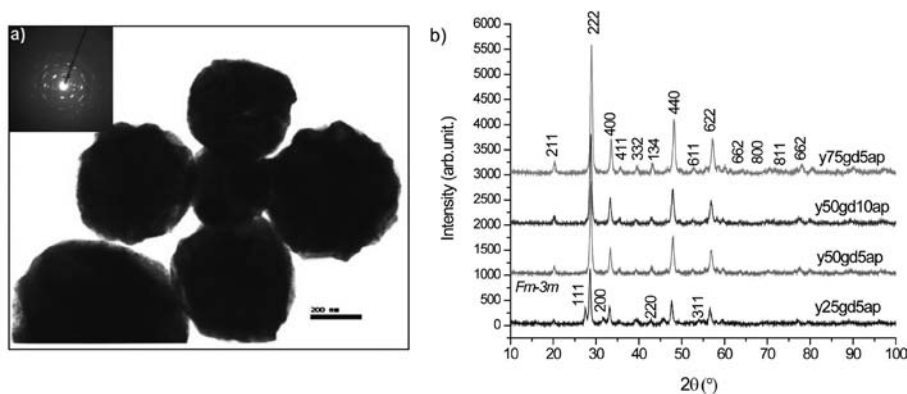


Fig. 14 TEM/SAED image for as-prepared $(Y_{0.50}Gd_{0.50})_2O_3:Eu^{3+}$ powder with 10at% of Eu^{3+} (left) and XRD diffraction patterns of the as-prepared samples for $(Y_{1-x}Gd_x)_2O_3:Eu^{3+}$ system indentifying $Ia3$ phase as a primary phase in all the samples and for the sample $x=0.25$ peaks belonging to $Fm-3m$ are denoted (right).

phase with $Fm-3m$ space group was confirmed in ap samples^{20,69}. All the as-prepared samples were thermally treated at $1100^\circ C$ for 12h and in this case only $Ia3$ phase prevailed.

Observing the optical properties, the same characteristic emission spectra of Eu^{3+} ion were seen as in the case of pure $Y_2O_3:Eu^{3+}$ system. Detailed analysis of the emission spectra showed that in the case of $(Y_{1-x}Gd_x)_2O_3:Eu^{3+}$ system a linear increase of maximum Stark splitting (ΔE) occurs with the increase of gadolinium content (**Table 3**), i.e. with the increase of lattice parameters. Since maximum splitting of the 7F_1 manifold is affected by crystal field strength parameter in a proportional way, the increase of ΔE value with the increase of gadolinium content could be treated as a clear indication of almost perfect mixing in solid solutions of $(Y,Gd)_2O_3:Eu^{3+}$ system^{20,98}.

When doped with 5at% mixed $(Y_{1-x}Gd_x)_2O_3:Eu^{3+}$ oxides, thermally treated at $1100^\circ C$, had similar lifetime values of 5D_0 emitting level in comparison to yttria with same doping concentration (around $1.4 \mu s$). In the case of $x=0.50$, doping was done with 5 and with 10at% of Eu^{3+} and in these cases 5D_0 lifetime of the sample with higher doping concentration was significantly smaller i.e. $0.86 \mu s$. It indicated concentration quenching and that $(Y_{1-x}Gd_x)_2O_3:Eu^{3+}$ with $x=0.50$ and 10 at% of Eu^{3+} had inferior properties than the material in bulk form. Relatively high values of 5D_1 lifetimes for thermally treated $(Y_{1-x}Gd_x)_2O_3:Eu^{3+}$ powders with 5at% revealed, as in the case of $Y_2O_3:Eu^{3+}$, implied homogeneous distribution of the doping ion.

3.4. $Y_3Al_5O_{12}$ (YAG): Ce^{3+}

The $Y_3Al_5O_{12}$ (YAG) is optically isotropic mate-

Table 3 Main structural characteristics derived through Rietveld refinement and characteristics of the luminescent measurements for $(Y_{1-x}Gd_x)_2O_3:Eu^{3+}$ system annealed at $1100^\circ C$ ²⁰

	$(Y_{1-x}Gd_x)_2O_3:Eu^{3+}$			
	y _A gd _B T A- yttrium content; B-doping concentration of Eu^{3+} (at%); T-annealing temperature			
	y ₇₅ gd ₅ 1100	y ₅₀ gd ₅ 1100	y ₂₅ gd ₅ 1100	y ₃₀ gd ₁₀ 1100
cs (nm)	155.94	202.63	55.25	191.36
a (Å)	10.667	10.724	10.771	10.730
ms (%)	0.0329	0.0563	0.0333	0.0195
${}^5D_0 \rightarrow {}^7F_0$ (C_2), nm	579.9	580.0	580.0	579.9
${}^5D_0 \rightarrow {}^7F_1$ (S_0), nm	581.6	581.6	581.4	581.4
${}^5D_0 \rightarrow {}^7F_1$ (C_2), nm	586.8	586.9	587.1	586.9
	592.3	592.3	592.2	592.2
	598.5	598.3	598.2	598.4
ΔE (cm^{-1})	333.2	324.7	316.1	327.5
τ (${}^5D_0 \rightarrow {}^7F_2$) (ms)	1.36	1.25	1.32	0.86
τ_{avr} (${}^5D_1 \rightarrow {}^7F_2$) (μs)	14.3	13.9	13.6	/

rial with high thermal conductivity. Doped with rare earth ions it represents very useful phosphor material for variety of display applications including cathode ray tube, low voltage field emission display, and backlight source. Specially cerium doped YAG (YAG:Ce³⁺), as a yellow-emitting component for the production of a white light, is a comprehensively studied previous years due to urgent demand for alternative light source in an illumination and display area. The broad Ce³⁺ emission band originates from the 4f-5d electronic transition with intensive side bands due to vibronic coupling to the lattice and local vibration modes in the YAG lattice. Due to this YAG:Ce³⁺ easily convert blue emission from blue light emitting diode (LED) into white LED. Even a lack of cerium emission toward the red region can be suppressed by a co-doping (Tb³⁺) or cation substituting (Ga³⁺ or Gd³⁺) making presently this material to be the phosphor of choice in commercial white LEDs¹⁰⁰.

First publication related to luminescence investigation in YAG:Ce³⁺ system dated from 1967¹⁰¹. Compared with this traditionally produced garnet by solid-state reaction between the component oxides, today's phosphor materials usually produced through soft-chemistry processes possess many advantages thanks to their certain structural and morphological characteristics. The field of aerosol processing was intensively developed in the last 10 years and many phosphorous materials have been produced up to now⁴⁷. Processing of YAG:Ce³⁺ powder *via* spray pyrolysis (ultrasonic and FEAG) has been previously reported^{102,103}. Significant advance is shown due to the mixing of starting reactants at molecular scale, but obtaining of the pure garnet phase was hindered by retaining of amorphous phase in synthesized powders. Therefore, annealing process at high temperatures was applied for the crystallization and activation of cerium-doped YAG particles. In latter work¹⁰⁴, it was shown that the PL intensity of YAG:Ce³⁺ particles was strongly affected by doping concentration of cerium, annealing temperature, mean particle size, and particle morphology. The non-aggregated spherical particles of YAG:Ce³⁺ (1at%) annealed at 1300°C showed the maximum photoluminescence emission. Several papers devoted to the same topic were reported in the following years, highlighting the complexity of synthesis - structure relation towards achieving optimized phosphors properties. It was shown that concentration of nitrates solution and the flow rate of nitrogen used as a carrier gas have the major impact on the productivity of the spray pyrolysed particles¹⁰⁴. Significant mor-

phological and functional enhancement through BaF₂ flux introduction in common nitrates solution during spray pyrolysis resulted in the intensification of the maximum peak intensity of the prepared YAG:Ce³⁺ phosphor powders in comparison to that of the commercial phosphor powders¹⁰⁵. The addition of urea into nitrate precursor contributes to nanoparticles formation due to its combustion in the flame zone and improves their optical performance¹⁰⁶. Further enhancing of the YAG:Ce³⁺ luminescence efficiency can be realized through Tb³⁺ co-doping due to occurring of the effective energy transfer from Tb³⁺ to Ce³⁺ in YAG host lattice¹⁰⁷. But in all of above reports in-situ generation of garnet phase during spray pyrolysis is omitted or associated with Y₄Al₂O₉, (YAM) or YAlO₃ (YAP) phases appearing so additional thermal treatment of processed powder is obligatory. The technique of spray pyrolysis was employed also to produce homogeneous solid solutions in the Al₂O₃-Y₂O₃ system at temperatures as low as 150-300°C, owing to the prevention of segregation of the precursors prior to YAG phase crystallization¹⁰⁸. Another attempt has been made using "single-source" precursors (alkoxides and glycolates) instead of "multiple-source" precursor¹⁰⁹. The lack of formation of YAG in all the spray pyrolysis experiments was ascribed to the short heating times and fast heating rates, which resulted in the formation of kinetic products.

Rationalization of the sequence for nanocrystalline YAG:Ce³⁺ phase evolution in the particles synthesized by ultrasonic spray pyrolysis method through variation of processing parameters or precursors composition was also the topic of our research^{10,70-74}. It was shown that particle morphological and structural characteristics are dependent on the applied synthesis methodology, especially regarding the precursors solution modification. Synthesis from common nitrates precursors was performed at 900°C in a tubular flow reactor using the air to carry the aerosol. Short residence time during synthesis resulted in multi-phase powder generation. Beside garnet phase, YAM and Y₂O₃ were also detected⁷¹. Synthesized particles were submicronic in size, highly spherical and unagglomerated (**Fig. 15**). They exhibit rough surface implying that are built from primary nanoparticles⁷⁰. Their general morphology did not change significantly with annealing, but their roughness increase further due promoted crystallization affecting their specific surface⁷². Incorporation of Ce³⁺ ions at the host is confirmed with the broad emission having peak maximum at 533nm⁷⁰. The interpretation of the thermo- and radio- luminescence signals from

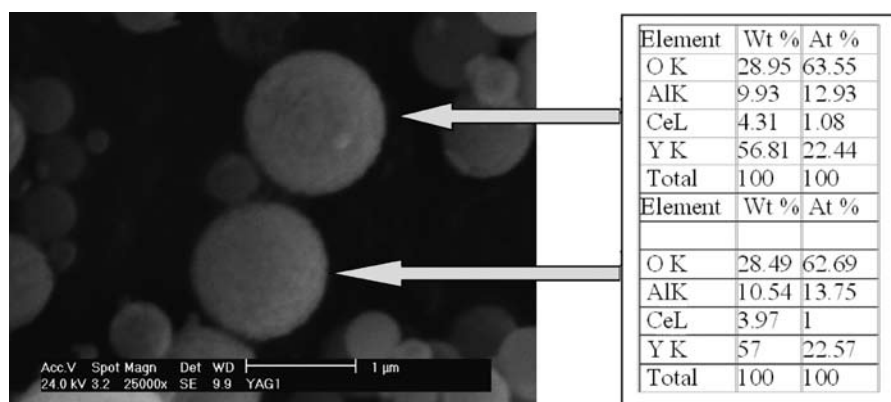


Fig. 15. SEM of the YAG:Ce³⁺ particles obtained through spray pyrolysis of nitrate solution at 900°C and annealed at 1000°C (6h); corresponding EDS analysis.

the YAG:Ce³⁺ powders implies that the cerium ions are not readily accommodated on the YAG lattice sites during synthesis⁶⁵. Even after annealing cerium ions do not offer a favourable excitation decay path; instead, there are broad emission bands typical of the host lattice defect sites and a very weak luminescence via the cerium on pathway near 300nm. The complexity of the temperature dependence of the TL as a function of wavelength also suggests that a variety of independent defect sites contributes to the TL. They also indicated numerous anomalies in the temperature dependence of their luminescence lifetime data.

To investigate the nature of the multiphase powder obtaining, an amorphous material with composition corresponding to yttrium aluminum garnet phase with same content of cerium has been synthesized at 320°C using a similar spray pyrolysis route. Precursor-derived amorphous phase crystallized at temperatures as high as 900 and 1000°C gave multiphased powders with different compositions after 3h of annealing (YAG, YAP, YAM), while prolongation of treatment at higher temperature result in pure YAG phase formation (Fig. 16)⁷³.

In order to achieve additional heating during YAG:

Ce³⁺ synthesis urea-assisted spray pyrolysis was employed¹¹¹. This route can be regarded as a self-combustion synthesis confined within a droplet where urea acts as an *in-situ* source of thermal energy due to its decomposition. The as-prepared non-agglomerated amorphous powder has broad particle size distribution (200-1400nm) (Fig. 17). They were additionally thermally treated in air at 1000 and 1100 °C for 6h preserving their morphological characteristics. Despite of precursor modification during synthesis, performed annealing did not yield pure YAG:Ce³⁺ product. While lower temperature is favorable for YAP and YAM phase segregation, increase of heating temperature enhanced YAG phase formation with YAM phase retention.

Having this in mind, preservation of the molecular homogeneity during precursor synthesis was done through polymerization with an organic complexing agent EDTA and ethylen glycol (EG)⁷⁴. Two reactions are involved, a complex formation between EDTA and metals (via four carboxylate and two amine groups) and esterification between EDTA and EG. Ultrasonically generated aerosol droplets were decomposed at 600°C in argon atmosphere. Following the initial attempt in providing pure YAG:

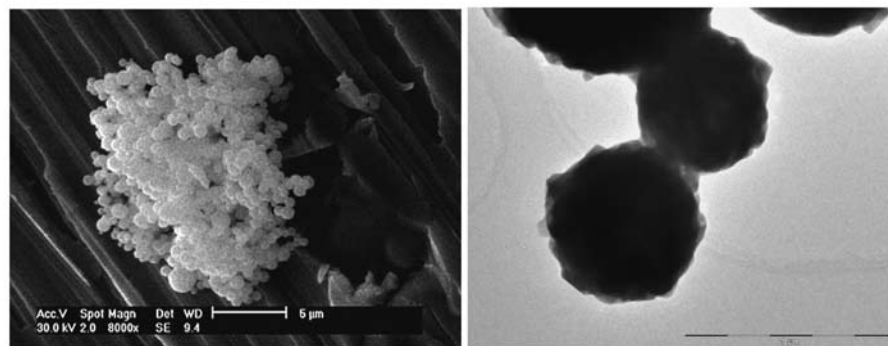


Fig. 16 SEM and TEM of the YAG:Ce³⁺ particles obtained through spray pyrolysis of nitrate solution at 320°C and annealed at 1000°C (6h).

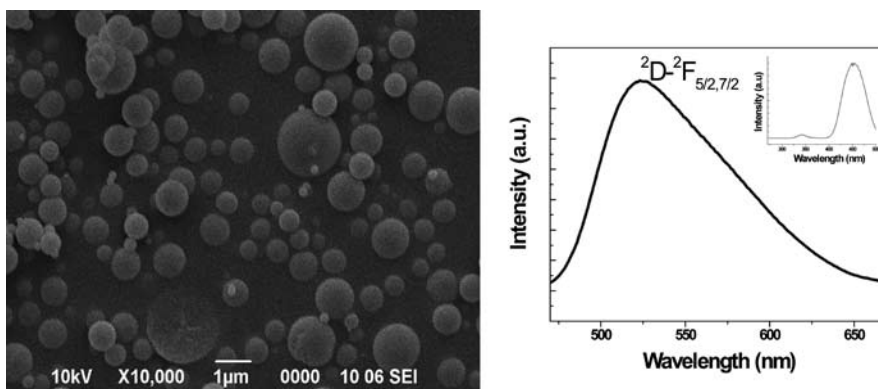


Fig. 17 SEM of the as-prepared YAG:Ce³⁺ particles obtained through urea-assisted spray pyrolysis at 900°C; PL spectra of particles treated at 1100°C (3h).

Ce³⁺ phase generation the particles were additionally thermally treated for 3h in air at 1000°C and 1100°C. Comprehensive structural analysis implied that garnet phase was formed without contamination of other phase having different aluminum yttrium composition even at the lower annealing temperature and in a much shorter time. The spherical dense particles comprised grained-like structure, since they are composed of nanosized garnet monocrystals (**Fig. 18**). Although uncompleted, cerium incorporation in garnet matrix is confirmed by broad green-yellow emission spectra in the range of 470-670 nm peaking at 521nm. With this optimization of the spray pyrolysis reaction conditions towards synthesis of pure, un-agglomerated YAG:Ce³⁺ particles with spherical shape and filled morphology were achieved.

4. Conclusions

Aerosol route represents a versatile synthesis method for processing novel functional materials. An

insight into the diversity of this method and materials that could be produced was given within this paper with the highlight on hot-wall aerosol synthesis of phosphor particles based on Gd₂O₃:Eu, Y₂O₃:Eu, (Y_{1-x}Gd_x)₂O₃:Eu and Y₃Al₅O₁₂:Ce which are a part of the current research in the Institute of Technical Sciences of SASA, Serbia. As it was summarized, the syntheses from the aerosol are found to be of great value since they result in well defined phosphor powder characteristics essential for achieving higher brightness and resolution in displays. Particularly, it was shown that spray pyrolysis is one of the simplest among them and is capable in ensuring particle spherical morphology, good crystallinity and uniformity in size and shape. Those characteristics enhance uniform distribution of the luminescent centre in the host matrix influencing final luminescence properties.

Targeted cubic crystal structure of RE₂O₃:Eu oxide powders (RE=Gd,Eu) was obtained in all as-prepared samples and it persisted as the solely phase through-

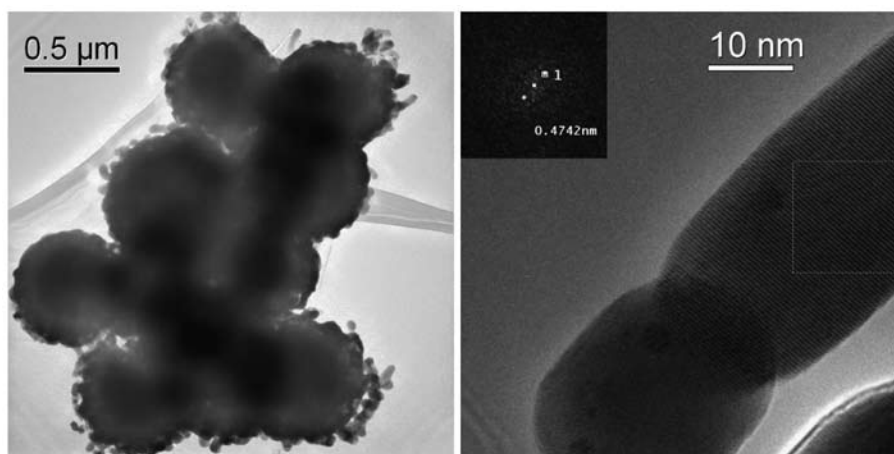


Fig. 18 TEM/HRTEM/FFT of the YAG:Ce³⁺ particles obtained from polymeric precursor solution through spray pyrolysis at 900°C; annealed at 1100°C; FFT inset confirm *Ia-3d* phase formation (211 plane).

out the thermal treatment (1000-1200°C /12h) which led to the improvement of crystallinity. Appearance of secondary fcc *Fm-3m* phase in as-prepared samples of Gd₂O₃:Eu³⁺ and mixed oxide with highest content of gadolinium (Y_{0.25}Gd_{0.75})₂O₃:Eu³⁺ was identified through XRD and TEM/SAED analysis. Additionally, in the case of Gd₂O₃:Eu system HRTEM analysis revealed local appearance of a metastable, monoclinic phase at temperatures above 1100°C associated with a high content of interfaces and high defect content. Generally, in the case of RE₂O₃:Eu oxides a good control over morphological features was accomplished. Controlled synthesis parameters led to the formation of powders consisted out of spherical, non-agglomerated particles with narrow size distribution (300-800nm). TEM/HRTEM analysis revealed their nanostructural nature (primary particles as low as 20 nm) and filled morphology. Functional characterization of RE₂O₃:Eu revealed typical emission spectra of Eu³⁺ ion incorporated into rare earth oxides with dominant red emission peak at 611nm. The development of local defect structure, depending on the time-temperature history of phosphor processing, may influence the emission spectra causing broader luminescent lines. For (Y,Gd)₂O₃:Eu oxides the increase of Gd content in the yttria matrix had an influence on the spectra and it was observed throughout the increase of maximum Stark splitting (ΔE) of the ⁷F₁ manifold. Such behavior was treated as a clear indication of almost perfect mixing in solid solutions of (Y,Gd)₂O₃:Eu³⁺ system. Based on the fluorescence decay curves of the ⁵D₀ emitting level of Y₂O₃:Eu³⁺ and (Y,Gd)₂O₃:Eu³⁺ systems it was concluded that applied synthesis method led to the formation of nanostructured powders having longer lifetimes in comparison to Y₂O₃:Eu³⁺ in its bulk form. Also, these analyses showed that concentration quenching occurs for the case of 10 at% doping concentration of Eu³⁺ in comparison to 5 at% due to lower values of ⁵D₀ lifetimes.

In the case of YAG:Ce³⁺ the control over their morphological properties was not completely achieved due to the fact that fully dense particles were not generated from nitrate precursors. Additionally, applying the concept of low temperature aerosol decomposition resulted in preservation of the desired powder morphology but formation of YAG phase was still followed by YAM and Y₂O₃ phases. The drawback was in the fact that high heating rates and short residence time, inherent to spray pyrolysis process, led to the formation of kinetically stable phases rather than the thermodynamically stable target YAG phase. Since

spray pyrolysis offers different approaches for controlling of the particle morphology and composition, obtaining of the YAG:Ce³⁺ particles with spherical and filled morphology was done through introduction of polymeric precursor solutions. The absence of intermediate phases implied that observed differences in solubility of yttrium and aluminum sources (liable for sequential precipitation and phase segregation) could be prevailed through homogeneous dispersion of Y³⁺ and Al³⁺ ions into polymeric organic network formed by esterification. Enhancement in PL intensity of synthesized particles indicated reduced dimensionality of their primary entities (crystallites) and homogeneity distribution of cerium ion in the YAG host lattice.

Acknowledgement

The authors are grateful to the Ministry of Science and Technology of the Republic of Serbia for financial support (Project #142010), NEDO International Joint Research Grant Program 01MB7 and COST 539 Action. The authors gratefully acknowledge Dr. Satoshi Ohara, JWRI, Osaka University, Japan for kind assistance as well as the contribution of Dr. M. Dramicanin, Institute "Vinca", Serbia, in the preparation of this article. FEI Holland is greatly acknowledged for nanotomography measurements.

References

- 1) Tuller, H. (1997): Solid State Electrochemical Systems- Opportunities for Nanofabricated or Nanostructured Materials, *J. Electroceram.*, 1(3) pp.211-218.
- 2) Messing, G.L. Zhang S.-C. and Jayanthi, G.V. (1993): Ceramic Powder Synthesis by Spray Pyrolysis, *J. Amer. Ceram. Soc.*, 76 (11) pp.2707-805.
- 3) Gurav, A. Kodas, T. Pluym T. and Xiong, Y. (1993): Aerosol Processing of Materials, *Aerosol Sci. Technol.*, 19, pp. 411-52.
- 4) Kodas, T. T. Hampden-Smith, M. J. (1999): Aerosol Processing of Materials, Wiley-VCH .
- 5) Milosevic, O. (1999): Aerosol Synthesis of Nanostructured Materials"; in *Advanced Science and Technology of Sintering*, Edited by B. Stojanovic, M.V.Nikolic and V. Skorokhod, Kluwer Academic/Plenum Publishers, New York, pp.103-111.
- 6) Madler, L. (2004): Liquid-fed Aerosol Reactors for One-step Synthesis of Nano-structured Particles, *KONA Powder and Particle Journal*, 22, pp.107-119.
- 7) Okuyama K. and Lengorro I. W. (2003): Preparation of Nanoparticles via Spray Route, *Chem.Eng. Sci.*, 58, pp.537-547.
- 8) Gurav, A., Kodas, T., Kauppinen, E., Joutsensaari,

- J. and Zilliacus, R. (1994): Phase evolution and gas-phase particle size distributions during spray pyrolysis of (Bi,Pb)-Sr-Ca-Cu-O and Ag-(Bi,Pb)-Sr-Ca-Cu-O powders. *Nanostr. Mater.*, 4 (5), pp.583-589.
- 9) Fukui, T., Ohara S. Naito, M. and Nogi, K. (2003): Performance and stability of SOFC anode fabricated from NiO/SYZ composite particles, *J. Euro. Cer. Soc.*, 23 (15), pp.2963-2967.
 - 10) Milosevic, O., Mancic, L., Rabanal, M.E., Yang, B and Townsend, P.D. (2005): Structural and Luminescence Properties of $Gd_2O_3:Eu^{3+}$ and $Y_3Al_5O_{12}:Ce^{3+}$ Phosphor Particles Synthesized via Aerosol, *J.Electrochem. Soc.*, 152, pp.G707-713.
 - 11) Pratsinis S.E. and Vemury, S. (1996): Particle formation in gases: a review, *Powder Techn.* 88, pp.267-273.
 - 12) Zachariah M. R. and Huzarewicz, S. (1991): Aerosol processing of YBaCuO superconductors in a flame reactor, *J. Mater. Res.*, 6(2), pp.264-269.
 - 13) Helble, J. J.(1998): Combustion aerosol synthesis of nanoscale ceramic powders, *J.Aerosol Sci.*, 29 (5-6), pp.721-736.
 - 14) Tani, T., Watanabe N. and Takatori, K. (2003): Emulsion combustion and flame spray synthesis of zinc oxide/silica particles, *J.Nanopart.Res.*, 5(1-2), pp.39-46.
 - 15) Mancic, L., Milosevic, O., Marinkovic, B., de Silva Lopes, M.F. and Rizzo, F. (2000) "The influence of urea on the formation process of Bi-Pb-Sr-Ca-Cu-O superconducting ceramics synthesized by spray pyrolysis method" , *Mat. Sci. Eng.: B*, Vol 76(2), pp.127-132.
 - 16) Lee, S., Son, T., Yun, J., Kwon, H., Messing, G.L. and Jun, B. (2004): Preparation of BaTiO₃ nanoparticles by combustion spray pyrolysis, *Mater. Lett.*, 58, pp.2932-2936.
 - 17) Langlet, M., Joubert, J. C. (1992): The pyrosol process or the pyrolysis of an ultrasonically generated aerosol, in: C.N.R.Rao (Ed.), *Chemistry of Advanced Materials*, Blackwell Scientific Publications, Oxford, pp.55-78.
 - 18) Smith, A.(2000): Pyrosol deposition of ZnO and SnO₂ based thin films: the interplay between solution chemistry, growth rate and film morphology, *Thin Solid Films*, 376, pp.47-55.
 - 19) Tucic, A., Marinkovic, Z.V., Mancic, L., Cilense, M., Milosevic, O. (2003): Pyrosol preparation and structural characterization of SnO₂ thin films, *J.Mat.Process.Techn.*, 143-44, pp.41-45.
 - 20) Marinkovic, K. (2009): Structural, morphological and functional properties of nanostructured rare-earth oxides obtained through aerosol synthesis, Master Science Thesis, Belgrade University.
 - 21) Lang, R. J. (1962): Ultrasonic atomization of liquids, *J. Acoust. Soc. Am.* 34, pp.6-8.
 - 22) Liu, T. Q., Sakurai, O., Mizutani, N., Kato, M. (1986): Preparation of spherical fine ZnO particles by the spray pyrolysis method using ultrasonic atomization technique, *J. Mat. Sci.*, 21 pp.3698-3702.
 - 23) Lenggoro, I. W., Okuyama, K., Fernandez de la Mora J., and Tohge, N. (2000): Preparation of ZnS nanoparticles by electrospray pyrolysis, *J. Aerosol Sci.*, 31 (1) pp.121-136.
 - 24) Chang, H-W., Okuyama, K. (2002): Optical properties of dense and porous spheroids consisting of primary silica nanoparticles, *Aerosol Sci.*, 33, pp.1701-1720.
 - 25) Ocaña M. and Matijevic, E. (1990): Preparation of uniform colloidal dispersions by chemical reactions in aerosols—V. Tin(IV) oxide, *J.Aerosol Sci.*, 21(6), pp.811-20.
 - 26) Nukiyama, S., Tanasawa, Y. (1993): An experiment on the atomization of liquid, *Transactions of the Japan Society of Mechanical Engineering*, 5, pp.136-143.
 - 27) Maric, R., Fukui, T., Ohara, S., Yoshida, H., Nishimura, M., Inagaki T. and Miura, K. (2000): Powder Prepared by Spray Pyrolysis as an Electrode Material for Solid Oxide Fuel Cells, *J. Mater. Sci.*, 35, pp.1-8.
 - 28) Gonzales-Carreño, T., Morales, M.P., M. Gracia M. and Serna, C. J.(1993): Preparation of uniform g-Fe₂O₃ particles with nanometer size by spray pyrolysis", *Mater. Lett.* 18, pp.151-155.
 - 29) Cho, S-Y. Lee J-H. and Park, S-J. (1993): Preparation of spherical SnO₂ powders by ultrasonic spray pyrolysis, *J.Am.Ceram. Soc.* 76 (3) pp.10-15.
 - 30) Fukui, T., Ohara S. Naito, M. and Nogi, K. Morphogy and Performance of SOFC Anode Fabricated from NiO/YSZ Composite Particles, *J. Chem. Eng. Jpn.*, 34 (7), pp.964-966.
 - 31) Chang, Y., Park S.B. and Kang, Y.W (1995): Preparation of high surface area nanophase particles by low pressure spray pyrolysis, *Nanostr. Mater.* 5, pp.777-791.
 - 32) Li, Q., Sorensen, C.M., Klabunde K.J. and Hadjipanayis, G.C. (1993): Aerosol spray pyrolysis synthesis of magnetic manganese ferrite particles, *Aerosol Sci. Techn.* 19, pp.453-467.
 - 33) Senzaki, Y., Caruso, J., Hampden-Smith, M.J., Kodas T.T. and Wang, L. M., (1995): Preparation of strontium ferrite particles by spray pyrolysis, *J. Amer. Ceram. Soc.* 78(11) pp.2973-2976.
 - 34) Marinkovic, Z. V., Mancic, L., Maric, R., Milosevic, O. (2001): Preparation of nanostructured Zn-Cr-O spinel powders by ultrasonic spray pyrolysis, *J.Europ.Ceram. Soc.*, 21 (10-11) pp.2051-2055.
 - 35) Koch W. and Friedlander, S. K. (1990): Particle growth by coalescence and agglomeration, *J.Aerosol Sci.*, 21(1) pp.S73-S76.
 - 36) Okuyama, K., Lenggoro, I.W. (2003): Preparation of nanoparticles via spray route, *Chemical Engineering Science*, 58, pp.537-547.
 - 37) Pluym, T.C., Powell, Q. H., Gurav, A.S., Ward T.L. and Kodas, T.T. (1993): Solid silver particles production by spray pyrolysis, *J.Aerosol Sci.* 24 (3) pp.383-392.
 - 38) Marinkovic, Z.V., Mancic, L., Milosevic, O. (2004): Nature of structural changes in nanocrystalline ZnO powders under linear heating conditions, *J. Euro. Cer. Soc.*, 24, pp.1929-1933.
 - 39) Jayanthi, G.V., Zhang S.C. and Messing, G.L. (1993): Modeling of solid particle formation during solution aerosol thermolysis, *Aerosol Sci.Techn.* 19, 478-490.

- 40) Xiong Y. and Kodas, T. T. (1993): Droplet evaporation and solute precipitation during spray pyrolysis, *J.Aerosol Sci.* 24 (7) pp.893-908.
- 41) Milosevic, O., Gagic, V., Vodnik, J., Mitrovic, A., Karanovic, Lj., Stojanovic, B., Zivkovic, Lj. (1997): Synthesis and deposition of ZnO based particles by aerosol spray pyrolysis, *Thin Solid Films*, 296, pp.44-48.
- 42) Milosevic, O., Mirkovic, M., Uskokovic, D. (1996): Characteristics and formation mechanism of BaTiO₃ powders prepared by twin-fluid and ultrasonic spray-pyrolysis method, *J.Am. Ceram.Soc.*, 79 (6) pp.1720-22.
- 43) Odier, P., Dubois, B., Clinard, C., Stroumbos, H. and Monod, P. (1990): Processing of ceramic powders by the spray pyrolysis method; influence of the precursors, examples of zirconia and YBa₂Cu₃O₇, in: *Ceramic Trans - Ceramic Powder Science III*, G.L. Messing, S. Hirano, H. Hausner ed., American Ceramic Society, Westerville, OH.
- 44) Xiong, Y., Lyong S.W. and Kodas, T.T. (1995): Volatile metal oxide evaporation during aerosol decomposition, *J.Am.Ceram.Soc.* 78 (9) pp.2490-2496.
- 45) Patil, P.S. (1999): Versatility of chemical spray pyrolysis technique, *Mater. Chem. Phys.*, 59, pp.185-198.
- 46) Uskokovic D. and Jokanovic, V. (2006): Molecular designing of fine particles using aerosol synthesis, in *Advances in Dielectric Materials and Electronic Devices*, ed. American Ceramic society, Ceramic Transactions, 174, pp.3-14.
- 47) Jung, S., Kang, Y.C., Kim, J.H. (2007): Generation of phosphor particles for photoluminescence applications by spray pyrolysis, *J.Mater. Sci.*, 42, pp.9783-9794.
- 48) Fukui, T., Oobuchi, T., Ikuhara, Y., Ohara, S. and Kodera, K. (1997): Synthesis of (La,Sr)MnO₃-YSZ Composite Particles by Spray Pyrolysis, *J.Am.Ceram.Soc.*, 80, pp.261-263.
- 49) Fukui, T., Ohara, S. and Mukai, K. (1998): Long-Term Stability of Ni-YSZ Anode with a New Microstructure Prepared from Composite Powder” , *Electrochem. Solid-State Lett.*, 1, pp.120-122.
- 50) Milosevic, O., Maric, R., Ohara, S., Fukui, T. (2001): Aerosol Synthesis of Phosphor Particles Based on Eu Activated Gadolinium Oxide Matrices, *Ceramic Transactions*, 112, *Ceramic Processing Sci. VI*, pp.101-106.
- 51) Fukui, T., Ohara, S., Naito, M. and Nogi, K. (2003): Synthesis of NiO-YSZ Composite Particles for an Electrode of Solid Oxide Fuel Cells by Spray Pyrolysis, *Powder Technology*, 132, pp.52-56.
- 52) Matsumoto, M., Kaneko, K., Yasutomi, Y., Ohara, S. and Fukui, T. (2002): Synthesis of TiO₂-Ag Composite Powder by Spray Pyrolysis” , *J. Ceram. Soc. Japan*, 110, pp.60-62.
- 53) Cribier, J-F, Ohara, S. and Fukui, T. (2003): Preparation of ZnO based Particles in a Microgravity environment”, *J. Mater. Sci. Lett.*, 22, pp.37-40.
- 54) Milosevic, O., Jordovic, B., Uskokovic, D. (1994): Preparation of fine spherical ZnO powders by an ultrasonic spray pyrolysis method, *Materials Letters* 19, (3-4) pp.165-170.
- 55) Milosevic, O., Uskokovic, D.(1993): Synthesis of BaTiO₃ and ZnO varistor precursor powders by reaction spray pyrolysis, *Mat. Sci. Eng. A* 168 (2) pp.249-252.
- 56) Djinic, V. M., Mancic, L. T., Bogdanovic, G. A., Vuclic, P. J., del Rosario, G., Sabo T.J. and Milosevic, O.B. (2005): Aerosol synthesis of pure and Pt-doped ZnO particles using nitrate and pdda-Pt(IV) complex solutions, *J. Mater. Res.*, 20 (1) pp.102-113.
- 57) Grguric-Sipka, S., Sabo, T., Mancic L. and Milosevic O. (2004): Aerosol synthesis of ruthenium doped ZnO fine particles, *J.Aerosol.Sci.*, 35, pp.S183-184.
- 58) Janackovic, Dj., Jokanovic, V., Kostic-Gvozdenovic, Lj., Zivkovic, Lj., Uskokovic, D. (1996): Synthesis, Morphology and Formation Mechanism of Mullite Particles Produced by Ultrasonic Spray Pyrolysis” , *J.Mater.Res.*, 11 (7) pp.1706-1716.
- 59) Martin, M.I., Rabanal, M.E., Gomez, L.S., Torralba, J.M., Milosevic, O. (2008): Microstructural and morphological analysis of nanostructured alumina particles synthesized at low temperature via aerosol route, *J.Eur.Ceram.Soc.*, 28, pp.2487-2494.
- 60) Stopic, S., Ilic, I., Nedeljkovic, J., Rakocevic, Z., Uskokovic, D. (1999): Influence of Additives on the Properties of Spherical Ni Particles Prepared by Ultrasonic Spray Pyrolysis”, *J.Mater. Res.*, 14, (7) pp.3059-3065.
- 61) Cerovic, Lj. Milonjic, S., Zivkovic, Lj., Uskokovic, D. (1996): Synthesis of Spherical b-Silicon Carbide Particles by Ultrasonic Spray Pyrolysis”, *J.Am.Ceram.Soc.*, 79, pp.2215-17.
- 62) Saponjic, Z.V., Rakocevic, Z., Dimitrijevic, N.M., Nedeljkovic, J.M., Jokanovic, V., Uskokovic, D.P (1998): Tailor Made Synthesis of Q-TiO₂ Powder by Using Quantum Dots as Building Blocks, *Nanostruct. Mater.*, 10, pp.341-348.
- 63) Mancic, L., Milosevic, O., Marinkovic, B., da Silva Lopez, M.F., Rizzo, F. (2000): Rapid Formation of High Tc Phase in Bi-Pb-Sr-CaCu-O System, *Physica C*, 341-348, pp.503-504.
- 64) Mancic, L., Milosevic, O., Labus, N., Ristic, M. (2001): High Tc Superconducting Powders Synthesis from Aerosol” , *J.Euro.Ceram.Soc.*, 21, pp.2765-2769.
- 65) Wang, Y., Milosevic, O., Gómez, L., Rabanal, M.E., Torralba, J.M., Yang, B., Townsend, P. D. (2006): Thermoluminescence responses from europium doped gadolinium oxide *Journal of Physics: Condensed Matter*, 18, pp.9257-9272.
- 66) Rabanal, M.E, Gómez, L.S, Khalifa, A., Torralba, J.M., Mancic, L., Milosevic, O. (2007): Structural properties of europia-doped-gadolinia synthesized through aerosol, *Journal of European Ceramic Society* 27 (13-15) pp.4325-4328.
- 67) Gómez, L. S., Rabanal, M.E., Torralba, J. M., Mancic, L., Milosevic, O. (2007): Structural and morphological study of nanoceramics prepared by spray pyrolysis. *Ceramic Transactions, Characterization & Control of interfaces for High Quality Advanced materials. The*

- American Ceramic Society, eds. Kevin Ewsuk et al. Vol. 198, pp.193-197
- 68) Marinkovic, K., Mancic, L., Gomez, L., Rabanal, M.E., Dramicanin, M., Milosevic, O., Nanostructured $(Y_{1-x}Gd_x)_2O_3:Eu^{3+}$ powders obtained through aerosol synthesis, ICCCI 2009, Kurashiki, September 6-9th, Japan
 - 69) Marinkovic, K., Mancic, L., Gomez, L.S., Rabanal, M.E., Dramicanin, M., Milosevic, O. (2009): Photoluminescent properties of nanostructured $Y_2O_3:Eu^{3+}$ powders obtained by aerosol synthesis, ICOM 2009, Herceg Novi, 27-30th August, Montenegro.
 - 70) del Rosario, G., Ohara, S., Mancic, L., Milosevic, O. (2004): Characterisation of YAG:Ce powders thermal treated at different temperatures, *Appl. Surf. Sci.*, 238 (1-4) pp.469-474.
 - 71) Milosevic, O., Mancic, L., Ohara, S., del Rosario, G., Vulic, P. (2004): Aerosol synthesis and phase development in Ce-doped nanophased Yttrium-aluminium garnet ($Y_3Al_5O_{12}:Ce$) particles, *Ceramic transactions, Characterisation and Control of Interfaces for High Quality Advanced Materials*, eds. K.Ewsuk, K.Nogi, M.Reiterer, A.Tomsia, S.J.Glass, R.Waesche, K.Uematsu, M.Naito, American Ceramic Society, 146, pp.435-441.
 - 72) Mancic, L., del Rosario, G., Marinkovic Stanojevic, Z., Milosevic, O. (2007): Phase evolution in Ce doped yttrium aluminium based particles derived from aerosol, *J.Eur.Cer.Soc.*, 27, pp.4329-4332.
 - 73) Kandic, Lj., Marinkovic, K., Mancic, L., del Rosario, G., Milosevic, O. (2007): Low Temperature Aerosol Synthesis of YAG:Ce³⁺ Nanostructures: Comparative Study of the XRPD Micro structural Parameters, *Mat. Sci.Forum*, 555, pp.395-400.
 - 74) Mancic, L., Marinkovic, K., Marinkovic, B., Dramicanin, M. and Milosevic, O. (2009): YAG:Ce³⁺ nanostructured particles obtained via spray pyrolysis of polymeric precursor solution, *J.Eur.Cer.Soc.*, in press, doi:10.1016/j.jeurceramsoc.2009.05.037.
 - 75) Jugovic, D., Uskokovic, D. (2009): A review of recent developments in the synthesis procedures of lithium iron phosphate powders, *Journal of Power Source*, 190, pp.538-544.
 - 76) Rack, P. D. , Holloway, P. H. (1998): The srtructure, device physics and material properties of thin film electroluminescent displays, *Mater. Sci. Eng.*, 4, pp.171-219.
 - 77) Ropp, R. C. (1991): *Luminescence and the Solid State*, Elsevier Science Publishers B. V., New York.
 - 78) Maghrabi, M., Townsend, P.D., Vazquez, G. (2001) Low temperature luminescence from the near surface region of. Nd:YAG, *J. Phys.: Condens. Matter*, 13, pp.2497-515.
 - 79) Kang, Y.C., Lenggoro, I.W., Park, S.B. and Okuyama, K. (2000): YAG-Ce phosphor particles prepared by ultrasonic spray pyrolysis, *Mater. Res. Bull.*, 35, pp.789-798.
 - 80) Zych, E., Brecher, C., Wojtowicz, A.J. and Lingertat, H. (1997): Luminescence properties of Ce-activated YAG optical ceramic scintillator materials, *J. Lumin.*, 75, pp.193-203.
 - 81) Kang, Y. C., Park, S. B., Lenggoro, I.W., Okuyama, K. (1999): Gd₂O₃:Eu phosphor particles with sphericity, submicron size and nonaggregation characteristics, *Journal Phys. Chem. Solids* 60, pp.379-384.
 - 82) Jung, D.S., Hong, S.K., Lee, H. J., Kang, Y.C. (2006): Gd₂O₃:Eu phosphor particles prepared from spray solution containing boric acid flux and polymer precursor by spray pyrolysis, *Opt. Mater.*, Vol. 28(5) pp.530-535.
 - 83) Pires, A. M., Santos, M.F., Davolos, M.R., Stucchi, E.B. (2002): The effect of Eu³⁺ ion doping concentration in Gd₂O₃ fine spherical particles, *J. Alloy Compd.*, 344, pp.276-279.
 - 84) Koo, H., Ju, S., Jung, D.S., Hong, S.K., Kim, D.Y., Kang, Y.C. (2006): Morphology Control of Gd₂O₃:Eu phosphor particles with cubic and monoclinic phases prepared by high temperature spray pyrolysis (2006): *Jap. J. Appl. Phys.*, 45 (6A) pp.5018-5022.
 - 85) Kim, E. J., Kang, Y.C., Park, H.D., Ryu S.K. (2002): UV and VUV characteristics of (YGd)₂O₃ phosphor particles prepared by spray pyrolysis from polymeric precursors, *Mater.Res.Bull.*, 2159, pp.1-10.
 - 86) Gómez, L. S., Sourty, E., Freitag, B., Milosevic, O., Rabanal, M. E., A three dimensional study of Gadolinium oxides doped with europium formed by aerosol method using electron tomography, to be published.
 - 87) Bae, J.S., Yi, S.S., Kim, J. H., Shim, K.S., Moon, B.K., Jeong, J.H., Kim, Y. S. (2006): Crystalline-phase-dependent red emission behaviours of Gd₂O₃:Eu³⁺ thin-film phosphors, *Applied Physics A* , 82, (2) pp.S.369-372.
 - 88) Seo, D.J., Kang, Y.C., Park, S. B. (2003): The synthesis of (Y_{1-x}Gd_x)₂O₃:Eu phosphor particles by flame spray pyrolysis with LiCl flux. *Appl. Phys. A*, 77, pp.659-663.
 - 89) Bhargave, R. N., Gallagher, D., Welker T. (1994): Doped nanocrystals of semiconductors-a new class of luminescent materials *J. Lumin.*, 61, pp.275.
 - 90) Wan, J., Wang, Z., Chen, X., Mu, L., Qian, Y. (2005): Shape tailored photoluminescent intensity of red phosphor Y₂O₃:Eu³⁺. *Journal of Crystal Growth.*, 284, pp.538-543.
 - 91) Tissue, B. M. and Yuan, H. B. (2003): Structure, particle size and annealing of gas-phase condensed Eu³⁺: Y₂O₃ nanophosphors, *J.Solid State Chem.*, 171, pp.12-18.
 - 92) Allieri, B., Depero, L. E., Marino, A., Sangalleti, L., Caporaso, L., Speghini, A., Bettinelli, M. (2000): Growth and microstructural analysis of nanosized Y₂O₃ doped with rare-earths, *Mater. Chem. Phys.*, 66, 164-177.
 - 93) Mitric, M., Onnerud, P., Rodic, D., Tellgren, R., Szytula, A., Napijalo, M.Lj. (1993): The preferential site occupation and magnetic properties of GdxY_{2-x}O₃, *J. Phys.Chem.Solids*, 54, 967-972.
 - 94) Dosev, D., Guo, B., Kennedy, I.M. (2006): Photoluminescence of Eu³⁺: Y₂O₃ as an indication of crystal struc-

- ture and particle size in nanoparticles synthesized by flame spray pyrolysis *Aerosol Sci.*, 37, 402-412.
- 95) Malta, O., Antic-Fidancev, E., Lemaitre-Blaise, M., Milicic-Tang, A., Taibi, M. (1995): The crystal field strength parameter and the maximum splitting of the 7F_1 manifold of the Eu^{3+} ion in oxides, *Journal Alloys and Compounds*, 228, pp.41-44.
 - 96) Pons Y Moll, O., Huignard, A., Antic-Fidancev, E., Aschehoug, P., Viana, B., Millon, E., Perrière, J., Garapon, C., Mugnier, J. (2000): Eu^{3+} - and Tm^{3+} -doped yttrium oxide thin films for optical applications, *Journal of Luminescence*, 87-89, pp.1115-1117.
 - 97) Tallant, D.R., Seager, C.H., Simpson, R.L. (2002): Energy transfer and relaxation in europium-activated Y_2O_3 after excitation by ultraviolet photons, *Journal of Applied Physics*, 91, pp.4053-4064.
 - 98) Andrić, Ž., Dramićanin, M.D., Mitrić, M., Jokanović, V., Bessiere, A., Viana, B. (2008): Polymer complex solution synthesis of $(\text{YxGd1-x})_2\text{O}_3:\text{Eu}^{3+}$ Nanopowders, *Optical Materials*, 30, pp.1023-1027.
 - 99) Gomez, L. S. (2009): Sintesis y caracterization de oxidos nanoestructurados de gadolinio e ytrio dopados con europio obtenidos mediante el metodo de spray pirolisis, PhD Thesis, University Carlos III, Madrid.
 - 100) Yang, H., Lee, D-K., Kim, Y-S. (2009): Spectral variations of nano-sized $\text{Y}_3\text{Al}_5\text{O}_{12}:\text{Ce}$ phosphors via codoping/substitution and their white LED characteristics, *Materials Chemistry and Physics* 114, pp.665-669.
 - 101) Blasse, G., Bril A. (1967): Investigation of some Ce-activated phosphors, *Journal of Chemical Physics*, 47(12) pp.5139-5245.
 - 102) Kang, Y.C., Park S.B., and Lenggoro, I.W., Okuyama, K. (1998): Preparation of non aggregation YAG-Ce phosphor particles by spray pyrolysis, *Aerosol Sci.*, 29, pp.S 911-S912.
 - 103) Kang, Y.C., Lenggoro, I.W., Park, S.B., Okuyama, K. (2000): YAG:Ce phosphor particles prepared by ultrasonic spray pyrolysis. *Mater. Res. Bull.*, 35, pp.789-798.
 - 104) Qi, F.X., Wang, H.B., Zhu, XZ. (2005): Spherical YAG: Ce^{3+} Phosphor Particles Prepared by Spray Pyrolysis, *Journal of Rare Earths*, 23, 4, pp.397-400.
 - 105) Lee, S.H., Jung, D.S., Han, J.M., Koo, H.Y., Kang, Y.C. (2009): Fine-sized $\text{Y}_3\text{Al}_5\text{O}_{12}:\text{Ce}$ phosphor powders prepared by spray pyrolysis from the spray solution with barium fluoride flux, *J. Alloys and Compounds* 477, pp.776-779.
 - 106) Purwanto, A., Wang, W.N. Ogi, T., Lenggoro, I.W., Tanabe, E., Okuyama, K. (2008): High luminance YAG: Ce nanoparticles prepared from urea-added aqueous precursor by flame-process, *Journal of Alloys and Compounds*, 463, (1-2) pp.350-357.
 - 107) Hyun K.J., Lee, W. (2007): Enhanced luminescent properties of $\text{Y}_3\text{Al}_5\text{O}_{12}:\text{Tb}^{3+}, \text{Ce}^{3+}$ phosphor prepared by spray pyrolysis, *Journal of Luminescence* 126, pp.469-474.
 - 108) Ullal, C.K., Balasubramaniam, K.R., Gandhi, A.S., Jaram, V. (2001): Non-equilibrium phase synthesis in $\text{Al}_2\text{O}_3\text{-Y}_2\text{O}_3$ by spray pyrolysis of nitrate precursors, *Acta Materialia* 49 (14) pp.2691-2699.
 - 109) Nyman, M., Caruso J, HampdenSmith, M.J. (1997): Comparison of solid-state and spray pyrolysis synthesis of yttrium aluminate powders, *J.Amer.Ceram.Soc.* 80 (5) pp.1231-1238.
 - 110) Marinkovic, K., Mancic, L., Pavlovic, V.B., Dramicanin, M., Milosevic, O. (2008): Urea-assisted self-combustion aerosol synthesis of $\text{Y}_3\text{Al}_5\text{O}_{12}:\text{Ce}^{3+}$, YUCOMAT, September 8-12 2008, Herceg Novi, Montenegro, p.139.

Author's short biography



O. Milosevic

Olivera B. Milosevic, Research professor at the Institute of Technical Sciences of Serbian Academy of Sciences and Arts (ITS SASA), Belgrade, Serbia, was born on August 13th 1955. in Belgrade (Serbia). She graduated Chemical engineering at the Faculty for Technology and Metallurgy, Belgrade University and from the same University she received her M.Sc. and D.Sc. degrees in Materials Science. She is awardee of the Japanese Science and Technology Agency Fellowship in 1999, when she joined Japan Fine Ceramic Center, Nagoya, Japan as a Visiting Researcher. She participated as a Visiting Professor at the University Carlos III, Madrid, Spain, Department for Materials Science and Engineering, in 2001, 2002, 2003 and 2005/2006 and is awardee of a one year Sabbatical grant from the Ministry of Science and Education, Madrid, Spain. She is invited as Visiting professor to join JWRI, Osaka University as JSPS fellowship awardee in 2010.

The main field of her scientific work has been related to the advanced materials processing with particular emphasis in research and development of nanophased functional materials (ceramics and composites) using chemical reactions in aerosols. The significance of her researches is confirmed with more than 200 scientific papers in relevant scientific journals and presentations at the International Conferences. Her results have been cited more than 200 times in scientific literature. Most of her work she delivered either as plenary or invited lectures at Hiroshima University, Japan, Konan University, Kobe, Japan, Japan Fine Ceramic Center, Nagoya, Japan, Microcoating Technology, USA etc., Beijing Normal University, China, "Jozef Stefan" Institute, Slovenia, Osaka University, Japan etc. She currently leads the research activities focused to the innovative processing methods for 1D and 3D nanoscaled functional materials. Dr. Olivera B. Milosevic is a full member of the International Institute for the Science of Sintering (IISS) and the Engineering Academy of Serbia, a member of the European Microscopic Society, Serbian Chemical Society and Serbian Crystallographic Society.



L. Mancic

Lidija Mancic was born on August 18th 1968 in Zajecar, Serbia. She received her BSc (1992) and M.Sc. (1996) degrees at Belgrade University, Technical faculty in Bor – Inorganic Chemistry Department, and D.Sc. (2004) in the field of Materials Science at the Centre for Multidisciplinary Studies, Belgrade University. Since 1996 she has worked in ITS SASA on the synthesis and characterization of superconductors and semiconductors (ultra-dispersed and nano-powders, bulk and films using chemical reactions in aerosols). Since 2006 she has been engaged in research devoted to one-dimensional nanomaterials processing through hydrothermal route at Pontificia Universidade Catolica do Rio de Janeiro within the framework of her post-doc studies. She is a reviewer for several peer reviewed journals in the area of material science.



M. E. Rabanal

Maria Eugenia Rabanal was born on March 12th, 1969 in Madrid, Spain. She received her BSc (1993) and Master (1996) degrees at the University Complutense in Madrid, Spain in the field of Physical Chemistry. In 2002 she received her Ph.D. in Materials Science at the University Carlos III, Madrid, Spain, working on soft magnetic materials and high energy mechanical milling process. She was a pre-doctoral fellow along the course 1999/2000 at the Physics Department in the Trinity College in Dublin. She got a position in 1998 as an Assistant professor at Department of Materials Science and Engineering and Chemistry Engineering of the University Carlos III of Madrid, Spain where she has presently the permanent position as a lecturer. Her current research activities are focused on structural, morphological and functional characterization of advanced materials using a variety of experimental techniques. She has more than 60 publications in international journals and communications at International Conferences.

Author's short biography



L. S. Gomez

Luz Stella Gómez Villalba was born on May 26th 1963 in Columbia. She received her BSc (1988) at the National University of Columbia in the field of geology and her PhD (2008) in the field of Materials Science at the University Carlos III, Materials Science and Engineering Department, Madrid, Spain. In the period from 1988-2001 she was engaged at INGEOMINAS, Colombian Institute of Researchers in geology, mining and chemistry (Colombia) where she conducted research work in the field of petrology and mineralogy. She is presently engaged at ECONOMIC GEOLOGY INSTITUTE- Superior Council of Scientific Researchers (CSIC)- Universidad Complutense de Madrid (Madrid- Spain) where she realized researches in nanotechnology applied to geomaterials in cultural heritage conservation. Her current research interest includes the structural characterization of nanophase materials with expertise in the field of Transmission Electron Microscopy and XRD powder diffraction.



K. Marinkovic

Katarina Marinkovic was born on March 11th, 1978 in Belgrade, Serbia. She received her BSc in Chemical Engineering in 2003, and M.Sc. in Material Science in April 2009, both at the Faculty of Technology and Metallurgy, Belgrade University, Serbia. She works as a research assistant in ITS SASA since 2006. in the area of conducted synthesis of nanostructured powders and thin films through aerosol methods. Within COST 539 Action she got a one month Short Term Scientific Mission (STSM) at the University Carlos III, Madrid, Spain, November-December 2006. She has published several papers in peer reviewed journals and presentations at international Conferences.

Structural Joining of Ceramics Nanoparticles: Development of Photonic Crystals for Terahertz Wave Control by Using Micro Stereolithography[†]

Soshu Kirihara

Smart Processing Research Center, Joining and
Welding Research Institute, Osaka Universit¹

Abstract

Structural joining is new concept of materials processing to create novel functional materials with special patterns and morphologies. Nanometer sized ceramics particles are bound continuously with resin materials solidified by laser beam irradiations to form micrometer order structures exactly. In this paper, fabrication processes of alumina photonic crystals with a periodic diamond structure will be introduced. Periodic arrangements of dielectric constants can control electromagnetic waves in terahertz frequency ranges through spatial wave diffractions. Three dimensional dielectric lattices were designed by using graphical application of a computer aided designing (CAD) software, and acrylic diamond structures with alumina nanoparticles dispersion were formed by using micro stereolithography (μ -STL) of a computer aided manufacturing (CAD) system. Fabricated precursors were dewaxed and sintered in the air to obtained full ceramics photonic crystals. The terahertz wave properties were measured by terahertz time domain spectroscopy (TDS) device. A complete photonic band gap to reflect the terahertz wave perfectly was observed, and showed good agreement with a theoretical simulation of plane wave expansion (PWE) method. Moreover, localization of the terahertz wave were observed in point or plane defects introduced into the diamond photonic crystals trough an electromagnetic field analysis of transmission line modeling (TLM) method.

Keywords: Phonic Crystal, Band Gap, Dielectric Material, Terahertz Wave, Stereolithography

1. Introduction

Periodically arranged structures of dielectric media are called photonic crystals¹⁻⁴. They have photonic band gaps in which no electromagnetic wave can propagate. If the periodicity is changed locally by introducing a defect, localized modes appear in the band gap⁵⁻⁸. Such localization function of electromagnetic waves can be applied to various devices, for example resonators, waveguides, and antennas. Three dimensional photonic crystals with a diamond structure are regarded as the ideal photonic crystal since they can prohibit the propagation of electromagnetic waves for any directions in the band gap^{9,10}. However, due to the complex structure, they

are difficult to fabricate. In our previous investigations, we have succeeded in fabricating micrometer order diamond structures by using stereolithography method of a computer aided design and manufacturing (CAD/CAM) processes¹¹⁻¹⁶. Photo sensitive resin slurry including with nanometer sized ceramic particles was solidified continuously through laser beam scanning to create dielectric lattice structures accurately. A complete photonic band gap formation in the terahertz wave frequency range was reported. Subsequently, structural modifications of the diamond lattice structures to control the terahertz wave propagations were investigated by using the CAD/CAM process practically¹⁷⁻²¹. In near future industries, electromagnetic waves in a terahertz frequency range with micrometer order wavelength will be expected to apply for various types of novel sensors which can detect gun powders, drugs, bacteria in foods, micro cracks in electric devices, cancer cells in human skin and other physical, chemical and living events²¹⁻²⁷.

[†] Accepted: August 25th, 2009

¹ 11-1 Mihogaoka Iaraki, 567-0047 Osaka, Japan
TEL: 81-6-6879-8693
FAX: 81-6-6879-8693
E-mail: kirihara@jwri.osaka-u.ac.jp

In this paper, the novel stereolithography process to fabricate the micro diamond photonic crystals by using the ceramic slurry with the nanoparticles will be introduced. And, the resonance and localization properties of the terahertz waves into various types of the structural defects introduced according to theoretical electromagnetic simulations will be demonstrated.

2. Photonic Band Gap Formation

Photonic crystals composed of dielectric lattices form band gaps for electromagnetic waves. These artificial crystals can totally reflect light or microwave at a wavelength comparable to the lattice spacings by Bragg deflection as shown in Fig. 1. Two different standing waves oscillating in the air and dielectric matrix form higher and lower frequency bands in the first and second Brillouin zones, respectively. The band gap width can be controlled by varying structure, filling ratio, and dielectric constant of the lattice. Structural modifications by introducing defects or varying the lattice spacing can control the propagation of light or microwaves. The band diagram of the photonic crystal along symmetry lines in the Brillouin zone is drawn theoretically. The Maxwell's equations (1) and (2) can be solved by means of plane wave propagation (PWE) method²⁸, where ω and c denote frequency and light velocity, respectively. Electronic and magnetic field $E\omega(r)$ and $H\omega(r)$ are described with the following plane wave equations (3) and (4), respectively. The periodic arrangement of dielectric constant $\epsilon(r)$ can be obtained as equation (5) from the crystal structure. G and k are reciprocal vector and wave vector, respectively.

$$\left[\nabla \times \left(\frac{1}{\epsilon(r)} \nabla \times \right) \right] \mathbf{H}_{\omega}(r) = \left(\frac{\omega}{c} \right)^2 \mathbf{H}_{\omega}(r) \dots (1)$$

$$\left[\frac{1}{\epsilon(r)} \nabla \times \nabla \times \right] \mathbf{E}_{\omega}(r) = \left(\frac{\omega}{c} \right)^2 \mathbf{E}_{\omega}(r) \dots (2)$$

$$\mathbf{H}_{k,n}(r) = \sum_G \mathbf{H}_{k,n}(G) e^{i(k+G) \cdot r} \dots (3)$$

$$\mathbf{E}_{k,n}(r) = \sum_G \mathbf{E}_{k,n}(G) e^{i(k+G) \cdot r} \dots (4)$$

$$\frac{1}{\epsilon(r)} = \sum_G \frac{1}{\epsilon(G)} e^{iG \cdot r} \dots (5)$$

3. Applications of Photonic Crystals

Fig. 2 shows expected applications of photonic crystal for light and electromagnetic wave control in various wavelength ranges²⁹. Air guides formed in a photonic crystal with nanometer order will be used as the light wave circuit in the perfect reflective structure. When a light emitting diode is placed in an air cavity formed in a photonic crystal, an efficient laser emission can be enhanced due to the high coherent resonance in the micro cavity. While, millimeter order periodic structures can control microwaves effectively. Directional antennas and filters composed of photonic crystals can be applied to millimeter wave radar devices for intelligent traffic system (ITS) and wireless communication system. The perfect reflection of millimeter wave by photonic crystal will be useful for barriers to prevent wave interference. Terahertz waves with micrometer order wavelength are expected to apply for various types of sensors to detect other physical, chemical and living events. The micrometer order photonic crystals can be applied for the terahertz wave cavities, filters and antennas.

4. Geometry of Artificial Crystals

Typical photonic crystal structures were shown in

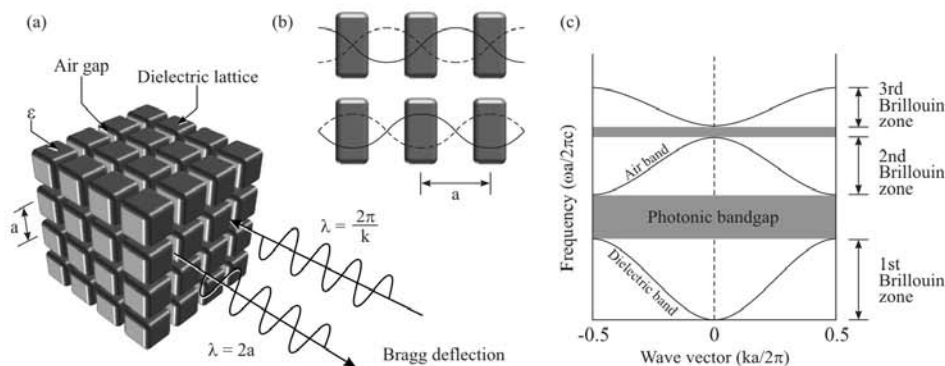


Fig. 1 Principles of photonic band gap formations in periodic arrangements of dielectric materials. Two different standing waves with higher and lower frequencies are formed in a photonic crystal, and a forbidden gap is formed between these frequencies.

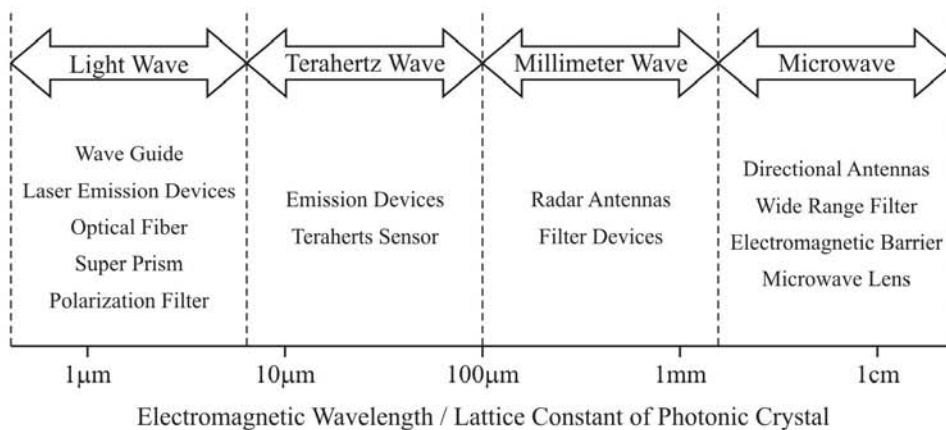


Fig. 2 Expected applications of the photonic crystal in various electromagnetic wavelengths.

Fig. 3. A woodpile structure (a) with simple structure of stacked rods can form the perfect photonic band gap. Photonic crystals composed of GaAs or InP were fabricated by using semiconductor process techniques³⁰. A light wave circuit (b) in the periodic structure of arranged AlGaAs pins is processed by using electron beam lithography and etching techniques³¹. A layered structure (c) composed of Si and SiO₂ with the different dielectric constants realize light wave polarization and super prism effects³². These layers are stacked by using self-organized growing in alternate sputtering and etching. An inverse opal structure (d) is composed of air spheres

with FCC structure in TiO₂, Si, Ge or CdS matrix³³. At first, polystyrene spheres are arranged by using self-organization in colloidal solutions. Then, the slurry of these dielectric media is infiltrated into the periodic structure and sintered. The optical fiber (e) with photonic crystal structure can guide light efficiently along the central core³⁴. Silica fibers and glass capillaries were bundled by wire drawing at high temperature. Diamond type photonic crystals (f) composed of TiO₂, SiO₂ or Al₂O₃ can fabricated by using stereolithography and successive sintering process. The wider perfect band gap is obtained in microwave and terahertz wave frequency ranges.

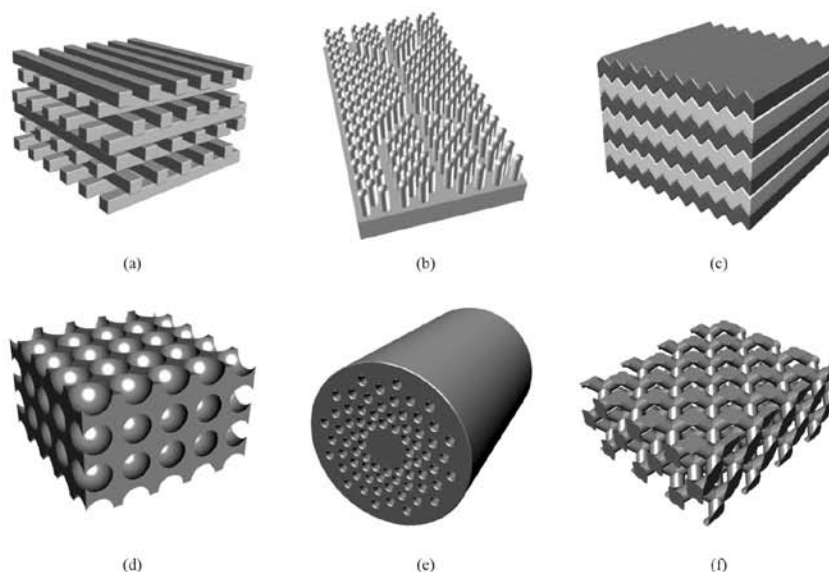


Fig. 3 Typical periodic structures of the photonic crystals with woodpile structure (a), patterned substrate (b), stacked layer (c), inverse opal structure (d), bundled fiber (e), and diamond structure (f).

5. Design of Diamond Structure

Electromagnetic band diagrams of diamond structures were calculated to determine their geometric parameters by the PWE method. The dielectric constant of the lattice used in the calculation was 10 for alumina. **Fig. 4** (a), (b), and (c) show a unit cell of the diamond structure, the definition of the aspect ratio, and the calculated complete band gap width as a function of the aspect ratio, respectively. According to **Fig. 4** (c), the band gap becomes the widest when the aspect ratio is 2.0. The wider the band gap, the easier it is to localize the electromagnetic waves when a defect is introduced. When the aspect ratio is 1.5, the lattice rods become thick and the band gap width is approximately 84% as much as that of 2.0. Thus, the aspect ratio of the diamond structure was designed to be 1.5. The lattice constant was $500 \mu\text{m}$. The whole structure was $4 \times 4 \times 2 \text{ mm}$ in size, consisting of $8 \times 8 \times 4$ unit cells.

6. Fabrication of Dielectric Lattices

The three dimensional diamond lattices were designed by using a computer graphic application (Toyota Caelum Co. Ltd., Thinkdesign ver. 7.0). The graphic data was converted into a stereolithography (STL) file of a rapid prototyping format. After the slicing process of the three dimensional model into a series of two dimensional cross sectional data into thin sections, this data file was transferred to micro stereolithography equipment (D-MEC Co. Ltd., Japan, SI-C1000). In our system, photo sensitive acrylic resin dispersed with alumina particles of 170 nm in diameter at 40 vol. % was fed over the substrate from a dispenser nozzle. The highly viscous ceramic/

resin paste was fed with controlled air pressure. It was spread uniformly by moving a knife edge. The thickness of each layer was controlled to $10 \mu\text{m}$. A two dimensional pattern was formed by illuminating visible laser of 405 nm in wavelength on the resin surface. The high resolution has been achieved by using a digital micro-mirror device (DMD) and an objective lens. **Fig. 5** shows a schematic illustration of the micro stereolithography system. The DMD is an optical element assembled by mirrors of $14 \mu\text{m}$ in edge length. The tilting of each tiny mirror can be controlled according to the two dimensional cross sectional data by using a computer. The three dimensional structure was built by stacking these micro patterns layer by layer. In order to avoid deformation and cracking during dewaxing, careful investigation for the dewaxing process is required. The precursors with diamond structures were heated at various temperatures from 100°C to 600°C while the heating rate was $1.0^\circ\text{C}/\text{min}$. The dewaxing process was observed in respect to the weight and color changes. Nanometer sized alumina particles could be sintered at 1500°C . The heating rate was $8.0^\circ\text{C}/\text{min}$. The density of the sintered sample was measured by the Archimedes method. The microstructure of the lattices was observed by using scanning electron microscopy (SEM).

7. Measurement of Electromagnetic Wave

In recent years, terahertz waves have received extensive attentions and investigations since they have a lot of interesting and applicable features in various fields such as materials, communication, medicine, and biology. It is possible to detect gun powders and ceramic blades hidden in bags, clothes,

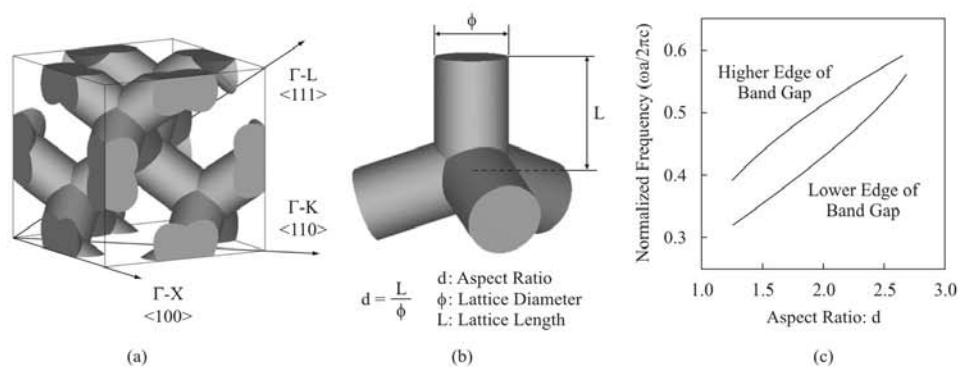


Fig. 4 A CAD image of a unit cell of diamond structure (a), definition of aspect ratio (b), and band gap width as a function of aspect ratio (c).

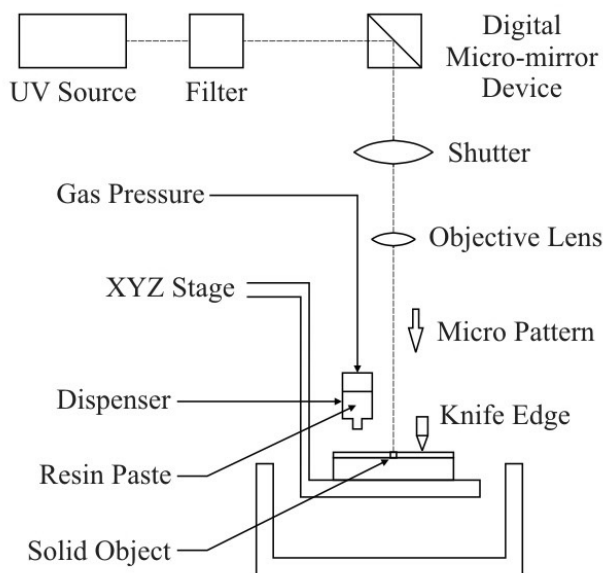


Fig. 5 A schematically illustrated free forming system of a micro stereolithography machine by using computer aided design and manufacturing (CAD/CAM) processes. (D-MEC Co. Ltd., Japan, SF-C 1000, <http://www.d-mec.co.jp>).

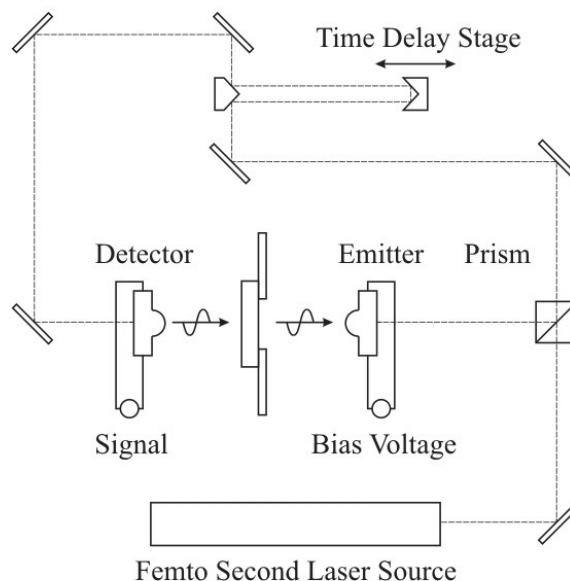


Fig. 6 The schematically illustrated measuring system of a terahertz wave analyzer by using a time domain spectroscopic (TDS) detect method (Advanced Infrared Spectroscopy, Co. Ltd. Japan, J-Spec 2001, <http://www.aispec.com>).

and envelopes by using terahertz waves since they can penetrate plastic, paper, and clothes without radiation damage to living bodies⁴. It is also possible to identify toxic drugs because they have spectral fingerprints or absorption spectra⁵. Moreover, they can distinguish cancerous areas from healthy areas due to the different absorption rates⁶. A terahertz wave attenuation of transmission amplitudes through the diamond photonic crystals were measured by using a terahertz time domain spectrometer (TDS) apparatus (Advanced Infrared Spectroscopy Co. Ltd., Japan, Pulse-IRS 1000). **Fig. 6** shows the schematic illustration of the measurement system. Femto second laser beams were irradiated into a micro emission antenna formed on a semiconductor substrate to generate the terahertz wave pulses. The terahertz waves were transmitted through the micro patterned samples perpendicularly. The dielectric constant of the bulk samples were measured through a phase shift counting. Diffraction and resonance behaviors in the dielectric pattern were calculated theoretically by using a transmission line modeling (TLM) simulator (Flomerics, UK, Microstripes Ver. 7.5) of a finite difference time domain (FDTD) method.

8. Alumina Photonic Crystals

An alumina dispersed resin precursor fabricated by the micro stereolithography is shown in **Fig. 7**. The lattice constant of the formed diamond structure was

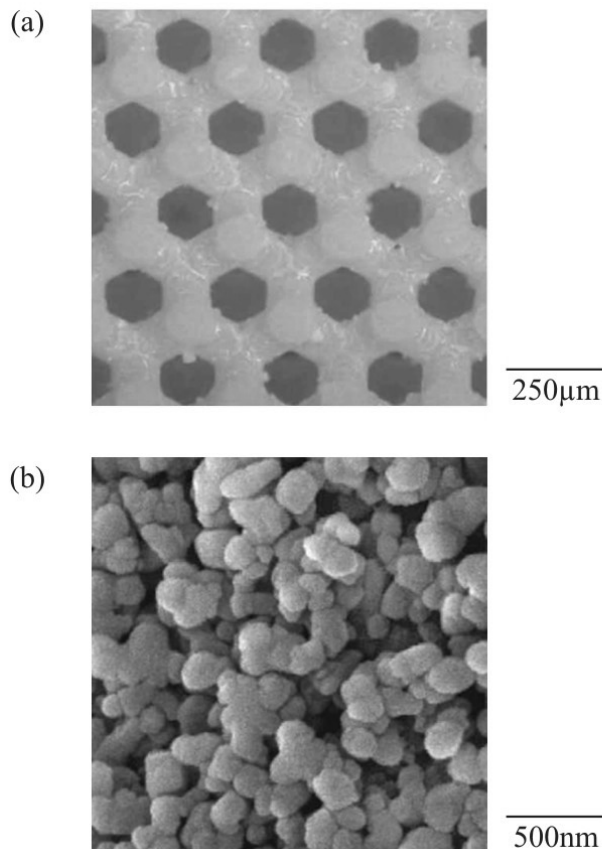


Fig. 7 The photonic crystal with the diamond structure composed of acrylic lattices with nano alumina particles dispersion formed by the micro stereolithography.

500 μm . The spatial resolution was approximately 0.5 %. The weight and color changes as a function of temperature are shown in **Fig. 8**. The sample color changed into black at 400°C due to carbonizing of resin. It became white at 600°C suggesting burning out of resin. Thus, the dewaxing process is considered to start at 200°C and complete at 600°C. The dewaxing temperature was optimized to be 600°C. Through the dewaxing and sintering processes, ceramic diamond structures were successfully obtained. **Fig. 9** shows (111), (100) and (110) planes of the sintered diamond structure composed of the micrometer order alumina lattice. The lattice constant was measured as 375 μm . The deformation and cracking were not observed. The linear shrinkage on the horizontal axis was 23.8 % and that on the vertical axis was 24.6 %. It is possible to obtain the uniform shrinkage by designing an appropriate elongated structure in the vertical direction for compensation to the gravity effect. The relative density reached 97.5 %. Dense alumina microstructure was formed, and the average grain size was approximately 2 μm . The measured dielectric constant of the lattice was about 10.

9. Terahertz Wave Spectroscopy

The terahertz wave attenuation of the transmission amplitude through the alumina diamond structure for Γ -L <111>, Γ -X <100> and Γ -K <110> crystal direction is shown in **Fig. 10**. The forbidden gap is formed at the frequency range of 0.32 - 0.49, 0.35 - 0.53

and 0.35 - 0.52 THz in transmission spectra for Γ -L <111>, Γ -X <100> and Γ -K <110> directions, respectively. A common band gap was observed in every direction at the frequency range from 0.35 to 0.49 THz, where the electromagnetic wave cannot transmit through the crystal and is totally reflected in all directions. The measured band gap frequencies were compared with calculation results by the plane wave expansion method as shown in **Fig. 11**. The band diagram of the photonic crystal along symmetry lines

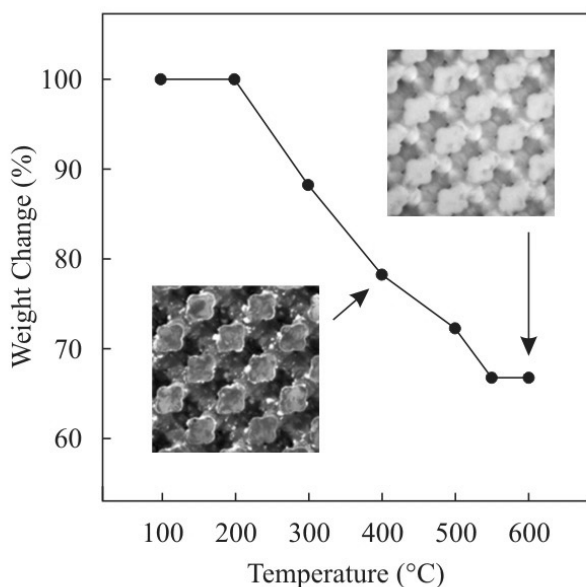


Fig. 8 The weight change as a function of temperature and the lattice color after dewaxing at 400 and 600°C in heating temperatures.

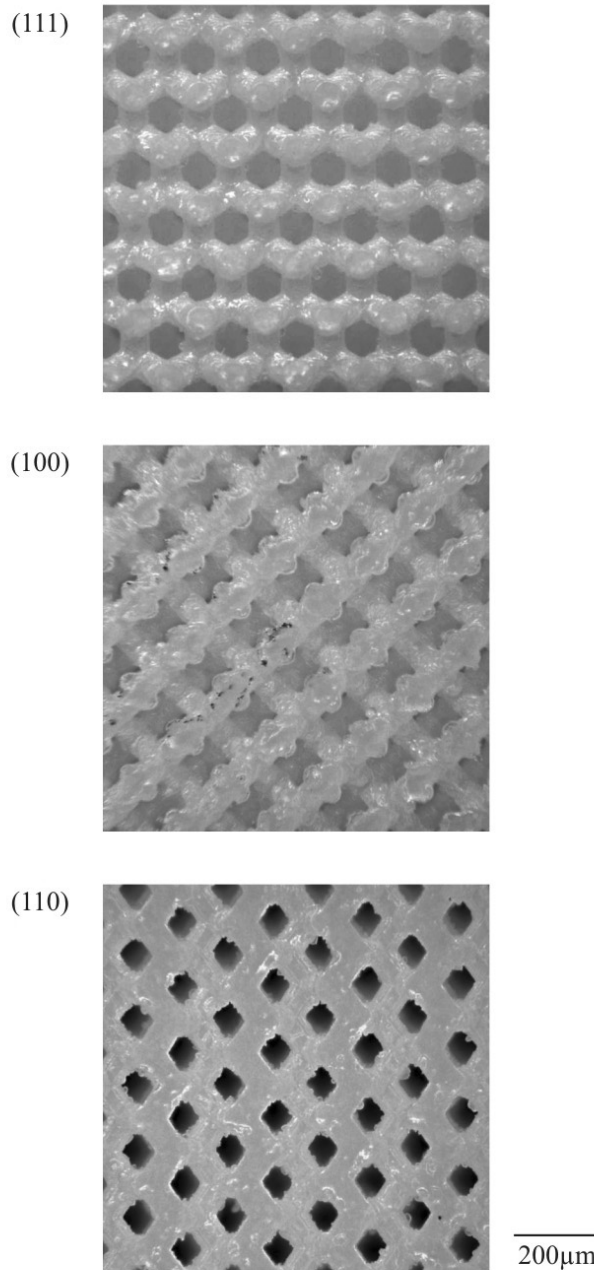


Fig. 9 Crystal planes of (111), (100) and (110) in alumina photonic crystals with the diamond structure fabricated by using the micro stereolithography. Sintering density of alumina lattices is 98.5 %. Dielectric constant of the lattice is 10.

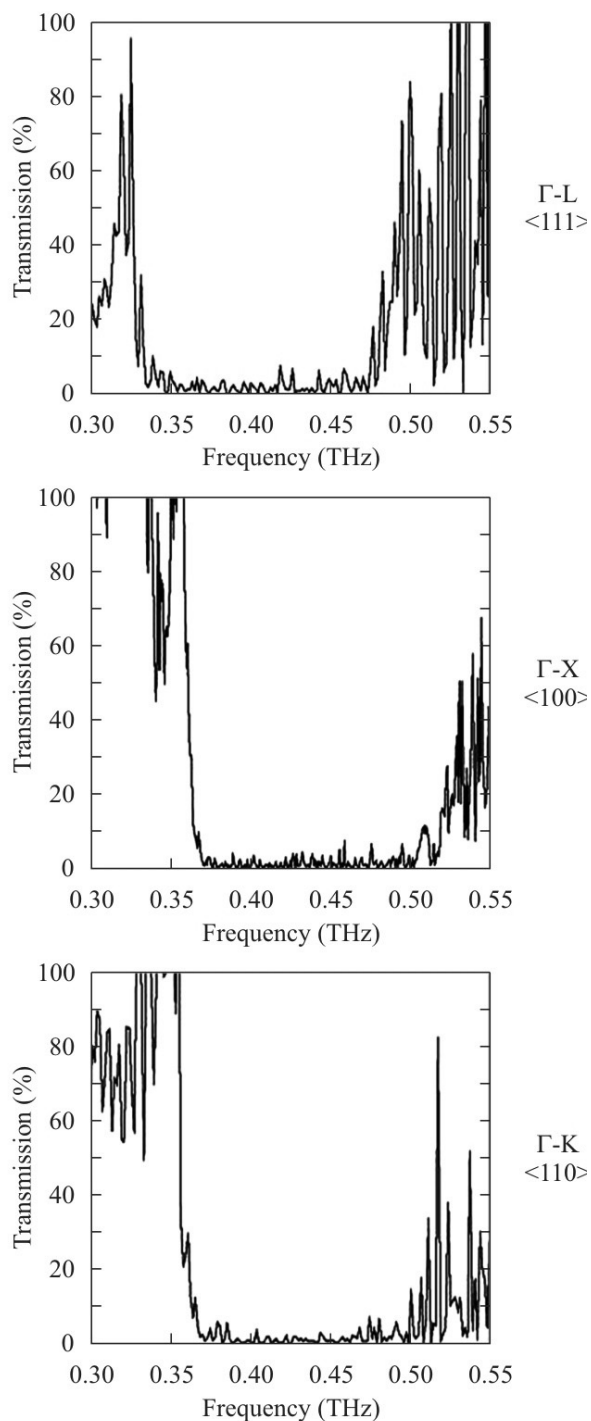


Fig. 10 Terahertz wave Attenuations of transmission amplitude for Γ -L $\langle 111 \rangle$, Γ -X $\langle 100 \rangle$ and Γ -K $\langle 110 \rangle$ directions in the alumina photonic crystal with the diamond structure by using terahertz time domain spectroscopy.

in the Brillouin zone is drawn theoretically by the PWE method. The opened circles mean the higher and lower edges of the measured band gaps. These frequency ranges of opaque regions corresponded to the calculation. According to the photonic band dia-

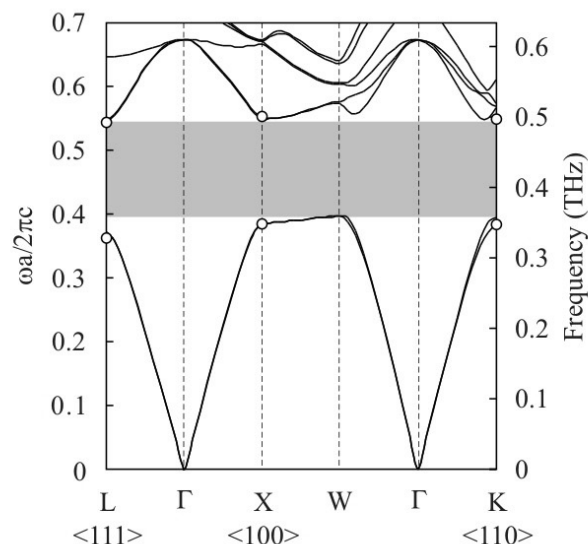


Fig. 11 A photonic band diagram calculated by plane wave expansion (PWE) method. Opened circles are measured edge frequencies of photonic band gaps. The dielectric constant of the lattice was 10. The frequency range with gray color indicates the perfect band gap in common for all directions.

gram, it was demonstrated that a complete photonic band gap opened between 0.35 and 0.49 THz. When a gap is formed, there are two types of the standing wave modes with the wavelength corresponding to periodicity of the dielectric lattices at the frequencies of the each band edges as shown in **Fig. 1**. The lower frequency mode concentrates the wave energy in the dielectric region, whereas the higher frequency mode concentrates in the air region.

10. Point Defect of Air Cavity

A diamond structure introduced by an air cubic defect with the same dimension as the unit cell is **Fig. 12**. The transmission spectrum along the Γ -X $\langle 100 \rangle$ direction is shown in **Fig. 13**. Two peaks were observed in the band gap at the frequencies 0.42 and 0.46 THz, respectively. Measured peak frequencies were compared with the simulation by the TLM method as seen in **Fig. 14**. They were in good agreement with the simulation. The first peak in **Fig. 13** was named mode A, while the second one mode B. The electric field distributions of these modes were simulated by the TLM method. **Fig. 15** (a) and (b) show cross sectional images of the distributions. In the images, the red area indicates that the electric field intensity is high, whereas blue and green area indicates it is low. Thus, it was considered that the mode A concentrated the oscillation energy of a half wavelength with an antinode in the cube. Also, the

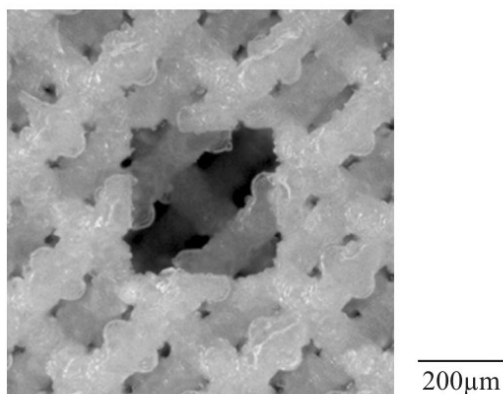


Fig. 12 A alumina lattice with the diamond structure introduced by an air cubic defect. The edge length of the air cavity is same size of the lattice constant.

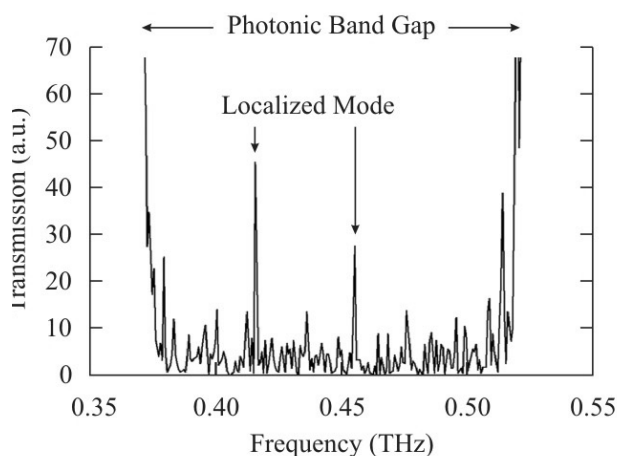


Fig. 13 A transmission spectrum of a defect introduced structure as a function of frequency. Two localized modes of transmission peaks are formed in the photonic band gap.

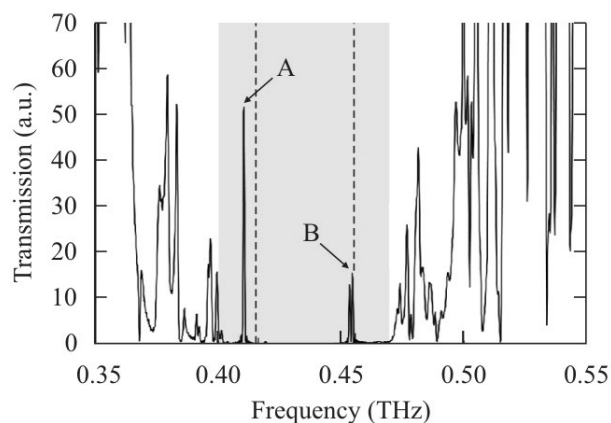


Fig. 14 The simulated spectrum of the defect introduced structure as a function of frequency. Dashed lines are frequencies of measured transmission peaks. The frequency range with gray color indicates the perfect band gap in common for all crystal directions.

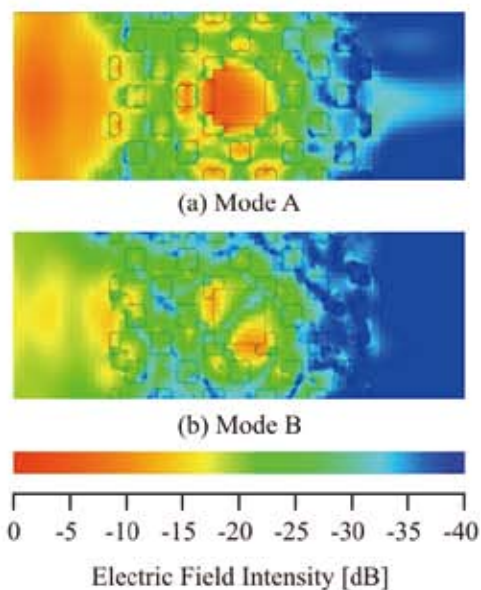


Fig. 15 Electric field distributions of localized mode A (a) and mode B (b) simulated by transmission line modeling (TLM) method of a finite difference time domain (FDTD).

mode B concentrated the energy of a half wavelength on the sides of the cube with a node in the cube. Therefore, it was confirmed that the defect introduced structure localized terahertz waves.

11. Plane Defect of Twinned Lattices

Twinned diamond structure composed of the mirror symmetric alumina lattices is shown in **Fig 16**. The plane defect forms parallel to the (100) crystal plane. The transmission spectrum for the Γ -X <100> crystal direction of the twinned diamond structure is shown in **Fig. 17**. The localized mode forms in the photonic band gap. At the transmission peak of 0.41 THz in frequency, the incident terahertz wave localized in the plane defect, and the amplified wave propagated to the other side of the crystal sample. The measured band gap region and the peak frequency of the localized mode were compared with the calculated spectrum by the TLM method as shown in **Fig. 18**. They were in good agreement. Subsequently, the electric field distribution in the twinned diamond lattices was simulated. **Fig. 19** shows cross sectional images of the distributions. Incident terahertz wave is resonate and localized in the plane defect region between the twinned diamond lattices. The amplified electromagnetic wave by multiple reflections can transmit through the photonic crystal. Therefore, the transmission peak will be formed in the band gap. The three dimensional photonic band gap structure

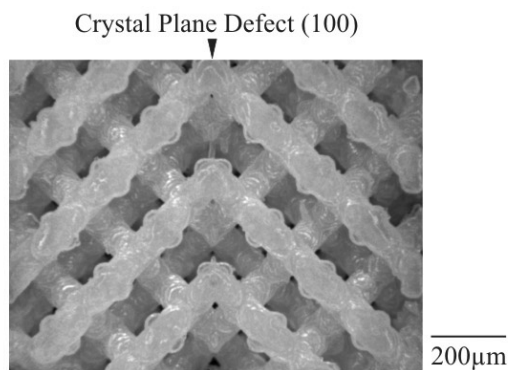


Fig. 16 A modified photonic crystal introduced by a plane defect parallel to (100) layers between twinned diamond lattices with a mirror symmetric arrangement for Γ -X <100> direction.

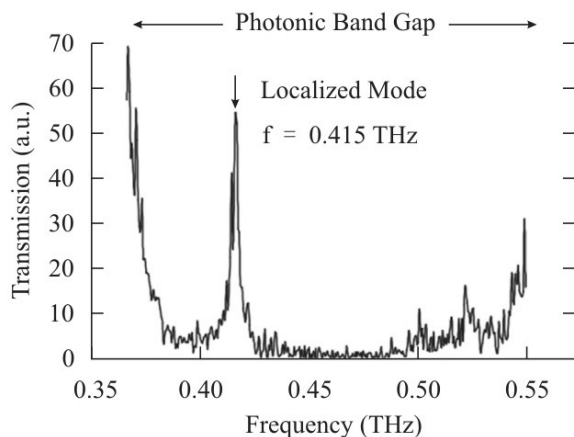


Fig. 17 The localized mode in the photonic band gap formed by the twinned diamond structure composed of the alumina lattices.

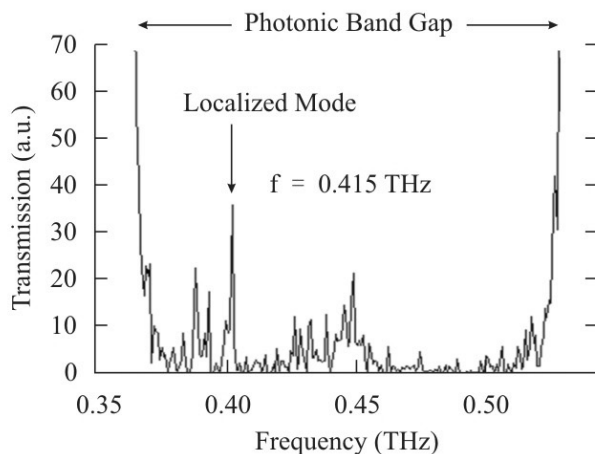


Fig. 18 The localized mode of the transmission peak in the photonic band gap formed by the twinned diamond structure. The perfect dielectric lattice forms the band gap to prevent the electromagnetic wave propagations, and the structural defect forms the localized mode to permit the transmission.

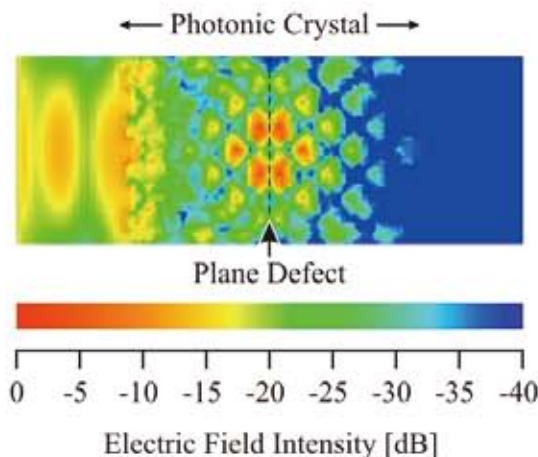


Fig. 19 The intensity distribution of electric field in the twinned diamond structure calculated by the TLM method. Incident terahertz wave are localized by multiple reflections in the plane defect between two dielectric lattice structures.

to form the localized mode can be applied to the terahertz wave filters.

12. Terahertz Wave Beam Emitter

A modified diamond photonic crystal with the plane defect between the twinned lattice structures is shown in **Fig. 20**. The lattice structures of one and two periods were arranged on the right and left side of the plane defect, respectively. The incident direction of the terahertz wave was from the left to the right. In the measured transmission spectrum, one localized mode peak was observed in the band gap at the frequencies of 0.41 THz. The measured

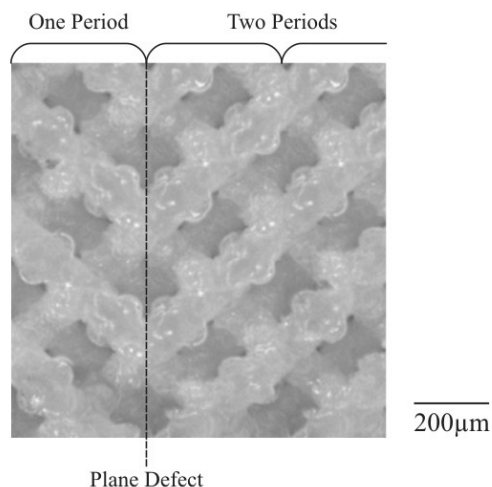


Fig. 20 An asymmetric twinned diamond structure. One and two periods of diamond lattices were formed on the left and right sides of the plane defect, respectively.

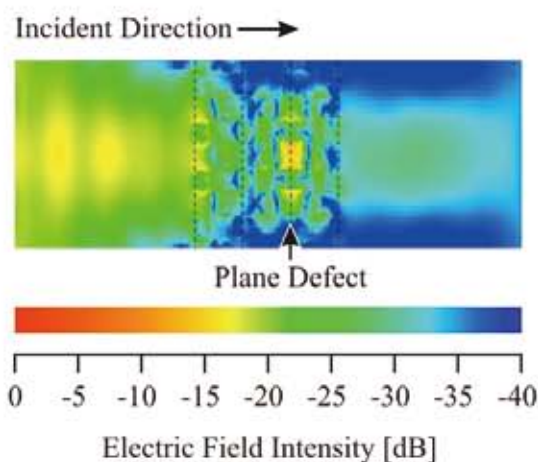


Fig. 21 The cross sectional image of the electric field intensity in the asymmetric twinned diamond structure calculated by the TLM method. The incident terahertz wave can transmit and propagate through the twinned lattice structure from the left to right side as an amplified plane wave.

band gap region and peak frequency of the localized mode were compared with calculations by the TLM method. They had good agreement. Subsequently, the electric field distribution in the twinned diamond lattices was simulated. **Fig. 21** shows cross sectional images of the distributions. Incident terahertz wave is resonate and localized in the plane defect region. The amplified electromagnetic wave by multiple reflections can transmit preferentially for the right direction through the diamond lattice with only one period of the diffraction lattices. On the right side of the sample, the radiation pattern shows the plane wave expansion. The micro photonic crystal with the twinned ceramic lattice of the diamond structure can be applied to a terahertz beam emitters.

13. Conclusion

Three dimensional micrometer order photonic crystals with a diamond structure composed of acrylic resin including alumina nanoparticles at 40 vol. % by using micro stereolithography a structural joining process. By the careful optimization of process parameters regarding dewaxing and sintering, dense alumina micro lattice structures were fabricated successfully. The sintered photonic crystal of alumina formed a complete band gap at the terahertz region from 0.35 to 0.49 THz. Localized modes were obtained by introducing a point defect of air cubic cavity and a plane defect between twinned diamond structures, which were in good agreements with the simulation by TLM method. It is expected that these three dimensional photonic band gap structures can

be applied to control terahertz waves.

Acknowledgments

This study was supported by Priority Assistance for the Formation of Worldwide Renowned Centers of Research - The Global COE Program (Project: Center of Excellence for Advanced Structural and Functional Materials Design) from the Ministry of Education, Culture, Sports, Science and Technology (MEXT), Japan.

References

- 1) Ohtaka, K. (1979): "Energy band of photons and low energy photon diffraction", *Physical Review B*, Vol. 19, No. 10, pp.5057-5067.
- 2) Yablonovitch, E. (1987): "Inhabited Spontaneous Emission in Solid-state Physics and Electronics", *Physical Review Letter*, Vol. 58, No. 20, pp.2059-2062.
- 3) John, S. (1987): "Strong Localization of Photons in Certain Disordered Dielectric Superlattices", *Physical Review Letter*, Vol. 58, No. 23, pp.2486-2489.
- 4) Temelkuran, B., Bayindir, M., Ozbay, E., Biswas, R., Sigalas, M., Tuttle, G. and Ho, K. (2000): "Photonic Crystal-based Resonant Antenna with Very High Directivity", *Journal of Applied Physics*, Vol. 87, No. 1, pp.603-605.
- 5) Soukoulis, C. (1996): "Photonic Band Gap Materials", Kluwer Academic Publisher, Netherlands.
- 6) Noda, S., Yamamoto, N., Kobayashi, H., Okano, M. and Tomoda, K. (1999): "Optical properties of three-dimensional photonic crystals based on III-V semiconductors at infrared to near-infrared wavelengths", *Applied Physics Letters*, Vol. 75, No. 16, pp.905-907.
- 7) Kirihara, S., Takeda, M., Sakoda, K. and Miyamoto, Y. (2002): "Control of Microwave Emission from Electromagnetic Crystals by Lattice Modifications", *Solid State Communications*, Vol. 124, No. 4, pp.135-139.
- 8) Kanehira, S., Kirihara, S. and Miyamoto, Y. (2005): "Fabrication of TiO₂-SiO₂ Photonic Crystals with Diamond Structure", *Journal of the American Ceramic Society*, Vol. 88, No. 6, pp.1461-1464.
- 9) Ho, K., Chan, C. and Soukoulis, C. (1990): "Existence of a Photonic Gap in Periodic Dielectric Structures", *Physical Review Letter*, Vol. 65, No. 25, pp.3152-3165.
- 10) Kirihara, S., Miyamoto, Y., Takenaga, K., Takeda, M. and Kajiyama, K. (2002): "Fabrication of Electromagnetic Crystals with a Complete Diamond Structure by Stereolithography", *Solid State Communications*, Vol. 121, No. 8, pp.435-439.
- 11) Chen, W., Kirihara, S. and Miyamoto, Y. (2007): "Fabrication and Measurement of Micro Three-Dimensional Photonic Crystals of SiO₂ Ceramic for Terahertz Wave Applications", *Journal of the American Ceramic Society*, Vol. 90, No. 7, pp.2078-2081.

- 12) Chen, W., Kiri-hara, S. and Miyamoto, Y. (2007): Three-dimensional Microphotonic Crystals of ZrO_2 Toughened Al_2O_3 for Terahertz wave applications, *Applied Physics Letter*, Vol. 91, No. 15, 153507-1-3.
- 13) Chen, W., Kiri-hara, S. and Miyamoto, Y. (2007): Fabrication of Three-Dimensional Micro Photonic Crystals of Resin-Incorporating TiO_2 Particles and their Terahertz Wave Properties, *Journal of the American Ceramic Society*, Vol. 90, No. 1, pp.92-96.
- 14) Chen, W., Kiri-hara, S. and Miyamoto, Y. (2008): Static Tuning Band Gaps of Three-dimensional Photonic Crystals in Subterahertz Frequencies, *Applied Physics Letters*, Vol. 92, pp.183504-1-3.
- 15) Kanaoka, H., Kiri-hara, S. and Miyamoto, Y. (2008): Terahertz Wave Properties of Alumina Microphotonic Crystals with a Diamond Structure, *Journal of Materials Research* Vol. 23, No. 4, pp.1036-1041.
- 16) Miyamoto, Y., Kanaoka, H. and Kiri-hara, S. (2008): Terahertz Wave Localization at a Three-dimensional Ceramic Fractal Cavity in Photonic Crystals, *Journal of Applied Physics*, Vol. 103, pp.103106-1-5.
- 17) Takano, H., Song, B., Asano, T. and Noda, S. (2005): Highly Efficient in-Plane Channel Drop Filter in a Two-Dimensional Heterophotonic Crystal, *Applied Physics Letters*, Vol. 86, No. 24, pp.241101-1-3.
- 18) Kiri-hara, S. and Miyamoto, Y. (2009): Terahertz Wave Control Using Ceramic Photonic Crystals with Diamond Structure Including Plane Defects Fabricated by Micro-stereolithography, *The International Journal of Applied Ceramic Technology*, Vol. 6, No. 1, pp.41-44.
- 19) Kiri-hara, S., Niki, T. and Kaneko, M., "Terahertz Wave Behaviors in Ceramic and Metal Structures Fabricated by Spatial Joining of Micro-stereolithography, *Journal of Physics*, in printing.
- 20) Kiri-hara, S., Niki, T. and Kaneko, M., "Three-dimensional Material Tectonics for Electromagnetic Wave Control by Using Micro-stereolithography", *Ferroelectrics*, in printing.
- 21) Kiri-hara, S., Tsutsumi, K. and Miyamoto, Y., "Localization Behavior of Microwaves in Three-dimensional Menger Sponge Fractals Fabricated from Metallodielectric Cu/polyester Media", *Science of Advanced Materials*, in printing.
- 22) Van Exter, M., Fattinger, C. and Grischkowsky, D. (1989): Terahertz Time-domain Spectroscopy of Water Vapor, *Optics Letters* Vol. 14, Iss. 20, pp.1128-1130.
- 23) Clery, D. (2002): Brainstorming Their Way to an Imaging Revolution", *Science*, Vol. 297, pp.761- 763.
- 24) Kawase K., Ogawa, Y., Watanabe, Y. and Inoue, H. (2003): Non-destructive Terahertz Imaging of Illicit Drugs Using Spectral Fingerprints, *Optics Express*, Vol. 11, Iss. 20, pp.2549-2554.
- 25) Woodward, R., Wallace, V., Arnone, D., Linfield, E. and Pepper, M. (2003): Terahertz Pulsed Imaging of Skin Cancer in the Time and Frequency Domain, *Journal of Biological Physics*, Vol. 29, No. 2-3, pp.257-259.
- 26) Wallace, V., Fitzgerald, A., Shankar, S. and Flanagan, N. (2004): Terahertz Pulsed Imaging of Basal Cell Carcinoma ex Vivo and in Vivo, *The British Journal of Dermatology*, Vol. 151, No. 2, pp.424-432.
- 27) Oyama, Y., Zhen, L., Tanabe, T. and Kagaya, M. (2008): Sub-Terahertz Imaging of Defects in Building Blocks, *NDT&E International*, Vol. 42, No. 1, pp.28-33.
- 28) Haus, J. (1994): A brief review of theoretical results for photonic band structures, *Journal of Modern Optics*, Vol. 41, No. 2, pp.195-207.
- 29) Kawakami, S. (2002): "Photonic Crystals", CMC, Tokyo,.
- 30) Noda, S. (2000): Three-dimensional photonic crystals operating at optical wavelength region, *Physica B*, Vol. 279, No. 1-3, pp.142-149.
- 31) Baba, T. and Fukuya, N. (2001): Light propagation characteristics of defects waveguides in a photonic crystal slab, *Photonic Crystals and Light Localization* (edited M. Soukoulis), Kluwer Academic Publishers, Netherlands,.
- 32) Kosaka, H., Kawashima, T., Tomita, A., Notomi, M., Tamamura, T., Sato, T. and Kawakami, S. (1999): Photonic crystals for micro wave circuits using wavelength-dependent angular beam steering, *Applied Physics Letter*, Vol. 74, No. 8, pp.1370-1378.
- 33) Cregan, R., Mangan, B., Night, J., Birks, T., P. Russell, S., Roberts, P. and Allan, D. (1999): Singlemode photonic bandgap guidance of light in air, *Science*, Vol. 285, No. 5433, pp.1537-1539, September,.
- 34) Vos, W., Sprik, R., Blaaderen, A., Imhof, A., Lagendijk, A. and Wegdam, G. (1996): Strong effects of photonic band structures on the diffusion of colloidal crystals, *Physical Review B*, Vol. 53, No. 24, pp.16231-16235.

Author's short biography



Soshu Kiriwara

Soshu Kiriwara is an Associate Professor in Osaka University, Japan. He belongs to Smart Processing Research Center in Joining and Welding Research Institute. His current research includes micro tectonics by using spatially structural joining of ceramics and metals nanomaterials.

Surface Modification for Improving the Stability of Nanoparticles in Liquid Media[†]

Motoyuki Iijima and Hidehiro Kamiya*
 Institute of Symbiotic Science and Technology,
 Tokyo University of Agriculture and Technology¹

Abstract

Nanoparticles are now an indispensable material for science and technology such as in materials, medicals, and cosmetics areas. Controlling the dispersion stability of nanoparticles in various liquid media is an essential issue to control the properties of the final products. At the beginning of this review, we will introduce several reasons why it is difficult to control the stability of nanoparticles in liquid media. Then, we will briefly review the surface modification techniques to overcome the difficulties of handling nanoparticles in liquids. Two types of surface modification concepts, post-synthesis surface modification and in-situ surface modification, which is a surface modification on manufactured particles and surface modification during the particle synthesis, respectively, will be introduced.

Keywords: polymeric dispersants, silane coupling agents, nanoparticle synthesis, ligand exchange, colloid stability

1. Introduction

Today, nanoparticles have already become an indispensable material for industries because of their unique size dependent properties such as electrical, magnetic, mechanical, optical and chemical properties, which largely differ from those of their bulk materials¹⁻⁵. Since nanoparticles have different surface structures and surface interactions compared to the sub-micron sized particles, nanoparticles have an extremely high tendency of adhesion and aggregation. Thus, it is quite important to develop techniques to control the dispersion/aggregation phenomena of nanoparticles to apply them into functional materials and products. In terms of aqueous media dispersions, DLVO theory is a quite useful tool to control and characterize the dispersion phenomena. However, it is still a challenging issue to control the stability of suspension with highly loaded nanoparticles or suspensions in organic media. Surface modification of nanoparticles is one of the mostly accepted methods to improve the dispersion stability of nanoparticles in those challenging conditions. On modifying nanoparticle surface, it is quite important to design the surface structure based on the type of nanoparticles and

the liquid media. In this review, we will first introduce some reasons why nanoparticles form aggregates so easily. Then, various surface modification techniques will be reviewed for the dispersion of various nanoparticles into various liquid media.

2. Difficulties of Handling Nanoparticles

Brownian motion is one of the inneglectable phenomena for handling nano-sized particles. The three dimensional mean transfer distance (Δx) by the Brownian motion can be stated as eq.1, where D_B and Δt is Brownian diffusion coefficient and time, respectively. The Brownian diffusion coefficient in Eq.1 can be stated as eq.2 where k is Boltzmann constant, T is the absolute temperature, μ is the viscosity of media and d_p is particle size. From eq.1 and eq.2, it is clear that the Brownian motion increases as the particle decreases. Thus, nanoparticles have very high chances to make an approach and collision with other nanoparticles whatever the media is. Since van der Waals attractive force also works among nanoparticles, the generation of potential barrier among nanoparticles is necessary to prevent strong aggregations.

$$\Delta x = \sqrt{6D_B\Delta t} \quad (1)$$

$$D_3 = \frac{kT}{3\pi\mu d_p} \quad (2)$$

[†] Accepted: August 29th, 2009

¹ Koganei, Tokyo 184-8588, Japan

* Corresponding author

TEL & FAX: 81-42-388-7068

E-mail: kamiya@cc.tuat.ac.jp

The DLVO theory⁶⁾, which involves van der Waals attractive force and electro static interactions from electrical double layer, is one of the tools to control potential barrier between particles in aqueous media. In the case of sub-micron sized particles, it is quite easy to control their dispersion stability by the electrical double layer which can be tuned by the surface potential of particles and the counter ion concentration. However, in the case of nano-sized particles, it is difficult to improve their dispersion stability only by the DLVO interactions because of the small potential barrier. For an example, **Fig. 1** shows the effect of particle size and the surface potential on the potential curves calculated by the DLVO theory. The x-axis and the y-axis is the total potential (V_T) normalized by kT and the surface distance, respectively. The counter ion concentration was fixed to be 1.0 mM. When the particle size and the surface potential was 100 nm and 88.5 mV, respectively, a large potential value, which $V_T/kT > 30$, was calculated. This V_T/kT value is large enough to prevent the nanoparticles from aggregation. Contrary, when the particle size was reduced down to 30 nm with same surface potential value, the normalized surface potential reduces to $V_T/kT < 10$. In this condition, since the potential barrier generated by the electric double layer is small, it is expected that the particles will strongly aggregate. In order to obtain the large potential barrier as $V_T/kT > 30$ for 30 nm nanoparticles, it is necessary to increase the surface potential up to 177 mV, which is difficult to obtain even by adsorbing polyelectrolytes.

From the potential curve calculated by the DLVO theory as shown in **Fig. 1**, we can estimate the required surface potential to let the particle be in the dispersed state. In the case of high concentration suspensions, it is also important to take in account

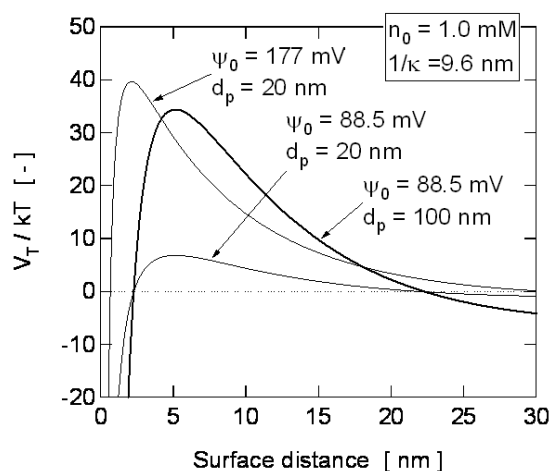


Fig. 1 Example of the potential curves calculated by DLVO theory.

the surface distances among the particles. In **Fig. 1**, we can observe that the maximum potential was obtained when the surface distance is several nanometers. When the particle concentration is high and the particles stay near than this distance, the particles will be trapped in the van der Waals force and form aggregates. **Fig. 2** shows the relationships between the volume fraction of particles and mean surface distance calculated by eq.3 which was reported by Woodcock⁷⁾. In the case of sub-micron sized particles, the mean particle surface distance will approach near to several nanometers when the volume fraction is over 60 vol%. Contrary, in the case of nanoparticles, the mean particle surface distance will reduce to several nanometers when the volume fraction is only 20 vol%. The mean particle surface distance will be smaller at low solid concentration in the case of nanoparticles. An additional surface repulsive force such as steric repulsive force will be necessary at this condition where the mean particle surface distance approaches near than several nanometers.

$$h = dp \cdot \left(\sqrt{\frac{1}{3\pi \cdot F} + \frac{5}{6}} - 1 \right) \quad (3)$$

Nanoparticles also possess unique surface structure compared to the sub-micron sized particles^{8,9)}. For an example, we have synthesized SiO₂ particles with various diameters by sol-gel method and characterized their surface structure by FT-IR. It was found that the peak of free silanol groups increases as the particle size reduces. It is expected that the large curvature of nanoparticles increased the average distance of silanol groups and reduced the possibility of hydrogenation. This difference of surface structure affected largely the surface force interactions

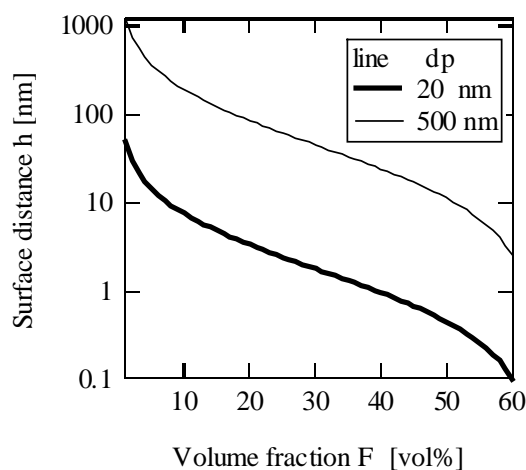


Fig. 2 Relation between solid volume fraction and mean particle surface distance.

and dispersion stabilities. **Fig. 3** shows the surface force interaction curves of SiO₂ particles with various diameters measured by AFM colloid probe method. The theoretical force curve calculated by DLVO theory is also shown in this figure. In all particle diameters shown in **Fig. 3**, it can be observed that the measured force curves fits with the theoretical force curves until the surface distance approaches near to several nanometers. However, in case of particles larger than 60 nm, the van der Waals attractive was not detected when the particles were approached near than several nanometers. This was due to the repulsive force from the hydrogenated silanol groups. This repulsive force from hydrogenated silanol groups was effective to improve the stability of particles in aqueous media. Contrary, in the case of 8 nm SiO₂ nanoparticles, the repulsive force from hydrogenated silanol groups were not detected so that there is only less chance to improve the dispersion stability in liquid media.

3. Surface Modification of Nanoparticles for the Improvement of their Dispersion Stability in Various Liquid Media.

In section 2, we have described the difficulties of stabilizing nanoparticles in liquid media. In order to improve the dispersion stability of nanoparticles in liquid media, it is necessary to modify the particle surface by polymeric surfactants or other modifiers to generate an effective repulsive force between

nanoparticles.

3.1 Post-synthesis surface modifications

3.1.1 Polymer dispersants

The adsorption of polymeric dispersant is one of the simplest surface modification techniques to improve the dispersion stability of nanoparticles in liquid media. In terms of dispersing hydrophilic nanoparticles into aqueous media or in organic solvents with high polarities, anionic polymer dispersants or cationic polymer dispersants are widely used to generate steric repulsive force from the polymer chains and to increase the surface charge. For an example for anionic surfactants, various types of polycarboxylic acids and their salts such as polyacrylic acid (PAA)¹⁰⁻¹³, polyacrylic acid sodium salts (PAA-Na)¹⁴⁻¹⁶, and co-polymers of polyacrylic acid and maleic acid¹⁷ are used to disperse many kinds of oxide nanoparticles as like BaTiO₃¹⁰, TiO₂^{14, 17}, Al₂O₃^{11, 16}, MgO¹², and Fe₂O₃¹⁵. For an example of cationic surfactant, polyethyleneimine (PEI) is widely accepted¹⁸⁻¹⁹. The relationships among pH of suspension, solid fraction of the suspension, dissociation ratio of polymer dispersant, molecular weight of polymer surfactant, surface charge of nanoparticles and the size of the particle are quite essential to the adsorption ratio of surfactants and the degree of steric repulsive force. Kakui et al.¹⁷⁻¹⁸ have reported the effect of particle size and the molecular weight of branched PEI on the viscosity of Al₂O₃/ethanol suspension at fixed solid concentration. It was found that in the case of

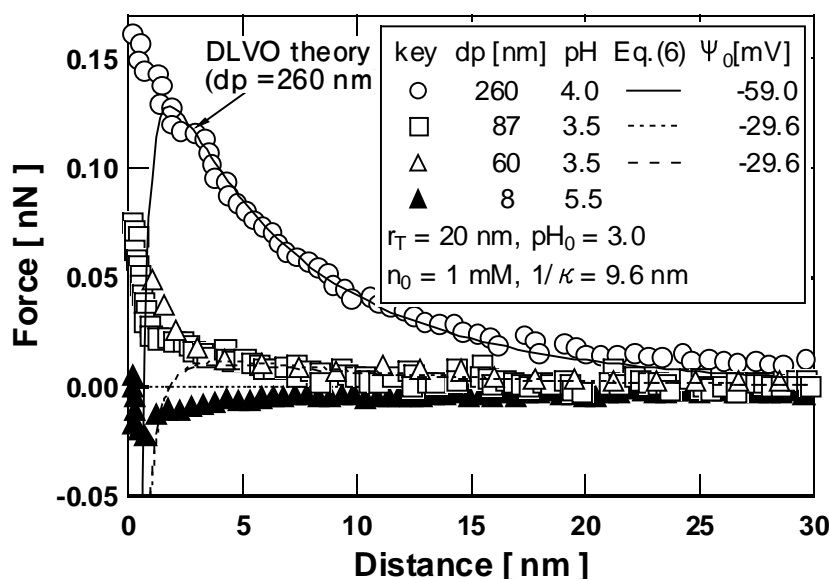


Fig. 3 Force curves between sol-gel derived SiO₂ particles with different particle diameter measured by colloid probe AFM.

sub-micron sized particles, the smallest viscosity was obtained when the molecular weight of PEI was 10,000. Contrary, in the case of 7 nm Al_2O_3 nanoparticles, the suspension viscosity reduced drastically when the molecular weight was 1800. As shown in **Fig. 2**, the mean surface distance will drastically reduced at same solid fraction when the particle size is reduced to several ten nanometers from sub microns. It is expected that large sized polymer surfactant were not able to travel among the particles when the particle size was nanosized. Thus, when the high molecular weight surfactant was used for nanoparticles, the surfactant was not able to be adsorbed on the surface and could not possess an effective repulsive force to improve the dispersion stability of the suspension. Similar effects are also reported on the TiO_2 aqueous suspension. The effect of solid fraction of TiO_2 nanoparticles and the molecular weight of PAA-Na on the suspension viscosity were reported.¹⁴ **Fig. 4** shows the apparent viscosity of TiO_2 suspension of various solid fractions treated with PAA-Na with various molecular weights. It can be observed that the optimum molecular weight to obtain the minimum

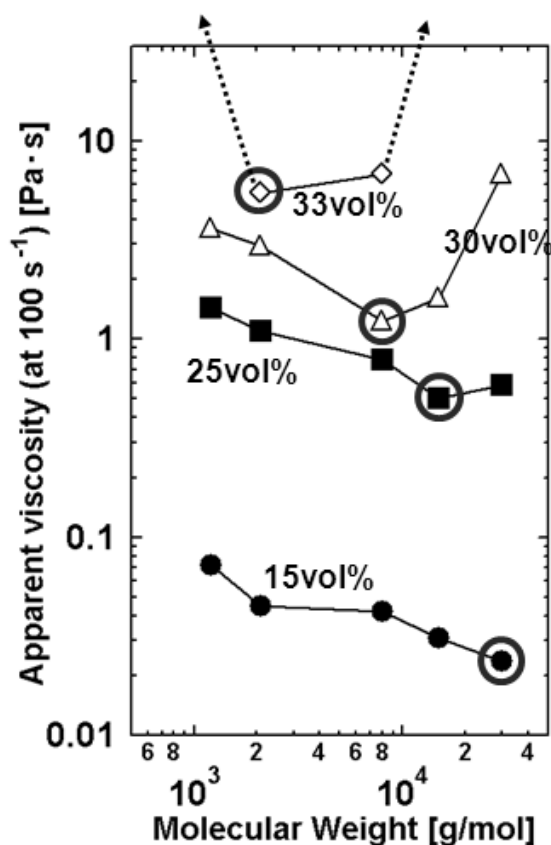


Fig.4 Effect of molecular weight on the TiO_2 /water suspension viscosity at various solid fractions.

apparent viscosity of suspension reduces as the solid fraction increases. It was found that the suspension viscosity drastically reduces when the size of polymeric dispersants adsorbed on TiO_2 were near to the mean surface distance calculated by Eq.3. Even if we are using the same TiO_2 nanoparticles, the smaller molecular weighted surfactant reduces the suspension stability at high solid content where the larger molecular weighted surfactant reduces the suspension stability at low solid content.

Not only the molecular weight but also the structure of the polymer surfactant can affect on the dispersion stability of nanoparticles. One example is the use of polymer dispersant with hydrophilic group and hydrophobic group²⁰. **Fig. 5(a)** shows the force curve between TiO_2 nanoparticles in water treated by PAA-NH_4^+ or a copolymer of PAA-NH_4^+ and polyacrylic acid methyl, measured by AFM colloid probe method. It was measured that TiO_2 modified by PAA-NH_4^+ had larger steric repulsive force and reduced the apparent suspension viscosities (**Fig. 5(b)**). It is expected that the loop-train structure can be controlled by tuning the ratio of hydrophilic site and the hydrophobic site. Another example is the use of comb type polymers such as PAA backbones with PEO chain^{10, 16, 21}. These comb polymers are also applied to improve the stability of various oxides, such as BaTiO_3 and Al_2O_3 , and the particles adsorbed with these polymers are reported to be well stabilized under wide range of pH and ion concentrations.

On dispersing hydrophobic nanoparticles, such as SiC, CNT, and coals, in aqueous media, the copolymers with hydrophilic group and hydrophobic group is often used for anionic surfactants.²²⁻²⁴ The hydrophobic segments are for the adsorption of dispersant on hydrophobic particles and the hydrophilic segments are for the improvement of compatibility with aqueous media. The hydrophilic segment also plays an important role for the generation of effective repulsive force by the electrical double layer interactions. For the hydrophobic segments, an aromatic compound such as styrene is used to make an effect adsorption on hydrophobic particles by hydrophobic interactions and pi-pi interactions. In the case of the use of cationic polymers, PEI is also applicable to hydrophobic particles and various reports can be found which improves the stability of SiC and CNT in aqueous media by PEI.²⁵

3.1.2 Chemical surface modifications

Surface modifying the particle surface chemically is an also useful technique to improve the stability of

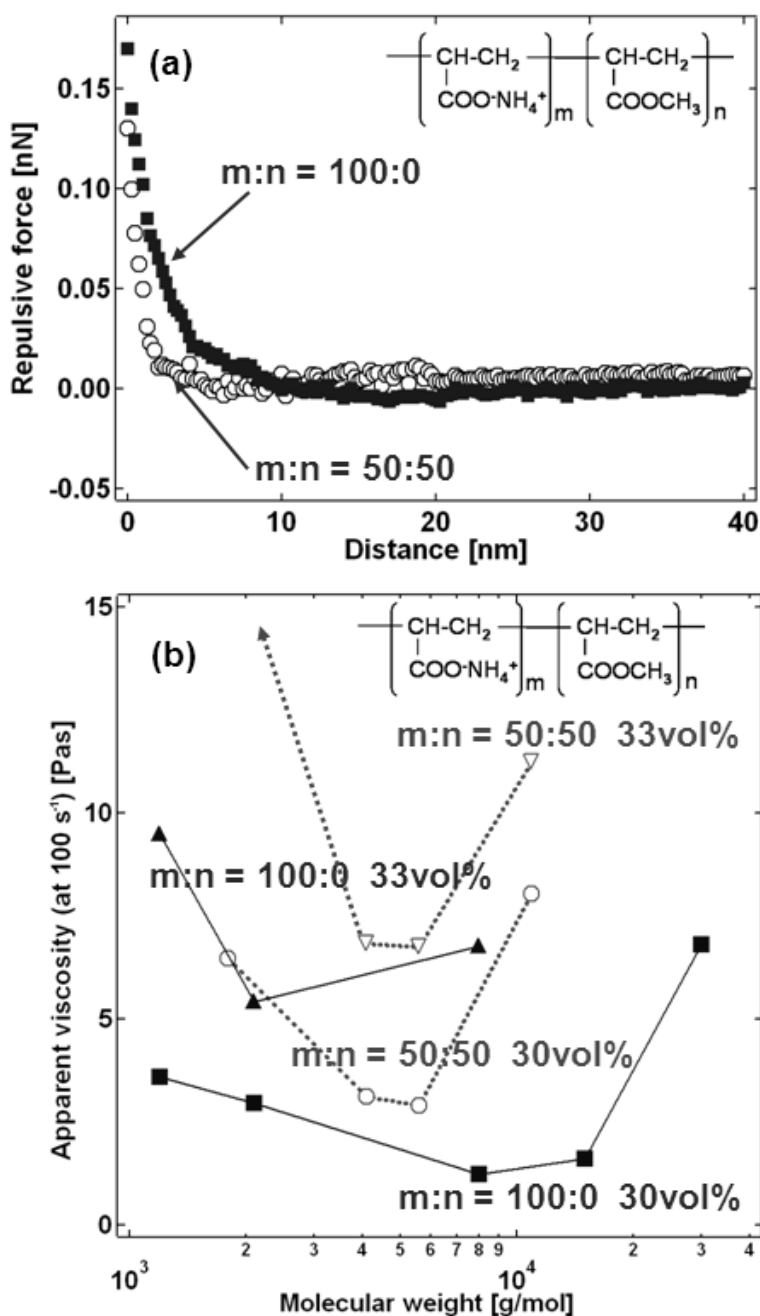


Fig. 5 (a) Force curves measured between TiO₂ nanoparticles treated by anionic polymer dispersants and the (b) apparent viscosity of corresponding TiO₂/water suspensions.

nanoparticles in various liquid media. On modifying the oxide nanoparticle surface, silane coupling agent, which has 1~3 alkoxy groups and 3~1 organic functional groups, are used from the 1960s. Metal-OH group on the particle surface is used as a reaction site. The first purpose of the silane coupling agents was to improve the compatibility of hydrophilic particle surface with hydrophobic polymer surface by introducing various organic functional groups on particle surface. Ever since Plueddemann have reported

the concept of silane coupling agents²⁶, numerous researchers have modified the particle surface to improve the compatibility of particle/polymer surface and to improve the properties of composite materials²⁷⁻²⁸. The surface modification of nanoparticles by silane coupling agents is also useful to improve the dispersion stability in organic media. The first example is grafting various polymers on particle surface by using silane coupling agents. Typically, various reactive groups such as amines, epoxides and vinyls

are firstly introduced on the particle surface by silane coupling agents, and then polymers are grafted from or grafted to the particle surface. For examples, the particle surface was modified by aminopropylsilane, and then PEG chains were further grafted to the particle by using epoxy terminated PEG²⁹. Various radical polymers such as polyvinylpyrrolidone (PVP) can be grafted on vinyl functionalized particle surface.³⁰ Radical polymer brushes such as PMMA can also be grafted from the amino functionalized surface by reversible addition – fragmentation chain transfer polymerization (RAFT)³¹⁻³².

Another example is designing steric silane networks on particle surface by controlling the reaction of silane alkoxides. Chaimberg et al., have reported that the amount of silane coupling agent chemisorbed on oxide supports differs drastically by changing the surface modification procedures.³³ The type of solvents, pH, and amount adsorbed water on particles largely affected to the chemisorbed content of silane coupling agents. Having an impression from this report, we have modified the surface of fumed silica nanoparticles in MEK with slight amount addition of pH controlled water.³⁴ It was found that when 3-glycidoxypropyltrimethoxysilane were modified with slight amount addition of acidic water, a relatively large steric repulsive force was measured by colloid probe AFM method while that modified with slight amount addition of base water possessed small steric repulsive force. It was also reported that the MEK suspension of particles with large measured steric force had lower viscosity and the silane network on the particle surface played an important role for improving the suspension stability.

On chemically modifying hydrophobic particles such as carbides and carbon related materials, it is necessary to design the surface by a chemistry that entails the reaction with the surface functional group on the particle surface. In case of carbon related particles, the unsaturated hydrocarbon which mostly related to the defect of graphite rings are one of the useful functional groups. For example, we have modified the surface of SiC nanoparticles by using various azo radical initiators such as 2,2'-azobisisobutyronitrile (AIBN) and 2,2'-azobis (2-methylpropionamide) dihydrochloride (AMPA).³⁵ It is reported that the intensity ratio of D band and G band (D/G) measured by raman spectroscopy reduced by modifying the SiC nanoparticle, which is an evidence of reaction between unsaturated hydrocarbon on SiC surface and radical initiators. By choosing the structure of azo radical initiators, the surface properties of SiC

nanoparticles can also be tuned. When AIBN was introduced on the SiC surface, the particles possessed anionic characteristics that they were stable in basic aqueous solution while that possessed cationic characteristics and were stable in acidic aqueous solution then they were modified by AMPA (**Fig. 6**). By applying this possibility of radical reactions at the surface of carbon related particles, various polymers can be also grafted on the particle surface. For example, ATRP radical initiators were first generated on the surface of CNT and then PMMA was grafted from the surface.³⁶ There are also examples of surface modification techniques which directly react with the graphite ring on the particle surface. It is reported that biradical groups such as nitrene compounds can be reacted with double bonds on carbon related materials.³⁷ The particle surface can be tuned by applying various nitrenes with reactive functional groups such as amine, carboxyl, and bromide groups.³⁸ The use of 1,3-dipolar cycloaddition of azomethine ylides, which can be generated by condensation of an R-amino acid and an aldehyde, are also applicable to fictionalization of carbon related materials.³⁹

In the case of post-synthesis surface modifications, it is possible to improve the dispersion stability of nanoparticles in various solvents. However, there are large difficulties in redispersing them into solvents near to their primary particle size. This is because nanoparticles strongly aggregate when they were collected as dried powder. In order to redisperse this aggregated dry powder into solvents near to their primary particle size, the mechanical milling method

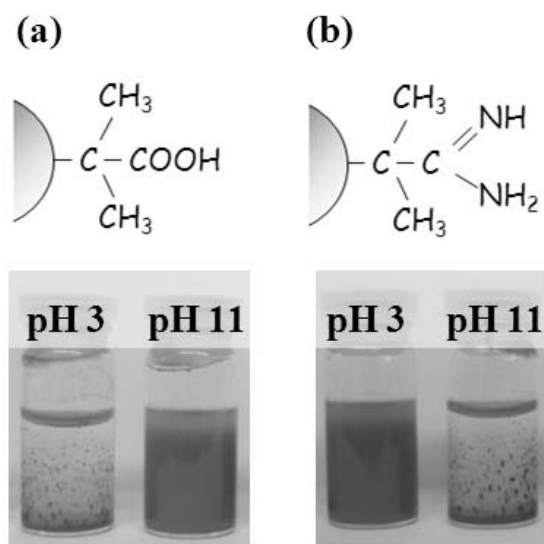


Fig. 6 Surface structure and the stability of surface modified SiC nanoparticle in pH controlled water after modified by (a) AIBN and (b) AMPA.

using small bead has recently developed.⁴⁰ As reducing the bead size down to 15-30 μ m, the aggregation size reduced to their primary particle size as about 10 nm where the particles were still aggregated when the bead size was larger than 100 μ m in diameter. This method and other physical technique, for example, ultrasonic dispersion, can applied to redisperse various nanoparticle into liquid media by the simultaneous processing of the surface modification introduced above and the bead milling.

3.2 In-situ surface modifications

3.2.1 Synthesis of nanoparticles redispersible near to their primary particle size

In order to re-disperse nanoparticles into solvents without aggregations, an in-situ surface modification route, which conduct surface modification during the nanoparticle synthesis, have been investigated by many researchers. A reverse micelle method is one of such method that particle synthesis reaction occurs in the reverse micelle structures.⁴¹ Various metals⁴²⁻⁴³, oxides⁴⁴⁻⁴⁵, and non oxide semiconductors⁴⁶⁻⁴⁷ can be synthesized by this method. Since the particles are synthesized in the reverse micelle structure, the obtained nanoparticles are redispersible into organic solvents with low-polarities. A thermal decomposition method, which involves the thermal decomposition of organometallic compounds in high boiling solvents are also widely accepted methods to obtain nanoparticles with high crystallinity and sharp size distributions.⁴⁸ The organometallic compounds can be for example, carbonyl-metals,⁴⁹⁻⁵⁰ metal acetylacetonates⁵¹ and metal-surfactant complexes.⁵²⁻⁵³ In the former two cases, capping agents such as trioctylphosphine oxides (TOPO), oleic acid and oleyl amines are dissolved in the synthesis solution to prevent the aggregation of nanoparticles. In the case of surfactant-metal uses such as metal oleate, the surfactant acts as the capping agents. It is reported that these thermal decomposition routes has possibility of particle size tuning in nanometer scale.⁵³ Not only metals,^{52,54} oxides,^{49,52,53} and nonoxide semiconductors,⁵⁵⁻⁵⁶ but also complicated compounds such as fluorides⁵⁷ and phosphine nanoparticles⁵⁰ are able to be synthesized by these methods. Since the prepared particles are capped with surfactants, they are typically redispersible into low-polar organic solvents. Nonhydrolytic sol-gel reaction,⁵⁸⁻⁶⁰ which is a reaction between metal halides and alkoxides or ethers, with the presence of capping agents such as TOPO and fatty acids are another accepted routes to prepare nanoparticles redispersible into low-polar solvents.

On preparing nanoparticles dispersible in aqueous or high-polar solvents, a polyol method is also widely accepted by many researchers.⁶¹⁻⁶⁴ Typically, nanoparticle reagents those soluble in high polar solvents, such as metal salts and metal complexes, are dissolved in polyol media (e.g. ethylene glycol, diethylene glycol, triethylene glycol) and then aged at temperature near to the boiling temperature. Many oxides⁶¹⁻⁶², sulfides⁶³ and fluorides⁶⁴ those redispersible into high polar solvents can be prepared by this method.

Based on abovementioned methods, various nanoparticles including metals, oxides, sulfides, and fluorides that are redispersible into many solvents can be synthesized by in-situ surface modification techniques. Contrary, a large difficulty lies in terms of engineering an in-situ surface modification technique to carbon related nanoparticles, because the particle synthesis temperature is extremely high. However recently, there are several reports of synthesis of carbon related materials those dispersible in solvents near to their primary particle size. The first example is the synthesis of carbogenic nanoparticles by thermal decomposition of various ammonium citrate salts such as octadecyl ammonium citrate salts and 2-(2-amonoethoxy)-ethanol salts.⁶⁵ It was reported that the citrate groups decomposes into carbogenetic nanoparticles while the organic ammonium salts act as a surface modifier. Hydrophilic and hydrophobic carbogenic nanoparticles about 7 nm were prepared by using octadecyl ammonium salts and 2-(2-amonoethoxy)-ethanol salts, respectively. Another example is the application of laser irradiation method. Graphite powders were dispersed into PEG and Nd:YAG laser was irradiated to the suspension.⁶⁶ After 2hours of irradiation, the suspension was centrifugated and the resulted supernatant contained PEG modified carbon nanoparticles which diameter was about 3 nm.

The surfactant capped nanoparticles which were synthesized by in-situ surface modification procedure can also further be modified in order to tune their surface properties. Ligand exchange method, which exchanges the capped surfactant, is a typically accepted method and has a large benefit in controlling the particle surface by keeping their dispersion stability. The surface structure can be controlled by exchanging various capping agents which has thermo-sensitivity⁶⁷ and that increases compatibility with aqueous solution⁶⁸⁻⁶⁹, polymers⁷⁰, or biomolecules⁷¹⁻⁷². For examples, hydrophobic ligands on Fe₃O₄⁶⁷, and FePt⁷² nanoparticles were exchanged to

PEG based ligand to improve the biocompatibility of nanoparticles. 2-mercaptothanol capped ZnS nanoparticles were modified with a tailor-made surfactant which contains polymerizable functional group in order to improve the compatibility with radical polymerizable polymers.⁷⁰⁾ Silane coupling agent, which was introduced above, can also be attached by ligand exchange route. For example, oleic acid stabilized ferrite magnetic nanoparticles were ligand exchanged by various silane coupling agents which has amine, carboxylic acid, or PEG group⁷³⁾. After the ligand exchange procedure, ferrite magnetic nanoparticles were able to redisperse in aqueous media without strong aggregations. This ligand exchange by silane coupling agents can also be applied to various metals and oxides such as Au, Ag, and Fe₃O₄.⁷⁴⁾ The use of mixed silane alkoxides are also a useful tool to tune the surface properties for their redispersion in various types of solvents.⁷⁵⁾ For an example, we have modified the surface of TiO₂ nanoparticles by mixed silane alkoxides with hydrophobic group (decyltrimethoxysilane: DES) and hydrophilic group (3-aminopropyltrimethoxysilane: APTMS). When TiO₂ were only modified by DES, the surface modified particles were only redispersible into low polar solvents such as toluene while that became redispersible into high polar solvents by modifying the particles by DES and APTMS (**Fig. 7**). By applying these methods, various reactive groups can be introduced on the particle surface without formation of strong aggregations. Since the particles are controlled to be not aggregated during the entire process, from the particle synthesis to surface modification procedure, it is a useful process to engineer the particle surface for nanotechnology

applications.

4. Conclusion

The reason for the difficulties for dispersing nanoparticles in liquid media, and various surface modification technique to overcome the difficulties of nanoparticle dispersions have briefly reviewed. The post synthesis surface modification have a benefit for easy processing whereas the controlled in-situ surface modification have a benefits for the possibility of engineering the nanoparticle surface without aggregations, e.g. surface modified nanoparticles are redispersible into liquid media near to their primary particle size. By selecting the surface modification procedure by time and circumstances, a nanoparticle suspension which are useful for further material processing can be designed.

Acknowledgments

This review was conducted as a part of project supported by a Grant-in-Aid for Scientific Research (B) (20360346) from the Japan Society for the Promotion of Science.

References

- 1) Marignier, J. L., Belloni, J., Delcourt, M. O., and Chevalier, J. P. (1985): Microaggregates of non-noble metals and bimetallic alloys prepared by radiation-induced reduction, *Nature*, 317, pp.344-345.
- 2) Alivisatos, P. (1996): Semiconductor Clusters, Nanocrystals, and Quantum Dots, *Science*, 271, pp.933-937.
- 3) Ozin, G. A. (1992): Nanochemistry: Synthesis in diminishing dimensions, *Adv. Mater.*, 4, pp.612-649.
- 4) Jun, Y.-W., Huh, Y.-M., Choi, J.-S., Lee, J.-H., Song, H.-T., Kim, S., Yoon, S., Kim, K.-S., Shin, J.-S. and Cheon, J. (2005): Nanoscale Size Effect of Magnetic Nanocrystals and Their Utilization for Cancer Diagnosis via Magnetic Resonance Imaging, *J. Am. Chem. Soc.*, 127, pp.5732-5733.
- 5) Kimberly, D., Dhanasekaran, T., Zhang, Z. and Meisel, D. (2002): Size-Dependent Melting of Silica-Encapsulated Gold Nanoparticles, *J. Am. Chem. Soc.*, 124, pp.2312-2317.
- 6) Verwey, E. J. W. and Overbeek, J. Th. G. (1947): "Theory of the stability of lyophobic colloids", Elsevier Publishing Company.
- 7) Woodcock, L. V. (1987): Developments in the non-Newtonian rheology of glass forming systems, *Lecture Notes in Phys.*, 277, pp.113-124.
- 8) Kamiya, H., Mitsui, M., Takano, H. and Miyazawa, S. (2000): Influence of particle diameter on surface silanol structure, hydration forces, and aggregation behavior of alkoxide-derived silica particles, *J. Am.*

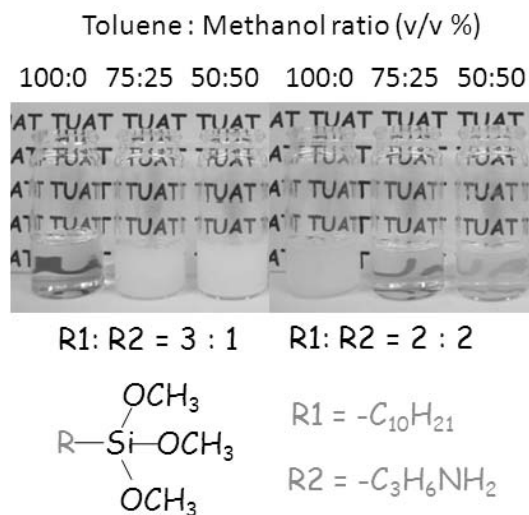


Fig. 7 Dispersion stability of TiO₂ nanoparticles modified by mixed silane alkoxides.

- Ceram. Soc., 83, pp.287-293.
- 9) Iijima, M., Tsukada, M. and Kamiya, H. (2007): Effect of particle size on surface modification of silica nanoparticles by using silane coupling agents and their dispersion stability in methylethylketone, *J. Colloid Interface Sci.*, 307, pp.418-424.
 - 10) Yoshikawa, J., Lewis, J. A. and Chun, B. -W. (2008): Comb polymer architecture, ionic strength, and particle size effects on the BaTiO₃ suspension stability, *J. Am. Ceram. Soc.*, 92, pp.S42-S49.
 - 11) Palmqvist, L. and Holmberg, K. (2008): Dispersant Adsorption and Viscoelasticity of Alumina Suspensions Measured by Quartz Crystal Microbalance with Dissipation Monitoring and in Situ Dynamic Rheology, *Langmuir*, 24, pp.9989-9996.
 - 12) Prabhakaran, K., Kumbhar, C. S., Raghunath, S., Gokhale, N. M. and Sharma, S. C. (2008): Effect of concentration of ammonium poly(acrylate) dispersant and MgO on coagulation characteristics of aqueous alumina direct coagulation casting slurries, *J. Am. Ceram. Soc.*, 91, pp.1933-1938.
 - 13) Laarz, E., Meurk, A., Yanez, J. A. and Bergstrom, L. (2001): Silicon nitride colloidal probe measurements: interparticle forces and the role of surface-segment interactions in poly(acrylic acid) adsorption from aqueous solution, *J. Am. Ceram. Soc.*, 84, pp.1675-1682.
 - 14) Sato, K., Kondo, S., Tsukada, M., Ishigaki, T. and Kamiya, H. (2007): Influence of solid fraction on the optimum molecular weight of polymer dispersants in aqueous TiO₂ nanoparticle suspensions, *J. Am. Ceram. Soc.*, 90, pp.3401-3406.
 - 15) Nsib, F., Ayed, N. and Chevalier, Y. (2006): Dispersion of hematite suspensions with sodium polymethacrylate dispersants in alkaline medium, *Colloids and Surf. A*, 286, pp.17-26.
 - 16) Lyckfeldt, O., Palmqvist, L. and Carlstroem, E. (2009): Stabilization of alumina with polyelectrolyte and comb copolymer in solvent mixtures of water and alcohols, *J. Euro. Ceram. Soc.*, 29, pp.1069-1076.
 - 17) Kakui, T. (2004): "Analysis of Action Mechanism of Polymer Dispersant and Dispersion Control of Fine Particles in Liquid Phase for Dense Suspensions", Doctoral thesis, Tokyo University of Agriculture and Technology.
 - 18) Kakui, T., Miyauchi, T. and Kamiya, H. (2005): Analysis if the action mechanism of polymer dispersant on dense alumina suspension using colloidal probe AFM, *J. Euro. Ceram. Soc.*, 25, pp.655-661.
 - 19) Tang, F., Uchikoshi, T., Ozawa, K. and Sakka, Y. (2006), Effect of polyethyleneimine on the dispersion and electrophoretic deposition of nano-sized titania aqueous suspensions, *J. Euro. Ceram. Soc.*, 26, pp.1555-1560.
 - 20) Kamiya, H., Fukuda, Y., Suzuki, Y., Tsukada, M., Kakui, T. and Naito, M. (1999): Effect of polymer dispersant structure on electrosteric interaction and dense alumina suspension behavior, *J. Am. Ceram. Soc.*, 82, pp.3407-3412.
 - 21) Kirby, G. H., Harris, D. J., Li, Q. and Lewis, J. A. (2004): Poly(acrylic acid)-poly(ethylene oxide) comb polymer effects on BaTiO₃ nanoparticle suspension stability, *J. Am. Ceram. Soc.*, 87, pp.181-186.
 - 22) Xue, C.-H., Shi, M.-M., Yan, Q.-X., Shao, Z., Gao, Y., Wu, G., Zhang, X.-B., Yang, Y., Chen, H.-Z. and Wang, M. (2008): Preparation of water-soluble multi-walled carbon nanotubes by polymer dispersant assisted exfoliation, *Nanotechnology*, 19, 115605/1-115605/7.
 - 23) Kakui, T. and Kamiya, H. (2004): Effect of Sodium Aromatic Sulfonate Group in Anionic Polymer Dispersant on the Viscosity of Coal-Water Mixtures, *Energy & Fuels*, 18, pp.652-658.
 - 24) Delozier, D. M., Watson, K. A., Smith Jr. J. G., Clancy, T. C. and Connell, J. W. (2006): Investigation of Aromatic/Aliphatic Polyimides as Dispersants for Single Wall Carbon Nanotubes, *Macromolecules*, 39, pp.1731-1739.
 - 25) Zhang, T., Zhang, Z., Dong, M., Zhang, J., Lin, Q. and Jiang, D. (2007): The influence if polyethylene imine on the gelcasting of SiC with two different initiators, *J. Am. Ceram. Soc.*, 90, pp.3748-3752.
 - 26) Plueddemann, E. P., Clark, H. A., Nelson, L. E. and Hoffman, K. R. (1962): Silane coupling agents for reinforced plastics, 39, p.135.
 - 27) Owen, M. J. (2002): Coupling agents: chemical bonding at interfaces, *Adhesion Sci. Eng.*, 2, pp.403-431.
 - 28) Plueddemann, E. P. (1970): Adhesion through silane coupling agents, *J. Adhesion*, 2, pp.184-201.
 - 29) Emoto, K., Alstine, J. M. V. and Harris, J. M. (1998): Stability of Poly(ethylene glycol) Graft Coatings, *Langmuir*, 14, pp.2722-2729.
 - 30) Chainmberg, M., Parnas, R. and Cohen, Y. (1989): Graft Polymerization of Polyvinylpyrrolidone onto Silica, *J. Appl. Polym. Sci.*, 37, pp.2921-2931.
 - 31) Li, C., Han, J., Ryu, C. Y. and Benicewicz, B.C. (2006): A Versatile Method to Prepare RAFT Agent Anchored Substrates and the Preparation of PMMA Grafted Nanoparticles, *Macromolecules*, 39, pp.3175-3183.
 - 32) Li, C. and Benicewicz, B. C. (2005): Synthesis of Well-Defined Polymer Brushes Grafted onto Silica Nanoparticles via Surface Reversible Addition-Fragmentation Chain Transfer Polymerization, *Macromolecules*, 38, pp. 5929-5936.
 - 33) Chaimberg, M. and Cohen, Y. (1990): Note on the Silylation of Inorganic Oxide Supports, *J. Colloid and Interface Sci.*, 134, pp.576-579.
 - 34) Iijima, M., Tsukada, M. and Kamiya, H. (2007): Effect of surface interaction of silica nanoparticles modified by silane coupling agents on viscosity of methylethylketone suspension, 305, pp.315-323.
 - 35) Iijima, M. and Kamiya, H. (2008): Surface Modification of Silicon Carbide Nanoparticles by Azo Radical Initiators, *J. Phys. Chem. C*, 112, pp.11786-11790.
 - 36) Liu, M., Zhu, T., Li, Z. and Liu, Z. (2009): One-Step in Situ Synthesis of Poly(methyl methacrylate)-Grafted Single-Walled Carbon Nanotube Composites, *J. Phys. Chem. C*, 113, pp.9760-9765.

- 37) Holzinger, M., Abraha, J., Whelan, P., Graupner, R., Lay, L., Hennrich, F., Kappes, M. and Hirsch, A. (2003): Functionalization of Single-Walled Carbon Nanotubes with (R)-Oxycarbonyl Nitrenes, *J. Am. Chem. Soc.*, 125, pp.8566-8580.
- 38) Gao, C., He, H., Zhou, L., Zheng, X. and Zhang, Y. (2009): Scalable Functional Group Engineering of Carbon Nanotubes by Improved One-Step Nitrene Chemistry, *Chem. Mater.*, 21, pp.360-370.
- 39) Georgakilas, V., Kordatos, K., Prato, M., Guldi, D. M., Holzinger, M. and Hirsch, A. (2002): Organic Functionalization of Carbon Nanotubes, *J. Am. Chem. Soc.*, 124, pp.760-761.
- 40) Inkyo, M., Tahara, T., Iwaki, T., Iskandar, F., Hogan Jr. C. J. and Okuyama, K. (2006): Experimental investigation of nanoparticle dispersion by beads milling with centrifugal bead separation, *J. Colloid and Interface Sci.*, 304, pp.535-540.
- 41) Pileni, M.-P. (2003): The role of soft colloidal templates in controlling the size and shape of inorganic nanocrystals, *Nature Mater.*, 2, pp.145-150.
- 42) Petit, C., Lixon, P. and Pileni M.-P. (1993): In-situ Synthesis of Silver Nanocluster in AOT Reverse Micelles, *J. Phys. Chem.*, 97, pp.12974-12983.
- 43) Park, J., Joo, J., Kwon, S. G., Jang, Y. and Hyeon, T. (2007): Synthesis of Monodisperse Spherical Nanocrystals, 46, pp.4630-4660.
- 44) Liu, C., Zou, B. S., Rondinone, A. J. and Zhang, Z. J. (2000): Reverse Micelle Synthesis and Characterization of Superparamagnetic $MnFe_2O_4$ Spinel Ferrite Nanocrystals, *J. Phys. Chem. B*, 104, pp.1141-1145.
- 45) Vestal, C. R. and Zhang, Z. J. (2003): Synthesis and magnetic characterization of Mn and Co spinel ferrite-silica nanoparticles with tunable magnetic core, *Nano Lett.*, 3, pp.1739-1743.
- 46) Quinlan, F. T., Kuther, J., Tremel, W., Knoll, W., Risbud, S. and Stroeve, P. (2000): Reverse Micelle Synthesis and Characterization of ZnSe Nanoparticles, *Langmuir*, 16, pp.4049-4051.
- 47) Yang, H. and Holloway, P. H. (2003): Enhanced Photoluminescence from CdS: Mn/ZnS core/shell quantum dots, *Appl. Phys. Lett.*, 82, pp.1965-1967.
- 48) Murray, C. B., Kagan, C. R. and Bawendi, M. G. (2000): Synthesis and characterization of monodisperse nanocrystals and close-packed nano-crystal assemblies, *Annu. Rev. Mater. Sci.*, 30, pp. 545-610.
- 49) Willis, A. L., Turro, N. J. and O'Brien, S. (2005): Spectroscopic Characterization of the Surface of Iron Oxide Nanocrystals, *Chem. Mater.*, 17, pp.5970-5975.
- 50) Park, J., Koo, B., Yoon, K. Y., Hwang, Y., Kang, M., Park, J.-G. and Hyeon, T. (2005): Generalized Synthesis of Metal Phosphide Nanorods via Thermal Decomposition of Continuously Delivered Metal-Phosphine Complexes Using a Syringe Pump, *J. Am. Chem. Soc.*, 127, pp.8433-8440.
- 51) Saita, S. and Maenosono, S. (2005): FePt Nanoparticles with a Narrow Composition Distribution Synthesized via Pyrolysis of Iron Ethoxide and Platinum Acetylacetonate, *Chem. Mater.*, 17, pp.3705-3710.
- 52) Park, J., An, K., Hwang, Y., Park, J.-G., Noh, H.-J., Kim, J.-Y., Park, J.-H., Hwang, N.-M. and Hyeon, T. (2004): Ultra-large-scale synthesis of monodisperse nanocrystals, *Nature Mater.*, 3, pp.891-895.
- 53) Park, J., Lee, E., Hwang, N.-M., Kang, M., Kim, S. C., Hwang, Y., Park, J.-G., Noh, H.-J., Kim, J.-Y., Park, J.-H. and Hyeon, T. (2005): One-nanometer-scale size-controlled synthesis of monodisperse magnetic iron oxide nanoparticles., 44, pp. 2872-2877.
- 54) Shen, C., Hui, C., Yang, T., Xiao, C., Tian, J., Bao, L., Chen, S., Ding, H. and Gao, H. (2008): Monodisperse Noble-Metal Nanoparticles and Their Surface Enhanced Raman Scattering Properties, *Chem. Mater.*, 20, pp.6939-6944.
- 55) Hines, M. A. and Scholes, G. D. (2003): Colloidal PbS Nanocrystals with Size-Tunable Near-Infrared Emission: Observation of Post-Synthesis Self-Narrowing of the Particle Size Distribution, *Adv. Mater.*, 15, pp.1844-1849.
- 56) Murray, C. B., Kagan, C. R. and Bawendi, M. G. (1995): Self-Organization of CdSe Nanocrystals into Three-Dimensional Quantum Dot Superlattices, *Science*, 270, pp.1335-1338.
- 57) Li, Z., Zhang, Y. and Jing, S. (2008): Multicolor Core/Shell-Structured Upconversion Fluorescent Nanoparticles, *Adv. Mater.*, 20, pp.4765-4769.
- 58) Trentler, T. J., Denler, T. E., Bertone, J. F., Agrawal, A. and Colvin, V. L. (1999): Synthesis of TiO_2 Nanocrystals by Nonhydrolytic Solution-Based Reactions, *J. Am. Chem. Soc.*, 121, pp.1613-1614.
- 59) Niederberger, M., Garnweitner, G., Pinna, N. and Antonietti, M. (2004): Nonaqueous and Halide-Free Route to Crystalline $BaTiO_3$, $SrTiO_3$, and $(Ba,Sr)TiO_3$ Nanoparticles via a Mechanism Involving C-C Bond Formation, *J. Am. Chem. Soc.*, 126, pp.9120-9126.
- 60) Chen, Z., Huang, L., He, J., Zhu, Y. and O'Brien, S. (2006): New nonhydrolytic route to synthesize crystalline $BaTiO_3$ nanocrystals with surface capping ligands, *J. Mater. Res.*, 21, pp.3187-3195.
- 61) Feldmann, C. (2003): Polyol-Mediated Synthesis of Nanoscale Functional Materials, *Adv. Func. Mater.*, 13, pp.101-107.
- 62) Wan, J., Cai, W., Meng, X. and Liu, E. (2007): Monodisperse water-soluble magnetite nanoparticles prepared by polyol process for high-performance magnetic resonance imaging, *Chem. Comm.*, pp.5004-5006.
- 63) Zhao, Y., Zhang, Y., Zhu, H., Hadjipanayis, G. C. and Xiao, J. Q. (2004): Low-Temperature Synthesis of Hexagonal (Wurtzite) ZnS Nanocrystals, *J. Am. Chem. Soc.*, 126, pp.6874-6875.
- 64) Wang, F. and Liu, X. (2008): Upconversion Multicolor Fine-Tuning: Visible to Near-Infrared Emission from Lanthanide-Doped $NaYF_4$ Nanoparticles, 130, pp. 5642-5643.
- 65) Bourlinos, A. B., Stassinopoulos, A., Anglos, D., Zboril, R., Karakassides, M. and Giannelis, E. P. (2008): Surface Functionalized Carbogenic Quantum Dots, 4,

- pp. 455-458.
- 66) Hu, S.-L., Niu, K.-Y., Sun, J., Yang, J., Zhao, N.-Q. and Du, X.-W. (2009): One-step synthesis of fluorescent carbon nanoparticles by laser irradiation, *19*, pp.484-488.
- 67) Chanana, M., Jahn, S., Georgieva, R., Lutz, J. -F., Bäuml, H. and Wang, D. (2009): Fabrication of Colloidal Stable, Thermosensitive, and Biocompatible Magnetite Nanoparticles and Study of Their Reversible Agglomeration in Aqueous Milieu, *Chem. Mater.* 21, pp.1906-1914.
- 68) Azzam, T., Bronstein, L. and Eisenberg, A. (2008): Water-Soluble Surface-Anchored Gold and Palladium Nanoparticles Stabilized by Exchange of Low Molecular Weight Ligands with Biamphiphilic Triblock Copolymers, *Langmuir*, 24, pp.6521-6529.
- 69) Zhang, Q., Song, K., Zhao, J., Kong, X., Sun, Y., Liu, X., Zhang, Y., Zeng, Q. and Zhang, H. (2009): Hexanedioic acid mediated surface-ligand-exchange process for transferring NaYF₄:Yb/Er (or Yb/Tm) up-converting nanoparticles from hydrophobic to hydrophilic, *J. Colloid Interface Sci.*, 336, pp.171-175.
- 70) Lü, C., Gao, J., Fu, Y., Du, Y., Shi, Y. and Su, Z. (2008): A Ligand Exchange Route to Highly Luminescent Surface-Functionalized ZnS Nanoparticles and Their Transparent Polymer Nanocomposites, *Adv. Func. Mater.*, 18, pp.3070-3079.
- 71) Nikolic, M. S., Krack, M., Aleksandrovic, V., Kornowski, A., Förster, S. and Weller, H. (2006): Tailor-Made Ligands for Biocompatible Nanoparticles, *Angew. Chem. Int. Ed.*, 45, pp.6577-6580.
- 72) Hong, R., Fischer, N. O., Emrick, T. and Rotello, V. M. (2005): Surface PEGylation and Ligand Exchange Chemistry of FePt Nanoparticles for Biological Applications, *Chem. Mater.*, 17, pp.4617-4621.
- 73) De Palma, R., Peeters, S., Van Bael Margriet, J., Van den Rul, H., Bonroy, K., Laureyn, W., Mullens, J., Borghs, G. and Maes, G. (2007): Silane ligand exchange to make hydrophobic superparamagnetic nanoparticles water-dispersible, *Chem. Mater.*, 19, pp.1821-1831.
- 74) Jana, N. R., Earhart, C. and Ying, J. Y. (2007): Synthesis of Water-Soluble and Functionalized Nanoparticles by Silica Coating, *Chem. Mater.*, 19, pp.5074-5082.
- 75) Iijima, M., Kobayakawa, M. and Kamiya, H. (2009): Tuning the stability of TiO₂ nanoparticles in various solvents by mixed silane alkoxides, *J. Colloid Interface Sci.*, 337, pp.61-65.

Author's short biography



Motoyuki Iijima

Dr. Motoyuki Iijima graduated from Tokyo University of Agriculture and Technology in 2004, and from the graduate school of Tokyo University of Agriculture and Technology in 2005. He received the Ph.D. degree of Engineering from Tokyo University of Agriculture and Technology in 2007. He was a Research Fellow of the Japan Society for the Promotion of Science during 2007. Currently, he is an Assistant Professor of Institute of Symbiotic Science and Technology of Tokyo University of Agriculture and Technology since 2008.



Hidehiro Kamiya

Dr. Hidehiro Kamiya graduated from Nagoya University in 1981, and from the graduate school of Nagoya University in 1983. He received the Ph.D. degree of Engineering from Nagoya University in 1986. He became a Research Associate in the Department of Material Engineering of Nagoya Institute of Technology in 1986 and an Assistant Professor in the Department of Chemical Engineering of Nagoya University in 1991. He joined the Department of Chemical Engineering of Tokyo University of Agriculture and Technology as an Associate Professor in 1993. Currently, he is a Professor of Institute of Symbiotic Science and Technology of Tokyo University of Agriculture and Technology since 2003.

Smart Powder Processing for Advanced Materials[†]

Makio Naito*, **Hiroya Abe** and **Akira Kondo**

Joining and Welding Research Institute, Osaka Univ.¹

Toyokazu Yokoyama

Hosokawa Micron Corp.²

C. C. Huang

Hosokawa Micron Powder Systems³

Abstract

Smart powder processing stands for novel powder processing techniques that create advanced materials with minimal energy consumption and environmental impacts. Particle bonding technology is a typical smart powder processing technique to make advanced composites. The technology has two main unique features. Firstly, it creates direct bonding between particles without any heat support or binders of any kind in the dry phase. The bonding is achieved through the enhanced particle surface activation induced by mechanical energy, in addition to the intrinsic high surface reactivity of nanoparticles. Using this feature, desired composite particles can be successfully fabricated. The second feature of this technology is its ability to control the nano/micro structure of the assembled composite particles. As a result, it can custom various kinds of nano/micro structures and can produce new materials with a simpler manufacturing process in comparison to wet chemical techniques. In this paper, its application examples for making advanced materials will be explained.

These two features lead to the achievement of minimizing energy consumption and environmental impacts when producing advanced materials. By making use of the particle bonding principle, a new one-pot processing method to synthesize nanoparticles without applying extra heat was developed. Furthermore, by carefully controlling the bonding between different kinds of materials in the composite particles, effective separation of elemental components can be achieved. It leads to the development of a novel technique for recycling advanced composite materials and turns them to high-functional applications. In this paper, these approaches will also be introduced. It is our goal to signify the particle bonding technology as a potential advanced processing technique for producing powder materials.

Keywords: Smart powder processing, Particle bonding, Nanoparticles, Composite particles, Advanced materials, Energy reduction, Recycling, Fumed silica compact, SOFC

1. Introduction

Recently, various novel powder processing techniques were rapidly developed for advanced material production due to the growing of high-tech industry, especially in consideration of energy consumption and the environmental issues such as the recycling of

waste materials. Smart powder processing stands for novel powder processing techniques that create advanced materials with minimal energy consumption and environmental impacts. Particle bonding technology is a typical smart powder processing technique to make advanced composites¹⁻⁵⁾. The technology has two main unique features. Firstly, it creates direct bonding between particles without any heat support or binders of any kind in the dry phase. The bonding is achieved through the enhanced particle surface activation induced by mechanical energy, in addition to the intrinsic high surface reactivity of nanoparticles. Using this feature, desired composite particles can

[†] Accepted: August 25th, 2009

¹ 11-1, Mihogaoka, Ibaraki, Osaka, 567-0047 Japan

² Shodai-Tajika 1-9, Hirakata, Osaka, 673-1132 Japan

³ 10 Chatham Road, Summit NJ 07901 USA

* Corresponding author

TEL: 06-6879-8660, FAX:06-6879-8680

E-mail:m-naito@jwri.osaka-u.ac.jp

be successfully fabricated. The second feature of this technology is its ability to control the nano/micro structure of the assembled composite particles. As a result, it can custom various kinds of nano/micro structures and can produce new materials with a simpler manufacturing process in comparison to wet chemical techniques.

Fig. 1 showed the examples of unique microstructures created by the particle bonding technique, which led to various kinds of applications such as multi-layered composite particles for the drug delivery systems (DDS)⁶⁾, self-assemble structures for electronic devices, composite porous materials for fuel cell electrodes, and nano-porous materials. In this paper, first, its application examples for advanced material production would be explained, including the development of fuel cell electrodes⁷⁻²⁴⁾ and high efficient thermal insulation materials²⁵⁻²⁷⁾.

Furthermore, by making use of these features, a new one-pot processing method to synthesize nanoparticles without applying extra heat was developed. A rapid synthesis of perovskite type lanthanum manganite and related compounds starting from a mixture of industrial grade powders was demonstrated²⁸⁻³³⁾. Also, particle bonding with electric discharge is an interesting phenomenon for controlling surface structure of nanoparticles³⁴⁾. These results suggest that particle bonding technique is a promising approach to minimize energy consumption when synthesizing nanoparticles, while existing processes require a long manufacturing route including firing at high temperatures. In this paper, the development of

novel powder processing for energy reduction would be introduced.

Finally, by carefully controlling the bonding between different kinds of materials, separation of composite structure into elemental components is possible, which leads to the development of novel technique to recycling advanced composite materials and turns them to high-functional applications. In this paper, the development of novel method to recycle glass-fiber reinforced plastics (GFRP) would be introduced and particle bonding principle was found to be a potential advanced processing technique for producing powder materials³⁵⁾.

2. Production of Composite Particles

So far, various kinds of composite particles have been produced by particle bonding process. The typical one is a core particle coated with fine guest particles. Bonding fine particles on the surface of core particle was already proposed. **Fig. 2** showed the particle bonding process³⁾ by Mechanofusion System⁴⁾. The process is carried out in two steps. First, the surfaces of fine particles and core particles are mechanically activated, as a result, fine particles adhere onto the surfaces of core particles. Then, as the second step, fine particles and core particles interact to each other while fine particles also adhere onto the fine-particle layer on the surfaces of core particles. Therefore, by changing the kind of fine particle materials during the processing, we can easily make multi-layered composite particles or functional gradient

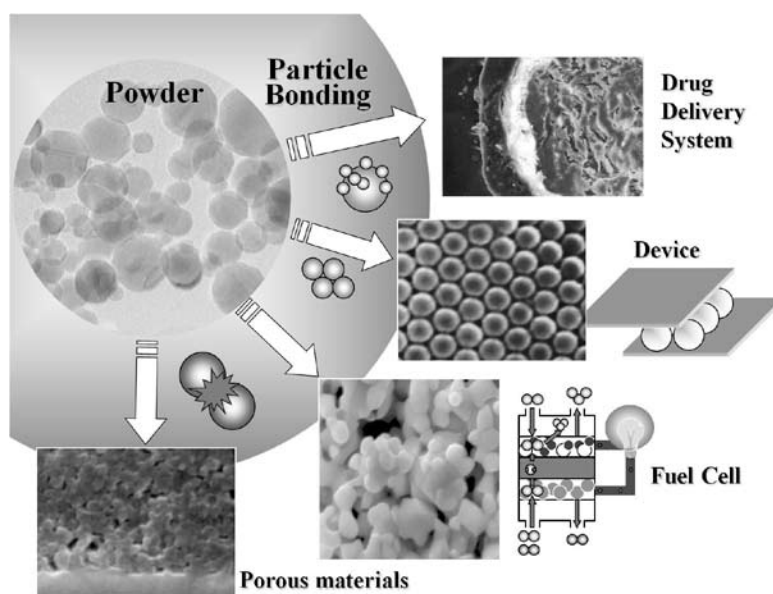


Fig. 1 Unique microstructure created by particle bonding process.

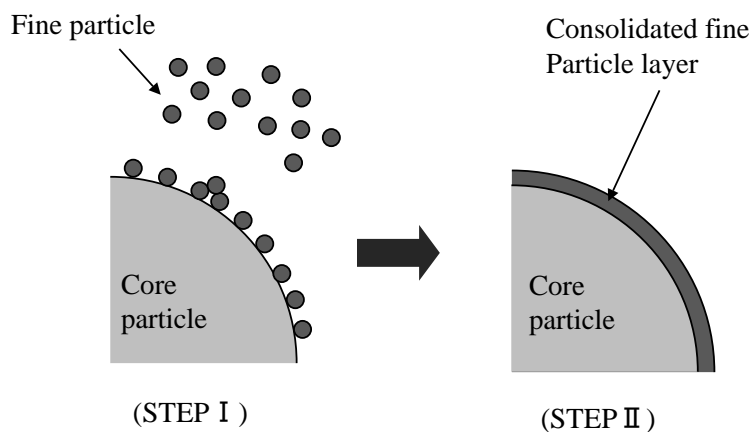


Fig. 2 Particle composite processed by Mechanofusion System.

particles.

There are a lot of factors affecting the particle composing process, and, its bonding mechanism depends on the combinations of core/fine particulate materials. However, as is well known, the contact surface between the powder materials receives extremely high local temperature and pressure, where mechanical stresses were actually given³⁶⁾. For example, authors previously reported that the local temperature at the interface between particles during particle bonding processing could be ten times higher than the apparent temperature of processing chamber³⁷⁾. Such a locally high temperature is expected to cause unique phenomena between fine particles and core particles, or among fine particles. For example, when coating nano titania particles on the glass beads, the peak of binding energy of Ti 2p shifted away from its original position after only 5 min of mechanical processing³⁾. It suggested that there was a chemical interaction on their surface during the processing.

3. Structural Control of SOFC Electrodes

Solid oxide fuel cell (SOFC) is a promising candidate for power generation in the 21st century because of its high energy efficiency and clean exhaust. Current R&D efforts focus on reducing its production cost and increasing the long-term stability of cells and stacks by lowering its operation temperature without losing power density. Prefabrication of the composite particles followed by electrode forming using particle bonding process is an ideal way to go, especially for controlling the microstructure of composite electrodes. Recently, we successfully fabricated various kinds of composite particles such as large core-particles coated with nanoparticles and

inter-dispersed composite mixture consisting of several kinds of nanoparticles using the particle bonding technique⁷⁻²⁴⁾.

Nickel-yttria stabilized zirconia (Ni-YSZ) is the most widely used SOFC anode material due to its excellent electrochemical properties at high temperatures. The electrochemical reaction (hydrogen oxidation) takes place at the triple-phase boundary (TPB) where Ni, YSZ and fuel gas meet. The reaction rate strongly depends on the catalytic activity of anode materials and the TPB length. Since the former significantly decreases with decreasing operation temperature, the latter must be increased as much as possible in the limited effective electrode volume to keep high electrochemical performance even at lower temperatures. For the TPB enlargement, the anode microstructure such as size and arrangement of Ni and YSZ must be controlled precisely.

Fig. 3 showed the process to fabricate SOFC anode using coated composite particles (CC), i.e. NiO large core-particle coated with YSZ nanoparticles. The composite particles provided well-organized electrode microstructure as shown in the figure, and resulted in good electrochemical performance¹²⁾. As a result, a prototype SOFC power plant system with a capacity of about 1kW was fabricated using the anode made by the CC particles and has been in services at an operating temperature of 700°C. Fig. 4 showed a LED display exhibiting the Japanese letters of HO-SOKAWA, which was installed at the top floor of the main building of Hosokawa Micron Corporation in Osaka and powered by the prototype SOFC system for long-term evaluation.

Particle bonding process can also create another type of composite particles. For example, Fig. 5 showed NiO-YSZ inter-dispersed composite particles

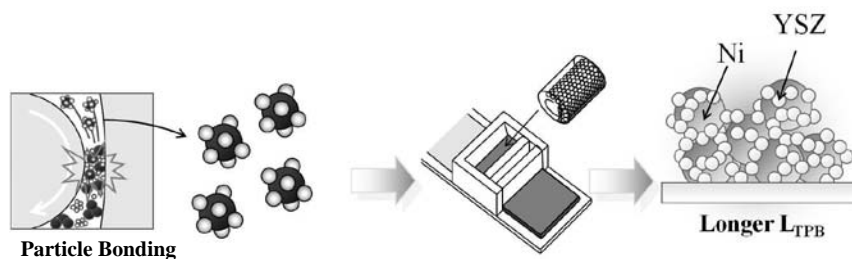


Fig. 3 Fabrication of composite anode by composite particles.



Fig. 4 LED display by SOFC power plant.

(IC) consisting of NiO and YSZ nanoparticles²⁴.

Fig. 5 (a) was the SEM micrograph of the composite particles. **Fig. 5 (b)** was the detailed structure of a composite particle observed by TEM. NiO and YSZ phases in the composite particle were identified by

EDS analysis in the micrograph. The micrograph indicated successful fabrication of the IC particles. NiO and YSZ nanoparticles were well dispersed and their sizes were in good agreement with those estimated from the specific surface area of starting particles (NiO: 160 nm and YSZ: 75nm)²⁴.

Fig. 6 showed SEM micrographs of the anode made of IC particles before the reduction, just after the reduction, and after the long-term stability test at 700°C for 920h. The anode made of IC particles before the reduction showed grain sizes smaller than 1 μm without abnormally large ones. NiO shrunk when it was reduced to Ni, and, porous structure evolved in the anode. Thus, the uniform porous structure after reduction suggested that NiO was uniformly distributed around the three-dimensional YSZ frame work in the entire anode. Even after the long-term stability test, no significant structural change was observed in the anode. The grain size was kept at about 0.5 μm, and no abnormally large grain was observed. The insignificant micro-structural change indicated that grain growth of Ni was insignificant in the anode made of IC particles under the testing conditions²⁴.

Fig. 7 showed anode polarization curves as a function of current density. The anode made of IC particles showed lower polarization than the anode made

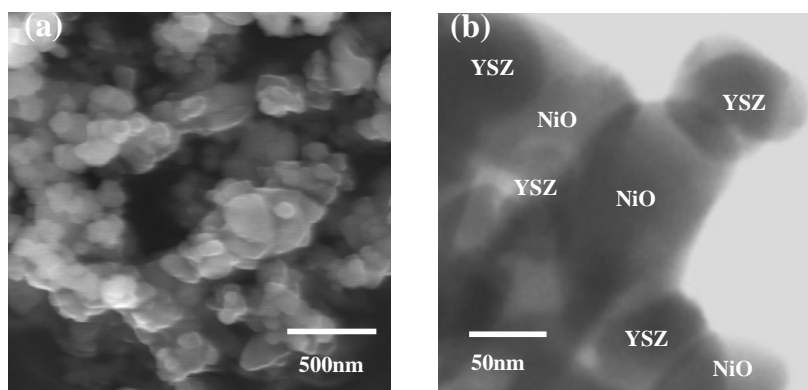


Fig. 5 Ni-YSZ inter-dispersed composite particles.
(a) SEM (b) TEM

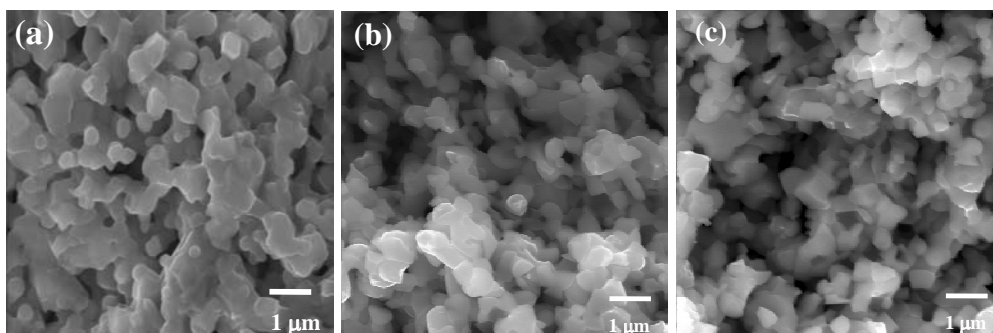
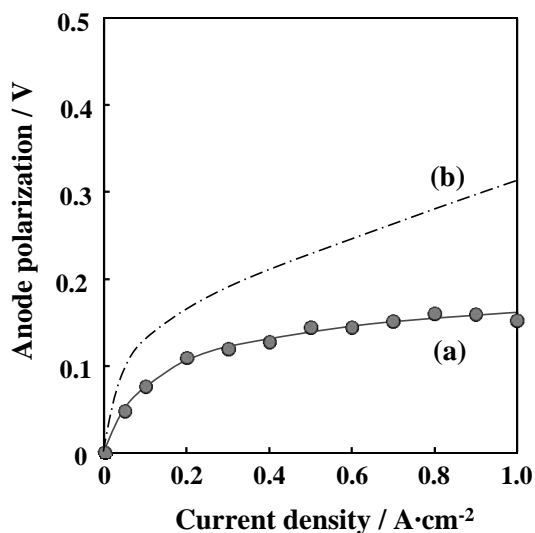


Fig. 6 Cross-sectional SEM images of the anode.
 (a) before reduction, (b) after reduction,
 (c) after the long-term stability test at 700°C for 920h



(a) Inter-dispersed composite particles (IC)
 (b) Coated composite particles (CC)

Fig. 7 Anode polarization as a function of current density.

of CC particles²⁴. It indicated that careful control of microstructure by the use of composite particles as starting materials was very important for improving the performance of anode. Further improvement on the electrode performance was expected by optimiz-

ing Ni-YSZ microstructure using particle bonding technique.

4. Nano-Porous Structural Control and its Application for Thermal Insulation

The second example is to make high efficient thermal insulation materials²⁵⁻²⁷. Interest in thermal insulation materials has been intensified globally, because escalating energy costs signified the importance of efficient thermal insulation. In this study, nanoparticle bonding process was used to make composite fibers coated with porous fumed silica layer in the dry phase. **Fig. 8** showed the proposed dry processing method to fabricate fumed silica compact by using composite fibers²⁶. Fiber glass composites porously coated with silica nanoparticles were fabricated at the first stage and then compacted into a board by dry pressing. The composites were produced by a particle bonding process without collapsing the fiber glass and nano-scale pores made by the fumed silica. The proposed method had the advantage of preventing contacts between fibers in the compacts due to the existence of coating layer. In addition, since fumed

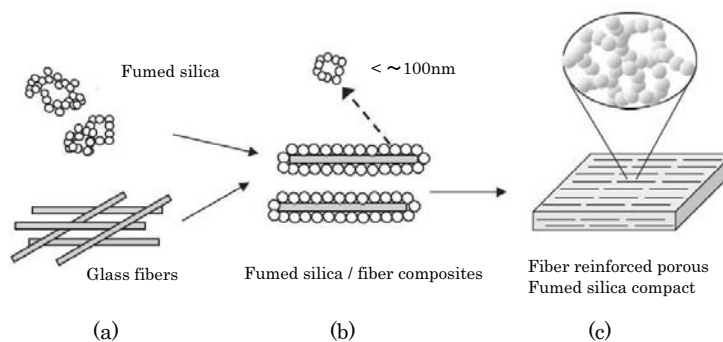


Fig. 8 Proposed dry processing method to fabricate fibrous fumed silica compacts: (a) mixing of raw materials; (b) particle bonding to coat glass fiber with fumed silica; (c) dry pressing of the composites from (b) to produce bulk body.

silica was fixed on the fibers, particle segregation rarely occurred during forming. Therefore, highly uniform dispersion of fibers in the compact could easily be achieved.

Fig. 9(a) showed a cross-sectional SEM image of a glass fiber coated with fumed silica found in the processed powder mixture. **Fig. 9(b)** showed the magnified TEM image of the coated fumed silica layer²⁵⁾. This layer was porously formed with a pore size of about 100 nm. The composite fibers were then successfully dry-pressed to make fiber reinforced fumed silica porous compact. **Table 1** showed the thermal conductivity of compact specimens with 80% porosity at 100°C and 400°C²⁶⁾. They were lower than molecular conductivity of still air (0.03 W/mK at 100 °C, 0.05 W/mK at 400°C) and at the same level as those obtained from silica aerogel³⁸⁾ and fumed silica compacts³⁹⁾. These results indicated that the obtained compacts had nano-scale porous structure. The remarkable attribute of composite fibers was achieving very low thermal conductivity with a relatively large amount of glass fibers. Mechanical strength of the compacts depends on their apparent density determined by the compressive strength. In this case, fracture strength ranged from 0.4 to 1.6 MPa, corresponding to apparent densities from 400 to 480 kg/m³, could be obtained. This made it possible to machine the compacts for various applications.

The present study demonstrated that the dry powder processing method as shown in **Fig. 8** provided fibrous fumed silica compacts with mechanical reliability and efficient thermal insulation. The specific feature of this method was to apply effective mechanical processing for making fumed silica fiber composites, instead of conventional mixing techniques. The

Table 1 Thermal conductivity of the fibrous fumed silica compacts prepared by particle bonding process

Specimen	Density [kg/m ³]	Porosity [%]	Thermal Conductivity [W/(m · K)]	
			@100°C	@400°C
#1	459	81.2	0.0266	0.0269
#2	485	80.1	0.0266	0.0282

powder mixture consisting of composite fibers was in a good mixing state and resulted in fumed silica compact with well-dispersed fibers. The existence of fumed silica layer on the glass fiber could prevent direct fiber-fiber contacts in the compact which avoided solid thermal transport through the fibers even at high fiber loadings. Thus, as mentioned above, fumed silica compacts with efficient thermal insulation and good mechanical strength were achieved in this study²⁶⁾.

Furthermore, the thermal conductivity of fumed silica compacts at higher temperature could also be kept at lower value by adding SiC powders as an opacifier. It was found that thermal insulation compacts made of powder mixture consisting of fumed silica: glass fiber: SiC at a mass ratio of 70:10:20 prepared by the particle bonding technique could achieve a thermal conductivity of 0.04 W/mK at 600°C⁴⁰⁾. By changing the kind of nanoparticle additives, it was expected that thermal conductivity of the compacts could be kept lower at even higher temperatures by particle bonding process in the future.

5. Development of One-pot Process for Synthesizing Nanoparticles

The first attempt to synthesize materials at low

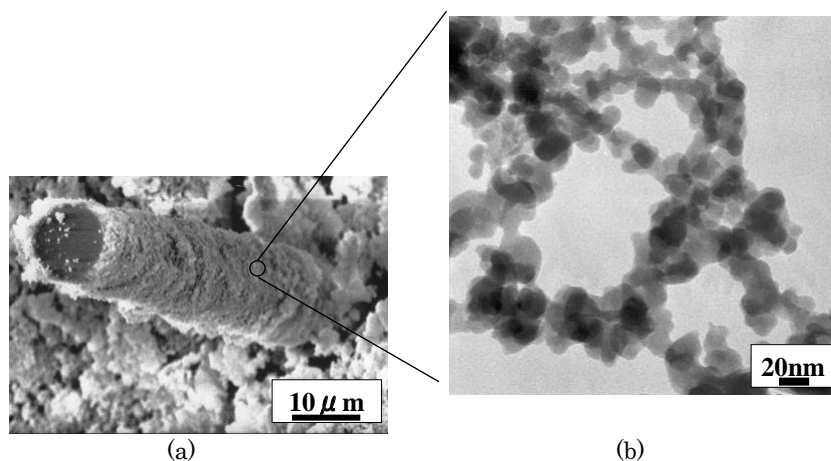


Fig. 9 (a) Cross-sectional SEM image of fumed silica/fiber composites
(b) TEM image of the coated fumed silica surface

temperature using particle bonding principle began with the research to create MgB_2 from magnesium and boron powders^{41, 42}. It was found that particle bonding process could combine the elemental powder components to form superconductive MgB_2 phase. Large magnesium particles (-330 mesh) and submicron amorphous boron particles (average particle size: $0.8 \mu m$) were mechanically processed by particle bonding technique. As a result, boron particles were embedded into the surface of magnesium particle at a depth of about $1 \mu m$, and, MgB_2 phase was found at this embedded region after annealing at a relatively low temperature under atmospheric pressure of argon.

The second attempt of applying particle bonding principle for low temperature reaction was to dope TiO_2 nanoparticles with nitrogen without any heat support, which usually requires annealing⁴³ at $500\text{--}600^\circ C$ under NH_3 flow. The high annealing temperature can lead to undesirable grain-size growth of TiO_2 nanoparticles. To overcome the problem, a new apparatus applying mechanical particle bonding technique with electric discharge was developed for this application¹. NH_3 (10%)/Ar plasma was generated at different gas pressures in a mechanical particle bonding processing chamber, where an anatase TiO_2 powder with a BET surface area of $300 m^2/g$ (equivalent to about 7 nm in diameter) was uniformly irradiated. When generated plasma irradiated at 300 Pa, the TiO_2 powder had a specific surface area of $283 m^2/g$, and, noticeable absorption in visible light range was observed. In addition, the powder showed an improvement of the photo-catalytic oxidation activity of

CH_3CHO under visible light. These results indicated that the presented plasma processing was capable of modifying TiO_2 nano-powder to improve its photo-reactivity without much reduction in specific surface area, which typically occurred when powder modification was carried out with annealing treatment³⁴.

Using the features of particle bonding technique, new one-pot processing to synthesize nanoparticles without any heat support was developed²⁸⁻³³. First, a rapid synthesis of perovskite type lanthanum manganite starting from a mixture of industrial grade powders was demonstrated. A traditional route to synthesize $LaMnO_{3+\delta}$ was through the solid state reaction of constituent oxide powders at $1300^\circ C$ **Fig. 10** showed conventional production process of $LaMnO_3$ materials from La_2O_3 and Mn_3O_4 powders. This process needs many manufacturing steps and the thermal reaction involved leads to particle size enlargement and limits the degree of chemical homogeneity.

On the other hand, a rapid mechano-chemical synthesis proposed by the authors was shown in **Fig. 11**. In this method, synthesis was achieved by one-pot processing of a mixture of industrial grade La_2O_3 and Mn_3O_4 . The one-pot processing was based on particle bonding technology, which applied mechanical forces such as compression and shear stresses repeatedly on the powder mixture without using media balls.

Fig. 12 showed the phase evolution as a function of processing time examined by XRD with the powder mixture processed under the presence of water vapor²⁸. In the experiment, the humid air (RH 70% at $25^\circ C$) was injected into the chamber before the mechanical processing. At the beginning, only the

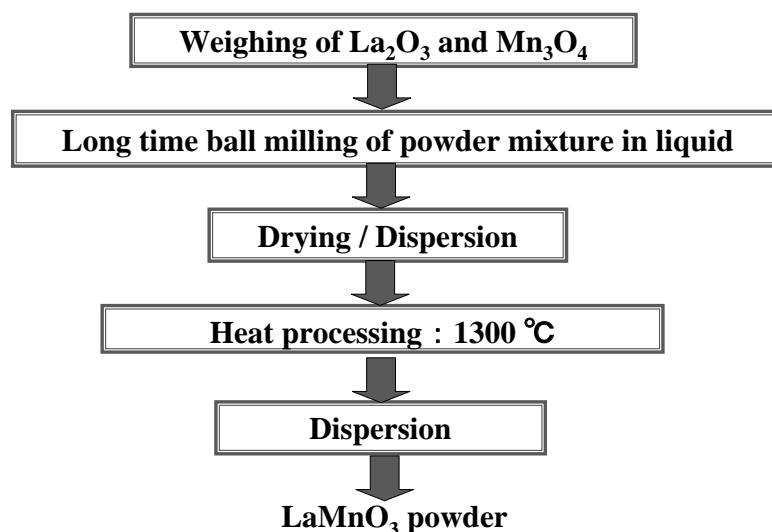


Fig. 10 Conventional production process of $LaMnO_3$ powder.

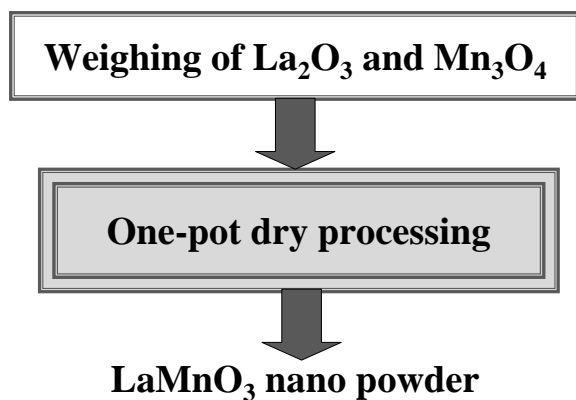


Fig. 11 One-pot processing to synthesize LaMnO₃ nano powder.

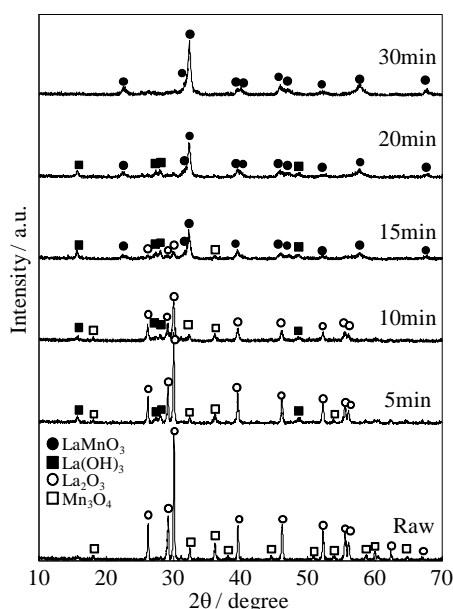


Fig. 12 XRD patterns of the powder mixture processed under RH 70%.

peaks corresponding to La₂O₃ and Mn₃O₄ were observed from the powder mixture. These peak intensities decreased drastically as processing time increased and almost disappeared after 15 min. in processing. Concurrent with the intensity decreases, the peaks related to La(OH)₃ appeared. Also, the peaks corresponding to LaMnO_{3+δ} started appearing after 15 min in processing and their intensities increased as processing time increased. After 30 min, the peaks completely transformed to single phase LaMnO_{3+δ} with disappearance of the La(OH)₃. The crystal structure of the synthesized powder was further identified to be LaMnO_{3+δ} by orthorhombic symmetry (JCPDS card 35-1353).

Fig. 13 showed the change of specific surface area (SSA) of the powder mixture with an increase

in processing time²⁸). The starting SSA of the powder mixture was 7.0m²/g. It increased quickly until 10 min. in processing and then kept almost constant. After 30 min in processing, it became 9.0m²/g. However, when processed in the dry air, the SSA of powder mixture increased only slightly; and, it was 7.5 m²/g after 30 min in processing. In this case, the XRD pattern of the powder mixture was almost identical to that of the starting state.

Adding to the synthesis of LaMnO_{3+δ}, strontium doped materials were also synthesized by the one-pot processing^{29,30}. Furthermore, BaTiO₃ was also rapidly synthesized by the one-pot processing shown in Fig. 11. In this case, industrial grade of TiO₂ and BaCO₃ powders were used^{32,33}

The one-pot reaction mechanism has not yet been fully understood. However, as mentioned in Figs. 12 and 13, the presence of a small amount of water played an important role on the reaction of La₂O₃ and Mn₃O₄. Further analysis would lead to the establishment of one-pot reaction mechanism to synthesize nanoparticles in the future.

6. The Development of Novel Recycling Process for GFRP

By making use of particle bonding principle between different kinds of materials, disassembling them is also possible and it can be applied to recycle waste composite materials. For example, glass fiber reinforced plastics (GFRP) is a typical composite material having the advantages of lightweight, high

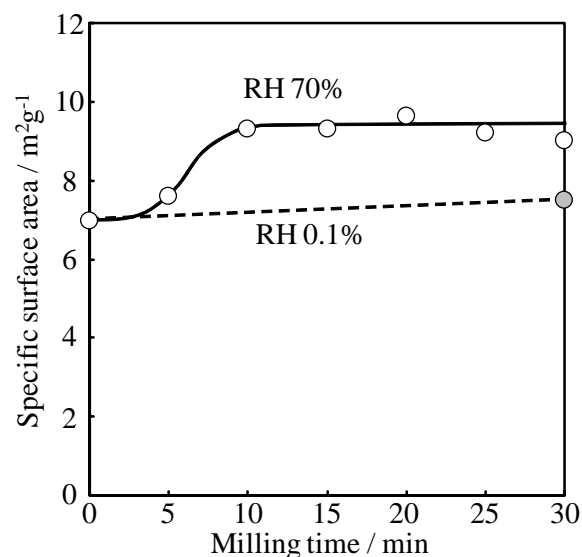


Fig. 13 Change of the specific surface area of powder mixture as a function of mechanical processing time.

strength and high weather resistance. Therefore, it has been used in various applications including boats, bath tubs, and building materials. Its production volume reached 460,000 tons in Japan in 1996, but decreased gradually since then. However, the volume of waste GFRP has increased every year. So far, almost all of the waste GFRP has been incinerated or disposed in landfill. Only 1-2 % of the waste GFRP is recycled as cement raw material or additives for concrete. Japan Reinforced Plastics Society started producing cement recycled from GFRP in 2002. The incineration of GFRP has problems of low calorific values on burning, and its residue needs to be disposed. In order to recycle the waste GFRP, some advanced chemical solvents and supercritical fluid⁴⁴⁾ have been studied. However, they have not been used in practice, because the chemical approach requires high temperature and high pressure operating conditions, which are not only costly but also generate by-products. In addition, the recycled materials do not have similar quality to that of the starting materials.

GFRP usually contains 40-50% of calcium carbonate filler and 20-30% of glass fibers. These materials must be recycled through simple and low energy process for profits. Therefore, we aimed to develop new recycling method to make advanced materials from the waste GFRP. **Fig. 14** showed the concept of an innovative recycling process of GFRP proposed by the authors³⁵⁾. It consisted of two unit processes based

on particle bonding principle. First, GFRP was separated into glass fibers and matrix resins, and then, the surface of separated glass fibers was coated by low cost nanoparticles. The coated composite glass fibers would be compacted to make porous materials as shown in **Fig. 8**. High functional materials having the properties of very low thermal conductivity, light weight, and easy machining are expected to obtain by applying the new process shown in **Fig. 14**.

The waste GFRP chip crushed down to about 1 cm was processed by an attrition-type mill, which applied similar mechanical principle to that of particle bonding process. When strong shear stress was applied to the chip layers for surface grinding, glass fibers began to separate from matrix resins on the chip surfaces. As a result, all glass fibers were effectively separated from other matrix components. The SEM photographs of the processed waste GFRP were shown in **Fig. 15**³⁵⁾. It was obvious that the glass fibers separated from matrix resins had their own shape by using this method (**Fig. 15(a)**). The length of the glass fibers ranged from about 100 μ m to over 1 mm. On the other hand, the glass fibers were destroyed when applying a vibration ball mill (**Fig. 15(b)**). In the vibration ball milling, mainly impact and compressive forces were applied to the material, which reduced glass fibers to particle form. These results showed that the proposed method using particle bonding principle was very effective in

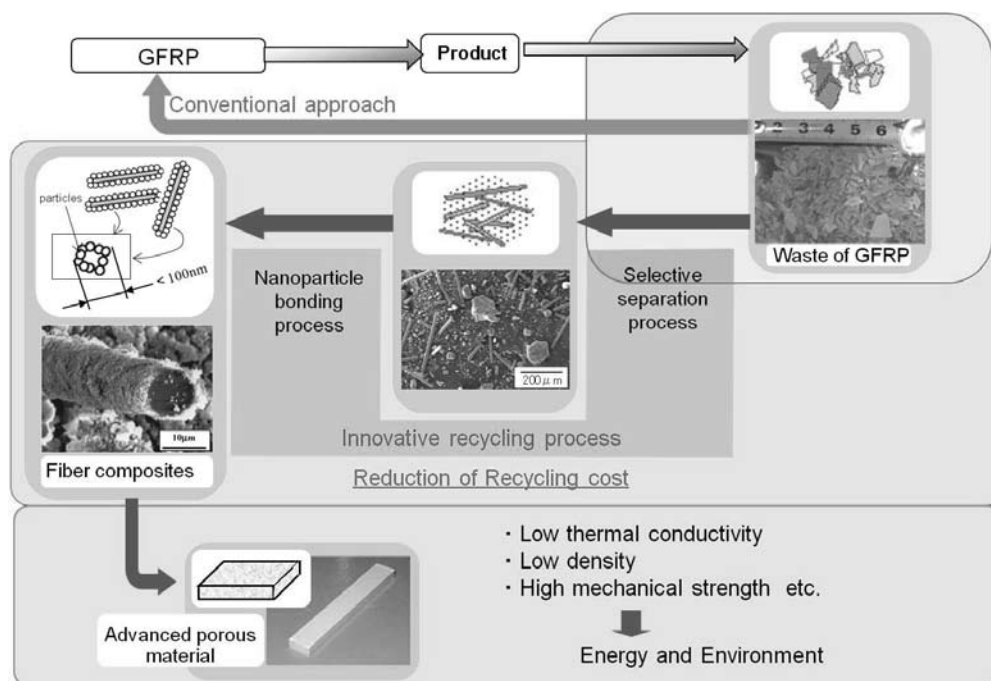
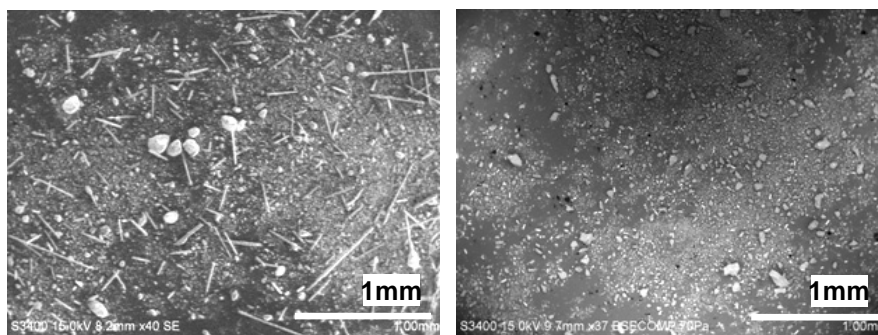


Fig. 14 Innovative recycling process for GFRP proposed by authors.



(a) (b)

Fig. 15 SEM photographs of processed powders by using the proposed method (a) and vibration ball mill (b).

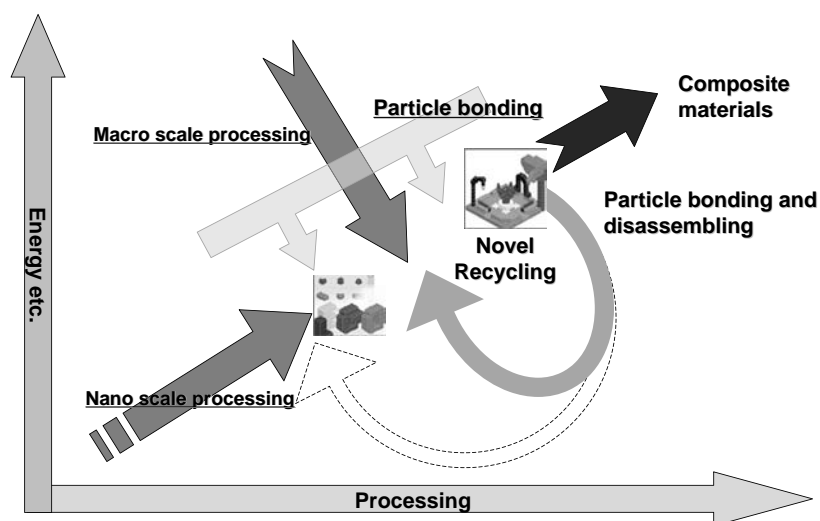


Fig. 16 Concept of smart recycling for composite materials based on particle bonding principle.

selective separation of glass fibers from other matrix components. Further experiments are now being carried out to make nanoparticle coated composite fibers from the recycled glass fibers for new material development.

Fig. 16 showed the concept of smart recycling of composite materials by using the particle bonding and disassembling between different kinds of materials. From the conventional recycling standpoint of view, each element of waste composite material must be returned back to its original state for repeated usage. However, it needs high recycling costs and the obtained element has lower quality than the virgin material. As a result, the recycling process cannot be practically used. On the contrary, the proposed recycling concept does not aim to obtain each original element, but develops further advanced materials using disassembled blocks of the waste composite

materials. In this case, how to apply bonding and disassembling the waste materials is the very key issue. As shown in **Fig. 16**, recycling waste back to its intermediate structure and then assembling it with another material to make further advanced materials would be more energy efficient than reclaiming the original elements. This concept will be a basis for the next generation of recycling system for advanced materials.

7. Conclusions

In this paper, particle bonding process was explained as a typical example of smart powder processing. This process enabled us to develop new composite materials. Based on its principle, the electrodes for SOFC and the high performance thermal insulator were developed. This process is also applicable

to other applications. In this paper, two examples were explained. The first one was to develop one-pot processing for nanoparticle synthesis from elemental powders without any heat support, and, the second was to develop new recycling process for waste composite materials and turn them into other advanced materials. It is believed that dry particle bonding technology can open the doors for various kinds of smart powder processing applications in the future.

References

- 1) Naito, M. and Abe, H. (2004): Particle Bonding Technology for Composite Materials – Microstructure Control and Its Characterization, *Ceramic Transactions*, 157, pp.69-76.
- 2) Naito, M., Abe, H. and Sato, K. (2005): Nanoparticle Bonding Technology for the Structural Control of Particles and Materials, *J. Soc., Powder Technol., Japan*, 42, pp.625-631.
- 3) Naito, M., Kondo, A. and Yokoyama, T. (1993): Applications of Comminution Techniques for the Surface Modification of Powder Materials, *ISIJ International*, 33, pp.915-924.
- 4) Yokoyama, T., Urayama, K., Naito, M., Kato, M. and Yokoyama, T. (1987): The Angmill Mechanofusion System and its Applications, *KONA Powder and Particle Journal* 5, pp.59-68.
- 5) Naito, M. and Yoshikawa, M. (1989): Applications of Mechanofusion System for the Production of Superconductive Oxides, *KONA Powder and Particle Journal*, 7, pp.119-122.
- 6) Fukumori, Y., Ichikawa, H., Uemura, T., Sato, K., Abe, H. and Naito, M. (2005): Process Performance of Dry Powder Coating for Preparing Controlled Release Microcapsules by a High Speed Mixer, *Proceedings of 8th International Symposium on Agglomeration, Bangkok, Thailand, March 16-18*, pp31-38.
- 7) Fukui, T., Ohara, S., Okawa, H., Hotta, T. and Naito, M. (2000): Properties of NiO Cathode Coated with Lithiated Co and Ni Solid Solution Oxide for MCFCS, *J. of Power Sources*, 86, pp.340-346.
- 8) Fukui, T., Okawa, H., Hotta, T., Naito, M. and Yokoyama, T. (2001): Synthesis of CoO/Ni Composite Powders for Molten Carbonate Fuel Cells, *J. Am. Ceram. Soc.*, 84, pp.233-235.
- 9) Fukui, T., Hotta, T., Okawa, H., Ohara, S., Naito, M. and Nogi, K. (2001): Performance and Morphology of a New Cathode Made from CoO/Ni Composite Particles for MCFCS, *Electrochemistry*, 69, pp.335-339.
- 10) Fukui, T., Ohara, S., Naito, M. and Nogi, K. (2001): Morphology Control of the Electrode for Solid Oxide Fuel Cells by Using Nanoparticles, *J. Nanoparticle Research*, 3, pp.171-174.
- 11) Fukui, T., Ohara, S., Naito, M. and Nogi, K. (2001): Morphology and Performance of SOFC Anode Fabricated from NiO/YSZ Composite Particles, *J. Chem. Eng., Japan*, 34, pp.964-966.
- 12) Fukui, T., Ohara, S., Naito, M. and Nogi, K. (2002): Performance and stability of SOFC anode fabricated from NiO/YSZ composite particles, *J. Power Sources*, 110, pp.91-95.
- 13) Fukui, T., Ohara, S., Okawa, H., Naito, M. and Nogi, K. (2003): Synthesis of Metal and Ceramic Composite Particles for Fuel Cell Electrodes, *J. European Ceram. Soc.*, 23, pp.2835-2840.
- 14) Fukui, T., Murata, K., Ohara, S., Abe, H., Naito, M. and Nogi, K. (2004): Morphology control of Ni-YSZ cermet anode for lower temperature operation of SOFC, *J. Power Sources*, 125, pp.17-21.
- 15) Murata, K., Fukui, T., Huang, C.C., Naito, M., Abe, H. and Nogi, K. (2004): Composite Powders Processed by Advanced Mechanical Method for the Fabrication of Cermet Anodes of Solid Oxide Fuel Cells, *J. Chem. Eng. Japan*, 37, 4, pp.568-571.
- 16) Fukui, T., Murata, K., Abe, H., Naito, M. and Nogi, K. (2004): Morphology and Performance of a Ni-YSZ Cermet Anode for Solid Oxide Fuel Cells, *Ceramic Transactions*, 146, pp.255-259, published by *J. Am. Ceram. Soc.*
- 17) Fukui, T., Murata, K., Huang, C.C., Naito, M., Abe, H. and Nogi, K. (2004): Morphology Control of SOFC Electrodes by Mechano-Chemical Bonding Technique, *The Ceramic Engineering and Science Proceedings*, 25, 3-4, pp.263-267, published by *Am. Ceram. Soc.*
- 18) Murata, K., Fukui, T., Abe, H., Naito, M. and Nogi, K. (2005): Morphology Control of La(Sr)Fe(Co)O_{3-a} Cathodes for IT-SOFCs, *J. Power Sources*, 145, pp.257-261.
- 19) Misono, T., Murata, K., Fukui, T., Chaichanawong, J., Sato, K., Abe, H. and Naito, M. (2006): Ni-SDC cermet anode fabricated from NiO-SDC composite powder for intermediate temperature SOFC, *J. Power Sources*, 157, pp.754-757.
- 20) Hagiwara, A., Hobara, N., Takizawa, K., Sato, K., Abe, H. and Naito, M. (2006): Preparation and evaluation of mechanochemically fabricated LSM/ScSZ composite materials for SOFC cathodes, *Solid State Ionics*, 177, pp.2967-2977.
- 21) Sato, K., Kondo, A., Abe, H., Naito, M. and Chaichanawong, J. (2007): Mechanical Synthesized La_{0.8}Sr_{0.2}MnO₃ Fine Powder for Cathode Material of Intermediate Temperature Solid Oxide Fuel Cell (IT-SOFC), *Ceramic Transactions*, 198, pp.225-230.
- 22) Hagiwara, A., Hobara, N., Shimada, H., Takizawa, K., Sato, K., Abe, H. and Naito, M. (2007): Evaluation of the Long Term Stability of LSM/ScSZ Composite Powder Materials for SOFC Cathodes, *Ceramic Transactions*, 198, pp.317-323.
- 23) Mori, H., Nonaka, N., Mizuno, M., Abe, H. and Naito, M. (2008): Development of a Geometrical Model for Optimizing Porous Anode Microstructure of Solid Oxide Fuel Cells, *J. Chem. Eng., Japan*, 41, pp.246-253.
- 24) Sato, K., Abe, H., Misono, T., Murata, K., Fukui, T. and

- Naito, M. (2009): Enhanced electrochemical activity and long-term stability of Ni-YSZ anode derived from NiO-YSZ interdispersed composite particles, *J. European Ceram. Soc.*, 29, pp.1119-1124.
- 25) Tahara, D., Itoh, Y., Ohmura, T., Abe, H. and Naito, M. (2004): Formation of Nanostructure Composites Using Advanced Mechanical Processing, *Ceramic Transactions*, 146, pp.173-177, published by Am. Ceram. Soc.
- 26) Abe, H., Abe, I., Sato, K. and Naito, M. (2005): Dry Powder Processing of Fibrous Fumed Silica Compacts for Thermal Insulation, *J. Am. Ceram. Soc.*, 88, pp.1359-1361.
- 27) Abe, I., Sato, K., Abe, H. and Naito, M. (2008): Formation of porous fumed silica coating on the surface of glass fibers by a dry mechanical processing technique, *Advanced Powder Technology*, 19, pp.311-320.
- 28) Sato, K., Chaichanawong, J., Abe, H. and Naito, M. (2006): Mechanochemical synthesis of LaMnO_3 fine powder assisted with water vapor, *Material Letters*, 60, pp.1399-1402.
- 29) Chaichanawong, J., Sato, K., Abe, H., Murata, K., Fukui, T., Charinpanitkul, T., Tanthapanichakoon, W. and Naito, M. (2006): Formation of strontium-doped lanthanum manganite ($\text{La}_{0.8}\text{Sr}_{0.2}\text{MnO}_3$) by mechanical milling without media balls, *Advanced Powder Technology*, 17, pp.613-622.
- 30) Chaichanawong, J., Sato, K., Abe, H., Naito, M., Charinpanitkul, T. and Tanthapanichakoon, W. (2007): Influence of Water Content of Starting Powder Mixture on the Mechanochemical Synthesis of Strontium Doped Lanthanum Manganite: *Ceramic Transactions*, 198, pp.199-204.
- 31) Ohara, S., Abe, H., Sato, K., Kondo, A. and Naito, M. (2008): Effect of water content in powder mixture on mechanochemical reaction of LaMnO_3 fine powder, *J. European Ceram. Soc.*, 28, pp.1815-1819.
- 32) Kondo, A., Sato, K., Abe, H., Naito, M. and Shimoda, H. (2007): Mechanochemical Synthesis of Barium Titanate from Nanocrystalline BaCO_3 and TiO_2 , *Ceramic Transactions*, 198, pp.375-380.
- 33) Ohara, S., Kondo, A., Shimoda, H., Sato, K., Abe, H. and Naito, M. (2008): Rapid mechanochemical synthesis of fine barium titanate nanoparticles, *Material Letters*, 62, pp.2957-2959.
- 34) Abe, H., Kimitani, T. and Naito, M. (2006): Influence of NH_3/Ar plasma irradiation on physical and photocatalytic properties of TiO_2 nanopowder, *J. Photochemistry and Photobiology A: Chemistry*, 183, pp.171-175.
- 35) Okuni, Y., Miura, M., Isu, N., Kondo, A., Abe, H. and Naito, M. : New Recycling Method to Make Advanced Materials from Waste FRP by using Attrition Type Milling Apparatus, *Mater. Res. Bull.*, in press.
- 36) Dacheville, F. and Roy, R. (1960): High-pressure Phase Transformations in Laboratory Mechanical Mixers and Mortars, *Nature*, 186, pp.34.
- 37) Nogi, K., Naito, M., Kondo, A., Nakahira, A., Niihara, K. and Yokoyama, T. (1996): New Method for Elucidation of Temperature at the Interface between Particles under Mechanical Stirring, *J. Japan Soc. Powder and Powder Metall.*, 43, pp.396-401.
- 38) Kwon, Y-G., Choi, S-Y., Kang, E-S. and Baek, S-S. (2001): Ambient-Dried Silica Aerogel Doped with TiO_2 Powder for Thermal Insulation, *J. Mater. Sci.*, 35, pp.6075-6079.
- 39) Smith, D.R. and Hust, J. G. (1989): Microporous Fumed-Silica Insulation Board as a Candidate Standard Reference Material of Thermal Resistance, NISTIR 89-3901, U.S., National Institute of Standards and Technology.
- 40) Ohmura, T., Abe, I., Ito, Y., Sato, K., Abe, H. and Naito, M. (2009): Development and Evaluation of Characteristics of Nanoporous Materials, *J. Soc., Powder Technol.*, Japan, 46, pp.461-466.
- 41) Abe, H., Naito, M., Nogi, K., Matsuda, M., Miyake, M., Ohara, S., Kondo, A. and Fukui, T. (2003): Low temperature formation of superconducting MgB_2 phase from elements by mechanical milling, *Physica C*, 391, pp.211-216.
- 42) Abe, H., Naito, M., Nogi, K., Kondo, A., Fukui, T., Ohara, S., Matsuda, M. and Miyake, M. (2004): Formation of MgB_2 Superconducting Phase from Mg and B Composite Particles Produced by Mechanical Mixing, *Ceramic Transactions*, 146, pp.277-282, published by J. Am. Ceram. Soc.
- 43) Asahi, R., Morikawa, T., Ohwaki, T., Aoki, K. and Taga, Y. (2003): Visible-Light Photocatalysis in Nitrogen-Doped Titanium Oxides, *Science*, 293, pp.269-271.
- 44) Iwaya, T., Tokano, S., Sasaki, M., Goto, M. and Shibata, K. (2008): Recycling of fiber reinforced plastics using depolymerization by solvothermal reaction with catalyst, *J. Mater. Sci.*, 43, pp.2452-2456.

Author's short biography



Makio Naito

Makio Naito received B.S., M.S. and Ph.D. degrees in chemical engineering from Nagoya University, Japan in 1980, 1982 and 1987, respectively. He was with Hosokawa Micron Corp. from 1982 to 1993 and engaged in the R&D of powder processing technology. He joined Japan Fine Ceramics Center (JFCC), Nagoya, Japan in 1993, where he has focused on powder characterization and powder processing technology in ceramics manufacturing. He was Vice Director of JFCC from 2000 to 2002, and then became a professor at Joining and Welding Research Institute (JWRI), Osaka University, Japan in 2002. He continued focusing on important studies on innovative powder and nanoparticle processing to develop advanced materials about energy and environmental issues. He was promoted to be the Director of Smart Processing Research Center, JWRI in 2007, and is also the Vice Director of JWRI from 2009. In addition, he has served as a Director of Hosokawa Micron Corp. from 2005. His publications cover a wide range of studies in the fields related to the advanced materials. He has authored or coauthored more than 500 technical articles, including more than 200 refereed journal articles. He has contributed to 47 books with 9 books as an editor. He has received many awards including Richard M. Fulrath Award from The American Ceramic Society.



Hiroya Abe

Hiroya Abe received B.S., M.S. and Ph.D. degrees in electrical engineering from Nagaoka University of Technology, Japan in 1990, 1992 and 1995, respectively. He was with Motorola Japan from 1995 to 1998, and with Japan Fine Ceramics Center (JFCC) from 1998 to 2002. Then, he joined at Joining and Welding Research Institute (JWRI), Osaka University, as an associated professor in 2002. His current interest is the development of smart materials and interfaces for functional joining technologies.



Akira Kondo

Akira Kondo received B.S. and M.S. degrees in chemical engineering from Nagoya University, Japan in 1989 and 1991, respectively. He received Ph D. degree in material science from Osaka University in 1999. He was with Hosokawa Micron Corp. from 1991 to 2005, where he engaged in the R&D of powder processing technology. He became a specially designated researcher at Joining and Welding Research Institute (JWRI), Osaka University, Japan in 2005, and is engaged in the R&D of powder processing for advanced materials.

Author's short biography



Toyokazu Yokoyama

Dr. T.Yokoyama is the Director of Powder Technology Research Institute of Hosokawa Micron Corporation (HMC), a global supplier of systems and materials related with powder and particle science and engineering. He graduated from Kyoto University in chemical engineering and received M.S. there in 1975. Then he spent six years in Europe to study powder technology at Karlsruhe University and to work as an engineer for Hosokawa Europe Ltd. in Germany and England. After another six-year work in the engineering and R&D divisions of HMC in Osaka specializing in powder technology, he worked at Nagoya University and obtained Ph.D. on the subject of ultrafine wet grinding. From 1992 to 2003, he was a general manager of Hosokawa Micromeritics Laboratory for R&D mainly in the field of powder and nanoparticle technology. His major interests are particle design and processing to produce advanced functional materials by mechanical composing methods as well as fine grinding and particle characterization.



Dr. C. C. Huang

Dr. C. C. Huang is the Director of Research and Development, Nanoparticle Technology and Micron Products at Hosokawa Micron Powder Systems, which is an operating unit of Hosokawa Micron International Inc., a global supplier of systems and equipment related to material sciences and engineering. He holds an M.S. degree in engineering from Illinois Institute of Technology and a Ph.D. degree in chemical engineering from West Virginia University. He has many years' experiences in industrial R&D, as well as academia, in the field of powder technology and science. Dr. Huang specializes in powder and nanoparticle processing, powder characterization, powder granulation, and fluidization. He has published over 30 articles and 8 patents, chaired several meetings, and continues to be an active member in a number of scientific and engineering societies.

Numerical Simulations of Pulverized Coal Combustion[†]

Ryoichi Kurose*

*Department of Mechanical Engineering and Science, and Advanced
Research Institute of Fluid Science and Engineering, Kyoto University¹*

Hiroaki Watanabe and Hisao Makino

*Energy Engineering Research Laboratory, Central Research Institute of
Electric Power Industry (CRIEPI)²*

Abstract

Coal is an important energy resource for meeting the further demand for electricity, as coal reserves are much more abundant than those of other fossil fuels. In pulverized coal fired power plants, it is very important to improve the technology for the control of environmental pollutants such as NO_x, SO_x and ash particles including unburned carbon. With the remarkable progress in the performance of computers, it is strongly expected that the computational fluid dynamics (CFD) would be a tool for the development and design of such suitable combustion furnaces and burners for the pulverized coal combustion. The focus of this review is to highlight our recent progress of CFD of the pulverized coal combustion in terms of Reynolds-Averaged Navier-Stokes (RANS) simulation and Large-Eddy Simulation (LES) together with some of future perspectives.

Keywords: Pulverized coal combustion, Numerical simulation, RANS simulation, LES

1. Introduction

Coal is an important energy resource for meeting the further demand for electricity, as coal reserves are much more abundant than those of other fossil fuels. In pulverized coal fired power plants, it is very important to improve the technology for the control of environmental pollutants such as NO_x, SO_x and ash particles including unburned carbon. In order to achieve these requirements, understanding the pulverized coal combustion mechanism and development of the advanced combustion technology are necessary. However, the combustion process of the pulverized coal is not well clarified so far since pulverized coal combustion is a very complicated phenomenon, in which the maximum flame temperature exceeds 1500°C and some substances which can hardly be measured, for example, radical species and highly reactive solid particles are included. Accordingly, development of new combustion furnaces and burners requires high cost and takes a long period

because the empirical process comprises many steps.

The computational fluid dynamics (CFD) of the pulverized coal combustion field is being developed with the remarkable progress in the performance of computers. This method, in which the governing equations of the combustion field are solved using a computer, is capable to provide the detailed information on the distributions of temperature and chemical species and the behavior of pulverized coal particles over entire combustion field that cannot be obtained by experiments. In addition, it facilitates the repeated review in arbitrary conditions for the properties of pulverized coal and the flow field at a relatively low cost. It is, therefore, strongly expected that the CFD becomes a tool for the development and design of combustion furnaces and burners.

DNS (Direct Numerical Simulation), LES (Large-Eddy Simulation) and RANS (Reynolds-Averaged Navier-Stokes) simulation are typical methods for the CFD of the combustion field in terms of turbulence model. DNS, which directly solves governing equations of fields of the flow, chemical species concentrations and temperature by setting the numerical grid space below the minimum eddies in these fields, has the highest numerical accuracy among the above mentioned methods. Although it is effectively ap-

[†] Accepted: August 24, 2009

¹ Yoshida-honmachi, Sakyo-ku, Kyoto 606-8501, Japan

² 2-6-1 Nagasaka, Yokosuka, Kanagawa 240-0196, Japan

* Corresponding author

E-mail : kurose@mech.kyoto-u.ac.jp

plicable to the basic research, its application to the combustion field at practical levels is very difficult as it requires a huge number of grid points and high loads to the computer. On the contrary, RANS simulation is most frequently used in practical applications. This method solves the governing equations by averaging them over the time and replacing resulted Reynolds stresses and turbulent scalar fluxes terms with turbulence models. It can considerably reduce the number of grid points and loads to the computer. However, RANS simulation has several problems, such as difficulty in selection of turbulence models and determination of parameter values contained in them and disadvantage in predicting the unsteady turbulent motions. Accordingly, attention is gathered on LES recently, which directly solves governing equations for relatively large eddies and calculates remaining small eddies using models. This is a sort of space averaging method and has certain advantages that the unsteady turbulent motions are evaluated and the number of parameters contained in models is reduced. Although LES poses high loads to computer compared with RANS simulation, it is likely to be applied to practical fields in near future when the progress of computer performance is taken into consideration.

The focus of this review is to highlight our recent progress of CFD of pulverized coal combustion in terms of RANS simulation and LES together with some of future perspectives. In Sec. 2, pulverized coal combustion test furnaces and a burner concerned for the present numerical simulations are described together with a brief concept of pulverized coal combustion boilers. Some of numerical results on LES and RANS are shown in Secs. 3 and 4, respectively. Finally, this review is concluded in Sec. 5.

2. Pulverized Coal Combustion Utility Boiler and Test Facilities for Basic Experiments and Numerical Simulations

In this review, numerical simulations of combustion fields in pulverized coal combustion boilers are focused on. The boiler is a system that transforms heat into steam. In general pulverized coal combustion boilers, pulverized coal is supplied from installed burners, which vertically line up at three locations, as shown in **Fig. 1**. The number of burners for a boiler is 10-40 and the coal feed rate for each burner is 10 tons/h at most. The utility boilers are generally classified into two types in terms of combustion system, namely opposed firing in which burners are placed

front and back a boiler (see **Fig. 1**) and corner firing in which burners are placed at four corners of a boiler. For these boilers, it is more important to understand the vertical flame interaction than the horizontal flame interaction, since the flames bended upward by upward main stream and buoyancy vertically affect the other flames each other.

In order to fundamentally investigate the flame interaction, CRIEPI (Central Research Institute of Electric Power Industry) utilizes a multi-burner pulverized coal combustion test furnace, in which three burners each with a coal combustion capacity of about 100 kg/h are vertically installed, at Yokosuka Research Laboratory, as shown in **Fig. 2**. The multi-burner furnace is connected to flue gas treatment equipments such as selective catalytic De-NO_x, electrostatic precipitator, gypsum limestone wet type De-SO_x, which are similar to those in utility boilers. The height, horizontal width, and depth of this furnace are 11, 0.9, and 1.9 m, respectively. Combustion air is injected into the furnace through the burner and staged combustion air ports located 2.0 m downstream from the upper-stage burner outlet. In addition, a single-burner pulverized coal combustion test furnace (see **Fig. 3**) is also used at Yokosuka Research Laboratory of CRIEPI to further understand the detailed structure of a singular flame. The coal combustion capacity of it is about 100 kg/h. The single-burner furnace is a cylindrical furnace so that the pure pulverized combustion behavior can be examined without flame bending and interaction. The diameter of this furnace is 0.85 m and the length is 8 m. Combustion air is injected into the furnace through the burner and staged combustion air ports located 3.0 m downstream from the burner. By comparing the combustion characteristics between these two test furnaces, it is expected to obtain the useful information in designing and operating the actual utility boilers.

The burner installed in the above test furnaces is the CI- α (CRIEPI-IHI Advanced Low-Pollution High-Ability) burner with a coal combustion capacity of about 100 kg/h. Pulverized coal is fed into the furnace with the primary air, and the secondary and tertiary air is supplied from the surrounding area of primary air. The CI- α burner is designed to promote mixing near the burner by means of recirculation flow produced by the straight motion of primary air and the strong swirling motion of the secondary and tertiary air (see **Fig. 4**). This recirculation flow lengthens the residence time of pulverized coal particles in the high-temperature field near the burner

outlet and accelerates the evolution of volatile matter and the progress of char reaction. Therefore, the amount of unburned carbon in fly ash is effectively reduced, but the NO_x concentration increases in this region. Then, the NO_x concentration is immediately reduced to N₂ in the reduction flame existing after the recirculation zone. Furthermore, this NO_x reduction effect is promoted by the staged combustion method, in which some of the combustion air separated from the burner is supplied via injection ports mounted on the rear of the furnace. Detailed descriptions of the CI-*a* burner and its performance can be found in our previous papers¹⁻³.

In our numerical simulations, the pulverized coal combustion fields in these single- and multi-burner furnaces with the CI-*a* burner have been simulated, since the experimental data useful for the validation of the numerical simulations are abundant for a variety of coals and combustion conditions.

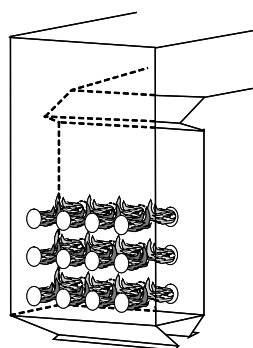


Fig. 1 Schematic of opposed firing boiler for pulverized coal combustion.



Fig. 2 Multi-burner furnace.



Fig. 3 Single-burner furnace.

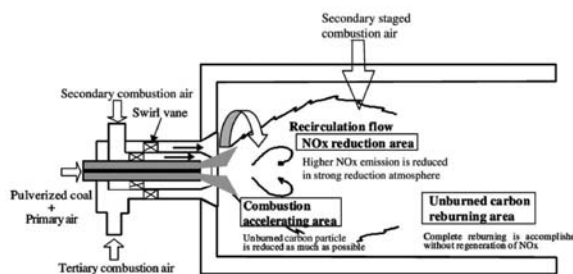


Fig. 4 Concept of CI-*a* burner.

3. Reynolds-Averaged Navier-Stokes (RANS) Simulation

3.1 RANS simulation method

The gas-phase time-averaged continuity equation and conservation equations of momentum, turbulent kinetic energy, dissipation, enthalpy and chemical species coupled with the renormalization group (RNG) *k-ε* turbulence model^{4,5} are solved using the SIMPLE algorithm⁶.

The schematic diagram of the pulverized coal combustion simplified for this calculation is shown in Fig. 5. Coal devolatilization is simulated by a first-order single reaction model (arrow (1)). Gaseous combustion between the volatilized fuel and air and the char burning rate are calculated using the combined model of kinetics and eddy dissipation models⁷ (arrows (3)-(5)) and Field et al.'s model⁸ (arrow (2)), respectively. The NO_x formation model is employed in a post-processing fashion, where a converged combustion flow field solution is first obtained before performing the NO prediction. For the formation of NO_x, three different mechanisms are employed, namely Zeldovich NO_x, prompt NO_x and fuel NO_x formation mechanisms indicated by arrows (6)-(9), respectively⁹⁻¹¹.

The details of the governing equations, mathematical models and numerical procedures for RANS simulations of pulverized coal combustion are described in our previous papers¹²⁻¹⁷.

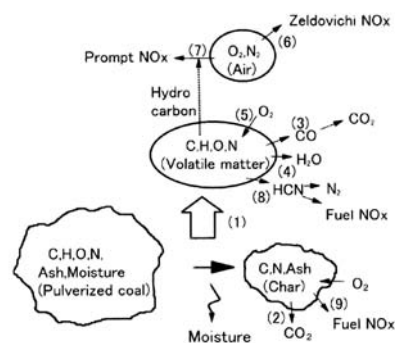


Fig. 5 Concept of pulverized coal combustion.

3.2 Effect of coal properties

Bituminous coal, whose fuel ratio is about 1.0 - 2.5, is largely used in utility boilers in Japan because of its high ignitability, high combustibility, and high calorific value. However, since the global demand for coal is considered to increase, it is desired to utilize not only the bituminous coal but also low-rank coals with high moisture and high ash contents. Therefore, it is very important to develop the numerical simulation code which can precisely capture the effect of coal properties on combustion characteristics.

(1) Numerical conditions

The simulated test furnace is the single-burner furnace with the CI- α burner. The computational domain and simplified burner geometry are shown in **Fig. 6**. A part of cylinder ($-\pi/6 \leq \theta \leq \pi/6$) is taken as the region of calculation. The feed rates of the primary, secondary and tertiary air are given to match with the actual experiments¹⁸⁻²⁰. The heat-value of coal is assumed to be equal to 2.74×10^6 kJ/h and the total flow rate of the primary, secondary and tertiary air are determined so that the excess concentration of O₂ at the outlet becomes 4 % (air ratio = 1.24). The rate of staged combustion (= volume flow rate of the staged combustion air/volume flow rate of the air for combustion) is 30%. The number of grid points is taken as $61(x) \times 58(r) \times 11(\theta)$ (the grid division in the directions of x and r are finely set in the vicinity of burner). It is assumed that the pulverized coal particles consist of particles with diameters of 5, 20, 40, 60, 80 and 100 μ m (the mean diameter of the pulverized coal is about 40 μ m).

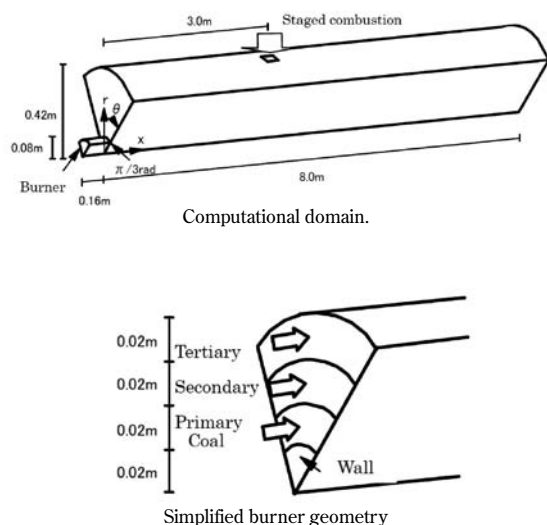


Fig. 6 Schematic of computational domain and burner.

(2) Bituminous coals

Table 1 lists the properties of five types of bituminous coal subjected to the test¹². **Fig. 7** compares the axial distributions of time-averaged gas temperature and O₂ and NO concentrations for Newlands coal with the experiments. **Fig. 8** shows the distributions of streamwise gas flow velocity, gas temperature and O₂ and NO concentrations (values of characteristic quantities increase as the color changes from blue to red). Qualitatively good agreement is shown between calculations and experiments for all distributions, which indicates that real pulverized coal combustion fields are well reproduced. The quantitative comparison of calculations and experiments, however, shows that the peak value of gas temperature of the former is higher than the latter and the temperature rapidly become lower in the downstream region than the latter. They differ in that the O₂ concentration is higher and the peak value of NO concentration is lower in the region of $x < 3$ m. Possible reasons for these differences are incomplete agreement of shape settings of furnace and burner with those in the experiments and insufficient accuracy of turbulence model in the region near the burner with strong fluid shear.

Figs. 9 and 10 compares the relationship of the unburned carbon fraction, Uc^* (proportion of unburned part for the combustible part in the coal), the combustion efficiency, $Ef (= 1-Uc^*)$ and the fuel ratio, FR (proportion of fixed carbon in the coal/proportion of volatile matters in the coal) and the relationship of the conversion of fuel N to NO, CR (proportion of N part converted to NO for N part in the coal) and FR/FN , respectively, with the experiments. It is experimentally known that Uc^* and CR increase with increasing FR and FR/FN , respectively. It is confirmed from these figures that similar increasing tendency are obtained in the calculations without any contradiction, although they show quantitative differences.

Table1 Bituminous coal properties.

Coal	Newlands	Wambo	Plateau	Workwarth	Blair Athol
Proximate analysis					
Moisture ^{*1} [wt%]	(2.2)	(3.5)	(5.9)	(1.5)	(7.9)
Volatile matter ^{*2}	28.4	35.7	41.3	31.4	29.6
Fixed carbon ^{*2}	56.4	54.6	48.8	57.5	62.5
Ash ^{*2}	15.2	9.7	9.9	11.1	7.9
Heating value [kcal/kg]	6970	7380	7170	7050	6950
(high) ^{*2}	6730	7080	6870	6770	6710
(low) ^{*2}					
Ultimate analysis					
C ^{*2} [wt%]	71.8	74.2	71.9	73.6	74.6
H ^{*2}	4.45	5.62	5.47	5.10	1.52
N ^{*2}	1.59	1.82	1.3	1.59	1.54
O ^{*2}	6.44	8.27	11.8	8.36	11.2
S ^{*2}	0.48	0.42	0.41	0.35	0.23
FR ^{*3} [-]	1.99	1.53	1.18	1.83	2.11
FR/FN ^{*4} [-]	1.25	0.84	0.91	1.15	1.37

*1: As received. *2: Dry basis. *3: Fuel ratio (Fixed carbon/Volatile matter)
*4: Nitrogen content

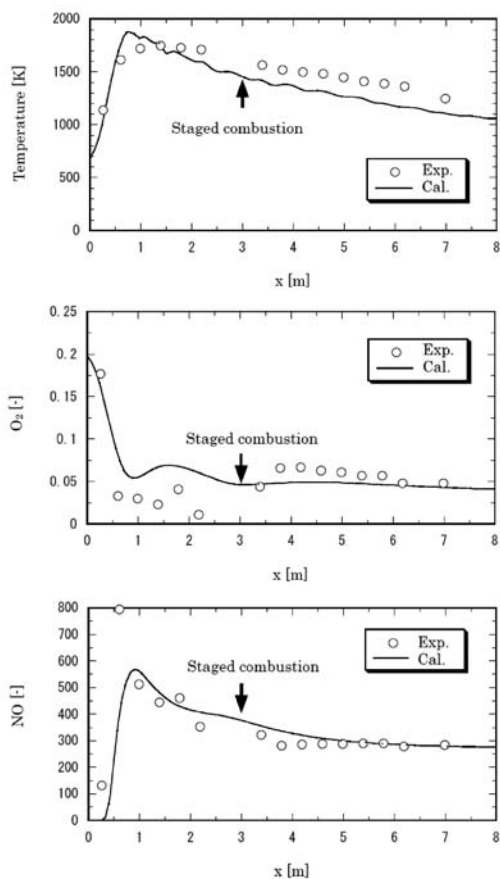


Fig. 7 Axial distributions of gas temperature and O_2 and NO concentrations (Newlands coal).

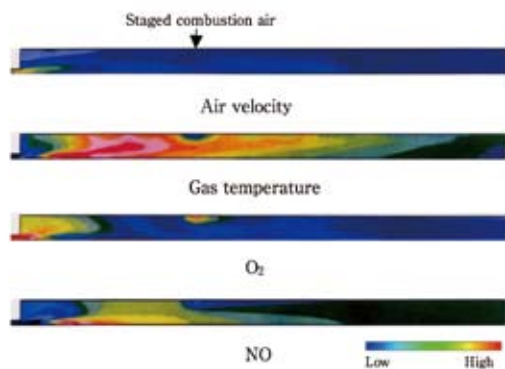


Fig. 8 Distributions of streamwise air velocity, gas temperature and O_2 and NO concentrations (Newlands coal).

(3) Effects of ash and moisture contents

Table 2 shows the coal properties of high ash coal, namely Ikeshima coal (Japanese bituminous coal), which have almost the same fuel ratio and carbon, hydrogen, nitrogen and oxygen contents on a dry ash free basis, but different ash content of 36, 44 and 53 wt%⁽¹³⁾. These samples are prepared by the floatation separation. The ash contents of the tested coals are higher than those of usual coals, which are fired in the thermal power stations in Japan. **Fig. 11**

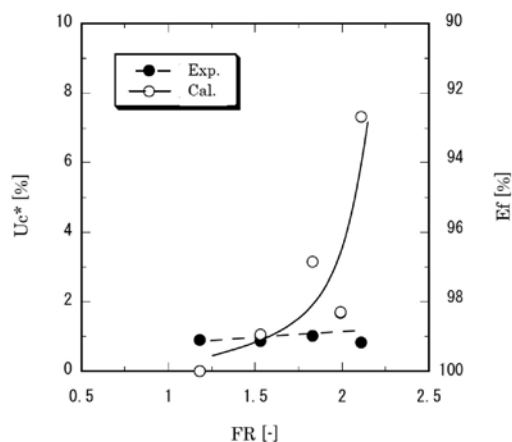


Fig. 9 Relation between Uc^* and FR .

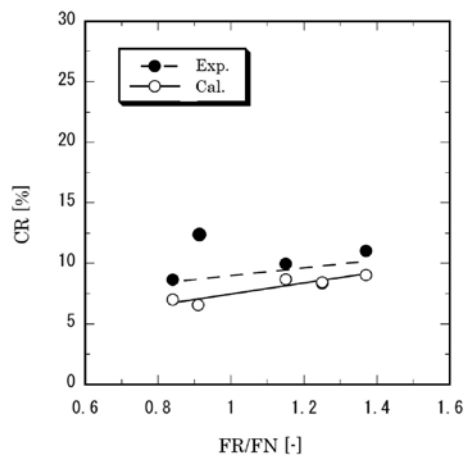


Fig. 10 Relation between CR and FR/FN .

shows the comparisons of NOx concentration and unburned carbon fraction, Uc^* , at the furnace exit with the experiments. The numerical trends are found to be in general agreement with the experiments. As the ash content increases, both the NOx concentration and Uc^* at the furnace exit increase. The results suggest that the present numerical simulation for the pulverized coal combustion is applicable for the pulverized coal combustion at least to know the qualitative effects of the ash. It is considered that the discrepancies between calculations and experiments are probably due to that the shapes of the furnace and the burner modeled in the calculations are not completely the same as those of the experiments and that turbulence model used are not sufficient, as described earlier. Also, compared to the experiments, the calculated Uc^* at the furnace exit is low especially for high ash content coals [**Fig. 11 (b)**]. It is speculated that this is attributed to the fact that the interaction between ash and combustible matter is not taken into account for the numerical model of char oxidization. To estimate these combustion char-

acteristics for high ash content coal more precisely, the char oxidization model, which takes the presence of ash into account, should be proposed.

To investigate the effects of the moisture in the coal, Kimoto et al.²⁰ imitatively increases the moisture content by injecting the steam generated by a steam-generation apparatus into the primary air. Therefore, numerical simulations in the same conditions are performed. It should be noted here that contrary to the introduction of coal moisture, the consumption of the latent heat of vaporization of the moisture is not necessary in this case. The test fuel is Newlands bituminous coal. The equivalent moisture content, MC (= mass of the moisture content in the coal/mass of the coal (dry basis) $\times 100$), are varied as 0, 17.6 and 42.8. Newlands coal originally contains 2.20 moisture, but the original 2.20 moisture is vapor-

ized through a pulverizer and the steam is removed. The present computations are carried out for $MC = 0, 20$ and 40 , and all the moisture in the coal is assumed to evaporate in transit to the furnace¹⁴). In **Fig. 12**, the variations of unburned carbon fraction, Uc^* , and NOx conversion, CR , at the outlet of the furnace are shown against MC , together with the experiments. It is found that Uc^* and CR for $MC = 0$ well correspond to the experiments, and that the increase of MC leads an increase in Uc^* and decrease in CR . These trends are similar to those given by the experiments although the effect of MC on Uc^* is weaker in these predictions than in the experiments. Although the difference in Uc^* is considered to be caused by the deficiency of the application of the char burning model used here, the model with higher accuracy has not been proposed yet.

Table2 High ash coal properties.

		Ikeshima-A (ash 36%)	Ikeshima-B (ash 44%)	Ikeshima-C (ash 53%)
Proximate analysis	Moisture ^a (%)	2.7	3.0	2.6
	Ash ^b (%)	36.0	44.4	52.6
	Volatile matter ^b (%)	30.5	26.6	22.9
	Fixed carbon ^b (%)	33.5	29.0	24.5
	Fuel ratio (%)	1.10	1.09	1.07
Ultimate analysis ^c	Carbon (%)	80.5	79.0	78.7
	Hydrogen (%)	7.5	7.9	8.0
	Nitrogen (%)	1.1	1.1	1.1
	Oxygen (%)	9.6	10.1	10.1
	Total sulfur (%)	1.5	1.8	2.3
	Combustible sulfur (%)	1.4	1.7	2.0
Heating value (low) ^b (MJ/kg)		20.9	18.4	14.8

^a Equilibrium moisture basis of coal at 75% relative humidity and room temperature.

^b Dry basis.

^c Dry ash free basis.

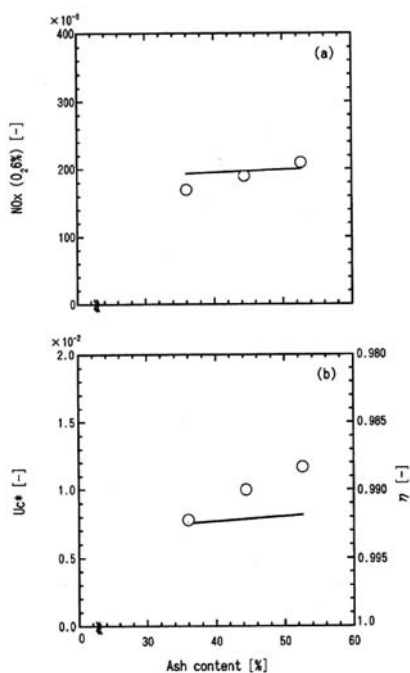


Fig. 11 Effects of ash content on NOx concentration and Uc^* ; \circ , experiment; —, calculation.

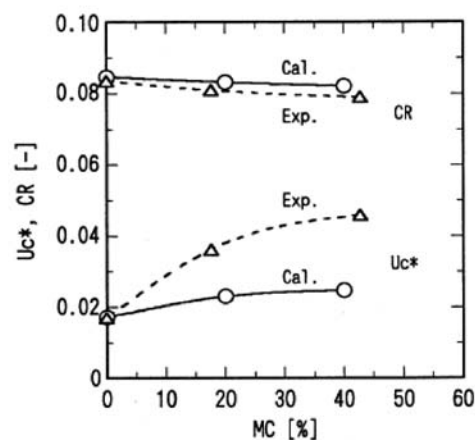


Fig. 12 Effects of moisture on Uc^* and CR .

3.3 Application to complex geometries

Although numerical simulations of the pulverized coal combustion fields have been conducted by many researchers, most of the burner geometries are strongly simplified as shown earlier, in spite of the fact that subtle differences in the burner shape significantly affect the coal combustion characteristics. Hence, the geometries of single- and multi-burner furnaces which install the CI- α burners are faithfully duplicated.

(1) Single-burner furnace

The test furnace considered is the single-burner furnace with CI- α burner. The numerical procedure and conditions are the same as those described earlier. The geometries of the computational domain and the CI- α burner are shown in **Fig. 13**. These are designed to faithfully match the actual geometries¹⁵⁾. The computational domain is half of the furnace, and a periodic condition is applied in the azimuthal direction. The swirl vane angles for secondary and tertiary air are set at 81° and 72°, respectively, which are optimum values for bituminous coal (these values are zero when the swirl force is zero). **Fig. 14** shows the predicted gas velocity vectors in the CI- α burner and near the burner. It is observed that the secondary and tertiary combustion air introduced from the outside in the normal direction are shifted in the azimuthal direction by swirl vanes and the swirling velocity reaches up to 30 m/s. Also, as expected from the previous experiment for coal flow using NO tracer gas²⁾, recirculation flow can be seen in the region near the burner. The swirling air, which is ejected along the burner throat with the maximum velocity of about 18 m/s, is divided into upstream and downstream flows near the side wall, and small recirculation flow around the burner (arrow A) and large recirculation flow in the central region along the z-axis (arrow B) are formed. **Fig. 15** show the comparison of axial distributions of gas temperature and chemical species concentrations. Overall, the calculated axial distributions of gas temperature and O₂ concentration are in better agreement with the experiments than those in the simplified-shape case (see **Fig. 7**), although there are some quantitative discrepancies, for example, the predicted gas temperature rises earlier and higher, the O₂ concentration shows larger values around the region just after the position where staged combustion air is injected. Although the figure is omitted here, it was found that the prediction of the NO_x concentration is improved compared to the simplified-shape case¹⁵⁾ and that

present numerical method can capture the general combustion characteristics of high-fuel-ratio coals¹⁶⁾.

(2) Multi-burner furnace

RANS simulation is also applied to a pulverized coal combustion field in the multi-burner furnace with three CI- α burners. The geometries of the computational domain is shown in **Fig. 16**. The swirl vane angles for secondary and tertiary air are set at 72° and 63°, respectively, which are optimum values for bituminous coal (these values are zero when the swirl force is zero). The thermal input of the coal combustion test furnace is 8.62×10^6 kJ/h (the coal feed rate for each burner is approximately 100 kg/h). The air ratio is 1.24, and the excess O₂ concentration at the furnace outlet is 4%. The staged combustion air ratio is set at 30%. The mass ratio of the pulverized coal (dry base) to the primary air is 1:2.2, and the mass ratio of secondary air to tertiary air is 1:6. Bituminous coal (i.e., Newlands coal) is chosen for the test fuels. **Fig. 17** shows the comparisons of distributions of gas temperature and chemical species concentrations between calculations and experiments²¹⁾. On the whole, simulated and experimental contour plots are consistent qualitatively, although there are some quantitative discrepancies, which might be caused by the deficiency of RANS simulation. Although the details are omitted here, this study also suggested the possibility that overall unburned carbon fraction of coal-fired plants can be reduced by supplying coal with a low combustibility to the middle- or lower-stage burner and supplying coal with a high combustibility to the upper-stage burner.

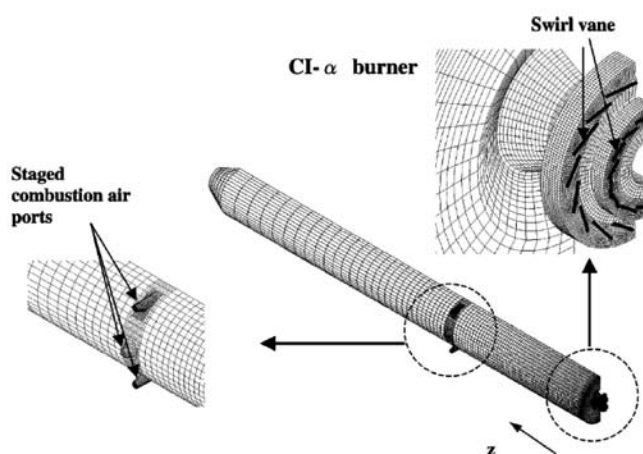
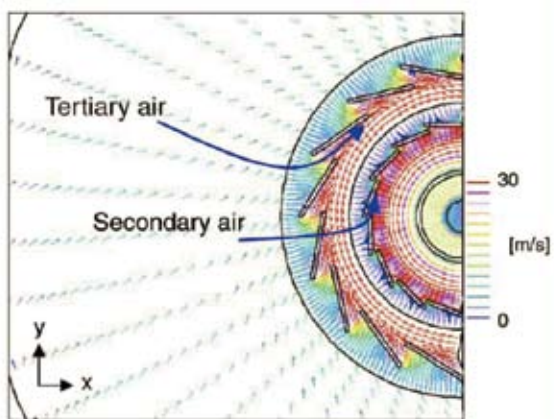
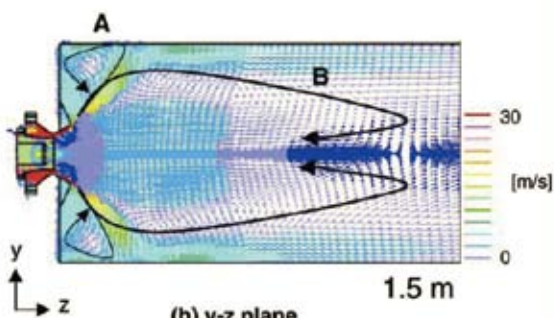


Fig. 13 Schematic of computational domain of single-burner furnace and CI- α burner.

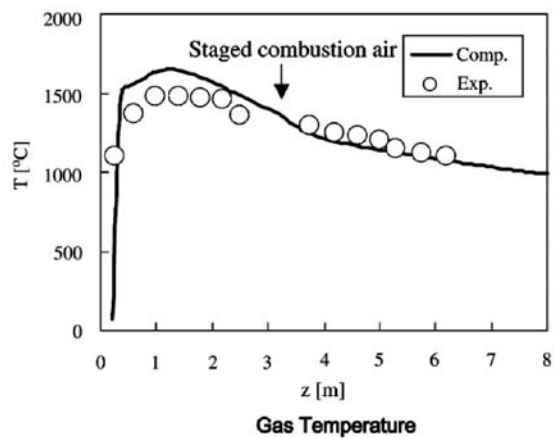


(a) x-y plane

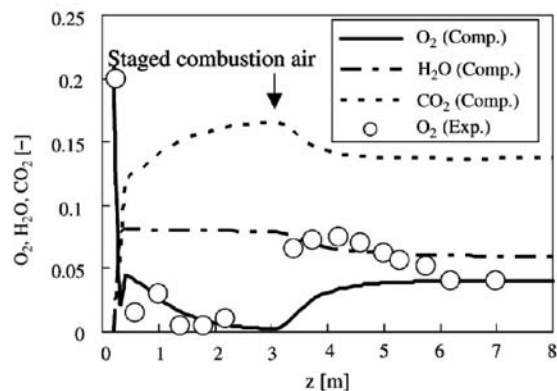


(b) y-z plane

Fig. 14 Gas velocity vectors in and near the CI- α burner (Newlands coal).



Gas Temperature



O₂, H₂O, CO₂ mole fractions

Fig. 15 Axial distributions of gas temperature and O₂, H₂O and CO₂ concentrations (Newlands coal).

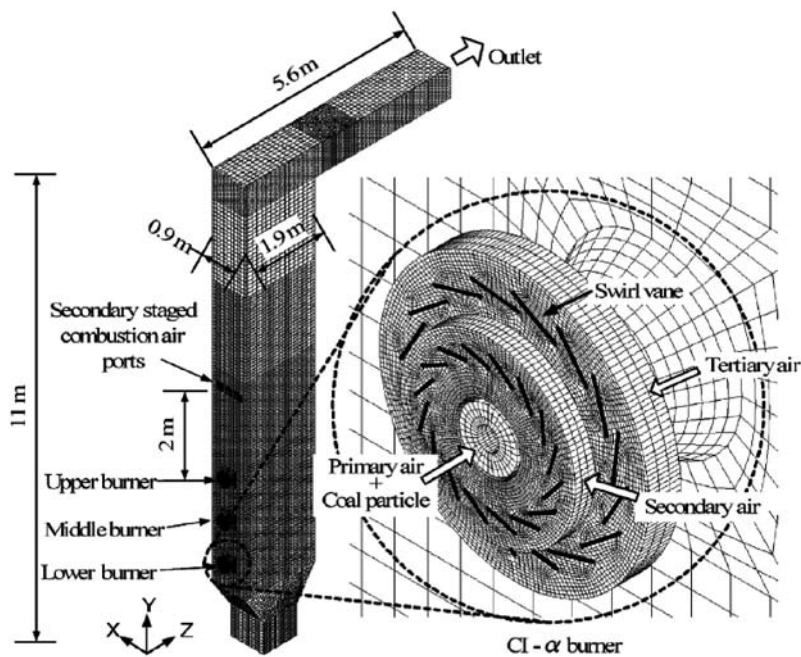


Fig. 16 Schematic of computational domain of multi-burner furnace and CI- α burner.

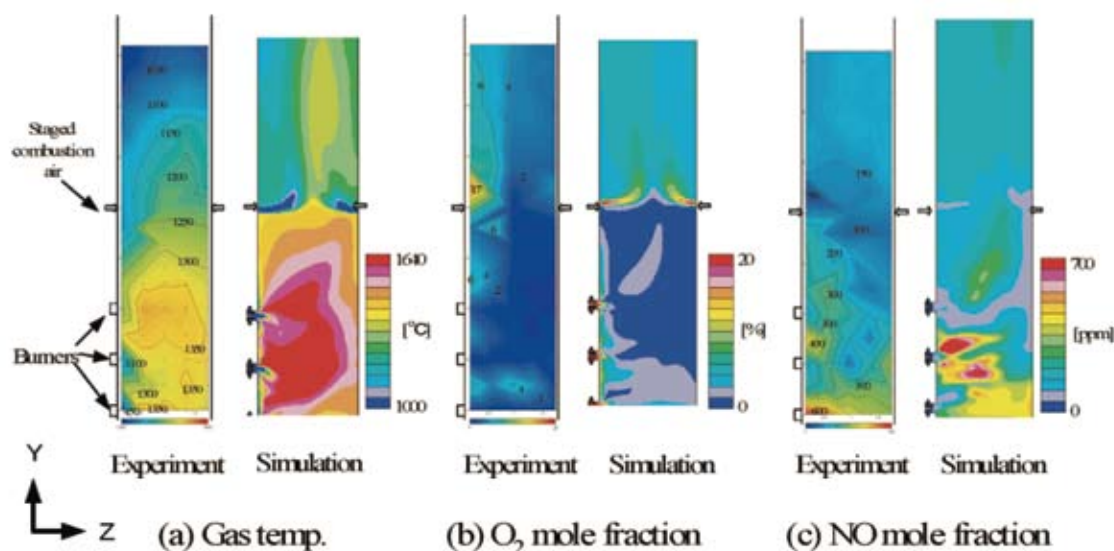


Fig. 17 Distributions of gas temperature and O₂ and NO concentrations (Newlands coal).

4. Large-Eddy Simulation (LES)

4.1 LES method

One of the LES solvers used here is the Front-Flow/red for unstructured grids, which has been originally developed at the Institute of Industrial Science of the University of Tokyo in the Frontier Simulation Software for Industrial Science project as a part of the IT program sponsored by the Ministry of Education, Culture, Sports, Science and Technology (MEXT), extended by CRIEPI, Kyoto University, and NuFD (Numerical Flow Designing, LTD). This solver is based on the SMAC/SIMPLE algorithms and the Finite Volume Method (FVM) with an unstructured grid system. The gas-phase continuity equation and conservation equations of momentum, enthalpy and species coupled with the dynamic Smagorinsky model^{22,23)} are solved. The mathematical models for the pulverized coal combustion are basically the same as those used in RANS simulation, as described earlier. The cold and combusting flow fields in the single-burner furnace with the CI- α burner are considered. The geometries of the computational domain and the CI- α burner are designed to faithfully match the actual geometries, as shown in Fig. 18. The swirl vane angles for secondary and tertiary air are set at 81° and 72°, respectively. The computational domain is divided in about 450,000 tetrahedral volumes with cone-shaped clustering on burner downstream for both LES and RANS simulation.

The details of the governing equations, mathematical models and numerical procedures for LES of pulverized coal combustion are described in our previ-

ous papers²⁴⁻²⁶⁾.

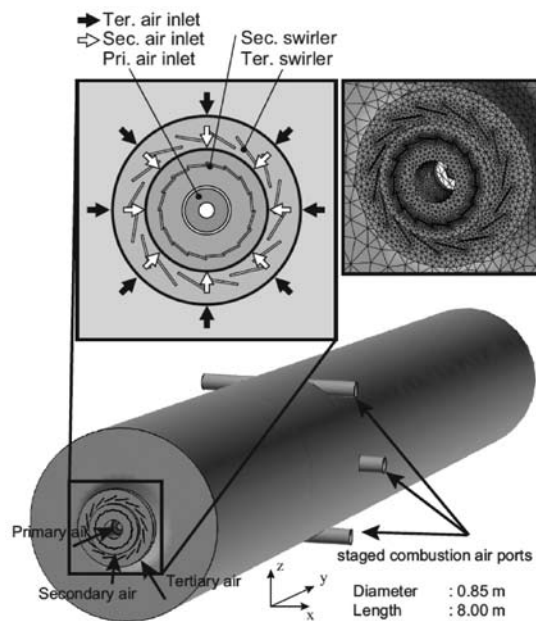


Fig. 18 Schematic of computational domain of single-burner furnace and CI- α burner.

4.2 Comparison between LES and RANS simulation

In order to verify the superiority of LES in capturing turbulent swirling flow behavior, LES results for the swirling cold (non-combusting) flows in the pulverized coal combustion furnace are compared with RANS simulation results using the same computational grid and the experiments²⁵⁾. In the experi-

ments, instantaneous streamwise and azimuthal air velocities are measured using the Ar Laser two-dimensional multi-scan Laser-Doppler velocimeter.

Fig. 19 shows the comparisons of distributions of axial velocity, U_z , on the flow direction plane and azimuthal velocity, U_θ , on the cross section plane at $z = 0.235$ m between LES and RANS simulation. Here, the distributions are shown by instantaneous value for LES and time-averaged value for RANS simulation, respectively. The deviation from the axisymmetric flow formed in the time-averaged flow field is observed in the instantaneous U_z distribution for LES. This deviation originates from the vortices created in the region near the burner outlet. It is also found that in the recirculation flow formed near the burner outlet, the backward flow velocity (negative U_z) for LES is smaller than that for RANS simulation. In addition, the outer positive U_z region does not expand to downstream near the side wall for LES, while it is remarkable for RANS simulation. Also, the region showing the ring-shaped large U_θ is less for LES than that for RANS simulation, which means that the swirling flow and the related recirculation flow for LES are weaker than those for RANS simulation.

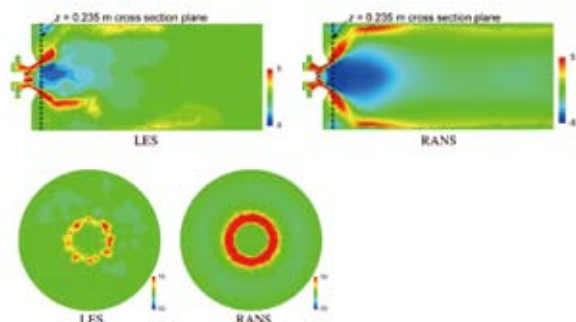


Fig. 19 Distributions of U_z on the flow direction plane (upper) and U_θ on the cross section plane at $z = 0.235$ m (lower).

Fig. 20 shows the comparisons of radial distributions of time-averaged axial velocity, U_z , and azimuthal velocity, U_θ at $z = 0.235$ m among LES, RANS simulation and experiments. Here, for the experiments, measured data in the entire range of the diameter is displayed. It should be noted here that since the secondary and tertiary air cannot be injected uniformly along the circumferential direction due to the limitation of the experimental equipment, the complete axisymmetric flow is not observed in the furnace. Therefore, although the detailed quantitative discussion cannot be done here, the behavior of the recirculation flow formed at $r = 0.015 - 0.12$ m for LES is similar to that for the experiments. On the other hand, the backward flow velocity of the recircu-

lation flow for RANS simulation is much larger than that for the experiments. Also, in the region where the peak value of U_θ appears around $r = 0.14$ m, U_θ for LES is slightly higher than that for the experiments, while U_θ for RANS simulation is about three times higher. From these comparisons, it is revealed that LES is much superior to RANS simulation to predict the axial velocity in the recirculation flow formed in the swirling flow and the azimuthal velocity around this recirculation flow. The superiority of LES to capture the behavior of the swirling and recirculation flows is considered due to the accuracy in predicting the momentum exchange in the strong shear flow, namely the mixing effect by the turbulence. It was also confirmed that the r.m.s. of axial velocity for LES is in general agreement with the experiments and that these superiority of LES is similarly observed in the cases where the swirl vane angles for secondary and tertiary air are changed.

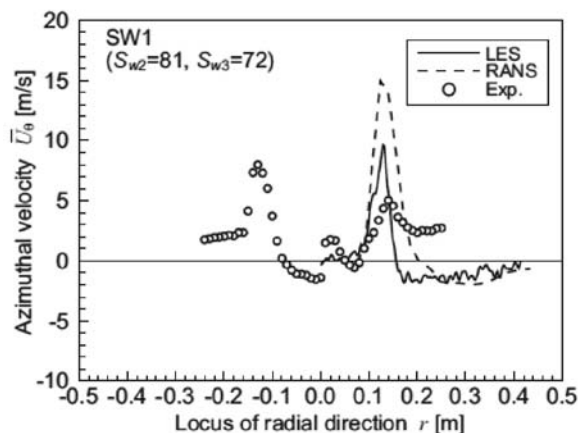
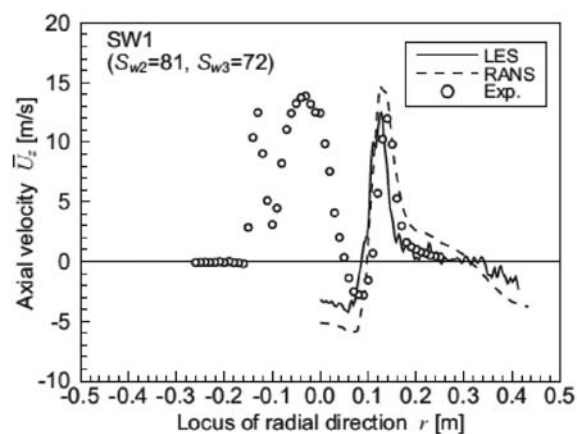


Fig. 20 Radial distributions of U_z and U_θ .

4.3 Challenges to pulverized coal combustion field

Very recently, LES has been applied to an actual pulverized coal combustion field in the single-burner furnace with the CI- α burner²⁶⁾.

Fig. 21 shows the predicted distributions of instantaneous axial velocity, gas temperature and O₂ concentration on the flow direction plane. It is observed that a swirling recirculation flow is formed in the central region close to the burner and its size and strength dynamically change with time. Also, this unsteady flow behavior strongly affects the ignition characteristics. **Fig. 22** shows the comparisons of axial distributions of time-averaged gas temperature and O₂ concentration between calculations and experiments^{18,27)}. The predicted distributions qualitatively agree with the experiment. Thus, unlike RANS simulation, LES can precisely capture this unsteady combusting flow motion, whose nature has a potential to greatly improve the numerical accuracy. In addition, LES has an advantage that the number of model parameters is much less than that for RANS simulation. However, for the LES of the pulverized coal combustion, there remain difficult challenges in terms of not only mathematical models on turbulent combustion and pollutant emissions but also computational costs.

5. Conclusions

In this review, our recent progress of Computational Fluid Dynamics (CFD) of pulverized coal combustion is discussed in terms of RANS (Reynolds-Averaged Navier-Stokes) simulation and LES (Large-Eddy Simulation). It can be said that regarding the

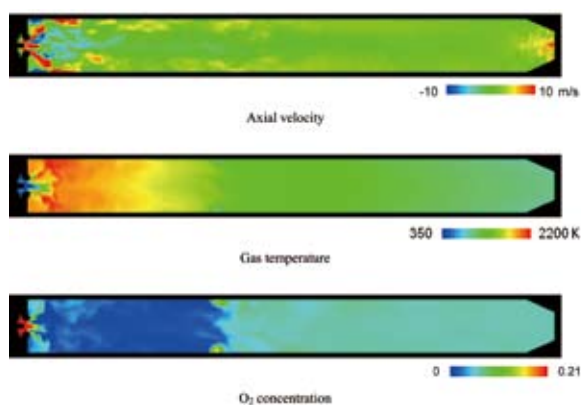


Fig. 21 Distributions of instantaneous axial velocity, gas temperature and O₂ concentration on the flow direction plane.

prediction of flow field, LES is much superior to RANS simulation and therefore expected to become a useful tool for the development and design of new combustion furnaces and burners in near future. However, the combustion of pulverized coal is a complicated phenomenon in which a wide variety of processes such as the devolatilization of pulverized coal, combustion of volatile matters and combustion at the surface of particles, in addition to the dispersion behavior of pulverized coal in the gas stream, simultaneously act to each other. Therefore, the pulverized coal combustion behavior is not fully understood and modeled yet. In particular, coal devolatilization model is found to strongly affect the numerical accuracy recently²⁸⁾. The improvement of turbulent combustion model is also necessary. The more sophisticated turbulent combustion model, in which the detailed reaction mechanism can be taken into consideration such as flamelet models often used for gaseous and spray combustion²⁹⁻³²⁾, is desirable. Furthermore, the application of LES to much larger and more complicated fields such in utility boilers is challenges in terms of numerical stability, accuracy and costs.

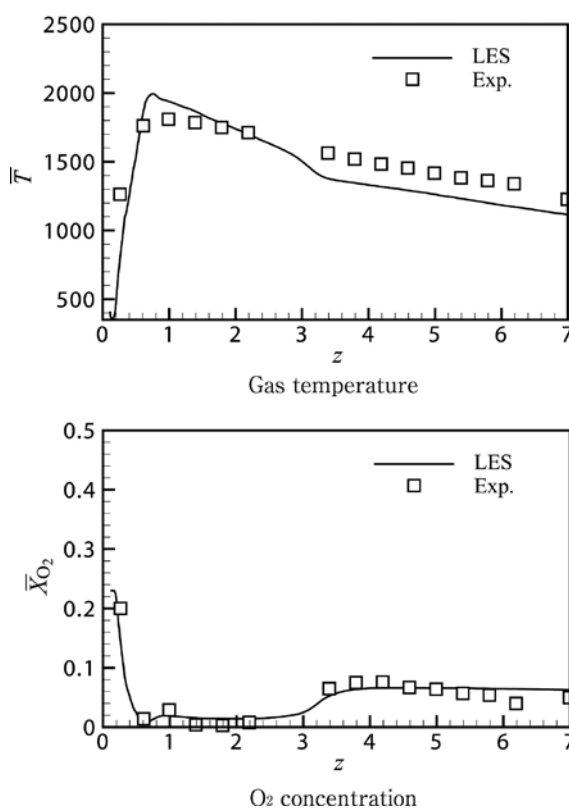


Fig. 22 Comparisons of axial distributions of time-averaged gas temperature and O₂ concentration between calculations and experiments.

Reference

- 1) Makino, H., and Kimoto, M. (1994): Low NO_x Combustion technology in pulverized coal combustion, *Kagaku Kogaku Ronbunshu*, 20, pp. 747-757.
- 2) Makino, H., Kimoto, M., Kiga, T., and Endo, Y. (1997): Development of new type low NO_x burner for pulverized coal combustion, *The Thermal and Nuclear Power*, 48, pp.702-710.
- 3) Makino, H., and Ikeda, M. (2001): The development of low NO_x combustion technology for various kinds of pulverized coal, In Proc. of 6th World Congress of Chemical Engineering, CD-ROM.
- 4) Yakhot, V., and Orszag, S. A. (1986): Low-Reynolds number approximation for turbulent eddy viscosity, *Journal of Scientific Computing*, 1, pp. 1-51.
- 5) Yakhot, V., Orszag, S. A., Thangam, S., Gatski, T. B., and Speziale, C. G., Development of turbulence models for shear flows by a double expansion technique, *Physics of Fluids*, 1992. A4, p. 1510-1520.
- 6) Patankar, S.V. (1980): "Numerical heat transfer and fluid flow", New York, Hemisphere.
- 7) Magnussen, B. F., and Hjertager, B. W. (1976): On the mathematical modeling of turbulent combustion with special emphasis on soot formation and combustion, In Proc. of 16th Symposium (International) on Combustion, Pittsburg, PA, The Combustion Institute, pp. 719-729.
- 8) Field, M. A. (1969): Rate of combustion of size-graded fractions of char from a low rank coal between 1200 K-2000 K, *Combustion and Flame*, 13, pp.237-252.
- 9) De Soete, G. G. (1975): Overall reaction rates of NO and N₂ formation from fuel nitrogen, In Proc. of 15th Symposium (International) on Combustion, Pittsburg, PA, The Combustion Institute, pp.1093-1102.
- 10) De Soete, G. G. (1990): Heterogeneous N₂O and NO formation from bound nitrogen atoms during coal char combustion, In Proc. of 23th Symposium (International) on Combustion, Pittsburg, PA, The Combustion Institute, pp. 1257-1264.
- 11) Levy, J. M., Chan, L. K., and Beer, J. M. (1981): NO/Char reactions at pulverized coal flame conditions, In Proc. of 18th Symposium (International) on Combustion, Pittsburg, PA, The Combustion Institute, pp.111-120.
- 12) Kurose, R., Tsuji, H., and Makino, H. (2001): Numerical simulation of pulverized coal combustion in a furnace (Effect of moisture on coal on combustion characteristics), *Trans. of JSME (B)*, 67, pp.210-218.
- 13) Kurose, R., Ikeda, M., and Makino, H. (2001): Combustion characteristics of high ash coal in a pulverized coal combustion, *Fuel*, 80, pp.1447-1455.
- 14) Kurose, R., Tsuji, H., and Makino, H. (2001): Effects of moisture in coal on pulverized coal combustion quantities, *Fuel*, 80, pp.1457-1465.
- 15) Kurose, R., Makino, H., and Suzuki, A. (2004): Numerical analysis of pulverized coal combustion characteristics using advanced low-NO_x burner, *Fuel*, 83, pp.693-703.
- 16) Kurose, R., Ikeda, M., Makino, H., Kimoto, and M., Miyazaki, T. (2004): Pulverized coal combustion characteristics of high fuel ratio coals, *Fuel*, 83, pp.1177-1785.
- 17) Hashimoto, N., Kurose, R., Tsuji, H., and Shirai, H. (2007): A numerical simulation of pulverized coal combustion in a multi-burner furnace, *Energy & Fuels*, 21, pp.1950-1958.
- 18) Makino, H. (1995): "Emission characteristics and reduction technology for NO_x and unburned carbon fraction on pulverized coal combustion", Doctoral Dissertation (Kyoto University).
- 19) Ikeda, M., Kimoto, M., Miyazaki, T., and Makino, H. (1997): Influence of ash content on pulverized coal combustion characteristics - Combustion characteristics on high ash content coal investigated by coal combustion test furnace -, CRIEPI Report, W97023.
- 20) Kimoto, M., Ikeda, M., Miyazaki, T., and Makino, H. (1998): Influence of moisture in coal on pulverized coal combustion characteristics - Combustion characteristics of high moisture content coal investigated by coal combustion test furnace -, CRIEPI Report, W98002.
- 21) Tsuji, H., Kotsuji, T., Ikeda, M., and Shirai, H. (2006): Development of total evaluation system of coal for pulverized coal combustion and flue gas treatment (part 1) - Comparison between fly ash property of combustion test furnace and that of actual power station -, CRIEPI report, M05006.
- 22) Moin, P., Squires, K., Cabot, W., and Lee, S. (1991): A dynamic subgrid-scale model for compressible turbulence and scalar transport, *Physics of Fluids*, A 3, pp.2746-2757.
- 23) Pierce, C. D., and Moin, P. (1998): A dynamic model for subgrid-scale variance and dissipation rate of a conserved scalar, *Physics of Fluids*, 10, pp.3041-3044.
- 24) Kurose, R., and Makino, H. (2003): Large-eddy simulation of a solid-fuel jet flame, *Combustion and Flame*, 135, pp.1-16.
- 25) Watanabe, H., Kurose, R., and Komori, S. (2009): Large-eddy simulation of swirling flows in a pulverized coal combustion furnace with a complex burner, *Journal of Environment and Engineering*, 4, pp.1-11.
- 26) Watanabe, H., Tanno, K., Kurose, R., and Komori, S. (2009): Large-eddy simulation of coal combustion in a pulverized coal combustion furnace with a complex burner, *Turbulence, Heat and Mass Transfer 6* (Edited by K. Hanjalic', Y. Nagano, and S. Jakirlic') pp.1027-1030.
- 27) Kimoto, M., Makino, Tsuji, H., and Ikeda, H. (1994): Development of new pulverized coal burner for low NO_x and low unburned carbon combustion technology (Part 5), CRIEPI Report, W94013.
- 28) Hashimoto, N., Kurose, R., and Shirai, H. (2007): Numerical simulation of a pulverized coal combustion in a Furnace (Part 4) - Development of the model employing tabulated devolatilization process-, CRIEPI

- Report, W07006.
- 29) Peters, N. (2000): "Turbulent combustion", Cambridge University Press, Cambridge.
- 30) Watanabe, H., Kurose, R., Hwang, H.-S., Akamatsu, F. (2007): Characteristics of flamelet in spray flames formed in a laminar counterflow, *Combustion and Flame*, 148, pp.234-248.
- 31) Ihme, M., and Pitsch, H. (2008): Modeling of radiation and nitric oxide formation in turbulent nonpremixed flames using a flamelet/progress variable formation, *Physics of Fluids*, 20, 055110.
- 32) Baba, Y., and Kurose, R. (2008): Analysis and flamelet modeling for spray combustion, *Journal of Fluid Mechanics*, 612, pp.45-79.

Author's short biography



Ryoichi Kurose

Dr. Ryoichi Kurose is an Associate Professor of Department of Mechanical Engineering and Science at Kyoto University. He received a Ph.D. in Chemical Engineering from Kyushu University in 1998. He was previously employed at CRIEPI (Central Research Institute of Electric Power Industry) in Kanagawa, Japan as a Research Associate in the coal combustion group. His research interests are in turbulence and transport phenomena appearing in environmental and industrial flows. Main current subjects are interfacial air-water two-phase flows, dispersed two-phase flows, chemical reacting flows and combusting flows.



Hiroaki Watanabe

Dr. Hiroaki Watanabe is a Research Scientist of CRIEPI (Central Research Institute of Electric Power Industry) in Kanagawa, Japan. He received a M.E. degree in Mechanical Engineering from Waseda University in 1998 and a Ph.D. in Mechanical Engineering and Science from Kyoto University in 2008. Dr. Watanabe was employed at CRIEPI in 1998 as a Research Associate in the coal gasification group. Currently, his main research subjects are in computational energy sciences. This includes analysis and modeling of multiphase reaction phenomenon taking place in coal and spray combustion and gasification with RANS, LES and DNS.



Hisao Makino

Dr. Hisao Makino is an Associate Vice President of CRIEPI (Central Research Institute of Electric Power Industry) in Japan and a Deputy Director of Energy Engineering Research Laboratory of CRIEPI. He graduated from Kyoto University in 1977 and received a M.E. degree in Chemical Engineering from Kyoto University in 1979 and a Ph.D. in Chemical Engineering from Kyoto University in 1995. Dr. Makino was employed at CRIEPI in 1979 as a Research Associate in combustion research section. His research interests are powder technology and coal utilization technology for the energy supply and environmental protection. Main current subjects are an advanced combustion technology for pulverized coal, upgrading technology for low rank coal and flue gas treatment technology.

The Improvement and Upscaling of a Laser Chemical Vapor Pyrolysis Reactor[†]

Jan van Erven^{1*}, David Munao¹, Zhao Fu², Tomek Trzeciak³, Reyer Janssen³, Erik Kelder¹ and Jan C. M. Marijnissen¹

TU Delft, NanoStructured Materials¹

TU Delft, DEMO²

University of Exeter, Electromagnetic materials group³

Abstract

In this work, a new laser Chemical Vapor Pyrolysis (LaCVP) reactor is presented. The concepts behind the new reactor's design aim to improve and scale up the production of powders compared to conventional used laser CVP systems. For these purposes, the reaction zone has been studied in relation to the nozzle and the laser beam geometry. As a result, a new reaction zone comprising a rectangular nozzle and rectangular laser beam has been developed. The new reactor, including the new reaction zone, has great flexibility towards different type of materials that can be produced. Moreover, the advanced design of the reactor allows flexibility towards the use of various types of equipment, such as, nozzles, hoods, sampling equipment, etc.

First encouraging results of silicon synthesis using the new reactor are presented. The silicon nanoparticles were synthesized from silane (SiH₄) precursor in a N₂ atmosphere. The products have been characterized with TEM, XRD, TGA and FTIR analyses and compared with a commercial available one (Aldrich). The synthesized products show a narrow size distribution and small particle size, in comparison with the commercial material. Future work will include the further development of the system and investigation of the role of the experimental parameters on the product characteristics.

Keywords: Aerosol synthesis, laser CVP, nanoparticles, silicon, upscaling

1. Introduction

The discovery of novel materials, processes, and phenomena at the nanoscale, as well as the development of new experimental techniques for research provide fresh opportunities for the development of innovative systems and nanostructured materials. Nanostructured material can be made with unique nanostructures and properties¹. These new and advanced properties can be achieved when the product has specific size and morphological characteristics. Often, the requirements are that the nanoparticles have a spherical form, a narrow size distribution, are

highly pure and are not aggregated.

The generation of nanoparticles can be carried out by various liquid- and gas-phase processes. Liquid-phase processes usually involve a bottom-up approach, combining different techniques such as electro deposition², reductive precipitation³, hydrothermal and sol-gel syntheses^{4,5}. Wet routes can offer flexibility, but also introduce a higher probability of contamination and the need for separation/purification processes, which drastically increase the production costs and cause environmental pollution. Gas-phase processes are known to produce highly pure nanoparticles in a clean and efficient way. Industrially commercialized processes are the flame processes for the production of, for example, titania and carbon black⁶. Other types of gas-phase processes such as plasma⁷, spark discharge⁸ and tube furnaces⁹ have already been used for quite a while on a lab scale but are not yet implemented industrially. Extensive research has been done on the production of nanoparti-

[†] Accepted: September 25th, 2009

¹ Julianalaan 136,2628 BL, Delft, the Netherland

² Makeling 1,2628 BL, Delft, the Netherland

³ Stocker Road, Exeter, UK, EX44QL

* Corresponding author

E-mail: janvanerven@hotmail.com

TEL: (+31) 15-2783568, FAX: (+31) 15-2784945

cles using flame spray pyrolysis systems by Pratsinis and co-workers. They developed a scaled-up system with production rates of 200 g/hr¹⁰. A process that is capable of producing highly pure, non-aggregated and non-oxidized particles, with the potential to be scaled-up is the laser chemical vapor pyrolysis (laser CVP) process.

Laser CVP is a very suitable gas-phase process for the synthesis of a wide range of nanoparticles. The synthesis of nanoparticles by laser pyrolysis was developed at the Massachusetts Institute of Technology (MIT) at the beginning of the 1980s by Haggerty and Cannon^{11,12}. The process is based on the resonant absorption of a laser beam wavelength by the precursor gas. It is important to note that if nanoparticles are to be produced efficiently by laser pyrolysis it is necessary to use at least one reactant with an absorption band close to that of the laser emission wavelength. Despite this limitation, a wide variety of materials has already been produced via this technique such as: carbon clusters¹³, fullerenes¹⁴, metallic compounds (e.g. nickel¹⁵, iron¹⁶), oxidic compounds (e.g. iron oxide¹⁷, titania¹⁸, alumina¹⁹, silica²⁰), ceramic materials (e.g. nitrides²¹, carbides²²) and semiconductors (e.g. silicon^{23,24}). It is clear that this technique can offer a huge versatility toward products, and consequently, to the final application for which the material has been designed.

During the past two decades of research, laser CVP was also conducted extensively at TU Delft^{21, 25-27}. Although the previous systems proved to be viable to produce nanoparticles, the particles were neither uniform in size or composition. The non-uniformity originates from the non-uniform conditions inside the reaction zone, which is the intersection between laser beam and gas flow. Production rates of the studied systems were in the grams-per-hour range, but the system has a potential to be scaled-up to higher industrial rates.

The goal of the current research was to improve powder characteristics and to scale-up the production rate of the laser CVP process. In this paper, the results of the research are presented. The most remarkable achievement is the quality improvement accomplished with a newly designed reaction zone.

Although not all capabilities of the new reactor have been explored, some first encouraging results are presented. The material that was produced and characterized constitutes silicon nanoparticles. Silicon was chosen because it is of increasing interest, both in academic and industrial environments. This is due to its potential of being used in applications,

e.g. energy storage and conversion, biomedical, sensors and electronics²⁸⁻³¹. Two interesting samples are highlighted and compared with a commercial silicon sample.

2. Laser CVP Process

In laser chemical vapor precipitation, also called laser pyrolysis, a laser is employed as a heating source to produce particles. It is a gas-phase process in which precursor gases or vapors are heated by absorbing the energy of a laser beam. The process has been mostly used in conjunction with a CO₂ laser and, specifically, with its 10.6- μ m emission wavelength. A first requirement of this process is that the absorption band of at least one of the precursors is close to the emission band of the laser. This process is unique compared to other processes that use conventional heating sources where the heat from the source to the gas molecules is transported by a combination of conduction, convection and radiation processes.

In the case that none of the bands of the precursors overlap with the laser emission band, a sensitizer gas can be used. The sensitizer absorbs the energy and transfers it to the reactants by molecular collisions without playing a role in the decomposition or reactions. Sulfurhexafluoride (SF₆) was, for example used in the production of silicon nitride (Si₃N₄) from tetrachlorosilane (SiCl₄) vapors³², or in the production of nickel nanoparticles from nickelcarbonyl (Ni(CO)₄) vapor¹⁵.

The precursor gas flow is intersected by a laser beam, thus creating a well-defined and wall-free reaction zone. In the reaction zone, the precursors are heated extremely fast due to the unique heating process. The residence time in the beam, controlled by the flow rate and height of the laser beam, is in the order of several milliseconds with a heating rate in the order of 10⁶°C/s. In this short time, the precursors decompose and a reaction can occur if two or more precursors are used. The product molecules form nuclei, due to supersaturation, and grow in size. This process is stopped as the hot particles and gases mix with the cooler surrounding inert gas, with cooling rates in the order of 10⁵°C/s. Summarizing, the characteristics of the laser-heated process are:

- No contamination from other gases, liquid or solid precursors provided a pure carrier gas is used
- Absence of surfaces in the reaction zone on which, e.g. heterogeneous nucleation can occur
- Good control over the power intensity and the

well-defined reaction zone gives control over the exposure time, the nucleation rate and the growth rate of the particles

- Steep heating and cooling rates, in the order of 10^5 - 10^6 °C/s
- Possible multi-photon, unimolecular reactions³³⁾
- Unique reactions due to the specific heating process.

Although this technique is viable for the production of nanoparticles, improvements in the design will raise industrial interest. Identified shortcomings are:

- non-uniform conditions across the reaction zone lead to non-uniformity of the products in terms of particle size distribution and product composition
- low energy efficiency as most of the laser energy is not used (80% - 95%)
- inadequate control over the degree of agglomeration
- very limited production rate, limiting the applicability for industrial applications.

In this study, the focus is on the improvement of particle size uniformity and production rate. First, an analysis of a typical reaction zone is presented, followed by a new design concept, which gives the main directions for the construction of the new reaction zone.

3. New-design Reaction Zone

3.1. Typical reaction zone

The non-uniform conditions are a consequence of the reaction zone configuration. An example of a

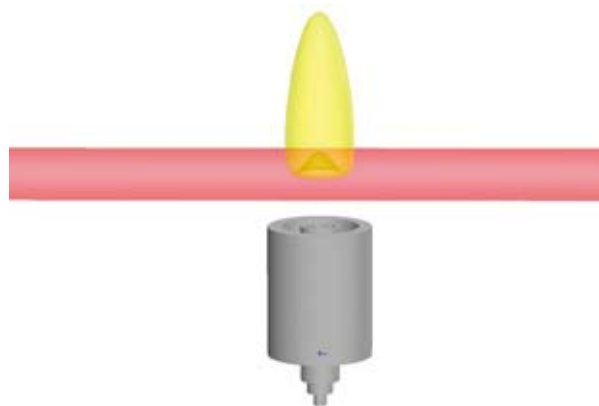


Fig. 1 Reaction zone as used by Kruis consisting of a round nozzle and a round laser beam.

reaction zone, introduced by Kruis²⁶⁾, is shown in **Fig. 1**.

The gases emerging from the nozzle have a parabolic velocity profile while the laser beam has a Gaussian intensity profile.

The reaction zone consists of a round nozzle and a round laser beam. Precursors enter the zone through the nozzle with a parabolic flow profile from the bottom and flow upwards. The gas flow is orthogonally intersected by a laser beam with a Gaussian intensity profile. The problem can be easily visualized, reducing its geometry from 3 to 2 dimensions (**Fig. 2**). In this case, it is possible to observe that the gas velocity profile matches the laser intensity profile only in center of the intersection zone. Although Kruis' reaction zone is used as an example, similar reaction zones used by other researchers suffer from the same deficits.

Because of these non-uniformities, different vol-

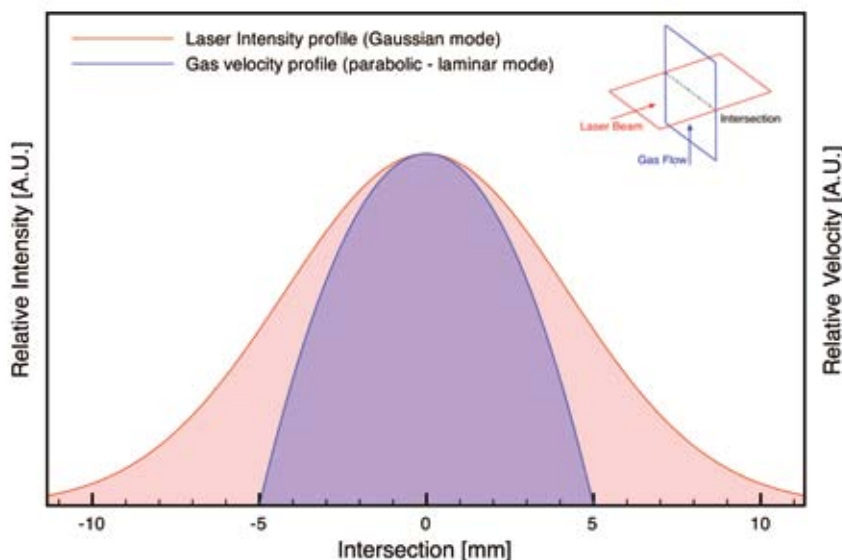


Fig. 2 Overlapping between gas velocity profile in the laminar mode and laser intensity profile in the Gaussian mode.

ume elements of the gas stream are subjected to different laser intensities and velocity histories, and this leads to a broad particle size distribution and possible chemical composition. Non-uniformities in size were observed by several authors^{26,34}. Flint and co-workers classified the particles in three categories³⁴: small (10 nm) particles found in agglomerates, larger (50 nm) particles in aggregates and single isolated larger (100 nm) particles. They developed a model for the silicon particle growth in a laser CVP system. The conclusion was that the silicon particle size and morphology is dependent on the time distribution of the particles above the melting temperature of silicon. This depends on the particle position in the flame as well as the residence time in the flame. Kruis observed similar results and reports several particle morphologies in the synthesis of silicon nitride²⁶.

Following this analysis, it was envisioned that for improving the powder characteristics, the gas flow geometry should match the laser beam geometry. The following aspects were thereby considered in the new design: laser and gas intersection, gas flow geometry, gas flow profile, mixing of reactants, laser beam geometry and laser beam intensity. Besides improving the powder characteristics, it was also envisioned to scale-up the production rate, which is typically in the g/hr range, to industrial rates that are in the kg/hr range.

Production rates in the kg/hr range have already been achieved by Nanogram using a rectangular nozzle configuration in the production of silica nanoparticles, however, their system has a non-uniform reaction zone²⁰.

3.2. Proposed reaction zone

As already mentioned, in order to overcome the non-uniformities in the final product it is essential that the gas flow geometry match the laser beam geometry. To achieve this, a new reaction zone is proposed. This concept, shown schematically in **Fig. 3**, consists of a rectangular gas flow with a flat velocity profile orthogonally intersected by a rectangular laser beam with a flat intensity profile.

To obtain this configuration, two problems had to be solved: how to get a flat velocity profile and how to obtain a rectangular laser beam. This will be described in detail in the next two sections followed by a description of the actual manufactured reaction zone.

3.3. Gas flow geometry and gas flow profile

To obtain the desired reaction zone a rectangular

gas flow is required, which can be achieved with a rectangular nozzle. The optimal size of the rectangular nozzle, that is, the width and length, are influenced by several factors. The width is dictated by the compromise between the production rate and acceptable intensity loss of the laser beam, and the length is determined by the production rate and laser beam width.

To minimize the intensity loss over the width of the nozzle, preferably a very thin slit should be used but this would limit the production capacity. A wide slit would have a high capacity but also an undesirable high intensity drop, creating a non-uniform energy distribution along the reaction zone. The intensity drop as a function of the penetration depth was calculated using the Lambert-Beer law. Initially, the system presented here was designed using a mixture of silane and ammonia for producing highly pure and narrow-sized silicon nitride. For calculating the intensity drop, the absorption coefficient of a mixture of silane and ammonia was therefore used. The result is shown in **Fig. 4**. A nozzle width of 2 mm was chosen which corresponds to a maximum intensity drop of 20%. For the silicon powders from silane presented in this study, the intensity drop as function of the penetration drop is probably less favorable. This can have an influence on the temperature profile.

The length of the nozzle is limited by the desired production rate and by the laser beam diameter. The laser beam diameter used in this study is 18 mm. Although expanding the laser beam is possible, it has experimental and financial consequences. It was therefore decided to keep the length of the nozzle at 10 mm, which is well within the laser beam diameter. Moreover, the theoretical production rate with this nozzle is approximately 100 grams per hour, which is a substantial improvement compared to the previ-

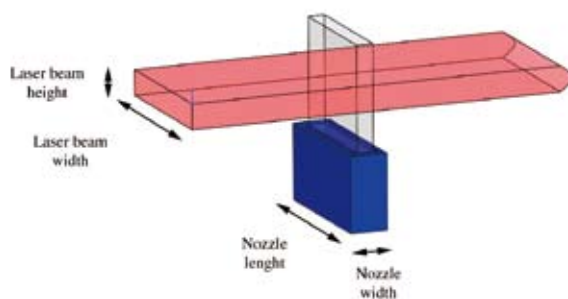


Fig. 3 Sketch of the proposed reaction zone. It consists of a rectangular nozzle out of which gases flow with a flat velocity profile. Gas flow is orthogonally intersected by a rectangular laser beam with a flat intensity profile.

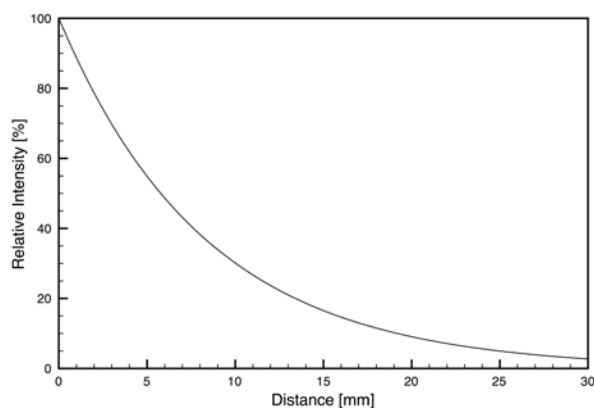


Fig. 4 Intensity drop as a function of the penetration depth for SiH_4 and NH_3 mixture (1:10) and for pure silane. The absorption coefficient for the SiH_4/NH_3 mixture is $1.2 \text{ cm}^{-1}\text{atm}^{-1}$ ³⁹.

ous reactors.

Although not yet mentioned, the literature and our own research indicate clearly that premixing of the precursor gas is important to obtain a homogeneous product. Sadakata mentions that the heterogeneity of the produced powder decreases with the change in mixing type of the gases from laminar diffusion, turbulent diffusion to premixing³⁶.

To obtain a flat velocity profile of the gases, a porous plate on top of the nozzle was considered.

3.4. Laser beam geometry and laser beam intensity

Besides having a rectangular and flat velocity gas flow, the intensity of the laser beam should match this geometry. In the proposed case, **Fig. 3**, this is a rectangular laser beam with flat intensity profile. There is to our knowledge no system that gives an exact rectangular shape and flat intensity profile but there are several ways to approximate it. Three alternative systems have been considered: 1) combination of several optical elements to shape the beam, 2) diffractive optical elements, and 3) a cylindrical lens.

A simple shaping system can be made by a combination of several optical elements consisting of a spatial filter, a beam expander and a cylindrical compressor, see **Fig. 5**. The spatial filter cuts off the edges and produces a rectangular beam. The beam expander enlarges it to the dimensions matching that of the

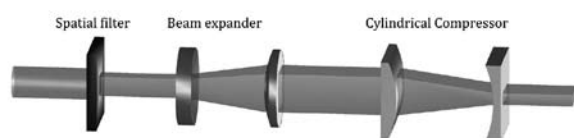


Fig. 5 Multiple optical elements shaping system.

reactant stream, and the cylindrical compressor sets the height of the beam, making it possible to control the residence time of the reactant gases in the laser beam. The main disadvantages of this solution are that several optical elements have to be aligned. In addition, they are expensive, as they have to be made from an IR-transparent material (generally inorganic mono-crystals such as zinc selenide (ZnSe)).

The second option considered was diffractive shaping optics (Diffractive Optics Element, DOE). Although an almost perfect rectangular laser beam can be obtained, the idea was abandoned due to experimental and financial constraints. The available DOE system proposed had a focal plane of approximately 150 mm from the diffractive element, while the minimum focal length, limited by the reactor design, needed to be 300 mm. Moreover it was expensive compared to the next option.

A relatively simple and economic solution is the use of a cylindrical lens. Cylindrical lenses have at least one surface that is formed in the shape of a cylinder, thereby focusing the beam into a line. The advantage of this system is that only one optical element is needed to perform the task. This is very attractive from an operational and financial point of view. A drawback of a cylindrical lens is that it does not shape the beam to an exact rectangular form and that it does not flatten the intensity profile. However, the used laser beam is wider than the rectangular nozzle and therefore the projection of the laser beam on the gas stream is approximately rectangular; see **Fig. 6** for a schematic representation.

The cylindrical lens cannot adapt the intensity profile to a flat one, and therefore another option was explored to achieve this goal. The laser intensity profile of the laser beam depends on the optical configuration of the laser cavity. Different laser transmission modes can be achieved by different optical configura-

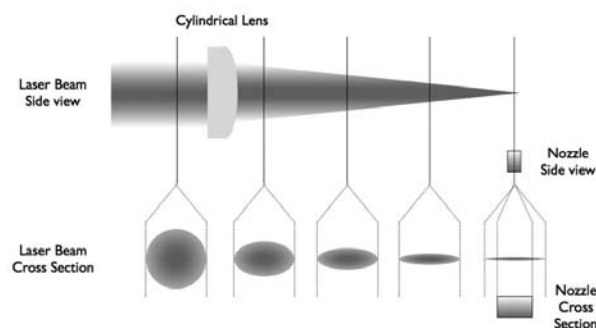


Fig. 6 Focusing action of a cylindrical lens. Top: side view. Bottom: cross-section. The beam is focused above the nozzle outlet. With the beam wider than the nozzle outlet, its elliptical section is approximately rectangular.

tions³⁷). The laser used in this study is able to provide a so-called D-mode profile which is graphically represented in **Fig. 7** (right), next to the standard Gaussian profile.

The laser intensity profiles can be visualized by pointing the CO₂ laser beam toward a Perspex block. This is shown in **Fig. 8**, with 3.8A being the unfocused Gaussian intensity profile, **Fig. 8B** the unfocused D-mode profile, **8C** the focused Gaussian using the cylindrical lens and **8D** the focused D-mode profile. The role of the cylindrical lens is clear: from a three-dimensional profile, the beam is focused on a line, giving a two-dimensional profile. Although not perfect, the intensity profile of the D-mode is much closer to a flat profile compared with a standard Gaussian profile.

3.4. New reaction zone

All mentioned flow requirements are condensed in

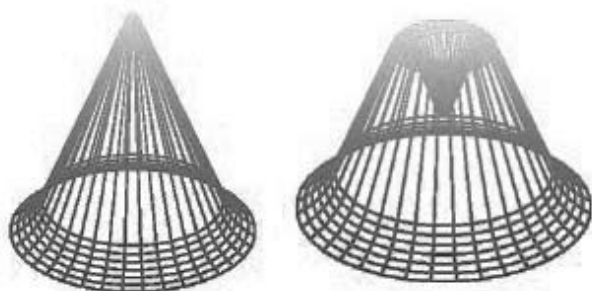


Fig. 7 Graphical representation of a Gaussian intensity profile (left) and the D-mode profile (right).

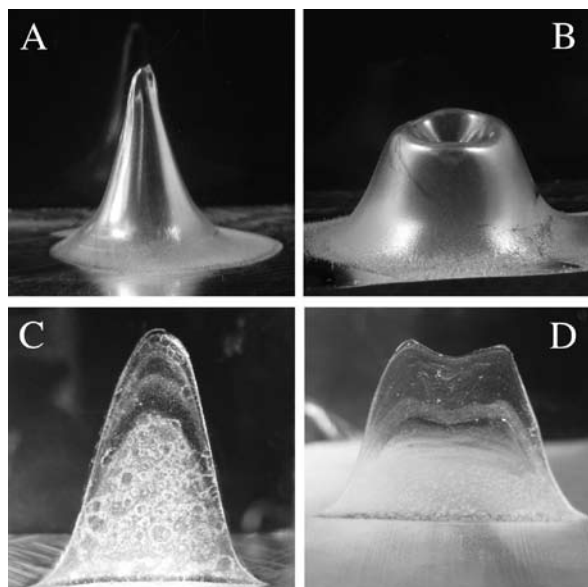


Fig. 8 Laser intensity profiles of the laser beam burned in a Perspex block. A) unfocused Gaussian, B) unfocused D-Mode profile, C) focused Gaussian profile, D) focused D-Mode profile.

the newly developed nozzle. A schematic 3D impression and pictures of the new nozzle are shown in **Fig. 9**.

The nozzle assembly consists of three pieces; the inner nozzle, a bottom cap and an outer shell. The stainless steel outer shell, with a rectangular opening in the center, serves as the outer nozzle and mixing chamber, while the inner nozzle is fixed inside and closed off at the bottom with the cap. Three tubes are used to feed the precursor gases (e.g. C₂H₄, SiH₄, NH₃) to the mixing chamber, and one tube provides the sheath gas to the outer nozzle. The precursors are premixed to improve the homogeneity of the product. An additional porous plate can be placed on top of the nozzle for flattening the gas velocity profile.

The middle picture in **Fig. 3.9** shows the new nozzle assembly from the top, without the bottom cap. Here, it is visible how the inner nozzle is positioned inside the outer shell. The whole nozzle assembly, including tubes, is manufactured from stainless steel 316. The inner nozzle has an inner dimension of 10 × 2 mm for the reasons mentioned in section 3.3. To create a very smooth gas flow out of the nozzle and avoid turbulence and dilution with the sheath gas, the thickness of the nozzle width was made as thin as possible, i.e., 100 μm. However, for manufacturing reasons, the bottom had to be 200 μm. The dimensions of the rectangular outer nozzle are 20 × 11 mm, so that the opening is 10 times bigger in area than the opening of the inner nozzle. This is done to permit using a sheath flow that is 10 times higher than the inner gas flow while maintaining the same exit velocity from both nozzles.

With this nozzle design and the optical set-up mentioned above, the matching between the laser intensity profile and the gas velocity profile is substantially improved all along the intersection in comparison with the one offered by the previous reaction zones (**Fig. 2** and **10**).

4. Experimental Set-up

The newly developed reaction zone was incorporated into a gas-tight reactor that forms the heart of the experimental set-up. The complete laser CVP set-up, with the reactor and its complementary units, is schematically shown in **Fig. 11**.

The set-up is divided into a number of sections; gas supply system, reactor, CO₂ laser + optics, filtration section, pump and exhaust system, and a control system that is not shown. In short, the system operates as follows. Gases are fed to the reactor using

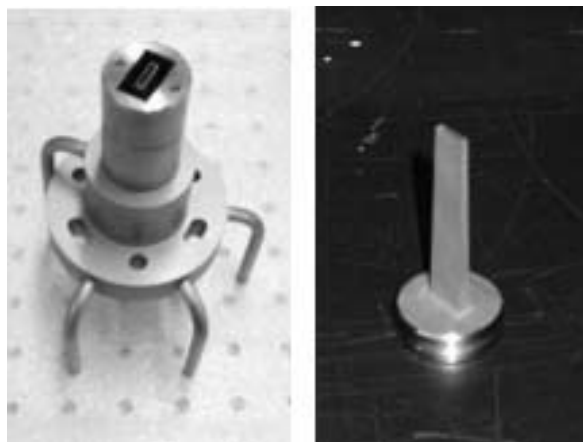
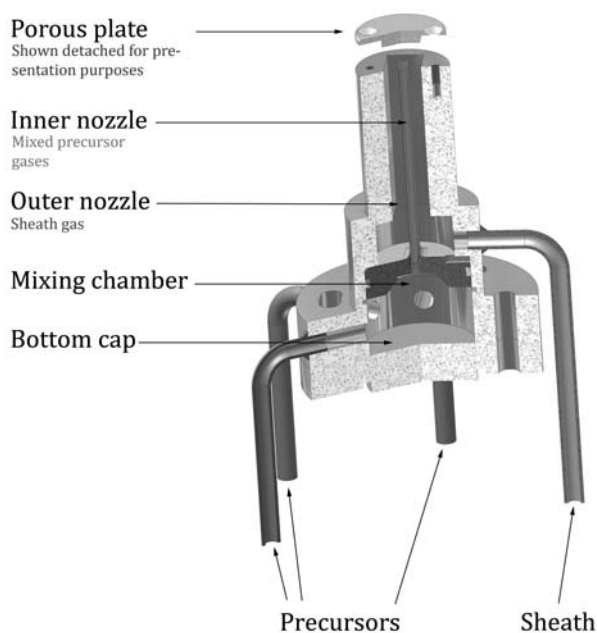


Fig. 9 Left: 3D impression of new nozzle, middle: photo of the nozzle assembly, right: inner nozzle.

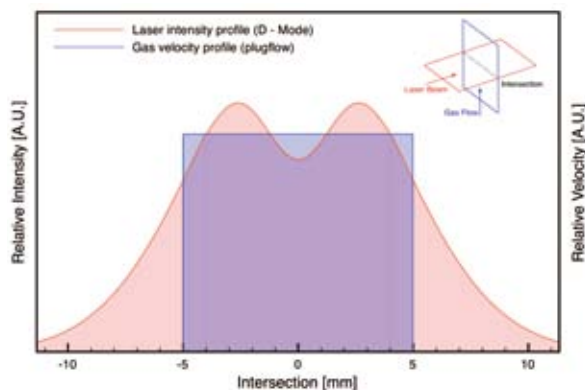


Fig. 10 Overlapping between flat gas velocity profile and laser intensity profile in the D-mode.

a gas supply system. The gases enter through the nozzle into the reactor where they are heated by a CO₂ laser beam. The beam is guided to the reactor by mirrors and shaped by a cylindrical lens to obtain the required form. Due to the heating, the gases start to react and form nuclei. The particles grow and leave the reactor with the gas stream at the top. The product stream enters the filtration section. Here, it is possible to direct the stream toward either a waste filter or a product collector. The product collector is used if it is desirable to extract the powder from the system for further processing or analysis. The waste filter is used for disposal of the powder when it is not desirable to collect the powder. The stream that is directed either through the waste filter or product collector is then transported through a second waste

filter to remove any remaining particles from the stream. To maintain a flow and to control the pressure in the system, a roughing pump is used. The pressure is regulated by using a pressure control loop that maintains the pressure in the reactor independent of the pressure drop across the system. The exhaust of the pump is connected to an exhaust stack that is equipped with an extra blower that dilutes the exhaust stream. The exhaust stack is equipped with a particle filter to prevent particles being emitted to the environment.

The sections are explained in more detail below. First the gas supply is described, followed by the reactor, CO₂ laser and optics, filtration section and the pump and after-treatment system.

4.1 Gas supply system

The gas supply system can supply the following gases to the system: silane (SiH₄), ammonia (NH₃), hydrogen (H₂), ethylene (C₂H₄) and nitrogen (N₂). For future work, preparations for expanding the system by the gases argon (Ar) and sulfur hexafluoride (SF₆) have been made.

The flow rates of the available gases are controlled by mass flow controllers (MFCs). Each gas has its own MFC except for H₂ and C₂H₄, which use the same MFC. This MFC has a calibration curve for each gas, which can be selected when using the designated gas. All MFCs can also be connected to nitrogen to flush the lines during start-up or shut-down of

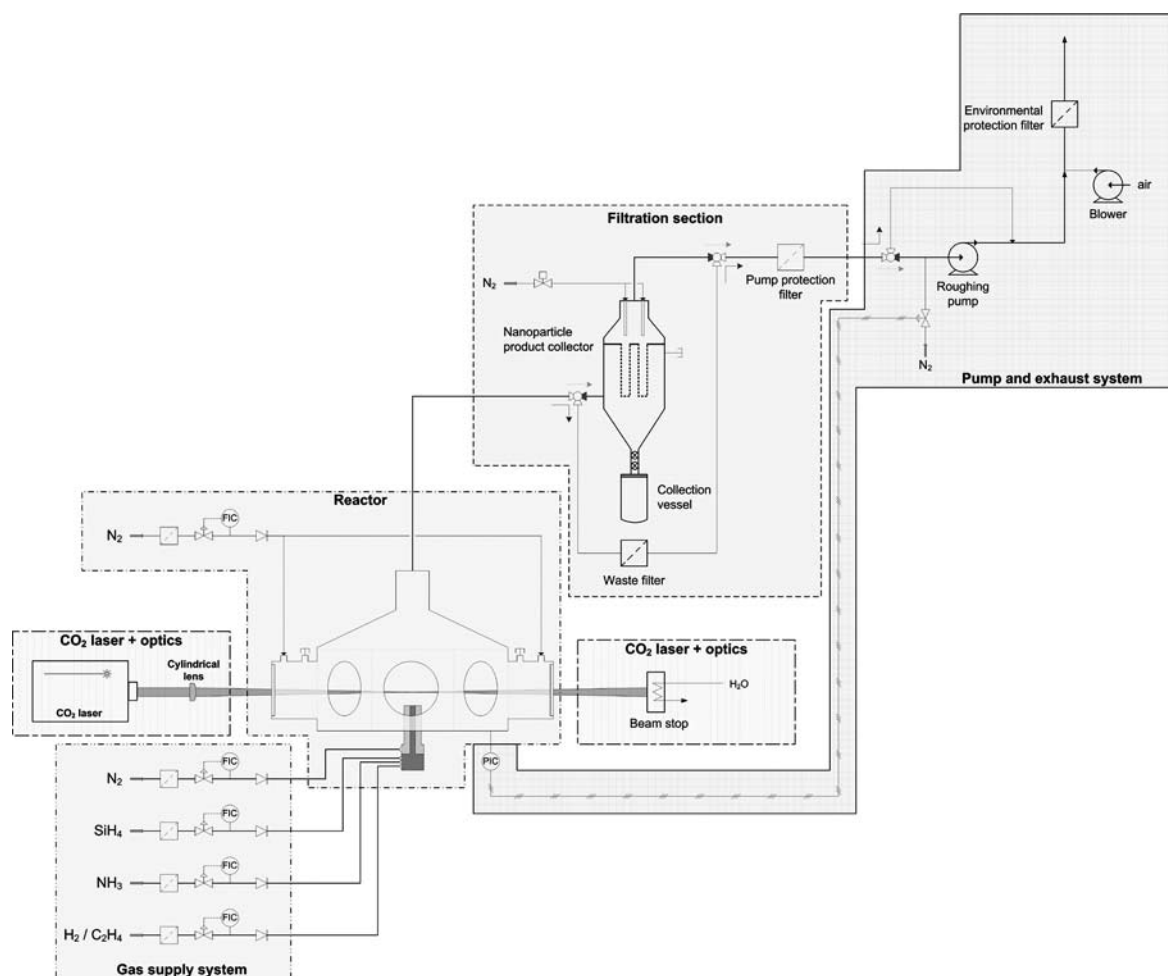


Fig. 11 Schematic representation of the set-up.

the system.

4.2 CO₂ laser and optics

The CO₂ laser is the energy source of the reaction. The CO₂ laser used in this study is a YZ-1500 laser from PRC lasers. The maximum output is 2 kW in continuous wave mode (CW) and 5 kW in pulsed mode. The emitted wavelength is 10.591 μm. The beam diameter is 18 mm when leaving the laser cavity and has a divergence of 0.5 mm/m.

The beam is operated in so-called D-mode (see Fig. 8 and 10). As outlined before, this will help in reducing the non-uniformities in the reaction zone, as the intensity profile is more uniform compared to the Gaussian distribution.

Two water-cooled copper mirrors (Ge-reflective surface, 2 inch diameter, from II-VI Incorporated) were used to guide the beam inside the reactor. Before entering the reactor, the beam is focused by a 1.5-inch diameter ZnSe cylindrical lens (II-VI Incorporated). The position of the beam above the nozzle can be adjusted in height, but for our experiments is

fixed at 5 mm. The optical windows used as a passage for the laser beam to enter and exit the reactor are ZnSe windows with an anti-reflective coating.

The optics are placed on an optical table as shown in Fig. 12. To avoid vibrations from the system or external sources to the optical table, the optical table is physically separated from the rest of the system and is equipped with air-suspended legs. In the table, a rectangular cut-out is made to accommodate the reactor, which is supported on a separate stand. The optical table has a dimension of 1.2m × 2.4m, providing plenty of space for optics and future planned measurement systems, such as in-situ measuring equipment for observing the particle formation processes in the reactor.

4.3 Reactor

To accommodate the reaction zone in a controlled atmosphere for generating oxygen-free nanoparticles, a reactor body was designed and built. A 3-D impression of the reactor is shown in Fig. 13.

The body as shown above is milled from one piece

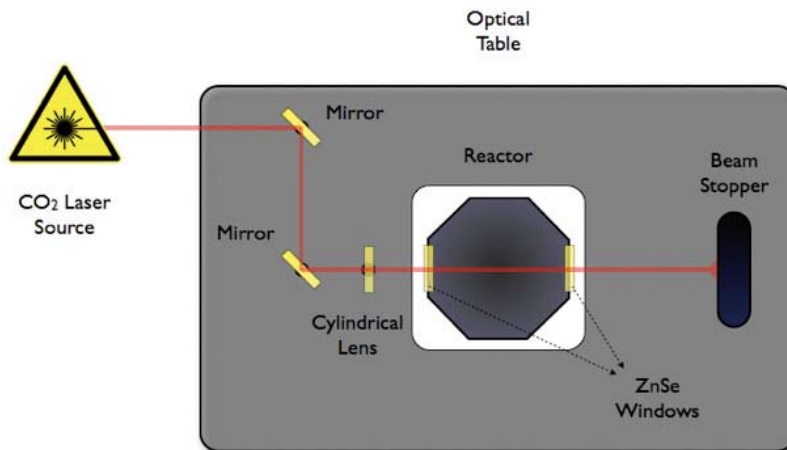


Fig. 12 Optical table and optical arrangement.

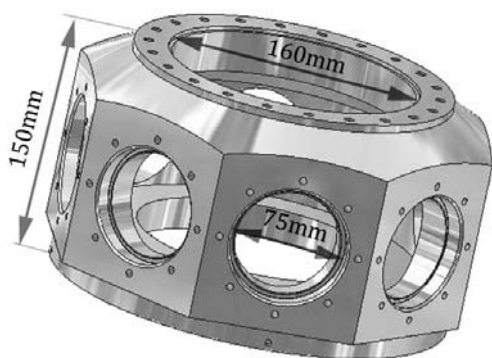


Fig. 13 3-D impression of the reactor. Eight identical ports provide good optical access. The top and bottom flanges provide connections for any kind of nozzle and chimney design.

of stainless steel 316. Creating it from a monobloc reduces the chance of leakages and increases the ability to withstand pressure differences. The reactor has 8 identical viewing ports that provide optical access for observation or measuring purposes. The equal-sized ports provide the opportunity of using various pieces of equipment on each port and of interchanging them without problem. The ports can accommodate optics with a diameter up to 75 mm and are fixed by flanges bolted to the reactor.

The bottom and top of the reactor each has a flange connection for easy mounting of parts or equipment. For example, at the bottom, a nozzle can be accommodated while at the top, an exhaust hood can be fitted. A 2D cut view and top view of the reactor with various parts as used in this study is shown in Fig. 14.

In the top and bottom of Fig. 14, the nozzle as presented in section 3.4 is shown. The nozzle is mounted

on a flange that is bolted to the bottom of the reactor body. Although not shown in this figure, it is possible to adjust the nozzle in height with respect to the flange on which it is mounted.

In the top figure, a flushing system is also shown. The purpose of the system is to keep the ZnSe win-

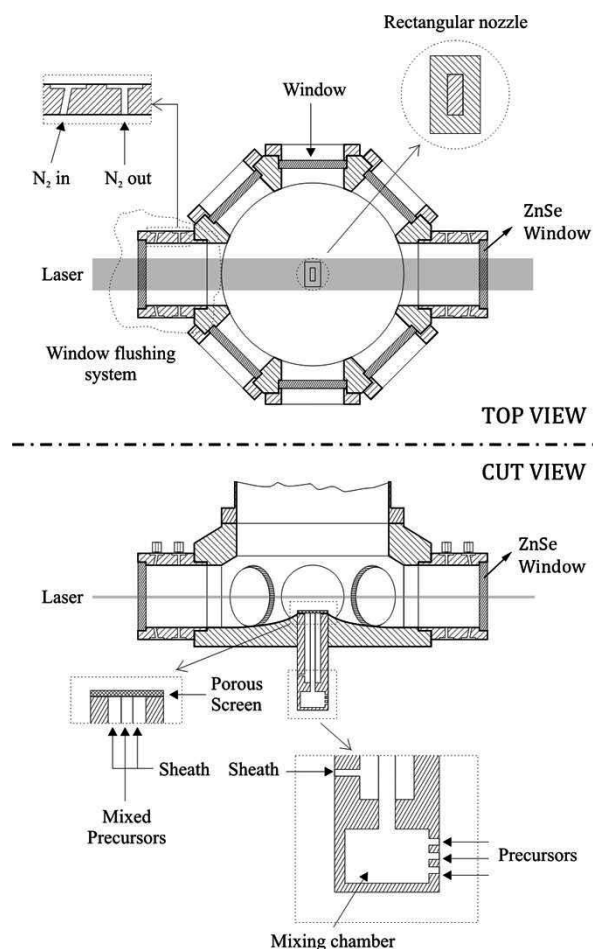


Fig. 14 2-D top view (top) and cut view (bottom).

dows free from particles originating from the flame. This is done because the ZnSe windows are susceptible to breakage. Breakage can happen if hot spots are created by deposited particles heating up on the surface. In the flushing system, a nitrogen flow is directed toward the window via 24 holes (N_2 in, **Fig. 14** top view) to create a sheet of nitrogen and a net gas flow toward the flame. The nitrogen can be withdrawn from the chamber (N_2 out, **Fig. 14** top view) to avoid possible disturbance of the flame in the reactor. In the experiments reported here, this withdrawal option is not used.

On top of the reactor body, a flange connection is fitted to permit any type of exhaust hood to be easily mounted. The function is to guide the particle-laden gas stream to the particle collection system and prevent particles depositing inside the reactor chamber. The exhaust hood is a conical chimney as depicted in **Fig. 15**.

As described in the previous section, the reactor is physically separated from the optical table. The reactor is placed on a stand that is fitted inside the optical table.

4.4 Particle collection section

The particle-laden gas stream exiting from the reactor is the input of the filtration section. This section consists of three filtration units (see **Fig. 11**): a product collection filter, a disposable waste filter and a disposable pump protection filter. The stream can be directed to the product collection filter or to the waste product filter. In this way, one can choose to keep the produced powder for further processing or, if this is not desirable, to dispose of it in the waste filter. Disposing of the powder is done mainly during start-up or shut-down procedures; the process is not stable in these phases and will not produce the required powders. If the process is stable and it is desired to keep the product, the stream is directed to

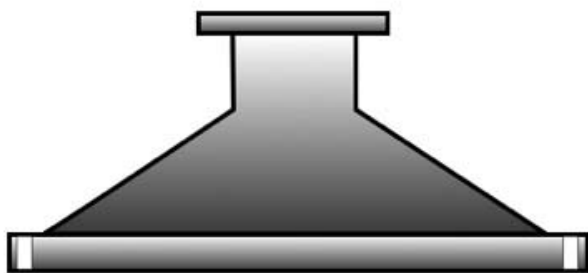


Fig. 15 Exhaust hood for guiding particles to the exhaust system.

the collection filter by switching a three-way valve.

The collection filter is a newly designed device because off-the-shelf solutions are not available for this production rate and for the particle sizes produced by the laser CVP system. The device was built within the TU-Delft facilities. It is based on surface filtration using high-temperature ceramic filters (Herding Alpha filter). Powder gathers on the filter's surface forming a compact filter cake. When the cake causes the pressure drop to exceed permissible values, the filters are cleaned by pulsing nitrogen in the opposite direction to the flow. The filter cake breaks off from the ceramic filters and is collected in a glass collection vessel. The filter and vessel can be closed off by two gate valves, allowing removal of the jar without letting oxygen enter either the vessel or filtration system.

The remaining waste gas, coming from either the collection filter or waste filter, is directed to a second filter (Camfill Farr 1D200). This filter is used to protect the pump by filtering out the remaining particles from the gas stream.

4.5 Pump and exhaust system

A pump is used to permit controlling the pressure and to keep a flow in the system. The pump used here is a dry roughing pump (ACP28G, Alcatel Vacuum Technology) as this pump is able to pump with an almost atmospheric inlet pressure.

To obtain control over the pressure in the reactor, an extra nitrogen flow is introduced just before the inlet of the pump. The amount of nitrogen injected is regulated by a proportional valve. The amount of nitrogen depends on the desired pressure in the reactor and the pumping speed of the pump. The proportional valve is regulated by a pressure reader and controller (PIC) connected to the reactor. If, for instance, the pressure in the reactor rises, the amount of nitrogen injected in front of the pump will decrease and vice versa.

The gases leaving the pump are vented in a stack which is connected to a blower. The stream is diluted about 10,000 times with outside air before finally being purged to the atmosphere. The dilution is performed to keep the level of exhaust gases within explosion or environmental limits. These levels will not be reached during normal operation but can be reached when anomalies occur during production.

4.6 Control system

Measurable values are monitored and control functions are performed by a Programmable Logic Con-

troller (PLC). The PLC is often used in industry as it is a reliable tool to control set-ups. Safety procedures are programmed in the PLC that intervene when an anomaly occurs in the set-up. When an anomaly is detected, the PLC will run a procedure that brings the equipment in a safe state. A PLC is chosen for this purpose as PCs are too unreliable for this task. The PLC is connected to a PC that runs Labview, which is the interface to the user. Sequential procedures or recipes are programmed in Labview that operate the equipment in a certain sequence to arrive at production state.

5. Experiments and Results

5.1 Synthesis conditions of silicon nanoparticles

The synthesis of silicon nanoparticles was carried out with SiH₄ as the gas precursor in a N₂ 5.0 atmosphere. The whole set-up is flushed with 10 l/min of N₂ overnight before synthesis takes place. The pressure of the reactor is kept at 800 mbara during flushing and synthesis procedures. Silane is fed to the inner nozzle and is diluted by nitrogen through the ammonia MFC. A correction factor was applied to determine the correct nitrogen flow. From the first set of experiments, two samples were chosen for a detailed analysis. For practical reasons, these two samples are named Si-1 and Si-2, respectively. The experimental parameters can be found in **Table 1**.

A picture of the flame of Si-2 synthesis is shown in **Fig. 16**.

5.2 Particle production

Analyses were carried out on the samples mentioned in section 5.1. The size and morphology of the product were studied via transmission electron microscopy and X ray diffraction. The surface chemistry and the thermal stability upon oxidation were investigated via infrared spectroscopy and thermogravimetric analysis, respectively. It is of extreme interest to compare the produced particles with a reference sample. In this case, nano-Si from Aldrich (CAS 7440-21-3) was chosen for this purpose. The commercial product's specifications given by Aldrich are: particles are synthesized via the same technique used in this work, laser CVP, and the particles are smaller than 100nm (TEM).

For the Si-1 sample, the primary particles are approximately 20 nm with a spherical shape and the particle size distribution seems to be narrow (see **Fig. 17B**). In the Si-2 case, the particle size distribu-

Table 1. Experimental parameters used during the synthesis of the representative samples

	Si-1	Si-2
Reactor P [mbara]	800	800
SiH ₄ Flow Rate [l/min]	0.24	0.12
N ₂ Dilution Flow rate [l/min]	2.16	2.28
N ₂ Sheath Flow rate [l/min]	11.34	14.34
Laser Power In [W]	510	890
Laser Power Out [W]	250	575

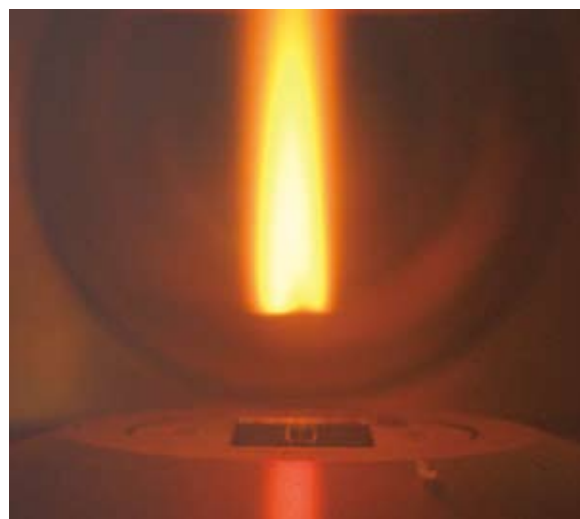


Fig. 16 Flame in the laser CVP reactor during Si-2 synthesis. The picture is taken from an optical window parallel to the laser beam.

tion is much broader (**Fig. 17C**). Small particles (20 nm) are surrounded by bigger ones (50-70nm), often sintered together in bigger aggregates of irregular geometry. There are many more aggregates in Si-2 (**17C**) compared to Si-1 (**17B**). A close-up of the Si-2 sample (**Fig. 17G**) shows a high crystallinity of the particle's core. The outer shell has a thickness of around 2 nm, is amorphous, and probably formed by an SiO_x passivation layer formed immediately after the synthesis, as a spontaneous reaction with small oxygen impurities³⁸. Looking at the TEM picture of the commercial particles (**Fig. 17A**), it is clear that our primary particles are much smaller and much more uniform in size than the Aldrich product. The commercial particles are around 100 nm in size, poly-dispersed, aggregated and their shape is not well-defined.

The two samples differ also in color (see **Fig. 18**). The first sample, Si-1, looks brownish while the second one, Si-2, is going more toward yellowish-green, which resembles the commercial powder color.

XRD spectra of the three samples are shown in **Fig. 19**. They were recorded with a Bruker AXS D8-Advance diffractometer. The crystallographic

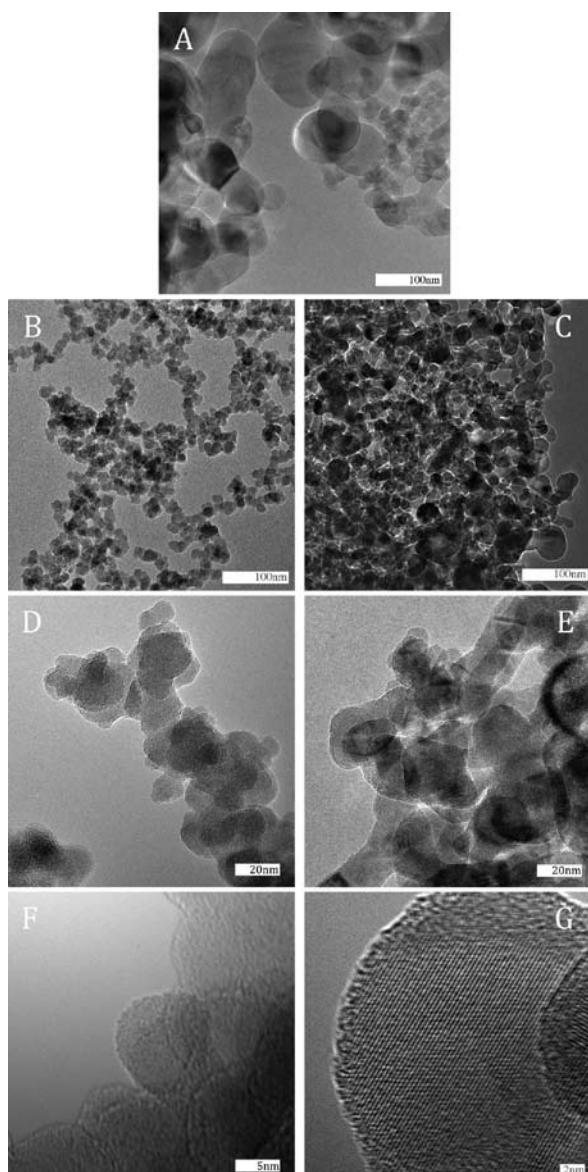


Fig. 17 TEM micrographs of analyzed powders. Fig. A shows the Aldrich powder. Figs. B, D and F show the Si-1 sample at different magnifications. Figs. C, E and G show the Si-2 sample at different magnifications. Fig. G shows the crystallinity of the particle core of the Si-2 sample.

distance between 111 planes is in good agreement with the calculated one from the electron diffraction pattern given by the TEM micrograph shown in **Fig. 17G**.

The crystallite sizes calculated with the Sheerer formula result in 4.8, 14.4 and 34.6 nm for the Si-1, Si-2 and Aldrich samples, respectively. It is important to keep in mind that the crystallite size can differ significantly from the primary particle size, especially in the case of polycrystalline particles. In all cases, reference peaks of silicon are found (PDF¹) number: 75-0590), whereas no evidence of crystalline silicon oxides phases are found. It is likely that the thin pas-



Fig. 18 Pictures of the produced powders. Left: Si-1 sample. Right: Si-2 sample.

sivation layer is amorphous, therefore not giving any significant contribution to the diffraction peaks. Its presence on the particles' surface is further confirmed by IR spectroscopy.

FTIR analysis was performed with a "Perkin Elmer Spectrum one FTIR". The powder of sample Si-1 was investigated in transmission mode. The sample was prepared as a solid pellet, after mixing the Si powder with dry KBr. The resultant spectrum is shown in **Fig. 20**. From the spectrum, it is clear that the sample contains water adsorbed on the surface ($\nu = 1628 \text{ cm}^{-1}$). Moreover, the surface is oxygen-terminated as confirmed by the stretching ($\nu 1s=1068$, $\nu 2s=806$, $\nu 3s=649 \text{ cm}^{-1}$) and bending ($\nu 1b=978$, $\nu 2b=470 \text{ cm}^{-1}$) vibrational modes of Si-OH and Si-O-Si groups. The outer shell of the particles behaves in the same way as silicon oxide³⁹⁾. The OH groups on the surface can be used for chemical modification of the particles⁴⁰⁾.

Different reactions can be carried out via surface chemical modification of the hydroxylated silicon surfaces, such as silanization, halogenation, amination, alkylation and alkoxylation. In this way, it is possible to tune the electronic and optical properties of the silicon nanoparticles, thus raising its number of possible applications in solid-state electronic devices⁴¹⁾.

As confirmed by the thermal analysis (PerkinElmer TGA7), the passivation layer is stable up to 200°C, as shown in **Fig. 21**. In excess of 200°C, the sample starts to increase its weight as a result of the oxidation reaction in the core of the particles. Good evidence of the chemical stability is the fact that upon air exposure, the powder does not change color, even

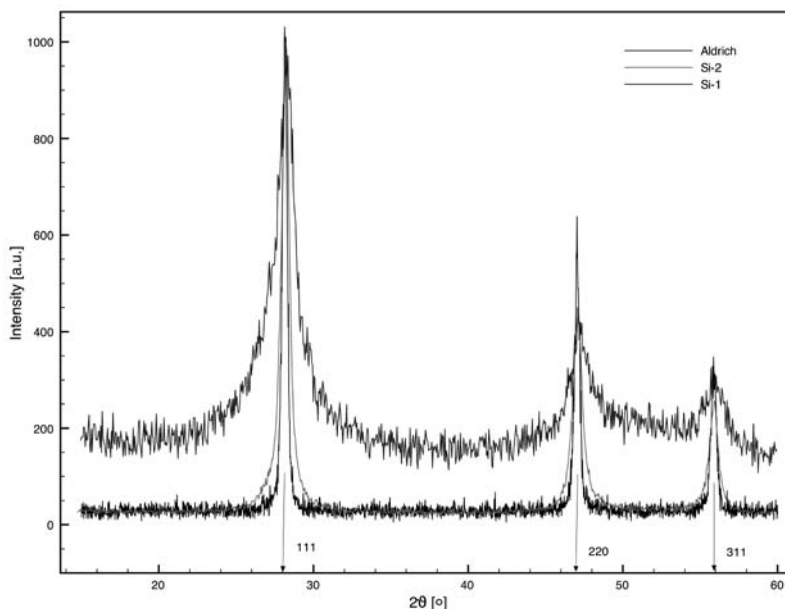


Fig. 19 XRD spectra of the produced silicon powder and the Aldrich powder.

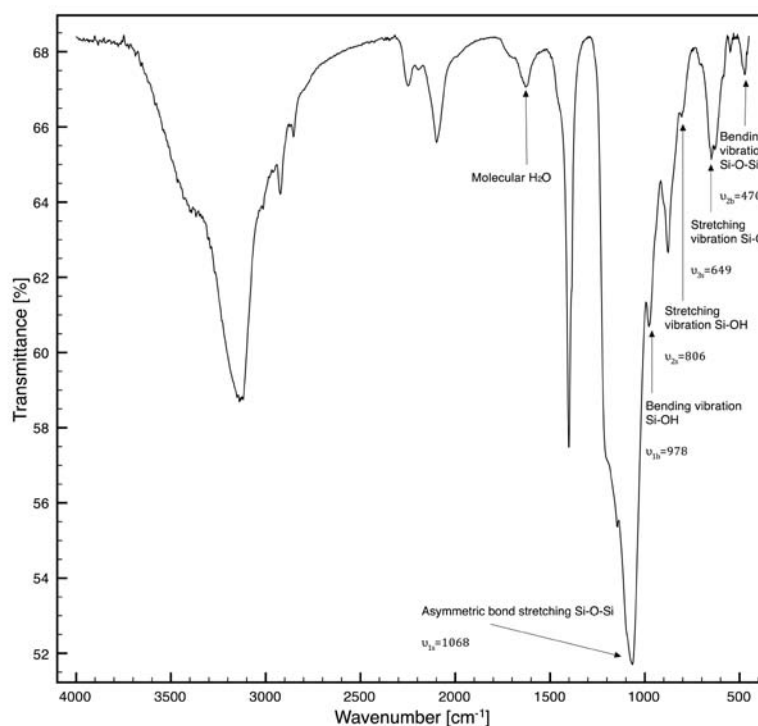


Fig. 20 FTIR spectrum of Si-1 sample.

after a period of a month.

Although the reactor was not tested at full production capacity, the maximum rate that is achievable with the current MFC is approximately 100 grams per hour. This increases the production rate by a factor of 10 compared to the previous lab scale reactors. The production rate of the Si-1 sample achieved so

far was approximately 16 grams per hour, although the synthesis was shorter than one hour. The current synthesis experiments run for approximately 20 minutes and yield 5 grams of silicon nanopowder. The synthesis was limited because of particle recirculation in the reactor. This was measured by an increase in energy absorption of the CO₂ laser beam

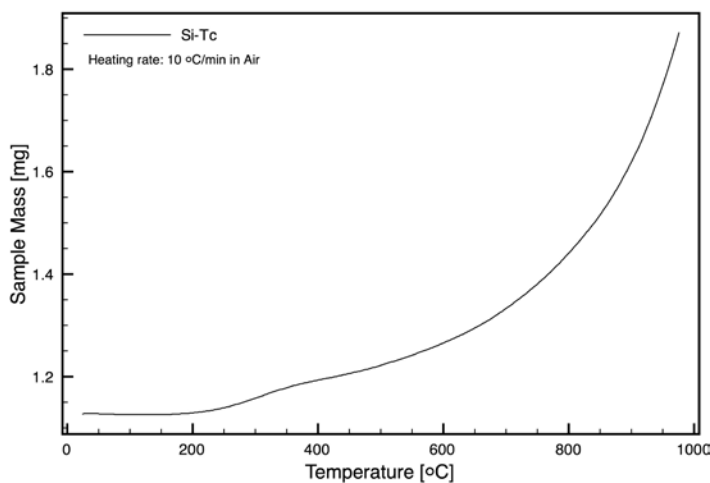


Fig. 21 TGA plot of Si-1 sample. Sample is thermally stable at room temperature. After a very small decrease in weight, probably due to the loss of adsorbed water, the sample gains weight due to oxidation, which starts after 200°C.

during the synthesis and was observed by particle deposition on the windows and internal walls of the reactor. The problem of recirculation is currently being addressed by using a different exhaust hood design. After successful testing, the production rate will be increased to explore the full capabilities of the system. It is important to note that these results are from the very first batch of experiments. Attempts will be made to improve the powder characteristics, which are already remarkable when compared to the commercial Aldrich material. For this purpose, the synthesis conditions (e.g. laser intensity, pressure, concentration of reactants, gas speed) related to the product features are currently under investigation. Until now, the porous plate was not used. In the future though, this will be used to obtain a flat gas velocity profile. It is anticipated that a flat velocity profile will improve particle characteristics.

6. Conclusions

The laser CVP process is a very promising technique for the production of highly pure nanoparticles with a narrow size distribution. To become industrially applicable, however, the synthesis apparatus must be improved. In this study, a new design is presented that focuses on the improvement of product homogeneity and on increased production rates.

The improvement of the product homogeneity, in size and composition, comprises the concept of a uniform reaction zone. For these purposes, the reaction zone was studied in relation to the nozzle and the laser beam geometry. In particular, in order to achieve mono-dispersed nanoparticles, it is important to have

a good match between the laser beam intensity profile and the gas velocity profile. In this way, different gas elements have the same probability of absorbing the same amount of energy, resulting in a uniform heating along the reaction zone and therefore in a mono-dispersed product.

The concept resulted in a newly built reaction zone that consists of a rectangular nozzle and an almost rectangular laser beam. The reaction zone is built into a new and flexible reactor that is capable of producing highly pure nanoparticles at production rates of between 10 and 100g/h. Its flexibility is reflected not only in the different types of materials that can be produced, but also in the modular configuration of the reactor body toward the auxiliary components (i.e. nozzles, hoods, investigation devices). The set-up consists of a main core, the reaction chamber, and the following auxiliary units: gas supply system, CO₂ laser and optics, filtration section, pump and exhaust system, safety control unit (PLC).

The system has not been tested extensively yet, but the first encouraging experimental results are shown here. Silicon was chosen as a first product due to the large number of applications already available for this kind of material. Silicon nanoparticles were synthesized from a SiH₄ precursor in an N₂ atmosphere. Different flow rates and laser powers were experimented, and two samples were chosen for a more extensive characterization. The products were characterized via TEM, XRD, TGA and FTIR analyses and compared with a commercially available one (Aldrich). The synthesized products show a narrow size distribution and small particle size compared with the commercial material. Silicon nanoparticles are

pure and chemically stable upon air exposure, thanks to a thin passivation layer on the particle surface.

Future work on the set-up will include a methodic characterization of the nanopowder in relation to the different experimental parameters used during the synthesis. In particular, the effect of laser intensity, precursor flow rates, as well as concentrations and reactor pressure will be analyzed in respect of the final product properties. The system will also be tested in order to investigate its maximum production rate in a continuous production process.

Acknowledgements

DEMO is acknowledged for their extensive work and intensive cooperation on the system with special thanks going to Nico Alberts, Gerard de Vos, Leen Groenewegen, Giel Hermans and Reyer Janssen. The authors would also like to thank the National Center for HREM, with special thanks to Ugo Lafont for his extensive work on the TEM.

References

- 1) Ford, M., S. Russo and J. Gale. Preface (2009): Proceedings of the international conference on nanoscience and nanotechnology (Melbourne, 25-29 February 2008). *Journal of Physics Condensed Matter*, 21(14).
- 2) Reetz, M. T. and W. Helbig (1994): Size-selective synthesis of nanostructured transition metal clusters. *J. Am. Chem. Soc.*, 116(16): pp.7401-7402.
- 3) Zhang, L. and A. Manthiram (1996): Generation of magnetic metal particles in zeolite by borohydride reduction at ambient temperature. *Journal of Materials Chemistry*, 6(6), pp.999-1004.
- 4) Brinker, C. J. and G. W. Scherer (1990): *Sol-Gel Science: the Physics and Chemistry of Sol-Gel processing*.
- 5) Alain, C.P. (1998): *Introduction to Sol-Gel Processing*.
- 6) Madler, L. et al. (2002): Controlled synthesis of nanostructured particles by flame spray pyrolysis. *Journal of Aerosol Science*, 33(2), pp.369-389.
- 7) Vollath, D. (2008): Plasma synthesis of nanopowders. *Journal of Nanoparticle Research*, 10(SUPPL. 1), pp.39-57.
- 8) Schwyn, S., E. Garwin and A. Schmidt-Ott (1988): Aerosol generation by spark discharge. *Journal of Aerosol Science*, 19(5), pp.639-642.
- 9) Sun, S. et al. (2008): Bundled tungsten oxide nanowires under thermal processing, *Nanotechnology*, 19(30).
- 10) Wegner, K. and S.E. Pratsinis (2004): Gas-Phase (Aerosol) Synthesis of Nanoparticles: Scale-up, in Presented at the Summer School in Winter (SSIW) 2004.
- 11) Cannon, W. (1982): SINTERABLE CERAMIC POWDERS FROM LASER-DRIVEN REACTIONS - 1. PROCESS DESCRIPTION AND MODELING., in *Journal of the American Ceramic Society*, pp.324-330.
- 12) Cannon, W. (1982): SINTERABLE CERAMIC POWDERS FROM LASER-DRIVEN REACTIONS - 2. POWDER CHARACTERISTICS AND PROCESS VARIABLES., in *Journal of the American Ceramic Society*, pp.330-335.
- 13) Ehbrecht, M. et al. (1993): CO₂-laser-driven production of carbon clusters and fullerenes from the gas phase, *Chem. Phys. Lett.*, pp.34-38.
- 14) Armand, X. (1997): Fullerene synthesis by laser pyrolysis of hydrocarbons, *Journal of Physics and Chemistry of Solids*, pp.1853-1859.
- 15) He, Y., X. Li and M. Swihart (2005): Laser-driven aerosol synthesis of nickel nanoparticles, *Chem. Mater.*, pp.1017-1026.
- 16) Alexandrescu, R. (2005): Combining resonant/non-resonant processes: Nanometer-scale iron-based material preparation via CO₂ laser pyrolysis, *Applied Surface Science*, pp.138-146.
- 17) Martelli, S. et al. (2000): Production of iron-oxide nanoparticles by laser-induced pyrolysis of gaseous precursors, *Applied Surface Science*, pp.353-359.
- 18) Curcio, F. (1990): Synthesis of ultrafine TiO₂ powders by a CW CO₂ laser, *Applied Surface Science*, pp.225-229.
- 19) Borsella, E. (1993): Laser-driven synthesis of nanocrystalline alumina powders from gas-phase precursors, *Applied Physics Letters*, pp.1345-1347.
- 20) Bi, X. et al. (2001): Synthesis of nanoscale optical materials using nano particle manufacturing (NPM, $\tilde{N} \epsilon$) technology., *Proceedings of SPIE - The International Society for Optical Engineering*, Beijing.
- 21) Tuinman, I. (1997): "The production of Si₃N₄ powders in a laser-driven aerosol reactor", PhD Thesis.
- 22) Kruis, F. E. et al. (1998): Particle formation paths in the synthesis of silicon nitride powder in a laser-heated aerosol reactor. *Journal of the European Ceramic Society*, 18(8), pp.1025-1036.
- 23) Fantoni, R. et al. (1989): Laser assisted synthesis of ultrafine silicon powder, *Applied Surface Science*, pp.308-315.
- 24) Kruis, F., A. Goossens and H. Fissan (1996): Synthesis of semiconducting nanoparticles, *J. Aerosol Sci.*,
- 25) Bauer, R. A. (1991): "Laser chemical vapor precipitation of ceramic powders", PhD Thesis..
- 26) Kruis, F. E. (1993): "Particle formation in a laser-heated aerosol reactor", PhD Thesis.
- 27) Besling, W. (1999): "In-situ raman spectroscopy and laser-induced fluorescence of high vibrationally-excited gas mixtures during laser-induced chemical vapor deposition of nanostructured materials" , PhD Thesis..
- 28) Kasavajjula, U., C. Wang and A. Appleby (2007): Nano and bulk-silicon-based insertion anodes for lithium-ion secondary cells, *J Power Sources*, pp.1003-1039.
- 29) Han, X. et al. (2007): Stacked SiO₂/Si nanonail array fabricated by spacer technology for biomedical appli-

- cations, in TRANSDUCERS and EUROSensors - Int. Conf. Solid-State Sensors, Actuators Microsystems, pp.1609-1612.
- 30) Forster, C. et al. (2005): Micro-electromechanical systems based on 3C-SiC/Si heterostructures, Mater. Sci. Eng. C, pp.804-808.
 - 31) Erdamar, O. et al. (2007): Effects of humidity and acetone on the optical and electrical properties of porous silicon nanostructures, in Phys. Status Solidi C Curr. Top. Solid State Phys., pp.601-603.
 - 32) Bauer, R.A. et al. (1991): Laser synthesis of low-agglomerated submicrometer silicon nitride powders from chlorinated silanes, Journal of the American Ceramic Society, pp.2759-2768.
 - 33) Longeway, P. A. and F.W. Lampe (1981): Infrared Multi-Photon Decomposition Of Monosilane, Journal of The American Chemical Society, pp. 6813-6818.
 - 34) Flint, J. and J. Haggerty (1990): A model for the growth of silicon particles from laser-heated gases, AEROSOL SCI. TECHNOL, pp.72-84.
 - 35) Haggerty, J.S. and W.R. Cannon (1991): "Laser-Induced Chemical Processes" , Book, pp.165-240.
 - 36) Sadakata, M., Y. Xu and A. Harano (1996): A systematic approach for the design of aerosol reactors, in Powder Technol., pp.261-266.
 - 37) Paschotta and Rüdiger (2008): "Encyclopedia of Laser Physics and Technology" , Book.
 - 38) Zhang, X.G. (????): Electrochemistry of Silicon and Its Oxide, Book.
 - 39) Slowing, I. et al. (2008): Mesoporous silica nanoparticles as controlled release drug delivery and gene transfection carriers, Adv. Drug Deliv., Rev., pp.1278-1288.
 - 40) Liu, Y. et al. (2009): Functionalization of silica nanoparticles with 4-isocyanato-4^a-(3,3^a-dimethyl-2,4-dioxo-azetidino)diphenyl methane, surface chemical reactivity and nanohybrid preparation, J. Colloid Interface Sci., pp.189-194.
 - 41) Aswal, D.K. et al. (2006): Self assembled monolayers on silicon for molecular electronics. Analytica Chimica Acta., 568(1-2), pp.84-108.
 - i) Powder Diffraction File, PDF, phase identification number for crystalline powders defined by the International Centre for Diffraction Data, ICDD.

Author's short biography



Jan van Erven

Jan van Erven, born in 1976 in the Netherlands, finished his master degrees in chemical engineering at the TU Delft in 2003. The goal of his master thesis was to investigate microscopically the oxidation of soot particles on a platinum catalyst. This involved the generation of platinum nanoparticles by electrospraying. After the masters he accepted a PhD position in the same research group, Nano Structured Materials. The aim of his work was to design and build an improved and up-scaled laser CVP reactor of which the results are presented in this work. Currently he is working part time as a researcher at Corus and is still bound to the university one day per week to assist David Munaó in continuing the development of the system.

Author's short biography



David Munaò

David Munaò is born in Rome, Italy, on November 23rd, 1981. He graduated in the University of Rome "La Sapienza" in 2007 in "Industrial Chemistry", Material Science division. His master thesis project regarded Polymer Electrolyte for Fuel Cells applications. His studies concerned mainly the electrochemical, chemical and physical properties of water-based 3D cross-linked polymer gels network and the role of ceramic nano-additive on the ionic conductivity of these systems. A fully working methanol based Fuel Cell has been assembled and its design has been studied and improved.

Being involved in the energy storage material field he moved to Delft in July '07 to begin a PhD position in the group of Dr. Erik Kelder. Being his group part of the European Network of Excellence for Li-Ion Battery technology development (ALISTORE) he is interested in improving the performance of new electrode materials, focussing on the anode side of the device. First encouraging results are obtained with nano-Silicon based materials produced via LaCVP setup. The reactor has been designed and engineered during the PhD period of his colleague, Jan van Erven, and has finally come to full production state with the strict collaboration of both of them.



Tomasz M. Trzeciak

Tomasz M. Trzeciak, born in 1976 in Poland, finished his master degrees in chemical engineering and processing at Warsaw University of Technology in 2002. The subject of his master thesis was theoretical investigation of transport and deposition of deformable fibrous particles in filter media. After the masters he accepted a PhD position in the Nano Structured Materials group (formerly Particle Technology group) at TU Delft. The aim of his work was theoretical modelling of phenomena involved in laser-CVP process as well as the design of experimental laser-CVP reactor unit. Currently he is working as a researcher at Exeter University investigating photonic effects in biological systems.



Jan C.M. Marijnissen

Jan C.M. Marijnissen is an Associate Professor and Head of the Aerosol Laboratory at Delft University of Technology, the Netherlands. He is a PERC Visiting Professor at the University of Florida, Gainesville, U.S.A. He holds a Masters degree from Delft University of Technology and a Ph.D. degree from the University of Minnesota, U.S.A. He has some thirty five years experience in the field of Mine Ventilation and Aerosol Technology. He has (co-)authored many articles and several books on Aerosol Technology and is a board member of different scientific associations and journals.

Hydrotextural Description of an Unsaturated Humid Granular Media: Application for Kneading, Packing and Drying Operations[†]

E. Rondet¹, M. Rundgsiyopas^{1,3}, T. Ruiz^{1*}, M. Delalonde² and J.P. Desfours¹

Laboratoire de Génie des Procédés - Eau et Bioproduits, U.M.R. CIRAD 016

Université Montpellier 2¹

Université Montpellier 1²

Mechanical Engineering Department, Faculty of Engineering, Burapha University³

Abstract

The kneading of a powder generates a product made of three phases (solid/liquid/gas) that interact through many interfaces. The respective proportions of each phase can vary according to the process parameters and the applied stress. After the initial operation of kneading, the medium can also be subjected to other stresses such as packing and thermal stresses or mechanical drying which will induce deep modifications in the relative proportions of the three phases. According to the twin influence of process strain and the nature of the three phases, the rheological behavior of the granular material can vary from that of a rigid solid to that of a more or less deformable plastic paste. The objective of this work is to depict, on a phase diagram, the potential states of each fraction constituting an unsaturated wet granular medium and their potential connectivity. From an experimental point of view, sorption isotherms and capillary retention curves allow determination of the two fluid phases state (liquid and gas). The hydrotextural diagram can be considered as a tool for the analysis and understanding of the mechanisms occurring during the processing (kneading and packing) or drying of wet granular media.

Keywords: state diagram, humid granular media, kneading, packing, drying, transformation path

1. Introduction

The ground is the most widespread wet granular medium. Nevertheless, many processes of product processing start with the wetting of a powder bed during a kneading stage.

Whatever their nature (agglomerates, dough or hard suspension), the wet media obtained can potentially be made up of three dispersed phases: solid, liquid and gas. These phases interact through the interfaces resulting from the divided character of the solid raw material. Many other of processing operations can succeed to this first step of kneading.

They generate a mechanical stress (tapping, packing or extrusion), a thermal or hydric stress (drying, osmotic dehydration), contributing to the evolution of the granular matrix towards its final application properties. These transformations combine the textural properties of the product and the process capabilities. The identification of the respective proportions of the “product” and “process” aspects in tropisms controlling the transformation is the object of a twin analysis that requires the follow-up of the relevant description parameters of the granular medium throughout the elaboration process.

Based on the relations of volume and mass conservation between the components of a granular medium at a representative elementary volume scale, the objective of this work is to propose a global representation to enable to depict the hydric and textural state of a wet granular medium in order to follow their evolution when process stresses are applied (compaction force, mixing stress, drying speed, etc.). The work presented here is a synthesis of many works performed on powder processing. The objective is

[†] Accepted: September 30th, 2009

¹ c.c. 05, place Eugène Bataillon, 34095 Montpellier cedex 5, France.

² 15 avenue Charles Flahault, B.P. 14491, 34093 Montpellier cedex 5, France.

³ 169 Long-Hard Bangsaen Road, Tambon Saensuk, Amphur Muang, Chonburi, 20131 Thailand

* Corresponding author :

TEL: +33467144617, FAX: +33467144787

E-mail: tr Ruiz@univ-montp2.fr

to focus on the hydrottextural variations of materials during the unit operation constituting the processing of powders. In this way, the use of the hydrottextural diagram permits following the transformation paths during processing from the wetting stage to drying. This representation of hydric, textural and rheological aspects corresponds to the definition of the thermodynamical approach of a system's states starting from a phase diagram. Applied to dispersed media as granular media, this macroscopic concept of a phase diagram was initiated by Matyas and Radhakrishna¹, to describe the hydrottextural state of an unsaturated soil subjected to hydromechanical stress. These authors showed that four parameters are necessary to completely define the state of an unsaturated soil: the water content (w , which is the ratio of the liquid mass to that of the solid) and the void index (e which is the ratio of the void volume to that of the solid phase) on the one hand, and the net mechanical stress and the capillary suction on the other hand. On state surfaces, which are diagrams built starting from experimental tests, it is possible to depict the "loading path." These paths symbolize the potential "trajectories" of a soil state subjected to mechanical and/or hydric stress, and are common in geotechnics.

Furthermore, the existence of particular state transitions such as the blocking transition (jamming transitions) observable on discrete systems (colloids, macromolecules, powders) for specific concentrations, inspired Liu & Nagel² who proposed a jamming phase diagram specific to the soft matter. This phase diagram established for "homogeneous" media is based on the temperature (T), the applied stress (Σ) and the reverse of compactness ($1/\phi$ where ϕ is the ratio of the apparent volume to that of the solid phase). When the particles are large enough to be insensitive to Brownian agitation (which is the case of the dry granular media), the system is defined as a zero-temperature system. Two parameters (compactness and applied stress) can describe the state of such a system. This type of representation is then used to depict the packing or the tapping of such materials³. When such media are composed of several components, it is necessary to supplement the description by parameters informing about the relative proportions of each component. In the case of a trisphasic media such as unsaturated wet granular media, it is necessary to take into account another parameter, for example the water content. The reverse of compactness and the void index are related by a linear relation: $1/\phi = 1 + e$, and it is thus possible to

note that the approaches of Matyas and Radhakrishna and Liu & Nagel are obviously isomorphous.

On this basis, we propose the development of a "hydrottextural diagram"^{4,5}, constituting the synthesis of the previously quoted works improved by the positioning of limits describing the connectivity state of the involved phases as well as their consistency state. The tests which make it possible to locate the state transitions of the wet granular medium will be briefly described. The first test allows the plotting of the water sorption isotherms which make it possible to identify the water proportion necessary to permit formation of the saturated monolayer and the appearance of the capillary condensation phenomenon (that marks the end of the hygroscopic field). Beyond this water content, the pendular state occurs during which the interstitial water generates capillary bridges between solid particles. The second test allows plotting of capillary retention curves mainly used in geotechnics. This test makes it possible to follow the variation of the water content of a sample with respect to the values of applied capillary suction increments. The curves established here for various compactness values allow identification of (i) the residual water content that corresponds to the value beyond which it becomes funicular (thus ensuring the connectivity of the liquid phase), and (ii) the water content of air inlet. Other geotechnical tests make it possible to identify the rheological consistency limits: the liquid and the plastic limit⁶. The depiction of all these limits depends on the intrinsic characteristics of the product and its affinity with the added wetting liquid phase. Stresses generated by the process (mechanical, hydric, etc.) will then lead to depiction of the produced states within the diagram. It is thus possible to anticipate and estimate the reaction of the granular medium to the stress imposed by the process. In this study, the hydrottextural diagram is specifically plotted for tests carried out on kaolin wetted by distilled water. The phase diagram of this mixture subjected to static packing is then shown. The texturing phenomena appearing during kneading, packing and drying of such a granular medium are specified.

2. Materials and Methods

2.1 Materials

The raw material chosen for this study is a cohesive powder: kaolin. This is a clay, classified in the category of non-swelling clays thanks to its structure made of rigid layers which prevent liquid penetration⁷. The true density (ρ_s^*) of the raw material

is measured with a helium pycnometer 1305 (Micromeritics) and is equal to 2580 kg/m^3 . A granulometric analysis, performed with a Malvern Master Sizer (Malvern instrument), allowed determination of the d_{50} which is equal to $8.8 \text{ }\mu\text{m}$ for kaolin native particles. Distilled water is used as the wetting liquid.

2.2 Determination of consistency limits and fluid percolation thresholds

Consistency limits are defined as the water content corresponding to changes in the product's mechanical behavior from solid to plastic and from plastic to pseudo-liquid. Atterberg limits^(6,8) are measured according to the French standards which define liquid limit (w_L) as the water content of transition between the plastic and the pseudo-liquid state⁽⁹⁾. The plastic limit (w_P) corresponds to the water content of transition between the solid and the plastic state⁽¹⁰⁾.

Fluid percolation thresholds and more generally hydrotextural limits are determined on cylindrical samples of the product according to two methods. The first method consists in identifying two specific water contents (w_{mono} and w_{capil}) on an isotherm curve established for several product samples of different initial solid volume fractions. These two values correspond to the water content allowing the saturation of the specific surface area by water molecules (w_{mono}) and to the outbreak of capillary condensation phenomenon (w_{capil})⁽¹¹⁾, respectively. Analysis of the isotherm curves by the BET⁽¹²⁾ and GAB⁽¹³⁾ approach makes it possible to define these specific water contents. From an experimental point of view, isotherm curves are plotted after experiments carried out in accordance with the gravimetric method conducted in an isotherm vessel where $T=25^\circ\text{C}$ and RH varies between 7 and 96%. The follow-up of the sample dimensions during the experiments allows determination of the solid volume fractions relative to w_{mono} and w_{capil} . Repetition of this experiment for various initial solid volume fractions makes it possible to obtain coordinates (w , ϕ) that delineate specific zones of the hydrotextural diagram⁽⁴⁾. The second test corresponds to a draining/imbibition experiment conducted on product samples over a controlled capillary suction⁽¹⁴⁾. This test is carried out with a pressure plate that makes it possible to identify the water contents for which the fluid phases are connected within the sample. The capillary suction curves (volumetric water content versus capillary suction for different values of sample compactness) make it possible to identify the residual water content (w_r) and the inlet air water content (w_i). w_r corresponds to the water content

for which the connectivity of the liquid phase is due only to water films at the particle surface⁽¹⁴⁾. The water content of the inlet air is the water content for which the gas phase is not connected anymore in the matrix. The repetition of this experiment for various initial solid volume fractions makes it possible to obtain coordinates (w , ϕ) that delineate specific zones on the hydrotextural diagram which correspond to those where liquid and gas phase are connected.

2.3 Kneading, packing and drying methods

Kneading. Wet masses are processed in a planetary mixer (Kenwood Major 1200). Rotation speed and dry load are constant and fixed at 70 rpm and 200 g, respectively. The wetting liquid is added steadily during 3 min. The wet mass is then homogenized for another 3 min before draining the mixer content on a smooth and clean surface. The water content, defined by the ratio of water to dry solid mass, ranges from 0% to 77%. Wet mass samples could be in two different states: an agglomerate bed at a water content lower than the plastic limit⁽⁵⁾, and a dough for higher water content values. We consider here the agglomerate state with two characteristic scales: the agglomerate scale and the bed bulk scale. Measurements of water content, compactness and saturation degree are in accordance with the methodology defined by Ruiz *et al.*⁽⁴⁾ and Rondet *et al.*⁽¹⁵⁾. To define these hydrotextural variables V_b , V_a (the bed bulk and agglomerates volumes, respectively), m_w and m_s (water and solid masses, respectively) must be assessed. The volume measurements are carried out by sampling the wet mass with a cylindrical metal ring (V_b) of 319 mm^3 ($\phi=7.22 \text{ mm}$; $h=7.81 \text{ mm}$), or by reading the displaced volume (V_a) after introducing weighed amounts of one or more agglomerates into paraffin, respectively. The wet masses sampled with the metal ring are weighed before and after drying in an oven (105°C over 24 h), the water content of each sample is evaluated by means of the m_s and m_w . Concerning the water content of the immersed agglomerates, this is evaluated on agglomerates of equivalent size taken in the same wet mass and placed in the oven (105°C over 24 h).

Packing. The samples are subjected to an uniaxial packing. This is carried out after the kaolin is kneaded with water, 20 g of this mixture is then placed in a cylindrical metal mold (2.54 cm in diameter and 19 cm long). Measurements are carried out using an instrumented press that controls the displacement rate of the piston in the mold (1 mm/s). The packing pressure resulting from this displacement is also

measured. During the test, the air is drained, which does not generate overpressure. The piston stops as soon as the net stress is equal to the set pressure (0.4; 1; 2; 4 MPa). The water content (w) and compactness (ϕ) of the sample are measured at the end of the test by weighing them before and after drying (105°C for 24h). The volume of the compact sample, necessary for calculation of its compactness, is deduced from the displacement of the piston at the end of the packing experiment.

Drying. The samples are dried in soft condition (constant and low temperature and immobile air). Thus, only the relative humidity (RH) of air could vary by using the saturated saline solutions method (7, 22, 33, 43, 63, 75, 85, 91 and 96%) at constant temperature 25°C. During the experiment, each sample (placed in different cells) was removed to measure its mass and dimensions. The samples were weighed on a balance (accuracy 0.01 milligram) to monitor the water loss, and their mean sizes were measured consecutively with a digital thickness micrometer (0.02 mm precision). Dry mass (m_s) is measured at the end of the experiment by placing the sample in an oven (105°C) for 24 hours. All these measurements do not exceed 2 minutes per manipulation and do not significantly disrupt the observed results.

3. Construction of the Hydrotextural Diagram

In accordance with Matyas and Radhakrishna¹⁾ and Liu and Nagel²⁾, the phase diagram of a wet granular medium is a graph plotted in the benchmark made up of compactness ($\phi = V_s/V_b$ with V_s and V_b being respectively the solid volume and the apparent volume at the bed bulk scale or the agglomerate scale), of water content ($w = m_w/m_s$) and of the operational parameter related to the transformation undergone by the product (Σ). However, independently of the

transformations which are applied to the triphasic medium, it is possible to note in the benchmark (w, ϕ) that particular hydrotextural states can be distinguished. For example, for each water content, the saturation state represents the solid volume fraction needed so as to saturate the granular media with water (**Fig. 1**).

It depends only on the ratio of the solid (ρ_s^*) and the real density of the liquid (ρ_w^*). If the constitution of a phase diagram makes it possible to establish a potential cartography of the states of the system, it becomes capital to identify the trajectories that the transformation path can take during the elaboration process (wetting/kneading, packing and drying).

Fluid phase states. The establishment of sorption isotherms of kaolin at different compactness makes it possible to identify the extent of the hygroscopic field of the product and then the transition towards the pendular state (**Fig. 2a**). The equilibrium water contents are depicted according to the relative humidity (RH). These isotherms are classified as a type 2¹¹⁾ and correspond to isotherms usually obtained with nonporous or macroporous adsorbents on the surface of which the adsorbed layer gradually thickens. This is characteristic of a multi-molecular adsorption. The GAB model¹³⁾ makes it possible to identify, for each isotherm, the water content necessary for saturation of the surface of the particles by a molecular monolayer (w_{mono}) and the water content that marks entry in the capillary field (w_{capil}). The capillary state is consecutive with the establishment of capillary menisci between the adsorbed water layers. The system has a sufficient interfacial energy to ensure the establishment of capillary bridges between grains. The Laplace pressure reaches the order of magnitude of the disjunction pressure. The localization of the coordinates (w_{mono}, ϕ_{mono}) and (w_{capil}, ϕ_{capil}) on the hydrotextural diagram makes it possible to de-

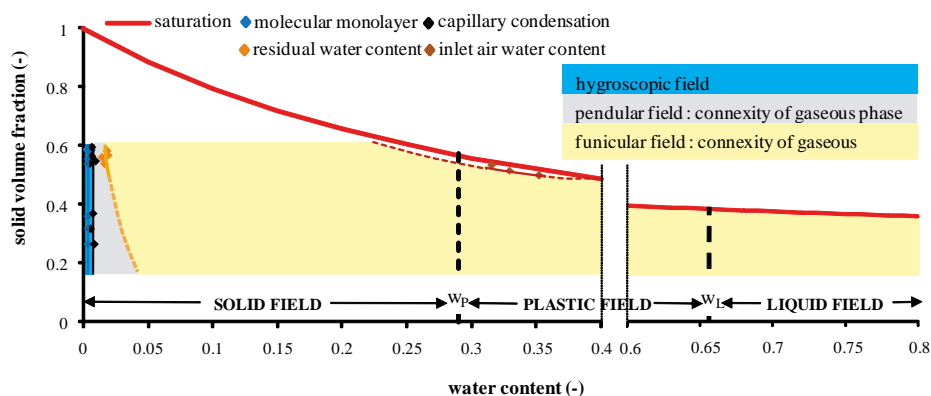


Fig.1 Hydrotextural diagram of kaolin.

limit a “hydrotextural” surface corresponding to the establishment of a saturated molecular mono-layer of adsorbed water and to the appearance of capillary bridges marking the end of the hygroscopic field and the entry in the pendular field (**Fig. 1**).

From the experimental results, the capillary retention curves can be depicted for each compactness value on a semi-logarithmic graph: volumetric water content ($\theta = V_w/V$) versus capillary pressure (**Fig. 2b**)¹⁶⁾. Let us mention that the experimental results presented are interpolated by the model of Fredlung and Xing¹⁴⁾, which allows a better recognition of the specific water contents w_i and w_r . The air inlet water content ($\theta_i \rightarrow w_i$) corresponds to the percolation threshold of the gas phase. When the medium is not saturated, and for water contents higher than w_i , the interstitial gas phase is entrapped in bubbles disconnected from each other. Beyond w_i the water is in the funicular state and the gas phase pressure exists at the global scale of the gaseous phase. The residual water content ($\theta_r \rightarrow w_r$) is the equivalent of the inlet air water content for the liquid phase. It marks the connectivity transition of the interstitial water and corresponds to the percolation threshold of water. For lower water contents, water is in the pendular state of “disjointed” menisci and adsorbed films. For higher water contents, the water pressure is a parameter that becomes representative of the total hydric state of the liquid phase (funicular state). The application of a hydrostatic pressure induced a flow of water (Darcian flow).

The positioning of these particular water contents on the hydrotextural diagram illustrates this fact and makes it possible to locate the characteristic zones of the two interstitial liquid phases with respect to the compactness state of the solid matrix (**Fig. 1**). The hygroscopic limit and the “lower” limit of the pendular field are slightly dependent on the compactness state of the granular network. Contrarily, the liquid

and gas percolation thresholds previously defined are extremely dependent on the value of the void volume. Between these percolation threshold curves corresponding to (i) residual water content for the liquid phase and (ii) to inlet air for the gas phase, the two fluid phases are simultaneously connected within the porous network. It is in this zone that the diphasic flows can take place and the intensive parameters such as densities are representative of the macroscopic phase state. Beyond this zone of tri-connectivity, at least one of the phases manifests a local state which it is advisable to consider statistically.

Rheological consistency limits. The granular medium is subjected to morphological changes as a function of the increase in water content: from a more or less pulverulent powder according to its cohesive nature, to the saturated state. Conversely, liquid/solid separation carried out by draining and/or drying shift the state of the system in the opposite direction without following the same path of hydrotextural transformation. From the dry states to the saturated states (of liquid), the rheological consistency of the mixture changes markedly by successively crossing the plastic limit and the liquid limit⁶⁾. The liquid limit (w_L) and plastic limit (w_P) of kaolin are close to $w_L \approx 0.66$ and $w_P \approx 0.29$, respectively. We checked that solid volume fractions which correspond to these water contents are located respectively on the saturation curve. This experimental result corroborates the observations of¹⁷⁾ showing that these Atterberg values correspond to a quasi-saturated state. The Atterberg limits make it possible to define three distinct fields of consistency (**Fig. 1**): solid, plastic and liquid. For the water contents higher than the plastic field, the medium behaves like a pseudo-liquid, creeping under its own weight.

The superposition of rheological, hydrotextural and, although not treated in this “isothermal” study, thermal aspects constitutes the hydrotextural dia-

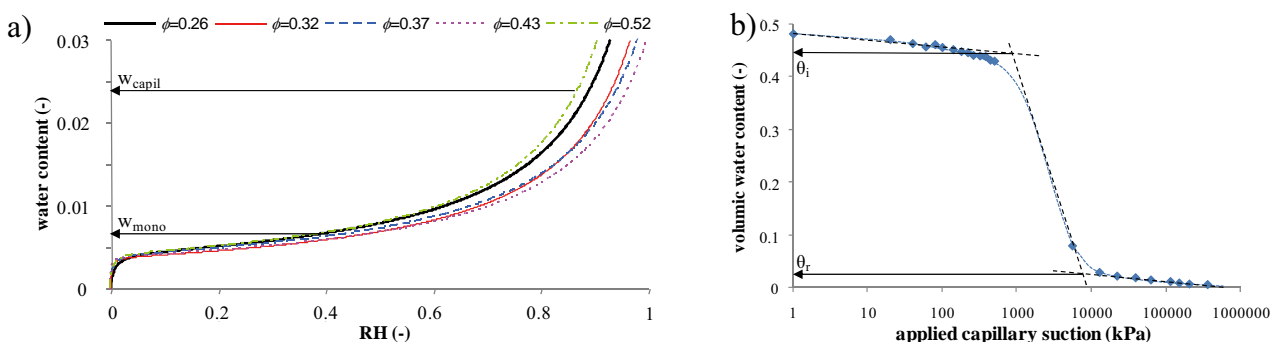


Fig.2 Desorption isotherms -a) and capillary retention curve -b) for kaolin at 25°C.

gram. This diagram counts the states potentially accessible by the tri or diphas mixture (dry or saturated). It reveals phase transitions primarily due to the connectivity of the components and to the rheological consistency of the mixture. The aptitude of the wet granular medium for state transformations is thus depicted within the same coherent framework. It is advisable, starting from this preliminary cartography, to introduce the influences of the transformation process applied to the system by integrating their specific operating capacities.

The aptitude of the mixture on the one hand and the process capability on the other hand; this dichotomy of principle is reunified within the phase diagram. Indeed, by regarding a particular transformation as kneading, packing or drying, it is consequently possible to analyze the influence of one or more representative operational parameters on the hydrotextral state. The phase diagram is then configured by adding the “operational” axis of the thermodynamic parameter which is characteristic of the transformation undergone (*i.e.* mixing energy, compressive stress, relative humidity, etc.).

4. Transformation Path on the Phase Diagram

The hydrotextral state of an unsaturated wet granular medium is initially characterized by its “distance” to the saturation state (dry or wet). Water content, compactness and saturation degree (S) (ratio of the liquid volume to that of the voids) are linked by a conservation balance⁴⁾:

$$\phi(w, S) = \frac{1}{1 + d_s^* \frac{w}{S}} \quad (1)$$

This equation derives from the saturation curve¹⁸⁾, taking into account the fact that for unsaturated states $w = S \cdot w_{sat}$ in equation (1) $d_s^* = \rho_s^* / \rho_w^*$. This relationship indicates that in a dry state ($w = 0$), compactness equals 1, which indicates that the solid apparent bulk density equals the real density of the solid particles. When the medium is saturated ($S = 1$), compactness depends only on the water content and the hydrotextral state is located on the saturation curve (**Fig. 1**). Between these two extreme states, the medium is not saturated and the relation between the saturation degree and the water content $S(w)$ is characteristic of the transformation path followed by the state of the medium during its transformation.

4.1 Kneading and wetting

At the agglomerate scale, Rondet¹⁹⁾ suggests a power law to describe the relation between the in-

crease in saturation degree and water content (**Fig. 3a**):

$$S(w) = \left(\frac{w}{w_{sat}} \right)^n \quad (2)$$

where w_{sat} is the water content corresponding to saturation of the agglomerate, and n is an exponent relative to the hydromechanical behavior of the agglomerates. Its value is lower than 1 for deformable media and equal to 1 for rigid and non-deformable materials. We observe that n is constant during agglomeration under defined process conditions. By reporting equation (2) in equation (1), we obtain the relation of compactness variation according to the water content during agglomeration morphogenesis:

$$\phi(w) = \frac{1}{1 + d_s^* w_{sat}^n w^{1-n}} \quad (3)$$

At the bulk scale, the authors proposed interpolation of the experimental dependence of the saturation degree on the water content (**Fig. 3a**), by means of a logistic law which corresponds to a sigmoid pattern:

$$S(w) = 1 - \frac{1}{1 + e^{\frac{w-w_m}{d}}} \quad (4)$$

where w_m and d are parameters corresponding respectively to the water content when the saturation degree equals 50% and the inverse value of the slope of the central part of the curve.

Fig. 3b depicts the hydrotextral diagram of kaolin. The texturation curves are plotted showing the variation of the solid volume fraction according to the water content at the two scales. At the bulk scale, three phases can be identified: (i) a phase of expansion during which the solid volume fraction is lower than that obtained in a dry state; (ii) a phase of gentle densification of the medium leading to a soft increase in the solid volume fraction until the water content reaches the percolation threshold previously defined⁵⁾ and from which the densification is very strongly accentuated; (iii) a final phase during which the medium reaches the saturation state and the solid volume fraction decreases. This phase of dilatation is extended until the granular medium reaches a suspension state. This texturing phenomenon, taking place between the dry and the saturated state, is the result of the interactions between the three phases constituting the unsaturated mixture. More explanation of these phenomena can be found in the references^{5, 15, 19)}.

4.2 Texturation by static packing

In the case of static compaction, Ruiz *et al.*⁴⁾ showed that the filling of the voids followed a sigmoid pattern (**Fig. 4**) and could be interpolated by eq. (4).

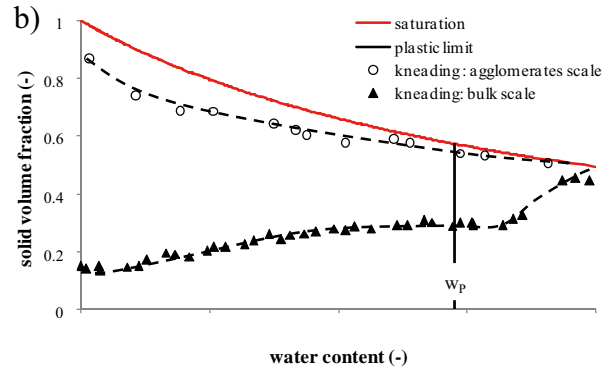
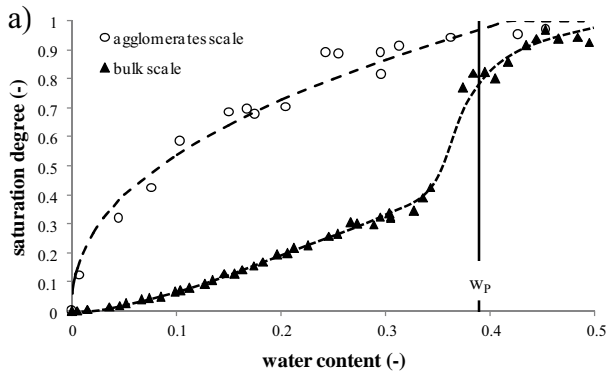


Fig.3 Textural evolution versus water content, at the agglomerate and at the bulk scale -a) saturation -b) solid volume fraction.

The two parameters of eq. (4) depend on the applied pressure. It is shown that a correlation between the normal compaction stress (σ) and the parameter w_m exist⁴⁾:

$$w_m \propto \frac{1}{a\sigma + b} \quad (5)$$

where a and b are fitting parameters, respectively, equal to 0.3499 and 1.1892, and whose physical meaning remains to be defined.

On the hydrotextural diagram (Fig. 5), these transformation paths reveal the same texturing phenomenon as that observed during kneading^{4,19)} due to the static compaction (0,4; 1; 2; 4 MPa).

By reporting equation 4 in equation 1, it is possible to obtain the mathematical expression of the transformation path (w, ϕ):

$$\phi(w) = \frac{1}{1 + d_s^* w \left[1 + e^{-\frac{w-w_m}{d}} \right]} \quad (6)$$

It is shown mathematically that the concomitant existence of the optima of expansion and densification implies that the w_m/d ratio is strictly higher than $0.02^4)$. In addition, it has been shown that these parameters are linearly dependent. This linear correlation is true

whatever the powder:

$$d = 0.2368w_m + 0.02 \quad (7)$$

The equations (5) and (7) make it possible to directly introduce the influence of the compaction stress applied in the expression of the transformation path (Eq. 6). Equation 6 describes a state surface specific to the packing of kaolin. The state surface is depicted in the phase diagram of figure 6. The transformation paths specific to the pressures applied in the experimental study (Fig. 5) correspond to projections of this surface in the plan (w, ϕ). Fig. 6 shows that the increase in the pressure submitted to the compact respects the texturing phenomenon (expansion, densification and dilution) by shifting it towards values of increasing compactness.

On Fig. 7, all the properties obtained from the sorption, draining/imbibition and consistency tests are overlaid on the transformation path. The texturing phenomenon can then be analyzed from various angles. The hygroscopic field extends from the dry state to the water content that allows capillary condensation and the formation of the first menisci. It is for higher water content that is reached the residual

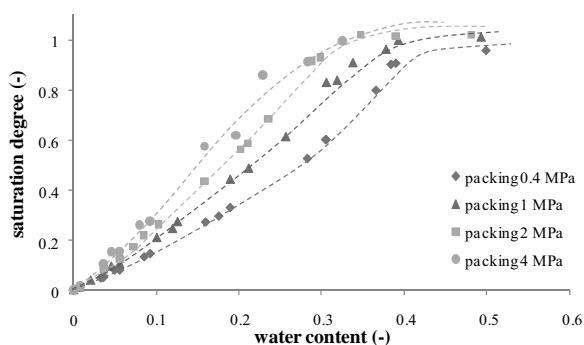


Fig.4 Loading path corresponding to voids filling for packed kaolin.

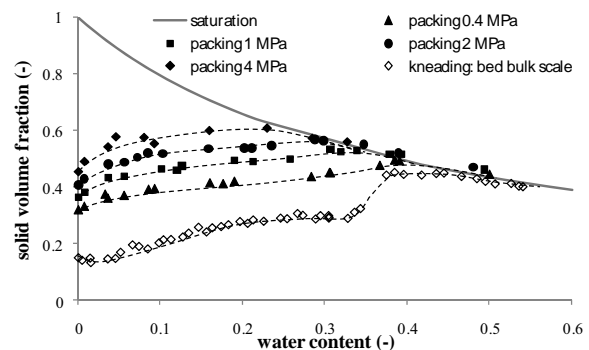


Fig. 5 Hydrotextural diagram of kaolin subjected to kneading (bed bulk scale) and uniaxial packing, in the benchmark (w, ϕ) – the texturing phenomenon.

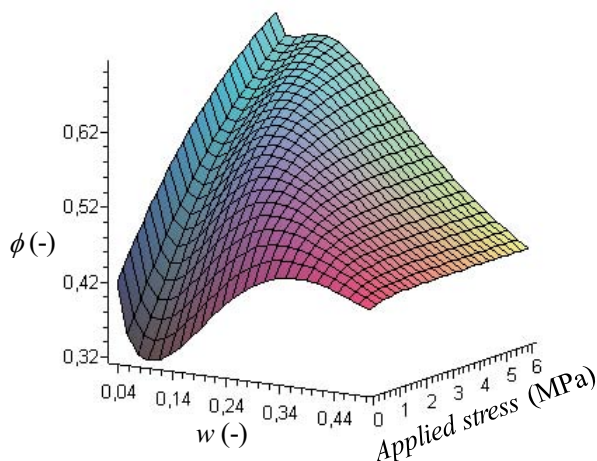


Fig.6 State surfaces of kaolin during packing in the phase diagram.

water content, which marks the end of the pendular field and the initiation of the liquid percolation within the matrix. From this limit on, the capillary bridges, whose number increases up to this point, will be gradually drowned by the successive water additions. The two fluid phases, water and gas, are then connected: water is in a funicular state. For higher water contents, it is possible to locate the water content of the inlet air beyond which the gas phase will remain in the matrix as entrapped air bubbles. This state is obtained for water contents close to 90%. These different water contents constitute important limits marking the change of the water state within the matrix. Whereas the water contents which ensure saturation of the molecular monolayer and capillary bridges (capillary condensation) are relatively independent of the compactness state of the medium, it is

not the same for the residual water content and inlet air water content, whose values increase as the compactness of the medium decreases. The medium densification does not induce a significant variation in the surface accessible to water but a reduction in pore size, caused by an increase in compactness, reduces the water quantity that is necessary to crossing the limit which marks the end of the pendular and funicular field. The superposition of these various fields on the evolution of the texturing phenomenon obtained after compaction enables us to link the succession of the three stages of the texturing phenomenon to the liquid phase state within the granular matrix (Fig. 7).

Concerning the expansion, the adsorbed water films are subjected to a disjunction pressure which counteracts the connection of grains, thus generating a reduction in compactness. Then, beyond the water content of capillary condensation, capillary menisci develop. These capillary bridges, whose number grows in the water content range corresponding to the pendular state, induce a capillary Laplace pressure and exert a traction between grains and induce a connection, or, in the case of packing, promote their local connection. The effect is all the more marked that the number of menisci increases. The densification slope is thus the more pronounced during the field where water is in the pendular state. With the increase in wetting, the antagonistic effects of the disjunction pressure and of Laplace pressure turn in favor of the capillarity, gradually extinguishing the expansion phenomenon to the detriment of densification. This phenomenon continues until the residual water content from which the connectivity of the liquid phase induces a progressive reduction

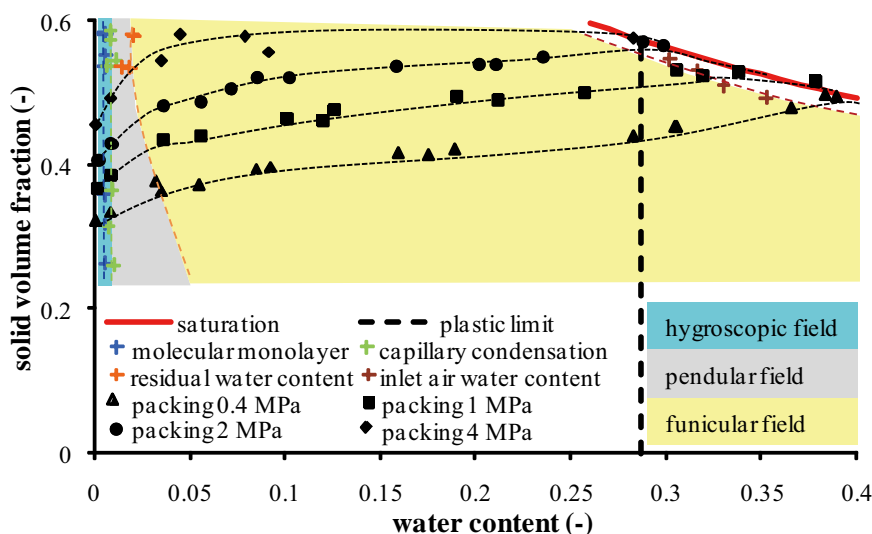


Fig.7 Complete phase diagram for kaolin submitted to packing stress.

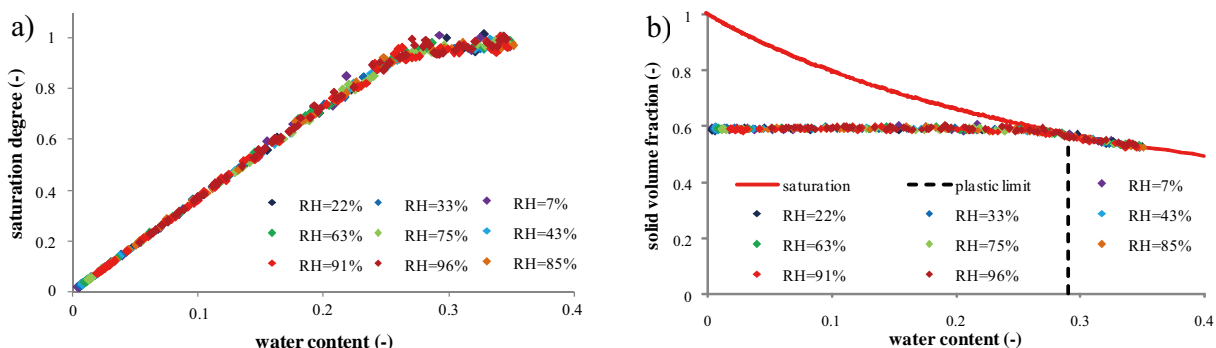


Fig.8 Evolution of –a) saturation degree and –b) solid volume fraction versus water content during drying at different relative humidity.

in the number of local capillary bridges. This pore filling results in a less pronounced densification slope up to the optimum of densification. This is obtained when all the menisci disappear and when capillary traction is exerted in the periphery of the sample as is the case in the capillary field. It is important to mention that the densification optimum corresponds systematically to the inlet air water content. The gas percolation threshold in the porous network is concomitant with the densification because the result of the capillary actions then reaches its paroxysm. These water contents correspond to saturation degrees close to 90%. Menisci corresponding to the liquid and air interface are circumscribed at the sample periphery and thus exert their action synergetically on the whole system, as is the case for the action of the surface tension around a water droplet. The densification optimum thus corresponds to the definition of the Proctor Optimum described in soil science¹⁶⁾. The progressive saturation of the medium decreases the capillary actions which will gradually disappear. Compactness thus decreases until the total saturation state beyond which it will be given by the saturation curve of the product. It is the dilution stage for which the saturated paste is comparable to a hard suspension²⁰⁾, then to a soft suspension when the solid phase is not connected anymore.

4.3 Texturation by drying

The drying of a saturated kaolin compact processed by static compaction implies shrinkage until compactness reaches its random close packing value ($\phi \approx 0.6$) corresponding to the shrinkage limit. At this value, the granular medium becomes rigid and an interstitial gaseous phase appears (Fig. 8). Before this value, the medium remains in a saturated state. After this value, the saturation degree varies with water content, and follows equation (2), with $n = 1$. The drying continues until the hygroscopic equilibrium

is reached. Relative humidity had no influence on the drying paths (Fig. 8b), except on the equilibrium water content given by the desorption isotherm. Texturing due to drying in soft conditions is easy to model, and the phase diagram is reduced to a single curve (Fig. 8b).

5. Conclusion

This experimental work is classified within the theoretical framework of establishing a state diagram for this particular soft matter class, i.e. the wet granular materials. The proposed diagram makes it possible to depict the hydric, textural and rheological states of a wet granular medium. Thanks to specific tests borrowed from multiple sciences treating the granular media, the hydrotextural diagram of kaolin is experimentally built. This voluntary multi-field approach is only a reflection of the phenomenological richness of the wet granular media. More pragmatically, this representation makes it possible to identify the repartition of the three dispersed phases within the mixture and its densification capacity during packing.

This phase diagram is thus a cognitive tool to enable the transformation path of a granular product during its processing to be followed. This work mentions, for example, the similarity between the effects of drying and draining on the evolution of the medium compactness. It finally makes it possible to understand, on a continuous medium scale, the succession of the various stages of the texturing phenomenon induced by the increase in water content. The experimental results make it possible to conclude that the succession of these various stages is linked with the water state within the matrix. Under the modulated effect of the capillary forces, the cohesion of the wet granular medium evolves, enabling it to adopt more or less compact configurations.

The state diagram of a wet granular media appears

that follows the example of its remote cousin the state diagram of “molecular” bodies, (i) like a tool for identification of the impact of the product and of the process on the transformation of a system, (ii) as the support of a twin product/process analysis for the processing of products with defined functionalities.

Nomenclature

d	inverse value of the slope of the central part of the curve ($S=f(w)$)	
d_s^*	ratio of the density of the solid to that of the liquid	[-]
d_{50}	median diameter	[mm]
e	void index	[-]
m_w	mass of water	[g]
m_s	dry mass	[g]
n	exponent relative to the hydromechanical behavior of agglomerates	[-]
S	Saturation degree, ratio of the liquid to voids volume	[-]
T	temperature	[°C]
V_a	volume of agglomerates	[cm ³]
V_b	volume of the agglomerates' bulk	[cm ³]
V_s	solid volume	[cm ³]
V_w	volume of water	[cm ³]
w	water content	[-]
w_{capil}	water content allowing initiation of capillary condensation phenomenon	[-]
w_i	inlet air water content	[-]
w_L	liquid limit	[-]
w_m	water content when the saturation degree equals 50%	[-]
w_{mono}	water content of saturation of the specific surface area by water molecules	[-]
w_P	plastic limit	[-]
w_r	residual water content	[-]
w_{sat}	water content corresponding to saturation of the agglomerate	[-]

Greek letters

θ	volumetric water content	[-]
ρ_s^*	density of the solid	[g.cm ⁻³]
ρ_w^*	density of the liquid	[g.cm ⁻³]
Σ	applied stress	[Pa]
	solid volume fraction	[-]
σ	normal compaction stress	[Pa]

References

1) Matyas E. L.; Radhakrishna H. S.: Volume change characteristics of partly saturated soils, *Geotechnique*, 18, 1968, 432-448.

2) Liu A. J.; Nagel S. R.: Jamming is not just cool any more, *Nature*, 396, 1998, 21-22.

3) Knight J. B.; Fandrich C. G.; Lau C. N.; Jaeger H. M.; Nagel S. R.: Density relaxation in a vibrated granular material, *Physical review E*, 51, 1995, 3957-3963.

4) Ruiz T.; Delalonde M.; Bataille B.; Baylac G.; Dupuy de Crescenzo C.: Texturing unsaturated granular media submitted to compaction and kneading processes, *Powder Technology*, 154, 2005, 43-53.

5) Rondet E.; Delalonde M.; Ruiz T.; and Desfours J-P: Hydrotextural and dimensional approach for characterising wet granular media agglomerated by kneading, *Chemical Engineering research and Design*, 86, 2008, 560-568.

6) Atterberg A.: Die Plastizität der Tone, *Internationale Mitteilungen Für Bodenkunde* 1, 1911, 10-43.

7) Coussy O.; Fleureau J-M.: « Mécanique des sols non saturés », 2002, Hermès Sciences Publications, Paris, France.

8) Mussy A.; Soutter M.: « Physique du sol », 1993, Edition Tec et Doc, Lausanne, Switzerland.

9) Standard NF P 94-052-1: Détermination des limites d'Atterberg. Limite de liquidité. Méthode du cône de pénétration, 1995.

10) French Standard NF P 94-051: Détermination des limites d'Atterberg. Limite de plasticité au rouleau, 1993.

11) Rouquerol F.; Luciani L.; Llewellyn P.; Denoyel R.; Rouquerol J.: Texture des matériaux pulvérulents ou poreux, *Techniques de l'Ingénieur, traité Opération unitaires*, 2003, article P 1050.

12) Brunauer S.; Emmett P. H. ; Teller E.: Adsorption of gases in multimolecular layers, *Journal of American Chemistry Society*, 60, 1938, 309-320.

13) Blahovec J.; Yanniotis S.: Modified classification of sorption isotherms, *Journal of Food Engineering*, 91, 2009, 72-77.

14) Fredlung D. G.; Xing A.: Equations for the soil-water characteristic curve, *Canadian Geotechnical Journal*, 31, 1994, 521-532.

15) Rondet E.; Delalonde M.; Ruiz T. ; Desfours J-P: Identification of granular compactness during the kneading of a humidified cohesive powder, *Powder Technology*, 191, 2009, 7-12.

16) Magnan J-P: Description, identification et classification des sols, *Techniques de l'Ingénieur, Traité Construction*, 1997, C 208.

17) Jefferson I.; Rogers C.: Liquid limit and the temperature sensitivity of clays, *Engineering Geology*, 49, 1998, 95-109.

18) Fleureau J. M., Kheirbek-Saoud S., Soemitro R., Taibi S., Behavior of clayey soils on drying-wetting paths, *revue Canadienne de Géotechnique*, 30, 1993, 287-296.

19) Rondet E.: Texturation capillaire de milieux granulaires humides. Ph. D. Thesis, Université des Sciences, Montpellier, (2008), http://hal.archives-ouvertes.fr/docs/00/33/05/01/PDF/These_rondet.pdf

20) Coussot P.; Ancey C.: Rheophysical classification of concentrated suspensions and granular pastes, *Physi-*

Author's short biography



Eric Rondet

After a university course focused on health and industrial formulation of health products, Eric Rondet obtained in 2005 a master's degree in process engineering. He prepared a PhD thesis on the capillary texturing of wet granular media in the Process Engineering - Water and Bioproducts Laboratory (UMR CIRAD 016) of Montpellier, and obtained his doctor's degree in 2008 from the University of Montpellier 2 (France). He then integrated the laboratory of Agropolymer and Emerging Technologies (UMR IATE - Montpellier SupAgro - INRA) for a study related to the agglomeration of cereal powders. Eric Rondet is currently an assistant professor in the Process Engineering- Water and Bioproducts Laboratory (UMR CIRAD 016).



Montana Rungsiyopas

Montana Rungsiyopas obtained her master's degree in Mechanical Engineering (Energy Technology) in 2001 from KMUTT (Thailand). She then worked as a lecturer in the mechanical engineering department, Burapha University (Thailand). She is now studying for her Ph.D. in the Process Engineering - Water and Bioproducts Laboratory (UMR CIRAD 016), at the University of Montpellier 2 (France). Her thesis is related to the theoretical analysis of mass and energy transfer connected with the deformation during the drying process of granular media. She will return to work in the mechanical engineering department of Burapha University as soon as she obtains her doctor's degree.



Thierry Ruiz

The path in the scientific world of Thierry Ruiz began with a mathematical course in the Science Faculty of Montpellier, followed by a Ph.D. which deals with non-equilibrium thermodynamics applied to the modeling of reactive mass transfer in porous media (Mechanic and Civil Engineering Laboratory of Montpellier). Assistant professor in the Process Engineering - Water and Bioproducts Laboratory (UMR CIRAD 016) since 1999, his works are focused on mass and energy transfers coupled with the morphogenesis of heterogeneous materials elaborated with soft matter (granular media, residual sludges, clay), where capillary interaction corresponds to the main texturing action.



Michèle Delalonde

Michèle Delalonde is a pharmacist from the pharmacy school at the University of Montpellier 1 (1983). She first specialized in writing Common Technical Documents (CTD) on novel drugs for different industrial partners. Afterwards, she obtained a master's degree in polymers for therapeutic applications and a PhD thesis focused on the rheological properties of wet masses. She obtained her doctor's degree in chemical and biological sciences for health in 1998. Currently, she works as an assistant professor in the Process Engineering - Water and Bioproducts Laboratory (UMR CIRAD 016). Her research works are actually focused on granular media and on the optimization of elaboration processes.

Jean-Pierre



Jean-Pierre Desfours began his career at the University of Montpellier 2 where he obtained his PhD on the electrical properties of magnetic semiconductors. An assistant professor at this university until 1987, he worked as a full professor in Marseille up to 1997. Since returning to the University of Montpellier, he has coordinated the Process Engineering- Water and Bioproducts Laboratory (UMR CIRAD 016). During his career, he has conducted research work and theses on different subjects in a large area of physics ranging from high-frequency electronic circuits, microchemical sensors and other devices, and his focus now lies on process engineering for the elaboration of materials from granular media.

Novel Material Properties Based on Flame-synthesized Nanomaterials[†]

Hartmut Wiggers

Institut für Verbrennung und Gasdynamik, University Duisburg-Essen¹

Abstract

The principles of high-temperature reactive particle formation in flames are characterized by a sequence of partly interacting rate processes in the gas flow, while the necessary energy is delivered by the exothermic combustion reaction heating the flow to high temperatures. A complete description of the precursor decomposition kinetics and the subsequent oxidation/hydrolysis reactions is rarely obtained, while the properties of the products manufactured such as size, morphology, phase composition, and crystallography are decisively influenced by these parameters. A precise understanding and control of the initial steps is therefore required to open up the possibility of tuning particle properties.

In the present study, the formation of oxidic particles in flame reactors is presented. It will be shown that the stoichiometry and crystallography of oxides such as ZnO, SnO₂ and TiO₂, and therefore their physical and chemical properties, can be adjusted depending on the reaction conditions. In addition to the synthesis of pure materials, coated particles as well as nanocomposites are accessible when a few requirements are fulfilled. In the case of immiscible oxides such as TiO₂ and SiO₂, composites consisting of separate phases are produced, while the formation of composites from miscible compounds usually requires a two-step process that tends to produce poorly mixed materials. Nevertheless, in the case of kinetically controlled synthesis, a one-step formation of nanocomposites from miscible oxides can be realized when the kinetics of precursor decomposition and particle formation of the participating oxides are quite different. This results in materials that exhibit new properties according to the used oxides. As an example, the one-step formation of homogeneously dispersed superparamagnetic Fe₂O₃ in fumed silica will be shown. Chemically, this material behaves like common silica but due to the superparamagnetic characteristics of the embedded iron oxide, it can be heated in a contactless manner by means of an alternating magnetic field. Applications focusing on contactless hardening and bonding become apparent.

Keywords: Flame synthesis, nanoparticles, TCO, nanocomposites, superparamagnetic Fe₂O₃, MagSilica®

1. Introduction

The formation of inorganic nanoparticles is used routinely today to produce a variety of bulk chemicals such as SiO₂, Fe₂O₃, TiO₂, Al₂O₃ and ZnO, amounting to millions of tonnes a year. They are used industrially as reinforcements, pigments, stabilizers, catalysts or catalyst supports, flowing aids, and multiple other applications. The formation of nanoparticles can be divided into two generally differing methods: wet-chemical and gas-phase synthesis. While wet-chem-

ical synthesis usually results in materials formed by thermodynamic control, gas-phase processes enable a kinetic control of nanoparticle formation. This method is therefore basically favored for the formation of metastable materials as doped nanoparticles and nanocomposites. As there is a variety of different reactor concepts such as hot-wall reactor, plasma reactor and laser reactor, the bulk synthesis for nano-sized inorganic particles is covered by flame reactors because they enable a cost-effective and versatile industrial process with high production rates. Moreover, flame reactors are designed for a broad range of operating conditions for the control of particle size, morphology and composition. Some useful studies on the flame synthesis of nanoparticles can be found in

[†] Accepted: September 30th, 2009

¹ Lotharstr. 1, 47057 Duisburg, Germany
TEL: (+49)203 379 3156, FAX: (+49)203 379 3087
E-mail: hartmut.wiggers@uni-due.de

the literature^{1, 2, 3, 4}.

Due to an increased understanding of size-dependent nanoparticle properties and probable applications thereof, an increasing demand for synthesis methods for the formation of specific nanoparticles with tuned properties has evolved. As the flame reactor is the workhorse for the gas-phase formation of nanoparticles, this paper addresses different possibilities for the formation of nanomaterials with specific properties by flame-synthesis. While we are interested in a precise understanding of the physics and chemistry of the oxidic particles themselves, impurities were neglected as far as possible. Because, for instance, Spicer et al. have already studied the possibilities for the formation of SiO_2/C nanoparticles in a premixed acetylene/oxygen flame⁵, we tried to avoid uncertainties resulting from such carbon-containing flames and complex hydrocarbon flame chemistry probably interacting with particle formation. Therefore, most of the results shown were obtained from experiments carried out in a low-pressure, premixed H_2/O_2 flame. The particle formation and growth were observed by means of a particle mass spectrometer (PMS) for the first few centimeters downstream of the flame-stabilizing burner head⁶. A typical result of such a PMS measurement taken during the formation of SnO_2 nanoparticles is shown in Fig. 1. Both PMS measurements and TEM investigation of thermophoretically sampled particles are always found to be in good agreement with respect to the mean particle diameter d_p and the standard deviation σ .

Typically, a reasonable particle growth is observed starting from about 80 mm downstream of the burner head (flow coordinate, height above burner), as shown in Fig. 2. The specification of the PMS en-

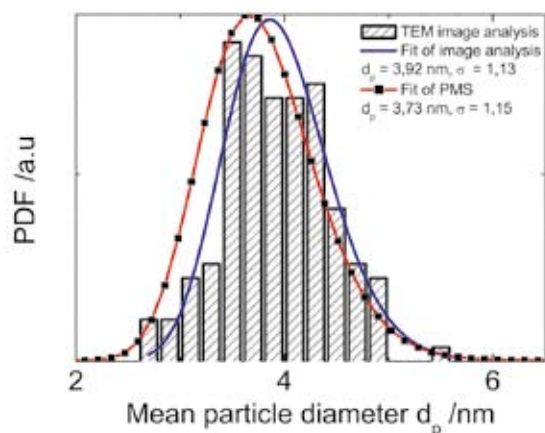


Fig.1 Comparison between PMS measurement and TEM analysis for the formation of SnO_2 nanoparticles taken at 110 mm height above the burner.

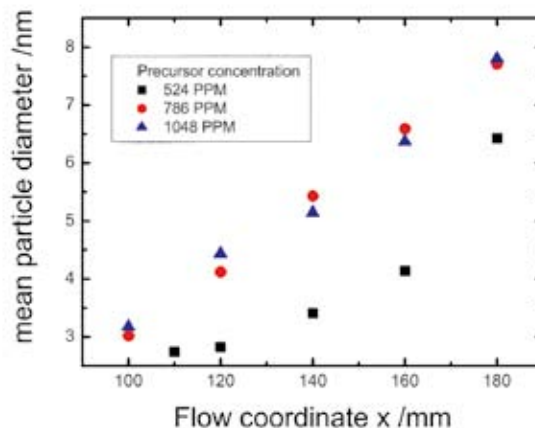


Fig.2 Particle growth of tin oxide nanoparticles downstream of the flame reactor as measured with a PMS.

ables measurement of the particles' size between 2 and 15 nm.

For further investigation, the as-prepared materials were usually sampled by thermophoretic deposition of the particles downstream of the reactor either on TEM grids or on a cooled substrate.

2. Oxidic Semiconductors

Semiconducting oxidic nanoparticles such as tin oxide and zinc oxide are seriously discussed as transparent conducting oxides (TCOs) for the formation of transparent conducting layers as they are used in flat panel displays and solar cells, while titania is used as the electron-conducting electrode in dye solar cells, the so-called Grätzel cells. Up to now, the market for TCOs has been dominated by indium tin oxide (ITO) and fluorine-doped tin oxide (FTO), mainly prepared by chemical vapor deposition (CVD), physical vapor deposition (PVD) and sputtering. These methods usually require expensive, low-pressure process steps and have the disadvantage that a lot of the material is not deposited on the substrates but is lost as so-called off-spray. Printing methods using nanoparticles such as ink-jet printing or roll-to-roll printing would allow minimizing the waste of the TCO, but these methods are still not able to completely resolve the issue of the high cost of ITO⁷. In addition, the electrical as well as the optical performance of printed layers based on nanoparticles mostly do not meet the requirements for TCO layers. This is mainly due to the two following drawbacks:

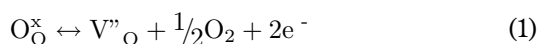
- 1 Agglomerates and bigger nanoparticles exceeding a size of about $1/10^{\text{th}}$ of the wavelength of the visible light decrease the transparency of a

printed layer due to scattering processes.

- The electrical properties of the printed films is poor compared to a common layer prepared by CVD or PVD due to poor electrical properties of the particles themselves as well as to poor particle-particle contacts.

While the first drawback can be engineered by adjusting the residence time as well as the time-temperature profile within the flame reactor, the second drawback is more difficult to solve.

Almost all oxidic semiconductors are n-type conductors, which means that the majority charge carriers are electrons. The electrons in the oxides originate from oxygen that is released from the lattice leaving behind two charge carriers, and can be described by the Kröger-Vink notation:



As a result, the adjustment of specific properties with respect to the electrical properties requires a tuning of the particle composition, especially its oxygen content during particle formation.

Several authors have shown that the fuel-to-oxygen ratio of flames has an important influence on nanoparticle properties such as morphology, size, crystallinity and stoichiometry^{8, 9, 10, 11}. In their works, the influence of the flame conditions on the stoichiometry and therefore on the electronic properties of several oxides are discussed.

In accordance with⁹, for all experiments the fuel-to-oxygen ratio Φ is defined as

$$\Phi = \frac{\text{mol of oxygen required for complete combustion}}{\text{mol of oxygen supplied}} \quad (2)$$

This means for $\Phi < 1$ that the flame is operated at lean conditions while $\Phi > 1$ corresponds to rich conditions.

Whereas in industrial synthesis processes Φ is usually fixed at a value around 0.5, our experiments were performed for values of Φ between 0.25 and 0.97 to investigate the influence of the fuel-to-oxygen ratio on the nanoparticles properties. Experiments performed at Φ close to one showed that almost no tin oxide or zinc oxide could be produced from organometallic precursors under this condition. Tin is known to exhibit stable oxidation states of 2 and 4, however, oxidation states that lie between 2 and 4 have been identified¹². X-ray diffraction (XRD) measurements of the powder received from synthesis at $\Phi = 0.85$ showed that the monoxide SnO is formed rather than the dioxide SnO₂. As is the case with many organometallic precursors, the Sn-precursor tetramethyltin (TMT) decomposes and forms Sn at-

oms within a few hundred microseconds by thermal decomposition. Thereafter, tin oxide is produced by a subsequent oxidation of the tin atoms^{13, 14}. As studied for many metals, atomic as well as molecular oxygen plays an important role for the oxidation of metal atoms and suboxides, respectively^{15, 16}. Therefore, the oxidation process leading to tin dioxide is expected to be incomplete because of the lack of oxidizing species. Hence, it is understandable that almost no tin oxide was found at $\Phi > 0.85$ due to the fact that mainly tin monoxide is formed. Its high vapor pressure prevents the material from condensation within the reaction chamber¹⁴.

Zinc oxide is an amphoteric material that forms zinc hydroxides during particle growth within the flame and which also has a high vapor pressure like tin monoxide¹⁷. As a result of the high vapor pressure of tin monoxide and zinc hydroxide at elevated temperatures, it was found that noticeable amounts of tin oxide and zinc oxide nanoparticles could only be produced when $\Phi > 0.7$.

The results of these investigations show that stoichiometric H₂/O₂ ratios may be inadequate for a sufficient oxidation of precursor material and the formation of the respective oxides is significantly dependent on the oxidation potential of the flame. A 1-dimension simulation of the gas-phase species that appear in hydrogen/oxygen flames typically used for nanoparticle synthesis was performed with CHEMKIN's PREMIX™. The underlying gas-phase temperature used for the calculation was measured with laser-induced fluorescence of traces of NO added to the burning gas¹⁸. Despite the concentration of the educt gases hydrogen and oxygen, the diluent argon, and the product water, it was only hydrogen, oxygen, and OH radicals that showed a noteworthy concentration along the reaction path while the concentration of HO₂ as well as H₂O₂ is negligible. Except for molecular oxygen, species with oxidizing and reducing properties for $\Phi = 0.5$ and 0.85 are shown in **Fig. 3**.

The simulation shown in **Fig. 3** indicates that in the case of $\Phi = 0.5$, the concentration of the oxidizing radicals O[•] and OH[•] (filled symbols) reaches the maximum shortly after entering the reaction zone at about 20 mm height above the burner head, and the portion of the reducing gases H and H₂ vanishes very fast. In the case of $\Phi = 0.85$, the concentration of O/OH compared to H/H₂ is clearly lower. A high concentration of oxidizing species is vital for the oxidation process and their concentration with respect to the height above burner is indicative of the degree of oxidation at that position. Hence, the oxidation of

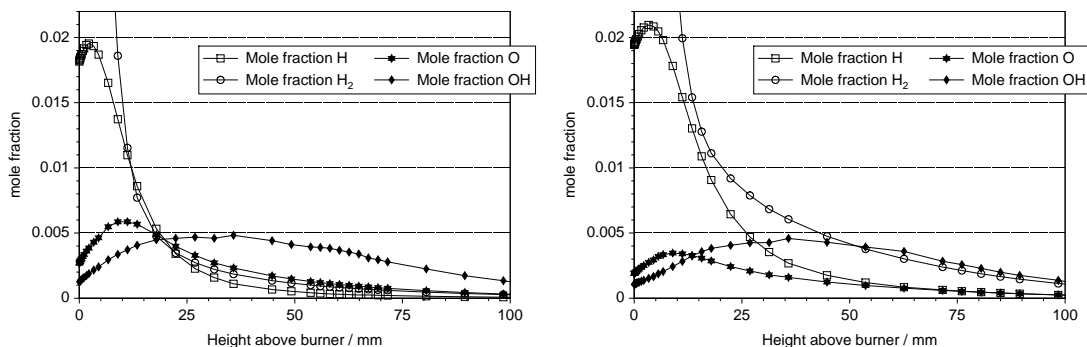


Fig.3 Mole fraction of O^\bullet , OH^\bullet , H^\bullet and H_2 in a $H_2/O_2/Ar$ premixed flame calculated with PREMIX™ for $\Phi = 0.5$ (left) and 0.85 (right).

the metal is assumed to be highly sensitive to the oxidation potential at the early particle formation due to no further increase of the concentration. As for low initial concentrations of oxygen, this concentration and the residence time within the reactor isn't sufficient for the formation of some materials with the highest possible oxidation state, and an oxygen-concentration-dependent stoichiometry is synthesized. As a result, the electrical as well as optical properties change due to the conditions during particle growth. **Table 1** summarizes some of the results obtained from electrical measurements on tin oxide powders.

To measure the resistivity, a few mg of the as-prepared powders were pressed into thin pellets with a diameter of 5 mm. The thickness was measured and the AC impedance of the pellets was investigated by putting them between 2 plane platinum electrodes¹⁹. The DC conductivity was extrapolated from the low-frequency data measured, and the resistivity was calculated by means of the geometrical data.

As a second example, the insufficient oxidation during the formation of TiO_2 nanoparticles via synthesis in the premixed flame reactor will be discussed. The synthesis of titania with a decreasing amount of oxygen results in colored material and the color can be tuned from white to pale yellow to pale blue. As previously reported, this change in color is strongly dependent on defects originating from oxygen vacancies that give rise to color centers^{20, 21, 22}. It is assumed that these defects are responsible for an increased catalytic activity of those materials²⁰.

Additionally, a high oxygen flow rate tends to favor the formation of the anatase phase, while a low oxygen flow rate promotes the formation of the rutile phase^{23, 24}.

Oxygen vacancies also play an important role in the defect luminescence of zinc oxide at around 2.25 eV, while simultaneously quenching the band gap and near-band gap luminescence in the blue around 3.25 eV. These oxygen defects can be prevented via a wet chemical route with subsequent surface termination^{25, 26}. An extreme excess of oxygen during the formation of zinc oxide from the gas phase can nevertheless also be successfully used to produce ZnO nanoparticles that show almost no defect luminescence, as can be seen in **Fig. 4**.

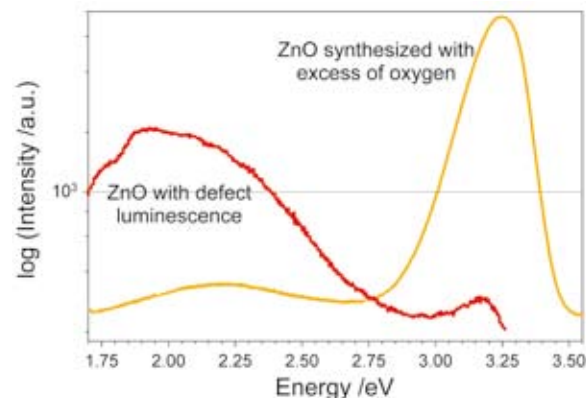


Fig. 4 PL spectra of ZnO from the gas phase synthesized at $\Phi = 0.5$ (red graph) and with extreme excess of oxygen.

Table 1 : Resistivity of as-synthesized tin oxide nanoparticles under ambient conditions synthesized at $0.98 < \Phi < 0.25$

Stoichiometry	Φ	Crystal structure	Color	Resistivity / Ωm
SnO_2	0.25	tetragonal (Rutile)	white	$14.8 \cdot 10^3$
$SnO_{1.74}$	0.63	tetragonal (Rutile)	light yellow	$7.4 \cdot 10^3$
$SnO_{1.4}$	0.85	tetragonal (PbO)	light gray	$4.8 \cdot 10^3$
SnO	0.98	tetragonal (PbO)	gray	$0.98 \cdot 10^3$

3. Nanocomposites

The kinetic and/or temperature control of particle formation in flame reactors not only opens a broad range with respect to their oxygen content, but also enables the formation of specific nanocomposites. Several authors have shown that, depending on flame conditions and temperature, different types of composites are accessible^{27, 28}. The authors have shown that both particles of one kind homogeneously embedded in a second material as well as homogeneous mixtures of two kinds of particles are accessible. They also found that the existence of a second phase may influence size, morphology and crystallinity. This paper will focus on the physicochemical properties of the composites. The $\text{TiO}_2/\text{SnO}_2$ and $\text{SiO}_2/\text{Fe}_2\text{O}_3$ systems will therefore be discussed in detail. The phase diagram of $\text{SnO}_2/\text{TiO}_2$ shows a big miscibility gap (see **Fig. 5**) and in thermodynamic equilibrium, a segregation of SnO_2 and TiO_2 is observed. A couple of scientists have investigated the properties and main differences of $\text{SnO}_2/\text{TiO}_2$ *composite* particles and films compared to *mixed oxides* (i.e. substitution of Ti with Sn in the TiO_2 lattice and vice versa) with respect to their photocatalytic potential^{29, 30, 31}.

The photocatalytic activity of titania mainly depends on the formation of electron-hole pairs (excitons) and the strong oxidation potential of the hole. In TiO_2 , excitons can be created under UV irradiation, and the composite material $\text{TiO}_2/\text{SnO}_2$ is expected to improve the transport of electrons from titania to tin oxide. The spatial separation of electrons and holes prevents the excitons from recombination and increases the photoactivity. In comparison to the composite material, the increase in photoactivity of the mixed oxides is expected to originate from an increase in band gap energy of the solid solution $\text{Ti}_{1-x}\text{Sn}_x\text{O}_2$.

Whereas usually, different routes for the formation

of composites and mixed oxides are required, flame synthesis has the ability to produce both composites as well as mixed oxides. Due to the high temperature gradient in flame reactors in the order of $10^4 - 10^6$ K/s³³, phase compositions can be quenched without segregation “freezing” the actual mixture. As has been shown by Akurati et al.³⁴, the flame synthesis of segregated $\text{TiO}_2/\text{SnO}_2$ nanocomposites is accessible probably due to a relatively low temperature within the particle formation zone, while experiments in our lab for $\text{TiO}_2/\text{SnO}_2$ mixtures ranging from 10/1 to 1/1 always showed complete solid solutions of both oxides³⁵. The XRD investigations approve this finding as the change in lattice constants of the synthesized materials behaves linearly in accordance with Vegard’s law. It was also found that with an increasing amount of tin substituting for titanium, the band gap energy for TiO_2 shifts from 3.2 eV to higher values.

Moreover, the electrical properties of the materials are also in accordance with these findings, resulting in an increasing conductance when changing the composition from almost insulating TiO_2 to more conducting SnO_2 (**Fig. 6**). The results presented in **Fig. 6** were obtained from impedance measurements taken at 200°C under synthetic air. They demonstrate that pure titania as well as the 10/1 mixture with tin oxide show poor conductance and DC behavior (pure electron transport) up to a few hundred hertz (G' keeps constant with increasing frequency). With an increasing amount of tin oxide, the conductance increases by about 2 orders of magnitude and DC behavior is observed up to a few kHz.

As has been shown, temperature control as well as oxygen control can dramatically influence nanoparticle as well as nanocomposite growth and properties. Furthermore, the kinetics of precursor decomposition and particle formation also plays an important role during the formation of nanocomposites. If the

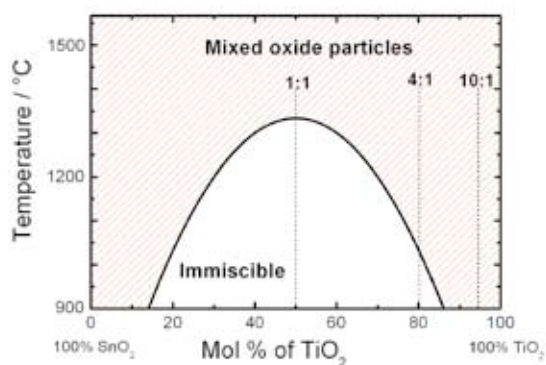


Fig. 5 Phase diagram of the $\text{SnO}_2/\text{TiO}_2$ system, adapted from³².

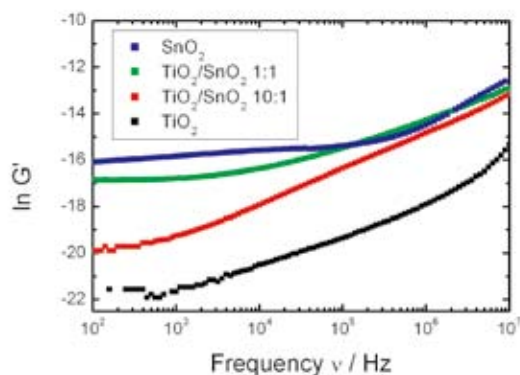


Fig. 6 Frequency-dependent conductance G' for different mixtures of TiO_2 and SnO_2 .

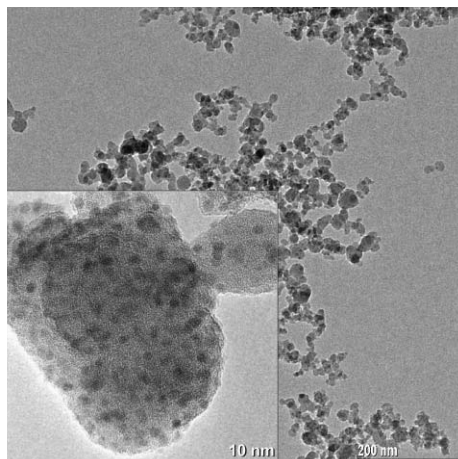


Fig. 7 TEM micrograph of γ -Fe₂O₃/SiO₂ nanoparticles. The overview shows the typical fractal geometry of fumed silica, while the inset gives a detailed insight into the homogeneous dispersion of iron oxide (dark specks) within the silica matrix.

evolution of different particles along the reaction path and, as a result, different time scales appear for the formation of the respective material, composites consisting of one material homogeneously dispersed within a second material may result. This principle was used for the formation of Fe₂O₃/SiO₂ nanocomposites.

The measurement of the magnetic properties of pure and nanosized γ -Fe₂O₃ (maghemite) exhibits a superparamagnetic behavior. Nevertheless, the decrease in blocking temperature with decreasing particle size wasn't observed as expected³⁶⁾ and is explained with magnetic interactions between the particles. Thus, a spatial separation is required to obtain size-dependent magnetic properties. Superparamagnetic materials do not retain any magnetization in the absence of an externally applied magnetic field. Due to this property, superparamagnetic nanoparticles are of great interest for applications that require a switchable magnetism, for example biomedical applications such as magnetic resonance imaging, hyperthermia, separation and purification of biomolecules, and drug delivery.

While iron silicates such as the Fe₂SiO₄ spinel that are found in nature usually have evolved under high pressure and in the presence of further cations such as Mg or Ca, it is not expected that iron silicates are formed by clean flame synthesis. This fact was used to engineer a material consisting of iron oxide homogeneously dispersed in silica. As the kinetic coefficients for the decomposition of the precursor iron pentacarbonyl (Fe(CO)₅) as well as for the oxidation of iron atoms reveal a very fast kinetic with respect to the formation of iron oxide³⁷⁾, the reaction rate coeffi-

cient of the matrix material source precursor must be larger compared to that of iron pentacarbonyl. Thus, the precursors tetramethylsilane (Si(CH₃)₄) and hexamethyldisiloxane (HMDSO) were chosen as a source precursor for the silica matrix^{38, 39)}. As the dilution of Fe₂O₃ in the silica matrix can be adjusted by means of the corresponding amount of precursor gases, their mean spatial arrangement is directly accessible during the synthesis, while the concentration of the precursors is proportional to the particle size. **Fig. 8** shows a representative TEM image of an Fe₂O₃/SiO₂ composite material illustrating the distribution of iron oxide within the silica matrix. The inset illustrates very clearly that the iron oxide nanoparticles are completely incorporated into the silica matrix. Thus, the chemistry of this "functionalized" silica is no different to that of common fumed silica.

SQUID measurements of the samples affirm that the iron oxide is superparamagnetic and from XRD measurements, a crystalline iron oxide phase is confirmed. From XRD investigations alone, it is not possible to distinguish between maghemite and magnetite (Fe₃O₄). However, Mössbauer spectroscopy at T = 4.2 K on pure iron oxide nanoparticles which are prepared under otherwise comparable conditions had revealed a single sextet with homogeneous line broadening, indicating that the particles are single-phase maghemite³⁶⁾. Furthermore, since the composites were synthesized at $\Phi = 0.4$, the full oxidation of iron resulting in Fe₂O₃ is expected.

From a couple of experiments with various precursor concentrations, Fe₂O₃/SiO₂ nanocomposites with similar loading but different size of Fe₂O₃ ranging from 9 to 28 nm in diameter were obtained. As expected for these spatially separated γ -Fe₂O₃ nanocrystals, a strong relation between the iron oxide particle size and magnetization was found, as can be seen from **Fig. 9**.

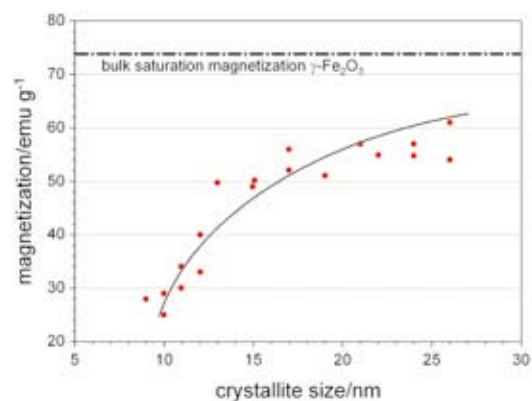


Fig. 8 Size-dependent saturation magnetization of γ -Fe₂O₃ nanoparticles dispersed in a silica matrix.

Within the size range of iron oxide particles that have been prepared, the bulk value for the saturation magnetization of γ -Fe₂O₃ is not reached. Therefore, if a higher magnetization is required, materials with a higher saturation are needed. Iron oxides make this possible with the aid of nanotechnology. While bulk magnetite Fe₃O₄ exhibits ferromagnetism at room temperature, nanosized magnetite switches to superparamagnetism with a size-dependent blocking temperature⁴⁰. In comparison to maghemite, the saturation magnetism of magnetite is significantly higher, achieving 92 emu/g. Hence, the tuning of the oxidation properties within a flame reactor and therefore tuning the stoichiometry by adjusting Φ again becomes important to force the formation of nanosized magnetite. The Evonik Degussa company has used this chance of product design to develop a superparamagnetic iron oxide/silica nanocomposite called MagSilica®⁴¹. It consists of nanosized magnetite and maghemite with iron oxide nanoparticles sized in the range of 5-40 nm. The saturation magnetization of this material is higher than that of a pure Fe₂O₃/SiO₂ nanocomposite. Due to the fact that flame reactors enable a cost-effective and versatile industrial process with high production rates, first attempts are made to use this material in large-scale applications such as ferrofluids and for the reinforcement of polymers and adhesives. Due to its superparamagnetic properties, the nanocomposite can be processed and manipulated by means of an alternating electromagnetic field, enabling heating and hardening of materials that usually contain fumed silica as additives. Contactless hardening, bonding and heating of materials containing the composite instead of classic fumed silica become apparent.

4. Summary

Flame synthesis is a cheap and established technology for the high-volume production of oxidic materials for bulk goods. It nevertheless still has the potential to produce sophisticated, engineered and tuned materials with specific properties. Together with the possibilities in tuning the oxygen content of flame-made materials and the composition and morphology of composites, a broad parameter range is accessible for a distinct formation of specific materials which meet the requirements of users in catalysis, optics and electronics.

Acknowledgments

The author thanks Profs. P. Roth, C. Schulz and

A. Lorke, University of Duisburg-Essen, for helpful discussions. I am also grateful to T. Hülser, C. Janzen, P. Ifeacho, J. Knipping, and V. Simanzhenkov for their productive and rewarding joint research on nanoparticles within the Collaborative Research Center "Nanoparticles from the gas phase". Financial support by the Deutsche Forschungsgemeinschaft (DFG) is gratefully acknowledged.

References

- 1) Roth, P. (2007): Particle synthesis in flames, Proc. Combust. Inst., 31, pp.1773-1788.
- 2) Pratsinis, S.E. (1998): Flame aerosol synthesis of ceramic powders, Prog. Energy Combust. Sci., 24(3), pp.197-219.
- 3) Mädler, L. (2004): Liquid-fed Aerosol Reactors for One-step Synthesis of Nano-structured Particles, KONA Powder and Particle Journal, 22 pp.107-120.
- 4) Stark, W. J. and Pratsinis, S.E. (2002): Aerosol flame reactors for manufacture of nanoparticles, Powder Technol., 126(2), pp.103-108.
- 5) Spicer P. T., Artelt, C., Sanders, S. and Pratsinis, S.E. (1998): Flame synthesis of composite carbon black-fumed silica nanostructured particles, J. Aerosol Sci., 29 (5-6), pp.647-659.
- 6) Roth, P. and Hospital, A. (1994): Design and Test of a Particle Mass Spectrometer (PMS), J. Aerosol Sci. 25(1), pp.61-73.
- 7) Hong, S. F., Kim, Y.H. and Han, J.I. (2008): Development of Ultrafine Indium Tin Oxide (ITO) Nanoparticle for Ink-Jet Printing by Low-Temperature Synthetic Method. IEEE Transaction on Nanotechnology 7(2), pp.172-176.
- 8) Huber, M., Stark, W. J., Loher, S., Maciejewski, M., Krumeich, F. and Bäiker, F. (2005): Flame synthesis of calcium carbonate nanoparticles, Chem. Commun.5, pp.648-650.
- 9) Grass, R.N. and Stark, W.J. (2006): Gas phase synthesis of fcc-cobalt nanoparticles, J. Mat. Chem. 16(19), pp.1825-1830.
- 10) Ifeacho, P. Hülser, T. Wiggers, H. Schulz, C. and Roth, P. (2007): Synthesis of SnO_{2-x} nanoparticles tuned between $0 \leq x \leq 1$ in a premixed low pressure H₂/O₂/Ar flame, Proc. Combust. Institute 31, pp.1805-1812.
- 11) Simanzhenkov, V., Wiggers, H. and Roth, P. (2005): Properties of flame synthesized germanium oxide nanoparticles, J. Nanosci. Nanotechnol., 5(3), pp.436-441.
- 12) Kennedy, M. (2004): "Investigation of tin oxide (Sn_nO_x) gas sensor", PhD thesis, Universität Duisburg-Essen,.
- 13) K. Takahashi, K., Giesen, A. and Roth, P. (2001): High temperature reaction of Sn(3P0) atoms with O₂ based on Sn and O-concentration measurements, Phys. Chem. Chem. Phys 3(19), pp.4296-4300.
- 14) Herzler, J. and Roth, P. (2003): High temperature gas phase reaction of SnOg with O₂, Phys. Chem. Chem.

- Phys 5(8), pp.1552-1556.
- 15) Belyung, D. P. and Fontijn, A. (1995): The $\text{AlO}+\text{O}_2$ Reaction System over a Wide Temperature Range, *J. Phys. Chem.*, 99(32) pp.12225-12230.
 - 16) Fontijn, A. (1998): Wide-temperature range observations on reactions of metal atoms and small radicals, *Pure & Appl. Chem.*, 70(2), pp.469-476.
 - 17) Kleinwechter, H., Janzen, C., Knipping, J., Wiggers, H. and Roth, P. (2002): Formation and properties of ZnO nano-particles from gas phase synthesis processes, *J. Mat. Sci.* 37(20), pp.4349-4360.
 - 18) Kronemayer, H., Ifecho, P., Hecht, C., Dreier, T., Wiggers, H. and Schulz, C.: Gas-temperature imaging in a low-pressure flame reactor for nano-particle synthesis with multi-line NO-LIF thermometry, *Appl. Phys. B*, 88(3) (2007) 373-377.
 - 19) Wiggers, H., Simon, U. and Schön, G. (1998): Conductivity Studies on AgSbO_3 with Channel Structure by Impedance Spectroscopy, *Solid State Ionics* 107(1-2), pp.111-116.
 - 20) Ihara T., Miyoshi M., Iriyama Y., Matsumoto O. and Sugihara S. (2003): Visible-light-active titanium oxide photocatalyst realized by an oxygen-deficient structure and by nitrogen doping, *Appl. Catal. B: Environ.*, 42(2), pp.403-409.
 - 21) Kuznetsov V.N. and Serpone N. (2006): Visible Light Absorption by Various Titanium Dioxide Specimens, *J. Phys. Chem. B*, 110(50), pp.25203-25209.
 - 22) Sekiya T., Yagisawa T., Kamiya N., Mulmi D.D., Kurita S., Murakami Y. and Kodaira T. (2004): Defects in Anatase TiO_2 Single Crystal Controlled by Heat Treatments, *J. Phys. Soc. Jpn.*, 73(3), pp.703-710.
 - 23) Akurati, K.K., Vital, A., Klotz, U.E., Bommer, B., Graule, T. and Winterer, M. (2006): Synthesis of non-aggregated titania nanoparticles in atmospheric pressure diffusion flames, *Powder Technol.*, 165(2), pp.73-82.
 - 24) Ifecho P., Kowalik A., Wiggers H., Roth P. and Schulz C. (2007): Synthesis and Characterization of High Surface Area TiO_2 Nanoparticles from Gas Phase Processes, *Proceedings PARTEC 2007*.
 - 25) Mahamuni S., Borgohain K. and Bendre B.S. (1999): Spectroscopic and structural characterization of electrochemically grown ZnO quantum dots, *J. Appl. Phys.*, 85(5), pp.2861-2865.
 - 26) Hsu N.E., Hung W.K. and Chena Y.F. (2004): Origin of defect emission identified by polarized luminescence from aligned ZnO nanorods, *J. Appl. Phys.*, 96(8), pp.4671-4673.
 - 27) Hung, C.H. and Katz, J.L. (1992): Formation of mixed oxide powders in flames: Part I. TiO_2 - SiO_2 , *J. Mater. Res.*, 7(7), pp.1861-1869.
 - 28) Hung, C. H., Miquel, P. F. and Katz, J. L. (1992): Formation of mixed oxide powders in flames: Part II. SiO_2 - GeO_2 and Al_2O_3 - TiO_2 , *J. Mater. Res.*, 7(7), pp.1870-1875.
 - 29) Shang J., Yao W. Q., Zhu Y.F. and Wu N. Z. (2004): Structure and photocatalytic performances of glass/ SnO_2 / TiO_2 interface composite film, *Appl. Catal. A*, 257(1), pp. 25-32.
 - 30) Yang J., Li D., Wang X., Yang X. J. and Lu L. D. (2002): Rapid synthesis of nanocrystalline TiO_2 / SnO_2 binary oxides and their photoinduced decomposition of methyl orange, *J. Solid State Chem.*, 165(1), pp.193-198.
 - 31) Lin, J., Yu, J.C., Lo, D. and Lam, S.K. (1999): Photocatalytic activity of rutile $\text{Ti}_{1-x}\text{Sn}_x\text{O}_2$ solid solutions, *J. Catal.*, 183(2), pp.368-372.
 - 32) Padurow, N.N. (1956): Mischbarkeit im System Rutil/Zinnstein, *Naturwissenschaften*, 43, pp.395-396.
 - 33) Tsantilis, S. and Pratsinis, S.E. (2004): Soft- and Hard-Agglomerate Aerosols made at High Temperatures, *Langmuir*, 20(14), pp.5933-5939.
 - 34) Akurati, K.K., Vital, A., Hany, R., Bommer, B., Graule, T. and Winterer, M. (2005): One-step flame synthesis of SnO_2 / TiO_2 composite nanoparticles for photocatalytic applications, *Int. J. Photoenergy*, 7(4), pp.153-161.
 - 35) Ifecho, P., Wiggers, H. and Roth, P. (2005): SnO_2 / TiO_2 mixed oxide particles synthesized in doped premixed $\text{H}_2/\text{O}_2/\text{Ar}$ flame, *Proc. Combust. Inst.*, 30, pp.2577-2584.
 - 36) Janzen, C. and Roth, P. (2001): Formation and Characteristics of Fe_2O_3 Nano-Particles in Doped Low Pressure $\text{H}_2/\text{O}_2/\text{Ar}$ Flames, *Combust. Flame*, 125(3), pp.1150 -1161.
 - 37) Woiki, D., Giesen, A. and Roth, P. (2002): A Shock Tube Study on the Thermal Decomposition of $\text{Fe}(\text{CO})_5$, *Proceedings of the 23rd Int. Symp. on Shock Waves*, p.447.
 - 38) Zachariah, M.R., Aquino, M.I., Shull, R.D. and Steel, E.B. (1995): Formation of superparamagnetic nanocomposites from vapor phase condensation in a flame, *Nanostruct. Mat.*, 5(4), pp.383-392.
 - 39) Janzen, C., Knipping, J., Rellinghaus, B. and Roth, P. (2003): Formation of silica-embedded iron-oxide nanoparticles in low-pressure flames, *J. Nanopart. Res.*, 5(5-6), pp.589-596.
 - 40) Stjern Dahl, M., Andersson, M., Hall, H.E., Pajeroski, D.M., Meisel, M.W. and Duran, R.S. (2008): Superparamagnetic Fe_3O_4 / SiO_2 Nanocomposites: Enabling the Tuning of Both the Iron Oxide Load and the Size of the Nanoparticles, *Langmuir*, 24(7), pp.3532-3536.
 - 41) Kroell, M., Pridoehl, M. and Zimmermann, G., Pop, L., Odenbach, S., Hartwig, A. (2005): Magnetic and rheological characterization of novel ferrofluids, *J. Magnetism Magn. Mater.* 289, pp. 21-24.

Author's short biography



Hartmut Wiggers

Dr. Hartmut Wiggers graduated from Münster University in chemistry and received his PhD from Essen University. During his postgraduate research he was involved in the characterization of charge carrier transport processes in semi-conducting and quantum-sized materials. He heads the nanomaterials group at the Institute for Combustion and Gas Dynamics at University Duisburg-Essen. His current research interests are the formation, chemistry and physics of crystalline, nanosized inorganic materials.

Drag on Gasborne Nanoparticles in the High Knudsen Number Regime[†]

T. Wu* and A. P. Weber

Institute of Particle Technology, Clausthal University of Technology¹

Abstract

At small Knudsen numbers (continuum regime) and sufficiently small Reynolds numbers, the friction resistance of particles with the carrier gas is described by means of the Stokes formula assuming no slip of the gas molecules at the particle surface. However, at high Knudsen numbers, this assumption does not hold anymore and the deviation from the continuum character is considered with the slip or Cunningham correction. In the present work, measurements of the separation curve of nanoparticles in a single-stage low-pressure impactor are presented to systematically investigate the disagreement of classical theory of friction resistance of nanoparticles in low-pressure flows. At the same time, the impaction process of nanoparticles is simulated with a CFD code based on the classic theory. An effective Cunningham correction is determined as a function of the Knudsen number from fitting the calculated separation curve to the measured one. Moreover, the so far unresolved finding of too low densities determined for metal nanoparticles by low-pressure impaction is explained for the first time.

Keywords: nanoparticle, Cunningham correction, high Knudsen number, drag

1. Introduction

Due to their unique properties, nanoparticles have found many practical applications such as protective coatings, self-cleaning surfaces and gas sensors to name only a few. In all these applications the handling of the nanopowders is essential for the quality of the deposit. To understand and control the deposition process, the drag coefficient of the nanoparticles has to be known. In addition, the correct interpretation of the results from nanoparticle measuring devices which are based on the motion of the particles relative to the carrier gas such as low-pressure impactors or low-pressure differential mobility analysers requires a sound knowledge of the friction forces. Stokes derived an analytical expression for the friction force in the continuum regime at small Reynolds numbers by assuming that the gas molecules exhibit no slip at the particle surface¹. The continuum drag formulation has been extended to a transition and free molecule regime by employing empirical fitting

functions called slip or Cunningham corrections. While the limiting behaviour of the Cunningham correction was given in the continuum regime and in the free molecule regime by the kinetic gas theory, the empirical constants for the transition regime were determined from experiments with micron and submicron oil droplets by Millikan assuming about 90% diffuse and 10% specular reflection of the gas molecules on the particle surface². However, recent calculations by Li and Wang showed that a transition to pure specular reflection occurs for very small nanoparticles leading to a reduced friction force³. Even stronger deviations from the Cunningham correction were observed in direct measurements of the velocity of nanoparticles in rectilinear acceleration by means of Laser Doppler Anemometry (LDA)⁴. However, no systematic investigation of the drag coefficient for nanoparticles at large mean free paths has been undertaken so far. Therefore, the present work aims at the compilation of experimental data to extract the influence of particle size, surface condition and Knudsen number on the drag coefficient in order to supply a working equation for the correct friction force for particle motion in the high Knudsen number regime. Further studies to explain the observed deviations from the classical Cunningham correction on the basis of molecular gas particle interactions are

[†] Accepted: September 30th, 2009-10-10

¹ Leibnizstrasse 19, D-38678 Clausthal-Zellerfeld, Germany

* Corresponding author:

TEL: 0049-5323-722117 FAX:0049-5323-722830

E-mail: tao.wu@mvt.tu-clausthal.de

beyond the scope of this contribution.

The article starts with the theory of particle behaviour in curve-linear motion which is the basis of inertial impaction. Then the experimental set-up is outlined and the separation results are presented. By comparison with CFD results, the correction function for the drag coefficient can be determined in absolute values. Finally, after discussing the consequences for the nanoparticle density determination based on low-pressure impaction, the results are condensed into the dependence of the correction function on the Knudsen number.

2. Basis of Particle Separation by Impaction

Here, the high Knudsen number regime to deposit nanoparticles was realized in a low-pressure impactor. After being accelerated through a nozzle, particles can be deposited in the subsequent curve-linear stream if their inertia is high enough compared with the drag in the carrier gas. For small Reynolds numbers ($Re < 0.25$), the friction force on the particle is given in one dimension by:

$$F_d = \frac{3\pi\eta \cdot x \cdot (v-w)}{Cc(Kn)} \quad (1)$$

which is proportional to the difference of gas and particle velocity ($v-w$) and inversely proportional to the Cunningham correction Cc , which in classic theory is only a function of the Knudsen number ($Kn = 2\lambda/x$):

$$Cc = 1 + Kn \cdot (1.257 + 0.4e^{-1.1/Kn}) \quad (2)$$

where the coefficients have been determined empirically^{5,6}.

The mean free path λ is related to the absolute pressure p by:

$$\lambda = \lambda_0 \cdot \frac{p_0}{p} \propto \frac{1}{p} \quad (3)$$

where $\lambda_0 = 65$ nm at ambient pressure and $p_0 = 10^5$ Pa at room temperature.

An important parameter to describe the efficiency of low-pressure impaction is the Stokes number which represents the ratio of inertia force F_i to drag force F_d :

$$Stk = \frac{F_i}{F_d} = \frac{\rho_p \cdot x^2 \cdot u \cdot Cc}{9\eta \cdot D_n} \quad (4)$$

where ρ_p is the particle density, u the outlet velocity at the nozzle exit, and D_n the nozzle diameter.

Based on continuity, the ideal gas law and the Cunningham correction (Eq. (2)), de la Mora et al.⁷ derived an expression for the Stokes number in a single-stage low-pressure impactor:

$$Stk = 0.178 \cdot \frac{\rho_p \cdot x \cdot \dot{m}_g \cdot c_0^3}{p^2 \cdot D_n^3} \quad (5)$$

where \dot{m}_g is the aerosol mass flow rate through the impactor, c_0 the velocity of sound and p the impaction pressure. In the classic impaction theory, the deposition process can be described by the Stokes number alone. Half of the particles will be separated at a value Stk_{50} which in turn gives a simple way of relating particle size and density as was shown by Kütz and Schmidt-Ott⁸:

$$Stk_{50} = 0.178 \cdot \frac{\rho_p \cdot x \cdot \dot{m}_g \cdot c_0^3}{p_{50}^2 \cdot D_n^3} = const \quad (6)$$

p_{50} is the impaction pressure at which 50% of particles are separated. Since all the other parameters in Eq. (6) are given by the geometry of the impactor and the flow rate of the carrier gas, the following ratio Y was so far assumed to be a constant:

$$Y = \frac{p_{50}^2}{\rho_p \cdot x} [\text{Pa}^2 \text{m}^2 / \text{kg}] \quad (7)$$

Eq. (7) was used extensively to determine the density of nanoparticles from single-stage low-pressure impaction measurements⁹. However, some inconsistencies with density data obtained with other techniques remained unresolved¹⁰. It will be shown in this study that the assumption of $Y = const$ does not hold true anymore in the high Knudsen number regime and that the reason for the deviation is related to the incorrect formulation of the Cunningham correction in this regime.

3. Experimental Set-up

The experimental set-up is represented in **Fig. 1**. It consists mainly of a particle generation process, charging and classification in a Differential Mobility Analyser (DMA, GRIMM model 55-40-26-Uni), particle impaction, monitoring of inlet particle concentrations and outlet aerosol charges. The metal particles were generated by spark erosion from electrodes of the required metal. The particles formed by nucleation and agglomeration were sintered completely as they passed through a downstream tube furnace to form dense spherical particles (**Fig. 2**). In the case of coated metal particles, the classified spherical particles passed an atmosphere saturated with Di-Ethyl-Hexyl-Sebacate (DEHS) vapour which condensed on the particles as they cooled. The coating thickness was adjusted by the temperature in the saturator. A second DMA is used to select a particle size after coating to permit determination of the coating thickness from the difference between the particle sizes before and after the coating. Pure oil droplets were generated by atomisation of DEHS with a pneumatic nebulizer (Topas model ATM 220). Because

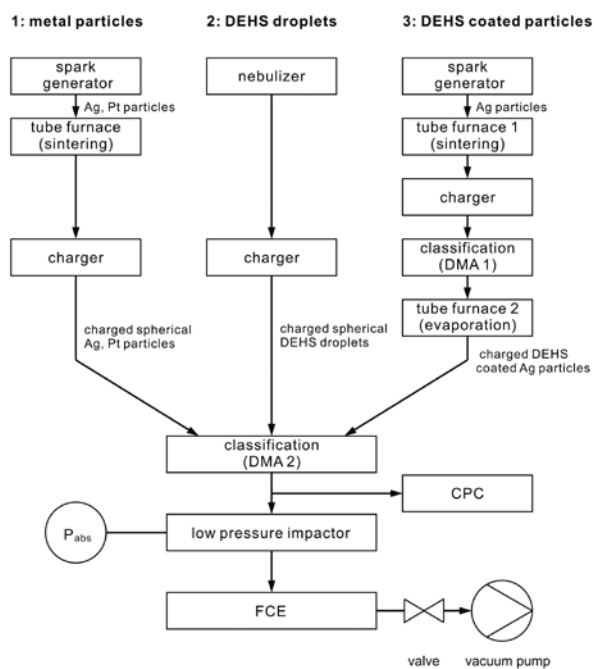


Fig. 1 Overview of the experimental set-up to investigate the separation behaviour of different particle types.

of surface tension, the droplets remain spherical in the carrier gas. However, due to the non-vanishing vapour pressure of DEHS in ultra-high vacuum, the shapes of DEHS-coated particles and the DEHS droplets could not be observed by means of TEM analysis. Before classification in the DMA, the particles were charged with a radioactive Kr-85 source (TSI model 3077). The size-selected particles were singly charged and monodisperse and entered the Low-Pressure Impactor (LPI). The particle number concentration in the outlet aerosol was measured with a Faraday Cup Electrometer (FCE), while the inlet concentration was recorded with a Condensation Particle Counter (CPC, GRIMM model 5.403). For a given particle size, the separation probability

increases with increasing particle velocity, leading to a decrease of the concentration of charged particles in the aerosol exit as measured with the FCE. The particle velocity was controlled through the chamber pressure in the impactor. The absolute pressure in the impaction chamber was varied by means of a low-pressure valve and monitored with the aid of a low-pressure gauge. The smaller the chamber pressure, the higher the gas and particle velocity.

The Low-Pressure Impactor (LPI) is shown schematically in **Fig. 3**. It consists of a critical orifice (150 μm in diameter), an accelerating nozzle (2 mm in diameter), an impaction plate and a pressure gauge. The aerosol enters at the top and exits from the bottom. The critical orifice keeps the inlet gas mass flow constant. To avoid interference of the gas flow through the critical orifice with the accelerating nozzle, they were separated by about 1m (as indicated in **Fig. 3**). The gasborne particles were accelerated in the nozzle towards the impaction plate. The particles which did not impact on the plate were measured downstream of the impaction surface with the FCE. In order to guarantee sticking of the impacting particles, the impaction plate was coated with a thin film of vacuum grease. For a given chamber pressure, the particle separation efficiency was calculated from the ratio of the FCE signal at this pressure related to the FCE signal at higher pressure where no impaction occurred (e.g. in **Fig. 4** for a pressure above 4500 Pa). Fluctuations of the particle concentration at the impactor inlet were measured with the CPC and taken into account for the separation curves.

4. Results and Discussions

4.1 Comparison of Y

A typical measurement of a separation curve for

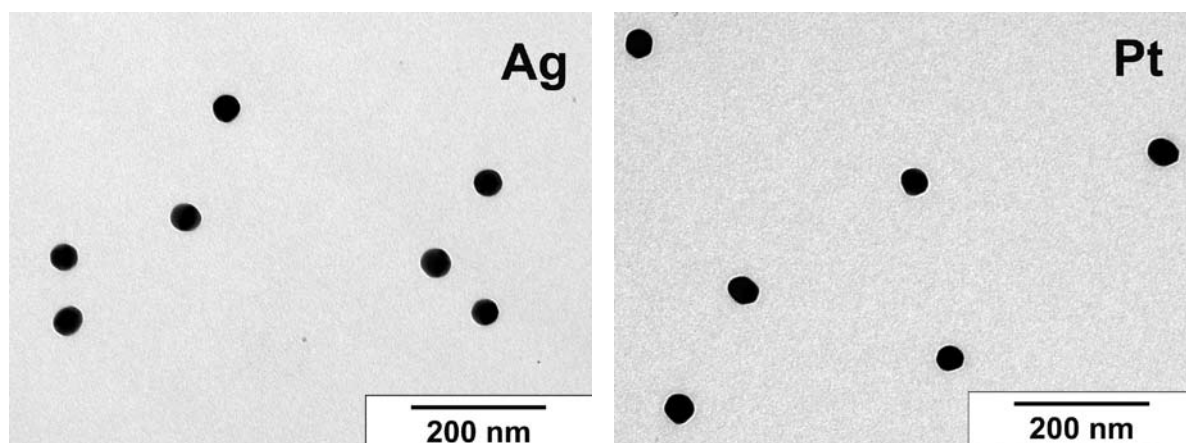


Fig. 2 TEM micrographs of the sintered and size-selected metal particles (left: 47 nm silver; right: 47 nm platinum).

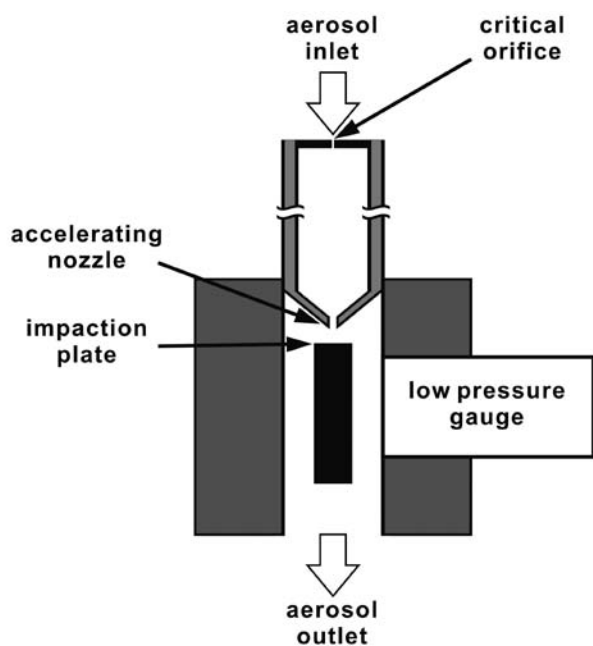


Fig. 3 Schematic of the low-pressure impactor.

DEHS droplets with a diameter of 454 nm is reproduced in Fig. 4. With decreasing pressure in the impaction chamber, the velocity of the gas jet increases and the particles also attain higher velocities. When reducing the pressure below 4200 Pa, particles start to deposit on the impaction plate by inertia, leading to a reduction of the aerosol electrometer signal (FCE) measured downstream of the impaction plate. At a pressure of about 2500 Pa, all particles are deposited and the electrometer signal drops to zero. The single-step drop of the curve indicates that no larger doubly charged droplets are present after the classification in the DMA. The value of p_{50} can be determined from such a curve as indicated in Fig. 4. According to Eq. (7), the particle size, particle density and p_{50} have to be known to determine Y . While the particle size is given from the classification and p_{50} is obtained from the separation curve, the particle density has to be estimated. For pure DEHS droplets, it is reasonable to assume the bulk density. However, since the droplets spend a few seconds in a low-pressure regime (minimum pressure for DEHS was 2000 Pa) between the critical orifice and the acceleration nozzle, their size may change due to evaporation which would lead to a decrease of the particle separation efficiency by impaction. In order to estimate this effect, the evaporation kinetics are approximated by the following equation which applies for $x < \lambda$ and includes the Kelvin effect¹¹:

$$\frac{dx}{dt} = \frac{2M(p - p_d)}{\rho_p \cdot N_a \cdot \sqrt{2\pi} \cdot mk_B T} \quad (8)$$

where p is the partial pressure of the DEHS vapour in the carrier gas and p_d is the partial pressure of DEHS vapour at the droplet surface, given by the Kelvin equation. Assuming no DEHS vapour in the carrier gas and maximum residence time and using literature values for surface tension and molar mass, a maximum size change by evaporation was obtained. Even for the smallest DEHS droplets of 124 nm, a size reduction of only a few nm was estimated. Therefore, the size change of the DEHS droplets due to evaporation in the low-pressure regime was neglected. In addition, the particle size reduction by evaporation would lead to a reduced separation efficiency in contradiction to the experimental results which show an improved separation efficiency as discussed below (e.g. Fig. 7).

For the completely sintered metal particles the bulk density was also assumed. This is explained on one hand by the TEM micrographs which show spherical dense particles and on the other hand by the sintering treatment used here which follows the procedure by Weber et al.¹² and Skillas et al.¹⁰. Using the direct mass determination of the silver aerosol particles with Inductively Coupled Plasma Spectroscopy (ICP), they showed that particles with bulk densities can be achieved by heating in a tube furnace for residence times of a few seconds. Exactly the same temperature treatment was also applied here so that the assumption of bulk density is justified. Platinum has a high melting point, so a high sinter temperature was used. Fig. 2 shows that the Pt particles also have a compact and spherical shape. So it can be assumed that the Pt particles have a bulk density, too. However, for the Ag particles coated with DEHS, an interpolation was used for the determination of the effective density. Using the diameter x_1 of the silver core and the diameter x_2 of the coated particles, the following equation was applied:

$$\rho_{eff} = \left(\frac{x_1^3}{x_2^3}\right) \cdot \rho_{Ag} + \left(1 - \frac{x_1^3}{x_2^3}\right) \cdot \rho_{DEHS} \quad (9)$$

where ρ_{Ag} is the density of silver, ρ_{DEHS} the density of DEHS.

In this way, the values of Y were determined for the metal particles (Ag, Pt), for the pure DEHS particles and for two types of DEHS-coated silver particles, i.e. with a thin and a thick DEHS coating. The results are shown in Fig. 5. For the metal particles, there is no difference in the Y values although the density of silver (10500 kg/m³) is less than half of the platinum density (21400 kg/m³). This indicates that the parameter Y does not depend on the particle density. It also becomes obvious that Y is not constant as

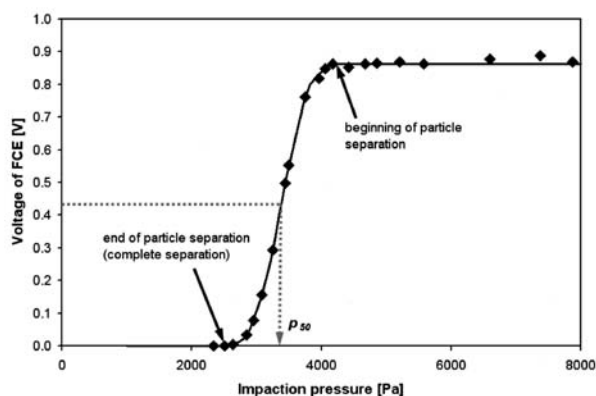


Fig. 4 Measured separation curve for 454-nm DEHS droplets.

assumed so far for the interpretation of low-pressure impactor density measurements. Moreover, there is a significant difference in the behaviour of oil surfaces and solid metal surfaces. Surprisingly, the silver particles with a thin DEHS coating show an intermittent behaviour. Since the coating thickness is rather small (a few nm) compared with the dimensions of the DEHS molecules (maximum length ca. 4 nm), layers of only a few molecules will form in the case of thin coatings. Although on a macroscopic level, oils wet extended metallic surfaces rather well, the situation may be different for the deposition of a limited number of DEHS molecules on the highly curved surface of Ag nanoparticles. On one hand, DEHS layers with a thickness of only a few molecules may not develop macroscopic surface tensions. And on the other hand, the surface may be contaminated to some extent, for instance by oxide states as observed before for Ni nanoparticles¹³⁾. Therefore, we hypothesize that the surface might rather consist of DEHS patches and of uncovered metal areas. This would support the hypothesis that the gas molecules are scattered in a different way from solid and liquid surfaces. But the exact dispersion of the thin DEHS coating on the surface of the particles is unknown. Hence reliable conclusions cannot be drawn at this state of knowledge. Once the whole surface of the silver particle is covered with DEHS, as in the case for thick coatings, the gas molecules do not differentiate between pure DEHS particles and DEHS particles with a silver core resulting in the same increase of the Y value as found in Fig. 5.

For large particles, it is expected that Y converges towards a constant value which is the same for solid and liquid particles. This extrapolation will be discussed in Fig. 9 on the basis of absolute values.

In order to interpret the variation of the parameter Y , we assume that the classic value for the Cun-

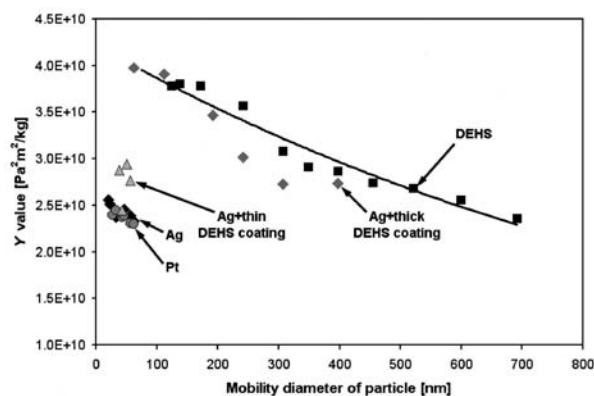


Fig. 5 Behaviour of parameter Y as a function of particles size for particles with solid (Ag, Pt) and liquid surfaces (DEHS).

ningham correction has to be adapted for the higher Knudsen number regime ($Kn \gg 1$) encountered here by multiplication with a function k :

$$C_{c,eff} = k \cdot C_{c,class} \quad (10)$$

According to Eq. (4), the function k also enters the Stokes number, changing it to a new effective value $Stk_{50,eff}$:

$$Stk_{50,eff} = k \cdot C_{c,class} \frac{\rho_p \cdot x^2 \cdot u}{9\eta \cdot D_n} = k \cdot Stk_{50,class} \quad (11)$$

To obtain the relationship between k and Y , the following equation is used:

$$Stk_{50,eff} = const \cdot \frac{k}{Y} \quad (12)$$

$Stk_{50,class}$ is the Stokes number calculated with the classic theory at 50% of the particle separation. The classic theory is suitable for small Knudsen numbers, i.e. relatively large particles, and short mean free paths of gas molecules, then k is equal to 1. At the present experimental conditions (low-pressure impaction of small particles), k decreases towards 1 with increasing particle size for all investigated materials (DEHS, Ag, Pt). The absolute value of k will be discussed in the next section.

With Eq. (10) and (1), the effective drag force can be written as:

$$F_{d,eff} = \frac{3\pi\eta \cdot x \cdot (v - w)}{k \cdot C_{c,class}} \quad (13)$$

Since Y is proportional to k , increasing Y means that the effective drag force of particles is less than that in the classic theory (with the classic C_c).

For the analysis here we will focus on DEHS droplets because the DEHS droplets have a definite compact spherical shape and their effective density is known. On the other hand, the atomizer supplies a variety of droplet sizes, so it is possible to investigate the particle dynamic properties over a large size

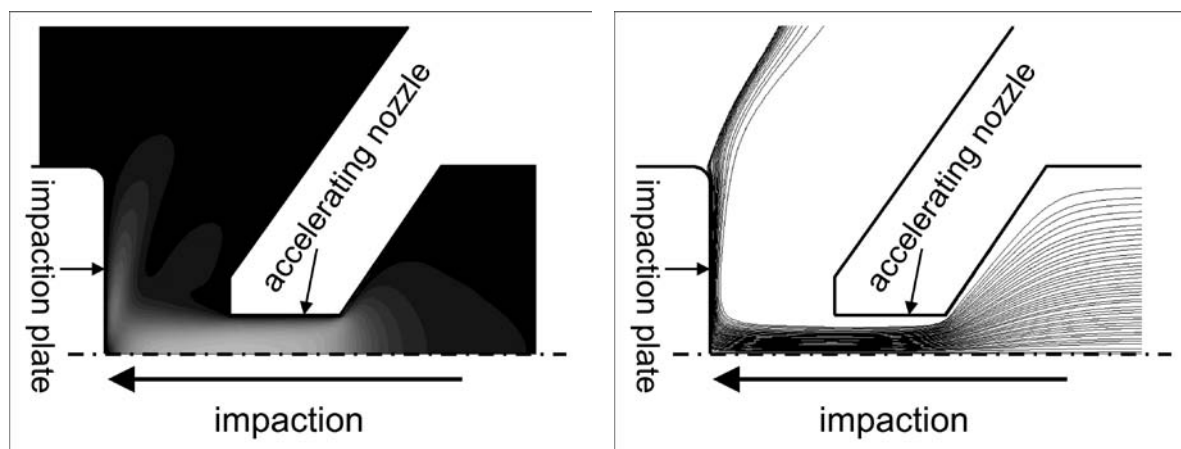


Fig. 6 Simulation results of impaction with 521-nm DEHS droplets by 3600 Pa using the classic C_c (left: gas flow; right: particle trajectories, the particle velocity is highest on the central axis and close to the gas velocity of 37 m/s).

range.

4.2 Determination of the factor k

The k values are unknown. But k is proportional to Y . If a k value can be found, then all the k values can be calculated by means of comparison of the Y values. For determining a k value, a CFD method is used.

Fig. 6 (left) shows the simulation results of the gas flow in the impactor. The brightness in flow zone indicates the gas velocities. The brighter the colour, the higher the gas velocity. As the impactor is axially symmetrical, a 2D model of half of the cross-section of the impactor is written. The gas is accelerated by the nozzle and the velocity increases. There is a velocity profile at the nozzle exit. In the centre, the gas velocity is at its maximum (37 m/s) and at the nozzle wall it is zero. Behind the accelerating nozzle the gas velocity decreases. On the surface of the impaction plate, the gas is diverted and a stagnation domain develops in the centre. According to their velocity relative to the gas, the particles are accelerated or decelerated due to the friction force. If the particle velocity is high enough, it can reach the impaction plate and is separated. Otherwise it is carried away by the gas. The calculation of the particle motion is based on the classic description of drag. A typical result of particle motion is shown in **Fig. 6 (right)** for DEHS droplets with a diameter of 521 nm. In this size range, diffusion is negligible and the particle motion can be calculated by inertia alone. On the central axis, particles have high enough velocities to reach the impaction plate. In the outskirt area, the particles exhibit lower velocities and may be carried away by the gas. Because of the inertia, the particles

are focused after entering the accelerating nozzle. If a particle can be separated, its track ends at the impaction plate. The separation grade can be calculated for a given particle size and chamber pressure from the particle trajectories.

A complete separation curve can be obtained by varying the pressure in the impaction chamber. The separation curve of the 521-nm DEHS droplets is shown in **Fig. 7**. Curve 1 is the simulation result by means of the classic friction theory ($k=1$). Curve 2 is the measured separation curve. There is clearly a difference between them. The measured separation efficiency is substantially larger than anticipated from the simulation, i.e. the droplets experience less friction than in theory. However, the curve shapes are similar. Assuming larger effective Cunningham corrections ($k>1$) will lead to a shift of the separation curve to the right as shown in **Fig. 7** for $k=1.0, 1.5, 2.0$ and 2.5 , respectively. In order to adapt the simulated separation curve to the measured p_{50} value for the

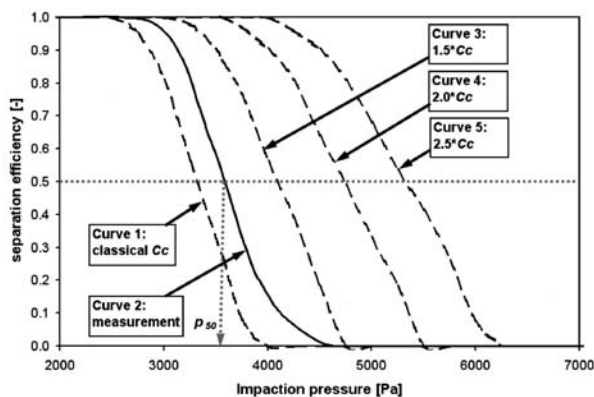


Fig. 7 Simulated (broken lines) and measured (solid line) separation curves of 521-nm DEHS droplets.

DEHS droplets of 521 nm, it is necessary to increase the Cunningham correction by a factor $k=1.167$:

$$C_{c,eff} = 1.167 \cdot C_{c,class}$$

Since k and Y are proportional to each other, it is sufficient to relate the values of k and Y for a certain particle size and p_{50} to obtain all corresponding values of k and Y . The results for DEHS droplets are shown in **Fig. 8**. For comparison, k was also obtained from simulation for all droplet sizes and their p_{50} (**Fig. 8** broken line). The curves for simulation and experimental results are close to each other indicating mutual confirmation of the two approaches. In addition, the measured k values of DEHS thick-coated silver particles fit in between the two lines.

The factor k for silver particles was calculated with the measurements and the same CFD procedure (**Fig. 8**). The k values for silver are close to the line of DEHS. It can be argued that the lines of silver and DEHS are actually the same. The small deviations are within the uncertainties in measurements and simulation as indicated in **Fig. 8**. In other words, k only depends on the parameter Y . Meaning that all the influences for this deviation from the classic theory such as surface condition and particle size are already included in this parameter Y . The function

between k and Y is independent of material, particle size, etc. and can be approximated by:

$$k = 4.35 \cdot 10^{-11} \frac{\text{kg}}{\text{Pa}^2 \text{m}^2} \cdot Y \left[\frac{\text{Pa}^2 \text{m}^2}{\text{kg}} \right] \quad (14)$$

where Y has the units of $\text{Pa}^2 \text{m}^2/\text{kg}$ and k is dimensionless. The proportionality constant in Eq. (14) depends on the impactor geometry and on the operation conditions. However, for a given impactor geometry and the flow conditions (type of carrier gas, temperature and gas mass flow rate at atmospheric pressure), the proportionality constant of Eq. (13) applies for all experiments performed in this study. If $k=1$ (in the area of the classic theory), the Y value or Stk_{50} is independent of material, particle size, pressure, etc., and is always a constant (see also broken line in **Fig. 9**).

4.3 Calibration of silver density by means of DEHS droplets

Important is that **Fig. 5** contains the key to explain the so far unresolved phenomenon that the densities of metallic nanoparticles determined with low-pressure impaction were substantially too low. The point is that the impactor had to be calibrated in order to evaluate Eq. (6). For this purpose, spherical particles of known density were employed – usually

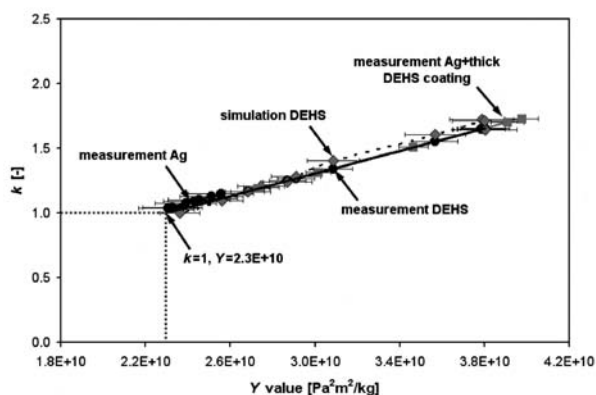


Fig. 8 The factor k as a function of the Y value.

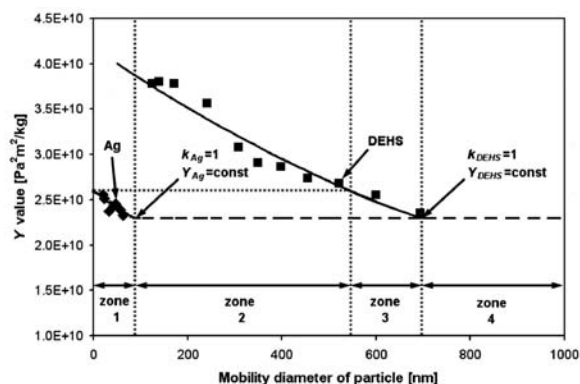


Fig. 9 Comparing the courses of trend lines from DEHS and silver measurements.

Table 1 Calibration of the silver particle densities with DEHS droplets in different particle size ranges

		x_{Ag}	
		Zone 1 ($k_{Ag}>1$)	Zone 2 to 4 ($k_{Ag}=1$)
x_{DEHS}	Zone 1 and 2 ($k_{DEHS}>1$)	a) $\frac{Y_{DEHS}}{Y_{Ag}} > 1$, $\rho_{Ag,calcul} < \rho_{Ag,eff}$	
	Zone 3 ($k_{DEHS}>1$)	b) The comparison of $\rho_{Ag,calcul}$ and $\rho_{Ag,eff}$ depends on the ratio $\frac{Y_{DEHS}}{Y_{Ag}}$ and can be different.	c) $\frac{Y_{DEHS}}{Y_{Ag}} > 1$, $\rho_{Ag,calcul} < \rho_{Ag,eff}$
	Zone 4 ($k_{DEHS}=1$)	d) $\frac{Y_{DEHS}}{Y_{Ag}} < 1$, $\rho_{Ag,calcul} > \rho_{Ag,eff}$	e) $\frac{Y_{DEHS}}{Y_{Ag}} = 1$, $\rho_{Ag,calcul} = \rho_{Ag,eff}$ (The classic theory is valid.)

oil droplets such as DEHS or DOS. However, for determination of the unknown density of the metal particles, the upper curve in **Fig. 5** was used and Y was assumed to be constant, leading to apparently changed densities. The degree of underestimation or overestimation depends on the sizes of the measured particles and the ones used for calibration. A detailed case differentiation is given in **Table 1**. Using rather large oil droplets (of about 700 nm) for the calibration, the correct calibration factor may have been chosen by chance. Going to smaller oil droplets, the underestimation of the real density may reach a factor close to 2 for particle sizes below 100 nm.

The particle density of silver is commonly obtained by comparison of the Stk_{50} by impaction of silver particles and of DEHS droplets. By combining Eqs. (6), (10) and (11), one obtains:

$$Stk_{50,eff} = k \cdot Stk_{50,class} = k_{Ag} \cdot 0.178 \cdot \frac{\rho_{Ag} \cdot x_{Ag} \cdot \dot{m}_g \cdot c_0^3}{p_{50,Ag}^2 \cdot D_n^3} \\ = k_{DEHS} \cdot 0.178 \cdot \frac{\rho_{DEHS} \cdot x_{DEHS} \cdot \dot{m}_g \cdot c_0^3}{p_{50,DEHS}^2 \cdot D_n^3} \quad (15)$$

From Eq. (15), the following expression for the silver density is obtained:

$$\rho_{Ag} = \frac{p_{50,Ag}^2}{p_{50,DEHS}^2} \cdot \frac{x_{DEHS}}{x_{Ag}} \cdot \rho_{DEHS} \cdot \frac{k_{DEHS}}{k_{Ag}} \quad (16)$$

In the classic theory, k is not considered, then ρ_{Ag} will be calculated with $\frac{k_{DEHS}}{k_{Ag}} = 1$. But actually $\frac{k_{DEHS}}{k_{Ag}}$ is often not equal to 1 for small particles, leading to a deviation from the correct particle density. Since k is proportional to Y , Eq. (16) may alternatively be written as:

$$\rho_{Ag} = \frac{p_{50,Ag}^2}{p_{50,DEHS}^2} \cdot \frac{x_{DEHS}}{x_{Ag}} \cdot \rho_{DEHS} \cdot \frac{Y_{DEHS}}{Y_{Ag}} \quad (17)$$

Since both k and Y depend on the particle size, the following combinations may occur (**Table 1** based on the zones 1 to 4 indicated in **Fig. 9**):

- Case a : x_{DEHS} in zone 1 and 2, x_{Ag} in all zones:
In this situation, is $\frac{Y_{DEHS}}{Y_{Ag}} > 1$ If the ρ_{Ag} is calculated with $\frac{Y_{DEHS}}{Y_{Ag}} = 1$ as in the theory, then the calibrated ρ_{Ag} is smaller than the effective ρ_{Ag} .
- Case b : x_{DEHS} in zone 3, x_{Ag} in zone 1:
In this case, the situations are complex. If $\frac{Y_{DEHS}}{Y_{Ag}} < 1$, the calibrated ρ_{Ag} is larger than

the effective ρ_{Ag} . If $\frac{Y_{DEHS}}{Y_{Ag}} = 1$, the calibrated ρ_{Ag} is exactly the same as the effective ρ_{Ag} . Otherwise, it is smaller.

- Case c : x_{DEHS} in zone 3, x_{Ag} in zones 2 to 4:
In this situation, is $k_{Ag}=1$, $k_{DEHS}>1$, $\frac{Y_{DEHS}}{Y_{Ag}}$ is always larger than 1, then the calibrated ρ_{Ag} is smaller than the effective ρ_{Ag} .
- Case d : x_{DEHS} in zone 4, x_{Ag} in zone 1:
In this situation, is $k_{DEHS}=1$, $k_{Ag}>1$, $\frac{Y_{DEHS}}{Y_{Ag}}$ is always smaller than 1, then the calibrated ρ_{Ag} is larger than the effective ρ_{Ag} .
- Case e : x_{DEHS} in zone 4, x_{Ag} in zones 2 to 4:
For large particles, $k_{Ag}=k_{DEHS}=1$. In this zone, the classic theory is valid.

De la Mora et al.¹⁴⁾ also found reduced densities in low-pressure impaction measurements and attributed this to contamination of the particle surface originating from the charging process with a radioactive source. However, their particles exhibited sizes of a few nanometres only (< 10 nm). In contrast, the particles investigated here were at least 20 nm or much larger, so that monolayers of contamination, when present at all, are negligible for the impaction behaviour.

4.4 The factor k as a function of the Knudsen number

The factor k is a function of Y , *i.e.* it is dependent on particle size and impaction pressure. In the presented impaction research, the impaction pressure – which can change the mean free path of gas molecules – and the particle size can influence both the frequency and strength of the interaction between particles and gas molecules. The Knudsen number indicates the ratio between the mean free path, and thus the impaction pressure and particle size. Therefore, it was attempted to describe the factor k as a function of the Knudsen number Kn as shown in **Fig. 10**.

For both materials, there is a critical Knudsen number Kn_0 , above which the function k increases strongly at first and then approaches a constant value for large Kn values. The asymptotic limit was obtained from **Fig. 9** by reducing the particle size ($x \rightarrow 0$), which in turn results in $Kn \rightarrow \infty$. For particles much smaller than the mean free path but still larger

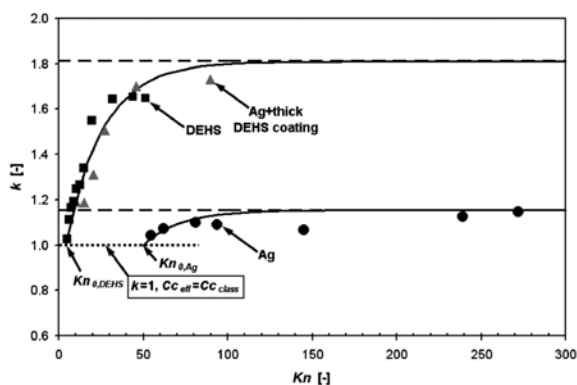


Fig. 10 The factor k as a function of the Knudsen number.

than the gas molecules, the friction coefficient f can be derived from the kinetic gas theory (formula of Epstein)¹⁵:

$$f = \frac{F_d}{v_{rel}} = \frac{2}{3} \cdot x^2 \rho_g \cdot \left(\frac{2\pi \cdot k_B T}{m} \right)^{1/2} \left[1 + \frac{\pi \alpha}{8} \right] \quad (18)$$

where ρ is the gas density and m is the molecular mass of the gas molecules. The accommodation coefficient α gives the fraction of diffusely scattered gas molecules, while $1-\alpha$ represents the fraction of specularly reflected gas molecules.

Based on Eq. (18), agreement between the measured and calculated drag forces are obtained for $\alpha = 0.09$ for 20 nm Ag particles and $\alpha = 0.34$ for 62 nm Ag particles, respectively. This indicates that even for particles as large as 62 nm, most of the gas molecules are specularly scattered in contradiction to the finding of Li and Wang³ who found that the transition from diffuse to specular reflection occurs at a particle size of a few nanometres. Therefore, we conclude that in the high Knudsen number regime, this transition can occur quite gradually, at least for the surfaces of solid particles. However, the friction coefficients observed for the DEHS droplets are out of the range of Eq. (18). The reason for this behaviour is so far unknown.

The behaviour of the function k was approximated by the following fit function:

$$k(Kn) = 1 + A \cdot [1 - \exp(-B \cdot (Kn - Kn_0))] \quad (19)$$

where A and B are constant. By fitting the function (19) to the measurements it was found that A and Kn_0 are dependent on the particle material or surface state while the value of B is about 0.045 independent of the particle material.

The Knudsen number is only inversely proportional to the impaction pressure p , but k is proportional to Y which is a function of impaction pressure p^2 and particle density ρ_p . Therefore, k is a function of Kn , p

and ρ_p . The influence of p and ρ_p is material-dependent. However, the curve progression of the relations between k and Kn are similar for all materials as indicated by the constant B value.

5. Conclusions

In the free molecular regime, small particles exhibit different drag properties than in the continuum regime, which is corrected by means of the Cunningham correction. But if the particles are sufficiently small in a high Knudsen number regime, they experience less friction than in the classic theory and their drag force cannot be well described with the classic Cunningham correction. In the experiments of low-pressure impaction it was found that the Stokes number Stk_{50} from the classic theory, which is calculated from the pressure p_{50} where 50% of particles are separated, is not constant. It depends not only on particle size, but also on the surface conditions of the particles. For correction of the theory, a factor k is introduced. In the free molecular regime, k is proportional to $Y = p_{50}^2 / (\rho_p \cdot x)$ and greater than 1. The classic friction force reduced by the factor k leads to the effective friction force.

For determination of the absolute value of k , a CFD method is used. The simulation result is adjusted to the measurement by means of variation of the Cunningham correction in the model. The deviation between the effective and classic Cunningham correction yields the factor k .

The function between k and Y is independent of other parameters, i.e. all interactions between gas molecules and particles are considered in the parameter Y . When $k=1$, different materials reach the same constant Y value. Once calibrated with standard particles such as oil droplets, the density of other particles can be determined from Stk_{50} . But if calibration and measured particles have different Y values, the calibration must be adjusted by k to avoid incorrect results for the particle density.

k is a function of particle size and impaction pressure. The impaction pressure determines the mean free path of gas molecules. Therefore, k depends also on the Knudsen number, which is determined by the mean free path and the particle size. But the relation between k and Kn is material-dependent, in particular the upper limit of k and the critical Knudsen number Kn_0 where k starts to increase above 1. Hence, the parameter Y may be more useful than the Knudsen number for interpretation of low-pressure impaction experiments since Y can be directly converted into a

k value using Eq. (14).

In the main, future work should address two issues. The drag behaviour of agglomerated nanoparticles in the high Knudsen number regime is so far largely unknown on a theoretical and experimental basis. However, agglomerates are encountered in most technical systems and a better understanding of the friction forces in a carrier gas is needed for better handling. The other issue is the fundamental explanation of the observed differences for the interaction of the gas molecules with solid and liquid surfaces. Here, molecular dynamics simulations as performed by Li and Wang¹⁶⁾ can be employed in future work to deepen the insight into the processes at the nanoparticle surface.

Nomenclature

Cc	Cunningham correction	[-]
c_0	velocity of sound	[m/s]
D_n	nozzle diameter	[m]
f	friction coefficient	[Ns/m]
F_d	drag force	[N]
F_i	inertia force	[N]
k	correction factor for Cc	[-]
k_B	Boltzmann constant	[J/K]
K_n	Knudsen number	[-]
M	molar mass of the liquid	[kg/mol]
m	mass of a vapour molecule	[kg]
\dot{m}_g	aerosol mass flow rate	[kg/s]
N_a	Avogadro's number	[mol ⁻¹]
p	pressure	[Pa]
p_0	ambient pressure	[Pa]
p_d	partial pressure of vapour at the droplet surface	[Pa]
Stk	Stokes number	[-]
T	temperature	[K]
u	outlet velocity by nozzle exit	[m/s]
v	gas velocity	[m/s]
w	particle velocity	[m/s]
v_{rel}	relative velocity, $v_{rel} = v - w$	[m/s]
x	particle diameter	[m]
Y	$p_{50}^2 / (\rho_p \cdot x)$ ratio proportional to Stk_{50}	[Pa ² m ² /kg]

Greek letters

α	accommodation coefficient for the fraction of diffusely scattered gas molecules	[-]
η	dynamic gas viscosity	[kg·m ⁻¹ ·s ⁻¹]
λ	mean free path of carrier gas molecules	[m]

ρ density [kg/m³]

Subscripts

1	silver core
2	coated particle
50	at which 50% of particles are separated
Ag	silver particle
$calcul$	calculated
$class$	classic
$DEHS$	DEHS droplet
eff	effective
g	gas
p	particle

References

- 1) Batchelor, G. K. (1967): "An Introduction to Fluid Dynamics", Cambridge University Press, ISBN 0521663962.
- 2) Millikan, R. A. (1923): The general law of fall of a small spherical body through a gas, and its bearing upon the nature of molecular reflection from surfaces, Phys. Rev. 22, 1.
- 3) Li, Z. and Wang, H. (2003): Drag force, diffusion coefficient, and electric mobility of small particles, I und II, Phys. Rev. E 68, 061206, 061207.
- 4) Reuter-Hack, K.; Weber, A. P.; Rösler, S. and Kasper, G. (2007): First LDA measurements of nanoparticle velocities in a low-pressure impacting jet, Aerosol Sci. and Technol. 41, pp.277-283.
- 5) Cunningham, E. (1910): On the velocity of steady fall of spherical particles through fluid medium, Proc. Roy. Soc. A 83, p.357.
- 6) Davies, C. N. (1945): Definitive equations for the fluid resistance of spheres, Proc. phys. Soc. 57, pp.259-270.
- 7) de la Mora, J. F.; Nagaraja, R. and McMurry, P. H. (1990): Inertial impaction of fine particles at moderate Reynolds numbers and in the transonic regime with a thin-plate orifice nozzle, J. Aerosol Sci. 21, pp.889-909.
- 8) Kütz, S. and Schmidt-Ott, A. (1990): Use of a low-pressure impactor for fractal analysis of submicron particles, J. Aerosol Sci. 21, Suppl. 1, S47-S50.
- 9) Schleicher, B.; Künzel S. and Burtscher H. (1995): In-situ measurement of size and density of submicron aerosol particles, J. Appl. Phys. 78, pp.4416-4422.
- 10) Skillas, G.; Tobler, L.; Beeli, C.; Burtscher, H.; Siegmann, K. and Baltensperger, U. (1999): On the density of silver nanoparticles. A comparison, J. Aerosol Sci. 30, Suppl. 1, S493-S494.
- 11) Hinds, W. C. (1982): "Aerosol Technology-properties, behavior, and measurement of airborne particles", John Wiley & Sons. Inc., ISBN 0-471-08726-2, 256.
- 12) Weber, A. P. Baltensperger, U., Gäggeler, H. W. and Schmidt-Ott, A. (1996): In situ characterization and structure modification of agglomerated aerosol particles, J. Aerosol Sci. 27, No. 6, pp.915-929.

- 13) Seipenbusch, M.; Weber, A. P.; Schiel, A. and Kasper, G. (2003): Influence of the gas atmosphere on restructuring and sintering kinetics of nickel and platinum aerosol nanoparticle agglomerates, *J. Aerosol Sci.* 34, pp.1699-1709.
- 14) de la Mora, J. F.; de Juan, L.; Liedtke, K. and Schmidt-Ott, A. (2003): Mass and size determination of nanometer particles by means of mobility analysis and focused impaction, *J. Aerosol Sci.* 34, pp.79-98.
- 15) Friedlander, S. K. (2000): "Smoke, Dust and Haze", 2nd Edition, Oxford University Press, p. 33.
- 16) Li, Z. and Wang, H. (2005): Gas-nanoparticle scattering: a molecular view of momentum accommodation function, *Phys. Rev. Lett.* 95.014502.

Author's short biography



Alfred P. Weber

Prof. Dr. Alfred Weber studied experimental physics and obtained his PhD in aerosol physics at ETH Zurich in 1993 on the characterization of the structure of agglomerated aerosol particles. From 1993 until 1995 he worked as a visiting scholar and lecturer in the group of Prof. Sheldon Friedlander in the Chemical Engineering Department at UC Los Angeles on tailoring nanoparticle agglomerates by understanding their restructuring kinetics. In 1996 he joined the group of Prof. Gerhard Kasper at the Institute of Mechanical Engineering and Applied Mechanics in Karlsruhe where he headed the groups of nanoparticle technology and particle measuring technology. He received the Smoluchowski Award at the International Aerosol Conference in 2001 for his work on the catalytic activity of aerosol nanoparticles. Since 2005, he has been a full professor for mechanical process engineering at the Clausthal University of Technology and director of the Institute for Particle Technology. His research focuses on the gas-phase synthesis of nanoparticles, their characterization and applications in functional coatings. Alfred Weber serves as a referee for various organizations and journals and is a member of the editorial board of the *Journal of Aerosol Science* and Chair of the Smoluchowski Award Committee. He gives the annual Clausthal course on "Particle Measuring Technologies" which was started by Prof. Kurt Leschonski in 1963.



Tao Wu

Dipl.-Ing. Tao Wu obtained his B.Eng. in 2001 from Tongji University, Shanghai, China, and his Dipl.-Ing. (M.Eng.) degree in 2005 from Clausthal University of Technology, Clausthal-Zellerfeld, Germany with the study of environmental engineering. For his master's thesis, he researched the optimization of pollutant emissions from a biomass thermal power plant at WULFF Deutschland GmbH (Germany). He graduated from the Institute of Mechanical Process Engineering (Particle Technology), Clausthal University of Technology in 2005 in the research groups of particle technology headed by Prof. Dr. rer. nat. Alfred P. Weber. His PhD work focuses on the characterisation of nanoparticles by means of low-pressure impaction, the fragmentation of nanoparticle agglomerates, the charging and bouncing process of nanoparticles by low-pressure impaction and their dynamic properties in low-pressure flows.

Good Laboratory Practice in Particle Measurement Calibration: Cascade Impactor[†]

Virgil A. Marple* and Bernard A. Olson

Particle Calibration Laboratory

University of Minnesota¹

Abstract

A laboratory often is faced with the task of calibrating particle inertial classifiers or investigating how instruments, or systems, respond to particles of specific sizes. Since, over time, multiple technicians may be involved in the calibrations, it is imperative that the procedures be uniform. For this purpose, "Good Laboratory Practice" (GLP) procedures as outlined in Code of Federal Regulations (CFR), Volume 21, Part 58 can be followed.

There are three main features of GLP that can be employed in calibrations with particles. They are: 1) all equipment that are used for measuring flow rates, pressure, volume, etc. are calibrated to NIST traceable standards, 2) a calibration protocol is written, and 3) Standard Operating Procedures (SOPs) are defined for all steps of the calibration process. The SOPs include management structure, document control, data handling, procedures for training personnel, calibration of the equipment, and the actual calibration for the device in question.

Although these GLP procedures are applied to nearly all calibrations performed in our laboratory, this paper will emphasize procedures suitable for the calibration of inertial classifiers, specifically cascade impactors.

Keywords: aerosol, calibration, particle, GLP, impactor

Introduction

It is necessary to have instruments that are accurately calibrated when measuring the size distribution and concentration of aerosol particles. Often the supplier of the instruments will provide calibration curves with the instruments. However, there are times when a calibration has to be performed in a laboratory. This may be during the course of developing a new instrument, or an independent calibration (other than that supplied by the manufacture) of a specific unit.

In the Particle Calibration Laboratory (PCL) at the University of Minnesota we have performed many of these types of calibrations. One such calibration was the archival calibration of the Next Generation Pharmaceutical Impactor (NGI) (Marple et al., 2003; Marple et al. 2004). Although all laboratories attempt

to use proper laboratory practices in their work, the PCL found that it was necessary to have a specific written procedure (protocol), which is followed through a set of Standard Operating Procedures (SOPs) so that the results of a calibration will be independent of the person doing the calibration. If the protocol and SOPs are followed, any person doing the calibration will take the same steps.

The procedures that were developed for our laboratory follows closely those outlined by the US Pharmacopoeia "Good Laboratory Practice for Nonclinical Laboratory Studies" (GLP) Code of Federal Regulations (CFR), Volume 21, Part 58. Some variations had to be made to these procedures to accommodate particle calibration of instruments, which we call Good laboratory Practice (GLP) for Particle Instrument Calibration.

In this paper, the GLP procedures that are followed to perform a calibration in the PCL are presented in detail. Since it is not possible to cover the calibration of the many different instruments used to analyze aerosol particles employing a wide variety of principles, the paper will reduce its scope to the calibra-

[†] Accepted: July 22nd, 2009

¹ 111 Church Street S. E. Minneapolis, MN 55455

* Corresponding author

TEL: 612-625-3441, FAX: 612-625-6069

E-mail: marple@me.umn.edu

tion of inertial classifiers, such as inertial impactors, cyclones, virtual impactors and body impactors. To further narrow the scope of the paper, the subject of the calibration will be a wide-range cascade inertial impactor covering the particle size distribution range from 20 μm at the upper stage to 0.05 μm at the last stage.

For readers not familiar with inertial impactors, a schematic is shown in **Fig. 1** of a cascade impactor, which consists of a series of stages. Each stage consists of a nozzle that directs a jet of particle-laden air at an impaction plate. Large particles will have enough inertia to slip across the air streamlines and strike the impaction plate. Smaller particles that do not strike the plate will proceed to the next stage where their inertia is increased due to a smaller nozzle that provides a higher velocity to the flow. Some of these smaller particles will impact on this second stage. Particles not collected here will proceed to the next stage where the nozzle is smaller and the process is repeated through all of the stages with each stage increasing the jet velocity. The net result after a known quantity of air has passed through the cascade impactor is the separation of the particles by aerodynamic size onto the various impaction plates.

The separation of the particles at each stage is characterized by the particle collection efficiency curve at each stage, where the particle collection efficiency for any particle size is defined as the fraction of particles passing through the stage nozzle(s) that are collected on the impaction plate (Marple et al., 2001). The experimentally determined collection efficiency curves for a typical cascade impactor are shown in **Fig. 2**.

Although the most important result of the calibration is the defining of the particle collection efficiency curves, it is also possible to determine particle inter-stage losses. Interstage losses are particles collected on surfaces other than the impaction plate.

In the following section a nine-step calibration protocol is presented, which if followed, will provide the same result independent of the researcher doing the calibration. The result of this calibration will be the experimental determination of the particle collection efficiency curve for each stage of a cascade impactor.

General Procedure for Calibration of an Inertial Impactor

The first step in performing a GLP calibration is to write a protocol for the calibration. The basic components of a protocol are as follows:

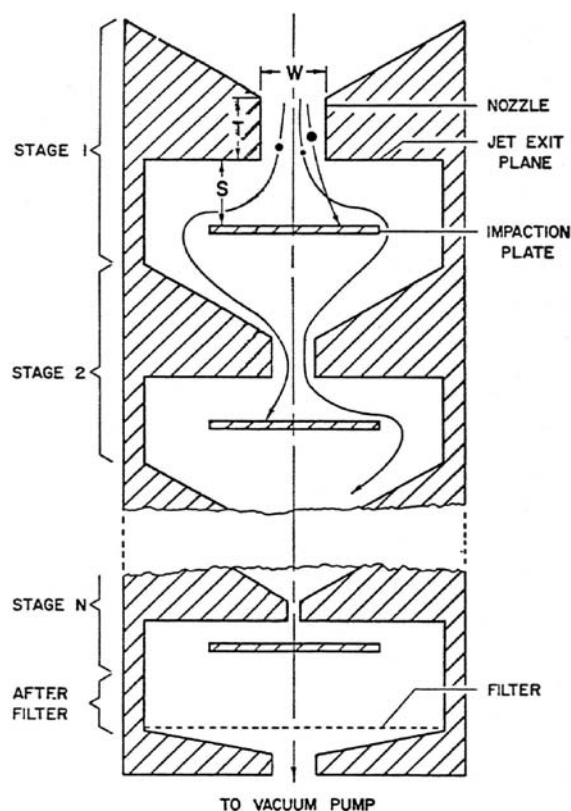


Fig. 1 Schematic diagram of a cascade impactor.

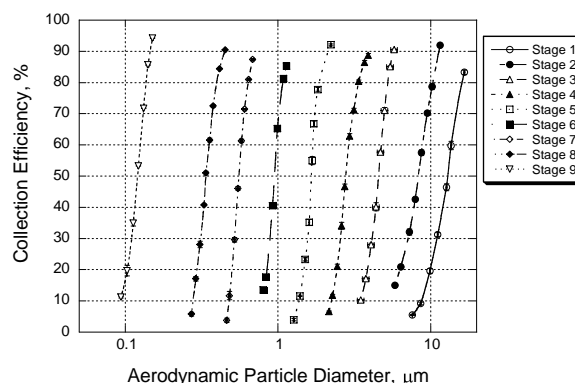


Fig. 2 Collection efficiency curves for a typical cascade impactor.

1. Purpose – Why and for whom is the calibration being performed?
2. Scope – Is the calibration being performed on a single unit or multiple units?
3. Objects to calibrate – This states what stages are to be calibrated, including any inlets, pre-separators, after filter sections and interstage loss determination.
4. Measurement matrix – This outlines the number of data points to be taken to define a stage efficiency curve (usually 3, 5 or 7 data points)

and about what percent efficiency these data points should be taken (usually at 5, 16, 40, 50, 60, 84 and 95% collection efficiency for seven point calibrations or some subset of these for fewer data points, but always one data point should be near the 50% collection efficiency). Also, the flow rate(s) and the precision of the flow rates should be defined here.

5. Validation of Ancillary Equipment – Each piece of equipment that is used for the calibration needs to be validated prior to the calibration being performed. This validation process is called Installation Qualification (IQ) as is a set of procedures to show that the equipment, once installed, is operating properly. The ancillary equipment includes:
 - a. flow rate measuring devices
 - b. pressure measuring devices
 - c. fluorometer
 - d. Aerodynamic Particle Sizer (APS)
 - e. Optical Particle Counter (OPC)

After IQ is completed the equipment needs to be checked on a regular basis during the calibration to ensure that it has not gone out of specification. This process is called Operational Qualification (OQ). An example validation (IQ and OQ) for the flow rate measuring equipment is given in Appendix A.

6. Methodology – This is the section that describes the actual calibration of the impactor. This defines the aerosol generator (usually a vibrating orifice aerosol generator (VOAG) for particles in the size range from 0.6 to 20 μm or a differential mobility analyzer (DMA) for particles in the size range of 0.02 to 0.6 μm) to be used in the calibration, and the material that will be used for the aerosol (usually oleic acid with a uranine fluorescent dye tracer for liquid particles or ammonium fluorescein for solid particles). Also defined in this section is the detection method to be used to determine the fraction of particles collected on the various surfaces. To fulfill this step, a number of Standard Operating Procedures (SOPs), listed in **Table 1**, must be followed. The details of the calibration procedure that must be described in this step of the protocol are quite voluminous, and has been moved to its own section following the last step (Step 9) of the protocol and titled “Methodology for calibration of an inertial impactor (Protocol step 6 continued)” so as not to overwhelm this list of protocol steps.

7. Data analysis – The particle collection efficiency data for each particle size at each stage taken in Step 6 must be analyzed to construct a particle collection efficiency curve and the 50% particle collection efficiency value (D_{p50}) for each stage. The data is also analyzed to determine the uncertainty of the data points and the corresponding uncertainty of the D_{p50} value.
8. Data report – The data report will include tables of collection efficiency versus particle aerodynamic diameter for each stage at each flow rate and all uncertainty values. In addition, this report must have a complete description of the impactor, including measurements of all nozzles and jet-to-plate distances. Large nozzle diameters can be measured using pin gauges but smaller nozzles need to be measured by optical methods. Automated optical measurement systems may have to be used if there are a large number of nozzles on a stage. All nozzle diameters measured should be included in the data report, along with the average, standard deviation, and minimum and maximum sizes. The report will also include a comprehensive description of the test methodology, including diagrams of the relevant apparatus used in the calibration, together with the actual test conditions (i.e., laboratory temperature, relative humidity, flow rate, barometric pressure).
9. Recording and retention of information - Experimental measurements, together with related observations, will be recorded and dated in a hard-back laboratory notebook with numbered pages. This notebook will be retained as part of the master file, together with hard copies of any relevant ancillary measurement data (e.g. APS, OPC) originally stored on computer. Hard copies of any calibration certificates and related documentation pertaining to ancillary equipment used in the calibration will also be retained in the master file.

Methodology for calibration of an inertial impactor (Protocol step 6 continued)

Two methods, the VOAG and DMA, are used to calibrate impactors in the size range of 0.02 μm to 20 μm . The methodology (Step 6 of the above protocol) must describe these methods in detail.

VOAG Method of Particle Generation and use as a Calibration Aerosol

Monodisperse particles of a desired size will be generated with the VOAG (Berglund and Liu, 1973) and passed through a multiplet reduction impactor (MRI) to remove all multiplet particles consisting of two or more coalesced primary particles. The impactor being calibrated will subsequently sample the aerosol that now contains only primary particles. The impactor will be assembled with all stages installed preceding and including that being calibrated. **Fig. 3** illustrates the calibration arrangement, showing the location of the VOAG and ancillary equipment with respect to the impactor. The after filter can be located immediately downstream of the stage being calibrated.

An Aerodynamic Particle Sizer[®] aerosol spectrometer (APS[®], model 3310, TSI, Inc.) will be used to sample the particle stream immediately before and after the measurement with the impactor to verify that the particles are monodisperse, since its size resolution is $0.02 \mu\text{m}$ at $1.0 \mu\text{m}$ and $0.03 \mu\text{m}$ at $10 \mu\text{m}$ aerodynamic diameter. This instrument will NOT be used to provide measurements of particle size for the purpose of defining the stage D_{50} value. Particle size will be determined from the operating variables of the VOAG.

The impaction plate of the stage being calibrated and the after filter will be washed separately with known quantities of 0.001 N aqueous solutions of sodium hydroxide, and the concentration of the uranine dye in the resulting solutions will be assayed using a fluorometer.

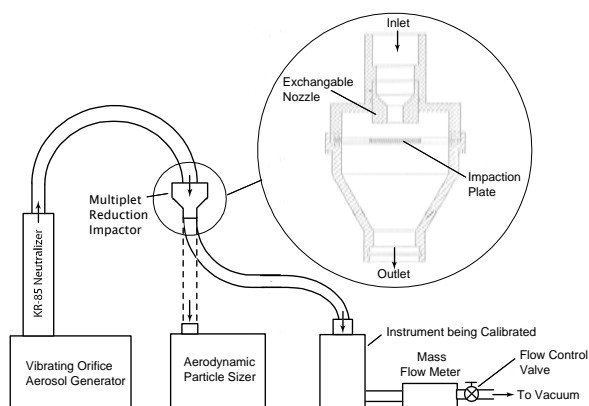


Fig. 3 Schematic diagram of the calibration setup using the vibrating orifice aerosol generator method.

DMA Method of Particle Generation and use as a Calibration Aerosol

A polydisperse aerosol, predominantly in the sub-micron size range, will initially be generated using a Collison-type pneumatic atomizer. This aerosol will subsequently be passed through a Kr-85 neutralizer to reduce the electrical charge on the particles and then the particles are size-classified using a differential electrical mobility analyzer (DMA), producing a monodisperse aerosol at the outlet (Liu and Pui, 1974). This aerosol will be subsequently sampled by the impactor to be calibrated, which will be assembled with all stages installed preceding and including the stage being calibrated. **Fig.4** illustrates the calibration arrangement, showing the location of the DMA and ancillary equipment with respect to the impactor. The impactor will be modified to provide a sample port downstream of the stage being calibrated. This modification will NOT affect the calibration, since the airflow pathway through the stage being calibrated will be unaffected. The CPC will be connected to this sample port. A modified impaction plate that provides a jet-to-plate distance of at least 50 nozzle

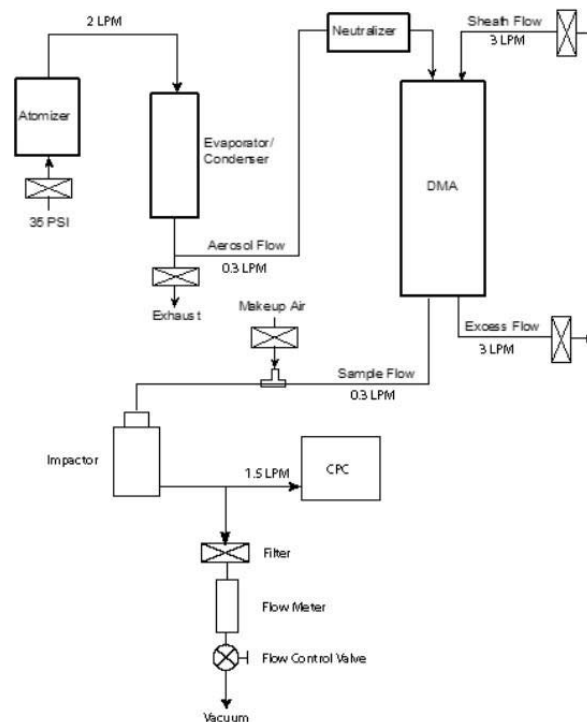


Fig. 4 Schematic diagram of the calibration setup using the differential mobility analyzer method.

diameters ($S/W \geq 50$) will be placed in the stage being calibrated to allow for a jet-to-plate distance large enough so that particle impaction will not occur. The number of particles counted with the CPC for a pre-determined sample period, depending on particle concentration, will be used as the upstream count. A standard impaction plate will then replace the modified impaction plate and the measurement repeated to obtain the downstream count. The collection efficiency for that stage at the particle size being generated will be defined by comparing upstream and downstream counts. A Laser Aerosol Spectrometer (Model HS-LAS, PMS, Inc., Boulder, CO) will be used to sample the particle stream immediately before and after the measurement to verify that the particles are monodisperse. This instrument will NOT be used to provide measurements of particle size for the purpose of defining the stage D_{50} value; this measurement will be determined from the operating variables of the DMA.

Uncertainty Analysis

The primary result of an impactor calibration is the particle collection efficiency versus aerodynamic particle diameter curves. Thus, the uncertainty in the generated particle size and the uncertainty of the measured particle collection efficiency values must be determined. These uncertainty calculations will depend on the type of particle generation system that is used and the method used to determine the fraction of particles collected at each stage.

If the VOAG is used to generate particles, the uncertainty values in each term of the fundamental equations that define the generated particle size must be determined by experimentation. For example, the flow rate of the liquid through the vibrating orifice of

the VOAG is one term in the equation for the generated particle size. Multiple measurements (at least three measurements) of this liquid flow rate must be measured and the standard deviation of the measurements used as the uncertainty of the liquid flow rate. In like manner, the uncertainty of all terms in the fundamental equation of the calculation of the particle size must be determined. Then a propagation of error technique, such as the Root-Sum-Square method, must be used to determine the effect of these individual uncertainties on the calculation of the uncertainty of the particle size generated. A similar analysis is used to determine the uncertainty of the particle size for the DMA method of generating aerosols.

This technique can also be applied to all terms that are used to calculate the particle collection efficiency for each determination of the collection efficiency. However, triplicate determinations of the collection efficiency can be made for each particle size for each stage and the standard deviation of the collection efficiencies used as the uncertainty in the collection efficiency instead of using a propagation of errors method.

Application of SOPs

To follow the GLP and implement the calibration protocol, a number of SOPs were written. Each time the calibration protocol is applied to an impactor calibration these SOPs must be followed. Some of the SOPs are only applied periodically as the need arises, some are applied at the beginning of each calibration day, and some are applied for each experimental calibration run that produces data.

Table 1 provides a list of SOPs followed for the calibration of a cascade impactor. Some of the SOPs are for training of lab personnel, some are for calibration of ancillary equipment to be used in the actual impactor calibration, and some are for the calibration itself. The SOPs for each of the particle generation techniques were also written.

Table 1 SOPs for calibration of cascade impactors

SOPs for Management of Calibration	
1	DOCUMENT CONTROL (how to handle instructional manuals, certificates and other calibration documents)
2	MANAGEMENT OF LABORATORY AND TRAINING OF TECHNICAL STAFF (program management structure, training responsibility and handling of training records)
3	HANDLING OF DATA (how data should be recorded and handled and where it should be kept)
4	DOCUMENT CHANGE CONTROL (defines what SOPs will be changed and who will approve and sign them)
SOPs for Performing Calibration with VOAG	
5	VOAG, DAILY OPERATION

6	VOAG, PARTICLE CALIBRATION
7	VOAG, CALIBRATION OF THE FREQUENCY GENERATOR
8	VOAG, CALIBRATION OF THE LIQUID SYRINGE PUMP
9	APS, DAILY OPERATION
10	DATA TRANSFER FROM THE APS
11	FLUOROMETER, DAILY OPERATION
12	CALIBRATION OF FLUOROMETER
13	MRI SETUP
14	URANINE, WEIGHING FOR CALIBRATING FLUOROMETER
15	PREPARATION AND HANDLING OF A LIQUID SOLUTION OF SODIUM HYDROXIDE IN WATER WITH A CONCENTRATION OF 0.001 N
16	PREPARATION AND HANDLING OF LIQUID SOLUTIONS OF URANINE AND SODIUM HYDROXIDE IN WATER BY VOLUME AND DILUTIONS
17	PREPARATION AND HANDLING OF LIQUID SOLUTIONS OF OLEIC ACID AND URANINE IN METHANOL: PARENT SOLUTION CONTAINING 5.0 PERCENT NON-VOLATILES BY VOLUME AND DILUTIONS

SOPs for Performing Calibration with DMA

18	OPERATION OF EVAPORATOR/CONDENSOR
19	OPERATION OF CPC
20	OPERATION OF DMA
21	CALIBRATION OF DMA
22	OPERATION OF LASER AEROSOL SPECTROMETER (LAS)
23	CALIBRATION OF LASER AEROSOL SPECTROMETER (LAS)
24	COLLISON-TYPE ATOMIZER OPERATION- DOS
25	CALIBRATION OF DMA LAMINAR FLOW METERS
26	VERIFICATION OF DMA MAGNEHELIC PRESSURE GAUGES
27	CALIBRATION OF DMA ROTAMETER
28	CALIBRATION OF DMA EXCESS FLOW CRITICAL ORIFICES
29	PREPARATION AND HANDLING OF LIQUID SOLUTIONS OF BIS (2-ethylhexyl) SEBACATE IN 2-PROPANOL PARENT SOLUTION CONTAINING 10 PERCENT SOLUTE BY VOLUME AND DILUTIONS

SOPs for Calibration and Operation of Ancillary Equipment

30	CALIBRATION OF REFERENCE PRESSURE GAUGE
31	CALIBRATION OF MANOMETER
32	OPERATION OF BAROMETER
33	CALIBRATION AND OPERATION OF DRY GAS FLOW METERS
34	CALIBRATION AND OPERATION OF PRESSURE TRANSDUCER
35	OPERATION OF SARTORIUS MODEL BP120S WEIGHT BALANCE
36	OPERATION OF SARTORIUS MODEL L610 WEIGHT BALANCE
37	OPERATION OF CAHN MODEL 31 MICROBALANCE
38	OPERATION OF TEMPERATURE AND RELATIVE HUMIDITY PROBE
39	CALIBRATION OF IMPACTOR FLOW
40	CALIBRATION AND OPERATION OF BUBBLE FLOW METER
41	OPERATION OF COLLISON-TYPE ATOMIZER- PSL
42	SILICA GEL DESICCANT

SOPs for General Laboratory Operations

43	LABORATORY ENVIRONMENTAL CONDITIONS
44	LABORATORY WATER SUPPLIES
45	LABORATORY CONSUMABLES EXCLUDING WATER
46	CLEANING OF GLASSWARE
47	CLEANING THE IMPACTOR
48	CLEANING OF APPARATUS

49	GLASSWARE HANDLING
50	STORAGE AND HANDLING OF CHEMICALS
51	LABELING OF CHEMICALS
52	USE OF TUBING AND CONNECTORS

A typical SOP is shown in Appendix B. The front page provides the title, date, and sign-off sheet for the author, study director and external reviewer. The page also lists the SOP title, document number, revision and if it supersedes any previous SOP. The next page lists the purpose, scope, safety requirements, responsibility and the action of the SOP in step-by-step instructions. As can be seen from Appendix B, the SOPs are written in great detail.

Conclusion

A Good Laboratory Procedure has been presented that governs the calibration of aerosol instruments. To simplify the description of the procedure, the procedure has been aimed at the calibration of one specific type of aerosol instrument, a cascade impactor. With very few changes in the protocol the procedure could be applied to the calibration of any inertial classifier. With further modifications the procedure could be applied to any aerosol-analyzing instrument. Although the procedure can theoretically be applied to any instrument, it is best suited for routine calibrations of rather standard instruments. For these types of applications, by following a well-defined protocol that is supported by detailed Standard Operating Procedures, calibrations can be performed on aerosol instruments with confidence that the calibration

results will be independent of the researcher doing the calibration. This assumes, however, that they are conscientious laboratory technicians.

References

- Marple, V.A., B.A. Olson, K. Santhanakrishnan and J.P. Mitchell (2003): Next Generation Pharmaceutical Impactor (A New Impactor for Pharmaceutical Inhaler Testing) – Part II: Archival Calibration, *Journal of Aerosol Medicine*, Vol. 16, No 3, pp.301-324.
- Marple, V.A., B.A. Olson, K. Santhanakrishnan and J.P. Mitchell (2004): Next Generation Pharmaceutical Impactor (A New Impactor for Pharmaceutical Inhaler Testing) – Part III: Extension of Archival Calibration to 15 L/min, *Journal of Aerosol Medicine*, Vol. 17, No 4, pp.335-343.
- Marple, V.A., B.A. Olson and K. L. Rubow (2001), *Inertial, Gravitational, Centrifugal and Thermal Collection Techniques*, Chapter 10, “Aerosol Measurement: Principles, Techniques and Applications, Second Edition” Eds. P.A. Baron and K. Willeke.
- Berglund, R.N. and B.Y.H. Liu (1973), Generation of Monodisperse Aerosol Standards, *Environ. Sci. Tech.* 7, pp.147-153.
- Liu, B. Y. H. and D. Y. H. Pui (1974): A Sub-micron Aerosol Standard and the Primary, Absolute Calibration of the Condensation Nucleus Counter, *J. Coll. Int. Sci.*, 47, pp.155-71.

APPENDIX A- VALIDATION OF ANCILLARY EQUIPMENT EXAMPLE

A.1 FLOW RATE MEASUREMENTS (VOAG- AND DMA-BASED PROCEDURES)

A.1.1 IQ:

Two dry gas meters (Model R-315, Rockwell International), maximum flow rate of 315 cubic-feet/hr (149L/min) (index 1/10 cubic-foot per revolution), will be flow certified for accuracy, before the start of the archival calibration of the NGI. This procedure will be performed by an external contractor (Energy Economics, Dodge Center, MN) using a Prover A #3079 certified using a NIST traceable one cubic-foot bottle AMCO #163, (NIST #4199).

Two bubble flow meters (model Gilibrator-2 with flow cell P/N 20826-S, Sensidyne, Clearwater, FL) with an operating flow rate range from 0.020L/min to 6L/min will be calibrated for accuracy by Sensidyne, before the start of the impactor calibration. This company uses a film flow meter MCL-103 as its primary standard traceable to NIST, as described in circular #602.

A.1.2 OQ:

A Rockwell dry gas meter will be used as a secondary standard to verify that the volumetric flow rate at the entry to the induction port of the NGI is within the specified limits (Sect. 4). The initial calibration of this 'test' dry gas meter will be checked at the end of the impactor calibration and the dry gas meter will be deemed to be within specification if its accuracy limits is within $\pm 1.0\%$ in the range from 30 to 100 L/min

A second (local reference) Rockwell dry gas meter will be used as an in-house secondary standard. This flow meter will be used for NO other purpose but to perform a weekly flow calibration check of the 'test' dry gas meter to be used for the calibration of the impactor in the range from 30 to 100 L/min. The 'test' dry gas meter will be deemed to be operating within specification if the difference between its indicated flow rate and that of the local reference dry gas meter is within $\pm 1.0\%$.

A Gilibrator model-2 bubble flow meter will be used as a secondary standard to verify that the laminar flow meters associated with the DMA are operating within specification. The initial calibration of this 'test' bubble flow meter will be checked at the end of the archival calibration exercise and the flow meter will be deemed to be operating within specification if its accuracy has remained within $\pm 1.0\%$ in the flow rate range of interest.

A second (local reference) Gilibrator model-2 bubble flow meter will be used as an in-house standard. This flow meter will be used for NO other purpose but to perform a weekly flow calibration check of the 'test' bubble flow meter to be used in the calibration of the impactor. The 'test' bubble flow meter will be deemed to be operating within specification if the difference between its indicated flow rate and that of the local reference bubble flow meter is within 2.0% in the flow rate range of interest.

APPENDIX B - STANDARD OPERATING PROCEDURE

TITLE: FLUOROMETER, CALIBRATION
 DOCUMENT: SOP-020
 REVISION: 1.0
 SUPERSEDES: NONE

**IMPACTOR CALIBRATION
 PARTICLE CALIBRATION LABORATORY**

UNIVERSITY OF MINNESOTA

	NAME	SIGNATURE	DATE
AUTHOR			
STUDY DIRECTOR			
EXTERNAL REVIEWER			

STANDARD OPERATING PROCEDURE

DOCUMENT: SOP-020

FLUOROMETER, CALIBRATION

PAGE: 1 OF 2

REVISION: 1.0

SUPERSEDES: NONE

PARTICLE CALIBRATION LABORATORY
UNIVERSITY OF MINNESOTA

PURPOSE: Calibration of fluorometer.

SCOPE: Impactor calibration

SAFETY: Use personal safety protection appropriate to chemicals.

RESPONSIBILITY: Operator/Supervisor

ACTION:

INITIAL TURN-ON AND DARK CURRENT SUBTRACTION

- 1) Familiarize yourself with the Aminco Fluorometer Instruction Manual.
- 2) Ensure that cell adaptor and lamp cover are in place.
- 3) Insert primary and secondary filter holders.
- 4) Set PHOTOMETER switch to off (out) position (twist counterclockwise and release) to disconnect meter.
- 5) Set MULTIPLIER switch to 100 (keep MULTIPLIER FINE ADJUST control turned fully clockwise to maximize meter sensitivity).
- 6) Set BLANK ADJUST switch to LOW.
- 7) Set DAMPING switch to OFF.
- 8) Remove cell adapter, turn cell adapter so that solid side is toward the PM tube and replace cell adapter cap.
- 9) Turn POWER switch to HV (high voltage). Power indicator light is indicating that PM tube is now active.
- 10) Allow at least 30 minutes for instrument to stabilize and record time.
- 11) Depress PHOTOMETER switch and lock (quarter twist clockwise). Meter is now connected to microphotometer's measuring amplifier.
- 12) Turn MULTIPLIER switch to different sensitivity settings until a needle deflection is noted. Adjust the BLANK ADJUST FINE control until the meter indicates zero. Continue to reset the MULTIPLIER switch and adjust the BLANK ADJUST FINE control until the MULTIPLIER switch is set to 0.1 (most sensitive position) and the meter indicates zero. The instrument is now zeroed and PM tube dark current subtracted.
- 13) Turn POWER switch to ON position.
- 14) Turn PHOTOMETER switch to off.

PAGE: 2 OF 2**CALIBRATION**

Note: when changing cell adapter, filters, or aperture plates, the high voltage must be removed from the PM tube by setting the Power switch to the ON position. Extraneous light striking the PM tube could cause tube fatigue. When changing samples, the PHOTOMETER switch MUST be in the off (out) position.

- 15) Prepare sample and blank solutions and add to clean cuvettes.
- 16) Select the aperture and 47B as primary filter. Place in primary filter holder.
- 17) Select 2A-12 as secondary filter and place in secondary filter holder.
- 18) Remove cell adaptor cap and remove cell adaptor.
- 19) Insert cuvette with blank into cell holder and replace cell adapter cap.
- 20) Set POWER switch to HV.
- 21) Set MULTIPLIER switch to the 0.1 position. Subtract the meter indication to zero with the BLANK ADJUST controls as follows:
 - A. Set BLANK ADJUST COARSE to LOW position.
 - B. Adjust BLANK ADJUST FINE control to obtain zero meter indication.
- 22) Set PHOTOMETER switch to off position.
- 23) Set aperture to 1-hole position and insert into primary filter holder.
- 24) Select the calibration standard solutions to cover the

complete range of the fluorometer. Fill the cuvettes with the calibration solutions.

- 25) Insert the lowest concentration standard solution into cell holder and replace cell cap.
- 26) Adjust meter sensitivity with MULTIPLIER switch, as required, and record meter indication in laboratory notebook (Note: Do not change the BLANK ADJUST FINE control during sample measurements as this will change the zero reference point. The MULTIPLIER switch can be set to different sensitivities as required).
- 27) Repeat steps 24 and 25 for the remaining solutions.
- 28) Insert cuvette with blank into cell holder and repeat step 25 to ensure that the meter indication is still zero. If it is not, re-zero and repeat steps 24 through 26.
- 29) Change the aperture from the 1-hole position to the 2-hole position and repeat steps 23 through 27. Once this is done replace the aperture 2-hole position to the 4-hole position and repeat steps 23 through 27.
- 30) Use linear regression analysis program to determine the R-squared value for each of the aperture settings.
- 31) If the R-squared value is greater than or equal to 0.9998 for any of the aperture settings, the fluorometer is deemed to be linear and it can be used for taking measurements. Print out copy of entries made in linear regression analysis program and attach to laboratory notebook.
- 32) If the R-squared value is less than 0.9998 any of the aperture settings, allow an additional 30 minutes for stabilization of the electronics (record time) and repeat calibration. If the R-squared value is still less than 0.9998, allow an additional 30 minutes (record time) for stabilization and repeat calibration. If the R-squared value is still less than 0.9998 the fluorometer cannot be used and the operator must refer to the Study Director for advice in accordance with SOP-003.

Author's short biography



Virgil A. Marple, Ph.D.

Virgil Marple is a Professor of Mechanical Engineering in the Particle Technology Laboratory of the Mechanical Engineering Dept at the University of Minnesota. Most of his research in the past 37 years has been in the area of aerosol physics and particle technology. He received his BSME from the University of Minnesota in 1962, his MSME from the University of Southern California in 1965, and his Ph.D from the University of Minnesota in 1970. Much of his research has been in the development of instrumentation to measure the size distribution and concentration of aerosol particles, as well as devices to generate these aerosols. In particular, he is known for his pioneering work in impactor design and development. This work has spanned the range from the first CFD analysis of the impactors in 1970 to the development of commercial cascade impactors, such as the Marple Personal Impactor, the Microorifice Uniform Deposit Impactor, and the Next Generation Pharmaceutical Impactor. In 1988 he was awarded the first American Association for Aerosol Research David Sinclair Award in recognition of sustained outstanding work in Aerosol Science and Technology. From 1970 to 2000 he has been involved in the study of CWP (black lung) in the coal mining industry, developing instrumentation, performing field studies as well as laboratory evaluation of samplers. He has been a consultant on aerosol problems to numerous companies, and is currently director of the Particle Calibration Laboratory, a laboratory dedicated to high quality particle calibration of inertial classifiers using "Good Laboratory Practice" techniques. He can be reached at marple@me.umn.edu.



Bernard A. Olson, Ph.D.

Bernard Olson is a research associate in the Particle Technology Laboratory of the Mechanical Engineering Department at the University of Minnesota. He received his BSME, MSME, and Ph.D. from the University of Minnesota. For the past 20 years his research has been in the design and testing of numerous aerosol sampling instruments. Most recent research projects include: Development of a Calibration Reference Device for Use with Test Standard ANSI/ASHRAE 52.2-2007, Method of Test to Evaluate Field Performance of Commercial Kitchen Ventilation Systems, Navy Prototype Aerosol Inlet Design and Fabrication, the Development of a Standard Test Method for Grease Particle Capture Efficiency of Commercial Kitchen Filters and Extractors (ASTM Standard 2519-05), Design of a 2.5 μ m Cut Pre-Classifer for the EPA Vehicle Exhaust Particulate Mass Measurement Module, Archival Particle Calibration of the Next Generation Pharmaceutical Impactor (NGI), and Development of a Micro-orifice Uniform Deposit Impactor with Cut Sizes Down to 10 Nanometers (Nano-MOUDI). He is currently the manager of the Particle Calibration Laboratory at the University of Minnesota's Mechanical Engineering Department. He can be reached at olso0209@umn.edu.

Improving Aerosol Dispersion through Processing and Dissemination Techniques[†]

S. Tedeschi^{1,2}, N. Stevens², K. Powers², A. Ranade³,
B. Moudgil^{1,2*}, and H. El-Shall,^{1,2}

Department of Materials Science and Engineering¹

Particle Engineering Research Center²

Particle Technology, LLC³

University of Florida

Abstract

The state of dispersion is a vital aspect of powder technology impacting both traditional and emerging technologies in many diverse areas of interest including health care, industry, the environment, and the military. In such applications, the properties and quality of the resultant product will be directly and noticeably affected by the degree to which the particles are dispersed. In any operation where satisfactory particle dispersion is imperative, a reduction in dispersion, or increased agglomeration, leads to poor efficiency and ultimately results in lower yields and increased cost. As powder technology moves into the nano-age, the challenges of maintaining and improving particle dispersion become increasingly important. Decreasing particle size into the submicron range can significantly increase the effect of surface forces leading to an increase in the cohesive forces of the powder, thus, making an understanding of dispersion even more essential.

In order to develop the knowledge base to understand and control aerosol dispersion, a fundamental study into significant powder characteristics and environmental conditions that influence dispersion has been conducted. This paper discusses the results of testing various techniques employed to improve the dispersion of sub-micron aluminum flakes such as using a fumed silica spacer to reduce interparticle contact area and, in turn, attractive van der Waals forces, as well as examining the effect of dissemination pressure on the state of dispersion of the particles. This research was conducted using statistical experimental design in order to efficiently study significant factors.

Keywords: particle, aerosol, dispersion, dissemination, statistical design, nanoparticle

Introduction

A great deal of work has been put forth to improve dispersion in several diverse fields. Although the research covers a large number of materials in many different areas and technologies, the efforts have focused on one or more main areas: improving drying methods¹⁻⁴), reducing attractive forces between particles⁵⁻¹⁰), increasing repulsive forces^{11, 12}), and developing mechanical dispersion devices¹³⁻¹⁶). Due to the complexity of the problem, however, most work has been empirical in nature and only incremental im-

provements have been seen¹⁷). The first step towards realizing a significant increase in aerosol dispersion is an understanding of the dominant causes of particle agglomeration and methods that can be used to effectively overcome them. This requires a systematic study of these factors and their effect on the dispersion of the resultant aerosol. In previous work, the efficacies of different drying methods were investigated and two novel CO₂ based drying methods developed¹⁸) as was the use of surface modification to control capillary adhesion¹⁹). During this research, the effect of humidity and hydrophobicity, flow aids and interparticle contact area, and dispersion methods have been studied and the results analyzed through the guidance of a statistical experimental design.

Much research effort has been directed at understanding powder dispersion through aerosolization. Ranade and Calabrese¹⁴) found that an annular geom-

[†] Accepted: July 22nd, 2009

¹ Gainesville, FL 32611-6400 USA

² Gainesville, FL 32611-6135 USA

³ Gainesville, FL 32608 USA

* Corresponding author

TEL: 352-846-1194 FAX: 352-846-1196

E-mail : bmoudgil@erc.ufl.edu

etry dispersion device configured such that the particles enter the air stream at the point of maximum energy, i.e. maximum turbulence created by an acceleration gradient, led to the best dispersion. Chew²⁰⁻²² investigated dry powder inhalers for pharmaceutical powders and found that the airflow was highly dependent on the device configuration but varied with the drug powder used such that no one configuration worked well with all powders due to differences in powder strength. Turbulence has also been experimentally studied with latex particles in conjunction with a numerical simulation developed by Endo²³. The simulation was compared to the experimental results and used to calculate the adhesion force of spherical particles, observing that the particle size distribution effected the number of contacts between particles and thus the degree of cohesive behavior of the bulk powder²⁴⁻²⁷.

Shear, turbulence, and impaction are dispersion mechanisms that are relatively easy to impart on a particle system and can be created simply by controlling device design. However, it is seen that these mechanisms alone are not entirely sufficient and further research is required, especially for particles under 1 μ m in size. It is therefore necessary to also study the powder properties to allow for processing steps during powder production to be implemented so that the cohesion of the powder is less than the forces provided by an appropriate dispersion device.

To consider practical ways to improve aerosol dispersion it is necessary to establish the forces involved that work against particle-particle separation. These forces include van der Waals, capillary and electrostatic forces. Controlling the influence of these forces on particle systems has been extensively researched in literature^{6, 14, 18, 19, 21, 28-45} and will be briefly discussed here.

With the exception of a few surfaces, most surfaces are not atomically smooth, and even at the atomic level there is some inherent roughness due to the size of atoms and their spacing within the crystal structure. If we consider two approaching surfaces, it is understood that the smoother the surface, the greater the contact area between the particles. If the surfaces are hence roughened, or the contact area between the particles is lessened through the addition of a mediating spacer particle, the overall contribution of van der Waals forces can be drastically reduced. The classical model for the effect of roughness on van der Waals forces was first postulated by Rumpf^{46, 47} and is shown in Equation 1.

$$F_{ad} = \frac{A}{6H_o^2} \left[\frac{rR}{r+R} + \frac{R}{\left(1 + r/H_o\right)^2} \right] \quad (1)$$

Here A is the Hamaker constant, H is the interparticle separation distance, R is the radius of the particle, and r is the radius of the asperity on the surface. This model, however, significantly underestimated the adhesion force. Recent work by Rabinovich and coworkers^{53, 54, 90} has further refined Rumpf model to better predict experimental results, and in its final form as the PERC Model is seen in Equation 2. Their work indicates that surface roughness on the nanometer scale (<2 nm rms) greatly increases the force of adhesion, and as the scale of roughness increases there is a subsequent decrease in adhesive forces.

$$F_{ad} = \frac{AR}{6H_o^2} \left[\frac{1}{\left(1 + \frac{32Rk_1rms}{\lambda^2}\right)} + \frac{1}{\left(1 + \frac{k_1rms}{H_o}\right)^2} \right] \quad (2)$$

The additional terms in this equation include the maximum peak-to-trough height between the surface asperities, k_1 , the root mean squared roughness, rms , and the average peak-to-peak distance between the asperities, λ .

The presence of moisture between surfaces will also have a profound effect on dispersion. As the presence of water increases between two surfaces, liquid bridges can form. If the contact angle of the liquid on the solid is less than 90° the surfaces will be drawn closer due to capillary action.

Work has also been done on methods to control or change the effect of capillary forces acting between two surfaces by increasing the surface roughness to minimize the formation of capillary bonds. Rabinovich and coworkers have investigated the effect of nanoscale surface roughness on the critical humidity required for the onset of capillary forces in such systems^{39, 48-51} and observed that the presence of roughness on surfaces on a nanoscale had a profound effect on the critical humidity required to induce capillary adhesion. Their study validated a simple analytical expression developed to predict the force of adhesion as a function of particle size, humidity, and roughness, which is most relevant for practical systems. A visualization of the effect of surface roughness is shown in **Fig 1**.

Electrostatic forces between particles are also necessary to consider for aerosol dispersion and have been broadly investigated^{11, 31, 35, 44, 52-59}. Static electricity arises when charges on the surface of a material are not free to move to neutralize each other or do

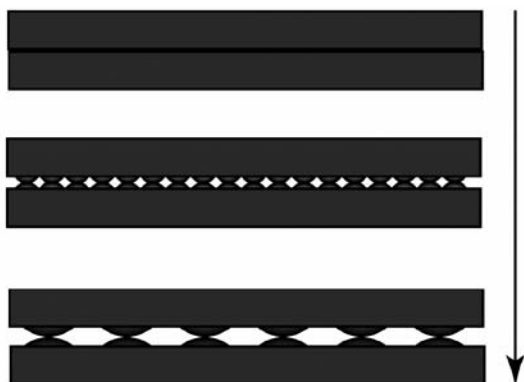


Fig. 1 Change in contact area with increasing roughness. The illustration shows the decrease in contact area that occurs with increasing surface roughness and is attributed to the difference in interparticle forces between smooth and rough surfaces.

so slowly⁵²⁾. These charges remain on the surface where they can interact with their surroundings. Particles with a similar net surface charge, greater in magnitude than the attractive forces, will experience columbic repulsion. However the affect of electrostatic forces on dispersion fall outside the bounds of the research presented here and will be left for future investigations.

The following investigation is directed at improving the dispersion of high aspect ratio particles by considering factors that affect dispersion as discussed above. A model system of aluminum flakes was used to investigate the effect of changing the interparticle contact area by the addition of 5-10 wt% spacer particles, the effect of relative humidity on the state of dispersion as well as the effect dispersion medium.

Materials and Methods

An aluminum flake material was used as a model

particle throughout this investigation (Sigma 1215, Sigma Technologies, Inc). These flakes are produced by physical vapor deposition and were delivered as a 70 wt% slurry in isopropyl alcohol. The flakes were rinsed 2-3 times by ultrasonication for 30 minutes (Misonix Sonicator 3000) in 50 mL of isopropanol (Fisher Scientific, USA) and separated by centrifugation (Beckman BH-2). The rinsing process removed any remaining product used in the PVD process.

For surface modification, 2% (vol.) solutions of n-octadecyltrimethoxysilane (ODTMS) were made as follows. 2 mL of silane and 0.5 mL of water was placed into 100 mL of ethanol (Fisher Scientific, 200 Proof), adjusted to a pH of 5 using glacial acetic acid (Aldrich, ACS Grade). 10 g of powder was slowly added to the solution while stirring and the solution was allowed to continue mixing for one hour. After the allowed time, the mixture was solvent exchanged to remove any excess silane via dilution and centrifugation (Beckman JA-21) and dried using a supercritical fluid drying process described elsewhere¹⁸⁾.

The spacer material used was a 10 nm mean diameter hydrophobic fumed silica, (Aerosil® LE2, Degussa). The spacer was added at 5 and 10 wt% to slurries of aluminum particles suspended in isopropanol. These slurries were then supercritically dried in a custom designed super critical drier (University of Florida, Paar Instruments).

The degree of dispersion of the aerosol particles was characterized using a lab-scale air dispersion chamber, fabricated in-house to integrate into a Thermo Electron Magna 760 Fourier Transform Infrared (FTIR) Spectrometer. The cylindrical chamber had an internal volume of five liters and positioned in side the FTIR such that the IR laser passed through sapphire crystal windows of the chamber to the detector.

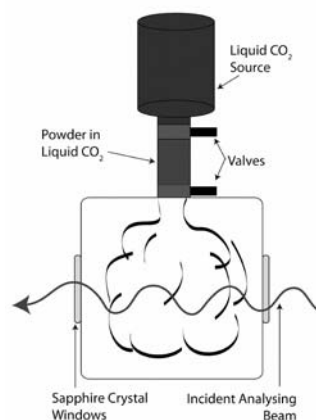


Fig. 2 The air dispersion chamber for the FTIR. A) The air dispersion chamber when positioned in the FTIR. B) A schematic diagram of the chamber showing the laser path through an aerosol cloud produced in the chamber.

The FTIR Air Chamber is shown in **Fig. 2**.

Prior to experimentation, the chamber was purged with nitrogen for 15 minutes. Powders were then dispersed into the chamber by one of two methods. The first method inducted the powder into the FTIR chamber by evacuating the chamber to -12.5 psig. The vacuum was quickly released dispersing the particles into the chamber by the venturi effect. Particles were also dispersed into the chamber by high pressure injection of either nitrogen gas (5-90 psi) or carbon dioxide (800 psi, gas and liquid).

The characterization of the size and dispersion of mixtures posed a unique challenge. Each material has a unique index of refraction, thus laser diffraction could not be used to characterize dispersion. A new method was developed using the attenuation of laser light in a settling chamber. Once the powder was disseminated, measurements of the laser transmission through the particle cloud were made over time and graphed as the negative log of one divided by transmission. The slope of this line is indicative of the settling rate since the transmission increases as the powder settling out of suspension in the air⁶⁰. A slower settling rate would result from a smaller particle size by increased dispersion. If a constant mass of material is used, and a constant concentration is assumed immediately after dissemination, the mass extinction coefficient of the Beer-Lambert Law, Equation 3, can be calculated and used to determine the airborne concentration over time. From this the degree of dispersion was determined and with it the efficacy of the processing and dissemination methods for that sample.

$$-\log\left(\frac{1}{T}\right) = M_e \cdot C \cdot PL \quad (3)$$

Here T is transmission of incident light passing through the dispersed sample, M_e is the mass extinction coefficient, C is concentration, and PL is the path length of the laser through the aerosol cloud and assumed to be the diameter of the chamber.

Settling times of interest were chosen to be one second, taken to be the maximum initial dispersion; ten seconds, a time of interest for both pharmaceutical powders and other aerosol applications; and one hundred seconds, a length of time considered to be in excess of most applications but interesting from the point of view of total aerosol lifetime.

Results and Discussion

High aspect ratio particles, such as flakes, pose

unique challenges for dispersion because their inherent high surface area to mass ratio. More specifically, the thickness of the flake is at least an order of magnitude smaller than the diameter the interparticle contact area between the flakes can be much higher while the mass which dispersive forces can be applied is very low. Associated with the high surface area are also high attractive surface forces, in particular van der Waals forces. For these reasons, once the surfaces come into contact, dispersion can become impossible. If the contact area between flakes is decreased, adhesion between the particles will be decreased and dispersion can be improved.

van der Waals forces are generally accepted to be significant only at short ranges, typically at separation distances less than 50 nm. Therefore, by maintaining some separation between the particles the van der Waals attraction will decrease. One way to achieve such an effect is through enhancement of surface roughness, shown in **Fig. 1**. First, the asperities on the surface lead to a less intimate contact and a lower total contact area between the particles. Second, the distance between the average surface planes is increased. The effect of roughness on van der Waals force can be seen by comparing the force distance curves calculated for smooth and rough surfaces, as shown in **Fig. 3**.

Here the theoretically calculated van der Waals force of attraction is plotted versus separation distance. Plot 1 shows the attractive forces for two smooth surfaces and Plot 2 shows the attractive

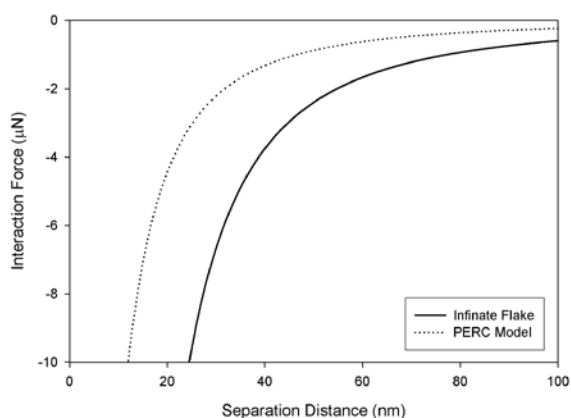


Fig. 3 Calculated van der Waals forces of a smooth and rough surface. Surface roughness has a large effect on interparticle forces. Plot 1 (solid) shows the calculation of van der Waals attraction for two smooth surfaces. Plot 2 (dotted) shows the effect of surface roughness incorporated by the PERC model^{53, 54} which not only decreases the contact area, but also separates the average surface plane of each body. A significant decrease in the calculated interaction force is seen.

forces for the same size flakes with a 4 nm RMS surface roughness as calculated by the PERC Model, Equation 2²¹). This increase in surface roughness is shown to have dramatically reduced interparticle attraction with ultimately leads to less agglomeration. By applying this concept to the high aspect ratio flakes under investigation, decreasing the attractive forces will lead to an improvement in dispersion.

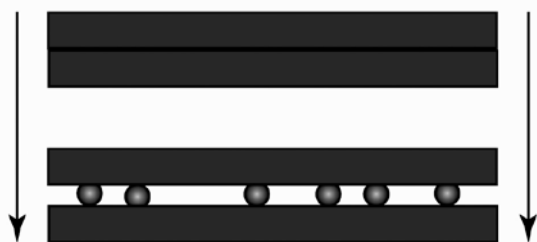


Fig. 4 Illustration of the change in contact area as a result of the addition of fumed silica. The particle surface cannot be changed to reduce contact area; however, fumed silica can be added to simulate the effect.

The surface roughness of the aluminum flakes cannot be altered easily, however, by adding spacer particles between the flakes, the effect of roughness can be simulated, as illustrated in **Fig. 4**. The fumed silica employed for this investigation was chosen because it had a diameter approximately the same size as the flake thickness (10 nm) and has a lower Hamaker constant than aluminum: 6.6×10^{-20} J as opposed to 1.5×10^{-19} J respectively²³). It was expected that the combination of these two effects would reduce the interparticle forces. A significant decrease in the magnitude of the theoretically calculated forces was found, as shown in **Fig. 5**.

This graph shows a comparison of the calculated force distance curve for smooth aluminum flakes 12 μ m in diameter and 12 nm thick along with the addition of 5-10 wt% fumed silica. The calculated forces go through an energy minimum at 5 wt% silica after which there is a slight increase in interaction forces at 10 wt% silica. At higher loadings of silica, there is a higher number of interparticle contacts and therefore an increase in the attractive forces. Based on these calculations, experiments were conducted to investigate the effect of adding fumed silica to the flakes.

For the first set of experiments, samples of bare aluminum flakes and those containing 5 wt% percent silica were disseminated using a partial vacuum pressure. As expected, the addition of silica resulted in a reduction of interparticle forces. **Fig. 6** shows a comparison of the airborne concentration of the vacuum disseminated aluminum and aluminum con-

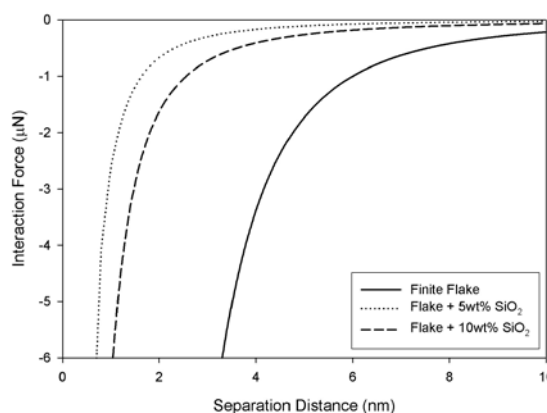


Fig. 5 Calculated van der Waals forces with the addition of silica between two flakes. A comparison of the calculated van der Waals forces for two smooth flakes is seen to be much higher than for two smooth flakes separated by silica spacer material. The Plot 1 (solid) shows the calculated van der Waals force for two smooth disks and Plot 2 (dotted) shows the calculation for two disks separated by 5 wt% of 10 nm fumed silica particles. Plot 3 (dashed) shows the calculation when 10 wt% silica is added. The spacer has the same effect as increasing surface roughness, but done without having to alter the flakes themselves. The Hamaker constant of silica is also lower than that of aluminum which also contributes to a decrease in van der Waals forces.

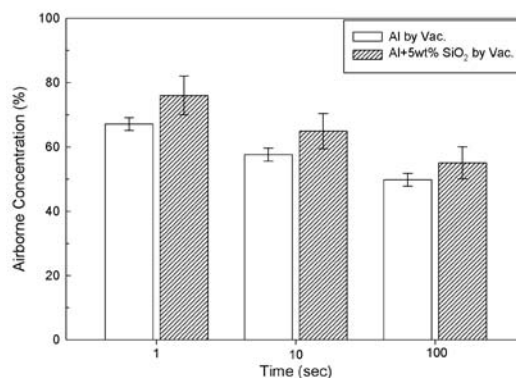


Fig. 6 Airborne concentration of aluminum particles by vacuum dissemination. The addition of 5 wt% silica to the aluminum demonstrated a 10-20% increase in airborne concentration.

taining the silica. The addition of the silica lead to a sixteen percent increase in airborne concentration of particles. It should be noted, however that complete dispersion was not achieved and other factors must be considered.

The effect of interparticle agglomeration due to capillary adhesion was subsequently investigated. Capillary forces between particles caused by the condensation of water from the atmosphere can lead to a significant increase in particle adhesion and in turn decrease the dispersability of the powder²⁴⁻²⁷). This was readily observed by the change in particle size distribution of aluminum flakes in **Fig. 7** after preconditioning at 20, 50, and 80% relative humidity for 48 hours. The particle size is seen to increase

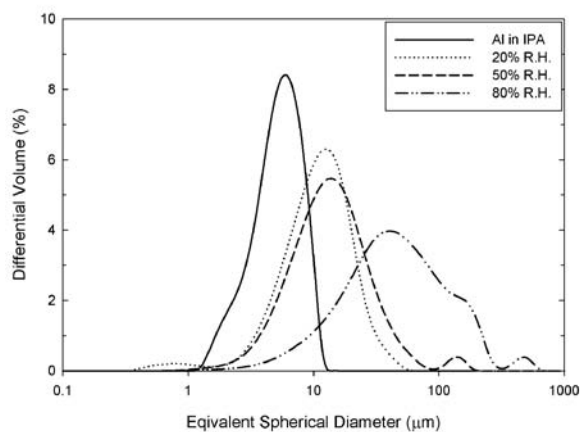


Fig. 7 Particle size of aluminum flakes at 20, 50, and 80% relative humidity. The graph represents change in particle size of the aluminum flakes after supercritical drying and conditioning for 48 hours at 20% relative humidity (dotted), 50% relative humidity (dashed), and 80% relative humidity (dash-dot). Plot 1 (solid) represents the primary particle size measured in isopropyl alcohol and provided as a comparison. The standard deviation for the measurement is $\pm 3 \mu\text{m}$. The change in particle size and distribution due to changes in the relative humidity can readily be seen.

with relative humidity as capillary forces increase the adhesion between the particles. The primary particle size is shown for comparison. The equation for the attractive forces due to the presence of liquid bridges between two spheres is given below⁵⁰.

$$F_{cap} = -4\pi R\gamma_{lv} \cos \theta \quad (4)$$

Here R is the radius of the capillary, γ_{lv} is the surface tension of the liquid phase, θ is the contact angle of the liquid at the particle surface, and the sign of the equation represents the force direction, which is cohesive in nature. By this reasoning, dispersion can be improved by controlling the capillary adhesion, i.e. increasing the contact angle through surface modification or by increasing the dispersion force through the use of a volatile medium. Research on the use of surface modification to control the contact angle is reported in detail elsewhere¹⁹) however only the relevant results will be discussed below. For this investigation, aluminum flakes were coated with a hydrophobic silane and the dispersion properties were examined using the FTIR Air Chamber.

The use of a volatile medium between the particles presents the opportunity to develop a radiating dispersion force from inside the agglomerate in addition to the traditional forces, such as turbulence and drag, an agglomerate would experience during dispersion. Liquid carbon dioxide was chosen as the volatile medium due to its environmental inertness, relatively low boiling point, high molar expansion ratio and

low toxicity. In its liquid form, CO_2 is stored at approximately 800 psi at room temperature and during release to the atmosphere The liquid undergoes a rapid molar volume increase of the order of 500%. The application of liquid CO_2 as a dispersive medium is shown illustrated in **Fig. 8**.

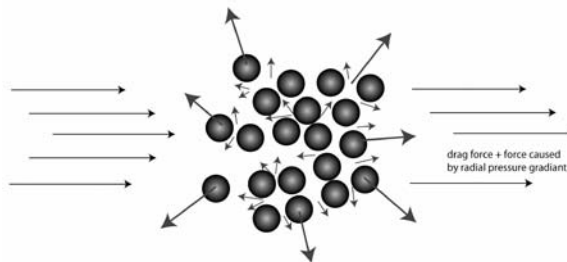


Fig. 8 Illustration of the dispersion effect of liquid carbon dioxide. Upon release, the liquid carbon dioxide will undergo a phase transformation from a liquid to a gas resulting in an increase in volume of approximately 500 times. The rapid vaporization of liquid carbon dioxide aids in the dispersion of the powder.

The airborne concentration of the bare and OD-TMS surface modified flakes at 50% relative humidity disseminated using liquid CO_2 can be seen in **Fig. 9**. No significant change in airborne concentration was observed. To further investigate this, bare aluminum flakes were conditioned at 20, 50, and 80% relative humidity for 48 hrs then disseminated into the air chamber using liquid CO_2 . As seen in **Fig. 10**, no significant change in airborne concentration or settling rate can be seen with increasing humidity. These results demonstrate that the use of liquid carbon dioxide to disperse and disseminate powder overwhelmed any effect of prior powder conditioning such as agglomeration due to capillary forces on dispersion.

The airborne concentrations, although independent of preconditioning humidity, was comparable to the dry aluminum alone and thus has room for

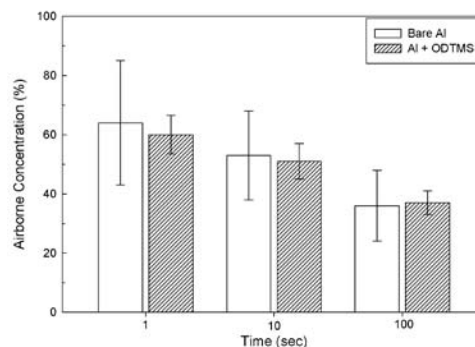


Fig. 9 Airborne concentration of surface modified aluminum flakes at 50% humidity. The plot shows the airborne concentration of bare aluminum flakes and ODTMS surface modified aluminum flakes. Surface modification does not improve dispersion over liquid CO_2 dissemination alone.

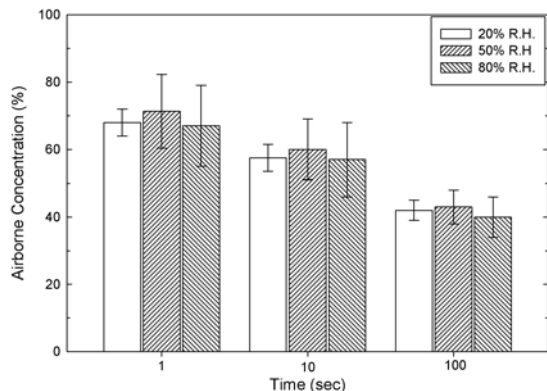


Fig. 10 Airborne concentration of bare aluminum at 20, 50, and 80% humidity. Using liquid CO₂ dissemination, the usual effect of increasing relative humidity on increasing agglomeration is no longer a factor due to the improved dispersion method.

further improvement. To do so the combination of both methods was used. The aluminum flakes and flake/silica mixtures were disseminated using the liquid CO₂ and the results can be seen by the increase in airborne concentration in **Fig. 11**. Although the dispersion of the bare aluminum did not improve, the addition of the spacer shows a 20% increase in airborne concentration over that of liquid alone. In addition, the settling rate of the mixture is shown to be slower, a second indication of improved dispersion.

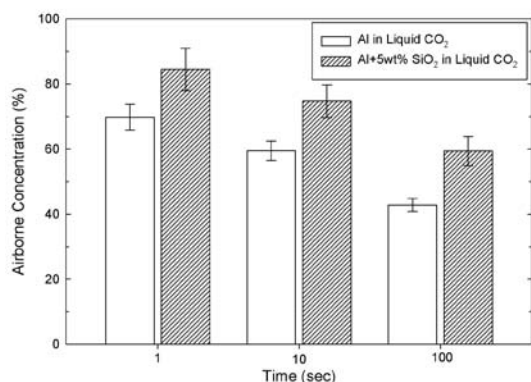


Fig. 11 Airborne concentration using liquid carbon dioxide and silica. The addition of 5 wt% silica has previously been shown to reduce the van der Waals forces between flakes by increasing the interparticle spacing. This also increases the volume of liquid carbon dioxide between the flakes and in turn the amount of pressure that can be generated upon dissemination.

Further analysis of the results was performed with the aid of a statistical design software package. A 3D representation of the results within the design space can be seen in **Fig. 12**. Each side of the cube represents one experimental factor with the corners signifying the minimum and maximum levels. The airborne concentration obtained from each level of each set of the three factors is designated by the number

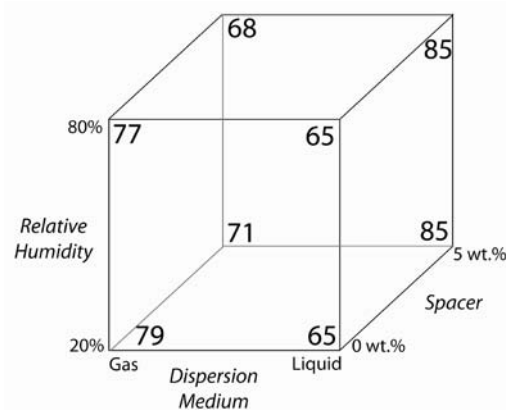


Fig. 12 Experimental design dispersion results. The figure shows the results for airborne concentration for all of the experiments used to investigate the effect of humidity, spacer, and dispersion medium. The conditions for optimum dispersion can be seen to result from 5 wt% spacer and liquid CO₂.

at each corner inside the cube. Since humidity did not show a significant effect on the airborne concentration experiments, it was not included in the analysis. From these results, the best conditions are found using liquid CO₂, 5 wt% silica, and using surface modification. Based on the data, an empirical model describing the effect of each factor on dispersion was developed by the software and given in Equation 5.

$$C_{air} = 73.55 + 0.70A(\text{Medium}) - 1.80B(\text{Surface Modification}) + 3.95C(\text{Spacer}) + 6.80AC + 1.80BC \quad (5)$$

In Equation 5, the factors that have a significant effect on airborne concentration are shown along with the magnitude of their effect according to the factor coefficient. The standard deviation for the coefficients was ± 0.6 . Half the coefficient value is the factor effect. It is seen that the spacer and the interaction between the spacer and the medium have the largest effect on dispersion. Using this model, a maximum airborne concentration can be calculated based on different levels of these parameters. Within this design space, a maximum airborne concentration of 85% is predicted and experimentally obtained.

Conclusions

Through this research, a systematic investigation of the effect of significant factors on powder dispersion in air has been conducted. An understanding of the effect of these factors on dispersion, and the magnitude of their effect, has been developed. Through the use of spacer particles, the interparticle contact area between the flake surfaces was reduced and in turn the adhesion forces were reduced. It was

demonstrated that the addition of 5 wt% of fumed silica as spacer particles resulted in a sixteen percent increase in airborne particle concentration using partial vacuum induction. The condensation of liquid after conditioning at elevated relative humidity levels lead to significantly agglomeration due to capillary adhesion. To overcome this challenge, a novel dispersion method was developed which employed the use of liquid carbon dioxide as a volatile dissemination medium. Through this method, the particles were dispersed in a liquid that underwent a high molar volume expansion during dissemination because of its phase change to a gas, the thermodynamically favored state at standard temperature and pressure, once released from the device. The expansion of gas added a radial force in addition to the shear normally produced through dispersion and dominated any effect of powder preconditioning, however it was not large enough to significantly improve dispersion. Once the spacer was added and disseminated using liquid CO₂ dissemination resulted in a significant increase in airborne concentration of 20% and a maximum airborne concentration of 85% was observed.

Future Work

Up to this point experiments have been performed to investigate the effect of important parameters on the interparticle size and airborne concentration. The effect of chosen parameters on interparticle forces has been theoretically calculated and compared to the experimental results. In order to obtain a better understanding of the effect of these factors on the interparticle forces, measurements of the forces on the macro and micro scale must be performed. A comparison of the change in magnitude of the interparticle forces as they relate to these factors will result in a correlation between the significant interparticle forces and their relationship to dispersion.

Acknowledgements

The authors acknowledge the financial support of the Particle Engineering Research Center (PERC) at the University of Florida the National Science Foundation (NSF) (Grant EEC-94-02989), the United States Army (Grant NSF-0244326EEC), Edgewood Chemical and Biological Center, and the Industrial Partners of the PERC for support of this research. Any opinions, findings, and conclusions or recommendations expressed in this material are those of the author(s) and do not necessarily reflect those of

the United States Army or the Industrial Partners of the PERC.

Reference

- 1) Shekunov, B.Y., et al. (2003): Aerosolization behavior of micronized and supercritically-processed powders, *Journal of Aerosol Science*, 34(5), pp.553-568.
- 2) Sellers, S.P., et al. (2001): Dry powders of stable protein formulations from aqueous solutions prepared using supercritical CO₂-assisted aerosolization, *Journal of Pharmaceutical Sciences*, 90(6), pp.785-797.
- 3) Sievers, R.E., et al. (2000): Supercritical fluid carbon dioxide technologies for fine particle formation for pulmonary drug delivery, *Abstracts of Papers of the American Chemical Society*, . 219, pp.33-34.
- 4) Kousada, Y. et. al. (1994): Generation of an Aerosol by the Boiling of Suspensions, *Aerosol Science and Technology*, 8(21), p.236.
- 5) Mullins, M.E. and M.B. Ranade (1984): Force of Adhesion and the Energy Required to Disperse Test Dust in Air, U.S.A. Chemical Research and Development Center, Editor.
- 6) Ranade, M.B. (1975): Research on Coatings or Surface Treatment of Metal Powders, A.F.C.R. Laboratory, Editor.
- 7) Ranade, M.B. (1984): Surface Treatment on Metal Powders for Dispersion Improvement, C.R.A.D. Center, Editor.
- 8) Hooton, J.C., et al. (2004): An atomic force microscopy study of the effect of nanoscale contact geometry and surface chemistry on the adhesion of pharmaceutical particles, *Pharmaceutical Research*, 21(6), pp.953-961.
- 9) Vold, M.J. (1961): The Effect of Adsorption on the van der Waals Interaction of Spherical Colloidal Particles, *Journal of Colloid Science*, 16(1).
- 10) Mizes, H., et al. (2000): Small particle adhesion: measurement and control. *Colloids and Surfaces a-Physicochemical and Engineering Aspects*, 165(1-3), pp.11-23.
- 11) Ren, J., et al. (2001): Electrostatic dispersion of fine particles in the air. *Powder Technology*, 120(3), p.187.
- 12) Ren, J., S.C. Lu, and F.Q. Tang (2003): The voltage-current characteristics and dispersion effect of RLW electrostatic disperser, *Powder Technology*, 135, pp.261-265.
- 13) Masuda, H., Higashitani, K., Yoshida, H., ed. (2006): "Powder Technology Handbook". Third ed., Taylor and Francis Group, LLC, Boca Ratone, FL.
- 14) Calabrese, R.V. and M.B. Ranade (1993): Pneumatic Nozzle Dissemination of Powders into Air, U.S.A.R. Office, Editor.
- 15) Hickey, A. (1997): A New Millenium for Inhaler Technology. *Pharmaceutical Technology*, 21(6), pp.116-125.
- 16) Masuda, H. and K. Gotoh (1996): Dry dispersion of fine particles, *Colloids and Surfaces A, Physicochemical and Engineering Aspects*, 109, p.29.
- 17) Tedeschi, S.T. (2007): Improving Aerosol Dispersion

- Through and Understand of Interparticle Forces, in Materials Science and Engineering, Ph. D. Dissertation., University of Florida, Gainesville.
- 18) Tedeschi, S., et al. (2008): Novel Supercritical Fluid Processing Techniques for the Production of an Aerosol, Powder Technology, In Peer Review.
 - 19) Stevens, N., et al. (2008): Controlling Unconfined Yield Strength in a Humid Environment through Surface Modification, Powder Technology, In Peer Review.
 - 20) Chew, N.Y.K., D.F. Bagster, and H.K. Chan (2000): Effect of particle size, air flow and inhaler device on the aerosolization of disodium cromoglycate powders, International Journal of Pharmaceutics, 206(1-2), pp.75-83.
 - 21) Chew, N.Y.K. and H.K. Chan (1999): Influence of particle size, air flow, and inhaler device on the dispersion of mannitol powders as aerosols. Pharmaceutical Research, 16(7), pp.1098-1103.
 - 22) Chew, N.Y.K., et al. (2002): Characterization of pharmaceutical powder inhalers: estimation of energy input for powder dispersion and effect of capsule device configuration, Journal of Aerosol Science, 33(7), pp.999-1008.
 - 23) Endo, Y., S. Hasebe, and Y. Kousaka (1997): Dispersion of aggregates of fine powder by acceleration in an air stream and its application to the evaluation of adhesion between particles. Powder Technology, 91(1), pp.25-30.
 - 24) Chew, N.Y.K. and H.K. Chan (2002): Effect of powder polydispersity on aerosol generation, Journal of Pharmacy and Pharmaceutical Sciences, 5(2), pp.162-168.
 - 25) Raula, J., et al. (2007): Study of the dispersion behavior of I-leucine containing microparticles synthesized with an aerosol flow reactor method, Powder Technology, 177(3), p.125.
 - 26) Zeng, R.J. and B. Rand (2000): Particle size distribution, powder agglomerates and their effects on sinterability of ultrafine alumina powders, Journal of Materials Science & Technology, 16(4), pp.393-396.
 - 27) Zeng, X.M., et al. (1999): Effects of particle size and adding sequence of fine lactose on the deposition of salbutamol sulphate from a dry powder formulation, International Journal of Pharmaceutics, 182(2), pp.133-144.
 - 28) Coelho, M.C. and N. Harnby (1978): Effect of Humidity on Form of Water-Retention in a Powder, Powder Technology, 20(2), pp.197-200.
 - 29) F. Soulié, F.C., M. S. El Youssoufi, C. Saix (2006): Influence of liquid bridges on the mechanical behavior of polydisperse granular materials, International Journal for Numerical and Analytical Methods in Geomechanics, 30(3), pp.213-228.
 - 30) Gopalkrishnan, P., I. Manas-Zloczower, and D.L. Feke (2005): Investigating dispersion mechanisms in partially infiltrated agglomerates: Interstitial fluid effects, Powder Technology, 156(2-3), pp.111-119.
 - 31) Gupta, R., D. Gidaspow, and D.T. Wasan (1993): Electrostatic Separation of Powder Mixtures Based on the Work-Functions of Its Constituents, Powder Technology, 75(1), pp.79-87.
 - 32) He, Y.H. (1999): A criterion for particle agglomeration by collision, Powder Technology, 103(2), pp.189-193.
 - 33) Ho, C.A. and M. Sommerfeld (2002): Modeling of micro-particle agglomeration in turbulent flows, Chemical Engineering Science, 57(15), pp.3073-3084.
 - 34) Holmes, N.S. and L. Morawska (2006): A review of dispersion modeling and its application to the dispersion of particles - An overview of different dispersion models available, Atmospheric Environment, 40(30), p.5902.
 - 35) Kunkel, W.B. (1950): The Static Electrification of Dust Particles on Dispersion into a Cloud, Journal of Applied Physics, 21(8), pp.820-832.
 - 36) Musante, C.J., et al. (2002): Factors affecting the deposition of inhaled porous drug particles, Journal of Pharmaceutical Sciences, 91(7), pp.1590-1600.
 - 37) Quon, R.A., A. Ulman, and T.K. Vanderlick (2000): Impact of humidity on adhesion between rough surfaces, Langmuir, 16(23), pp.8912-8916.
 - 38) Rabinovich, Y.I., et al. (2000): Adhesion between nanoscale rough surfaces - I. Role of asperity geometry, Journal of Colloid and Interface Science, 232(1), pp.10-16.
 - 39) Rabinovich, Y.I., et al. (2002): Capillary forces between surfaces with nanoscale roughness. Advances in Colloid and Interface Science, 96(1-3), pp.213-230.
 - 40) Shaw, D.T. (1978): "Fundamentals of Aerosol Science", New York, Wiley and Sons, Inc.
 - 41) Soulie, F., et al. (2006): Influence of liquid bridges on the mechanical behavior of polydisperse granular materials, International Journal for Numerical and Analytical Methods in Geomechanics, . 30(3), pp.213-228.
 - 42) Viguie, J.-R., et al. (2007): Study of agglomeration of alumina nanoparticles by atomic force microscopy (AFM) and photon correlation spectroscopy (PCS), Colloids and Surfaces A: Physicochemical and Engineering Aspects, 302(1-3), p.269.
 - 43) Yoon, R.-H., D.H. Flinn, and Y.I. Rabinovich (1997): Hydrophobic Interactions between Dissimilar Surfaces, Journal of Colloid and Interface Science, . 185(2), p.363.
 - 44) Yurteri, C.U., et al. (2002): Electrostatic effects on dispersion, transport, and deposition of fine pharmaceutical powders- Development of an experimental method for quantitative analysis, Particulate Science and Technology, . 20(1), pp.59-79.
 - 45) Zimon, A.D. (1969): "Adhesion of Dust and Powder", New York, Plenum Press.
 - 46) Rumpf, H. (1974): Die Wissenschaft des Agglomerierens, Chem.-Ing.-Tech, . 46, pp.1-11.
 - 47) Rumpf, H., K. Sommer, and K. Steier (1976): Mechanismen der Haftkraftverstärkung bei der Partikelhaftung durch plastisches Verformen, Sintern und viskoelastisches Fließen, Chem. Ing. Tech, . 48, pp.300-307.
 - 48) Ata, A., Y.I. Rabinovich, and R.K. Singh (2002): Role

- of surface roughness in capillary adhesion, *Journal of Adhesion Science and Technology*, . 16(4), pp.337-346.
- 49) Nguyen, A.V., et al. (2003): Attraction between hydrophobic surfaces studied by atomic force microscopy, *International Journal of Mineral Processing*, . 72(1-4), pp.215-225.
 - 50) Rabinovich, Y.I., M.S. Esayanur, and B.M. Moudgil (2005): Capillary Forces between Two Spheres with a Fixed Volume Liquid Bridge: Theory and Experiment. *Langmuir*, . 21(24), pp.10992-10997.
 - 51) Rabinovich, Y.I. and R.H. Yoon (1994): Use of Atomic Force Microscope for the Measurements of Hydrophobic Forces between Silanated Silica Plate and Glass Sphere. *Langmuir*, . 10(6), pp.1903-1909.
 - 52) Reist, P.C. (1993): "Aerosol Science and Technology", Second ed., New York, McGraw-Hill, Inc. 379.
 - 53) Cadle, R.D. (1975): "The Measurement of Airborne Particles", New York, John Wiley and Sons, Inc.
 - 54) Kunkel, W.B. (1951): Comment on Static Electrification of Dust Particles on Dispersion into a Cloud. *Journal of Applied Physics*, 22(1), pp.103-104.
 - 55) Nakajima, Y. and T. Sato (2003): Electrostatic collection of submicron particles with the aid of electrostatic agglomeration promoted by particle vibration. *Powder Technology*, 135, pp.266-284.
 - 56) Watanabe, T., et al. (1995): Submicron Particle Agglomeration by an Electrostatic Agglomerator. *Journal of Electrostatics*, 34(4), pp.367-383.
 - 57) Laitinen, A., et al. (1996): Bipolar charged aerosol agglomeration with alternating electric field in laminar gas flow, *Journal of Electrostatics*, 38(4), pp.303-315.
 - 58) Boisdron, Y. and J.R. Brock (1970): On Stochastic Nature of Acquisition of Electrical Charge and Radioactivity by Aerosol Particles, *Atmospheric Environment*, 4(1), pp.35-&.
 - 59) Pauthenier, M. and R. Guillien (1932): Direct electrometric study of the limited charge of a conductor sphere in an ionised electric field. *Comptes Rendus Hebdomadaires Des Seances De L Academie Des Sciences*, 195, pp.115-116.
 - 60) Fuks, N.A., (1964): "The mechanics of aerosols", Rev. and enl. ed. Oxford, New York, Pergamon Press; [distributed in the Western Hemisphere by Macmillan. xiv, 408 p.

Author's short biography



Stephen T. Tedeschi

Dr. Tedeschi is currently a patent analyst at Landon-IP specializing in the Materials Science. During the time of this work he was a Materials Science and Engineering doctoral candidate at the Particle Engineering Research Center, University of Florida where his research was focused on the improvement of aerosol dispersion. Dr. Tedeschi's research interests include powder flow, dispersion and aggregation of fine particulates in liquid and gas, and the use of particles for the attenuation of regions of the electromagnetic spectrum.



Nathanael I. Stevens

Dr. Stevens is a research scientist at the Particle Engineering Research Center, University of Florida. His appointment at the University of Florida began in 2006 after receiving his Ph.D. from the Ian Wark Research Center at the University of South Australia in 2005 where his research was focused on surface modification, mineral flotation and in-situ contact angle analysis of particulates. Dr. Stevens' research interests include powder flow, dispersion and aggregation of fine particulates, supercritical fluid processing and applied surface chemistry.

Author's short biography



Kevin Powers

Dr. Kevin Powers is currently serving as the Associate Director of the research and development facility at the Particle Engineering Research Center, University of Florida. He has been at UF since 1993. Prior to this appointment, Dr. Powers served as an Assistant Professor of Chemistry at the USAF Academy, Colorado Springs and also as an Instructor Pilot for the United States Air Force. Dr. Powers major research interests include particle characterization, nanoparticle toxicology, engineered particulates, supercritical fluid processing, interfacial phenomena, and photocatalysis.



A. Ranade

Dr. M. B. (Arun) Ranade is a chemical Engineer with over 35 years of experience in particle technology with emphasis on aerosol engineering at leading research and development institutions. As a visiting scientist at the University of Florida Particle Engineering Research Center (PERC) he is active in aerosol generation from solid, liquid and vapor phases for many applications including nanoparticle production in flame reactors, dissemination of military obscurants and standards for environmental analyses.



Brij M. Moudgil

Brij Moudgil is a Distinguished Professor of Materials Science and Engineering at the University of Florida where he currently holds the Alumni Chair in Materials Science and is also the Director of the Particle Engineering Research Center. He served as the president of the Society for Mining, Metallurgy, and Exploration (SME) for the year 2006-2007. His research interests are in polymer and surfactant adsorption, dispersion and aggregation of fine particles, nanotoxicity, multifunctional nanoparticles for bioimaging, diagnosis, and therapy, nanoparticulate processing and separation technology for enhanced performance in mineral, chemical, microelectronics, pharmaceuticals, advanced materials, and resource recovery & waste disposal applications. He received his B.E degree in Metallurgical Engineering from the Indian Institute of Science, Bangalore, India and his M.S and Eng. Sc.D degrees in Mineral Engineering from the Columbia University. In 2002 he was elected as a member of the U.S National Academy of Engineering for his contributions to mineral processing and professional leadership in the particle community. He can be reached at bmoudgil@erc.ufl.edu.



H. El-Shall

Dr. El-Shall is Associate professor of Materials Science and Engineering and Associate Director for Research at The Particle Engineering Research Center of University of Florida. He has been at UF since 1994. He also served as Associate Director for beneficiation research at the Florida Institute of Phosphate Research from 1986-1992. Before that he has served as assistant professor of Mineral Processing at Montana Tech from 1980 to 19986. DR. El-Shall's major research interests include interfacial phenomena and nanoparticle science and technology and its applications in medicine, mineral industry, and waste treatment in various industries.

Modeling of Powder Deposition into Shallow Dies for Three Filling Methods[†]

Saed Sayyar Roudsari and Virendra M. Puri^{1,*}
Materials Research Institute
Department of Agricultural and Biological Engineering
Penn State University¹

Abstract

Fundamental understanding of the deposition of powders into dies is essential to optimizing processes such as compaction. Toward this end, models were developed and verified to simulate the filling characteristics for three deposition methods into shallow dies. Understanding of the filling process for shallow dies represents the key first step towards gaining fundamental knowledge of filling deep dies. The three different filling methods modeled were: the feed shoe, rotational rainy, and point feed, which represent the commonly used methods to fill dies and containers. A free flowing, spray dried battery powder mixture ($d_{50}=600 \mu m$) was filled into a circular shallow die (35 mm diameter x 6.5 mm deep) at 20 mm/s feed shoe speed equivalent to 26 g/min filling rate. A physics based explanation of the filling process, i.e., pressure vs. time for a specific location at the bottom of the die, is included that provides a rational basis for the use of Chapman-Richards model. In order to evaluate the goodness of the model, the average root mean square error (RMSE) and the mean value of average relative difference (ARD) of the models were calculated. The results showed that 1) the RMSE for feed shoe, rotational rainy, and point feed were 0.16 dm (dm=decimeter, fill head equivalent of measured pressure), 0.44 dm, and 0.32 dm, respectively, whereas, the ARD for feed shoe, rotational rainy, and point feed were 7%, 16%, and 11%, respectively; 2) the deposition profile for feed shoe and rainy fill were sigmoidal in shape, while for the point feed it was linear.

Keywords: die filling, mathematical model, deposition method, feed shoe deposition, raing fill, point feed

1. Introduction

Any industry that deals with particulate materials must have a clear understanding of particle behavior during the handling and processing operations. Generally, materials in particulate form are easier and more economical to handle due to the flexibility in producing a variety of finished products. Given the widespread use of powders, it would be impossible to improve the handling and processing techniques without a precise knowledge of how particulate materials behave under various conditions.

Developing a mathematical model is the ultimate goal for engineers to simulate the cause and effect in a surrogate device which is used to represent a real world system to understand the response under

various conditions (inputs) (Kessler and Greenkorn, 1999). Some engineering mathematical models are built based on purely experimental observations, which treat variables in a physically most intuitive manner. The objective is to determine simple correlations of the behavior of the dependent and independent variables. At a more fundamental level, physical, chemical, and/or biological laws, are used to form the basis for mathematical model. In this context, the parameters that are embedded in the model have well defined physical meaning. In this research, the latter approach was attempted to formulate a mathematical model for the powder deposition process in dies.

No continuum models and methods have been published to simulate the deposition characteristics in shallow dies. Xie (2006) developed an overall rate equation for feed shoe filling process for cylindrical dies using a battery powder mixture (BPM). The overall rate equation was $dP_p/d\tau = \alpha P_p F(\tau) + \beta$, where P_p is prorated pressure, τ is normalized time, α and β are coefficients, and $F(\tau)$ is a stage-specific deposi-

[†] Accepted: July 22nd, 2009

¹ University Park, PA 16802, USA

* Corresponding author

E-mail. address: vmpuri@psu.edu;

TEL – 814-865-3559, Fax – 814-863-1031

tion rate function. Although, the model successfully described the feed shoe deposition method, no clear and complete physical interpretation of α and β , and origin of $F(\tau)$ were presented (Xie and Puri, 2008). Therefore, the objective of this research was to develop and validate time-dependent models for feed shoe, rainy fill, and point feed filling methods based on process physics.

2. Mathematical Formulation

The two cornerstones of the deposition model are the overall force balance and mass balance equations. In this study, the static force balance was used as the basis for developing the prevailing dynamic conditions. Furthermore, it was assumed that the developed equations are point-specific located at the die bottom. In order to better describe and analyze the die filling process, it was divided into two stages: 1) powder deposition process into a die that is partially to nearly completely filled, and 2) powder deposition process during surcharge build-up. The analysis and mathematical formulations are described in the following subsections.

2.1. Analysis of powder within die

Force Balance in powder mass: The most widely used equation for predicting vertical and lateral pressure in dies, bins, and containers is the Janssen's equation (Manbeck and Puri, 1995). Janssen's solution assumes the bulk density of material (ρ_b), angle of internal friction (φ), and coefficient of friction between the die wall and powders (μ) are constant throughout the particle bed. In order to gain a better insight into the effect of loading conditions and, in particular, to simplify the mathematical simulation, the system was assumed to be axisymmetric, thus

pressure distributions vary with depth but not with location around the circumference. A schematic of the free body diagram of the cylindrical die and force balance on powder mass at depth is shown in **Fig. 1**.

Summing forces acting on the differential elements in the vertical direction (**Fig. 1b**) yields Equation (1) (Roudsari, 2007):

$$(P_v + dP_v)A + P_w C dy - P_v A - \rho_b g A dy = 0 \quad (1)$$

where: A = cross-section; C =die circumference; P_w =vertical friction on the wall; P_v =vertical pressure in the mass; P_h =lateral pressure; g = gravitational constant; μ =coefficient of friction; ρ_b = bulk density; and y = actual filled height of powder in the die.

Since the number of symbols used is large, for convenience these are listed also in the Nomenclature section.

Upon integration, Equation (1) yielded:

$$P_v = \frac{\rho_b g R}{k\mu} (1 - e^{-\frac{k\mu y}{R}}) \quad (2)$$

where, k is the ratio of lateral to vertical pressure within the powder mass ($k = \frac{P_h}{P_v}$) and $R=A/C$.

Mass balance in powder mass: The physical principle of mass balance is given in Equation (3).

$$\dot{m}_2 - \dot{m}_1 + \frac{dm}{dt} = 0 \quad (3)$$

where \dot{m}_2 = rate of outflow, \dot{m}_1 = rate of inflow, $\frac{dm}{dt}$ = accumulation rate. In the case of filling a container with no outflow, Equation (3) can be rewritten as:

$$\frac{dm}{dt} = \dot{m}_1, \text{ but } m_1 = \rho v = Q \text{ and } \dot{m}_1 = \dot{Q} \quad (4)$$

Also $\rho \frac{dv}{dt} = \rho \dot{Q}$, $v=A \cdot y$, where, v =volume, then:

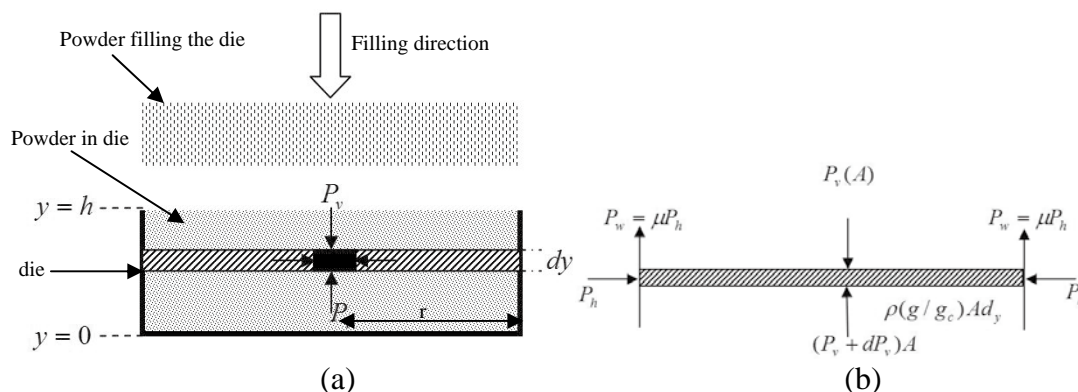


Fig. 1 Free body diagram of (a) cylindrical die during rainy filling process, and (b) force balance on powder mass inside the die (Manbeck and Puri, 1995).

$$A \frac{dy}{dt} = \dot{Q} \quad (5)$$

Next, Equation (2) can be rewritten in terms of general parameters γ_1 , γ_2 , and y , this reduces to:

$$P_v = \gamma_1(1 - e^{-\gamma_2 y}) \quad (6)$$

where, $\gamma_1 = \rho_b g R / \mu m$ and $\gamma_2 = k \mu / R$

Rearranging Equation (6) in terms of y and replacing in Equation (5) and integration leads to (Roudsari, 2007):

$$P_v = \frac{1}{\gamma_1} \left(1 - e^{\frac{-\gamma_2}{A\gamma_1^2} \dot{Q} t} \right)$$

Substituting $K = \frac{1}{\gamma_1}$ and $b = \frac{\gamma_2}{A\gamma_1^2} \dot{Q}$, yields:

$$P_v = K(1 - e^{-bt}) \quad (7)$$

Rewriting pressure P_v as equivalent height h^* $P_v / (\rho_p \times g)$: or $h^* = K(1 - e^{-bt})$ (8)

where K and b are experimentally determined parameters and ρ_p is the particle density.

2.2. Analysis of powder within surcharge mass

Equation (8) is a typical exponential response for pressure distribution in dies and containers; however, the most typical observed die filling pressure response was sigmoidal. For all three fill methods, there was always a powder surcharge that is a likely cause of the slowdown in pressure build-up. For the feed shoe, the pressure distribution is more complex and is believed to be caused by the cumulative effect of the feed shoe tube walls and powder head in the feed shoe tube. Since the surcharge of powders in a rainy fill provides a clearer explanation of the process physics, it is followed here. In addition, the point feed filling method's analysis is included.

As stated previously, the die was overfilled dur-

ing the filling process, which is a normal practice in industry. Following overfill, the excess powder is scraped off and the free surface of the powder is leveled. A simplified free body diagram of a heap (mound) of the surcharge powder above the die is shown in **Fig. 2**.

Following the force balance analysis carried out for filled powder below the die height ($y < h$), the vertical pressure was obtained as:

$$P_v = A(1 - e^{-b(H_0 - h)}) \quad (9a)$$

Or, in terms of equivalent height (h^*) and time (t) (Roudsari, 2007):

$$(H_0 - h) = \gamma_3(1 - e^{-\gamma_4(t - t_f)}) \quad (9b)$$

where, t_f = time to fill the die corresponding to $y = h$, and time at the end of filling process including surcharge $t > t_f$, and γ_3 and γ_4 are coefficients

Based on visual observations during experiments with the rainy fill method, the surcharge powder profile can be approximated by a spherical cap (ABCDEF) as shown in **Fig. 2a**. The vertical pressure as equivalent height from the surcharge powder is (Roudsari, 2007):

$$h^* = \frac{\rho_b \pi r^2 \theta}{\rho_p} \gamma_3 \left(1 - e^{-\gamma_4(t - t_f)} \right) + \frac{\rho_b \pi}{\rho_p} \frac{(\gamma_3)^3}{6} \left(1 - e^{-\gamma_4(t - t_f)} \right)^3 \quad (10)$$

where, ρ_b bulk density, g = gravitational constant, θ = (segment AC, **Fig. 2**)/ r , and r = radius of sphere.

The form of Equation (10) is sigmoidal, which is comparable to Chapman-Richards equation (Seber and Wild, 1989) shown below:

$$h^* = \alpha(1 - e^{-bt})^c \quad (11)$$

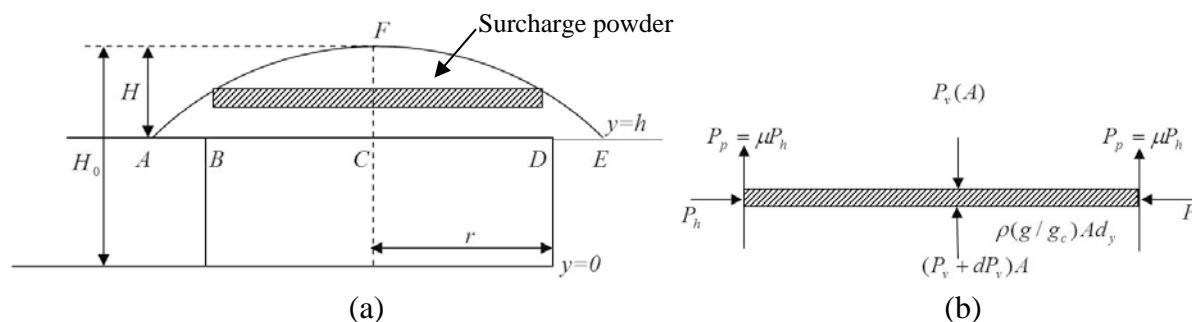


Fig. 2 (a) Free body diagram of dimension of surcharge powder for rainy fill, (b) force balance diagram of powder mass inside the surcharge powder mass above the die cross-section.

where α , b , and c are parameters. The interpretation of these coefficients is: (1) α represents the asymptotic equivalent height, i.e., the maximum h^* when time approaches ∞ ; for instance, when filling a deep die, (2) b represents the reciprocal of the characteristics time ($\frac{1}{b}$) of the deposition process exponent, i.e., the rapidity with which h^* is approached, and (3) c represents the build-up characteristics of pressure at bottom of the die due to the continuously increasing surcharge powder.

For the point feed method, the observed shape of surcharge powder was conical. For this fill method, the surcharge pressure (based on volume of the cone) can be written as (Roudsari, 2007):

$$h^* = \frac{\pi}{3} \frac{\rho_b}{\rho_p} \tan^3 \delta (\gamma_3)^3 \left(1 - e^{-\gamma_4(t-t_f)}\right)^3 \quad (12a)$$

where, δ is the cone half angle.

In the point feed fill method; the deposited powder's base expands until it reaches the walls of the die. During this time period, most of the die is unfilled, i.e., the walls of the shallow die do not directly influence the filling pressures. In this case, retaining the first non-zero term of the Taylor series for the Equation (12a) yields (Roudsari, 2007):

$$h^* = \beta(t-t_f)^c \quad (12b)$$

where, β is a coefficient determined from experimental data.

Equation (12b) is the generalized pressure build-up profile for the point feed fill method. As will be shown later $c \approx 1$ for BPM at slow filling rates. Given the generality of Equation (11), it was used for modeling the three filling methods.

3. Experimental Design

In this study, a battery powder mixture (BPM) was used to fill a shallow circular die of 35 mm in diameter that was 6.5 mm deep (i.e., $h=6.5$ mm). The bulk density and particle density of BPM were 1.65 g/cm^3 and 4.7 g/cm^3 , respectively (Xie, 2006). It is stable under ambient conditions. The granule size range of BPM powder was from less than 80 to 1000 μm with median size (d_{50}) of 600 μm . BPM powder is very friable; some granules easily fragment into finer granules during handling and transportation. Powder characteristics of relevance and importance during deposition and compaction have been reported in the literature (such as, Doelker, 1993; Hjortsberg and Bergquist 2002; Niesz, 1996, and Wu et al., 2003)

The second generation pressure deposition tester

(PDT-II) (**Fig. 3a**) was used to measure the powder pressure distribution characteristics (Xie and Puri, 2007). An innovative rotational rainy filling device (**Fig. 3b**) was designed and fabricated. This versatile device can be used to measure filling characteristics at different rotational speeds (Roudsari, 2007). The point feed (**Fig. 3c**) method with a funnel of 30 mm inlet diameter and 4.2 mm outlet diameter opening was used to fill the circular shallow dies. The pressure sensor strip, P-1500, was placed at the bottom of the die (**Fig. 3d**), which was connected to a data acquisition systems and data analysis software. There are 16 pressure sensors in one pressure sensor strip, the cross-section of each sensor is 2 mm \times 5 mm with center-to-center spacing of 2 mm. The pressure sensor strip was positioned at eight different angles, 22.5 degrees apart, which covered the entire die; i.e., 0° - 180° , 22.5° - 202.5° , 45° - 225° , 67.5° - 247.5° , 90° - 270° , 112.5° - 292.5° , 135° - 315° , and 157.5° - 337.5° . All sixteen sensors were exposed to record the pressure increase profile. The sensitivity of pressure sensor (P-1500) was 0.1% of the full scale range, or 5 Pa (4.8 mg on an area of 2 mm \times 5 mm). The highest pressure that the P-1500 can measure was 551.6 kPa (0.529 kg on an area of 2 mm \times 5 mm). The sensor calibration was repeated every 50 tests (Roudsari, 2007). Throughout this study, the data capture rate of 30 Hz per channel was used. Herein, results of BPM powder only are presented. The impact of particle size distribution and particle shape for a powder finer than BPM on the filling process is presented and discussed at length in Roudsari (2007).

4. Results and Discussion

4.1. Feed shoe filling process

A typical pressure profile obtained by the pressure sensor element located at the center during filling of the cylindrical die with the BPM at feed shoe speed of 20 mm/s is shown in **Fig. 4**. The plot represents the average of six runs to ensure that the experimental values had coefficient of variation generally less than 15% (Mittal et al., 2001; Wu et al., 2003; and Xie and Puri, 2006 and 2007). In order to convert the pressure profile of BPM, each pressure value was divided by the particle density (4.7 g/cc) multiplied by gravity ($\frac{P}{\rho_p \cdot g}$). As mentioned earlier, this can be interpreted as equivalent height (h^*). The equivalent height scale h^* is in dm, dm is decimeter, i.e., 1 dm=0.1 m. Due to the complexity, the entire pressure profile could not be simulated by one value each for coefficients α , b , and c of Equation 11. Therefore, the

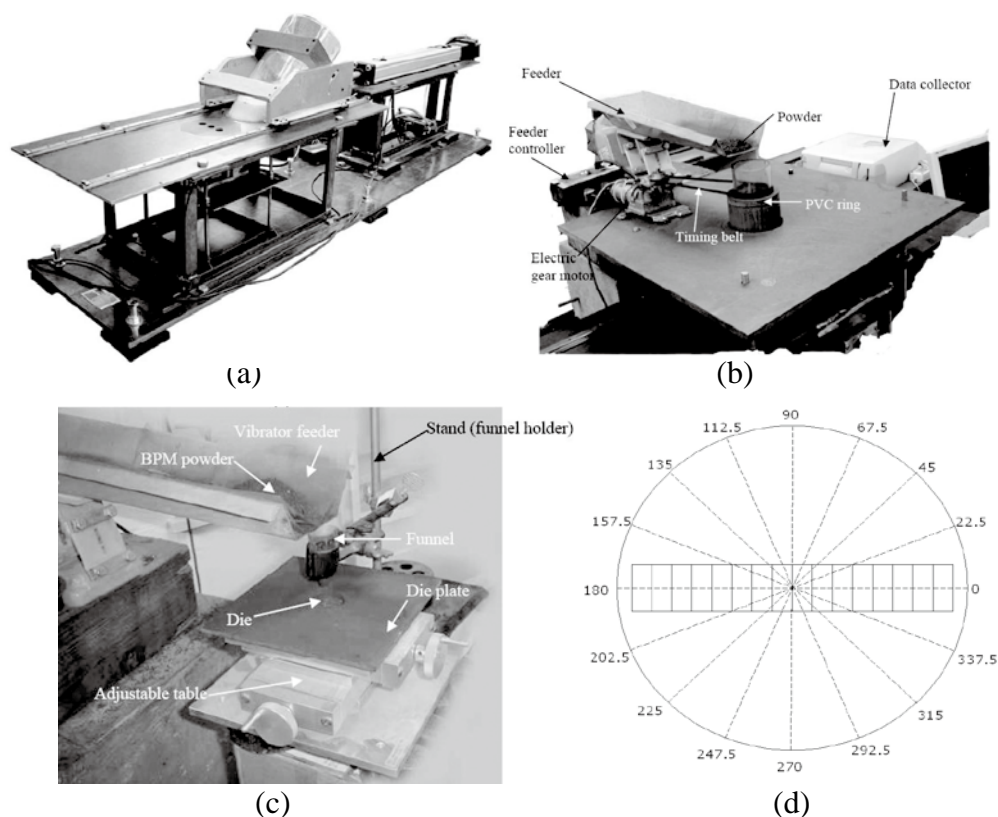


Fig. 3 Photographs of a) Second generation Pressure Deposition Tester, PDT-II, b) Rotational rainy fill, and c) Point feed; and d) Schematic of pressure sensor strip shown in one orientation at bottom of the die (Roudsari, 2007).

entire filling process was divided into various phases and Phase I was divided into two stages. Every phase was modeled using a simple rate equation. The positions of circular feed shoe tube during the filling process with reference to center of the die that were used to calculate the start and end times of various phases are given in Fig. 4 and 5.

4.1.1. Feed shoe filling phases

The feed shoe filling profile shown in Fig. 4 was divided into three distinct phases. Phase I was from time 0 to time T_1 which corresponded to forward stroke while the actual filling process occurred. Phase I was divided further into two stages which corresponded to feed shoe tube movement during the forward stroke. The two stages were, T_{1a} and T_{1b} where the first subscript denotes the phase and second represents the stage. During Phase II for time duration T_2 , the feed shoe started to leave the die. The pressure applied by the powder inside the feed shoe tube started to be released. Phase III for time duration T_3 was post-filling process during which time the powder gradually approached an equilibrium value.

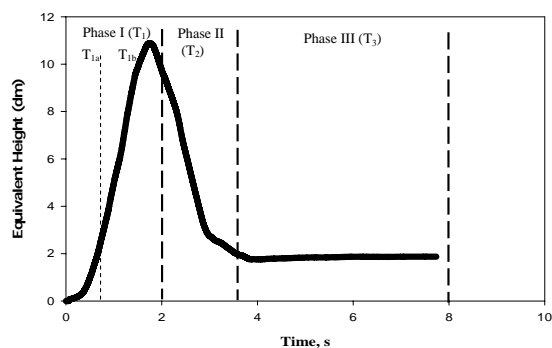


Fig. 4 Average filling pressure profile using feed shoe at 20 mm/s at the center of circular die with BPM powder.

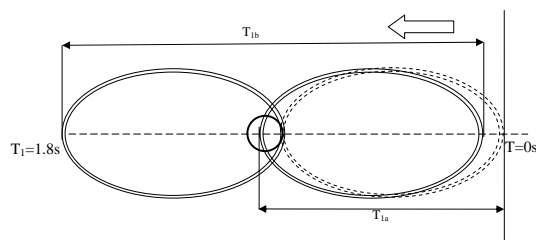


Fig. 5 Filling sequences in Phase I during the forward stroke showing feed shoe travel distance (in mm) and onset of stages described by T and its subscripts.

4.1.1.1 Phase I

In Phase I, actual filling of the die occurred during the forward stroke of feed shoe tube. The relative positions of feed shoe tube at two stages marked the start and end times are shown in **Fig. 5**. These particular positions of feed shoe tube with circular cross-section were used to identify and discriminate filling stages in Phase I. Corresponding to these positions, the specific times for the feed shoe tube to reach these positions are listed below:

T_{1a} : when feed shoe tube nose reached middle of the die, i.e., sensor location (0.49 s).

T_{1b} : when the back wall of feed shoe tube reached the leeward direction of the die (1.31 s).

Stage I (T_{1a}): The majority of filling was accomplished in this stage. The filling occurs rapidly showing an exponential deposition profile.

Stage II (T_{1b}): In this stage, the die was overfilled and surcharge powder covered the top of the powder mass.

At time 0, the feed shoe tube front wall reached the leeward direction of the die (**Fig. 5**), while only a small fraction of the powder in the front of feed shoe was available to enter the die. The filling rate is very low at this time. With the feed shoe movement and increase of time, more powder in the front wall of feed shoe tube filled the die. With the increase in time, the die continued to fill and the distance between the top surface of the powder in the die and the bottom of the powder in the feed shoe gradually decreased; at this time, the die was filled, i.e., could not accommodate more powder.

Two stages of the Phase I could be mathematically represented by the following rate Equation (13):

$$h^* = 32.63(1 - e^{-5.69t})^3 \quad (13)$$

The R-Square value of this regression was 0.97. Phase I is responsible for most of the powder filling during the deposition process, i.e., about 90% (Xie, 2006). During Phase I, the most pressure measured by the pressure sensor strip was exerted directly from the powder deposited into the circular die. Minimal-to-no pressure was exerted or influenced by the feed shoe wall.

4.1.1.2 Phase II

Based on experimental results, the rate Equation (11) of this phase can be simplified to:

$$\frac{dh^*}{dt} = m_2 \quad (14)$$

where m_2 = slope of the straight line. The slope m_2 = -6.79. The R-square value of this regression was 0.99.

4.1.1.3 Phase III

In this phase, the pressure reached an equilibrium state, and this state could best represent the pressure value of the end of filling process. The pressure profile decreased slowly in the beginning of this phase, followed by a close-to-horizontal profile. The reason for slow decline might be that some of the pressures at the end of forward stroke was gradually released. The rate of equivalent height Equation (11) in Phase III is simply $dh^*/dt = 0$

4.1.1.4 Overall equation for all the three phases

To effectively account for Phases II and III, the overall rate Equation (11) for shallow die can be represented alternately by Equation (15).

$$\frac{dh^*}{dt} = \alpha h^* F(t) + \beta \quad (15)$$

where α and β are coefficient, and $F(t)$ is a function of time. The specific form of function $F(t)$ and the corresponding applicable range of times are shown in **Table 1**. The Phases II and III did not have the function $F(t)$ (their α value was 0), since the changing rates of their pressure values were constant.

Root mean square error [RMSE, Equation (16)] and average relative difference [ARD, Equation (17)] values were used to determine the quality of the model predictions.

$$RMSE = \sqrt{\frac{\sum (h_{mod\ el}^* - h_{measured}^*)^2}{n - 1}} \quad (16)$$

$$ARD = 100 \frac{\sum \frac{|h_{mod\ el}^* - h_{measured}^*|}{h_{measured}^*}}{n} \quad (17)$$

where $h_{mod\ el}^*$ = modeled equivalent height,
 $h_{measured}^*$ = measured equivalent height,
 n = number of total data points.

RMSE and ARD for data were 0.16 and 7%, respectively.

Table 1 Model parameters for all three phases at the center ($r=0$ mm) of the cylindrical die filled with the BPM powder at 20 mm/s feed shoe speeds

Phase #	$h^*F(t)$	α	β	Time (second)
I	$h^*/(e^{5.69t} - 1)$	32.63	0	$0 \leq t \leq 1.8$
II	0	0	- 6.79	$1.8 \leq t \leq 3.4$
III	0	0	0	$3.4 \leq t \leq 7.8$

4.1.2 Model validation

Tables 2 and 3 show the coefficients for $r=4$ mm obtained from data points, and $r=2$ mm which was obtained from interpolation of $r=0$ mm and $r=4$ mm, respectively. The RMSE and ARD were 0.12 dm and 5%, respectively, which showed that the calculated values are in good agreement with measured values. The pressure profiles for measured and modeled data points at $r=2$ mm are shown in Fig. 6

Table 2 Model parameters for all three phases of at $r=4$ mm of the cylindrical die filled with the BPM powder at 20 mm/s feed shoe speeds

Phase #	$h^*F(t)$	α	β	Time (second)
I	$h^*/(e^{5.43t} - 1)$	29.87	0	$0 \leq t \leq 1.8$
II	0	0	- 6.13	$1.8 \leq t \leq 3.4$
III	0	0	0	$3.4 \leq t \leq 7.8$

Table 3 Model parameters for all three phases at $r=2$ mm, which were obtained from interpolation of $r=0$ mm and $r=4$ mm of the cylindrical die filled with the BPM powder at 20 mm/s feed shoe speed

Phase #	$h^*F(t)$	α	β	Time (second)
I	$h^*/(e^{5.56t} - 1)$	31.25	0	$0 \leq t \leq 1.8$
II	0	0	- 6.46	$1.8 \leq t \leq 3.4$
III	0	0	0	$3.4 \leq t \leq 7.8$

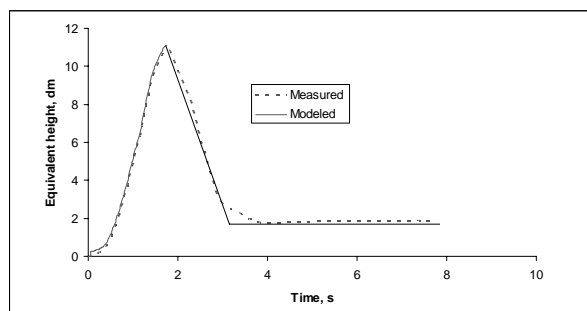


Fig. 6 Comparison of measured and modeled equivalent height for cylindrical die using feed shoe filling method at 20 mm/s feed shoe speed.

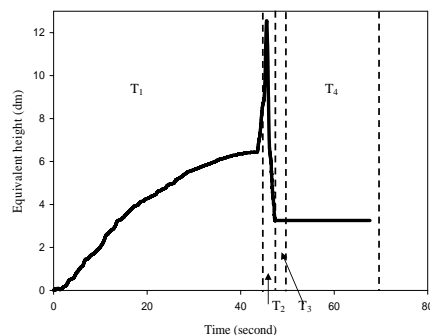


Fig. 7 Average filling pressure profile using rainy fill method at the center of circular die with BPM powder at 26 g/min filling rate.

4.2 Rainy fill

Fig. 7 shows a typical pressure profile for a cylindrical shallow die filled with BPM at 26 g/min filling rate. The plot represents the average of six runs with pressure sensor strip located at 0° - 180° orientation. The entire filling profile was divided into four phases as follows:

Phase I (T_1)= filling process (the rotational rainy filled the die completely at this phase (43 s);

Phase II (T_2)= leveling process (removing surcharge powder manually) (46 s);

Phase III (T_3)= end of leveling process (49 s);

Phase IV (T_4)= equilibrium period (end of filling process) (68 s).

4.2.1 Phase I

Phase I was the filling process during which the die was overfilled. In rotational rainy fill, the average time for this process was 43 seconds. The powder filling rate (the slope of mass ratio curve) increased rapidly with time and gradually decreased after 20 seconds. The die was over-filled after 20 seconds and surcharge powder started to accumulate after this time as discussed previously. Phase I had a sigmoidal shape curve which was represented by Equation (11); the specific form was $h^* = 19.32(1 - e^{-0.44t})^3$ with R-square of 0.94.

4.2.2 Phase II

During this phase, the surcharge powder was removed from the die. The leveling process generated high pressure inside the die due to increase in the shear stress among particles. The leveling process was accomplished manually by using a fiberglass tube (Roudsari, 2007). Based on experimental results, the rate Equation (11) reduces to:

$$\frac{dh^*}{dt} = m_2 \quad (18)$$

where m_2 = slope of the straight line ($m_2=0.16$). The R-square value of this regression was 0.94.

4.2.3 Phase III

During this phase, the rate Equation (11) takes on the following form:

$$\frac{dh^*}{dt} = m_3 \quad (19)$$

where m_3 = slope of the straight line ($m_3= -5.08$). The R-square value of this regression was 0.89. The main reason for Phase III not being a straight line might be due to the pressure release inside the die and

rearrangement that occurred after completion of the leveling process.

4.2.4 Phase IV

Phase IV was the last stage of rainy filling process, where the pressure became stable. The rate Equation (11) for Phase IV reduces to $dh^*/dt = 0$.

For the entire deposition process, the root mean square error (RMSE) and average relative difference (ARD) for rainy fill were 0.44 dm and 16%, respectively. The differences between measured data and model calculated values were relatively higher vs. feed shoe filling. The coefficient and specific form of the function $F(t)$ [Equation (15)], and the range of times are shown in **Table 4**.

4.2.5 Model validation

Tables 5 and **6** show the coefficients for $r=4$ mm obtained from data and $r=2$ mm obtained from interpolation of $r=0$ mm and $r=4$ mm, respectively. The RMSE and ARD for $r=2$ mm from interpolation values were 0.18 dm and 15%, respectively (**Fig. 8**), which are comparable with magnitudes to the $r=0$ and $r=4$ data sets; therefore, the model validation is acceptable.

Table 4 Model parameters for all four phases at the center ($r=0$ mm) of the cylindrical die filled with the BPM powder at 26 g/min

Phase #	$h^*F(t)$	α	β	Time (second)
I	$h^*/(e^{0.44t} - 1)$	19.32	0	$0 \leq t \leq 43$
II	0	0	0.16	$43 \leq t \leq 46$
III	0	0	- 5.08	$46 \leq t \leq 49$
IV	0	0	0	$49 \leq t \leq 68$

Table 5 Model parameters for all four phases at $r=4$ mm of the cylindrical die filled with the BPM powder at 26 g/min

Phase #	$h^*F(t)$	α	β	Time (second)
I	$h^*/(e^{0.55t} - 1)$	17.18	0	$0 \leq t \leq 43$
II	0	0	0.14	$43 \leq t \leq 46$
III	0	0	- 5.44	$46 \leq t \leq 49$
IV	0	0	0	$49 \leq t \leq 68$

Table 6 Model parameters for all four phases for $r=2$ mm, which were obtained from interpolation of $r=0$ mm and $r=4$ mm of the cylindrical die filled with the BPM powder at 26 g/min

Phase #	$h^*F(t)$	α	β	Time (second)
I	$h^*/(e^{0.49t} - 1)$	18.25	0	$0 \leq t \leq 43$
II	0	0	0.15	$43 \leq t \leq 46$
III	0	0	- 5.26	$46 \leq t \leq 49$
IV	0	0	0	$49 \leq t \leq 68$

4.3 Point Feed

Fig. 9 shows the entire filling profile for the point feed filling method. The complete filling process can be divided into four phases. Corresponding to each phase, a specific time with each phase of the filling process is listed below:

Phase I (T_1)= filling process (the point feed filled the die completely at this phase) (102 s);

Phase II (T_2)= leveling process (removing surcharge powder manually) (105 s);

Phase III (T_3)= end of leveling process (108 s);

Phase IV (T_4)= end of filling process (120 s).

4.3.1 Phase I

Phase I had almost constant deposition rate as explained previously. The powder filling increased with time. The die was filled with constant deposition rate at 26 g/min. For this phase, based on experimental results, the rate Equation (11) takes on the following form:

$$\frac{dh^*}{dt} = m_1 \quad (20)$$

where m_1 =slope of the straight line ($m_1=0.031$) and R-square was 0.99.

The filling profile for point feed method is consid-

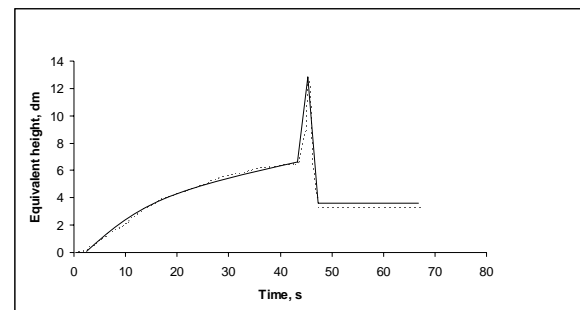


Fig. 8 Comparison of measured and modeled equivalent height for cylindrical die using rotational rainy fill at 26 g/min.

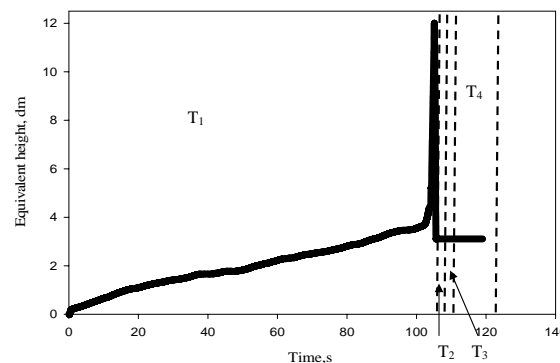


Fig. 9 Average filling pressure profile using point feed method at the center of circular die with BPM powder at 26 g/min filling rate.

erably different from feed shoe and rainy fill. The powder deposited in the die with the point feed method is not directly influenced by the die walls; hence, a nearly linear profile. Furthermore, the particles' accumulation profile continuously failed along angle of internal friction during the filling process which generated a constant head increase rate.

4.3.2 Phase II

During this phase, the leveling process occurred, i.e., the surcharge powder was removed manually from the die. The pressure rate rapidly increased due to increase in shear stress during the leveling process. The rate Equation 11 for this phase simplifies to: $\frac{dh^*}{dt} = m_2$, where $m_2=8.25$ (slope of the line) and R-square was 0.99.

4.3.3 Phase III

Phase III was end of the leveling process. The pressure quickly decreased after the surcharge powder was completely removed from the die. Due to high shear stress during the manual leveling process, the pressure was slowly released that resulted in a non-linear declining pressure profile; this was approximated by a straight line. Therefore, the rate Equation (11) for Phase III was:

$$\frac{dh^*}{dt} = m_3 \quad (21)$$

where $m_3= - 19.52$ (slope of the line) and R-square was 0.94.

4.3.4 Phase IV

Phase IV was modeled as a horizontal line. The modeled equivalent height was 3.11 dm. This was obtained by taking the average of all the data points within this phase. The rate Equation (11) for this phase was $dh^*/dt=0$.

For the entire deposition process, the root mean square error (RMSE) and average relative difference (ARD) for point feed filling method using a battery powder mixture at 26 g/min were 0.32 dm and 11%, respectively. The coefficient and specific form of the function $F(t)$ [Equation (15)] and the range of time are shown in **Table 7**.

4.3.5 Model validation

The model coefficients for $r=4$ mm obtained from data and $r=2$ mm which was obtained from interpolation of $r=0$ mm and $r=4$ mm are shown in **Tables 8** and **9**, respectively. The RMSE and ARD for $r=2$ mm for model calculated values were 0.14 dm and 8%, re-

spectively, which represents good validation for this study (**Fig. 10**).

The entire pressure increase profile for cylindrical die filled with battery powder mixture can be divided into different stages. All the stages could be simulated by a rate equation, based on the data collected and the physics of the filling process. The overall rate equation $dh^*/dt = \alpha hF(t) + \beta$ can serve as a quantitative tool for further investigation of different powders and die shapes.

Although the scope of this study was limited to one powder and one die shape, the parameters of simulation are general in nature and applicable to various

Table 7 Model parameters for all four phases at the center ($r=0$ mm) of the cylindrical die filled using point feed with the BPM powder at 26 g/min

Phase #	m	Time (second)
I	0.0311	$0 \leq t \leq 102$
II	8.25	$102 \leq t \leq 105$
III	-19.52	$105 \leq t \leq 108$
IV	0	$108 \leq t \leq 120$

Table 8 Model parameters for all four phases at $r=4$ mm of the cylindrical die filled using point feed with the BPM powder at 26 g/min

Phase #	m	Time (second)
I	0.055	$0 \leq t \leq 102$
II	8.87	$102 \leq t \leq 105$
III	-18.65	$105 \leq t \leq 108$
IV	0	$108 \leq t \leq 120$

Table 9 Model parameters for all four phases for $r=2$ mm, which were obtained from interpolation of $r=0$ mm and $r=4$ mm of the cylindrical die filled using point feed with the BPM powder at 26 g/min

Phase #	m	Time (second)
I	0.043	$0 \leq t \leq 102$
II	8.56	$102 \leq t \leq 105$
III	-19.08	$105 \leq t \leq 108$
IV	0	$108 \leq t \leq 120$

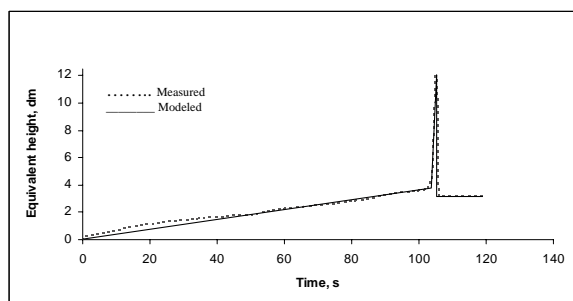


Fig. 10 Comparison of measured and modeled equivalent height for cylindrical die using point feed filling method 26 g/min.

powders and die shapes. In addition, the mathematical model permits consideration of simultaneous filling of multiple shallow dies. The mathematical models, which defines some or all of the deposition physics-based parameters, can be a very time efficient, cost effective, and reliable tool for identifying and addressing complex flow and filling issues.

Conclusions

Experimental data showed that the deposition profiles for feed shoe and rainy fill were sigmoidal in shape vs. a linear profile for point feed. For the complex filling profiles, a physics based model was used to explain the sigmoidal pressure build up profile for the feed shoe and rainy filling methods and the linear profile for the point feed. The following specific conclusions were arrived at from this study:

- 1) The overall rate equation for all three filling methods was: $dh^*/dt = \alpha hF(t) + \beta$.
- 2) The root mean square error (RMSE) for feed shoe, rainy, and point feed were 0.16, 0.44, and 0.32, respectively; whereas, the average relative differences (ARD) were 7%, 16%, and 11%, respectively.
- 3) For model validation, the RMSE values for feed shoe, rainy, and point feed were 0.15, 0.18, and 0.14, respectively; whereas, the ARD values were 5%, 15%, and 8%, respectively.

The validated powder deposition models can be used to optimize the slow filling of shallow dies so as to minimize defects associated with the filling process during compaction. Following the successful modeling of die filling at slow speeds, development and validation of models at higher deposition rates are ongoing. Incorporation of the particle characteristics through a multi-scale formulation of the deposition model would represent a leap-forward in the field of high pressure compaction.

Nomenclature

A	Cross-section
b	Parameter
c	Coefficient
C	Die circumference
$F(\tau)$	Stage-specific deposition rate function
$F(t)$	Deposition rate function
g	Gravitational constants
h	Die height
h^*	Equivalent height
H	Total height of powder in die

H_o	Surcharge height in die
k	Ratio of lateral to vertical pressure
K	Coefficient
m	Rate of outflow
\dot{m}_1	Mass
\dot{m}_2	Rate of inflow
P_w	Vertical friction on the wall
P_v	Vertical pressure in the mass
P_h	Lateral pressure
P_p	Prorated pressure
P	Pressure
\dot{Q}	Flow rate
r	Radius of sphere
R	hydraulic radius
t_f	Time of filling
t	Time
v	Volume
y	Actual filled height of die

Greek Letters

α	Coefficient
β	Coefficient
δ	Cone half-angle
φ	Angle of internal friction
ρ_p	Particle density
ρ_b	Bulk density
μ	Coefficient of friction
π	Normalized time
θ	Chord radius/r
$\gamma_1, \gamma_2, \gamma_3, \gamma_4$	Coefficients

References

- 1) Doelker, E. (1993): Assessment of powder compaction. Powder Technology and Pharmaceutical Processes (Handbook of Powder Technology, Vol. 9), edited by Dominique Chulia, pp. 403-471. Elsevier, New York.
- 2) Hjortsberg, E. and B. Bergquist (2002): Filling induced density variations in metal powder. Powder Metallurgy 45(2), pp.146-153.
- 3) Kessler, P. David, and Robert A. Greenkorn (1999): *Momentum, heat and mass transfer fundamentals*. Marcel Dekker, Inc.
- 4) Manbeck B. Harvey and V. M. Puri (1995): *Structure Loads in Grain Storage*. pp 465- 525. Chapter in Stored Grain Ecosystems, edited by Digvir S. Jayas, Noel D. White, and William E. Muir. Marcel Dekker, Inc.
- 5) Mittal, B., V. M. Puri and W. Shaffer (2001): Analysis of feed shoe powder deposition using real-time cumulative mass deposition tester. KONA Powder and Particle Journal, No.19, pp.144-155.
- 6) Niesz, D.E. (1996): A review of ceramic powder compaction. KONA Powder and Particle Journal, No.14, pp.44-51.

- 7) Roudsari, S. Saed (2007): Pressure Distribution Evaluation of Different Filling Methods for Deposition of Powders in Dies: Measurement and Modeling. Ph.D. Dissertation. The Pennsylvania State University, University Park, PA.
- 8) Seber, G. E. F. and C. J. Wild (1989): Nonlinear Regression. John Wiley and Sons. N. Y.
- 9) Wu, C. Y., A. C. F. Cocks and O. Gillia (2003): Die filling and powder transfer. Powder Metallurgy 39(4), pp.51-64.
- 10) Xie, X. and V. M. Puri (2006): Uniformity of powder deposition in dies using feed shoe - A review. Particulate Science and Technology, 24(4), pp.411-426.
- 11) Xie, X. (2006): Uniformity of Simultaneous Powder Deposition in Multiple Dies; Measurement and Modeling. Ph.D. Dissertation. The Pennsylvania State University, University Park, PA.
- 12) Xie, X. and V. M. Puri (2007): Simultaneous deposition of powder in three parallel cylindrical dies. Particulate Science and Technology, 25(3), pp.247-260.
- 13) Xie, X. and V. M. Puri (2008): Modeling of Simultaneous Deposition of Powder in Three Parallel-Oriented Cylindrical Dies. Particulate Science and Technology, 26(6), pp. 563-573.

Author's short biography



Saed Sayyar Roudsari

Saed Sayyar Roudsari was a graduate student in the Department of Agricultural and Biological Engineering at Pennsylvania State University from August 2004 to September 2007. He received his BS in Soil and Water Engineering from Iran and MS in Civil Engineering from North Carolina A&T State University. He is currently working as a professional engineer in County of Los Angeles Department of Public Works. He is an active member of ASABE, ASCE, and ISPE. This paper is a part of his Ph.D. work at Pennsylvania State University.



Virendra M. Puri

Virendra M. Puri, University Distinguished Professor, has been involved in research in the field of powder science, engineering, and technology for nearly three decades. He has served as the Acting Director of the NSF/IUCRC (Industry University Cooperative Research Center) – the Particulate Materials Center. Professor Puri has co-authored over 500 publications and co-inventor and holder of patents for four test devices in the area of powder flow, deposition and compaction. In addition, he has a Copyright for multi-purpose computational software dealing with powder processing applications. Professor Puri has been invited to serve on Editorial Boards, International Advisory Boards, and Chairpersons of several bulk solids-related publications and professional activities. He is Editor-in-Chief of *Particulate Science and Technology, An International Journal*. Professor Puri regularly offers seminars, courses, and workshops in powder mechanics to industry and academia. He has received several teaching and research awards.

Effect of Additives on the Dispersion Properties of Aqueous Based C/LiFePO₄ paste and its Impact on Lithium Ion Battery High Power Properties[†]

Jin-Hyon Lee, Hyun-Ho Kim, Sung Bok Wee, and Ungyu Paik*
 Division of Materials Science Engineering, Hanyang University¹

Abstract

Aqueous-based C/LiFePO₄ positive electrodes with high-rate capabilities are described with an intended application in lithium ion batteries. Pastes consisting of C/LiFePO₄ particles, sodium carboxymethyl cellulose (CMC), water-soluble elastomeric binder (WSB) and poly (acrylic acid) (PAA) were prepared in an aqueous medium and tape-cast onto an aluminum foil. It was found that the incorporation of PAA significantly decreased the apparent viscosity of the C/LiFePO₄ paste as well as shifted particle size distribution to lower value, which resulted in an improvement of the C/LiFePO₄ dispersion properties. A correlation was made between the dispersion properties and the electrochemical properties. The electrochemical properties indicated that the electrode with PAA exhibited a discharge specific capacity above 70 mAhg⁻¹ at 20C, which was about seven times higher than the discharge specific capacity without PAA at 20C which showed a discharge specific capacity of only 10 mAhg⁻¹. This was attributed to the formation of a resistance-imparting agglomeration, which is consistent with the dispersion properties of C/LiFePO₄ particles.

Keywords: lithium ion battery, olivine, poly (acrylic acid), dispersion, electrochemical properties

1. Introduction

Lithium iron phosphate (LiFePO₄) has received great attention as a promising alternative cathode material for rechargeable lithium ion batteries due to its high energy density, low cost, safety, and chemical stability.¹⁻³⁾ In particular, since the recall of several million notebook computer batteries due to the potential risk of explosion of lithium ion batteries, the safety issues of lithium ion batteries have become the center of public attention. This has resulted in an acceleration of the commercial use of LiFePO₄ due to its intrinsic safety and chemical stability as cathode materials, compared to the layered rock salt oxides LiCoO₂ and LiNiO₂ and the spinel LiMn₂O₄.

Generally, positive electrode films for commercial lithium ion batteries are prepared by a tape casting process⁴⁾ using a non-aqueous slurry whose suspending media consists of organic solvents. However,

since organic solvents are typically toxic and flammable^{5,6)}, various attempts have been made to switch from non-aqueous- to aqueous-based systems.⁷⁻¹²⁾ For example, Lee *et al.*⁸⁾, and Porcher *et al.*¹⁰⁾ investigated the stability of LiFePO₄ in an aqueous medium from the standpoint of dispersion and electrochemistry, respectively. Guerfi *et al.*⁹⁾ investigated the effect of a new water-soluble elastomer as a new binder for the LiFePO₄ cathode materials in a lithium ion battery. So far, few investigations have examined the correlation between dispersion properties and electrochemical properties in an aqueous medium. It is reported that the formation of an agglomeration caused by poor dispersion leads to degraded power properties at high C, because the agglomeration acts as a resistance.¹³⁾ According to Lee *et al.*⁸⁾, the addition of poly(acrylic acid) (PAA) significantly decreases the apparent viscosity of the LiFePO₄ paste, which results from the improved dispersion properties of LiFePO₄. However, direct evidence showing a correlation between the dispersion properties and rate properties was not provided.

In the present investigation, we investigated the effect of PAA on the dispersion properties of C/LiFe-

[†] Accepted: September 7th, 2009

¹ Seoul 133-179 Republic of Korea

* Corresponding author

upaik@hanyang.ac.kr (U. Paik)

TEL +82-2-2220-0502, FAX +82-2-2281-0502

PO₄ and its resulting high power properties of C/LiFePO₄ positive electrodes for applications in lithium ion batteries. A stable, aqueous-based C/LiFePO₄ slurry was prepared with a combination of two organic additives, namely carboxymethyl cellulose (CMC) and water-soluble elastomer binder (WSB), with and without PAA. CMC is used primarily as a thickening agent to prevent the C/LiFePO₄ particles from settling and segregating during processing. WSB and PAA were introduced as a binder and a dispersant for C/LiFePO₄, respectively. The effect of incorporating PAA into the suspension was characterized by measuring the electrokinetic response, particle size distribution and shear rheological behavior for the formulated suspension. Finally, the rate behavior of the coin cell fabricated by our formulated suspension was evaluated as a function of C rate.

2. Experimental

Carbon-coated LiFePO₄ (C/LiFePO₄) was obtained from a commercial source (Samsung SDI Co. Ltd., Korea) and had an average particle diameter of 300 – 500 nm. Dynamic light scattering measurements showed that the d₅₀ was 382 nm and the polydispersity index was 0.243. The carbon content, as stated by the manufacturer, was about 2 wt%. The BET surface was measured using N₂ and found to be 13 m²g⁻¹. Carbon black was used as a conducting agent. CMC (Dai-icel Co. Ltd., Japan) with an average molecular mass of 330,000 and a degree of substitution of DS=1.28 was used as a thickening agent. PAA (50% solution in water) with an average Mr of 5,000 was obtained from Polysciences, Inc. (Warrington, PA, USA). A water-soluble elastomer binder (Zeon Corp., Japan) was used as the elastomeric binder. Unless otherwise stated, concentrations of organic additives are expressed on a mass basis relative to the C/LiFePO₄ phase.

All suspensions were prepared with filtered de-ionized water (18MΩ resistance) and ultrasonicated for three min using a high-intensity submersible horn (5000A, Shimadzu Corp., Kyoto, Japan). The final pH values for all of the suspensions were between 8.9 and 9.3 and were not independently controlled.

For electrokinetic measurements, suspensions containing a C/LiFePO₄ mass fraction of 5% were prepared in deionized water, with and without PAA, and subsequently treated ultrasonically for 3 min. The treated suspensions were then allowed to equilibrate at room temperature for 12 h with magnetic stirring, after which they were ultrasonicated for an additional

3 min. The required amounts of CMC and WSB were then added, and the suspensions were equilibrated for an additional 12 h. Electrokinetic curves were determined using an electroacoustic analyzer (Model ESA-9800, Matec Applied Sciences, Hopkinton, MA, USA) operating nominally at 1 MHz.

Particle size distribution was measured at 25 ± 1°C using a Nano ZS (Malvern Instrument, Malvern, UK). The mass fractions of C/LiFePO₄ and carbon black were 40% and 0.83%, respectively. Sample preparation followed the same procedure previously described for ESA measurements. The required amount of carbon black was incorporated into the suspension after addition of CMC and WSB. Due to the high viscosity, the C/LiFePO₄ paste containing C/LiFePO₄ and carbon black was diluted by 5 wt%.

The rheological behavior of the C/LiFePO₄ paste containing C/LiFePO₄ and carbon black was determined at 25 ± 1°C using a controlled-stress rheometer (MCR501, Paar Physica, Stuttgart, Germany) with a concentric cylinder geometry (DG 27). The mass fractions of C/LiFePO₄ and carbon black were 40% and 0.83%, respectively. Sample preparation followed the same procedure previously described for ESA measurements. The required amount of carbon black was incorporated into the suspension after addition of CMC and WSB. The apparent viscosities of the C/LiFePO₄ suspensions were measured as a function of the ascending shear rate.

The discharge specific capacity of the fabricated coin cell was evaluated as a function of the number of cycles. The electrolyte was 1.3M LiPF₆ in a 3:7 volume mixture of ethylene carbonate (EC) and diethyl carbonate (DEC).

3. Results and Discussion

Fig. 1 shows the pH-dependent electrokinetic behavior of C/LiFePO₄ particulates as a function of used organic additives, CMC, WSB and PAA. The electrokinetic curves show that C/LiFePO₄ particles containing CMC and WSB with and without PAA exhibited a negative surface potential across the measured pH range. This resulted from the presence of a carboxyl functional group in the adsorbed layer of the CMC. In our previous investigation, we reported that the native carbon-coated C/LiFePO₄ particles showed a net negative charge across the normal pH range which implied that the bare surface of the C/LiFePO₄ particle rather than the carbon-coated area of the C/LiFePO₄ was mainly responsible for this negative surface potential.⁸⁾ CMC and PAA ion-

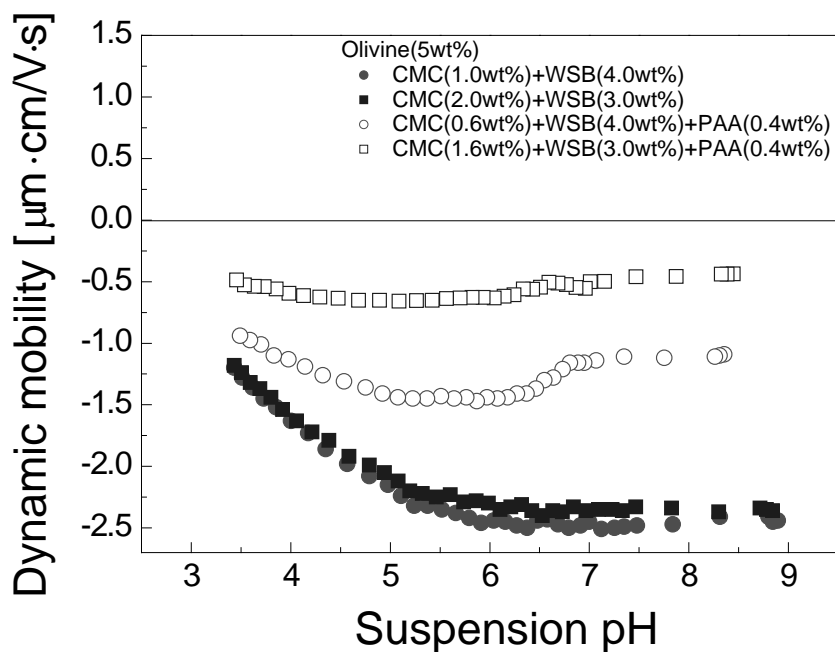


Fig. 1 Electrokinetic behavior of C/LiFePO₄ suspensions prepared at a solid mass fraction of 5% and containing CMC and WSB, with and without PAA.

ize with increasing pH to form a negatively charged macromolecule due to dissociation of carboxylic acid groups. Therefore, the adsorption of an organic additive on C/LiFePO₄ is mainly driven through hydrophobic interactions because of mutually repulsive electrostatic forces between the native C/LiFePO₄ and organic additives. However, in the acidic region, the adsorption of organic additives on C/LiFePO₄ can be driven by either hydrogen bonding or hydrophobic interaction due to the low degree of dissociation of organic additives. Furthermore, partial substitution of CMC with PAA resulted in a significantly decreased dynamic mobility. We investigated the effect of PAA on the development of surface potential for graphite¹⁴⁾ and C/LiFePO₄⁸⁾ and reported that the addition of PAA does not contribute to further development of electrokinetic potential (surface charge) of particulates. Therefore, it is possible to infer that the reduced amount of CMC is responsible for the reduced dynamic mobility of nanosized LiFePO₄.

Particle size distributions of 5wt%-diluted C/LiFePO₄ paste containing CMC and WSB with and without PAA were measured in order to evaluate the agglomeration state of C/LiFePO₄, and the results are shown in Fig. 2. It is found that the addition of PAA shifted particle size distribution to lower value, which is attributed to the improvement of dispersion properties of C/LiFePO₄ paste. These improved dispersion properties of C/LiFePO₄ originate from the

enhanced particle-particle interaction. It has been reported that PAA has a stronger adsorption affinity with hydrophobic surfaces than does CMC, and under basic conditions, PAA has a more favorable conformation for dispersion of particles due to electrostatic repulsive forces.¹⁴⁾

Rheological behaviors of C/LiFePO₄ paste containing CMC and WSB with and without PAA were characterized, and the results are shown in Fig. 3. All pastes show shear thinning behaviors, showing linear dependence of the viscosity on the shear rate. Shear thinning of the concentrated suspensions is known to appear because of structure formation (i.e., aggregation) and structure breakdown (because of the applied shear), with a concurrent increase in overall viscosity.¹⁵⁾ Furthermore, it was observed that the apparent viscosity of the paste decreased with an increase in the concentration of CMC. This was inconsistent with the previous results^{7, 16)} because CMC plays a role as a thickening agent, so the increase of CMC concentration results in an increase of the apparent viscosity of the paste. The decreased apparent viscosity of the paste may be attributed to the improvement of the dispersion properties of the C/LiFePO₄ or the effect of WSB. This issue will be addressed in future investigations. It was also noticeable that the addition of PAA significantly decreased the viscosity of the C/LiFePO₄ paste, which resulted from the improvement of dispersion properties of

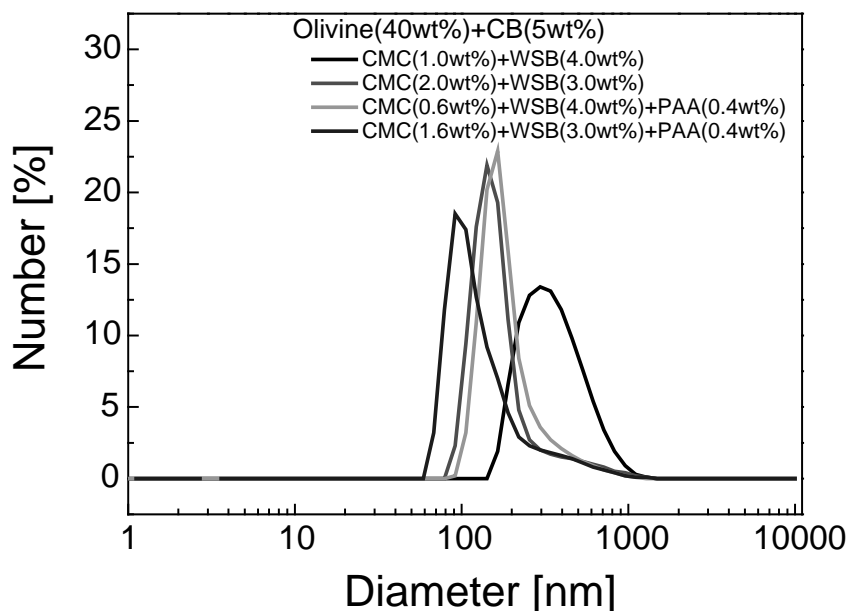


Fig. 2 Particle size distribution of 5wt%-diluted C/LiFePO₄ containing CMC and WSB with and without PAA.

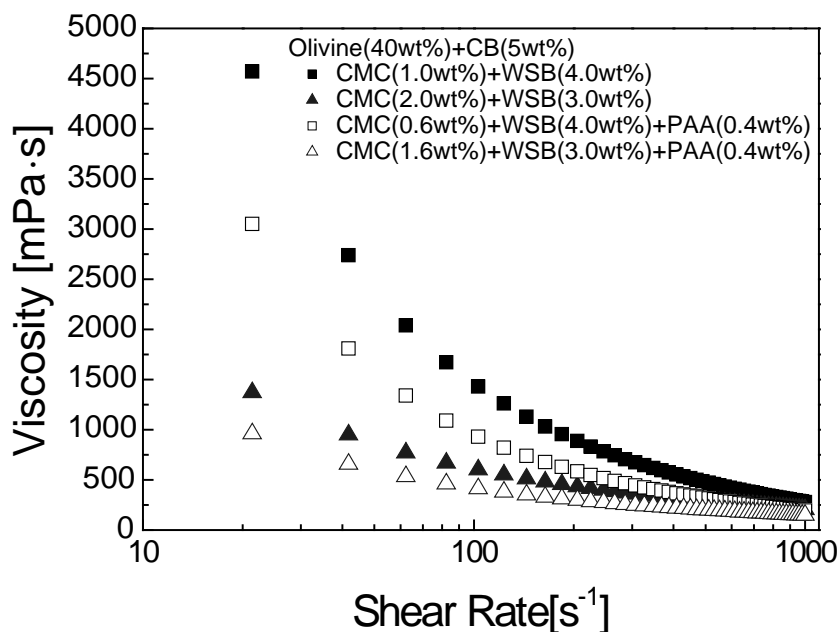


Fig. 3 Apparent viscosity vs. ascending shear rate for C/LiFePO₄ paste at a solid mass fraction of 40%.

C/LiFePO₄. This is well-consistent with the results for particle size distribution (Fig. 2) Therefore, it is clear that the addition of PAA contributes to the improvement of dispersion properties of C/LiFePO₄ through a steric stabilization.

The rate behaviors of the prepared C/LiFePO₄ positive electrodes were evaluated and are shown in Fig. 4. It was found that the specific discharge capacity of the C/LiFePO₄ electrode containing PAA was not

much different from that without PAA at 0.1C, showing about 160 mAh/g. However, at 20C, the electrode with PAA showed a specific discharge capacity that was about seven times higher than that without PAA. This is because the agglomeration of the solid phase resulted in an increase in the resistance of the agglomerated material, which decreased the conductivity of the active materials. This was consistent with the rheological behavior of the C/LiFePO₄ pastes.

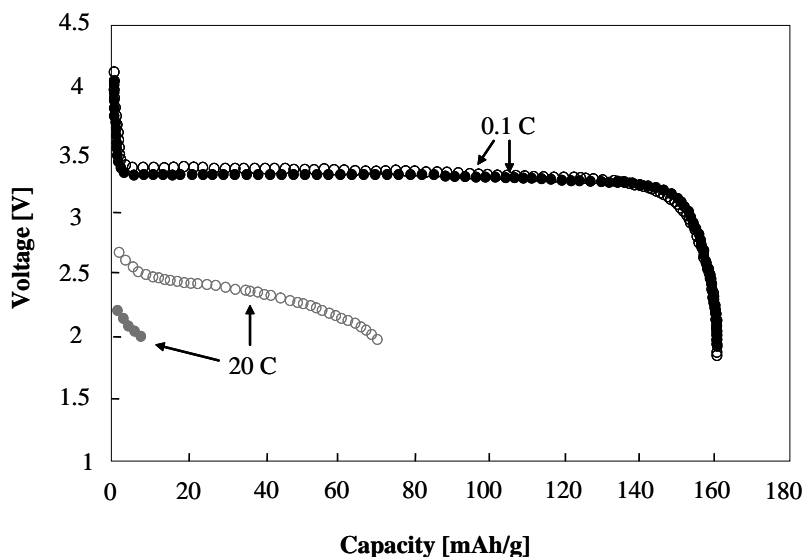


Fig. 4 Rate behaviors of prepared C/LiFePO₄ positive electrodes. Open symbol: electrode with PAA (C/LiFePO₄ : carbon black : CMC : WSB : PAA = 90 : 5 : 0.6 : 4 : 0.4), closed symbol: electrode without PAA (C/LiFePO₄ : carbon black : CMC : WSB = 90 : 5 : 1 : 4)

4. Conclusion

The dispersion properties of aqueous-based C/LiFePO₄ particulates and the resulting electrochemical behaviors were investigated. It was found that the incorporation of PAA resulted in a significant decrease in the viscosity of the C/LiFePO₄ paste as well as shift of particle size distribution to lower value. This indicated that the dispersion properties of C/LiFePO₄ particles were improved through steric interparticle forces. From the electrochemical performance, the electrode with PAA exhibited a specific discharge capacity about seven times higher than that without PAA at a high C-rate and 20C.

Acknowledgement

This work is the outcome of a Manpower Development Program for Energy & Resources supported by the Ministry of Knowledge and Economy (MIKE).

References

- 1) Padhi, A. K., Nanjundaswamy, K. S. and Goodenough, J. B. (1997): Phospho-olivine as Positive Electrode Materials as Rechargeable Lithium Batteries, *J. Electrochem. Soc.*, Vol. 144, pp.1188-1194.
- 2) Chen, Z. and Dahn, J. R. (2002): Reducing Carbon in LiFePO₄/C Composite Electrodes to Maximize Specific Energy, Volumetric Energy and Tap Density, *J. Electrochem. Soc.*, Vol. 149, pp.A1184-A1189.
- 3) Jiang, J. and Dahn, J.R. (2004): ARC studies of the thermal stability of three different cathode materials:

- LiCoO₂; Li[Ni_{0.1}Co_{0.8}Mn_{0.1}]O₂; and LiFePO₄, in LiPF₆ and LiBoB EC/DEC electrolytes, *Electrochem. Commun.*, Vol. 6, pp.39-43.
- 4) Yoo, M., Frank, C.W., and Mori, S. (2003): Interaction of Poly(vinylidene fluoride) with Graphite Particles. 1. Surface Morphology of a Composite Film and Its Relation to Processing Parameters, *Chem. Mater.*, Vol. 15, pp.850-861.
- 5) Paik, U., Lee, S., and Hackley, V. A. (2003): Influence of barium dissolution on the electrokinetic properties of colloidal BaTiO₃ in an aqueous medium, *J. Am. Ceram. Soc.*, Vol. 86, pp.1662-1668.
- 6) Lee, S., Paik, U., Hackley, V.A., Jung, Y.G. and Yoon, K.J. (2004): Microstructure and permittivity of sintered BaTiO₃: influence of particle surface chemistry in an aqueous medium, *Mater. Research Bulletin*, Vol. 39, pp. 93-102.
- 7) Lee, J.-H., Lee, S., Paik, U. and Y.-M. Choi (2005): Aqueous processing of natural graphite particulates for lithium-ion battery anodes and their electrochemical performance, *J Power Sources*, Vol. 147, pp. 249-255.
- 8) Lee, J.-H., Kim, J.-S., Kim, Y. C., Zang, D. S. and Paik, U. (2008): Dispersion properties of aqueous-based LiFePO₄ pastes and their electrochemical performance for lithium batteries, *Ultramicroscopy*, Vol.108, pp.1256-1259.
- 9) Guerfi, A., Kaneko, M., Peticlerc, M., Mori, M. and Zaghbi, K. (2007): LiFePO₄ water-soluble binder electrode for Li-ion batteries, *J. Power Sources*, Vol. 163, pp. 1047-1052.
- 10) Porcher, W., Moreau, P., Lestriez, B., Jouanneau, S. and Guyomard, D. (2008) : Is LiFePO₄ Stable in Water?, *Electrochem. Solid-State Lett.*, Vol. 11, pp. A4-A8.
- 11) Yu, D. Y. W., Donoue, K., Kadohata, T., Murata, T.,

- Matsuta, S. and Fujitani, S. (2008): Impurities in LiFePO₄ and Their Influence on Material Characteristics, *J. Electrochem. Soc.*, Vol.155, pp.A526-A530.
- 12) Martin, J. F., Yamada, A., Kobayashi, G. Nishimura, S., Kanno, R., Guyomard, D., and Dupre, N. (2008): Air Exposure Effect on LiFePO₄, *Electrochem. Solid-State Lett.*, Vol. 11, pp.A12-A16.
- 13) Patey, T. J., Hintennach, A., Mantia, F.L. and Novak, P. (2009): Electrode engineering of nanoparticles for lithium-ion batteries – Role of dispersion technique, *J. Power Sources*, Vol. 189, pp.590-593.
- 14) Lee, J.H., Paik, U., Hackley, V.A., and Choi, Y.M. (2006): Effect of poly (acrylic acid) on adhesion strength and electrochemical performance of natural graphite negative electrode for lithium-ion batteries, *J. Power Sources*, Vol. 161, pp. 612-616.
- 15) Paik, U., Hackley, V.A., Lee, H.-W. (1999): Dispersant –Binder Interactions in Aqueous Silicon Nitride Suspensions, *J. Am. Ceram. Soc.*, Vol. 82, pp.833-840.
- 16) Lee, J.H., Paik, U., Hackley, V.A., and Choi, Y.M. (2005): Effect of Carboxymethyl Cellulose on Aqueous Processing of Natural Graphite Negative Electrodes and their Electrochemical Performance for Lithium Batteries, *J. Electrochem. Soc.*, Vol. 159, pp. A1763-A1769.

Author's short biography



Ungyu Paik

Dr. Ungyu Paik is currently Distinguished Professor of the Division of *Materials Science Engineering*, and *Department of Energy Engineering* at Hanyang University, Korea. He is also Head of Research Center for Converging Technology in Advanced Gas Turbine System (ReCCoT) (sponsored by Korean Ministry of Knowledge and Economy) and Director of Global Research Laboratory for Nano Devices Processing Laboratory (sponsored by Korean Ministry of Education, Science & Technology). He acts as Technology counselor at Samsung SDI Corporate Research & Development Center and Hynix semiconductor. He received a Ph. D. degree from Department of Ceramic Engineering at Clemson University in 1991. His research interests are in control of the interparticle force of nano-ceramic particles and development of nano particle patterning technology. Newly expanded topics are focused on the next generation inorganic-organic hybrid electronics, dispersion stability of carbon nanotubes (CNTs), quantum dot in non-volatile memory, phosphor in plasma display panel (PDP), next generation photovoltaic devices (solar cell), and so on. He has published more than 150 technical papers in the scientific literature and hold 85 patents (including patent issues and applicants).



Jin-Hyon Lee

Mr. Jin-Hyon Lee is currently a Ph.D. candidate in the Division of Materials Science Engineering at Hanyang University. His research interests are focused on the design of dispersion system of carbon nanotube and active materials for the application of lithium ion battery positive/negative electrodes. He is also interested in the design of ink formulation for the application of ink-jet printed lithium ion battery.



Sung-Bok Wee

Mr. Sung-Bok Wee is a master course student in the Division of Materials Science Engineering at Hanyang University from 2008. His research interests are focused on the dispersion of active materials for the application of ink-jet printed lithium ion battery positive electrodes.

Author's short biography



Hyun-Ho Kim

Mr. Hyun-Ho Kim is a master course student in the Division of Materials Science Engineering at Hanyang University from 2008. His research interests are focused on the dispersion of active materials for the application of lithium ion battery positive electrodes. He is also interested in the synthesis of electrospun nanofiber for lithium ion battery electrode.

The 43rd Symposium on Powder Technology

The 43rd Symposium on Powder Technology was held on August 28, 2009 at Senri Hankyu Hotel in Osaka under the sponsorship of the Hosokawa Powder Technology Foundation and with the support of Hosokawa Micron Corporation. The symposium

was very successful as usual with the attendance of 160 including 36 academic people. The main subject was “Functionalization of Powder and Development of New Materials by Nanoparticle Technology”.

The 42th Symposium on Powder Technology

Subject: Nanoparticle Technology: New Development for Its Application and Commercialization

- | | |
|---|--|
| <ul style="list-style-type: none"> • Opening Address | <p>Prof. Jusuke Hidaka
(Doshisha Univ.)</p> |
| <p>Session 1 Chairperson: Prof. Jusuke Hidaka (Doshisha Univ.)</p> | |
| <ul style="list-style-type: none"> • Fundamentals of Ceramics Powder Forming Processes and Further Development for Novel Materials • Synthesis and Dispersion of Tailor-made Ceramic Nanocrystals | <p>Minoru Takahashi
(Nagoya Institute of Technology)</p> <p>Satoshi Ohara
(Osaka University)</p> |
| <p>Session 2 Chairperson: Prof. Yoshinobu Fukumori (Kobe Gakuin Univ.)</p> | |
| <ul style="list-style-type: none"> • Electrode structure and performance of Li-ion batteries • Creation of Boron Nitride Nanotubes and Possibility for a Series of novel nano-composite materials | <p>Yoshio Ukyo
(TOYOTA Central R&D Labs., Inc.)</p> <p>Hiroaki Kuwahara
(Teijin Limited)</p> |
| <p>Session 3 Chairperson: Prof. Makio Naito (Osaka Univ.)</p> | |
| <ul style="list-style-type: none"> • Improvement of “OISHISA” (Food Texture) by powder engineering • Nano particulate design and preparation for DDS & medical devices • Closing Address | <p>Yoshiki Yamazaki
(Taiyo Kagaku)</p> <p>Hiroyuki Tsujimoto
(Hosokawa Micron Corp.)</p> <p>Masuo Hosokawa
(Hosokawa Micron Corporation)</p> |



The 17th KONA Award

Dr. Minoru Takahashi, the executive director and vice president responsible for academic and evaluation affairs at Nagoya Institute of Technology (NIT), has been selected as the winner of the 17th KONA award. The award is sponsored by Hosokawa Powder Technology Foundation and given to the scientist(s) or group(s) who have achieved distinguished research work in the field of particle science and technology.

He received BS degree in 1973, MS degree in 1975 from mineral resources development engineering, and doctor of engineering in 1984 from the faculty of engineering in the University of Tokyo. He joined Ceramics Research Laboratory (CRL) in NIT as an assistant professor in 1975, and was promoted as a lecturer in 1986, an associate professor in 1987 and a professor in 1994. He took responsibility as the director of CRL from 2001 to 2002, and was appointed as the vice president of NIT in 2004 and has been in the current position since 2006. Prof. Takahashi has been elected as the new president of NIT. His term starts in April 2010.

For more than three decades, Dr. Takahashi has been engaged in the research of ceramics processing involving powder forming as the major subject at NIT, which is one of the excellent centers of ceramics researches in Japan. Excellent research achievements including a good number of lectures which Dr. Takahashi was invited to give at international conferences as well as scientific papers published in famous journals reveal that he is a world leading researcher in this area.

The style of his research is to find out the relationship between preparation of raw materials and forming characteristics both in experimental and theoretical approaches. His researches cover most of industrial forming processes such as die-pressing, extrusion, injection molding, slip casting and tape casting. In addition to the conventional forming methods, he tried the gel casting as a new forming method. He also developed a novel characterization method for a direct observation of particle dispersion structure in the slurry. The principle of this method is just to observe a thin slice of gelled slurry on an optical microscopy.

In recent years, Dr Takahashi has developed novel materials and new powder synthesis processes. For one example, electrical conductive ceramics have been successfully fabricated by combination of inert sintering and gel casting, converting polymer network in a gelled body to nano-carbon network. The conductivity could be controlled in a wide range depending on sintering atmosphere and temperature. Also he has developed unique and simple process called "bubble template" to synthesize hollow CaCO_3 particles. The hollow particles could be precipitated by reaction of CO_2 bubbles with a CaCl_2 solution.

Based upon Dr Takahashi's research achievements briefly described here, he was nominated as a candidate and finally selected as the winner of the 17th KONA award. On January 29, 2009, Mr. Masuo Hosokawa, President of the Foundation, handed the 17th KONA Award to Dr. Takahashi at the presentation ceremony held at Hosokawa Micron Corporation in Hirakata.



GENERAL INFORMATION

HISTORY OF THE JOURNAL

In the history of KONA Powder and Particle Journal, two organizations have been playing an important role. The one is the Council of Powder Technology, Japan (CPT) and the other is the Hosokawa Powder Technology Foundation (Hosokawa Foundation). The CPT was established in 1969 by Hosokawa Micron Corporation as a non-profit organization to enhance the activities of research and development on powder science and technology. The Hosokawa Foundation was established in 1991 as a public-service corporation approved by the Ministry of Education, Culture, Sport, Science and Technology of Japan. The issues from No.1 (1983) to No.12 (1994) of KONA were published by CPT and the issues from No.13 (1995) by the Hosokawa Foundation.

The aim of KONA in the early days was to introduce excellent Japanese papers to the world and thus KONA consisted of papers recommended by some Japanese academic societies and translated from Japanese to English. From the issue of No.8, the CPT changed its editorial policy to internationalize the KONA and to incorporate papers by authors throughout the world in addition to translated papers. In response to this change, three editorial blocks have been organized in the world; Asian-Oceania, American and European. The policy and system have not changed even after the Hosokawa Foundation has taken over from the CPT. From the issue of No.27(2009), publication of translated papers has been terminated and only original papers have been published. The CPT is active still today and collaborates with the Hosokawa Foundation.

AIMS AND SCOPE

KONA publishes papers in a broad field of powder science and technology, ranging from fundamental principles to practical applications. The papers describing technological experiences and critical reviews of existing knowledge in special areas are also welcome.

The submitted papers are published only when they are judged by the Editor to contribute to the progress of powder science and technology, and approved by any of the three Editorial Committees. The paper submitted to the Editorial Secretariat should not have been previously published except .

CATEGORY OF PAPERS

- Invited papers
Original research and review papers invited by the KONA Editorial Committees.
- Contributed papers
Original research and review papers submitted to the KONA Editorial Committees, and refereed by the Editors.

SUBMISSION OF PAPERS

Papers should be sent to each KONA Editorial Secretariat.

- Asia/Oceania Editorial Secretariat
Mr. T. Kawamura
Hosokawa Powder Technology Foundation
Shodai-Tajika,1-9, Hirakata, 573-1132 Japan
- Europe/Africa Editorial Secretariat
Dr. J. Stein or Mrs. P. Krubeck
Hosokawa Micron
Division of Hosokawa Alpine AG.
Welsersstr. 9-11, 51149 Koeln, GERMANY
- Americas Editorial Secretariat
Dr. C.C. Huang
Hosokawa Micron Powder Systems
10 Chatham Road, Summit NJ 07901 USA

Publication in KONA Powder and Particle Journal is free of charge.

PUBLICATION SCHEDULE

KONA is published annually. The publication date is December 25th.

SUBSCRIPTION

KONA Powder and Particle Journal is distributed free of charge to senior researchers at universities and laboratories as well as to institutions and libraries in the field throughout the world. The publisher is always glad to consider the addition of names of those who want to obtain this journal regularly to the mailing list. Distribution of KONA is made by each Secretariat.

Free electronic publication of KONA Powder and Particle Journal is available in
<http://www.kona.or.jp>

INSTRUCTIONS TO AUTHORS

(1) Manuscript format

- Electric files should be submitted to the Editorial Secretariat by online. Authors' short biography and photograph should be attached to the final version.
- The structure of manuscripts should follow the following order; title, authors, affiliations, abstract, keywords, main text, (acknowledgement), (appendix), (nomenclature), references. The items with parentheses are not mandatory. The text should be in single-column format. Figures and tables can be imported into the main text. If figures and table are collated in a separate section at the end of the article, indicate their approximate locations directly in the text. If symbols are defined in a nomenclature section, symbols and units should be listed in alphabetical order with their definition and dimensions in SI units. If symbols are not defined in a nomenclature section, they should be defined in the text.
- Full postal addresses must be given for all the authors. Indicate the corresponding author by the mark "*" after the name. Telephone and fax numbers and e-mail address should be provided for the corresponding author.
- Abstract should not exceed 200 words.
- The appropriate number of keywords is 5 or 6.
- Symbols and units should be listed in alphabetical order with their definition and dimensions in SI units.
- Concerning references, either the numbering system or the alphabetical system should be adopted. In the numbering system, references should be numbered in sequence starting at the beginning of the paper. References should be given in the following form:
 - 1) Carslaw, H. C. and Jaeger, J. C. (1960): "Conduction of Heat in Solids" , 2nd ed., Clarendon Press, Oxford, England.
 - 2) Howell, P. A. (1963): US Patent, 3, 334,603
 - 3) Jia, R. (1990): "Surface Properties of Coal and Their Role in Fine Coal Processing," Ph.D. Dissertation, University of California at Berkeley.
 - 4) Zhang, N. and Rosato, A. D. (2006): Experiments and Simulations on Vibration Induced Densification of Bulk Solids, KONA Powder and Particle Journal, No.24, pp.93-103.In the alphabetical system, all publications cited in the text should be presented in alphabetical order of the authors. In the text make references by name and year, e.g. Zhang and Rosato (2006). Reference to papers with more than 3 authors should show the name of the first author followed by "et al."

(2) Reprint

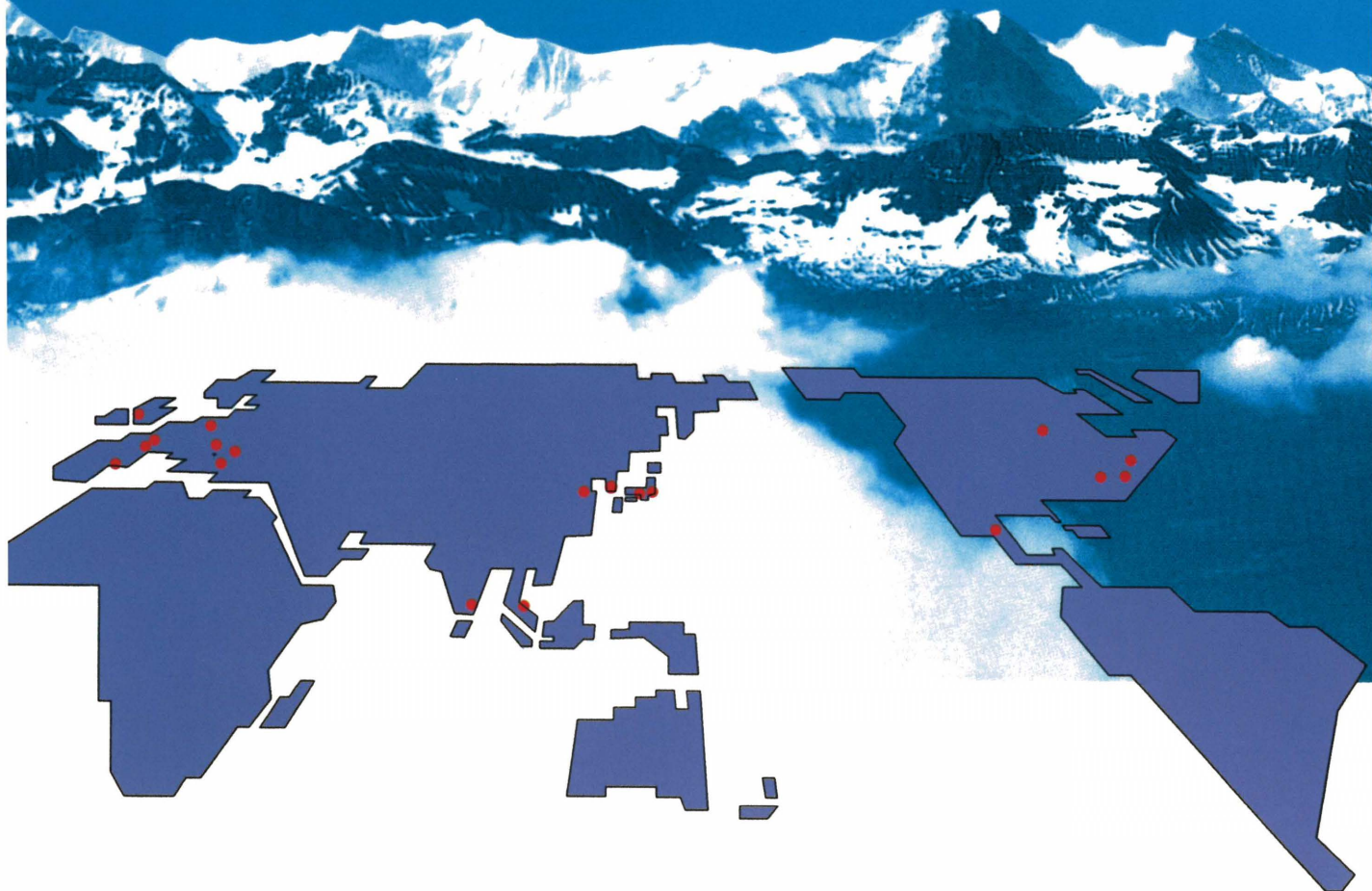
- The authors shall receive 50 free reprints. Additional reprints will be furnished when ordered with return of galley proof.

(3) Copyright and permission

- Original papers submitted for publication become immediately the property of the Hosokawa Powder Technology Foundation and remain so unless withdrawn by the author prior to acceptance for publication or unless released by the Editor. The original papers in KONA should not be reproduced nor published in any form without the written permission of the Hosokawa Foundation. Authors are responsible for obtaining permission from the copyright holder to reproduce any figures and photos for which copyright exists.

HOSOKAWA MICRON

Hosokawa Micron Ltd. is a member of the Hosokawa Micron Group, responding to global needs through an emphasis on materials science and engineering. The Group is an international provider of equipment and Technology for powder and particle processing, product recovery, plastics processing and confectionery products. The Group maintains facilities for research, engineering, manufacturing, and service in each of the world's major industrial markets.



Process Technologies for Tomorrow



HOSOKAWA MICRON

Headquarter Locations;
HOSOKAWA MICRON CORPORATION

<http://www.hosokawamicron.co.jp>